Ocean waves in geosciences

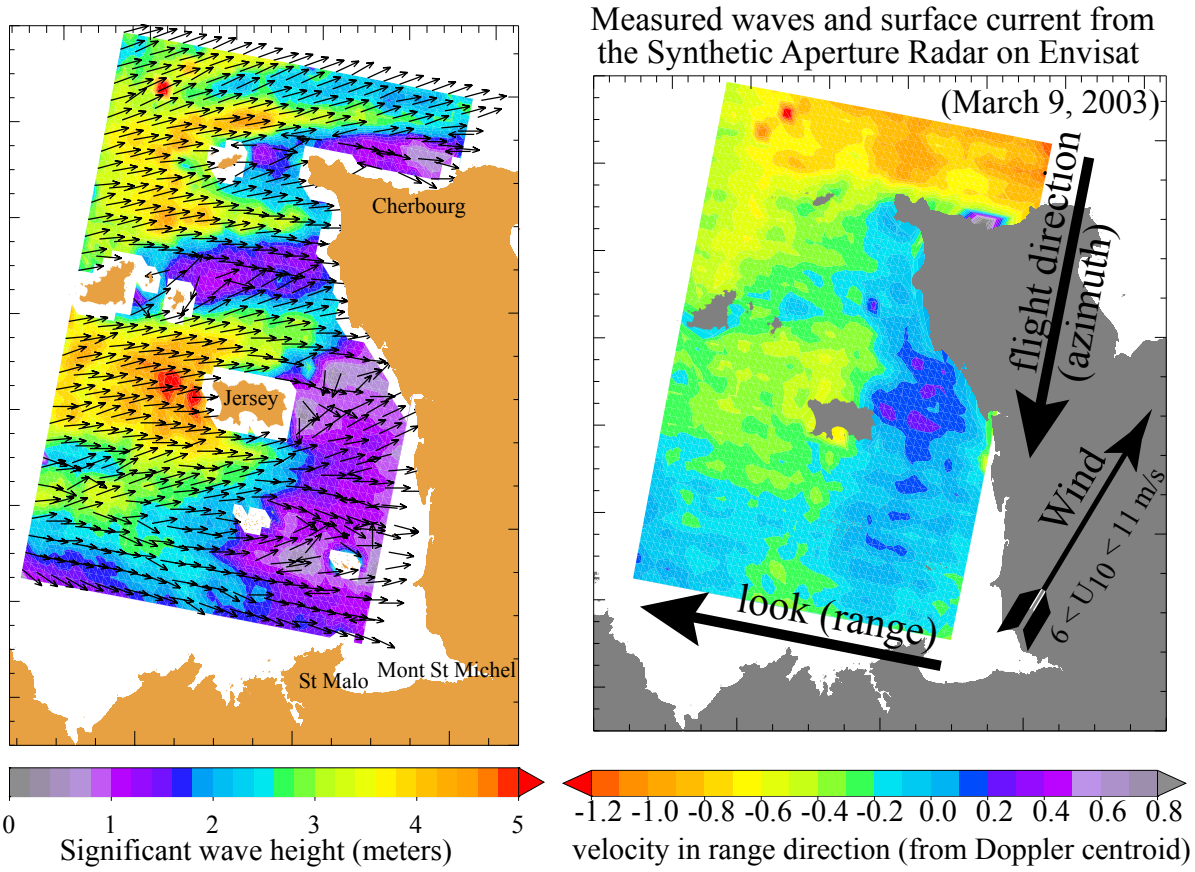

Fabrice Ardhuin,
Laboratoire d'Océanographie Physique et Spatiale, Brest, France
doi: 10.13140/RG.2.2.16019.78888/5 or 10.13140/RG.2.2.16019.78888/6 ...

January 18, 2021

Contents

Foreword

There are countless scholarly articles and books about ocean waves, with many different points of view, going from mathematical treatises to naval architecture. Among these we can single out the excellent textbooks by Kinsman (1965), Dean and Dalrymple (1991), and Holthuijsen (2007), the engineering manual from the U. S. Army Corps of Engineers (2002), and many excellent scientific monographs by Phillips (1977), Dingemans (1997), Young (1999), Lavrenov (2003), Janssen (2004), Lannes (2013) ...

So why another one?

First of all, scientific developments never stop, making these previous works not obsolete but less up to date and complete. This will happen with the present book, even if I am trying to update it on a regular basis. Second, and more important, all these books, except possibly the jewel by Phillips (1977) have a rather narrow scope, and do not cover aspects for which no monograph exist. I particularly think about microseisms or infragravity waves. Working with coastal engineers, geomorphologists and seismologists, has motivated me to bring to the forefront those results that are often obscure or very hard to follow. My point of view is that ocean waves play a very particular role in the Earth System, both as an important element of air-sea or land-ocean exchanges, and also as a deforming mirror that modifies our measurements of ocean properties using remote sensing and even in situ techniques. As a result, much insight and cross-fertilization can come from the integration of many geoscientifc fields, from microseisms to remote sensing, as well as applied disciplines such as marine meteorology or coastal and ocean engineering. At the very least, these different disciplines are providing new data and different points of view that complement each other in constraining our physical understanding of wave processes, and the parameterizations used in numerical models or remote sensing algorithms.

On these topics, I have tried to be clear without compromising the accuracy of the results, but this is a very difficult balance. If you find it unclear, do not hesitate to contact me and I will try again to clarify in the next revision.

I shall finish with a final warning: my selection of topics is clearly biased to my own tastes and interests, which are clearly favouring geosciences versus engineering. It does not mean that the topics ignored here are not important. For example, a good discussion of extreme waves and sea state analysis would be much more useful for all engineers than our development on three-dimensional wave-current interactions. For this you may go to section 4.3 of Holthuijsen (2007). This is my particular choice, and I hope that the present book will be a good combination of useful and interesting topics.

The document is organized in three parts, one relevant to waves in deep water, another providing additional information on coastal and shallow water aspects, and a third part that goes into some details that are probably not relevant for most readers. This book is designed to make it easier to read in electronic form, including hypertext links within the document and towards outside sources, such as the cited references.

This document, or part of it, is designed as a teaching material for the wave-related Master courses at University of Brest and ENSTA-Paris Tech. Because the present document is trying to follow the latest advances in research – and my imperfect understanding of these. The permanent evolution unfortunately leads to the presence of errors, more so in the last chapters. I thank Nicolas Rascle, Nadine Paugam, Clément Gandon, Nobuhiro Suzuki and Sophia Brumer for many corrections, Jean-François Filipot for contributions and help in translating chapter 3, and Philippe Bonneton for discussions and help on the structure and contents of chapter 13. This version It is still not finished and some (old) parts in chapter 15-24 and following are still in French and will be translated in the coming months. I thank you in advance for finding any dubious or strange contents, or broken links.

Part I

Waves in deep water

Chapter 1

Introduction

1.1 Waves in geosciences

From the ripples on a water puddle to large breaking waves on the beach, we have all seen waves. They can be familiar or threatening, possibly deadly for seasoned fishermen or yachtsmen (e. g. Pierson, 1972; Greenslade, 2001). Waves can exert huge forces: just try to stand up in the surf, in front of a two-meter tall wave that breaks. And two meters is a far cry from the maximum recorded wave height at sea, towering 32 m above the following crest (Liu et al., 2008). The most severe *sea state*, estimated from satellite radar altimetry, had a significant wave height of 20.1 m (Hanafin et al., 2012), which, as we shall see in this chapter, means that some wave heights probably exceeded 35 m.

Knowing and predicting the properties of waves is necessary for sea-going operations, the design of any marine structure such as a jetty, an offshore platform or a ship. Waves modify the fluxes of momentum between the ocean and atmosphere and thus influence more or less directly the oceanic and atmospheric circulation. Waves are also an important agent in the pick-up and transport of sediments, and the main source of background seismic motions.

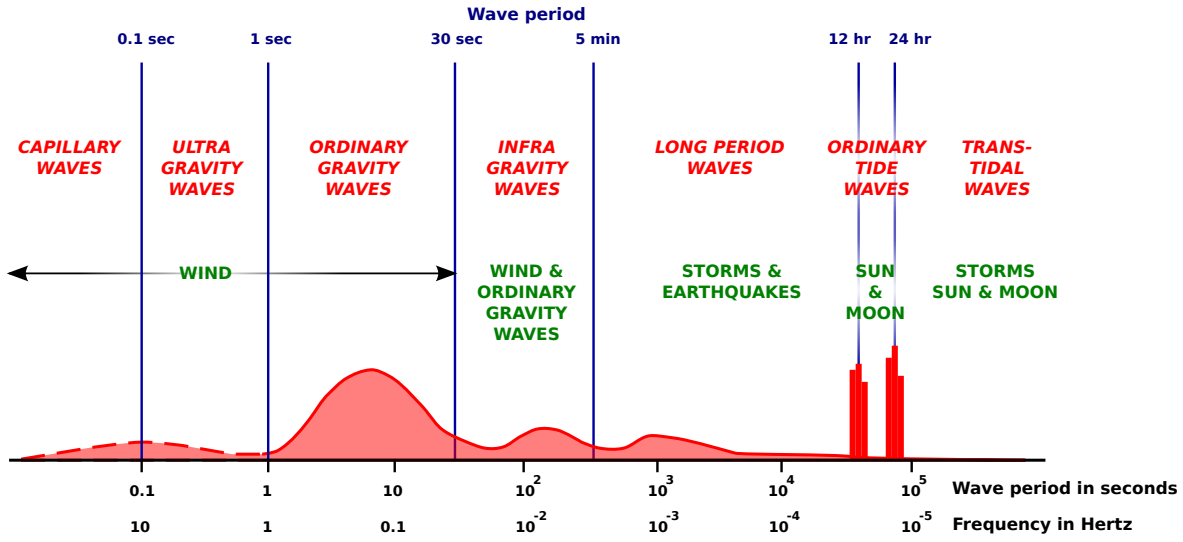

Figure 1.1: Classification of the spectrum of ocean waves according to wave periods. Adapted from Munk (1950).

To be more precise, we need now to introduce some classification of the different wave motions. A simple classification, as proposed by Munk (1950) and shown in figure 1.1, is based on the typical time scales of between the passing of two crests, which we shall call the period T, even though the motion does not repeat itself exactly and is not mathematically speaking periodic. As a result our periods T can be random numbers. This period classification is closely related to a physical classification that distinguishes between the different generation processes for these wave. Indeed, like any wave phenomenon, our waves can be defined by their

- **generation**,
- **propagation**
- and **dissipation**.

The goal of the present book is to describe and make understandable these three aspects, both qualitatively and quantitatively. This quantitative understanding allows an accurate forecast of local wave statistical properties, which we will call the sea state, as well as fluxes of energy and momentum between the atmosphere, ocean and solid Earth.

In this book, we will restrict ourselves to waves which are more or less directly generated by the wind, leaving out tsunamis. But before leaving them out, let's say a few words about tsunamis. Tsunami propagation and dissipation properties are the same as the wind-waves described here, but whats sets them apart from wind-waves is their very large wavelength, which cannot be generated by wind in the same way as the usual wind-waves. Hence their generation mechanisms are specific, namely earthquakes, landslides, and meteorite impacts, which are all important but rare events, leading to very different statistical properties compared to the waves continuously generated by the wind. Another slightly more common source of meteo-tsunamis are abrupt changes in wind properties. All these generation events are transient, and typically cause a depression or bump of the sea surface that appears very fast but on a very large scale. This depression or bump then radiates a train of waves, with a period of the order of 10 minutes that is given by the size of the initial surface perturbation. These waves are strongly amplified in shallow water. The first perturbation to arrive on land can be a trough. If you see the sea retreating rapidly, this is it ... do not rush out to pick up crabs, but instead run to high ground, as a big crest will likely follow and flood what was the dry land.

Instead of these transient wave trains, wind-generated waves are incessant and irregular. The time between the passing of two crests, which we define as the period T, is typically less than 30 s. This limit is related to wind speeds, as explained in chapter 5. These wind-waves also give rise to infra-gravity waves of periods 10 s to 10 minutes. For all these motions the average distance between two crests, which we shall call the mean wavelength L_m, increases with the mean period T_m. This wavelength goes from a few centimeters to about a kilometer. For wave shorter than a few centimeters, the effect of surface tension must be taken into account, and these short waves are called gravity-capillary waves.

Indeed, the **propagation** properties of waves is related to which of gravity or surface tension is the main restoring force that keep the water oscillating after an initial disturbance by a generating force. Gravity fights against surface slopes, setting up a pressure gradient that tends to reduce the sea level slope and is the main force for large wavelengths. Surface tension, instead, fights against surface curvature: it arises from the difference in thermodynamic properties of the interface between the two fluids, that are air and water. This difference gives an energy to their interface, which is proportional to the area of the interface: the more curved the surface the larger the energy, which is the equivalent of the gravitational potential energy. This force explains why water droplets are spherical, it is simply the geometry that minimizes the area (hence the energy) for a given volume. This surface tension also explains why short breaking waves are not energetic enough to generate bubbles and foam at the sea surface. The presence of a continuous layer of ice can also act like an elastic layer with an effect similar to surface tension. In this case even long waves can be influenced by the elasticity of the ice layer, this influence depends on the ice thickness (e.g. Squire et al., 1995).

Whether gravity or surface tension is the main restoring force, the work of these forces produces a motion with an associated kinetic energy. The oscillations of the air-sea interface are thus maintained by an exchange between potential and kinetic energy, until this energy is **dissipated**. Our waves are thus surface gravity waves, gravity-capillary or capillary waves for the shortest.

In the family of gravity waves, at the other extreme towards the large scales, the slow oscillations on time scales of several hours to several days are also influenced by the Coriolis force, caused by the rotation of the Earth, and the waves become inertial-gravity waves, also known as Kelvin and Poincaré waves. The main **generation** forces for these are the wind and the difference in the gravitational pull exerted by the Moon and Sun on the center and the surface of the Earth. Kelvin waves share many properties of gravity waves.

In practice, all these waves co-exist. Fortunately, it is often easy to sort them out and study them separately. Wind-waves and tides have very different periods and wavelengths, as illustrated by figure 1.2. There is no such clear separation between capillary and gravity waves, except at low wind speeds when there is clear gap in the wave spectrum around the wavelength of 1.7 cm. For waves longer than 20 cm, we will ignore the effect of the surface tension which will greatly simplify our calculations. However, surface

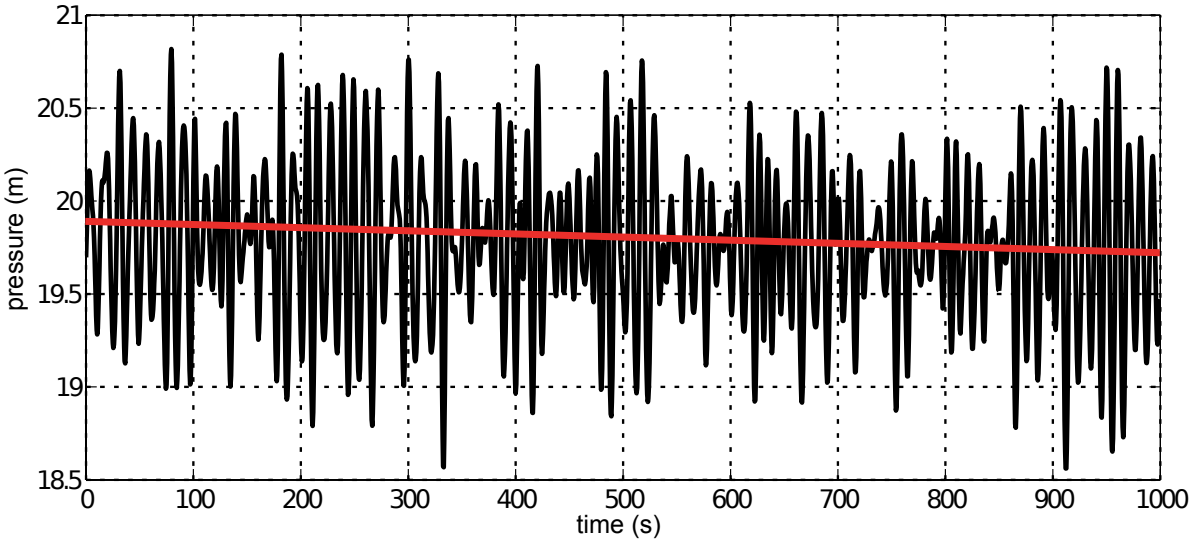

Figure 1.2: Example of the evolution of the bottom pressure in about 20 m of water in Bertheaume bay, France, on January 31, 2004.
The pressure in Pascals was converted here to an equivalent water height in meters by dividing the absolute pressure recorded by a Seabird 26 instrument, by the product $\rho_w g$ of water density $\rho_w \simeq 1026\text{kg/m}^3$, and gravity $g \simeq 9.81\text{m/s}^2$, after subtracting the atmospheric pressure recorded nearby, $p_a \simeq 10^5\text{Pa}$. The fast oscillation caused by a swell of significant wave height $H_s = 2.85$ m is superimposed on the tide that is gently falling, about 20 cm in 20 minutes, as shown by the red line.

tension should not be ignored in general, in particular when considering wave dissipation by breaking and the effects of small scale surface roughness, both important for radar and radiometric measurements of the ocean surface.

The **propagation** of waves is well known thanks to the works of Laplace, Poisson, Stokes, Airy, Rayleigh and Boussinesq in the 18th and 19th centuries, with later refinements. For a historical perspective, see Darrigol (2003) and Craik (2004). The questions of **generation** and **dissipation** are still very active research topics, with a fundamental problem posed by the multi-scale nature of real ocean waves: how short waves influence long waves and vice versa is very difficult to treat and measure. Because of the strong demand for results, successful forecasting methods have been developed on more or less empirical grounds. Modern wave forecasting started with swell forecasts for Morocco, in the 1920s (Gain, 1918; Montagne, 1922). This approach was generalized by Sverdrup and Munk (1947) who considered the full life cycle of waves, from generation by the wind to dissipation in the middle of the ocean and on beaches. This latter work was motivated by the planning of the allied amphibious operation Torch in Morocco in 1942, which led to a method later applied to Normandy and many Pacific islands. Their British colleagues, forming the W group at the admiralty, included Deacon, Darbyshire, Barber, Ursell and Longuet-Higgins who developed similar methods and introduced the spectral analysis of waves in 1945 (Ursell, 1999), paving the way for today's numerical wave models. The first numerical spectral wave model was developed by Gelci et al. (1957), the group that continued the Morocco wave forecasting effort in Casablanca.

Today, we can forecast with good confidence the main properties of the sea state and its consequences, including forces on a structure at sea, ship motions, working range of a radar... although the details of the generation and dissipation processes are not well known. This is a tribute to the flair of those who invented rules and equations to represent the complex and poorly known reality. However, given this empirical part, it is not surprising that the same models may not be accurate for secondary properties of the sea state, such as the distribution of the energy radiated in different directions or the statistics of short breaking waves.

Going against the long-term specialization and separation of geosciencies in many sub-disciplines, there has been a strong interest since the late 1990s in the interaction of waves with the atmosphere, ocean currents, turbulence, sediment motion, from the scale of the global ocean to the small scale of any particular beach. This is motivated by integrated approaches for climate projections or the understanding of sediment transport from sources to sinks. These efforts should be continued to properly understand

the interactions of waves and turbulence, and the multi-scale properties of the ocean surface. We hope that after reading the present book, that gives a broad view of what is known and tries to highlight what is still unclear, the reader will gather the courage to continue the exploration of ocean waves after Stokes, Boussinesq, Munk, Longuet-Higgins, Hasselmann, Zakharov, Katsaros, Phillips and many other less famous scientists who made today's knowledge possible.

Courage, though, may not be enough, and some tools will be needed to start for this journey, including a working knowledge of calculus and fluid mechanics.

The following books should be consulted for complements on different topics,

- Kinsman (1965) on general principles and wave measurements, in particular with arrays of sensors. Although a bit old, this book is very well written and easy to get into.
- Phillips (1977) for a comprehensive view, although not up to date, of upper ocean processes (waves, internal waves, turbulence ...)
- Mei (1989) for wave propagation, mass transport and wave-structure interactions
- Dean and Dalrymple (1991) gave a real textbook oriented towards engineering applications
- Komen et al. (1994) gives the fundamental – but not basic – concepts of numerical wave prediction in the open ocean, this is not an easy read
- Komar (1998) wrote a nice textbook for coastal geomorphology, an excellent starting point for those who do not have a strong physics background
- Young (1999) combined deep and shallow water waves, including also global wave climatology.
- the Coastal Engineering Manual (U. S. Army Corps of Engineers, 2002), replaced the Shore Protection Manual. This book is edited by the U.S. Army Corps of Engineers, the body in charge of shoreline defenses and management of ports and waterways. This combines general principles with empirical formulas for coastal engineering. This is freely available on the web.
- Janssen (2004) give the ECMWF perspective on wind and wave forecasting, with many theoretical details on wind-wave generation and nonlinear wave evolution.
- Holthuijsen (2007) A very well illustrated textbook centered on numerical wave modelling, specifically for coastal environments, although a bit weak on physical processes, such as bottom friction.

A lot of interesting material and teaching aids can be found on the web, from Tony Dalrymple's Java applets, to the UCAR Meted program targeted at meteorologists. A list of useful links will be proposed separately for each chapter.

Let us now beg the tides and currents to stop their flow, so that we may study waves quietly. We will see later, in chapters 7 and 16 how waves interact with other oceanic motions.

1.2 Wave motion: some observations

The random nature of ocean waves has long puzzled observers and made difficult all scientific investigations. Figure 1.2 gives a good example of a random sequence of high and low waves. Initially the forecasting of waves was formulated in terms of the highest wave. The notion of wave height distribution was only introduced after 1945, thanks to the development of wave recording devices, and the availability of computing power. Two types of methods have been developed to represent the random nature of the wave field. One of these is the spectral analysis, which will be heavily used in the following chapters. The other, is the wave-by-wave analysis, which we briefly describe here. More recent time-frequency analyses are a kind of hybrid of these two methods.

Both methods are very useful and have their own limitations. Spectral analyses is well suited for the wave forecasting, in particular at large scales, because it explicitly represents the dispersion of waves that have different periods. Spectral analysis decomposes the sea surface in elementary sinusoidal waves, it is thus very important to know the properties of these sinusoidal waves. This is the topic of chapter 2. However, some sort of wave-by-wave analysis must be use to investigate localized events associated to the finite amplitude of the waves, such as breaking, as discussed in section 5.3 and chapter 23.

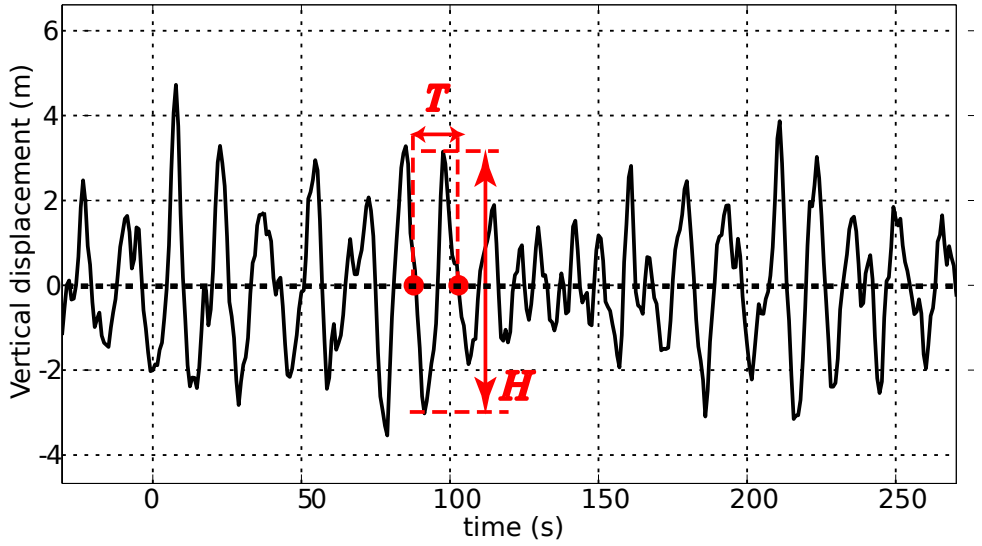

Figure 1.3: Principle of wave by wave analysis: a series of elevation records is broken in individual waves of duration T. The separation from one wave to the next is the zero down-crossing of the vertical displacement. This example was obtained from a Datawell Waverider buoy deployed offshore of Crozon, France, in May 2004.

1.3 Wave-by-wave analysis

1.3.1 Time series

Time series are the most common type of measurement these days, let us see what we can learn about waves from time series. We shall work with series of sea surface elevation, but we could have used any other physical quantity such as the velocity or pressure in the water or in the air.

We first define a single wave in time series by the time interval between two consecutive crossings of the mean sea level as the surface goes down. The choice of 'down' instead of 'up' is fairly arbitrary but it keeps the forward face of the wave, which is usually more interesting, within a single wave, whereas the rear face is split between two consecutive waves. For each wave we define a period T, which is the length of the time interval, and a height H, which is the difference between the maximum elevation (the crest) and the minimum elevation (the trough) during the perid.

From a sequence of heights, we can define a probability density function (PDF) dP as the limit, when dH goes to zero, of the probability P that a wave height is between H and $H + dH$, divided by dH. For a statistically stationary sea state, the surface elevation is well approximated by the sum of a large number of sine waves which are independent from one another. Applying the central limit theorem to this approximate model, we find that the surface elevation is a Gaussian process, with negative and positive anomalies around the mean sea level with statistics defined uniquely by the standard deviation of the sea surface elevation. As a result, and this was proven in the narrow frequency band limit by Rice (1944) and Cartwright and Longuet-Higgins (1956), the heights follow a Rayleigh distribution, as shown on figure 1.4,

$$dP(H) = \frac{2H}{H_{\rm rms}^2} \exp^{-H^2/H_{\rm rms}^2}. \tag{1.1}$$

This PDF is normalized to give $\int_0^\infty dP dH = 1$. The Rayleigh distribution is generally a good approximation for 98% of the distribution, sometimes even more. For extreme values, a better approximation was given by Tayfun (1980), taking into account the correlations among wave components due to second-order nonlinearities.

One useful result is that the probability that the height exceeds a given threshold $\widehat{H}$ is given by

$$P(H > \widehat{H}) = \mathrm{e}^{-\left(\widehat{H}/H_{\rm rms}\right)^2}. \tag{1.2}$$

This expression can be used to compute the height threshold $\widehat{H}$ associated to a fixed fraction of the wave population. For example $\widehat{H}_{1/3}$ is the height beyond which there are the highest 1/3 of the waves, and it is $\widehat{H}_{1/3} = (\ln(3))^{1/2}\, H_{\rm rms}$ which is nearly $1.05 \times H_{\rm rms}$.

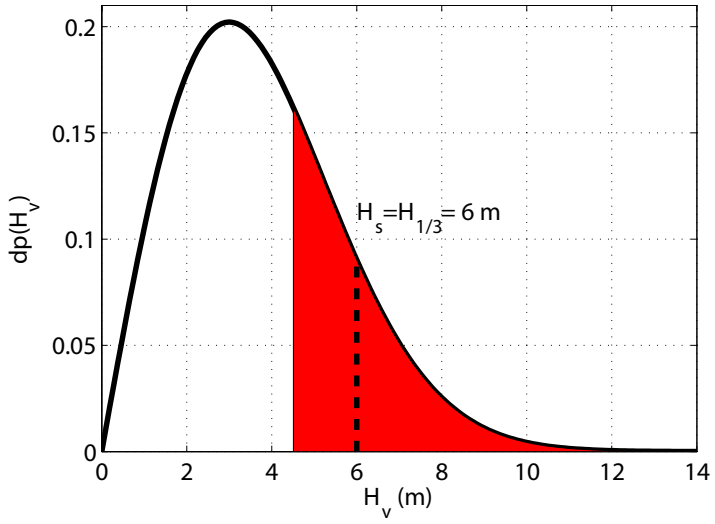

Figure 1.4: Rayleigh distribution of wave heights
$dp \times dH(H_v)$ is a probability for a single wave to have a height between H_v and $H_v + dH$. In red: the 1/3 of the highest waves in the distribution. The average height in this red part is $H_{1/3}$, which is one way to define the significant wave height H_s. In the following chapters we will rather define H_s as H_{m0}, equal to four times the standard deviation of the sea surface elevation. That other definition is recommended by the World Meteorological Organization and it gives a number very close to $H_{1/3}$.

A more widespread scale for the wave heights is given by integrating (1.2) to get the average height of the 1/3 highest waves. This is one definition of the significant wave height, denoted hautes $H_{1/3}$ or H_s. This scale roughly corresponds to the visual impression of wave heights, which was the most common source of measurements until the 1940s. More generally but still for a Rayleigh distribution, the average height of the $1/x$ fraction of the highest waves is,

$$\left[(-\ln(1/x))^{1/2} + \sqrt{\pi} \times \text{erfc}\left[(\ln(x))^{1/2}\right]/2\right] H_{\text{rms}} \tag{1.3}$$

where erfc is the complementary error function. For $x = 1/3$, this gives $H_{1/3} = 1.4157 \times H_{\text{rms}}$.

From the definition, the full Rayleigh PDF $p(H)$ is determined by H_{rms}. In practice the average $H_{1/3}$ is more commonly used, and there is also a lot of interest in the maximum height H_{max}, but that one depends on the length of the record. When recording more waves, H_{max} is likely to be higher. Waves that have a height H larger than $2.1H_{1/3}$ are called freak waves or rogue waves. If we follow the Rayleigh statistics, this correspond to 1 in 5700 waves. In practice, they are a bit more frequent for conditions with large average steepnesses, as predicted by Tayfun (1980). Also, for real waves the spectrum is not always narrow and on average $H_{1/3} \simeq 3.8m_0$ instead of $H_{1/3} \simeq 4.004m_0$, where m_0 is the standard deviation of the surface elevation (Goda, 1985).

In the context of the design of coastal or oceanic structures, there is a great interest in defining the maximum wave conditions that will occur over the expected lifetime of a structure, typically 50 to 100 years, or with a very low probability of occurrence to ensure maximum safety. For example, some sections of the Dutch dyke system are required by law to resist waves that occur only once in 10,000 years. The material and size of the structure is then designed to withstand these extreme conditions. If the extreme wave height and period is overestimated, the cost of construction is higher than it could have been. If the conditions are underestimated, the structure is likely to fail in a time shorter than the expected lifetime. This early failure happened for the first oil platforms built in the North Sea, in an age when there were no routine wave measurements.

For these extremes, the Rayleigh distribution does not hold, because the H_s is itself a random variable on the scale of days to centuries. The extreme wave statistics on these long time scales are determined by the distribution of extreme meteorological event, or, in shallow water, the joint distribution of water levels (including the astronomical tide) with weather events. These long term statistics are clearly different from the short term statistics. For short term, the sea state was a superposition of many independent wave trains, and we could use the central limit theorem. For long terms, we first need to determine the distribution of the significant wave heights H_s, and the probability that the height of a single wave

exceeds H_0 is then the conditional probability $p(H > H_0|H_s = H_{s0})$. The distribution of H_s follows a generalized Pareto distribution, and the probability $p(H > H_0)$ is given by integrating the conditional probability over H_{s0}.

Obviously, this requires stationary statistics. In some regions these statistics fluctuate with climatic patterns like the North Atlantic Oscillation, which particularly impacts the wave heights on the European Atlantic coast, or the El Nino-Southern Oscillation (ENSO) which has a strong impact on waves in the central Eastern Pacific or on the U.S. West coast (Bromirski et al., 2005). As an example, Edward Thornton, a renown specialist of nearshore dynamics, was asked in 1996 to provide some consulting advice for the construction of a wastewater pipeline in Monterey Bay, Central California. Construction started in 1997 in the middle of a very strong El Nino, the hundred-year wave height, which had been properly evaluated by Ed Thornton, was exceeded and the half-ton rocks protecting the pipe were too small to stay in place and were dispersed by the waves. For such a strong El Nino event, the storm waves that caused the damage on the U.S. West Coast were normal. One should thus use statistics with caution. Defining extreme wave heights is also very challenging in tropical areas where they are associated with hurricanes that have random tracks: a 20-year record of hurricane tracks generally does not contain all possible tracks, in particular the one of the next hurricane that will destroy this or that facility. Finally, there are also long-term trends associated with global change (e.g. Wang and Swail, 2004; Charles et al., 2012), especially in the Arctic where the trend in sea ice extent is leading to higher wave heights and periods (Stopa et al., 2016b).

1.3.2 Maps

Wave statistics from time series cannot represent all wave properties. Some of these, such as the length of crests, are defined from the spatial patterns in the wave field. This parameter, although secondary to the wave height, gives information on the spatial coherence of wave-induced motions and is thus very important when navigating a seaway or designing a structure that may be wider than the crest length.

Just like we have defined heights and periods, heights and lengths L can be defined in the case of waves propagating all in the same direction, say x. In that case, the crests are infinitely long in the other direction y. One important parameter is then the wave slope, defined from the ratio H/L. For sinusoidal waves, the maximum slope is $\pi H/L$.

Things get more complex when considering real waves that propagate in all directions. One can use the theory of random fields, developed by Adler (1981). In that theory, the crests are defined as subsets of the horizontal plane that are simply connected and that are above the mean sea level. Using this definition requires a bit of topology. In this context it becomes more difficult to associate a crest with a trough. There is a strong development of spatial statistics for ocean engineering and oceanography, thanks to the development of video measurement techniques (Fedele et al., 2009).

Chapter 2

Main properties of linear waves

This chapter explains how and why water moves in waves, once the waves have been generated. A more logical sequence might have been to study the generation process of the waves first, but it is much more complex and can only be understood once one knows how the waves move. The properties exposed in this chapter are thus common to all surface gravity waves, including tsunamis and wind waves.

In order to make things simple, we consider a flat, non-deformable bottom located at $z = -h$, and periodic waves in both space and time. This may sound very restrictive, but waves at sea generally behave as if the bottom were locally flat, and the periodicity allows us to study elementary waves that are later superimposed thanks to the quasi-linear wave motion, with some possible non-linear corrections to better fit the equations of motion. We will thus start with the linear wave theory of unidirectional and monochromatic waves that was first developed by Airy (1841), and which is a good approximation for waves of small height in not-too-shallow water. These are the typical conditions found in swells for depths larger than 50 m or so. Swells are the waves generated by winds in remote storms. It is also instructive for the oceanographer to play the game of differences, and find the common traits and main differences between these swells, and the tidal waves in shallow water that take the form of Kelvin waves. In fact, most of the wave properties derived here also apply to Kelvin waves. The main difference is the geostrophic balance along the crest of Kelvin waves that does not exist for shorter gravity waves for which the Coriolis force can be neglected for most properties.

We will try here not to get carried away by mathematics, which are necessary to arrive at quantitative predictions. Instead we will use the equations only as tools to help us reveal the wave motion in terms of forces, pressure and flow, which should help us navigate the many simplifying assumptions ot understand the role term.

2.1 Waves: a question of gravity, pressure, mass and vorticity

Before jumping into equations, we should make a few mechanical remarks. There is a motion in and above waves because the crests and troughs of the sea surface, located at $z = \zeta(x, y, t)$, correspond to different weights of water, which creates a pressure difference. We can already note that these pressure variations are of the order of $\rho_w g\zeta$, with ρ_w the water density and g the vertical apparent[1] acceleration of gravity. With a 1 m difference in height from crest to trough, we get a pressure difference of 10 kPa. What is important for the motion is the pressure *gradient*. With a wavelength of 200 m, this gives a crest-to-trough pressure gradient of the order of 100 Pa/m at the same level z, which drives a horizontal acceleration of 0.1 m/s^2.

The water set in motion must flow in an orderly way, following several principles. First, the mass of water is conserved, and for the slow velocities considered in this chapter, the flow is incompressible, hence non-divergent. We will also consider that the bottom does not deform under the waves. As a result, the horizontal convergence between a crest and the next trough must give rise to a vertical divergence. Besides, because the waves are generated by pressure forces, and propagated by pressure forces, the motion is, in a first approximation, irrotational. The vertical and horizontal velocities are thus strongly constrained by these two properties.

In summary, the free surface position ζ and gravity determine the near-surface pressure p, which gives the horizontal velocity u. The vertical velocity w is determined from the horizontal velocity using the

[1] Apparent means that this is not just Newton's general gravitation but it also includes the centrifuge acceleration due to the Earth rotation, giving $g \simeq 9.81\text{m s}^{-2}$.

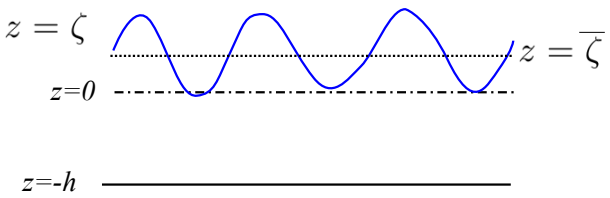

Figure 2.1: Definition of vertical levels: ζ is the sea level, $-h$ is the bottom, both defined relative to an arbitrary vertical datum $z = 0$. As a result the mean water depth is $D = h + \overline{\zeta}$.

zero divergence and vorticity conditions, and w also modifies the pressure field. We thus can express the problem of wave mechanics as a set of four equations for the four unknowns that are ζ, p, u and w.

2.2 Wave mathematics

We shall see that two important quantities, the wavelength L and period T are closely related for waves of small amplitude a. Here small, means that the slope ka and non-dimensional depth a/D are small, where $k = 2\pi/L$ is the wavenumber, and $D = h + \overline{\zeta}$, is the mean water depth. We remind the reader that $z = -h$ is the vertical position of the bottom, and $\overline{\zeta}$ is the mean sea surface elevation, both relative to an arbitrary datum $z = 0$.

These small parameters ka and a/D will appear repeatedly in this book. Their ratio gives a third parameter, which is independent of the wave amplitude, and that will be very important for the wave kinematics, this is the **non-dimensional depth** kD.

We will now go into the details of the linear wave theory, first laid out by Airy in the 19th century. It has the great advantages of being **linear**, hence any combination of the linear solution is also a solution of the equations of motion. More importantly, this linear model explains many of the waves properties, and is very accurate for swells in not-too-shallow water, and is not too far off for most wave properties, even for waves breaking in the surf zone.

Let us make two final remarks before we get into the equations. First, the linear waves exist only on paper, as all monochromatic waves are unstable, with a development of this instability that is faster for higher waves. This aspect is discussed in more details in chapters 5 and 18. Monochromatic waves are an acceptable solution for short evolution times, at least a few periods, possibly much more. Second, the choice of the Eulerian framework for the equations of motion is not a very good choice for the accuracy, as the linear Lagrangian theory is much more accurate than the Eulerian theory of Airy, because of the very simple balance between the pressure gradient and the fluid parcel acceleration. von Gerstner (1809) did find an exact theory that exactly satisfies the condition $p = p_a$ at the free surface, but it has an non-zero vorticity, which must be compensated by a sheared current. The use of Lagrangian equations is unfortunately more complex, and this is the main reason why we do not use it here. It is interesting to note, that mass conservation is linear in an Eulerian framework, while momentum conservation is non-linear, but the opposite is true for a Lagrangian framework.

2.3 Eulerian equations for wave motion

Our starting point is the conservation of mass and momentum applied to the ocean, with the former reduced to a zero divergence as we consider a constant density, which is true for the ocean within a few parts per thousand, and incompressible flow. The horizontal position is defined by the two-component vector $\mathbf{x} = (x, y)$ and the vertical is z. The corresponding velocities are $\mathbf{u} = (u, v)$ and w. Considering sea water as a perfect fluid, we apply the Navier-Stokes equations,

$$\frac{\partial \mathbf{u}}{\partial t} + \mathbf{u} \cdot \boldsymbol{\nabla} \mathbf{u} + w \frac{\partial \mathbf{u}}{\partial z} = -\frac{1}{\rho_w} \boldsymbol{\nabla} p + \nu \left(\nabla^2 \mathbf{u} + \frac{\partial^2 u}{\partial z^2} \right), \tag{2.1}$$

$$\frac{\partial w}{\partial t} + \mathbf{u} \cdot \boldsymbol{\nabla} w + w \frac{\partial w}{\partial z} = -g - \frac{1}{\rho_w} \frac{\partial p}{\partial z} + \nu \left(\nabla^2 w + \frac{\partial^2 w}{\partial z^2} \right), \tag{2.2}$$

$$\boldsymbol{\nabla} \cdot \mathbf{u} + \frac{\partial w}{\partial z} = 0, \tag{2.3}$$

where $\boldsymbol{\nabla}$ is the horizontal gradient operator. We thus have four scalar equations (2.1 has two horizontal components) for the four unknown that are u, v, w and p. Our problem will be well posed as soon as we define the boundary conditions, from the continuity of velocity and or stresses (pressure and shear stresses) and initial conditions. At the bottom, we only impose a free slip

$$w = -\mathbf{u} \cdot \boldsymbol{\nabla} h \quad \text{sur} \quad z = -h\left(\mathbf{x}\right) \tag{2.4}$$

which simplifies to $w = 0$ because we chose h to be constant

At the surface, we make the further hypothesis that for any horizontal position $\mathbf{x}$ there is only one value $z = \zeta$ of the free surface position (this excludes an overturning of the surface, as found in plunging breakers). The free surface is a material surface, which means that water parcels on the surface must stay on the surface. This can be expressed by the condition

$$\frac{\mathrm{d}}{dt}\left(z - \zeta\right) = w - \mathbf{u} \cdot \boldsymbol{\nabla}\zeta - \frac{\partial \zeta}{\partial t} = 0 \quad \text{at} \quad z = \zeta. \tag{2.5}$$

An interpretation of this surface kinematic boundary condition is that the vertical motion $\partial\zeta/\partial t$ is the combination of the vertical velocity w and the horizontal advection of the water parcels sliding along the surface $\mathbf{u} \cdot \boldsymbol{\nabla}\zeta$.

To that kinematic boundary condition we add the dynamic boundary condition that express the continuity of stresses at the air-sea interface. Neglecting the wind stress and surface tension, these reduce to a continuity of the pressure. In this chapter we will assume that the atmospheric pressure is takes the constant value p_a,

$$p = p_a \quad \text{at} \quad z = \zeta. \tag{2.6}$$

We now assume irrotational motion, so that the velocity field is given by the gradient of a velocity potential ϕ. Namely, $\mathbf{u} = \boldsymbol{\nabla}\phi$ and $w = \partial\phi/\partial z$. In this and all our notations, the classical operators (gradient $\boldsymbol{\nabla}$, Laplacian Δ ...) are restricted to the horizontal plane, in order to simplify notations. This assumption of irrotational wave motion is generally consistent with observations of real waves. Still, the vorticity can be very strong locally, for example in in the bottom and surface boundary layers or just after a wave has broken. Also, in the presence of sheared currents, the wave motion always has some vorticity, and a weak vorticity also arises from the Earth rotation. We finally start off by neglecting the viscous terms in the Navier-Stokes equations. This is justified by the fact that any significant wave-induced motion has scales of velocity U and length L that are large enough to make the Reynolds number UL/ν of the order of 10^4 or more.

All the assumptions made above remove some real features in the wave motion. Real waves always have some vorticity, which is also linked to the viscosity effects in the boundary layers. A rigorous treatment of these effects is possible and will be discussed in other chapters. We are here looking for the most simple solution that will capture most of the important properties of real waves.

Replacing velocities by gradients of ϕ in (2.1)–(2.2) one arrives at

$$\boldsymbol{\nabla}\left[\frac{\partial\phi}{\partial t} + \frac{1}{2}\left(\left|\boldsymbol{\nabla}\phi\right|^2 + \left(\frac{\partial\phi}{\partial z}\right)^2\right) + \frac{p}{\rho_w} + gz\right] = 0, \tag{2.7}$$

and

$$\frac{\partial}{\partial z}\left[\frac{\partial\phi}{\partial t} + \frac{1}{2}\left(\left|\boldsymbol{\nabla}\phi\right|^2 + \left(\frac{\partial\phi}{\partial z}\right)^2\right) + \frac{p}{\rho_w} + gz\right] = 0. \tag{2.8}$$

These two equations establish that the term in brackets is not a function of position and can only be a function of time $\gamma(t)$.

2.4 Small slope waves over a flat bottom: the Airy solution

So far, we had only assumed an incompressible flow (assumption A1), zero viscosity (A2), irrotational motion (A3), a flat bottom (A4).

We shall now linearize the equations, assuming that the wave amplitude is small enough to neglect the non-linear terms. This is verified in chapter 18, provided that a is much less than the wavelength L and a is much less than the mean water depth D.

This gives the linearized Bernoulli equation

$$\frac{\partial \phi}{\partial t} = -\frac{p}{\rho_w} - gz + \gamma(t), . \tag{2.9}$$

Assuming that waves are propagating [2] at a speed C, the motion is periodic as a function of $x - C(t)$ and thus $\gamma(t) = 0$. This gives the pressure as a function of the velocity potential,

$$p = -\rho_w g z - \rho_w \frac{\partial \phi}{\partial t}. \tag{2.10}$$

The Bernoulli equation states that the pressure is the hydrostatic pressure plus some correction due to the non-stationary motion. The static pressure term has been removed by the linearization.

The linearized kinematic boundary condition, which expresses the continuity of velocities, reads

$$w = \frac{\partial \phi}{\partial z} \simeq \frac{\partial \zeta}{\partial t} \quad \text{at} \quad z = \zeta, \tag{2.11}$$

which corresponds to a flat sea surface approximation. We can further approximate that the actual sea level is not too far from the mean sea level $z = \overline{\zeta}$.

The mass conservation equation was already linear,

$$\boldsymbol{\nabla} \cdot \mathbf{u} + \frac{\partial w}{\partial z} = 0 \tag{2.12}$$

and is equivalent to the Laplace equation for ϕ

$$\boldsymbol{\nabla} \cdot \mathbf{u} + \frac{\partial w}{\partial z} = \boldsymbol{\nabla}^2 \phi + \frac{\partial^2 \phi}{\partial z^2} = 0, \quad \text{at} \quad -h \leq z \leq \zeta. \tag{2.13}$$

Finally, the bottom kinematic boundary condition becomes,

$$w = \frac{\partial \phi}{\partial z} = 0 \quad \text{sur} \quad z = -h. \tag{2.14}$$

Taking ∂(2.9 at z=ζ)$/\partial t$ +$g\times$(2.11) we eliminate the unknown ζ, and obtain our wave equation

$$\frac{\partial^2 \phi}{\partial t^2} + g \frac{\partial \phi}{\partial z} = 0, \quad \text{at} \quad z = \overline{\zeta}. \tag{2.15}$$

Equations (2.14)–(2.15) are the bottom and top boundary conditions for Laplace's equation. The set of equation (2.13)–(2.15) is usually called the Euler equation. Its full non-linear form is given by (18.3).

2.4.1 Solution: Laplace equation and vertical profiles

Since we have a linear wave equation, it is natural to solve it using the Fourier transform that gives us a full basis of solutions. Without loss of generality, we thus look for solutions of the form,

$$\phi = \mathcal{R}\left(\widetilde{\phi}\,(z)\, \mathrm{e}^{\mathrm{i}\mathbf{k}\cdot\mathbf{x} - \sigma t}\right), \tag{2.16}$$

where $\mathcal{R}(a)$ is the real part of a. Replacing in Laplace's equation gives the Helmolz equation

$$-k^2 \widetilde{\phi} + \frac{\partial^2 \widetilde{\phi}}{\partial z^2} = 0. \tag{2.17}$$

Any solution is thus of the form

$$\widetilde{\phi}(z) = A \cosh(kz) + B \sinh(kz). \tag{2.18}$$

The bottom boundary condition imposes that $B = 0$, and we thus only keep the first term,

$$\widetilde{\phi}\,(z) = \Phi_0 \frac{\cosh(kz + kh)}{\cosh(kD)}. \tag{2.19}$$

Considering that the vertical velocity at the surface, where $z + h = D$, oscillates with a radian frequency σ to give a surface displacement amplitude a, we have

$$|\Phi_0| k \sinh(kD) / \cosh(kD) = \sigma a. \tag{2.20}$$

Hence, from Laplace's equation alone we get the orbital velocities. In particular, the amplitude of the horizontal velocity is, at the surface, $\sigma a / \tanh(kD)$.

[2] In the presence of standing waves, $\gamma(t)$ is an oscillating function of the order of ga^2/L, where a is the wave amplitude, first derived by Miche (1944a) and further considered by Longuet-Higgins (1950).

2.4.2 Solution: Momementum balance and dispersion relation

Replacing ϕ by (2.19) in the wave equation (2.15) gives the dispersion relation

$$-\sigma^2\Phi_0 + gk\tanh(kD)\,\Phi_0 = 0, \tag{2.21}$$

as given by de Laplace (1776),

$$\sigma^2 = gk\tanh(kD)\,. \tag{2.22}$$

This equation expresses the balance of forces between the horizontal pressure gradient which, just below the surface is is hydrostatic, with an amplitude $\rho_w gak$, and the horizontal acceleration, which has an amplitude $\sigma^2 a/\tanh(kD)$.

Hence waves have a lower phase speed $C = \sigma/k$ where D is reduced, for example near the shoreline. Contrary to a widespread misconception, this reduction of the phase speed has nothing to do with bottom friction. in fact the wave orbital velocity increases, and in the Airy theory there is no dissipation of energy.

2.4.3 Solution: polarization relations

Defining the phase of the free surface elevation,

$$\Theta = \mathbf{k}\cdot\mathbf{x} - \sigma t + \Theta_0, \tag{2.23}$$

with Θ_0 a constant between 0 et 2π, and the amplitude

$$a = \mathrm{i}\frac{\sigma}{g}\Phi_{\mathbf{k}}, \tag{2.24}$$

the elevation, velocities and pressure of the Airy (1841)[3] solution are given by the polarization relations

$$\zeta - \overline{\zeta} = a\cos\Theta, \tag{2.25}$$

$$\mathbf{u} = a\frac{\mathbf{k}}{k}\sigma\frac{\cosh(kz+kh)}{\sinh(kD)}\cos\Theta, \tag{2.26}$$

$$w = a\sigma\frac{\sinh(kz+kh)}{\sinh(kD)}\sin\Theta, \tag{2.27}$$

$$p = \overline{p}^H + \rho_w g a\frac{\cosh(kz+kh)}{\cosh(kD)}\cos\Theta, \tag{2.28}$$

where the hydrostatic pressure is $\overline{p}^H = -\rho_w g(z-\overline{\zeta}) + \overline{p}_a$ with p_a the atmospheric pressure. We also have

$$\phi = \frac{a}{k}\sigma\frac{\cosh(kz+kh)}{\sinh(kD)}\sin\Theta. \tag{2.29}$$

We obtain the displacements of water particles by integrating the velocity field in time. To a first order of approximation (at first order in $\varepsilon = ka$), we have the horizontal displacement

$$\widetilde{\xi}_h = -a\frac{\mathbf{k}}{k}\frac{\cosh(kz+kh)}{\sinh(kD)}\sin\Theta, \tag{2.30}$$

and the vertical displacement

$$\widetilde{\xi}_3 = a\frac{\sinh(kz+kh)}{\sinh(kD)}\cos\Theta. \tag{2.31}$$

Because of the wave propagation, the water parcels spend more time under the crest, where the horizontal velocity is larger, than under the trough, where the velocity is weaker. As a result there is a net, order ε^2 drift in the direction of propagation, even for linear waves. This is a Stokes drift - it is also called the wave (pseudo)-momentum. Like the energy and the wave action, the Stokes drift is an intrinsic quadratic property of the wave field. This aspect is discussed in more details in chapter 6.

[3] Although Laplace, Cauchy and Poisson gave all elements of this theory many years before Airy, the latter was the first to address the problem of a single propagating monochromatic wave train. Poisson solved several problems of greater complexity, including stationary waves and circular waves (Craik, 2004).

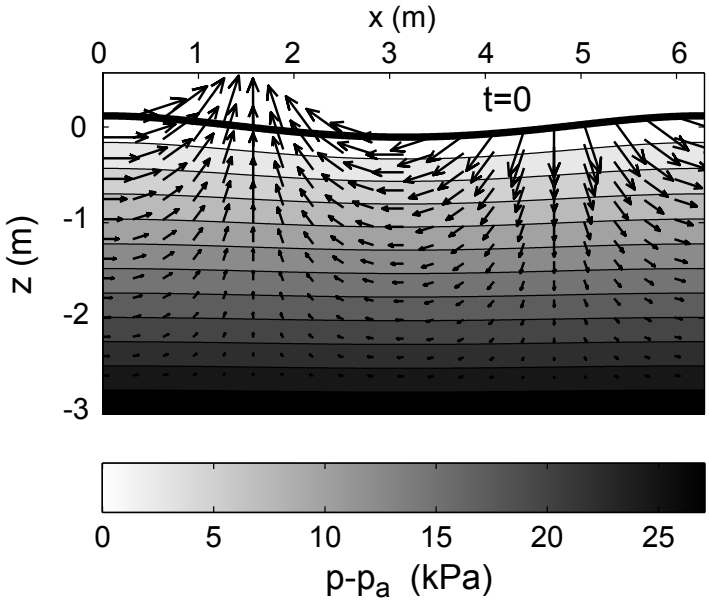

Figure 2.2: Pressure and velocity fields for a monochromatic wave of period $T = 2$ s in a mean water depth of $D = 3$ m.

Eq. (2.22)–(2.29) are all approximate solutions corresponding to the Airy waves. Stokes (1849) extended this Airy solution to take into account the non-linear terms of eq. (18.3), which improves the agreement with observations. In the deep ocean, all measurements confirm that waves are very nearly irrotational and well described by the theories of Airy and Stokes (see for example Thornton and Kraphol, 1974; Herbers et al., 1992). The general solution can be expressed as a series in powers of $\varepsilon_1 = ka$, which was shown to converge by Levi-Civita (1925). Many methods have been developed to obtain various numerical approximations of the exact solution (see §18.2).

2.4.4 Physical interpretation

The wave motion is maintained by the restoring force of gravity, which acts in quadrature to the velocity field, and thus always overshoots the equilibrium and creates crests where there were troughs. The acceleration induced by the pressure field feeds back into the pressure, and the motion *is not* hydrostatic. Near the surface, the pressure is nearly hydrostatic (figure 2.2). If the depth is large enough, at some level the vertical acceleration eventually cancels the pressure oscillations so that there is no significant motion at a depth much larger than the wavelength. This is typical of a surface wave, the motion decays exponentially from the surface, it is 'evanescent' or 'inhomogeneous'.

The flow is better understood by looking at the pressure p corrected for a hydrostatic pressure $p^H = p_a - \rho_w g(z - \overline{\zeta})$. This reveals a striking property, which is only true for $kD \gg 1$, the isobars of $p - p^H$ are also the streamlines. The streamfunction ψ is such that $u = \partial\psi/\partial z$, which gives

$$\psi = \frac{a}{k}\sigma \frac{\sinh(kz + kD)}{\sinh(kD)} \cos\Theta, \tag{2.32}$$

which is, for $kD \to \infty$ the pressure times $\rho_w g k$. This flow corresponds to a cyclostrophic equilibrium, with the pressure gradient balancing the centrifugal force of a water parcel turning around its circular orbit.

Wave motion has a maximum horizontal speed at the crest, in the direction of propagation. T Because of the Laplace equation, the motion decays away from the surface over a typical distance that is $1/k = L/2\pi$ when $kD >> 1$.

2.4.5 Kinematics: influence of the non-dimensional depth kD

The changes in kinematics and dispersion from deep to shallow water are related to the hyperbolic functions cosh, sinh and tanh, which are plotted in figure 2.5.

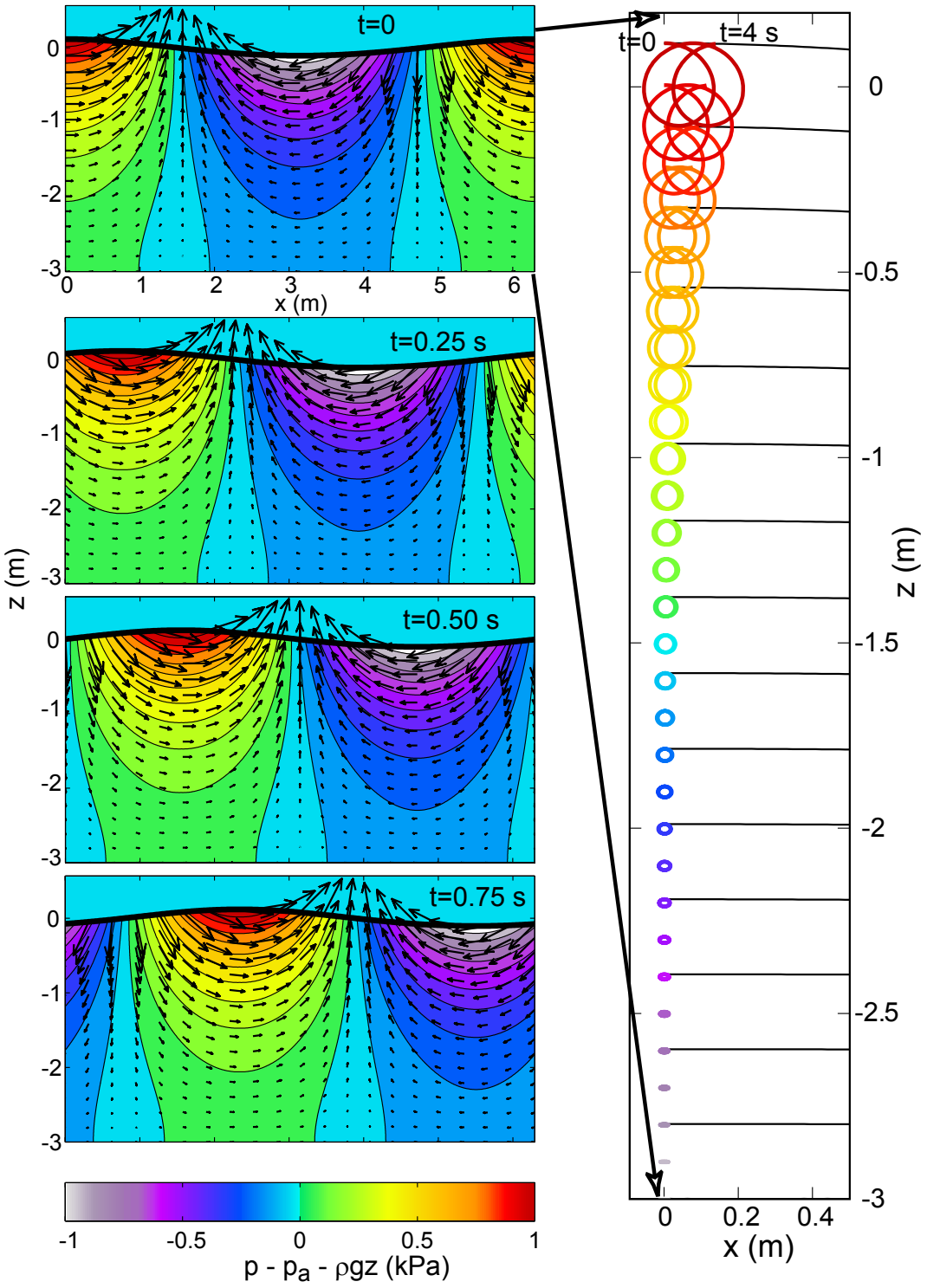

Figure 2.3: Left, in colors: pressure anomaly $p - p^H$ and velocities at different phases of the propagation of 2 s period wave in 3 m water depth, going from left to right. Right: trajectories of water particles.

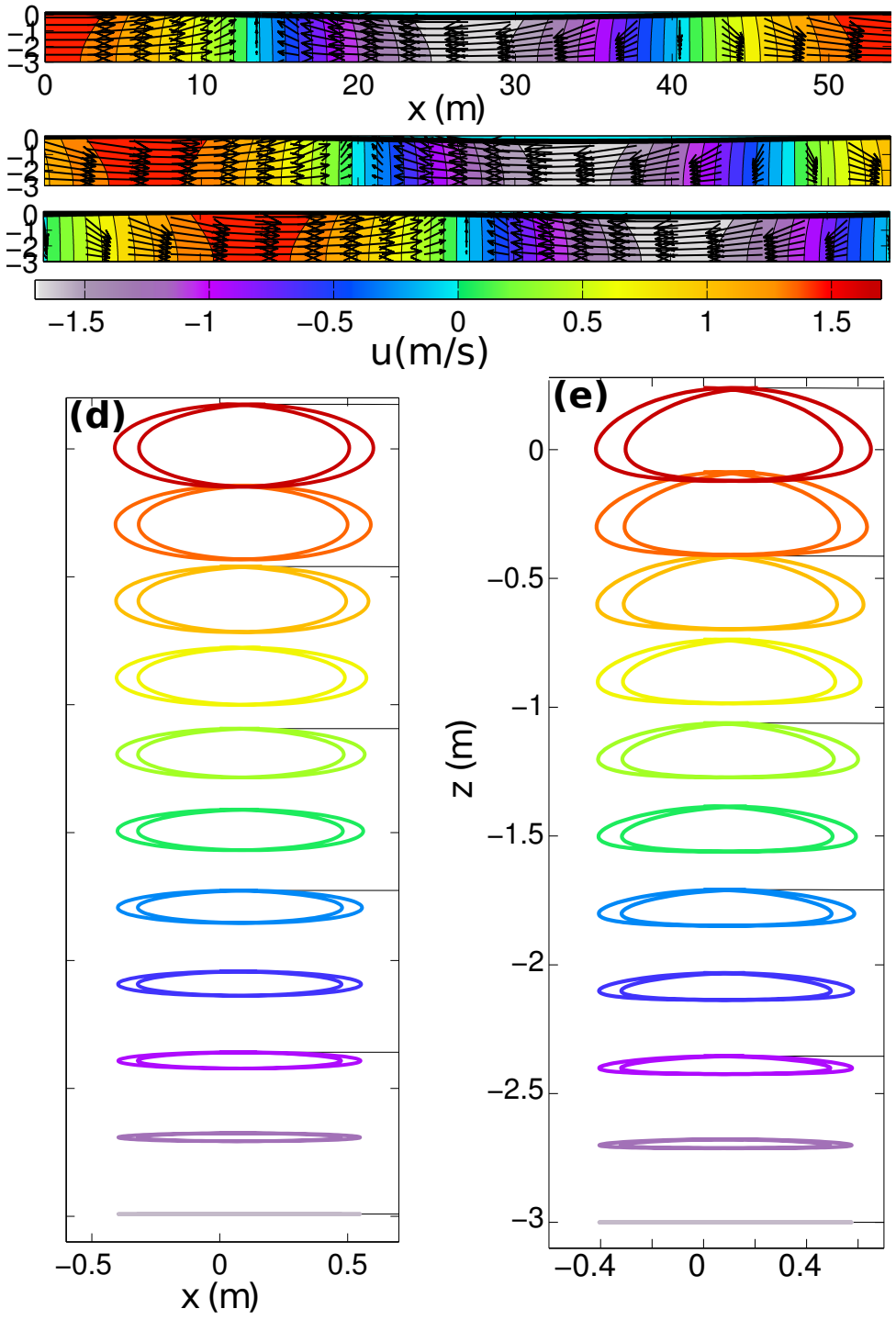

Figure 2.4: Velocity field in water for a wave train of period 10 s, and amplitude 18 cm in 3 m of water. Snapshots are shown for (a) $T = 0$, (b) 1.25 and (c) 2.5 s. The trajectories of water parcels are integrated over two Eulerian periods (20 s) for (d) linear waves, and (e) nonlinear waves with the same period and height, using streamfunction theory (see chapter 18). For the height chosen here, $H/D = 0.12$ and $H/L = 0.0067$, so that linear theory gives a fairly good approximation.

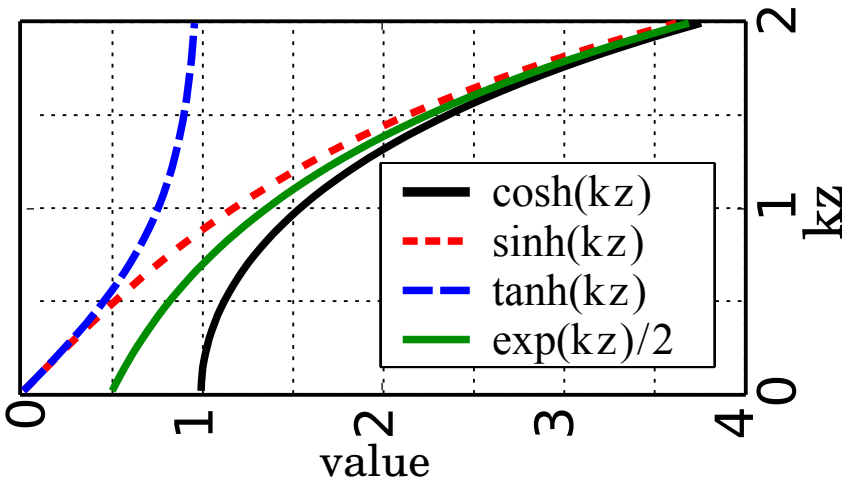

Figure 2.5: The main hyperbolic functions, used again and again in ocean wave theory.

Airy waves in deep water

A good number to remember is that, at a depth equal to half the wavelength, the motion amplitude is reduced by a factor $\exp(\pi) \simeq 25$ compared to the value at the surface. As a result, waves such that $D > L/2$ which corresponds to $kD > \pi$, are generally considered to be 'deep water waves'.

The dispersion relation becomes,

$$\sigma^2 \simeq gk, \tag{2.33}$$

the orbital velocities and pressures become

$$\mathbf{u} = a\mathbf{k}\frac{\sigma}{k}\mathrm{e}^{kz}\cos\Theta \tag{2.34}$$

$$w = a\sigma\mathrm{e}^{kz}\sin\Theta. \tag{2.35}$$

$$p = \overline{p}^H + \rho_w g a\mathrm{e}^{kz}\cos\Theta. \tag{2.36}$$

and displacements (2.30)-(2.31) are now

$$\widetilde{\xi}_h = -a\frac{\mathbf{k}}{k}\mathrm{e}^{kz}\sin\Theta, \tag{2.37}$$

$$\widetilde{\xi}_3 = a\mathrm{e}^{kz}\cos\Theta, \tag{2.38}$$

which is the parametric equation of a circle of radius $a\mathrm{e}^{kz}$. In first approximation, the water parcels follow circular orbits with diameters that vanish with deph.

Airy waves in intermediate water depth

For smaller water depths, the orbital velocity is significant near the bottom and the trajectories are now ellipses with horizontal major axis measuring $2a\cosh(kz+kh)/\sinh(kD)$, and a vertical minor axis $2a\sinh(kz+kh)/\sinh(kD)$ that shrinks from $2a$ at the surface, to zero at the bottom where the motion is back and forth along the bottom.

Airy waves in shallow water

For very shallow water (say $kD < 0.1$), the dispersion relation becomes

$$\sigma^2 = gDk^2, \tag{2.39}$$

and the velocities and pressure are

$$\mathbf{u} = a\mathbf{k}\frac{\sigma}{k\sinh(kD)}\cos\Theta \tag{2.40}$$

$$w = a\sigma\frac{(kz+kh)}{(kD)}\sin\Theta. \tag{2.41}$$

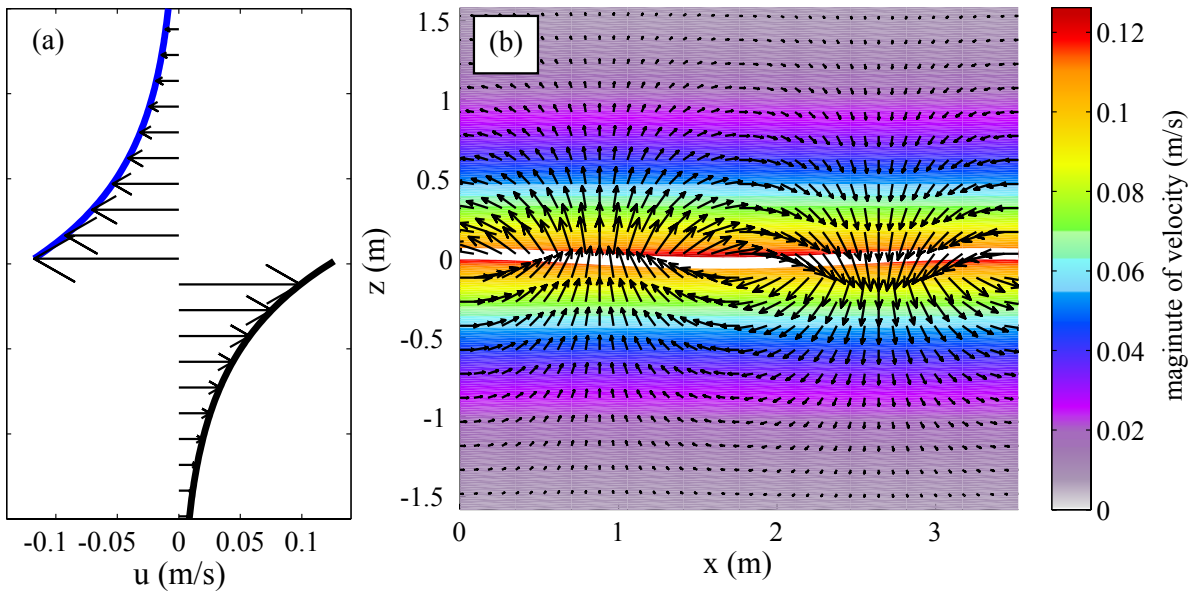

Figure 2.6: (a) Profile of the horizontal and vertical velocities on both sides of the sea surface at a wave crest ($x = 0$), and (b) velocity field, with the white line indicating the position of the free surface. These velocities correspond to waves of amplitude $a = 3$ cm, period $T = 1.5$ s, in $D = 3$ m water depth, which correspond to a wavelength $L = 3.5$ m, and a non-dimensional water depth $kD = 3.4$.

$$p = \overline{p}^H + \rho_w g a \cos\Theta = p^H. \tag{2.42}$$

This last expression states that the pressure is hydrostatic, just like in tidal waves. Tsunamis also nearly follow this shallow water limit.

The orbital displacement (2.30)-(2.31) are now

$$\widetilde{\xi}_h = -a \frac{\mathbf{k}}{k \sinh(kD)} \sin\Theta, \tag{2.43}$$

$$\widetilde{\xi}_3 = a \frac{(kz + kh)}{(kD)} \cos\Theta, \tag{2.44}$$

2.4.6 And in the air?

So far we have solved for the water motion. The same hypotheses of irrotational and incompressible flow will, in the air, produce the same equations and solutions. The only difference is that the bottom boundary condition is replaced by $\mathbf{u} \to 0$ as $z \to \infty$. The air motion over waves is thus similar to the water motion in deep water waves. The air pressure oscillates, with an amplitude that decays exponentially with elevation.

These results were confirmed by the measurements of Elliot (1972), who found a vertical decay that is slightly faster than e^{-kz}, due to the effect of the mean shear in the wind speed. When this shear is taken into account, the Laplace equation is replaced by the Orr-Sommerfeld equation, as detailed in chapter 22. Besides, the velocity jump at the air-sea interface, gives rise to a boundary layer that is laminar for low wave heights and wind speeds (Dore, 1978), but becomes turbulent otherwise (Perignon et al., 2014), probably leading to an important dissipation of long waves traveling across oceans that is discussed in chapter 22.

2.4.7 Dispersion

The velocity at which the wave crests or trough propagate is called the phase speed and is given by $C = \sigma/k$ which is also equal to the ratio L/T. Using the dispersion relation (2.22), we can eliminate σ

$$C = \frac{\sigma}{k} = \left[\frac{g}{k} \tanh(kD)\right]^{1/2}. \tag{2.45}$$

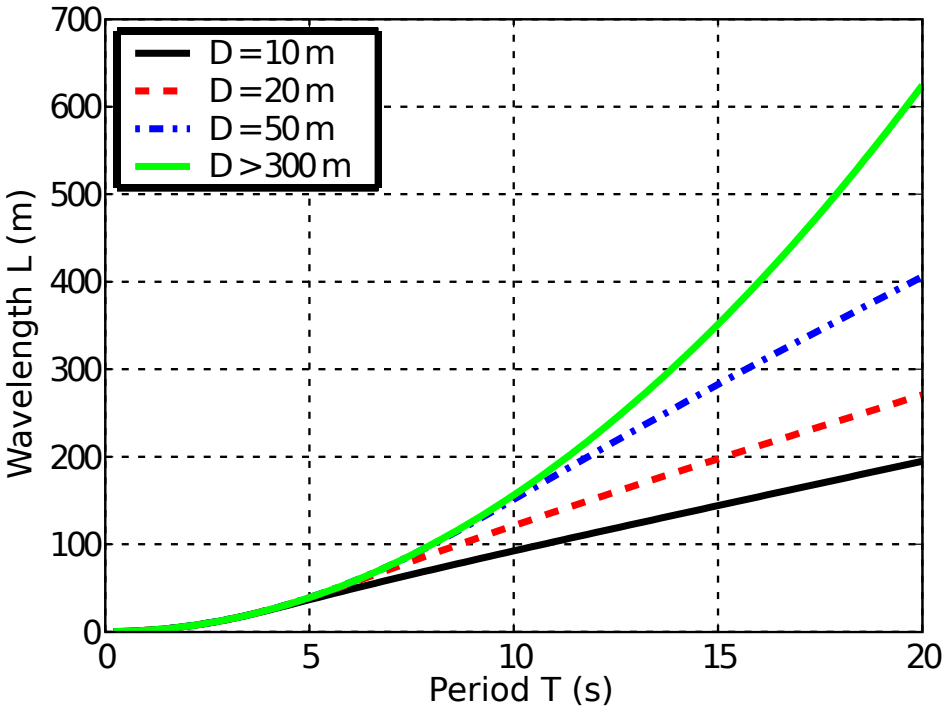

Figure 2.7: Wavelength as a function of the wave period and the water depth D, for linear waves in the absence of currents.

The phase speed is clearly a function of the wavelength, and thus waves are dispersive, meaning that wave packets that contain different components will spread over a larger space as they propagate, with the long waves traveling faster than the shorter waves. As a result, the waves arriving from a distant storm will always have a long period at the beginning and the average period will become shorter over time.

This dispersion property disappears in shallow water ($kD << 1$) where C goes to $(gD)^{1/2}$, independently of k. On figure 2.7, this gives a constant slope, for example for $D = 10$ m and $T > 5$ s).

We also note that, for a fixed period, the phase speed decreases with the water depth. This property is also true for a slowly varying water, in which case one can consider that the water depth is 'locally constant'. This variation of C is the cause of refraction (see chapters 7 and 12).

2.4.8 Energy

For any water particle, there is an oscillation of the kinetic and potential energies that are exchanged. Once integrated over the water depth and averaged over a wave period, that average is represented here by the overbar, the potential energy per unit horizontal surface is the vertical integral of the potential energy per unit volume $\rho_w g z$. In practice, we ignore the constant energy between the bottom and the mean sea level $\overline{\zeta}$, and we set our reference level such that $\overline{\zeta} = 0$,

$$\begin{aligned} E_p &= \overline{\int_0^{\zeta(\mathbf{x},t)} \rho_w g z \mathrm{d}z} = \rho_w g \overline{\frac{1}{2}(\zeta)^2} \\ &= \frac{1}{2}\rho_w g a^2 \overline{\cos^2(\mathbf{k}\cdot\mathbf{x} - \sigma t)} \\ &= \frac{1}{4}\rho_w g a^2. \end{aligned} \tag{2.46}$$

For the kinetic energy we integrate the kinetic energy per unit volume, $\left(|\mathbf{u}|^2 + w^2\right)$ to obtain a kinetic energy per unit horizontal surface,

$$\begin{aligned}
E_c &= \overline{\int_{-h}^{\zeta(\mathbf{x},t)} \frac{1}{2}\rho_w \left(|\mathbf{u}|^2 + w^2\right) \mathrm{d}z} \\
&\approx \frac{1}{2}\rho_w \left(\frac{agk}{\sigma \cosh(kD)}\right)^2 \left[\overline{\cos^2\Theta} \int_{-h}^{\overline{\zeta}} \cosh^2(kz+kh)\,\mathrm{d}z + \overline{\sin^2\Theta} \int_{-h}^{\overline{\zeta}} \sinh^2(kz+kh)\,\mathrm{d}z\right] \\
&\approx \frac{1}{4}\rho_w \left(\frac{agk}{\sigma \cosh(kD)}\right)^2 \int_{-h}^{\overline{\zeta}} \cosh(2kz+2kh)\,\mathrm{d}z \\
&\approx \frac{1}{4}\rho_w \left(\frac{agk}{\sigma \cosh(kD)}\right)^2 \frac{\sinh 2kD}{2k} \\
&\approx \frac{1}{4}\rho_w g a^2, \qquad (2.47)
\end{aligned}$$

$$E_t = E_c + E_p = \frac{1}{2}\rho_w g a^2 = \rho_w g E, \qquad (2.48)$$

where E is the variance of the sea surface elevation, here $E = a^2/2$. We have thus found that, to a first order of approximation, the average kinetic and potential energy E_c and E_p are equal.

Wave propagation is associated to a flux of energy. This flux of energy is transmitted by pressure forces from one water column to the next. This flux is the work of pressure forces given by eq. (2.28) with a velocity given by eq. (2.26). When integrated over the depth and averaged over a wave period, this gives the flux per unit crest length (i.e. per unit horizontal distance in the direction perpendicular to the propagation direction),

$$\begin{aligned}
W &= \overline{\int_{-h}^{\zeta} pu \mathrm{d}z} \\
&= \rho_w g a^2 \sigma \overline{\cos^2(\mathbf{k}\cdot\mathbf{x} - \sigma t)} \int_{-h}^{\zeta} \frac{\cosh^2(kz+kh)}{\sinh kD \cosh kD}\,\mathrm{d}z \\
&= E_t \frac{2\sigma}{\sinh(2kD)} \int_{-h}^{\overline{\zeta}} \frac{1}{2}\left[\cosh(2kz+2kh)+1\right]\mathrm{d}z \\
&= E_t \frac{2\sigma}{\sinh(2kD)} \left(\frac{\sinh 2kD}{4k} + \frac{D}{2}\right) \\
&= C_g E_t \qquad (2.49)
\end{aligned}$$

where

$$C_g = \frac{\sigma}{k}\left(\frac{1}{2} + \frac{kD}{\sinh 2kD}\right) = C\left(\frac{1}{2} + \frac{kD}{\sinh 2kD}\right). \qquad (2.50)$$

W is a flux of energy per unit distance and C_g the average speed at which the energy density E_t is radiated, which defines the group speed.

The full expression for the energy flux should also include the advective flux $u\left[\rho_w g z + 0.5\left(u^2+w^2\right)\right]$, but that part is negligible in the absence of currents.

This speed is called 'group speed' because it is indeed the speed at which a group of waves travels, because $C_g = \partial\sigma/\partial k$. Indeed, the superposition of two monochromatic waves of equal amplitude and similar frequencies gives a surface elevation

$$\zeta = a\cos\left[\left(k - \frac{1}{2}\Delta k\right)x - \left(\sigma - \frac{1}{2}\Delta\sigma\right)t\right] + a\cos\left[\left(k + \frac{1}{2}\Delta k\right)x - \left(\sigma + \frac{1}{2}\Delta\sigma\right)t\right], \qquad (2.51)$$

which writes

$$\zeta = 2a\cos(\Delta k x - \Delta\sigma t)\cos(kx - \sigma t). \qquad (2.52)$$

The first factor is the envelope of the group, with a length $2\pi/\Delta k$ and period $2\pi/\Delta\sigma$, that propagates at the speed $c' = \Delta\sigma/\Delta k$. This speed is, in the limit $\Delta k \to 0$, equal to $C_g = \partial\sigma/\partial k$. Two examples are shown in figure 2.9.

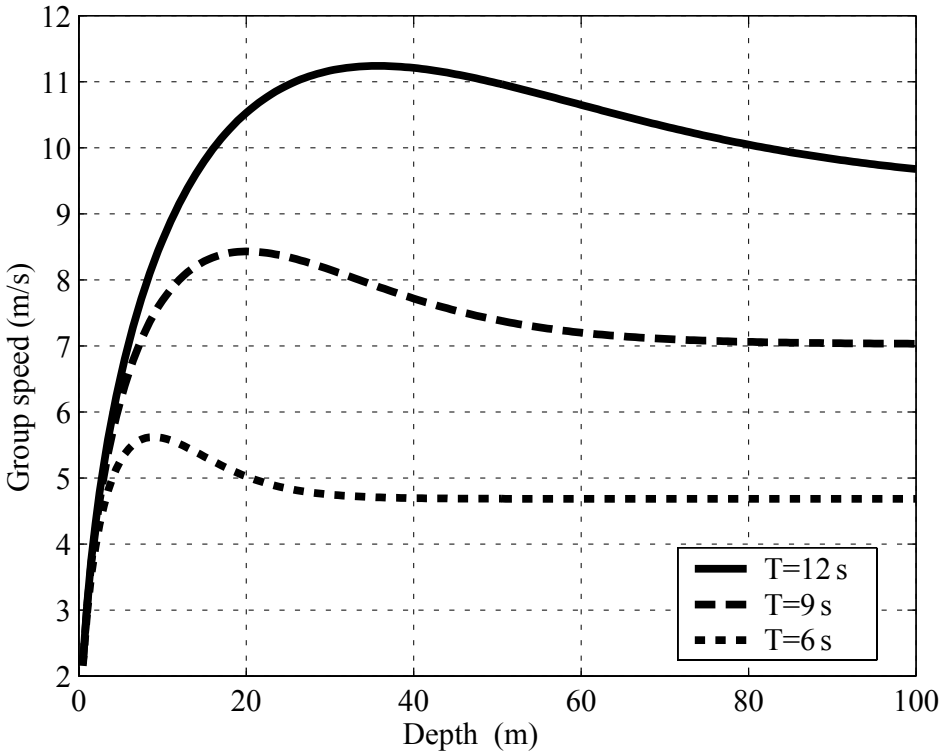

Figure 2.8: Group speed variation for linear waves with different periods, as a function of the water depth.

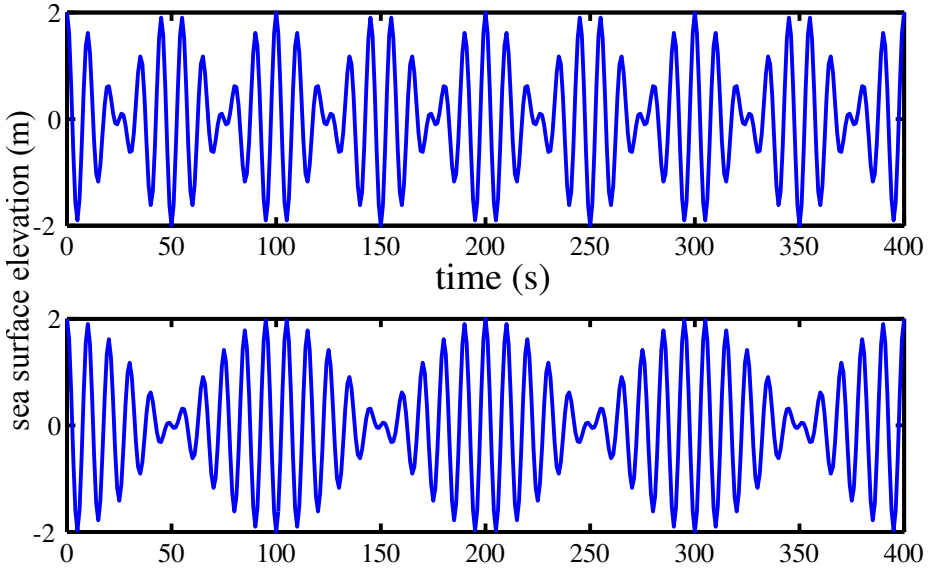

Figure 2.9: Wave groups produced by the superposition of two monochromatic waves. The top panel corresponds to $\Delta\sigma/\sigma = 0.2$, and the bottom panel $\Delta\sigma/\sigma = 0.1$. The narrower the spectrum, the larger the number of waves in the group.

Water depth:	general case	$kD \gg 1$	$kD \ll 1$
dispersion relation	$\sigma^2 = gk\tanh(kD)$	$\sigma^2 = gk$	$\sigma^2 = gDk^2$
phase speed	$C = \sigma/k = [g\tanh(kD)/k]^{1/2}$	$C = (g/k)^{1/2} = g/\sigma$	$C = \sqrt{gD}^{1/2}$
group speed	$C_g = C\left(0.5 + \frac{kD}{\sinh(2kD)}\right)$	$C_g = C/2$	$C_g = C$
Linear properties ($z < \zeta$)			
horizontal velocity	$\mathbf{u} = a\frac{\mathbf{k}}{k}\sigma\frac{\cosh(kz+kh)}{\sinh(kD)}\cos\Theta$	$\mathbf{u} = \frac{a\mathbf{k}\sigma}{k}\mathrm{e}^{kz}\cos\Theta$	$\mathbf{u} = \frac{a\mathbf{k}\sigma}{k^2D}\cos\Theta$
vertical velocity	$w = a\sigma\frac{\sinh(kz+kh)}{\sinh(kD)}\sin\Theta$	$w = a\sigma\mathrm{e}^{kz}\sin\Theta$	$w = \frac{z+h}{h}a\sigma\sin\Theta$
Quadratic properties			
Mean energy per unit surface	$E_t = \rho_w g E = \rho_w g a^2/2$	$E = \rho_w g a^2/2$	$E = \rho_w g a^2/2$
Stokes drift	$\mathbf{U}_s = \sigma\mathbf{k}E\frac{\cosh(2kz+2kh)}{\sinh^2(kD)}$	$\mathbf{U}_s = 2\sigma\mathbf{k}E\mathrm{e}^{2kz}$	$\mathbf{U}_s = \sigma\mathbf{k}E/(kD)^2$

Table 2.1: Main results of Airy wave theory with deep and shallow water limites. We remind that the phase is $\Theta = \mathbf{k}\cdot\mathbf{x} - \sigma t + \Theta_0$.

We note that for $kD \to \infty$, equation (2.50) gives $C_g = \sigma/(2k) = C/2$. Thus, in deep water the groups of waves travel at a speed that is half of the phase speed. Things are very different in shallow water ($kD \ll 1$), where $C_g = C$. In that shallow water limit, waves of all frequencies travel at the same speed (they are not dispersive) hence the groups also travel at that same speed. This is only true for linear waves. In chapter 18, we will see that phase and group speeds are also a function of the wave amplitude.

2.4.9 Energy and power

Eq. (2.49) gives the mean energy flux per unit crest length. For example, in the case of monochromatic waves with a height of 2 m, a period of 12 s and a water depth of 15 m, this flux is $W \approx 50$ kW m^{-1}. This means that if we take a surface facing the waves, 1 meter along the crest and the full water depth, there is 50 kW of mechanical power that goes through this surface. This is 5 MW for 100 m along the crests, which is the peak power of two 150 m high windmills. This number, for rather modest wave heights, shows the strong concentration of power in water waves. Unfortunately, this power is difficult to tap to produce electricity, in particular because it is very intermittent in most places.

2.4.10 Summary

We have obtained the main properties of regular linear waves, summarized in table (2.1). Because these Airy waves are solutions of the linearized equations of motion, they can be combined to obtain the general solution. Hence the surface elevation, velocities and pressure are given by the sum of monochromatic waves, each proportional to their amplitude a. We will see in the next chapter that it is also possible to add up the quadratic properties that are the energy and Stokes drift, which are proportional to the surface elevation variance $E = a^2/2$. These properties come from a series of assumptions, listed in table 2.2 and that will be discussed or removed in the following chapters that extend Airy theory, giving access to all sorts of corrections and allowing to determine the evolution of Airy waves caused by different forcing and dissipation processes. Indeed, we have determined here the eigenvectors of the linearized equations of motion: these are free waves that can exist without forcing. In practice, the forcing is necessary to generate these waves in the first place, and this forcing is balanced by dissipation when long time scales and large spatial scales are considered. That dissipation requires to include vorticity and viscous effects.

2.4.11 Extending Airy wave theory

What happens when we do not make one of the assumptions A1 to A13? In which conditions should we do this?

- A1. Except when considering acoustic and seismic noise generated by ocean waves, as in chapter 21, we can safely ignore compressibility effects.

- A2. Bottom deformations are relevant when considering acoustic and seismic noise generation. In fact, the bottom deformation should be considered for all acoustic wave propagation in the ocean.

Assumption	justification	consequences
A1. incompressible	$u \ll \alpha_w$	$\boldsymbol{\nabla} \cdot \mathbf{u} + \partial w/\partial z = 0$
A2. rigid bottom	bottom motion $\ll$ water motion	$w = -\mathbf{u} \cdot \boldsymbol{\nabla} h$ at $z = -h$
A3. inviscid	high Reynolds number	viscous stresses are zero
A4. irrotational	motion driven by pressure forces + (A3)	$\mathbf{u} = \boldsymbol{\nabla}\phi$, $w = \partial\phi/\partial z$
A5. flat bottom	bottom slopes usually $\ll 1$	with A2, $w = 0$ at $z = -h$
A6. sine wave	basis function of the Fourier transform	$\phi(z) \propto \cosh(kz + kh)$
A7. p_a constant on $z = \zeta$	$\rho_a \ll \rho_w$	no wave generation by the wind
A8. no surface tension	$\gamma \ll g/k^2$ for $L \gg 0.1$ m (in clean water)	no capillary waves
A9. $\varepsilon_1 = ka \ll 1$	$\varepsilon_1 < 0.44$ for periodic waves	with A10, gives linear equations
A10. $\varepsilon_2 = a/D \ll 1$	because it makes equations simpler	... but beware for $kD < 1$!
A11. no mean current	most often $U \ll C$ for dominant waves	simple dispersion $\sigma^2 = gk \tanh(kD)$
A12. constant density	$\rho'/\rho_w < 0.03$ for sea water	no internal waves
A13. no Earth rotation	$f_3 \ll \sigma$	

Table 2.2: Assumptions needed to derive Airy's theory. α_w is the sound speed in water, of the order of 1500 m s^{-1} (in the absence of air bubbles), and U is the mean current velocity. Finally ρ' is a scale for density perturbations relative to the mean ρ_w, and γ is the surface tension, such that $\gamma\rho_w(R_1 + R_2)$ is the additional pressure under a surface with radii of curvature R_1 et R_2, counted positive for a surface that is convex on the air-side, e.g. a crest.

- A3. In the boundary layers at the sea surface, and more importantly at the sea bottom, we will need molecular viscosity and turbulence effects (which can often be represented by an eddy viscosity). However, these layers are very thin, with a thickness of the order of $\delta = (\nu/\sigma)^{1/2}$, which is typically less than a millimeter for the kinematic viscosity of water $\nu \simeq 4 \times 10^{-6}$ m^2 s^{-1}, and wave periods $T > 1$ s, which is consistent with measurements of the water-side surface boundary layer by Banner and Peirson (1998). At the bottom, turbulence effects are important but the wave boundary layer is only a few centimeters thick.

- A4. For a viscous flow, the vorticity from the top and bottom boundary layers diffuses in the water column and in the air (Longuet-Higgins, 1953; Weber and Førland, 1990). Besides, there is also a weak vorticity caused by the Earth rotation, see A13 below.

- A5. The bottom boundary condition becomes $-\boldsymbol{\nabla}\phi \cdot \boldsymbol{\nabla} h = \partial\phi/\partial z$ (inviscid case), and is only satisfied exactly in the presence of at least two wave trains, one incident and one reflected. The incident wave train is also modified by diffraction effects. For small slopes, diffraction and reflection are generally weak, and the wave motion is well approximated by a "WKBJ" approximation: replacing the phase Θ by a function $S(\mathbf{x}, t)$ with $\mathbf{k} = \boldsymbol{\nabla} S$ and $\sigma = -\partial S/\partial t$ (see chapter 12). In this context *small* means that refraction or diffraction effects do not produce of significant variation of the wave amplitude at the scale of one wavelength. A more accurate approximation of the dispersion relation over a sloping bottom was given by Ehrenmark (2005), in the form $\sigma^2 = gk \tanh(kh\beta/\tan\beta)$, where β is the angle between the bottom and the horizontal. This correction is weak, only 4% for a slope $\beta = 10°$. For steep slopes, reflection becomes important and the separation of the variables $\mathbf{x}$ and z becomes meaningless. The velocity potential can be obtained numerically (e.g. Athanassoulis and Belibassakis, 1999; Belibassakis et al., 2001).

- A6. For a flat bottom this is not an assumption: we have the right to decompose the waves into sine waves because these are a complete basis. For small bottom slopes, the wave train is only *locally* equivalent to a sine wave. For steep slopes, the wave train can suffer strong distortions at the scale of one wavelength (e.g. Magne et al., 2007).

- A7. An atmospheric pressure oscillation on the scale of the wavelength can produce an amplification or attenuation of the waves, depending on its phase relative to the waves. This aspect is discussed in detail in chapters 5 and 22.

- A8. Due to surface tension, the pressure under the surface is increased by $-\gamma\left(\partial^2\zeta/\partial x^2+\partial^2\zeta/\partial y^2\right)$. This added pressure modifies the dispersion relation to give $\sigma^2=\left(gk+\gamma k^3\right)\tanh(kD)$. This modification is negligible for wavelengths larger than a few centimeters. The presence of a layer of ice at the sea surface has a similar effect on the waves, with added terms due to bending and inertia, and is significant for periods of 10 s and less (Liu and Mollo-Christensen, 1988) in the case of an ice layer thickness of one meter or more, and thicker layers have an influence on longer waves.

- A9. Non-linear effects associated to $\varepsilon_1\neq 0$ are fairly complex and will be discussed in chapters 5, 18 and 19. One particular consequence is that a monochromatic wave train is generally unstable (Benjamin and Feir, 1967). For waves in one dimension, as produced in the laboratory, this can create very high (freak) waves. Another consequence is that different wave trains interact, exchanging energy an momentum.

- A10. Non-linear effects associated to $\varepsilon_2\neq 0$ are important for $kD<1$ even if the wave height is small. This is particularly true near the shoreline, and the shape of waves can be strongly modified, as discussed in chapters 13 and 18.

- A11. Since the laws of physics are unchanged by a change of Galilean reference frame, a uniform current $\mathbf{U}$ in the absence of bottom friction only introduces a Doppler frequency shift, and all results established here remain valid, replacing Θ by $\Theta_D=\Theta+\mathbf{k}\cdot\mathbf{U}$. One can define an absolute frequency, as measured in the reference frame attached to the bottom,

$$\omega=\sigma+\mathbf{k}\cdot\mathbf{U}=\mathbf{k}\cdot\mathbf{U}+\left[gk\tanh\left(kD\right)\right]^{1/2}. \tag{2.53}$$

  For a current $\mathbf{U}(z)$ that varies only in the vertical, and in the limit $\varepsilon_1\ll 1$ and $\varepsilon_2\ll 1$, this dispersion relation generalizes to the form,

$$\omega\equiv\sigma+\mathbf{k}\cdot\mathbf{U}_A \tag{2.54}$$

  with the advection speed given by Kirby and Chen (1989),

$$\mathbf{U}_A=\mathbf{k}\cdot\int_{-h}^{\overline{\zeta}}\mathbf{U}(z)\frac{2k\cosh\left[2k(z+h)\right]}{\sinh(2kD)}\mathrm{d}z. \tag{2.55}$$

  Finally, when $\mathbf{U}$ also varies horizontally, the phase speed varies horizontally, so that refraction and diffraction effects appear, just like they do on a sloping bottom. These questions are addressed in chapter 7.

- A12. When the ocean is stratified, due to a vertical variation of temperature and/or salinity, the Airy waves are the 'external mode' in a family of waves that also include internal waves. Because the equations of motion are weakly nonlinear, these different modes are coupled, with an exchange of energy between surface waves and internal waves (Thorpe, 1966). This aspect is still relatively unexplored (Osborne and Burch, 1980; Kudryavtsev, 1994). This stratification can also be due to the presence of air bubbles near the surface or sediments near the bottom, with important consequences for the bottom boundary layer and wave dissipation. (e.g. Winterwerp et al., 2003; Styles and Glenn, 2000).

- A13. Taking into account the Earth rotation with a vertical Coriolis parameter f_3, a very weak transversal velocity component v appears, of the order f_3u/σ and in phase with w. This transversal component is important for the surface drift current (Hasselmann, 1970; Xu and Bowen, 1994; Ardhuin et al., 2004b; Rascle and Ardhuin, 2009). In the case of wind-generated waves, f_3/σ is typically of the order of 10^{-4}, so that the effect on the wave kinematics and dispersion is not measurable. There is also a very weak deviation of the propagation direction of the waves (Backus, 1962). This is still true for tsunamis which have much larger periods than wind-waves, typically a few minutes up to 30 minutes. Airy wave theory thus also applies to tsunamis, as long as non-linear effects are weak. On the contrary, for motions with longer periods, such as tides, the Earth rotation must be taken into account. This is why these waves are called inertia-gravity waves.

Chapter 3

Wave spectra and signficant wave height: theory and measurement

A detailed knowledge of the wave motion in any location is often not required, one may rather be interested in the evolution of some wave properties on distances much larger than the wavelength. A statistical approach is therefore preferred.

The most common method to represent the random nature of waves is the spectral analysis. It owes its success to the dispersive nature of waves (different components travel at different speeds), and it was made practical by the development of computer sciences in the 1960s and to the elegant Fast Fourier Transform (FFT) algorithm. Those curious to know how a spectrum can be calculated without a computer can read the amazing account of the rotating system invented by Barber et al. (1946) with variable speed to read off different spectral components off a wave record printed on paper .

With the Fourier method, a record of wave elevation $\zeta(t)$ is decomposed into a superposition of sine waves, each with a particular period. If the record has the three dimensions, $\zeta(x, y, t)$ this decomposition can be done in frequency, wavelength and propagation direction. The phases of theses sine waves are generally random, namely, the phase of one component in one record and the next record are not correlated at all. The only slowly varying quantity is the spectral density, defined as the amount of elevation variance per unit spectral bandwidth. The procedure can be applied to other variables, not just the elevation: pressure, velocity ... This slow variation of the spectrum allows a numerical prediction of ocean wave spectra.

3.1 Frequency spectrum

The spectral analysis that is applied to wave measurements is fairly different from the harmonic analysis which is used for studying tides. Tides are described as a sum of discrete components whose frequencies are very well known as they are associated with astronomical motions. For tides we thus have a finite set of frequencies at which the amplitude and phase can be determined with great accuracy. Waves are described as a the sum of a many components with energy at *all* frequencies. There is no gap in the wave spectrum, and the phases are completely random, uniformly distributed between 0 and 2π while the amplitudes also have random fluctuations. The result of the spectral analysis is a wave spectrum that describes the wave energy distribution as a function of frequency. The practical method used to compute wave spectra from time series of surface elevation or pressure is detailed in Chapter 17.

Figure 3.1 shows how a tide elevation signal is already quite well reproduced by the superposition of only two sine waves (these two waves are called S2 and M2). On the contrary for the high frequency signal, dominated by waves, one, two or three sines waves (black, red and green) are far from sufficient for representing the initial signal (blue). Indeed, to reconstruct the wave signal a great number of sine waves with relatively close frequencies are required. For simplicity, let us start with one realization m of an elevation time series, that can be expressed in terms of a Fourier series,

$$\zeta_m(t) = \sum_{i=1}^{N} a_{m,i} \cos(2\pi f_i t + \Theta_{0,m,i}) \tag{3.1}$$

Where $a_{m,i}$, f_i and $\Theta_{0,m,i}$ are the Fourier amplitudes, frequencies and phases of the Fourier mode i, found for the realization m of the sea state. As explained above, N must be a large number. In practice

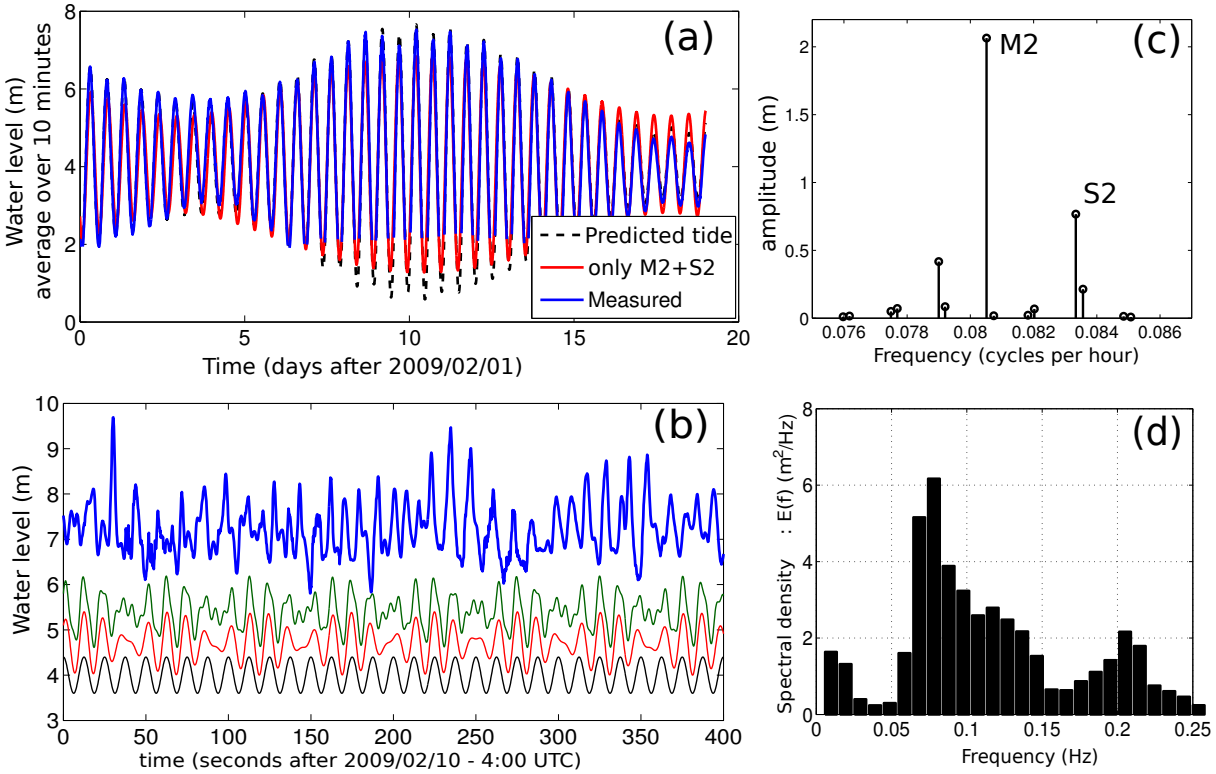

Figure 3.1: Example of surface elevation time series (a and b) deduced from pressure measurements collected as the foot of Western cliff of Banneg Island, Molene Archipelago. The corresponding spectra for the high and low frequency part illustrate the difference between a tide spectrum, presented as a function of amplitude and a wave spectrum. Below: a sample of the initial elevation signal and one, then two, then three sine waves are combined to approximate the initial signal. In the case of tides, the fit is already good with 2 components. In the case of waves, the detailed shape of the elevation cannot be reproduced without many components.

the phases are nearly random and uniformly distributed over $[0, 2\pi]$ [1]. The ensemble mean of the Fourier amplitudes, expressed as function of the frequencies, $A(f_i) = \langle a_{m,i} \rangle$ is called the amplitude spectrum. For waves, identical sea state realizations can only be obtained in controlled laboratory experiments. Instead, the sea state is assumed stationary and the ergodicity theorem is evoked to replace the ensemble mean by a temporal mean. In practice, M samples of a given (stationary) wave record simulate M realizations of the sea state and provide an equivalent ensemble mean.

For such random signals, the 'power' spectrum is preferred to the amplitude spectrum. As demonstrated in the previous chapter, the mechanical wave energy per unit surface of ocean, for an sine wave of amplitude a is $\rho_w g a^2/2$. As a consequence, the energy spectrum is

$$\left\langle \frac{1}{2} a_{m,i}^2 \right\rangle = \frac{1}{M} \sum_{m=1}^{M} \frac{1}{2} a_{m,i}^2, \tag{3.2}$$

With this definition, the values taken by the spectrum decrease proportionally to the spectral resolution Δf that is the inverse of the length of time over which the spectral analysis is performed. In order to avoid this dependency on the record length, it is customary to work with a power spectral density (PSD for short),

$$E(f_i) = \frac{1}{\Delta f} \left\langle \frac{1}{2} a_{m,i}^2 \right\rangle. \tag{3.3}$$

In the limit of large record lengths, the frequency interval Δf tends towards zero, and we obtain the

[1] The phases are not exactly random for an actual sea state, waves are slightly asymmetric, the front face being steeper than the back, and the crests sharper than troughs (e.g. Agnon et al. (2005)). For most applications, these effects can be neglected.

continuous wave energy frequency spectrum,

$$E(f) = \lim_{\Delta f \to 0} \frac{1}{\Delta f} \left\langle \frac{1}{2} a_i^2 \right\rangle . \tag{3.4}$$

While wave are irregular, the spectrum is relatively smooth, evolving slowly in space and time, with a typical time scale of a few hours. This regularity that contrasts with the apparent irregular motion of the sea surface, allows for a predictive numerical modeling. Note further, that for convenience we continue to call (abusively) 'energy' the elevation variance E which has units of length squared. The true energy, in Joules per unit surface, is in fact $\rho_w g E$.

This approach can be generalized to waves travelling in all directions. The Fourier representation of the sea surface elevation becomes,

$$\zeta_m(x, y, t) = \sum_{i=1}^{N} \sum_{j=1}^{M} a_{m,i,j} \cos(2\pi f_i t - k_i \cos(\theta_j) x - k_i \sin(\theta_j) y + \Theta_{0,m,i,j}), \tag{3.5}$$

as illustrated by figure 3.2

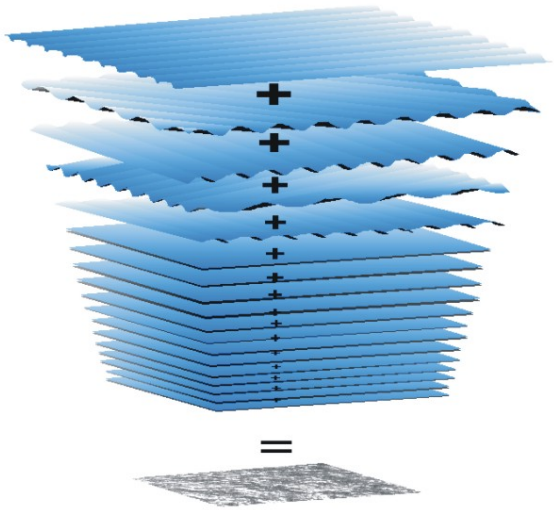

Figure 3.2: Reconstruction of a given sea state from the superposition of a great number of plane waves each with a particular direction and wavelength. Illustration of equation 3.5. After Pierson et al. (1955).

In this expression k_i and f_i are related by the linear dispersion relation and θ_j is the direction of propagation of the Fourier mode (i,j). In the same fashion as for the frequency, the continuous frequency-direction wave energy density spectrum,

$$E(f, \theta) = \lim_{\Delta f \to 0} \lim_{\Delta \theta \to 0} \frac{1}{\Delta f \Delta \theta} \left\langle \frac{1}{2} \rho_w g a_{i,j}^2 \right\rangle . \tag{3.6}$$

Keeping only the wave energy and its distribution reduces the representation of the waves properties to a manageable amount of information, but some information is lost in the process. Indeed, it is not possible to reconstruct the sea surface from the spectrum, especially because the phases are not conserved. In practice, the phase couplings are often negligible, and any reconstructed sea surface with random phases is statistically similar to the initial wave field. In this sense, for a Gaussian sea surface elevation, the spectrum contains the full statistics of the sea surface.

3.1.1 Wavenumber or frequency?

Depending on the measurement method, the numerical model or the application, one may want to perform the spectral analysis in the wavenumber or frequency space. The following relations between the frequency and wavenumber spaces, assume that waves follow the linear dispersion relation. The rule is simple, the variance of a given quantity does not depend on the coordinates in spectral space. The variance is the spectral density times the spectral width, hence,

$$E(f,\theta)d\theta df = E(k,\theta)d\theta dk \tag{3.7}$$

which yields

$$E(f,\theta) = \frac{\partial k}{\partial f}E(k,\theta) = \frac{2\pi}{C_g}E(k,\theta) \tag{3.8}$$

In the same manner,

$$E(f,\theta) = \frac{2\pi}{C_g}E(k,\theta) = \frac{2\pi}{C_g}kE(k_x,k_y) \tag{3.9}$$

The relationship must be used with caution for the high frequency part of the spectrum, because long waves modulate the frequency of shorter waves, which causes a deviation from the linear dispersion relation. This is significant at frequencies higher than three times the wind sea peak frequency (Leckler et al., 2015; Peureux et al., 2018).

Finally, and we shall see why in chapter 7, when the effects of currents on waves are included, numerical models usually work with the action spectrum instead of the energy spectrum. This action spectrum is usually defined as

$$A(k,\theta) = \frac{1}{\sigma}E(k,\theta) = \frac{1}{\sigma}E(k_x,k_y) \tag{3.10}$$

For instance, the numerical model WAVEWATCH III (Tolman and Booij, 1998) calculates the evolution of $A(k,\theta)$ discretized over N frequencies and M directions, through the variable ASPEC(I,J) with $1 \leq I \leq N$ and $1 \leq J \leq M$. However, the model output is transformed back to $E(f,\theta)$.

The spectrum is the primary variable of wave forecasting model, and, as such, it is important to be familiar with its physical meaning. Figure 3.3 illustrates the relation between the sea surface and spectrum shapes.

The reader is invited to try to recomposed a sea surface in the physical space from the spectrum produced by a numerical model,

$$\zeta(x,y,t) = \sum_m^M \sum_n^N \sqrt{2E(f_m,\theta_n)\Delta_f\Delta_\theta}\cos\left[k_m\cos\theta_n x + k_m\sin\theta_n y - \sigma_m + \Theta_0(m,n)\right], \tag{3.11}$$

where Δ_f and Δ_θ are the spectral resolutions, and M and N are the number of frequencies and directions used to discretize the spectrum. Rigorously, M and N should be taken infinite, but we may start with the typical resolution of a spectral wave model, of the order of 30 frequencies and 24 directions, with a significant level of energy in maybe only 20 components.

The component amplitude $\sqrt{2E(f_m,\theta_n)\Delta_f\Delta_\theta}$ is consistent with the fact that the total variance elevation is the sum of the amplitudes squared divided by two, or the spectrum integral over the entire spectral domain. The phase $\Theta_0(m,n)$ can be taken randomly distributed over $[0,2\pi]$. The resulting surface will look smoother than an actual sea state, and the observed crest-trough asymmetry will not be reproduced. This is due to the random phase assumption that disregards the phases coupling between spectral components. These issues are further addressed in §18.3.2.

3.2 Using spectra

Skipping here the technical details necessary for a practical estimation of the spectrum (see chapter 17), we now have a spectrum. Very nice, but what can we do with it?

3.2.1 Transfer function

Depending on the application, one can transform the elevation variance spectrum. For a variable A (for instance the bottom pressure), related to the surface elevation through a linear relation:

$$A = M\zeta, \tag{3.12}$$

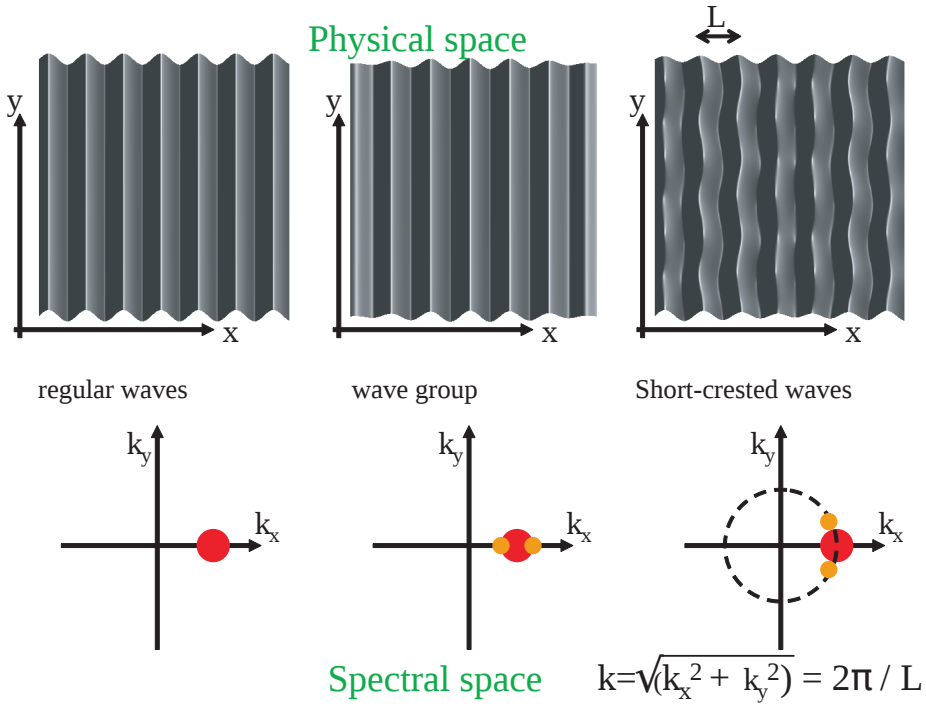

Figure 3.3: Relation between spectral and physical spaces. Schematic spectra of monochromatic waves (left panel) and modulated in terms of wavenumber or direction. For the last two cases, the surface is composed of three components.

where M is a complex number that takes values in the spectral space, the variance spectral density of A, E_A is

$$E_A(k_x, k_y) = |M|^2 E(k_x, k_y) \text{ or } E_A(f, \theta) = |M|^2 E(f, \theta) \tag{3.13}$$

or any other equivalent expression in other spectral coordinates.

For instance, the bottom velocity variance will be given from the polarization relation (2.25)–(2.31), that yield $M = \sigma \cos(\theta)/\sinh(kD)$, with θ the angle between the x-axis and the wave direction of propagation. We hence get the spectrum of the x-component of the bottom velocity.

3.2.2 Spectral and integral parameters: H_s, T_p ...

It can be inconvenient to describe a sea state by a two-variable function. Even when it is discretized into a numerical model, typically over 30 frequencies and 24 directions meaning 720 spectral components, which is a lot of numbers to describe a sea state. This information can be summarized into a few meaningful parameters.

As the spectrum is a decomposition of sea surface variance, the most important parameter is certainly the variance E, often abusively called energy. From the elevation variance E, we get a length scale $\sqrt{E}$. Going back to sine waves, the variance is $a^2/2$ with a the wave amplitude. Hence $\sqrt{2E}$ is an equivalent amplitude for random waves. More precisely, it is the root mean square amplitude. The root mean square wave height for a random wave is thus twice this amplitude $H_{rms} = 2\sqrt{2E}$.

For practical applications, the most widely used height scale is the *significant wave height* H_s that corresponds to the visual feeling given by the sea. From the wave height distribution we can define $H_{1/3}$ (see chapter 1). From the spectrum we define,

$$H_s \equiv H_{m0} \equiv 4\sqrt{E} = 4\sqrt{\int_0^\infty \int_0^{2\pi} E(f, \theta) d\theta df} \tag{3.14}$$

In practice $H_{m0} \simeq H_{1/3}$, this property can be demonstrated in the limit of a narrow spectrum (Longuet-Higgins, 1952). Following the recommendations of the World Meteorological Organization, we shall consider H_{m0} to be *the* definition of the significant wave height H_s. The "$m0$" index indicates that it is

based on the zeroth moment of the spectrum. The p-th moment of the spectrum is defined as,

$$m_p = \int_0^\infty \int_0^{2\pi} f^p E(f,\theta) d\theta df \tag{3.15}$$

In many cases, the directional information is not available, and we only have the frequency spectrum,

$$E(f) = \int_0^{2\pi} E(f,\theta) d\theta \tag{3.16}$$

This distribution of the energy as a function of frequency contains information on the typical time scales of the signal. $E(f)$ generally exhibits a sharp maximum around the frequency f_p, $E(f_p) = E_{max}$. f_p is the peak frequency, corresponding to the peak period $T_p = 1/f_p$. This peak period can be noisy in the presence of several peaks. The frequency distribution can also be characterized from the spectral moments,

$$T_{m0,p} = \left[\left(\int_0^{f_{\max}} \int_0^{2\pi} f^p E(f,\theta) d\theta df \right) / \left(\int_0^{f_{\max}} \int_0^{2\pi} E(f,\theta) d\theta df \right) \right]^{-1/p}. \tag{3.17}$$

The most widely used periods are $T_{m0,-1}$, $T_{m0,1}$, $T_{m0,2}$. Each of these has a more or less weight on low frequency part of the spectrum. If one is interested in an effect proportional to f^2, as is the case of the wave forces exerted on a structure, it is reasonable to use $T_{m0,2}$. Besides, $T_{m0,2}$ is very close to the mean period T_z given by wave-by-wave analysis. Note however that $T_{m0,2}$ depends on the choice of f_{max}. The values of the different periods for a typical spectrum are shown in figure 3.4.

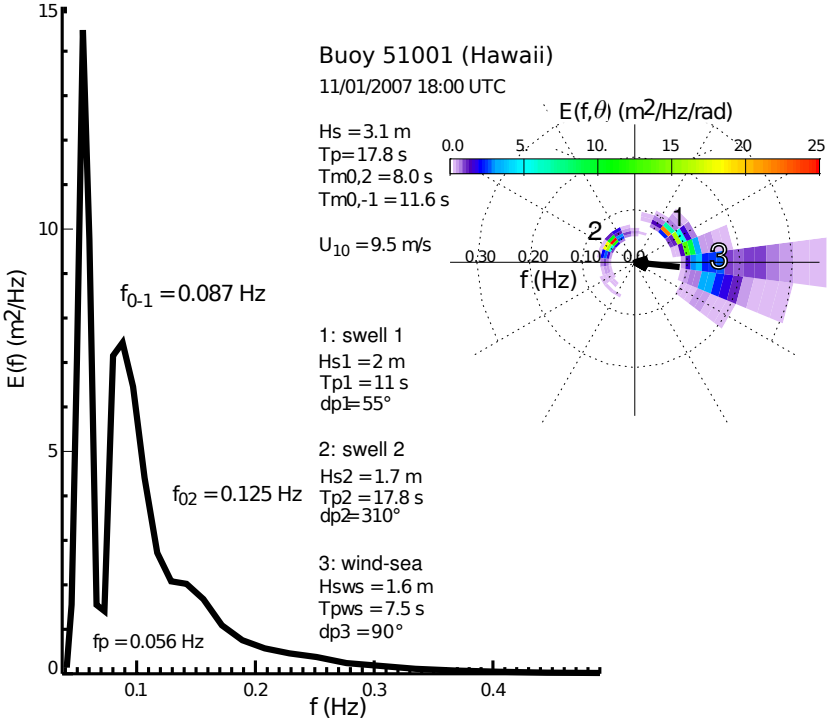

Figure 3.4: Typical example of a oceanic spectra in tropical area, measured by buoy 51001, moored 350 km North West of Kauai island, on January 11, 2007. The different peak and mean periods are indicated along with the parameters produced by a decomposition of the spectrum into a primary swell, secondary swell and wind sea. This analysis is generally not possible without directional information. Note that the wind sea only appears as a soft "shoulder" to the right of the secondary swell, while it comes from a different direction. This shows the possible difficulty of separating swell and wind sea from a frequency spectrum. Also note that the significant wave height H_s is less than the sum of H_{s1}, H_{s2}, H_{sws}, of the three systems: the energy can be summed but the wave heights cannot. Namely $H_s = \sqrt{H_{s1}^2 + H_{s2}^2 + H_{sws}^2}$.

Finally, we define,

$$a_1(f) = \int_0^{2\pi} \cos\theta E(f,\theta)d\theta / \int_0^{2\pi} E(f,\theta)d\theta, \tag{3.18}$$

$$b_1(f) = \int_0^{2\pi} \sin\theta E(f,\theta)d\theta / \int_0^{2\pi} E(f,\theta)d\theta, \tag{3.19}$$

$$\tag{3.20}$$

that can be estimated from the elevation spectrum $E(f)$ and the elevation-horizontal displacements co-spectra, E_{xz} and E_{yz} (see eq. (17.8) (17.9).

The mean wave direction at frequency f is,

$$\theta_m(f) = \arctan(a_1(f)/b_1(f)), \tag{3.21}$$

and the directional spreading, as defined by Kuik et al. (1988) is the standard deviation (in radians) of the spectral width in the limit of a narrow spectrum,

$$\sigma_\theta(f) = \left[2(1-(a_1^2(f)+b_1^2(f))^{1/2})\right]^{1/2}. \tag{3.22}$$

For an equal energies in opposite directions, σ_θ is maximum at $\sqrt{2}$ radians, which is 81 °.

The directional wave properties of the dominant waves, can also be characterized with the mean direction and directional spreading of the spectral peak: $\theta_m(f_p)$ and $\sigma_\theta(f_p)$. $\theta_m(f_p)$ is often referred to as "main direction", while the mean direction would rather be an average over the entire spectrum,

$$\theta_M(f) = \arctan\left(\int_0^\infty b_1(f)E(f)df / \int_0^\infty a_1(f)E(f)df\right) \tag{3.23}$$

With all these directions, one must be careful with the directional convention. The directions are usually counted from North (direction 0), progressing clockwise (90 east, 180 south, 270 West). However, depending on the authors, the direction convention is either meteorological (direction from where the waves or wind are coming, this is the convention used in the present manuscript) or oceanographic convention (direction toward which the waves or currents are moving). Be careful!

3.3 Random waves *in situ* observations

The most common usage of wave time series is the determination of the frequency spectrum $E(f)$ and, when more than one variable are measured, the directional wave spectrum $E(f,\theta)$ may be estimated. Details of this processing given in chapter 17. In practice, the most common in situ instruments for wave measurements are surface-following buoys or bottom-mounted pressure gauges or ADCPs.

3.3.1 Wave gauges

These are reference sensors that directly measures the free surface elevation $\zeta(x,y,t)$ at a fixed horizontal position (x,y). The measure is done through the electrical resistance or capacity of one (or two) conducting wires forming a loop closed by the sea surface. This type of sensor is widely used in the laboratory, but it is not so common at sea because this requires a fixed platform and the wires are susceptible to damage by small floating debris. Also, the large wave heights encountered in the field require long enough gauges. These wave gauges can also be mounted on a buoy that filters out the long waves through its motion (Graber et al., 2000). Wave gauges are most often associated in an array (see below) of several gauges synchronized and mounted on a single platform so as to provide a wave direction estimation (Cavaleri et al., 1981).

The direct measurement of surface elevation can also be performed by radar and LIDAR systems, which determine the distance to the sea surface from the travel time of an electromagnetic or sound wave, and that can likewise be arranged in an fixed array or integrated in a scanning system.

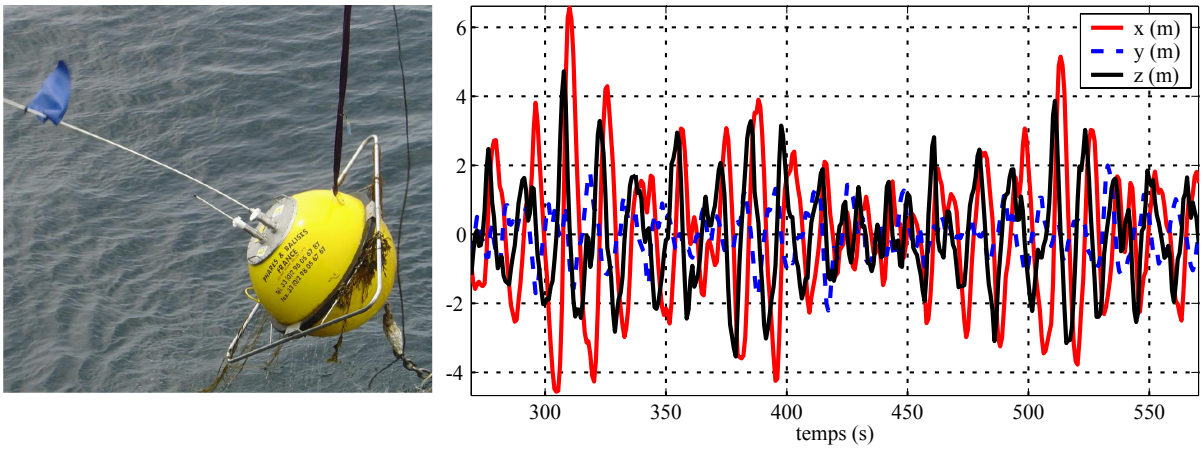

Figure 3.5: Left panel: Deployment of a Datawel Waverider buoy, 0.9 m of diameter, equipped with a (long) HF radio antenna and with a (short) Orbcomm satellite antenna for data transfer. Right panel: examples of displacements measured by this buoy offshore Crozon in May 2004. (same time series as in figure 1.2). Of course, the 10 m high waves were not measured by the times of the buoy deployment.

3.3.2 Wave buoys

Buoys measure either the successive positions and velocities, determined by a global navigation satellite system (such as the Global Positioning System - GPS) or vertical acceleration recorded by a buoy floating at the free surface that give after a double integration in time, a surface elevation signal $\zeta(x, y, t)$. Depending on the type of instrument and on the presence of currents, the horizontal position (x, y) is not fixed but nearly follows the wave orbital motion. This later property may be annoying for purists of the wave profile, as it partly filters out the free surface nonlinearity (the linear Lagrangian motion involves a part of the Eulerian motion). In addition to the heave measurement, that was for long the most common, the wave direction can be determined by measuring the horizontal accelerations that yields, through double integration, the horizontal displacement x and y (figure 3.3.2). The use of precise satellite positioning now allows a direct measure of the horizontal position, which can present certain advantages, especially for very low frequency waves. Several models are commercialized by Oceanor and Datawell, based on this concept.

The largest buoys generally use a measurement of the components $\partial\zeta/\partial x$ and $\partial\zeta/\partial y$ and of the local free surface slope: pitch and roll as the first prototypes of Longuet-Higgins et al. (1963) and Cartwright and Smith (1964). This is the case of the US National Data Buoy Center (NDBC) 3-m diameter buoys. Details of buoy processing are given in chapter 17. Both methods, acceleration and pitch-roll allow, thanks to the three signal covariance, the determination of the first four Fourier coefficients of the angular distribution, also known as angular moments,

- a_1 and b_1, defined by (3.18)–(3.19) and calculated from the co-spectra E_{xz} and E_{yz} (equations 17.8–17.9)
- a_2 and b_2, defined as a_1 andf b_1 but with $\cos\theta$ and $\sin\theta$ replaced by $\cos 2\theta$ and $\sin 2\theta$, respectively.

A more complete measure of the directional spectra from floating buoys has been developed but has not been as successful as expected: the cloverleaf buoy that consists in three pitch-roll buoy linked to each other (Mitsuyasu et al., 1975). In principle this layout provides a measure of the surface curvature and the Fourier coefficient up to a_8 and b_8. From a conventional buoy, one has to infer the function $S(f, \theta)$ from only the four independent number a_1, b_1, a_2 and b_2. This is not so much a measurement problem, but rather one of choosing a statistical estimator. There are many method for this. Among these, the Maximum Entropy Method (MEM Lygre and Krogstad, 1986), has the advantage of conserving the angular moment a_1, b_1, a_2 and b_2. The MEM method tends however to to give a bimodal shape (two-peak spectra), which is often (Ewans, 1998) but not always realistic (Benoit et al., 1997).

Other recent analysis techniques aim at increasing the the directional resolution of this kind of measurements. For instance, Donelan et al. (1996), have proposed an interesting method based on a wavelet transform. Unfortunately their method assumes that for any given frequency the wave field is dominated by waves coming for one single direction, which is not the case. This analysis yields a very

high directional resolution, and can be interesting to detect the presence of waves from a given direction, but it cannot be interpreted as a directional spectrum as it leads to a low bias in the directional spreading. Other methods can be biased and should be avoided. This is the case of the maximum likelihood method (MLM) which yields output spectra that are systematically too broad and have moments a_1, b_1, a_2 and b_2 that are different from the input parameters.

3.3.3 Pressure gauges

When surface elevation measurements are too expensive or not possible, which may be due to strong currents incompatible with mooring lines, breaking waves in the surf zone, a usually good alternative is the measurement from bottom-mounted sensors. The most common and robust are pressure gauges that can be used to measure tidal elevations at the same time. To recover the surface elevation from the pressure signal, we can invert the linear transfer function given by eq. (2.28), namely, for a sensor at a height h_d over the bottom, $M = \rho_w g \cosh(kh_d)/\cosh(kD)$. The water depth D is also given by the measurement of the mean pressure once it is corrected for the atmospheric pressure. Because the elevation to pressure transfer function M decreases when k increases, it is usually impossible to recover wave elevations for frequencies above a cut-off value f_c. That value f_c is a function of water depth, instrument noise, background noise (usually due to currents)... but also of the directional wave spectrum. Indeed, figure 3.6 shows an example of data recorded in 100 m depth, in which the second order pressure is larger than the linear pressure for frequencies above 0.13 Hz. As discussed in chapter 21, this second order spectrum is a function of the frequency spectrum $E(f)$ but also of the directional wave distribution. In that case, it is not possible to recover $E(f)$ for frequencies above 0.12 Hz. For example, on day 4, the yellow-orange sloping line at frequencies 0.05 to 0.1 Hz is a due to swell waves arriving from a distance of about 4000 km (see explanations in chapter 4, eq. (4.12)). At the same time, there is a fainter blueish line at twice these frequencies which is caused by the second order effect. The vertical blue stripes above 0.13 Hz are caused by the tidal current effects on the directional wave spectrum (Ardhuin et al., 2013).

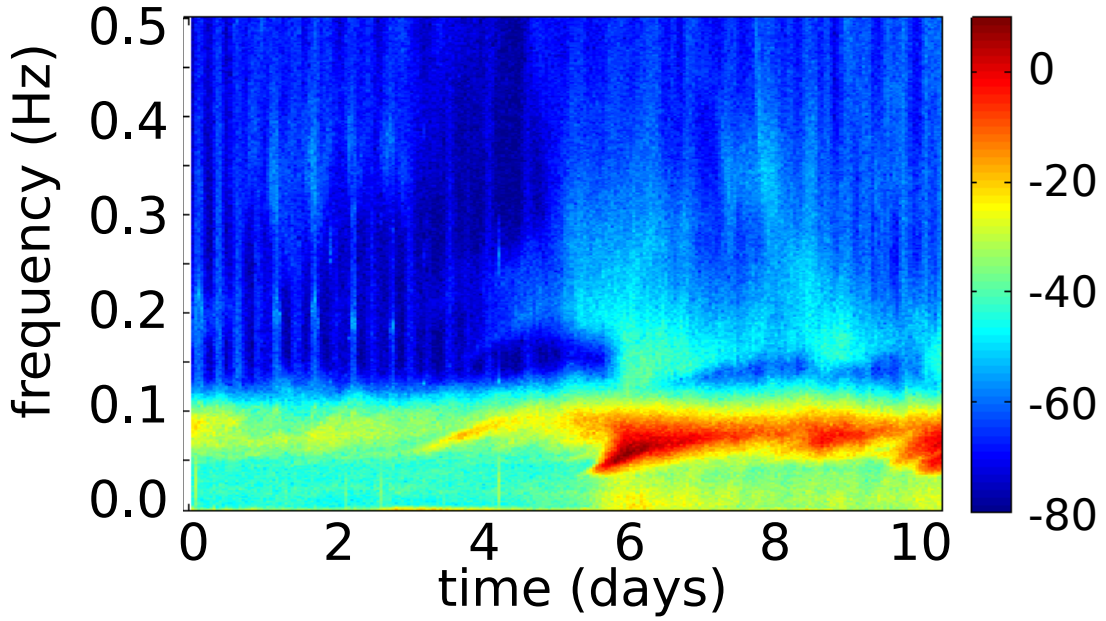

Figure 3.6: Bottom pressure spectra
Time-frequency diagram of the pressure recorded over 11 days in 100 m depth off the French Atlantic coast in October 2015. The colors show the pressure level in dB relative to 1 m^2/Hz times $\rho_w^2 g^2$. These measurements were performed by a very sensitive Paroscientific piezo-electric sensor, included in a RBR-duo system, with a noise level below -80 dB. At our depth of 100 m, the usual linear pressure signal, with a level between -40 to 10 dB, can be used to recover the surface elevation spectrum for frequencies below 0.12 Hz. At higher frequencies, the pressure is dominated by a second order effect due to waves in opposite directions (e.g. Miche, 1944b; Ardhuin et al., 2013). That effect has very important consequences for seismology, as discussed in chapter 21.

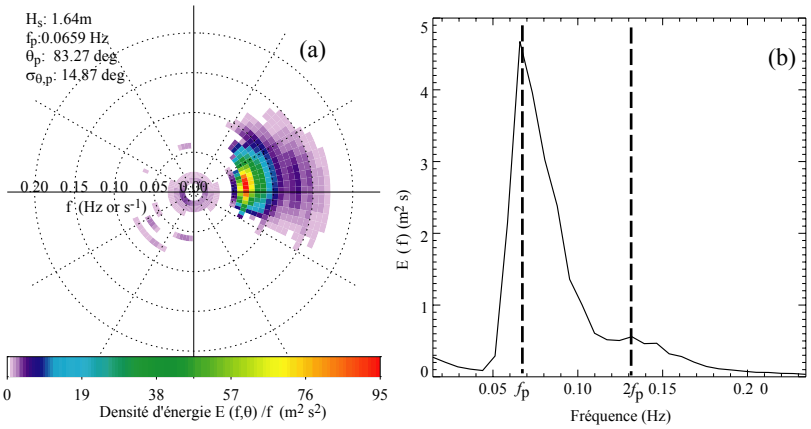

Figure 3.7: (a) Example of frequency-direction wave spectra, divided by frequency, computed from 8m depth pressure measurements in Duck, NC, October 19, 1994, 7:00 (EST). (b) Corresponding Frequency spectra whose secondary peak matches the first harmonic of the spectral peak ($f = 2f_p$), and which is likely due to the effect of nonlinear interactions that are of great importance in shallow water.

3.3.4 P-U-V sensors

As indicated by its name, this sensor measures the pressure p and the two horizontal components of the velocity, u and v. It is indeed the combination of two instruments: a current meter (acoustic, electromagnetic because a high sampling rate is required) and a pressure sensor, often piezo-electric. This instrument is of particular interest as it is designed to be installed on the sea bottom. It is the simplest mooring you may imagine, if one is not too worried about fishermen, for instance... Besides it is delicate to recover real time data (cables, acoustical modems with surface buoys...).

We have seen in Chapter 1 that the fluid pressure and velocities exponentially decay from the surface to the bottom with a typical scale which correspond to the wave length $2\pi/k$. The "P-U-V" sensor is thus perfect if one wish to measure the agitation at the bottom. To measure the wave heights one may use the theory that provide transfer functions between pressure, velocities, elevation, etc (equation 3.13). In this situation, the closer to the surface, the more reliable will be the measurement (e.g. an instrument mounted on a floating of fixed platform).

3.3.5 Sensor arrays and ADCPs

A set of wave gauge can be combined to record more covariances between the measurements. This kind of measure allowed to get the first accurate spectra (Donelan et al., 1985) and is particularly used for the air-sea interaction studies, for which the short waves spectrum is crucial (Graber et al., 2000; Pettersson et al., 2003). It is essential to synchronize the sensors with an accuracy that is small compared to the measured wave period. Similar techniques are employed in RADAR and SONAR technologies to determine the sources of echoes. The original array processing algorithms used for waves were actually developed for seismology.

These techniques have been largely applied to pressure sensors arrays with a number of statistical methods for the spectrum estimation (e.g. Davis and Regier, 1977; Long and Hasselmann, 1979; Pawka, 1983; Herbers and Guza, 1990). An example of a spectrum is given in Figure 3.7 determined from a coherent array of pressure sensors deployed in 8m depth on the site of the US Army Corps Field Research at Duck, North Carolina. For large arrays, the underwater instruments positioning much be very accurate. An acoustical positioning is generally used. The directional resolving power of the array generally increases with the number of sensors in the array (see Kinsman, 1965). Arrays of pressure sensors are excellent reference instruments for measuring the spectra of dominant waves, but they are relatively expensive to deploy and maintain. O'Reilly et al. (1996) used such an array for the validation of directional properties of two different types of buoys.

A recent and convenient alternative is the use of current profilers (ADCP). The combination of the velocities measured by different acoustic beams, allows, in principle, for an interesting measure of the directional spectra. However, the typical noise of up-looking ADCPs does not allow a higher angular resolution than that of a simple P-U-V (Herbers and Lentz, 2010). The main benefit of ADCPs, however,

is the use of measurements close to the sea surface, where the wave motion is less attenuated than at the bottom.

3.4 Optical measurements

Waves are usually the first thing that you see when looking at the sea. But turning beautiful pictures into numbers for scientific analysis is not so easy. We will not discuss here the techniques that are mostly used in the laboratory (e.g. light refraction across the air-sea interface), but instead we present the main methods in use for application to real ocean waves.

3.4.1 From stereo-photography to stereo-video

The first methods used to measure wave shapes were based on stereo-photography: pairs of photographs taken at the exact same time can be analyzed to produce a 3D map of the sea surface (Schumacher, 1939). The basic principle is to determine the $(x, y, z = \zeta(x, y))$ coordinates of points that have been identified in both images. This identification can be done using automatic correlation analysis. The pair of pictures can be obtained from a single platform to cover a modest area and reveal interesting details about the wave shapes (Banner et al., 1989), typically less than 30 by 30 m, or from a pair of aircraft to get a view of a much broader region (Cote et al., 1960; Holthuijsen, 1983) and produce a full directional wave spectrum. Now that everyone is carrying a digital camera around, and that stereo

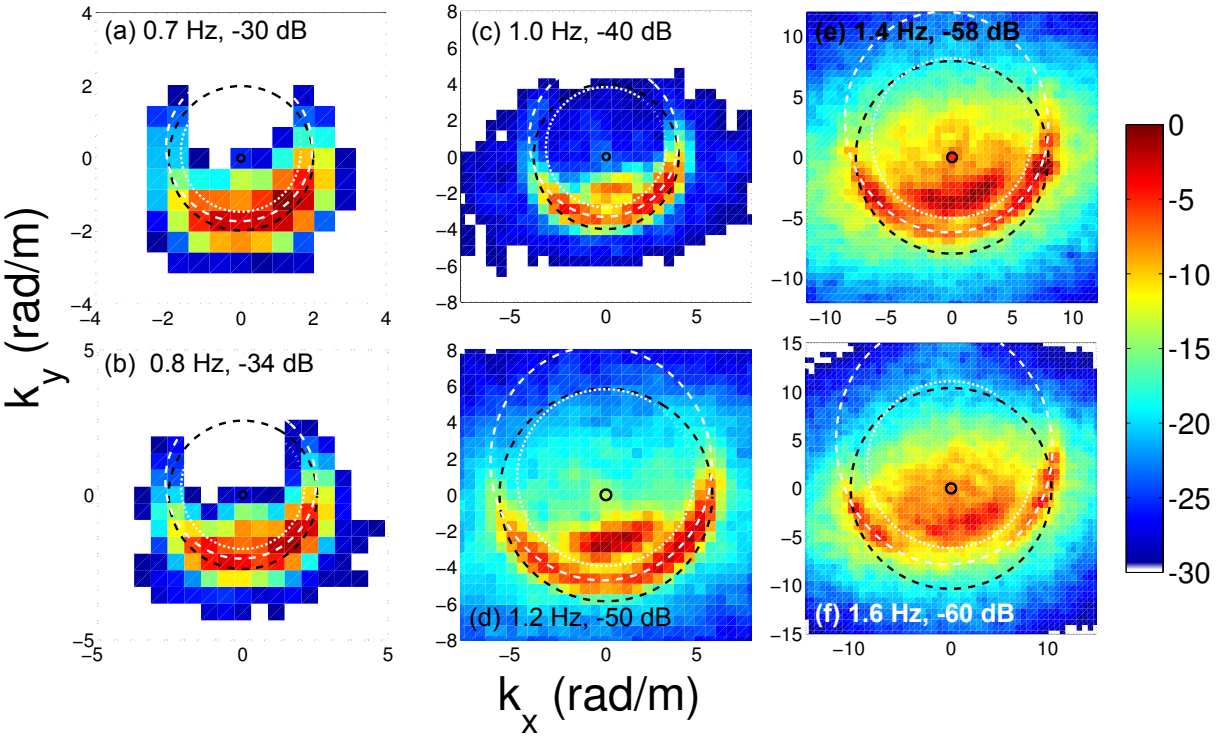

Figure 3.8: Slices of the double-sided spectrum for positive apparent frequencies 0.7, 0.8, 1.0, 1.2, 1.4 and 1.6 Hz. The energy appears in the direction from where it is coming. For each panel the color scale spans 30 dB with the dark red corresponding to the power indicated on the figure (e.g. -30 dB) relative to 1 m^4/Hz. Note that 1.4 and 1.6 Hz are twice 0.7 and 0.8 Hz, so that the first harmonic of the components in (a) and (b) appear at approximately twice the wavenumbers in panels (e) and (f). In each panel, the linear dispersion relation without current is plotted in black, and the white dashed line gives the linear dispersion with a uniform current $U = 0.15$ m/s oriented towards the trigonometric angle 99 degrees. The white dotted line marks approximately the separation between the linear part of the spectrum and the faster non-linear components (Adapted from Leckler et al. 2015).

processing is much more common, there are many opportunities to measure the full evolution of the sea surface in space and time $\zeta(x, y, t)$. Recent efforts by Benetazzo (2006) and Gallego et al. (2011) have demonstrated the capabilities of stereo processing, leading to new applications (Fedele et al., 2013;

Leckler et al., 2015). Latest developments include auto-calibration and the proper motion corrections needed for ship deployments. A general issue that remains is that not all light conditions are favorable. Alternatively, the use of more expensive infrared cameras or polarization cameras is a very interesting extension for overcoming the variability of lighting conditions and the lack of texture at small scale for a correlation analysis (Sutherland and Melville, 2013; Laxague et al., 2015).

The great advantage of having the full surface $\zeta(x, y, t)$, is that we can now measure a 3D spectrum, without the need to use linear wave theory. This is most important for the short wave components, for which nonlinear contributions are important. Figure 3.8 shows slices of the 3D spectrum at a constant frequency. These are obtained from a stereo-video system installed 11 m above the water in a platform in the Black Sea. The image processing uses the epipolar method: the position of the sea surface is obtained only by a knowledge of the geometry of the camera system. This record from October 4, 2011, was acquired when the wind speed was 14 /s and the wave peak frequency is $f_p = 0.33$ Hz (Leckler et al., 2015). The Non-linear contributions to the frequency spectrum dominate for $f > 4f_p$. For example at $f = 1.2$ Hz, there is more energy in the peak located near $(k_x = 0, k_y = -3)$ than along the linear dispersion relation shown wit the white dashed line. Such non-linear effects are also important for the statistics of extreme wave heights, as shown by Fedele et al. (2013); Benetazzo et al. (2017).

3.4.2 Using polarization and/or light intensity

Such a stereo system has difficulties in measuring waves with frequencies higher than 1.4 Hz that have small heights. Other measurement techniques that are directly sensitive to slopes are better suited for these shorter components: these include polarimetry (Zappa et al., 2008) or a measurement of the radiance that can also be combined with the epipolar method (Gallego et al., 2011; Yurovskaya et al., 2013).

Such a technique can also be applied to high resolution airborne or satellite imagery (with pixel sizes less than 30 m in order to resolve waves). Kudryavtsev et al. (2017) have particularly taken advantage of the 1.5 s to 4.5 s time lag in the acquisition of the different color channels of the MultiSpectral Instrument on board Sentinel-2. Clouds or haze obviously limit the application of optical methods, which is why radar is often preferred for wave remote sensing.

3.5 Radar remote sensing

Since the invention of radar, the sea was found to be an important source of echoes, at all radar frequencies (from decametric to micro waves). This is due to the dielectric properties of sea water. An active radar measures a electromagnetic power received by its antenna. This power (in Watts) is normalized by the antenna-target distance, the antenna size, the emitted power. This is the normalized radar cross section (NRCS), often represented by the symbol σ_0. σ_0 depends on the surface geometry, of the measurement (incidence angle, range direction) and of the electromagnetic properties (polarization, wave length). In particular, σ_0 highly depends on the radar wavelength and of the wave radar incidence angle relative to the surface.

A down-looking (nadir) radar will see high σ_0 with a glassy sea surface. If waves are present, the surface echoes may be considered as the incoherent superposition of the facet echoes.

Radar altimeter data are, the source of measurements of H_s available at global scale and used for operational wave forecasting through data assimilation. Contrary to other observation systems, H_s is directly determined, without the use of a spectral analysis. The usual arrangement is a radar antenna looking straight down - at the nadir - on the the sea surface. The choice of the radar frequency is dictated by a number of considerations, including atmospheric absorption – we want to be able to measure a returning echo from the sea surface – and the size of the antenna – low frequencies give large wavelength that require a proportionally large antenna to have a narrow beam. The radar wavelength and frequency are related by the speed of light c, namely $f_r = c/\lambda_r$.

Ocean waves have been monitored from space continuously since the lauch of ERS-1 using altimeters and SARs, as summarized in figure 3.9

3.5.1 Conventional or 'delay' altimetry

The first main principle of the analysis of the radar echoes is the determination of the distance, usually called range, based on the delay of a radar pulse to travel from the transmitting antenna to the target and back to the receiving antenna. Usually the two antennas are the same piece of hardware and this is

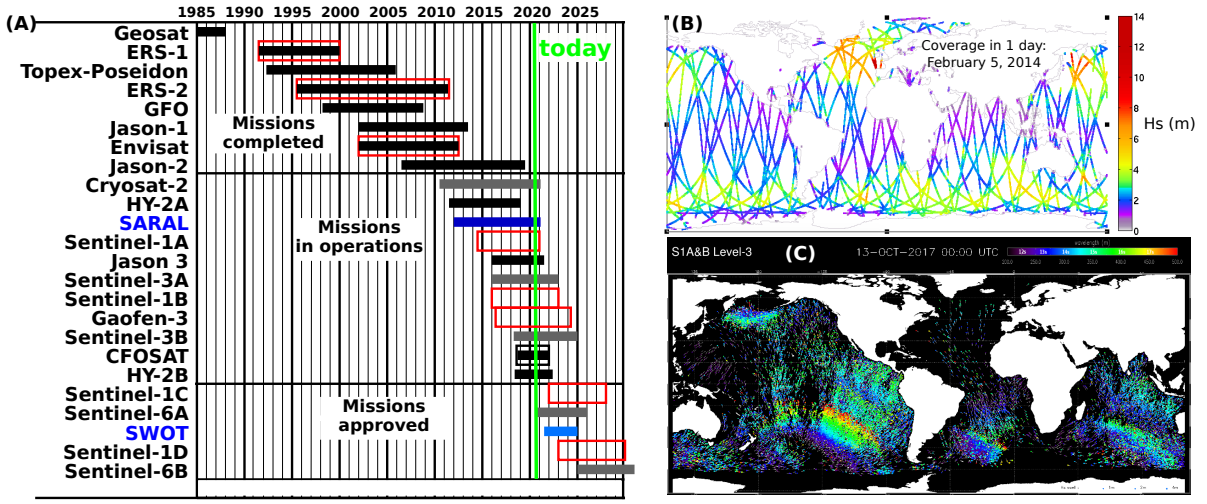

Figure 3.9: Satellite missions with sea state monitoring objectives.
Time coverage of satellite missions from 1985 to 2030, including nadir and near-nadir altimeters (solid bars), and missions monitoring ocean wave spectra (open boxes) using C-band Synthetic Aperture Radars (red), and real aperture radars in Ku-band (black) or Ka-band (blue). The lighter color (grey and blue) bars correspond to altimeters using Delay-Doppler processing. Source: CEOS database http://database.eohandbook.com/). (B) example of 1-day coverage for Hs measurements with 4 satellite altimeters (C) snapshot of a 'fireworks' plot, the showing the height (size of symbols) peak periods (colors), and directions (barbs) of swell partitions derived from Sentinel-1A and Sentinel-1B wave mode data. Such plots are produced routinely by CMEMS.

called a 'monostatic system'. Because the radar pulse has a finite duration which limits the resolution of the time measurement, it is customary to use a varying carrier frequency f_r that is modulated as chirps: f_r is increased linearly between f_0 and f_0+B during a radar pulse. This change in frequency allows to determine the precise time, within a pulse, when the echo was sent. As a result, the resolution in range dr is determined by the frequency bandwidth B, with $dr = c/(2B)$.

for all types of radars, it is thus better to use a larger bandwidth, but this is usually limited by atmospheric absorption windows or regulations. Hence, for satellite altimeters, B is limited to 320 MHz in Ku-band giving $dr = 48\ cm$, and and 500 MHz in Ka band, giving $dr = 30\ cm$. Because of issues with rain attenuation, all altimeters since GEOS-3 (1975-1979) have used Ku-band, in general jointly with another frequency, in C-band, except for the ongoing SARAL/AltiKa mission which uses only Ka-band.

Each radar pulse emitted by the radar antenna is reflected by a ocean area that expands with time, starting from the blue disk in the middle of figure 3.10.c, and expanding to the outer rings. The shape of the blue disk is only correct for a flat sea surface, and is distorted when waves are higher than dr. As a consequence, the power received by the altimeter grows with time, until the illuminated area falls out of the main lobe of the radar antenna. Because the rise-time typically spans a few range gates, the wave height typically comes from a region of the ocean that is between 4 and 7 km in diameter. In the case of the largest sea state in figure 3.10.a, the return power spreads over about 35 range gates, from number 26 to number 61, i.e. a distance of 10.5 m, close to the root mean square wave height $H_{rms} \approx H_s/1.4$. The power in range gates beyond 50 comes from the sea surface that is not directly under the satellite but on a circle around it, and is still illuminated by the radar beam.

Over a flat surface, the power rises very rapidly to a high value and decays. The decay is faster for a narrow radar beam as is the case on SARAL. Over a wavy surface, the radar receives echoes from wave crests firsts and wave troughs later: this difference in travel time between crests and troughs spreads the echoes over time. Brown (1977) showed how the shape of the 'waveform', i.e. the received power return, is generally (under a number of simplfiying assumptions) a convolution of the radar antenna pattern and the distribution of the surface elevation ζ. As a result, the slope of the 'wave form leading edge' is proportional to H_s.

Another interesting parameter that can be derived from the waveforms is the mean square slope (mss). Indeed, the backscattered power σ_0 is nearly inversely proportional to the mss (Vandemark et al., 2002). For display purposes the waveforms shown in figure 3.10 have been scaled: you can see that the

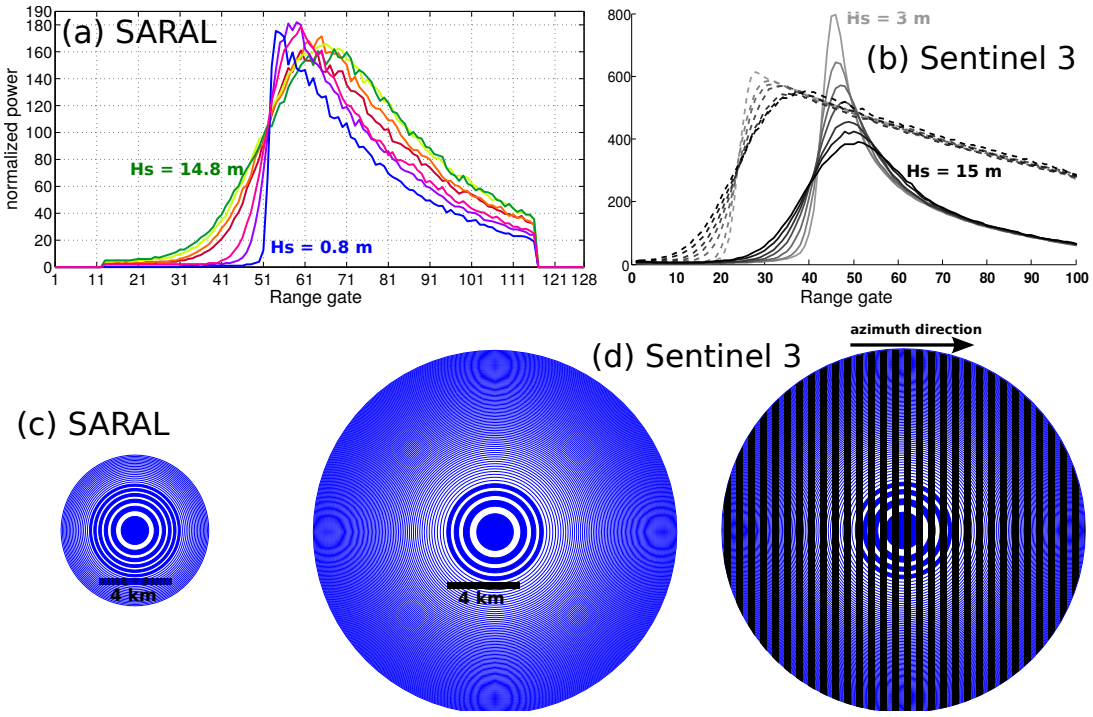

Figure 3.10: Altimeter waveforms and footprints

Example of altimeter waveforms for different wave heights. (a) These waveforms were selected along the ascending track of SARAL/AltiKa on February 5, 2014, beteen 05:29:49 and 06:20:07 UTC. Each waveform shows the the power measured by the radar as a function of time: time is discretized with intervals of 2×10^{-9} s corresponding to 30 cm range intervals usually called 'range gates'. The corresponding wave heights are 0.8, 3.2, 4.6, 9.7, 10.7, 13.2, and 14.8 m. Data is available from CNES/Aviso ftp. Each waveform shown here was obtained for 1 s of data, as the median of 40 conscutive waveforms. (b) Similar waveforms from Sentinel 3 using delay-only (dashed) and delay-doppler (solid) for Hs = 3,5,7,9,11,13 and 15 m, for cycle 23 orbit 349, on 25 October 2017 in the Pacific. (c) Spatial coverage of footprints corresponding to the 3-dB antenna lobe pattern, for an unrealistic flat sea surface with a uniform roughness, with the first 11 range gates painted alternatively blue and white, starting from center. (d) Footprint for Sentinel 3, with the 7 seven range gates colored blue and white, with the azimuth resolution of the Doppler processing indicated by the grey stripes.

noise level (power in gates 11 to 21) which should be nearly the same for all sea states is scaled to lower values for lower sea states that generally have low values of both H_s and mss. Because the mss is not a very common parameter in applications, many authors have derived empirical estimates of peak or mean periods from H_s and σ_0.

Finally it should be noted that the main application of the altimeters was the mapping of the sea surface height (SSH) for the determination of the geoid, and the measurements of ocean currents and tides. The measured mean sea level can be much more accurate than dr, thanks to averaging. Waves play an important role in the estimation of the mean sea level because of a range bias induced by wave non-linearities, that is on average of the order of 3 % of Hs (e.g. Minster et al., 1991). This is known as the sea state bias.

Also, because H_s and SSH are estimated jointly using a parametric fit to the waveform, there are important correlated errors in the two parameters (e.g. Dibarboure et al., 2014). As a result, without any particular editing or fitting of the waveforms, the variability of H_s at scales shorter than 80 km is expected to be mostly due to the error in the fitting procedure that can be associated to non-uniform radar backscatter and other effects.

3.5.2 delay-Doppler altimetry

Another principle that can be used to refine the position and/or to measure the velocity of targets along the satellite flight path is the Doppler effect, which also relies on a shift in frequency: targets ahead of

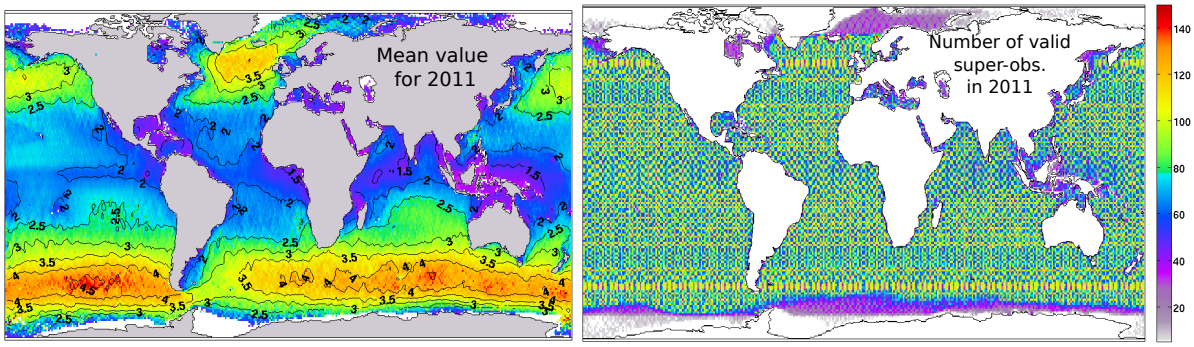

Figure 3.11: Global coverage of satellite altimeters
Over one day, the 3 satellites Jason 2, Cryosat 2 and SARAL/AltiKa covered all the oceans and seas with a density high enough to capture all the important storms. In a year, the full ocean is covered at a resolution of 1 degree in latitude and longitude. Data provided by ESA and CNES and processed by Ifremer. The spatial cover depends on the orbits shape. The number of tracks per 1 degree x 1 degree box (bottom panel) varies from 20 to 160 over a year: the coverage is less frequent close to the pole because Jason 2 has a more oblique orbit that does not cover the latitudes beyond 66 degrees. Also, sea ice produces echoes that differ from those of water and prevent the estimation of the wave height.

the radar are moving towards it, and hence have a higher frequency, while targets that are behind along the satellite path are moving away. Typical low Earth orbits give a satellite velocity around $V = 7$ km/s. Hence, a Ka-band system at 36 GHz frequency will see a Doppler shift of the order of $Vf_r/c = 840$ kHz, which is further reduced by the incidence angle θ_r. For a 0.5° antenna aperture, θ_r will normally vary between 0 and 0.5°, and the Doppler will be limited to 7.3 kHz.

A slicing of the radar echoes according to their Doppler shift allows a high-resolution mapping of the surface along the satellite track. This principle is used on Cryosat-2 and Sentinel-3, with a 300 m resolution along the track, as shown on figure 3.10.d. In that case the basic data has now one extra dimension, making a 'stack' of waveforms. For practical purposes, this stack is converted to a single 'SAR mode' waveform, such as the solid lines shown in figure 3.10.b. At such a resolution, the surface elevation due to very long swells propagating along the track can be resolved. A natural limit to this along-track resolving power is the fact that the sea surface is moving up and down with the waves. Indeed, an orbital velocity of $u = 2$ m/s gives a $uf_r/c =$ Doppler shift that can be mis-interpreted as a difference in incidence angle θ_r such that $(uf_r/c) = (V \sin\theta_r f_r/c)$, this corresponds to a horizontal displacement $uH_r/V \simeq 200$ m for a radar altitude $H_r = 800$ km.

3.5.3 Synthetic Aperture Radars (SARs)

As explained, in section 3.5.1, the separation of echoes in the range direction is easily achieved by combining the delay and frequency modulation of the chirped radar signal, with a resolution in distance that is thus controled by the frequency bandwidth. In the other direction (azimuth), the simultaneous echoes can be separated by their Doppler shift. This is perfect if targets are fixed relative to the ground, and a very good resolution can be obtained, both in the range and azimuth directions (about 10 m for Envisat, 5 m for Sentinel 1 in wave mode and 1 m in spotlight mode for TerraSAR-X). This processing produces a map of the surface backscatter in delay-Doppler coordinates. Unfortunately these positions are distorted from true geographic positions when the surface is moving toward the radar. With a vertical velocity w, targets are displaced by $\delta = w \cos\theta_i R/V$ along the azimuth direction. With a Sentinel-1 altitude $H_r = 693$ km and a typical speed over ground $V = 7.5$ km/s, when looking at an incidence angle of 23° the distance R is close to[2] $H_r/\cos\theta_i$ and the factor H_r/V is about 92 s^{-1}, i.e. a very small velocity $w = 10$ cm/s gives a displacement in azimuth of $\delta = 9.2$ m. A high speed train traveling at 100 m/s along tracks at 45° with the range direction at an azimuth angle of 23° has a radial velocity of 28 m/s, would be displaced 2.7 km in the azimuth direction, at a location that is 2 km *away* from the tracks! Figure 3.12 shows an example of targets displaced from their true locations according

[2]That approximation assumes a locally flat Earth. The exact value is obtained from the law of cosines in the triangle made of the satellite position, the target position and the center of the Earth, i.e. $R^2 + 2RR_e \cos\theta_i + R_e^2 - (H_r + R_e)^2 = 0$, where R_e is the radius of the Earth.

to their azimutal speed.

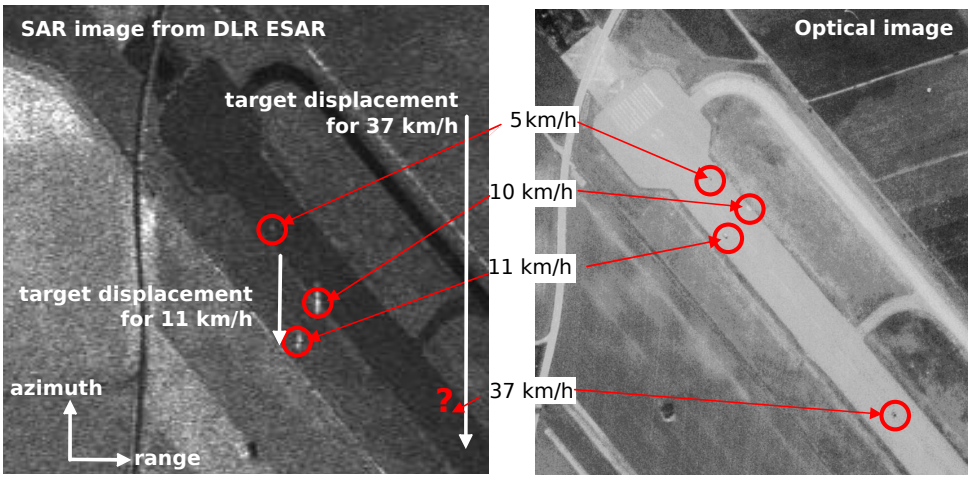

Figure 3.12: Where is the fast car? it is in the optical picture, but out of the SAR 'image'! Images of cars with different velocities along an airport runway in a nominally processed radar image (left) and a reference optical image (right), adapted from Palubinskas et al. (2005). The SAR acquisition was made from a Do-228 aircraft flying at only 88 m/s and altitude 3.94 km, giving a ratio $H_r/V = 44$ s^{-1}.

In the case of waves motion a velocity bunching effect appears, the echoes on the image are shifted from their actual position depending on the surface velocity towards the satellite creating a pattern of brighter areas, where the displaced targets are 'bunched together', and darker regions. This mechanism is often the main cause of the wave-induced σ_0 modulation in the open ocean. In ice-covered water, this is probably the only mechanism present that creates wave patterns in SAR images. This bunching in the azimuth direction is very similar to the light patterns at the bottom of a shallow pool that are caused by light refraction, as illustrated in figure 3.13.

In the case of a monochromatic wave train propagating in the azimuth (y) direction, with wavenumber k_y, and not located right under the satellite but at an icidence angle θ_i, the target displacement in the SAR image due to the velocity towards the satellite is

$$\delta = (W\cos(k_y y - \sigma t)\cos\theta_i + U\sin(k_y y - \sigma t)\sin\theta_i)\, H_r/(V\cos\theta). \tag{3.24}$$

where U and W are the amplitudes of the horizontal and vertical velocities given by eqs. (2.26)-(2.27).

Assuming a uniform radar power scattered from the sea surface σ_0, and taking the y dimension along the azimuth, the SAR image intensity is the incoherent sum at the displaced positions y' of the power coming from the true pixe positions y, it is thus given by the inverse of Jacobian of the transformation $y \to y' = y + \delta$, (see eq. 21 in Hasselmann and Hasselmann, 1991),

$$J = |dy'/dy|\,, \tag{3.25}$$

for a monochromatic wave of amplitude a it is,

$$I'_{SAR}(y) = \sigma_0/J = \sigma_0/\left|1 - C_{AR}\sin(k_y y - \sigma t)\right|. \tag{3.26}$$

The important parameter for image patterns is the coefficient c in Alpers and Rufenach (1979),

$$C_{AR} = k_y(W + U\tan\theta_i)H_r/V. \tag{3.27}$$

For $C_{AR} << 1$, eq. (3.26) can be linearized, but as C_{AR} increases, the SAR displacements become strongly nonlinear and for $C_{AR} = 1$, the Jacobian is zero and I'_{SAR} becomes infinite just like the light intensity at the focal point of a lens. In our figure 1.f, with a wave period of 10 s traveling in the azimuth direction, $C_{AR} = 1$ corresponds to an amplitude of the elevation $a = 0.42$ m, which, for random waves of the same energy would be a significant wave height $H_s = 4\sqrt{(a^2/2)} = 1.2$ m. For $C_{AR} > 1$, each bright line becomes a doublet. The two lines of the doublet progressively drift apart as the amplitude increases, pulling the minimum intensity to lower and lower values, up to the point where lines from different doublets meet, at $C_{AR} \simeq 4.6$. Beyond this value there is no region of very low intensity anymore.

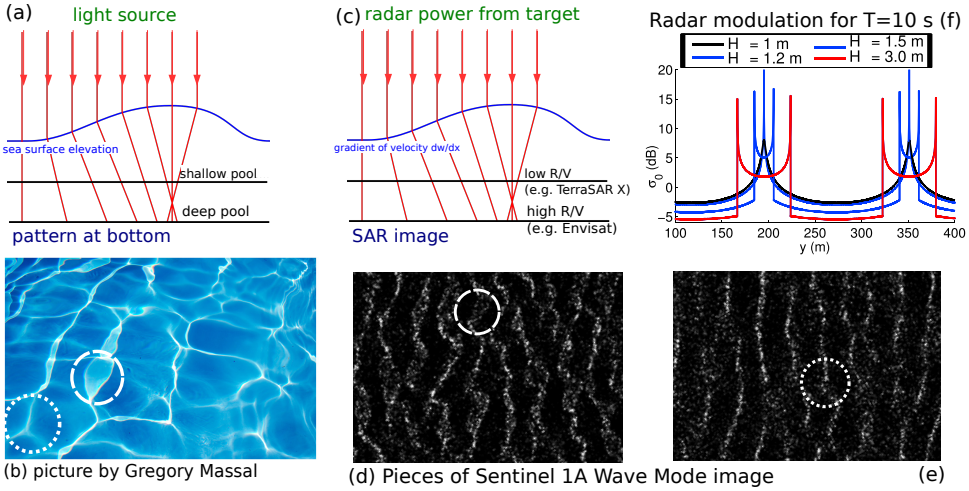

Figure 3.13: Patterns in SAR images
Analogy between (a,b) light patterns at the bottom of a shallow pool, and (c,d,e) velocity bunching effects in SAR images of ocean waves. (d) and (e) are taken from a wave mode Sentinel 1A image, acquired on 9 September 2014 at 04:48:16 UTC, at 10 and 35 km inside of the sea ice. In (d), almost all crests are doubled, for example in the region within the dashed circle. In (e) the lines are less bright and not doubled (for example within the dotted circle). This is easily simulated, as shown in (f), with the variations of image intensity expected from a sinusoidal monochromatic wave of wavelength 156 m (Adapted from Ardhuin et al., 2017a).

In practice, except far inside the sea ice cover, there are also short wave components in the wave spectrum $E(\mathbf{k})$. From a SAR processing point of view, these short waves are equivalent to Gaussian random vertical oscillations of $< v^2 >$ leading to random displacements in the SAR image that are larger than their wavelengths and that do not produce any pattern. These short waves also reduce the contrast of longer components. Hasselmann and Hasselmann (1991) gave a theoretical derivation of the impact of random waves on a SAR image spectrum $E_S(\mathbf{k})$, their eq. (55), with a simplified derivation by Krogstad (1992). In practice the short wave effect is a reduction in the image spectrum by an exponential factor,

$$E_S(\mathbf{k}) \simeq \exp(-k_y^2 < v^2 > H_r^2/V^2) E_l(\mathbf{k}) = \exp(-k_y^2 \lambda_c^2/(2\pi)^2) |M_S|^2 \left(E(\mathbf{k}) + E(-\mathbf{k})\right)/2, \quad (3.28)$$

in which $E_l(\mathbf{k})$ is a linearized spectrum, based on a modulation transfer function M_S that includes a linearized velocity bunching term, a hydrodynamic term due to the short scattering waves modified by longer waves, and a tilt term due to the change in local slope along long waves (Hasselmann et al., 1985a; Hasselmann and Hasselmann, 1991). All terms depend on the incidence angle, and these last two terms depend on the polarization of radar waves, horizontal or vertical, and on wind speed and wave age. The image is completely blurred at the scale of the random displacements and the resolution of 1 or 5 m is useless.

The azimuthal cut-off wavelength is $\lambda_c = 2\pi\sqrt{< v^2 >} H_r/V$, in which $< v^2 >$ is the orbital velocity variance. This cut-off effect is so dominant that it can actually be used to measure the surface orbital velocity variance from SAR images (Stopa et al., 2016c). A minor difficulty is the separation of the part of the wave spectrum that produces patterns in the SAR image and the shorter part that only introduces blurring. Looking at many ERS SAR data, Kerbaol (1997) concluded that, in the case of a wind sea, the velocity variance $< v^2 >$ should be restricted to waves shorter than a factor f_L times the peak wavelength, with $f_L \simeq 0.33$ for a mean short wave direction in the range direction and $f_L \simeq 0.15$ in the azimuth direction.

Combining all these effects with some empirically derived MTFs, it was possible to estimate the heights of swells within 25% of buoy measurements using wave mode data from Envisat (Collard et al., 2009). The full significant wave height, including the waves shorter than λ_c that are not resolved in the SAR image, can also be estimated by combining all image parameters (Li et al., 2011).

Several aspects of SAR processing are the subject of active research, including the measurement of high winds or currents, and improvements in the estimates of wave parameters in particular in ice-covered regions.

Figure 3.14 shows an example of waves around the ice edge: in the water (buoy S15), the waves

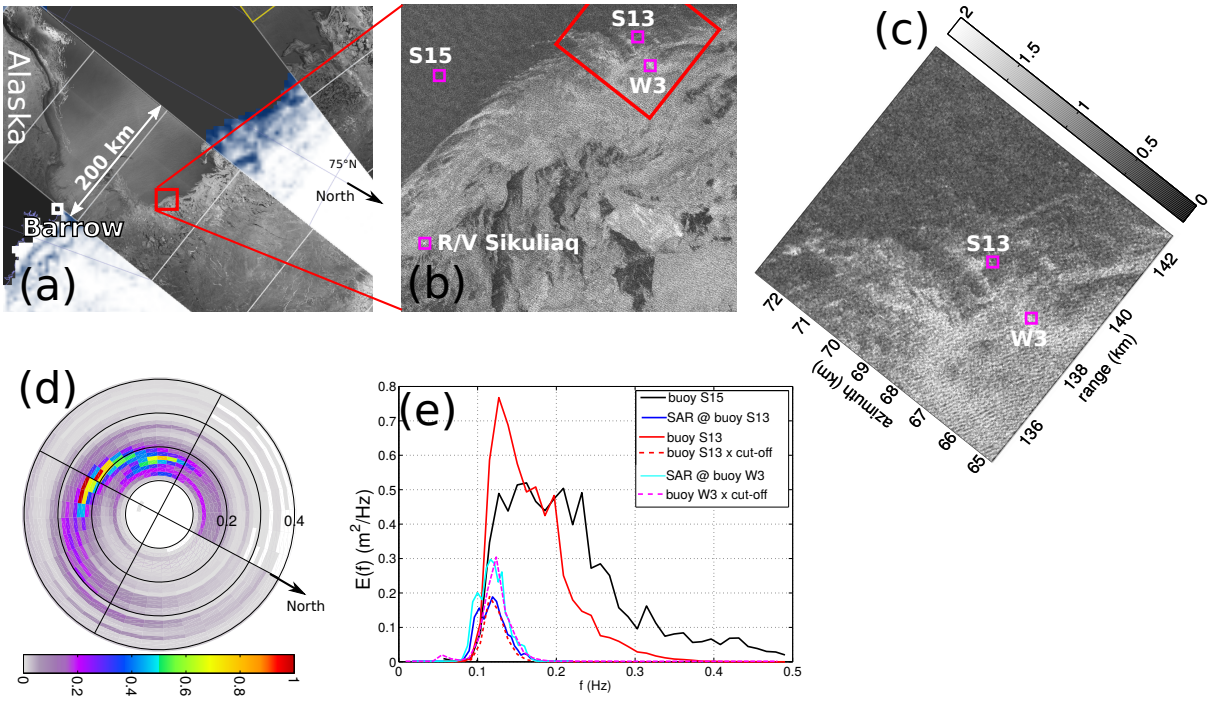

Figure 3.14: Context of the Sentinel-1A image acquired on November 1st, 2015, at 17:23 UTC, and available in situ data. The full image at full resolution can be viewed at http://bit.ly/22JFruo. (a) SAR-derived roughness (gray scale) showing open water between the Alaska shoreline, to the West of Barrow, and the measurement locations in the red box. (b) Location of the R/V Sikuliaq and some of the measurement buoys. Note that buoy S15 is in open water. (c) piece of the SAR image around the buoys S13 to W3. (d) Directional spectrum estimated from S15 data using the Maximum Entropy Method. (e) Comparison of spectra derived from in situ data and the SAR image around buoy S13 and buoy W3. In each panel the spectrum at the offshore buoy S15 is indicated for reference. The 'cut-off' effect is the reduction of wave spectrum according to eq. (3.28). Adapted from Ardhuin et al. (2017a).

cannot be seen by the SAR because, with a peak wavelength of 100 m, they are much shorter than the 290 m cut-off wavelength. Waves only appear in the ice with an increasing SAR spectral density which is not due to an increase in wave height, but a reduction in the cutoff wavelength from $\lambda_c = 114$ m at S13 to $\lambda_c = 87$ m at W3. Hence a correct estimation of λ_c is critical for a proper estimation of wave heights either in the open ocean or in ice-covered water. Another important practical problem, especially in ice-covered region, is the presence of non-wave features in the image: boats, slicks, variations in wind speed, leads in ice... these usually show up in the low frequency part of the spectrum, and, in figure 3.14 they probably are the reason for the spurious bump at $f = 0.1$ Hz.

Since SAR images are characterized by high resolution (5 m in the Sentinel-1 wave mode, 10 m in Interferometric Wide swath mode), and large coverage, they provide a unique opportunity to measure the spatial patterns in the wave field, as shown on figure 3.15.

3.5.4 The wave spectrometer and the matching wavefront technique

Whereas a SAR resolves the wave patterns in an image to produce a wave spectrum, it is possible to measure the 2D wave spectrum when high resolution – finer than half the wavelength – is only available in range, using the stationary phase technique.

When echoes are combined from narrow strip in range (red band in figure 3.16.a), the Fourier transform of these echoes in the range direction selects only the modulations by waves that are perfectly aligned with the direction θ_0 to which the radar is looking, all other components do not have this stationary phase and their modulations cancel out. Hence, the Fourier analysis of radar echoes provides a 1D spectrum $E(k, \theta_0)$ in the look direction. A successive acquisition in different directions provides the full directional spectrum $E(k, \theta)$. This is the principle of the wave spectrometer and it has been demonstrated with the airborne instrument RAWS, developed by NASA (Jackson et al., 1985), STORM

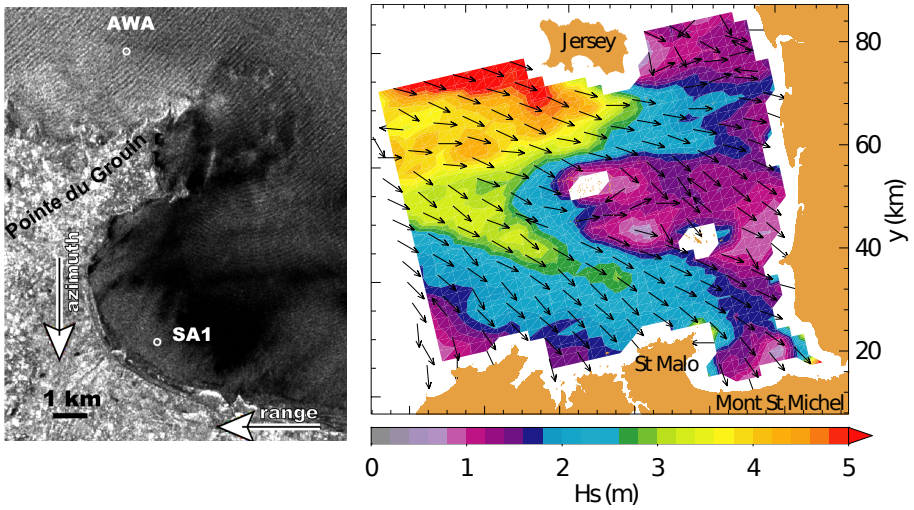

Figure 3.15: Left: Sample of a SAR image, recorded by Envisat on March 9 2003, over French coast. The grey level is a function of the radar cross section that is modulated by waves. Right: Full image processed into wave spectra, with significant wave height and peak direction. AWA et SA1 are positions of in-situ instruments, used for validation (Collard et al., 2005).

and KuROS developed jointly by CNES and CNRS (Hauser et al., 1992; Caudal et al., 2014). The first satellite wave spectrometer is SWIM, and it flies on the China-France Ocean Satellite (CFOSAT, Figure 3.16), which was launched on October 29, 2018.

For larger incidence angles, the measurements cover a larger area of the ocean, but there is more sensitivity to the wind speed in the radar back-scatter. Hence, the SWIM design is limited to 10 degrees of incidence. A larger incidence also requires a more powerful radar, because the reflectivity decreases with incidence angle.

It is also possible to analyze the Doppler of the backscattered signal, as done one KuROS. This additional measurement allows to remove the 180 degree ambiguity on the wave propagation direction, but it also provides an indepedant measuremnt of the wave spectrum via the orbital velocities, and finally it contains the signature of surface currents. This Doppler capability was included in the proposal for a sea Surface KInematics Multiscale (SKIM) that was submitted to the Earth Explorer 9 call of ESA, now under evaluation. Because the current velocity projection on the line of sight is increases for large incidence angles, the SKIM design goes a little beyond the SWIM incidence angles, with 12 degrees (Ardhuin et al., 2017b).

3.5.5 Grazing angle radar

Rotating radars are usually deployed at the coast, for ship traffic monitoring, or on ships, for navigation safety, providing a detection of ships, land, and sea ice. Most of these radar work in X-band, with a wavelength around 3 cm, but S-band can also be used. These radars also record many echos from the sea surface due to waves. This 'sea clutter' is another case of the saying, *somebody's noise is somebody else's signal*. The clutter greatly limits the detection of ships at sea, but wave and current information can be extracted from it (Young et al., 1985). Because of the low elevation afforded from a ship, the incidence angle is now grazing. Hence, the sea surface exhibits shadows behind wave crests and the relationship between the backscatter image and the sea surface is fairly nonlinear. Still, the wave spectrum may be related to the radar image spectrum using a transfer function (figure 3.17). The analyses procedure uses a sequence of several images, in order to decrease the noise. The 3D (frequency-wavenumber-direction) spectrum is estimated to filter the data into 'wave patterns' that follow the linear gravity wave dispersion relation, and other echoes and noise. This kind of system generally gives a good spectral energy distribution, but the gain (proportionality factor between the radar image spectrum and the surface elevation spectrum) is not very accurate, leading to typical errors of 20% or more on the estimate of H_s. An additional measurement form an altimeter, or a motion sensor giving heave or pitch/roll from a ship, can provide an independent measure of this gain. In systems that allow a measurement of the Doppler signal (e.g. Farquharson et al., 2005), the orbital velocities may be measured, but the radar really measures the velocities of scatterers which – at this incidence – contains also the phase velocities

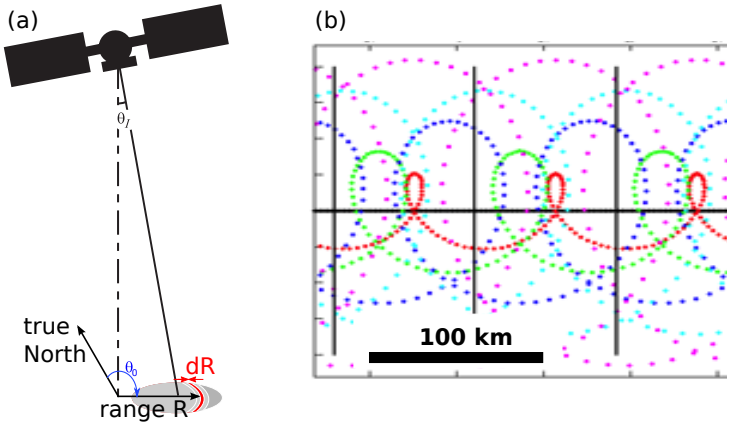

Figure 3.16: Measurement principle the SWIM radar that on CFOSAT. (a) geometry of the measurements for one cycle in direction θ_0. The resolution in range dR is of the order of 10 m, but the azimuth resolution is 18 km. Using different incidence angles θ_I (0, 2, 4, 6, 8 and 10 degrees) and rotating around the nadir provides estimates $E(k, \theta_0)$ in all direction θ_0. (b) Coverage of the SWIM instrument on CFOSAT: each colored dot is the center of a 19 km diameter footprint.

of steep waves.

A side-product of the dispersion relation analysis is are maps of surface currents, with sub-kilometer resolution, and water depth if the water is shallow enough. This is probably the best instrument available today for the measurement of sub-mesoscale currents over a footprint of about 10 km in diameter. A full exploitation of the dispersion relation can also provide an estimate of the vertical current shear near the surface (Lund et al., 2015).

3.5.6 Surface wave radar

An extreme case of grazing angle occurs when the radar waves propagate along the surface. This kind of propagation is possible in the HF-VHF range (from 2 to 50 MHz). This surface wave allows indeed to get information beyond the horizon.

The radar reflection is well explained by Bragg theory, with the maximum backscatter power at the Doppler frequency f_D occuring for electromagnetic incident and reflected wave numbers vectors $\mathbf{k}_i$ and $\mathbf{k}_r$ that match with the wavenumber $\mathbf{k}_w = \pm\mathbf{k}_i \mp \mathbf{k}_r$ and and the wave frequency $f_D = f$, where f and $\mathbf{k}_w$ are related by the linear dispersion relation. In the monostatic configuration where the receiving and transmitting antenna are almost at the same place, we have $\mathbf{k}_i = \mathbf{k}_e$, $\mathbf{k}_r = -\mathbf{k}_e$, and $\mathbf{k}_w = 2\mathbf{k}_2$.

The observed Doppler spectrum can be interpreted as the superposition of simple reflections (or first order reflections) and multiple reflections. The extraction of sea state spectra is possible from the second order that is a convolution of the spectrum (see for instance Wyatt, 2000). These second order echoes are weaker than first order echoes at Bragg frequencies.

The main echoes are used for currents measurement. Their frequency provides a measurement of the Bragg wave phase velocity. The deviation of this phase velocity from the expected linear wave phase speed can be interpreted as a surface drift current (Ardhuin et al., 2009a). This current also includes non-linear corrections to the phase velocity, which is like a filtered Stokes drift (Stewart and Joy, 1974; Broche et al., 1983; Ardhuin et al., 2009b). The secondary peaks, filled with black patterns, are caused by either the multiple reflection of radar waves, or the single reflection off nonlinear wave components. In some cases a peak can be seen at the frequency $\sqrt{2}f_B$ which corresponds to the reflection from the first harmonic of waves with wavenumber $\mathbf{k} = \pm\mathbf{k}_e$, which have a frequency, $2\sqrt{gk_e}$ in deep water. Because different wave components have different sensitivities to the current profile, it is possible to use that peak to measure the vertical shear of the current (Ivonin et al., 2004).

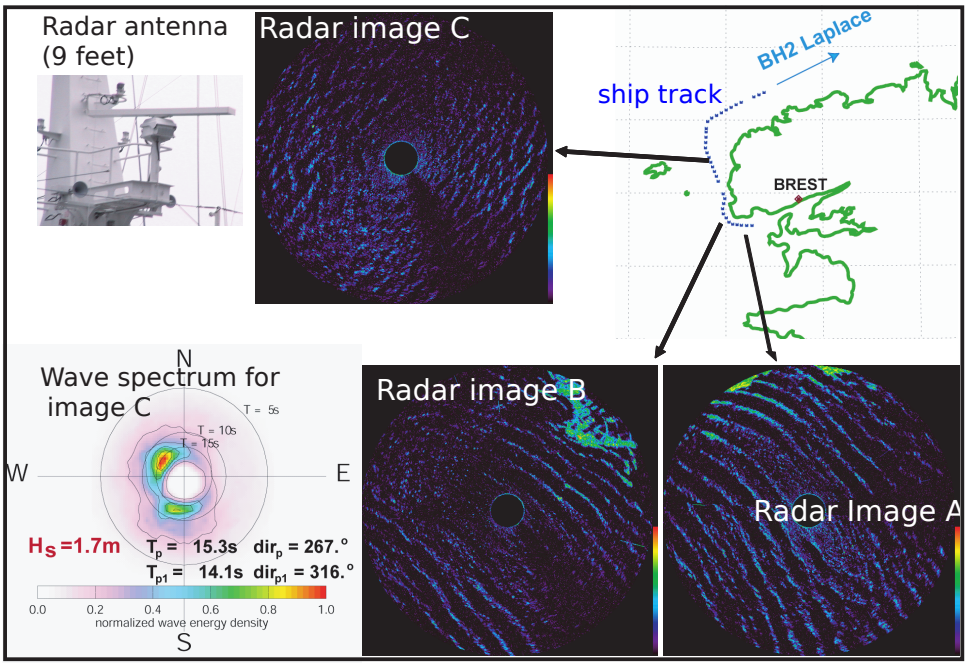

Figure 3.17: Examples of radar images recorded with a grazing radar (WAMOS system, Oceanwaves GmbH), onboard the Hydrographic vessel Laplace. The measurements were undertaken on March 2003, with a very long and high swell from the West ($H_s = 6$ m, $T_p = 26$ s). The spectrum shown here was obtained in the shadow of Ouessant. The swell forms two wave systems that go around the islands by the west and north directions.

3.6 The limitations to the usual spectral description of ocean waves

The spectrum describes the whole statistical properties of waves, provided the components are effectively independent. Yet, this is not exactly true as waves are slightly nonlinear. Two main relations exist between components: the presence of harmonics and the modulations. The first effects comes from the fact that a single nonlinear wave train corresponds to several spectral components whose wave number and frequency are multiple of that of the carrier wave. Rigorously speaking, one needs the 3D spectrum $E(f, \mathbf{k})$, see for example figure 3.8, to discern these harmonic waves that do not follow the linear dispersion. The 3D spectrum estimation requires specific instruments, mapping the surface in space and time. The link between the 3D spectrum and the linear part of the spectrum is the topic of ongoing research. The calculation technique of dressed and undressed spectrum presented by Elfouhaily et al. (2003) is a possible approach: the undressed spectrum corresponds to the linear part and the dressed part to the nonlinear spectral contents. To lowest order, however, the full spectrum can be obtained by the second order correction (Janssen, 2009; Leckler et al., 2015).

The modulation effect is a bit more complex. Typically, short waves in the presence of much longer waves see their environment modified. In particular, the apparent gravity felt by short waves is the standard gravity plus the vertical acceleration induced by the longer waves motion. In the same fashion, the long waves orbital velocities acts as a variable current on the short waves. These effects are one of the likely causes of the higher breaking rate of short waves at the crest of long waves (Dulov et al., 2002; Guimaraes, 2018). The short wave spectra is hence modulated by the long waves. In practice, for the wind sea, such effects are weak for waves with frequency less that three times the peak frequency (Banner et al., 1989). This factor 3 on the frequency corresponds to a factor 10 on the wavelength (in deep water).

Modulations can be caused by other effects than the presence of other waves. In particular, if the medium in which the wave propagate is not homogeneous, then the wave field will contain wavelengths that are interferences between the medium and the waves, and that do not correspond to the linear dispersion relation. These non-homogeneities can be variations in water depth, current, gravity, surface tension ... If these occur at scales similar to the wavelength, the result will be a scattering of the waves,

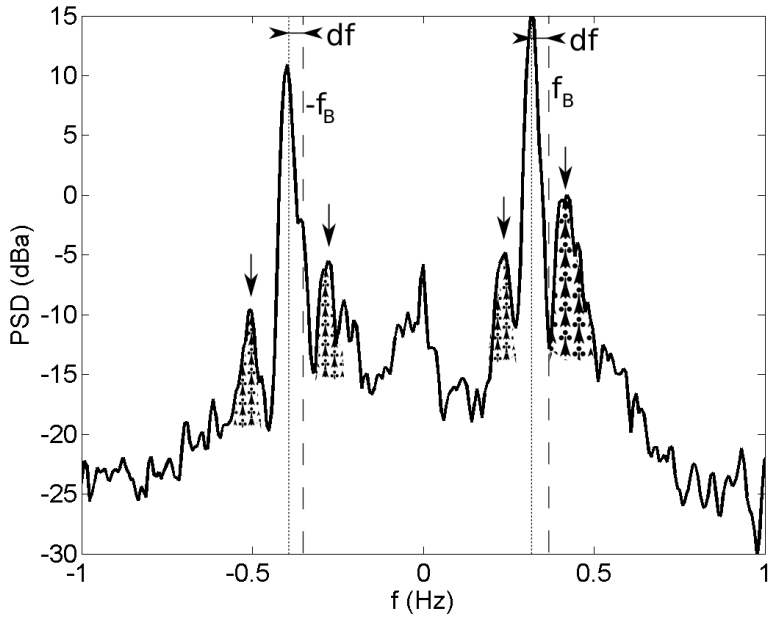

Figure 3.18: Example of Doppler spectrum from a HF radar.
This measured spectrum comes from the Porspoder radar (Finistere, France). The radar frequency is 12.4 MHz, corresponding to a wavelength $L_e = 2\pi/k_e = 24$ m. The main echo is due to Bragg scattering, which selects the ocean waves with a wavelength $L_e/2 = 12$ m that propagate towards ($f > 0$) or away from the radar ($f < 0$). Multiple scattering by waves with wavenumbers $\mathbf{k}_1$ and $\mathbf{k}_2$, such that $2\mathbf{k}_e = \mathbf{k}_1 + \mathbf{k}_2$ gives the 'second order echoes'. At first order, i.e. for linear waves, the waves of wavenumber $k_w = 2k_e$ have a frequency $f_B = \pm\sqrt{g2k_e} = \pm 0.36$ Hz in deep water. The anomaly df of the two highest peaks in the Doppler spectrum indicate that the phase speed $2\pi f/k$ is different from the linear wave theory without current. the main reason for that difference is usually the presence of a current, with a velocity $U_r = 2\pi df/(2k_e)$ in the direction of the radar.

such as the Bragg scattering caused by underwater topography that is described in chapter 12, or the generation of seismic waves over a sloping bottom in chapter 21.

Chapter 4

Measured waves: main parameters and wave spectra

A casual observation of the sea is enough to figure out that, the stronger the wind, the higher the height H and length L of the waves. From one location to another, it is also obvious that L and H change with the water body: a large lake can hold bigger waves than a pond, and waves in the Pacific, the largest water body on Earth, can reach close to 40 m high, with wavelengths above 600 m. Finally, within the same water body, the heights and lengths increase when moving downwind. The present chapter aims at providing a quantitative summary of observed wave properties, including useful empirical prediction formulae. These were the basis of wave forecasting methods (e.g. Pierson et al., 1955) before the advent of numerical models (Gelci et al., 1957).

4.1 Wind-sea growth

A wide range of visual observations were systematically gathered by Sverdrup and Munk, as early as 1941, in order to come up with a wave forecasting method for the U.S. Navy, faced with the delicate task of landing on the swell-battered beaches of Morocco. This work, initially classified, was only published as a landmark report after the war (Sverdrup and Munk, 1947). The miscelaneous observations were organized thanks to dimensional analysis with wave variables H and T expressed as a function of the wind speed U_{10} as measured at 10 m above the sea surface, the fetch X, the duration t over which of the wind has blown and the acceleration of gravity g. The fetch X is the length of the region over which the waves have been generated. In the open ocean X is not easy to define precisely, and it can be taken as an order of magnitude, in relation with a representative wind speed U_{10}: the region where winds are very high is typically smaller than the region where winds are lower, so that the choice of the wind speed will modify the fetch.

The use of U_{10} as the variable representing the strength of the wind is also fairly arbitrary. Many studies have debated the possibly better choice of the friction velocity in the air, $u_{\star a} = (\tau_a/\rho_a)^{1/2}$. unfortunately, the scatter of wave parameters as a function $u_{\star a}$ is almost as large as when U_{10} is used. Since U_{10} is more often measured than $u_{\star a}$, it turns out to be more practical.

In the most simple case, represented in figure 4.1, a uniform wind speed blowing perpendicularly offshore from a straight shoreline. In such conditions Sverdrup and Munk found that we may express the dimensionless wave energy $\widetilde{E} = H^2 g^2/U_{10}^4$, as a function of the dimensionless fetch

$$X^\star = Xg/U_{10}^2 \tag{4.1}$$

and duration

$$t^\star = tg/U_{10}. \tag{4.2}$$

A similar result was obtained for the dimensionless wave period $1/f_p^\star = Tg/U_{10}$. For random waves, it is now customary to use

$$E^\star = Eg^2/U_{10}^4 \tag{4.3}$$

and

$$f_p^\star = f_p U_{10}/g \tag{4.4}$$

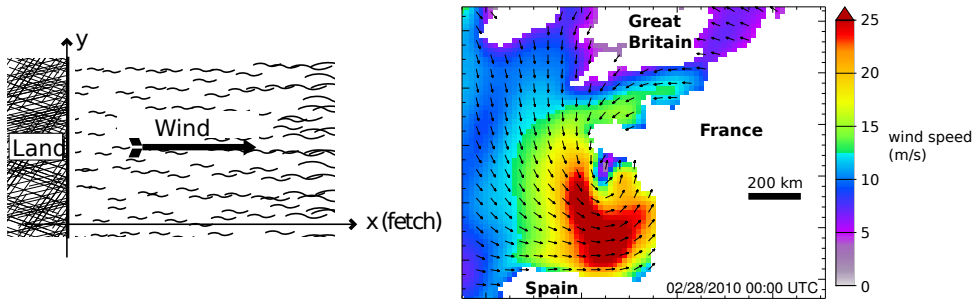

Figure 4.1: Definition of fetch.
Left: idealized conditions, Right: a real case corresponding to the 2010 Xynthia Storm, which caused severe coastal flooding in France: the wind speed varies rapidly in space and time, making it very difficult to define a fetch for an equivalent constant wind. The Xynthia storm crossed the bay of Biscay in 6 hours going to the North-East, as a result the waves had little time to develop.

where E and f_p are the free surface elevation variance and the frequency of the elevation spectral peak, respectively. Figure (4.2) shows values measured for $t^\star > 10^5$, for which the sea state does not depend on duration anymore, during the Shoaling Waves Experiment (SHOWEX) in 1999, off the North Carolina Outer Banks. The figure also includes a comparison with the average measured values during other experiments Kahma and Calkoen (1992); Kahma (1981).

4.1.1 Full development and wave age

For large fetches, the wave energy and peak frequency appear to tend to an asymptotic limit. This is very difficult to verify for moderate to strong winds, because the required non-dimensional fetch $X_0^\star = 2.2 \times 10^4$ is already 220 km for $U_{10} = 10$ m/s. In practice we have very few observations for steady and uniform winds over a non-dimensional fetch larger than $X^\star > 10^4$. In search of such conditions, Pierson and Moskowitz (1964) have carefully selected 55 records obtained from weather ships. From these measurements they estimated the asymptotic values

$$E^\star = 0.00402 \tag{4.5}$$

and

$$f_p^\star = 0.123. \tag{4.6}$$

The stage of development of waves, limited by fetch or duration, can be defined by the wave age,

$$A = C_p/U_{10} \tag{4.7}$$

where $C_p = 2\pi f_p/k_p$ is the phase speed at the peak of the spectrum. This parameter can be used to separate the wind sea, which is generated by the local wind and corresponds to young waves, with ages less than 1.2, and swell, for which the local wind has almost no effect, and which corresponds to older waves, with ages larger than 1.2. Donelan et al. (1992) showed that the wave growth stops or at least becomes very slow, when $C_p/U_{10} > 1.2$, confirming the analyses of Pierson and Moskowitz (1964). This means that, for a fully developped sea state, the dominant waves are propagating 20% faster than the wind speed.

4.1.2 Fetch limitation

The region where the wind is faster than a given value of U_{10} is always finite. This can limit the wave energy and peak frequency to a value lower than what would happen in a larger region. A practical important problem is the actual value reached by the wave height and peak period is such a limited area. With the non-dimensional fetch at full development $X_0^\star \simeq 2.2 \times 10^4$, all measurements lead to empirical wave growth formulae that are close to

$$C_p/U_{10} \simeq 1.2 \left(\min \left\{ \frac{X^\star}{X_0^\star}, 1 \right\} \right)^{0.33}, \tag{4.8}$$

$$H_s \simeq 0.26 \frac{U_{10}^2}{g} \left(\min \left\{ \frac{X^\star}{X_0^\star}, 1 \right\} \right)^{0.5}. \tag{4.9}$$

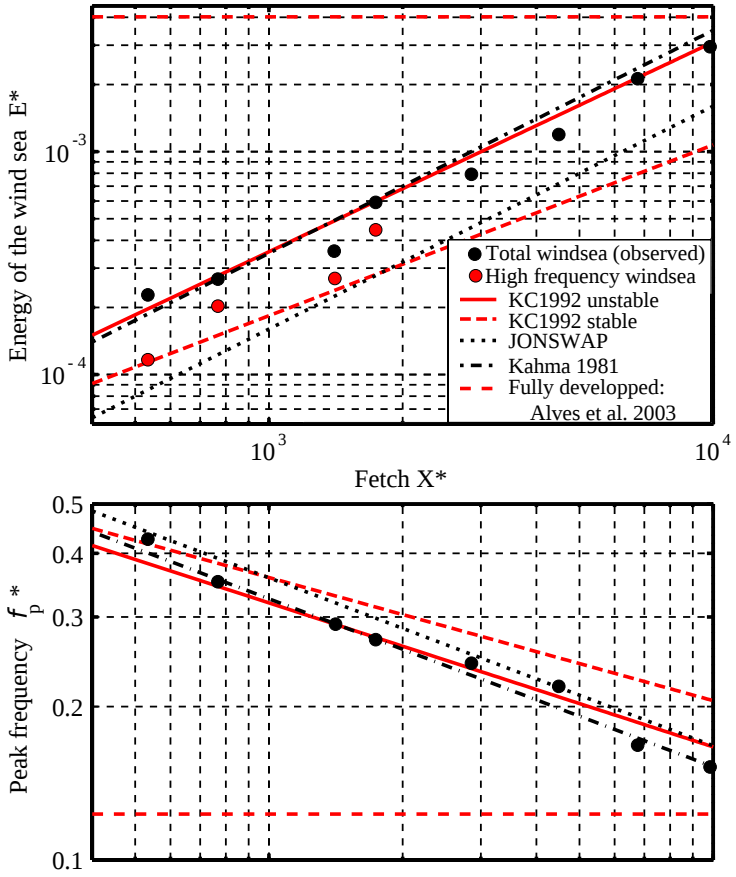

Figure 4.2: Growth of waves with fetch, measured during SHOWEX. The wind is blowing at an angle of 70 degrees relative to the shoreline, which generates a double peak in the wind sea for the shortest fetches. Very close to shore, the high frequency part of the wind sea (in red) is in the wind direction, while an 'alongshore wind sea' (in black) grows to lower frequencies, in the direction of the largest available fetch. For comparison, several empirical growth curves are superimposed, as given by Kahma et Calkoen (1992), and Kahma (1981) from other datasets, and the expected 'full development' proposed by Pierson and Moskowitz (1964), as re-analysed by Alves and Banner (2003).

We remember that in deep water,

$$T_p = \frac{2\pi C_p}{g}, \tag{4.10}$$

which yields T_p from C_p.

The empirical growth laws (4.8)–(4.9) are a practical set of equations to obtain a quick estimate of the order of magnitude of the sea state, with heights within a factor two of the measurements, as shown in figure 4.2. Many variants of thes equations have been published, with numerical values of the proportionality coefficients that may vary by a factor 2 (Kahma and Calkoen, 1992). These differneces are probably due, among other things, to the variations of the wind which is never exactly stationary nor uniform, and not exactly perpendicular to the shoreline... which is itself never quite straight and infinitely long. A careful analysis by Young (1998) reveals that some of the differences between the different datasets may be due to differences between the air and sea temperature, which modify the properties of the turbulence in the atmospheric boundary layer. The details of how that impacts the wave growth is still not understood. One possible factor is that the wind tends to be less regular (more gusty) in unstable conditions when the water is warmer than the air. It is well understood that this increased gustiness can lead to higher waves for mature waves ($X^\star > 10^4$, see Abdalla and Cavaleri, 2002).

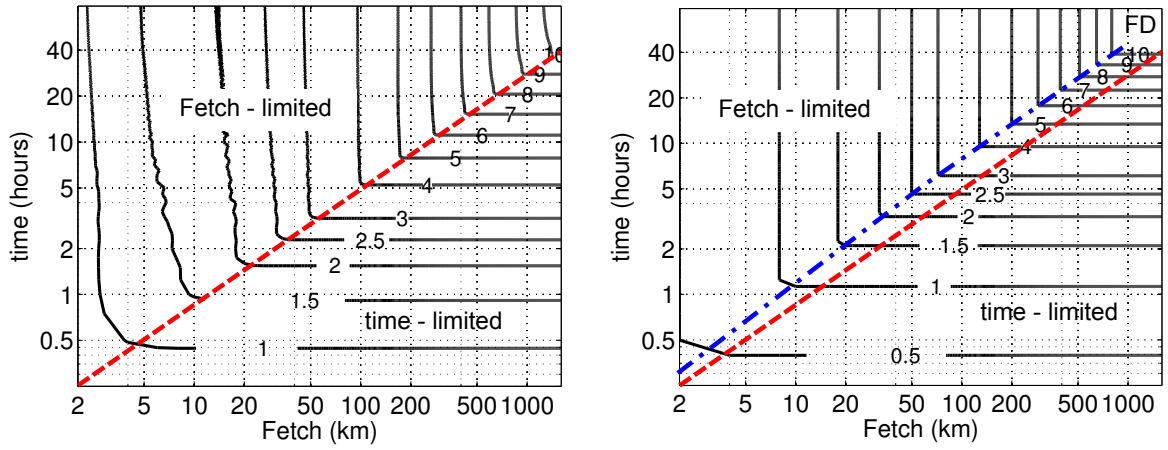

Figure 4.3: Estimation of significant wave height (H_s, contours) as a function of fetch and duration for the idealized case of an infinitely long coast with a wind blowing perpendicularly offshore at a speed $U_{10} = 20m/s$. In the left panel the estimate is given by a numerical integration of the wave action equation, defined in the next chapter, using parametrizations for the wind-wave growth and dissipation from Rascle and Ardhuin (2013) and non-linear wave-wave interactions from Hasselmann et al. (1985b) using the WAVEWATCH III model, with a third order numerical scheme Tolman (1995). The right panel combines eq. (4.9) and eq. (4.11). Both give the time-limited growth for large fetches and the fetch-limited growth for large durations, with no more growth when waves reach full development at $H_s \simeq 10.8$ m. The dashed line is the same in both panels. In the left panel, the model gives a slow increase of the wave height even after the time limitation has been exceeded: this is because the infinitely long shoreline allows the growth of very oblique components that travel very long distances alongshore. That effect is not represented in the empirical formula of eq. (4.11). It is a well documented effect for oblique fetches when the wind is not perpendicular to the coast (Ardhuin et al., 2007), but there is no description of this phenomenon for winds perpendicular to shore.

4.1.3 Time limitation

If the wind has started to blow only a short time ago, with $t^\star < 10^5$, the sea state parameters can be estimated, replacing $X^\star$ by

$$X' = (t^\star/70)^{1.3}. \tag{4.11}$$

4.1.4 Double limitation

In practice, the sea state is often limited by both time and fetch. The sea state parameters are then given the lowest of the two values for H_s and C_p/U_{10} between the one obtained with $X^\star$ and the one obtained with X' (see CERC, 1977). For an alternative estimation, one may read Hwang and Wang (2004). This double limitation is illustrated by figure 4.3.

4.2 Swell

In addition to the wind sea, which is related to the local wind, the sea state often contains an important swell contribution, which are waves radiating away from their area of generation. Swells are defined as the waves for which the source of energy from the wind is zero or negative, in practice it corresponds to waves travelling at a phase speed C faster than the wind speed U_{10}, or at angle relative to the wind $\theta_w - \theta_u$ such that $U\cos(\theta_w - \theta_u) < C$. This definition is often extended to allow the peak of a fully developped wind sea, which can travel at a phase speed of 1.2 U_{10}, to be classified as wind sea. This extension is equivalent to adding the source of energy from the nonlinear wave-wave interactions to the source of energy from the wind in order to separate wind seas and swell. Because the wind is neither steady nor uniform the boundary between wind sea and swell is rather fuzzy.

Swells is most important in large oceanic basins, in particular near their eastern boundary as the dominant winds generally blow from west to east where it can account for more than 90% of the wave energy (e.g. Chen et al., 2002). The swell is the part of the sea state that cannot be amplified by the

local wind because they are too fast, or travel at an angle too oblique to the local wind. This swell can be composed of distinct individual swells, travelling in different directions and with different dominant frequencies, these swells are the result of the evolution of wind seas that propagate out of their generation area. Swells, when they exist, generally have longer periods than the wind sea because short waves are rapidly dissipated away from their generation area. They are thus the result of storm conditions, with winds strong enough to generate large period waves, as given by eq. 4.8. The stronger and larger the storm, the longer the swell period.

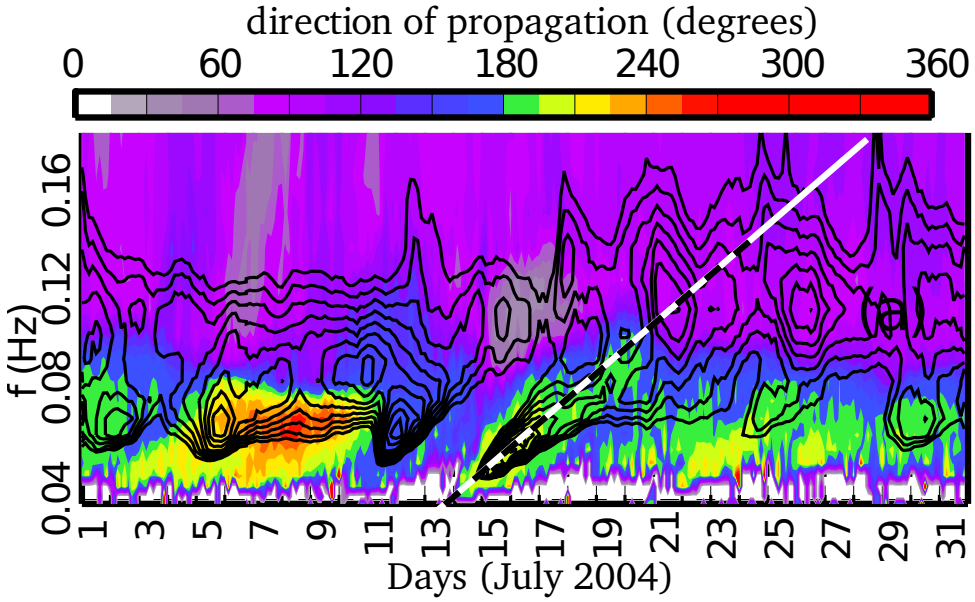

Figure 4.4: Example of the evolution of wave energy and mean direction as a function of frequency and time, over one month, measured at the Christmas Island buoy (Kiritimati, Kiribati), in the middle of the Pacific. Contour values equally spaced between 0.1 and 1.4 correspond to the logarithm of the spectral density $E(f)$, colors correspond to the mean direction for each frequency. The oblique dashed line from 15 July at 0.05 Hz to 18 July at 0.8 Hz correspond to eq. (4.12) with a distance $R\alpha = 6100$ km between storm and observation point. The intersection between this line and the axis $f = 0$ gives the date of the storm: July 9, when a severe storm was indeed present south of New Zeland. (taken from Collard et al., 2009).

Modern swell studies started during the colonial war between France and Morocco in 1906. In the absence of safe harbors on the atlantic coast of Morocco, the disembarkment of troops and supplies used small shuttle boats that could be destroyed by heavy swells. Such an event made the harbor of Casablanca unavailable for several months. Swell forecasting for Morocco became a an important matter, and the first method was based on the propagation of swells from the mid-atlantic Azores Islands where visual observations were made several times a day (Gain, 1918). This method was used in the swell forecasting office of Casablanca in the early 1920s (Montagne, 1922), where the first modern numerical wave models were invented (Gelci et al., 1957).

In the Pacific or Indian oceans, it is very common to find at the same time and place several swells coming from distinct storms (e.g. Figure 3.4), that may have happened 10,000 km away and a week before (Darbyshire, 1957; Munk et al., 1963). Owing to the large distances travelled by swells, the sphericity of the Earth must be taken into account. The re-derivation of linear wave theory in that case shows that the swell that propagated along a straight line on a flat ocean, now travel on the shortest path on the sphere, which are the great circles: the circles that have their centers at the center of the Earth, such as the meridians.

The height and period of swells depend on the height and period of waves in the strom, and the propagation distance outside of the storm. Storms generate waves with a wide range of periods up to about 1.2 times the peak period T_p. This mixture of waves 'disperses', and because the group speed $C_g = gT/(4\pi)$ in deep water, is a function of the period T, the largest period swell arrive first, followed by shorter swells. At very large distances, the storm from which the swell radiates can be considered a

point in space and time. The evolution of the peak period at a remote observatiokn position follows,

$$T_{\rm ps}(t) = \frac{4\pi R\alpha}{g(t-t_0)}, \tag{4.12}$$

where R is the Earth radius, t_0 is the time of the storm, and α is the spherical distance, i.e. the angle – in radians – at the center of the Earth between the storm and the observation point. This relationship very well verified, as shown in figure 4.4.

Swell heights decrease during propagation due to the dispersion from the source, and also due to dissipation. Dispersion is the main effect for swell periods larger than 12 s, and corresponds to a stretching of the wave fronts in the direction perpendicular to propagation, just like circles becoming larger away from a stone dropped in a pond. There is also a stretching of the wave train in the propagation direction due to the different group speeds, the longer wave periods contribute to a longer wave train away from the storm, while the shorter wave periods are travelling slower behind. This spatial spreading of the swell field is illustrated with numerical model results in figure 4.5, taken from Delpey et al. (2010). Neglecting

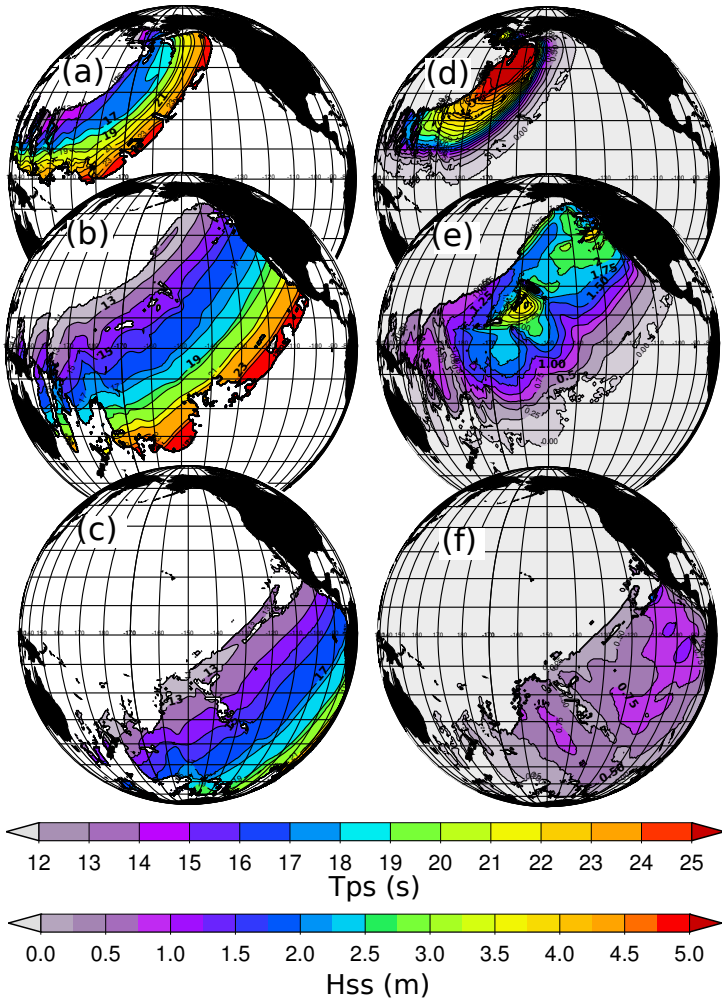

Figure 4.5: Swell radiated from a storm.
(a,b,c) peak periods of the swell T_{ps} and (d,e,f) significant swell heights H_{ss} from a realistic numerical model of the storm of February 24, 2004, centered at (160° E, 42° N). The maps correspond to February 27th (top) March 1st (middle) and March 6th (bas) at 00h UTC, which is 3, 6 and 9 days after the storm (reproduced from Delpey et al., 2010).

dissipation effects, and for distances of the order of 4000 km or more from the storm center, the decrease in swell height following the peak in space and time is given by

$$H_{ss}(\alpha) = H_{ss}(\alpha_0)\sqrt{\frac{\alpha_0 \sin\alpha_0}{\alpha \sin\alpha}}. \tag{4.13}$$

In practice, the height is further reduced by islands and continents where it breaks and dissipates on the shore. Dissipation in deep water is locally weak but can add up to a significant effect over long propagation distances (Ardhuin et al., 2009a). Even with these effects, it is possible to record swells coming from the antipodes (e.g. Munk et al., 1963).

4.3 Frequency spectra

4.3.1 The early days

The first measurements of wave spectra from time series were performed in 1944, as part of the efforts of Group W at the British Admiralty, after the amphibious assault on Normandy (Barber et al., 1946; Ursell, 1999). These records, and the many others that followed, revealed that for frequencies above the spectral peak, the decrease in energy takes always the same form. Phillips (1958) introduced the idea of an equilibrium region for $f > f_p$, and proposed that gravity was the only determining factor for that part of the spectrum which was controlled by wave breaking. Dimensional analysis leads to the shape

$$E(\sigma) = \alpha_P g^2 \sigma^{-5} \quad \text{soit} \quad E(f) = \alpha_P \, (2\pi)^{-4} \, g^2 f^{-5}, \tag{4.14}$$

where $\alpha_P \approx 0.008$ is now called Phillips' constant. The non-dimensional energy $E(\sigma)\sigma^5/g^2$ is constant in this model: the surface is thus fractal without any particular scale. In other words, these waves are self-similar and have all the same shape, whether they are large or small. These ideas were also developed

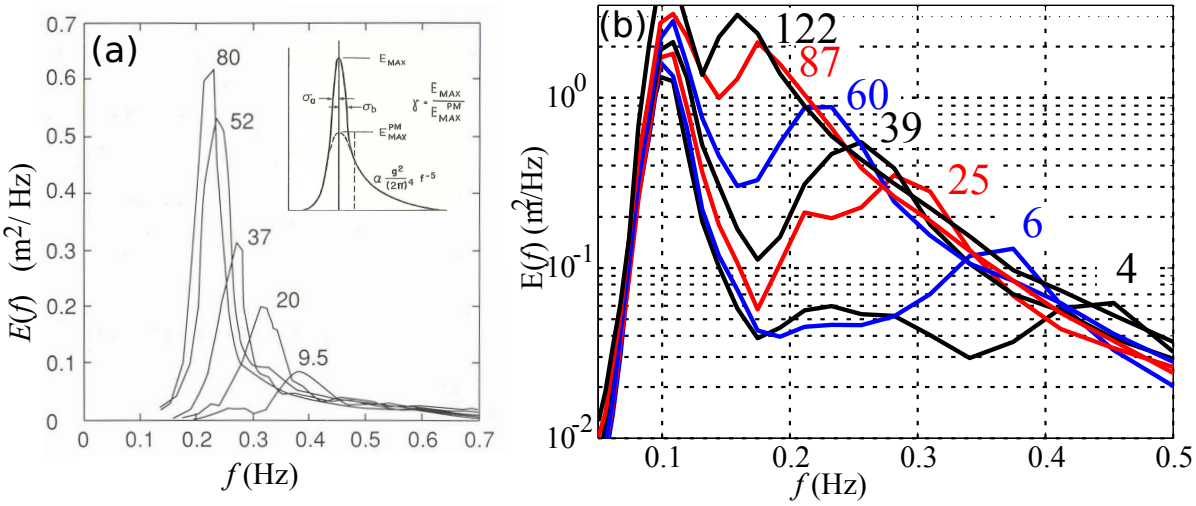

Figure 4.6: Evolution of the wave spectrum with fetch.
(a) measured spectra on September 15, 1968 at 11h during JONSWAP, with, inset, the proposed parameters for the JONSWAP spectrum. Numbers indicate the fetch in kilometers. (b) spectra measured on November 3rd, 1999, averaged from 13h to 17h during SHOWEX, using Datawell Mark III waverider buoys. Note that the scale is logarithmic. In the SHOWEX case, the wind speed is 10 m/s, 20 degrees from the shore-normal. The peak around $f = 0.1$ Hz corresponds to swell arriving from the Atlantic, against the wind. The instrument at the shortest fetch reveals two peaks in the wind sea, at 0.25 and 0.45 Hz. The analysis of wave directions, not shown here, show that the first peak is propagating alongshore, and the second is in the wind direction. The existence of the first peak is due to the oblique 20° angle between the wind and the shore-normal.

by Kitaigorodskii (1962), and led Pierson and Moskowitz (1964) to propose an empirical shape for the full spectrum, based on fully developed sea states,

$$E(f) = E_{PM}(f) = \alpha_P g^2 \, (2\pi)^{-4} \, f^{-5} \exp\left[-\frac{5}{4}\left(\frac{f}{f_p}\right)^{-4}\right]. \tag{4.15}$$

At short fetch, it was soon realized that this spectral shapes could be significantly different. The peak is particularly narrower for young sea states. Also, the values of the spectral density $E(f)$ for a given frequency f can be larger than those found for old seas: this overshoot of the spectral peak was first

discussed by Barnett and Sutherland (1968), and further investigated during the 1968-1969 Joint North Sea Wave Project (JONSWAP, see Hasselmann et al., 1973), figure 4.6).

Based on these observations, a 'peak enhancement' was added to the Pierson-Moskowitz (PM) shape,

$$E(f) = E_{PM}(f)\gamma^{\exp\left[\frac{-(f-f_p)^2}{2\sigma_{A/B}^2 f_p^2}\right]}. \tag{4.16}$$

This may look a bit complex, but each parameter plays a fairly clear role, illustrated in figure 4.6.a. $\gamma \simeq 3.3$ is the 'peak enhancement-factor', if equal to 1 then the spectrum is a PM spectrum, $\sigma_{A/B}$ is the relative width over which this enhancement applies. It was found that $\sigma_A \simeq 0.07$ if $f < f_p$ and $\sigma_B \simeq 0.09$ otherwise. Using (4.16) and (4.8) one can estimate C_p and $f_p = g/(C_p 2\pi)$ as a function of the wind speed. This gives the average spectral shape measured in the North Sea during JONSWAP.

4.3.2 The modern era

More recent obvservations, starting with Toba (1973), have shown that, at frequencies between f_p and $3f_p$, the spectrum was not following f^{-5} but f^{-4}. This shape can be obtained by including the wind speed or friction velocity in the dimensional analysis, it also corresponds to a constant flux of energy towards high frequencies due to the non-linear wave-wave interactions. In passing, we can see that it is always easy to find a theory for anything after the observations have been made. This f^{-4} decrease near the spectral peak is particularly well verified by the wave gauge array data of Donelan et al. (1985), which was one of the first clean measurements of the spectrum in both frequency and directions. Donelan et al. (1985) also proposed a spectral shape that reconciles the peak enhancement of the JONSWAP data with the mature wave spectral shape of Pierson and Moskowitz (1964). The adjustment given here in eq. (4.8) is an adaptation by Elfouhaily et al. (1997), giving the proper asymptotes for wave energies and periods. Further analysis by Long and Resio (2007) have shown that there is in general a transition from f^{-4} at frequencies above the windsea peak to f^{-5} at higher frequencies, and the frequency where this transition occurs appears to be a function of wave age.

This discussion of the detailed shape of the wave spectrum at frequencies beyond $2f_p$ may sound unimportant because it affects a very small fraction of the wave energy. However, that part of the spectrum supports most of the energy flux from the wind to the waves, and thus defines the roughness of the sea, and thus the growth rate due to the wind for the entire spectrum. Also, these short waves dominate the surface slopes, which strongly affect ocean remotely sensed properties such as sea level, surface salinity and wind speed and direction. Measurements of the sun reflection by the ocean performed by Cox and Munk (1954) give a very good estimate of the mean square slope (mss),

$$\text{mss} = \int \left(k_x^2 + k_y^2\right) E(k_x, k_y) \mathrm{d}k_x \mathrm{d}k_y \simeq \int \frac{(2\pi f)^4}{g^2} E(f) \mathrm{d}f, \tag{4.17}$$

where the second equality uses the linear wave approximation. In order to have a finite value of the mss, $E(f)$ must decrease faster than f^{-5} towards the high frequencies. Elfouhaily et al. (1997) and Kudryavtsev et al. (1999) have used this argument and detailed remote sensing data to propose a parametric shape of the wave spectrum that is a function of wind speed and wave age, and includes a strong decrease for $k > 10k_p$, taking also into account the effect of surface tension (see also Dulov and Kosnik, 2009; Yurovskaya et al., 2013). A few proposed parametric spectral shapes for gravity waves are compared in figure 4.7. In practice there is a very strong variability of the observed specta around these average shapes due to spatial and temporal variations in wind speed and direction. It should also be noted that for $f > 4f_p$ there can be a dominant contribution of non-linearities, as revealed in stereo-video imagery (see figure 3.8 in the preceding chapter).

4.4 Directional spectra

4.4.1 Early parameterizations

The distribution of wave energy as a function of directions, is still very much debated because of the difficulty of measuring details of that distribution. Indeed, a wave buoy only measured 5 parameters for each direction (e.g. Kuik et al., 1988), and even ADCP systems are generally too noisy to go beyond the mean direction and possibly spreading at each frequency (Herbers and Lentz, 2010). There are, however,

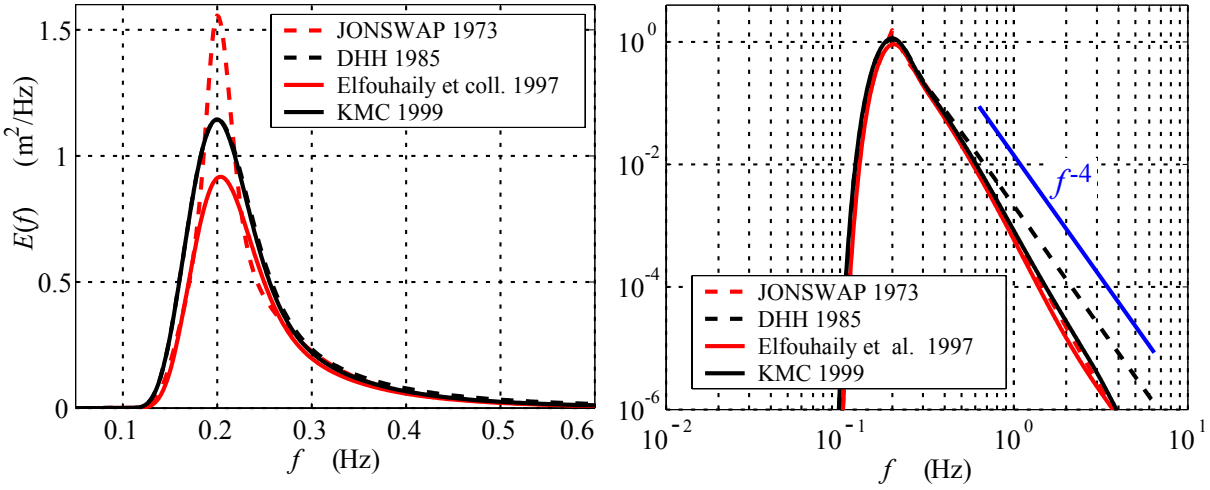

Figure 4.7: Example of proposed parametric wave spectrum shapes, for $U_{10} = 10$ m s^{-1} et $X = 50$ km. Left: using a linear scale and right, the same spectra with a logarithmic scale. The slope of the curves in log scale gives the power n of the dependance $E(f) \propto f^{-n}$. Note the transition from $n = 4$ for $f < 2f_p$ to $n > 5$ at higher frequencies, broadly consistent with the analysis of Long and Resio (2007). We have extended here the Donelan et al. (1985) spectrum beyond its range of validity, namely for $f > 3f_p$, in order to better visualize its f^{-4} decay.

important constraints on the high frequency directional distribution, with a surface slope variance which is almost the same in the downwind and crosswind directions.

The frequency-direction spectrum $E(f, \theta)$ is often decomposed into a frequency spectrum and a normalized directional distribution

$$E(f, \theta) = E(f)S(f, \theta) \tag{4.18}$$

with the normalization

$$\int_0^{2\pi} S(f, \theta)\mathrm{d}\theta = 1. \tag{4.19}$$

The first parameterizations of $S(f, \theta)$ used the fact that S is a periodic function and that buoys can provide the first terms in its Fourier decomposition,

$$S(f, \theta) = \frac{1}{2\pi} + a_1(f)\cos(\theta) + b_1(f)\sin(\theta) + ... \tag{4.20}$$

This was soon abandonned because S can be negative for some directions if the series is truncated. Longuet-Higgins et al. (1963) proposed another distribution that is always positive

$$S(f, \theta) = \cos^{2s}\left((\theta - \theta_m)/2\right), \tag{4.21}$$

which is symetric about the direction of the maximum θ_m, and narrower for larger s. This shape is still widely used, although s cannot be readily measured, whereas the directional spreading σ_θ (defined in chapter 3), is directly related to co-spectra of measured displacements or velocities. The width of the directional spectrum is generally minimum at the spectral peak, and increases towards both higher and lower frequencies. The mean direction, even for the wind sea, can differ significantly from the wind direction, in particular at short fetch (see figure 4.9).

Among other proposed forms, the one by Donelan et al. (1985) is based on theoretical solutions for non-linear wave groups,

$$S(f, \theta) \propto \frac{1}{\cosh^2\left[\beta\left(\theta - \theta_m\right)\right]} \tag{4.22}$$

and observations suggest $\beta = 2.44(f/0.95f_p)^{1.3}$ for $0.56 < f/f_p < 0.95$ and $\beta = 2.44(f/0.95f_p)^{-1.3}$ for $0.95 < f/f_p < 1.6$. That particular shape has been used for the estimation of the wind direction from HF radar data because they have non-zero values in the direction opposite to the wind direction, consistent with radar data. Unfortunately they still have a single maximum.

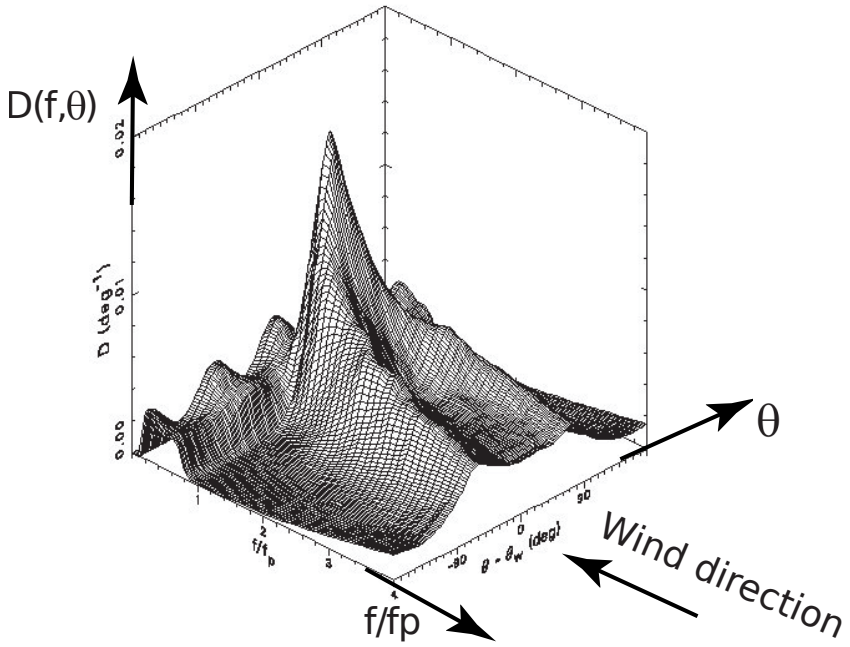

Figure 4.8: Average spectral distribution measured in Currituck sound for $U_{10} > 7$ m s^{-1} (From Long and Resio 2007).

4.4.2 Bimodality of the directional spectrum

Indeed, detailed observations using arrays (Young et al., 1995; Long and Resio, 2007) or surface mapping systems with radar or optical imagery (Hwang et al., 2000; Romero and Melville, 2010; Leckler et al., 2015) have clearly revealed that for $f > f_p$ the wind sea generally has two peaks on either side of the wind direction, as shown in figure 3.8 and 4.8. Such a distribution is called bimodal. For frequencies $f > 3f_p$ these peaks are 60 to 80 degrees away from the wind direction, at least for young waves ($C_p/U_{10} < 1/3$). There is no simple parametric form for these bimodal spectra, and their general shape for more mature waves is not established. Also, numerical models have a hard time reproducing clearly bimodal spectra, as discussed by Alves and Banner (2003). In general, for the dominant waves, we only have a good knowledge of the mean direction and directional spreading. One example of these two parameters is shown in figure 4.9).

As a result, applications that require a detailed knowledge of the directional spectrum, such as the interpretation of double-frequency acoustic and seismic noise, have to deal with large uncertainties. In fact, underwater acoustic data is one important source of measurements that can be used to better constrain our knowledge of the directional wave spectrum (Tyler et al., 1974). This source of data is now better understood (Ardhuin et al., 2013) and is still being explored (Farrell and Munk, 2008; Duennebier et al., 2012; Peureux and Ardhuin, 2016). This aspect is detailed in chapter 21.

At high frequencies, remote sensing using HF (e.g. Kirincich, 2016) or microwave radars can also constrain the directional distribution, and specific spectral shape parameterizations have been proposed by, for example, (Elfouhaily et al., 1997) and (Kudryavtsev et al., 2003) to provide wave spectra consistent with radar observations. With more data available now in new microwave bands such as L band (e.g. Yueh et al., 2013), and detailed wave shape measurements from stereo-video and polarimetric systems, there will certainly be improvements in the coming years.

4.4.3 Swell spectra

The spectrum of a swell system is simply a wind sea spectrum that has dispersed and dissipated. Due to the dispersion, it is much more narrow than a wind sea spectrum, and this narrowness increases with the distance from the storm. This narrow peak may be parameterized by a Gaussian, with a frequency bandwidth that is proportional to the size of the storm and inversely proportional to the spherical distance α from the storm (Collard et al., 2009). The directional width is also increased by the storm size and reduced by the distance, with one important difference due to the Earth sphericity. Indeed, beyond one

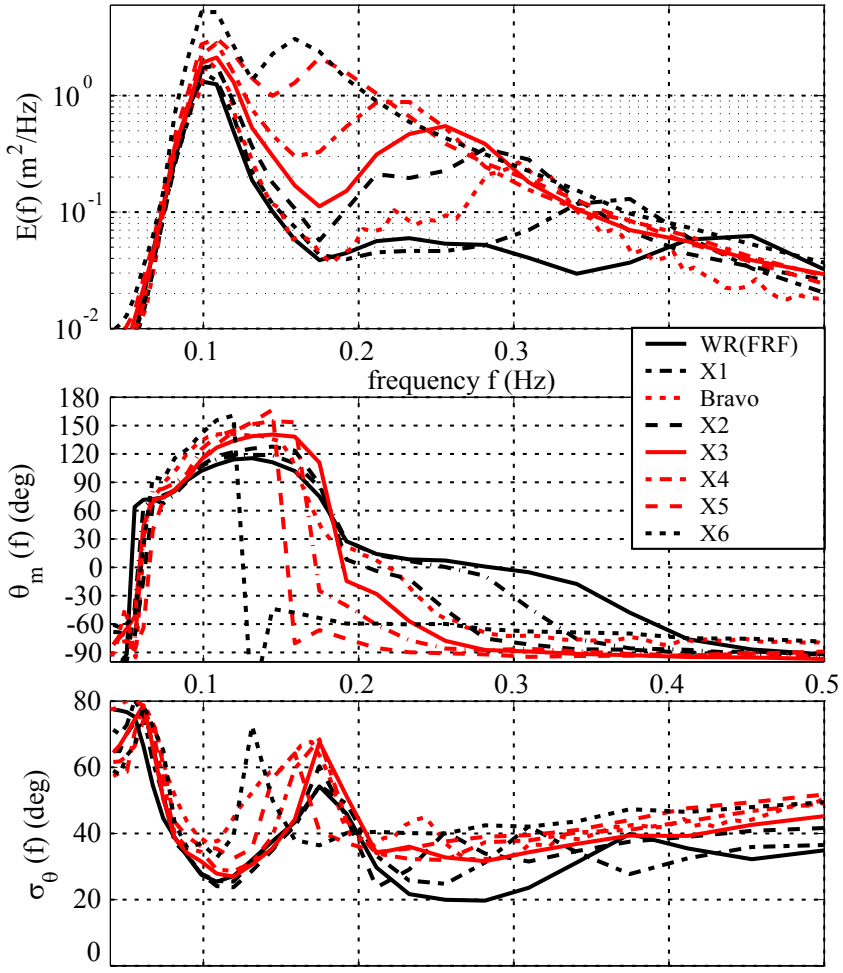

Figure 4.9: Example of measured directional parameters
Measurements during SHOWEX on November 3rd 2003, in presence of a 1 m swell opposing the wind sea. The wind direction is from 270° and the shoreline faces 70°. The different wave systems are clearly separated by a local maximum of the directional spreading σ_θ.

quarter of the Earth circumference, the directional width increases if no land has blocked the swell, and is proportional to $1/\sin(\alpha)$. Hence, the decrease in wave height given by eq. (4.13) corresponds to a narrowing of the spectrum, not to a reduction of the spectral density. Indeed, in absence of disspation, for deep water and without current, the spectral densities $E(f,\theta)$ are conserved during propagation. Namely $E(\lambda_0,\phi_0,t_0,f,\theta_0) = E(\lambda',\phi',t',f,\theta')$, where the point of coordinates (λ,ϕ,t) is on the same great circle as the point (λ_0,ϕ_0,t_0), and such that the azimuth of the great circle changes from θ_0 to θ.

4.5 Summary

4.5.1 Important parameters

We have seen that the most important factor that control the wind sea are

- the wind speed U_{10}
- the fetch X
- the duration t over which the wind has been blowing.
- The depth D, which was not discussed here. The reader may follow Young (1999).

Other parameters also have a quantitative effect,

- the shape of the fetch area
- the air-sea temperature difference $T_a - T_{\text{sea}}$ and the larger gustiness when this difference is negative.
- strong currents C (if $U/C > 0.1$).
- rain. That latter factor is not well known and is probably not so important in general.

The parameters of the first list have effects that are well understood. For the second list, the complex situations usually require the use of a numerical wave model in order to get a reliable estimate of the sea state parameter... but even in the models not all of these effects are well understood and thus not well parameterized in the models. The next chapter will present the main concepts used in numerical models for the evolution of waves in deep water.

4.5.2 Spectral shape

Wave spectra estimated from measurements have a wide variety of shapes, in particular close to coastlines where the fetch limitation on wave growth gives mean direction that can vary with frequency. In the open ocean, multiple swell systems that come from remote storms are also often present. (e.g. figure 3.4). The wind sea exhibits a clearly marked peak, where directional spreading has a local minimum, and a decrease of the spectral density $E(f)$ proportional to f^{-4} up to 2 to 3 times the wind sea peak frequency. For higher frequencies, the spectral density decreases like f^{-5} or faster.

In the directional distribution, there is always some energy in all directions, as revealed by high frequency radar data (e.g. Barrick et al., 1974; Tyler et al., 1974) but it can be very small. The wave spectrum generally has a marked bimodality at frequencies between 2 and at least 4 times the wind sea peak frequency, with two maxima on either side of the wind direction. This spectral shape is the result of different processes that, as we will see in the next chapter, can be represented in an equation for the evolution of the spectrum.

Chapter 5

Spectral wave evolution in deep water

It is now well understood that ocean waves derive most of their energy from the wind, and lose most of it to the ocean turbulence as they break. We shall see also in the next chapter that waves also carry some horizontal momentum, which, for monochromatic waves of phase speed C has a density per unit horizontal surface equal to $\rho_w gE/C$ and points in the wave propagation direction. The generation of waves by the wind is thus associated to vertical fluxes of horizontal momentum and energy going from the wind to the wave field. This flux of momentum generally accounts for more than 70% of the total momentum flux going from the atmosphere to the ocean, this total flux is usually called the wind stress. That air-sea momentum flux does not remain in the wave field, but rather it is lost by wave dissipation, mostly due to wave breaking, and ends up in the ocean currents. Most of this momentum loss happens at the same place where waves were generated: the wave field is thus largely 'transparent' to this momentum flux. However, a few percent of this momentum flux propagates away across ocean basins and is transformed into changes in sea level – this is known as wave set up – and currents on the beaches where waves break. These currents are the longshore currents. This transformation of wave momentum in the nearshore is the topic of chapter 16.

Besides, the generation or attenuation by the wind and dissipation associated to breaking, a third mechanism is very important for the evolution of the waves in deep water. It is the non-linear evolution of the waves which can be understood as a wave-wave scattering process: waves components exange energy and momentum, some components grow and others decay. In order to make things simple, we will consider now each of these three mechanism separately.

5.1 Generation of waves by the wind

The fraction of the wave energy that is in the water is $(\rho_w - \rho_a)/\rho_w \simeq 99.9\%$. Hence the transfer energy from wind to waves involves a flux of energy through the sea surface. Because the surface is a material surface, this flux cannot happen by advection, it thus requires the work of stresses on the surface, either the tangential stresses τ or the normal stresses, i.e. the pressure p. In the case of tangential stresses, the work is the correlation of the along-surface shear stress with the along-surface orbital velocity. The work of normal stresses is the correlation of pressure times the velocity normal to the surface (see figure 5.1). A quantification of these energy fluxes thus require the identification of processes that produce pressure and shear stresses on the surface. The first hypotheses on wave generation followed the theory of hydrodynamic instabilities. The air flow over a water surface is a particular case of a sheared flow in a stratified medium that may lead to the Kelvin-Helmholtz (KH) instability. This may indeed be important for very high winds speeds (Soloviev et al., 2014), but it cannot explain the initial growth of waves under moderate winds. In particular, KH theory predicts instabilities for an air-water interface for wind speeds above 6,5 m s^{-1} (Jeffreys 1925), but ripples already appear on the water surface for winds as low as $U = 1,1$ m s^{-1} (Kahma et Donelan 1988).

This initial growth of ripples is rather well explained by the effect of turbulence in the air advected by the wind Phillips (1957). That process is very soon overtaken by the feedback caused by the wave-induced pressure oscillations in the air, as the airflow is modified by the presence of waves. When waves travel slower than the wind projected in their propagation direction, the pressure is slightly higher on

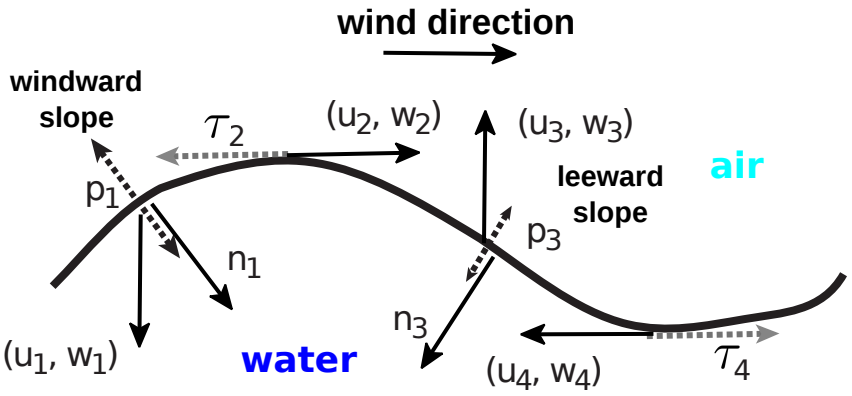

Figure 5.1: Fluxes at the air-sea interface, at four phases of the wave profile: 1 windward slope, 2 crest, 3 leeward slope, 4 trough. The energy flux from the atmosphere to the ocean is the work of the stresses acting on the sea surface, $[p\mathbf{n} + \tau] \cdot (u, w)$, with $\mathbf{n}$ the unit normal vector pointing to the water side. As a result, if the air pressure is higher on the windward slope, then $p_1 w_1 \left.\frac{\partial \zeta}{\partial x}\right|_1 > p_3 w_3 \left.\frac{\partial \zeta}{\partial x}\right|_3$ and the pressure-related flux is positive towards the water side. Likewise, if the shear stress τ is opposed to the velocity vector (as here), the flux τu induced by shear stresses is negative (i.e. energy goes from the water to the air). Similarly, the momentum flux is the average stress acting on the surface. Because of the surface slope, the vertical flux of horizontal momentum is the average of $p\partial\zeta/\partial x$ plus the average of τ_x.

the windward face, typically of the order of a few Pascals, and lower on the leeward side. In a first approximation, the amplitude of the pressure fluctuations is proportional but shifted in phase compared to the amplitude of the surface elevation, we shall thus use complex amplitudes for the pressure dPa and the elevation dZ,

$$dPa = \rho_w g \, (\alpha + \mathrm{i}\beta) \, dZ, \tag{5.1}$$

where α represents the in-phase oscillations and β the oscillations in quadrature. Here we will take $\alpha = 0$ for simplicity as we shall see that it is not important for wind-wave growth. The boundary condition on the continuity of pressure at the sea surface (eq. 22.25) writes,

$$\frac{\partial^2 dZ}{\partial t^2} + \sigma^2 \, (1 + \mathrm{i}\beta) \, Z = 0. \tag{5.2}$$

When $\beta \ll 1$, the solution to first order in β is

$$\begin{aligned}
\zeta &= a(t) \cos \Theta_1, && (5.3)\\
\phi &= \frac{g a(t)}{\sigma} F_{CC} \sin\theta_1 + \beta g \frac{a}{2\sigma} F_{CC} \cos \Theta_1, && (5.4)\\
p &= -\rho_w g z + \rho_w g a(t) F_{CC} \cos\psi - g\beta a F_{CC} \sin \Theta_1, && (5.5)\\
\frac{\mathrm{d}a(t)}{\mathrm{d}t} &= \frac{\beta\sigma a(t)}{2}, && (5.6)\\
\frac{\mathrm{d}}{\mathrm{d}t}\frac{a^2(t)}{2} &= \beta\sigma \frac{a^2(t)}{2} && (5.7)
\end{aligned}$$

where $F_{CC} = \cosh(kz + kh)/\cosh(kD)$, and $\Theta_1 = \mathbf{k} \cdot \mathbf{x} - \sigma t$. In the absence of other processes, this surface pressure yields an exponential growth or decay of the wave energy, depending on the sign of β.

It is an interesting exercise to also compute the Eulerian-mean flux of momentum at each depth, $\langle uw \rangle$, and prove that it has the same profile as the Stokes drift, given in the next chapter. This means that when the wind generates waves, the wave momentum increases in the water column, storing the momentum flux across the air-sea interface.

5.1.1 Measuring and parameterizing wind-wave generation

With an air pressure that is proportional to the surface elevation, the energy growth in eq. (5.7) can be written as,

$$S_{\mathrm{in}}(f, \theta) = \sigma\beta E(f, \theta). \tag{5.8}$$

The magnitude of the non-dimensional growth rate β is a key parameter to determine the energy balance with dissipative and non-linear processes, and, as a result, the shape of the wave spectrum. Numerical wave models all use semi-empirical parameterized expressions, with β a function of the relative direction between the wind and the waves, and a function of the ratio of the wind speed and the phase speed.

In most model parameterizations, β is inspired from theoretical results (e.g. Miles, 1959; Fabrikant, 1976; Miles, 1996), with empirical adjustments to the few available measurements of pressure over waves, or numerical simulations of air flow over waves, or observed wave groth (Plant, 1982), or measurements of pressure-slope correlations (Snyder et al., 1981; Donelan et al., 2005, 2006).

5.1.2 Parameterizations based on observations

Snyder et al. (1981) performed an important field experiment in the bight of Abaco, in the Bahamas, in order to reconcile the previous diverging observations by Dobson (1971) and Snyder and Cox (1966). Their measurements performed under light to moderate wind speeds are summarized by a growth rate

$$\beta = \max\left\{0, 0.25\frac{\rho_a}{\rho_w}\left[28\frac{u_\star}{c}\cos\left(\theta_\star - \theta\right) - 1\right]\right\}. \tag{5.9}$$

where ρ_a and ρ_w are the densities of air and water, and $u_\star = \langle u'w'\rangle^{1/2} = \sqrt{\tau_a/\rho_a}$ where τ_a is the air-sea momentum flux per unit horizontal surface, usually called 'wind stress'. This parameterization is used in the 'Cycle 3' of the WAM model (WAMDI Group, 1988).

The measurements by Snyder et al. (1981) have been confirmed by other experiments, for example in the North Sea by Hasselmann and Bösenberg (1991). Unfortunately these measurements at sea are made only with moderate wave heights and wind speed, and only for waves around the spectral peak.

Besides, most wind measurements at sea consist of mean wind speed and direction at a fixed height, typically 5 m, without the rapid fluctuations needed to estimate the friction velocity $u_\star$. A link between this wind speed and the wind stress is provided by assuming that the turbulent momentum flux $\langle u'w'\rangle$ is constant with height (which is not so true near the surface in the presence of waves), and that the mixing can be parametrized by an eddy viscosity of the form $\nu_T = l^2\partial U/\partial z$ where the mixing length is given by $l = \kappa z$ with von Kármán's constant $\kappa = 0.41$. Under these assumptions, the wind speed profile is a logarithmic as a function of height,

$$U\left(z\right) = \frac{u_\star}{\kappa}\ln\left(z/z_0\right), \tag{5.10}$$

starting from 0 at the roughness height z_0. There are many discussions on the proper way to estimate z_0, but a first reasonable guess is provided by the dimensional analysis of Charnock (1955),

$$z_0 \simeq \alpha_{CH}u_\star^2/g, \tag{5.11}$$

where $\alpha_{CH} \simeq 0.015$ is Charnock's 'constant'.

From this type of expression, several adjustement have been proposed, in particular it appears that the Charnock coefficient may vary with wave age, with an increase for young waves. This is how Janssen (1991) parameterized the numerical results of a coupled wave-atmosphere boundary layer model.

For very young waves, with $U_{10}/C_p > 3$ there are also clear signs of strong air flow detachment from the sea surface, which leads to an increase of β and decrease for extremely young waves when the air flow is fully detached (Donelan et al., 2006; Babanin et al., 2007). This detachement of the air flow and attenuation of the short waves by the wind (Soloviev et al., 2014) are possible explanations, together with the effect of sea spray (Andreas, 2004), for the reduction of the drag coefficient $C_d = u_\star^2/U_{10}^2$ in hurricane conditions. This is a very active topic of research with important consequences for the understanding and forecasting of extreme storm surges (e.g. Resio and Westerink, 2008).

5.1.3 Short waves and multiple-scale interactions

For the high frequency part of the spectrum, say $f > 3f_p$, there are no direct measurements of the pressure-slope correlations. The growth parameterizations are thus inferred from the observation of wind-wave growth (e.g. Plant, 1982), and numerical simulations that are consistent with an energy source term S_{in} proportional to $u_\star^2\cos^2\left(\theta_\star - \theta\right)$. Besides, approaching the sea surface from above, a growing fraction of the momentum flux is carried by the wave orbital motion, in the form of a correlation $\overline{uw}$. A likely consequence is that the short waves, which are affected by the air layers closest to the

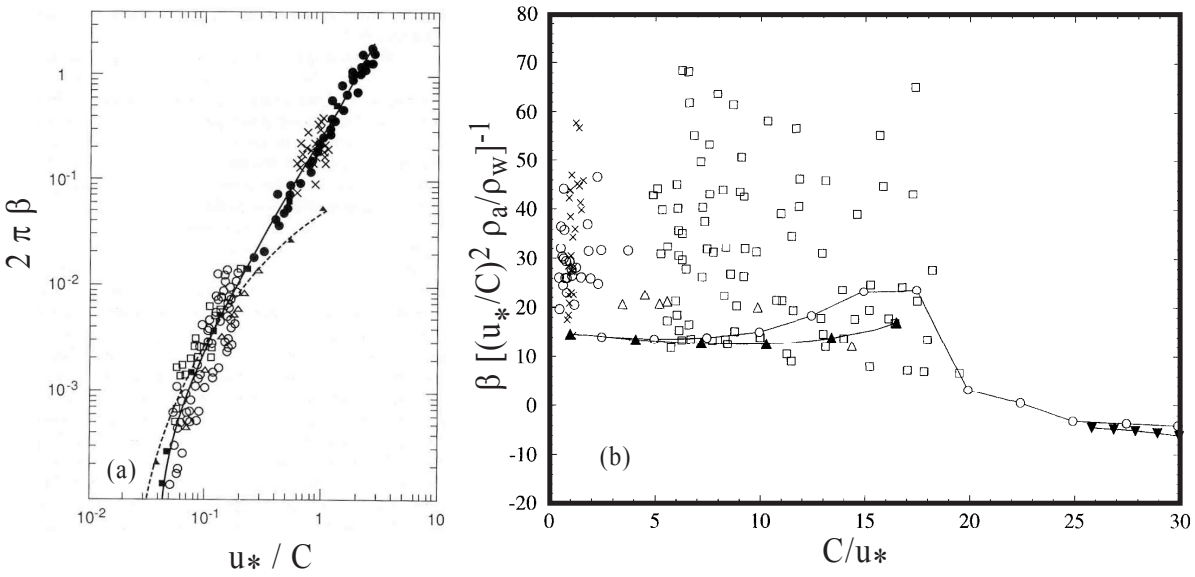

Figure 5.2: Growth rate of waves propagating in the wind direction, combining observations and theory. a. solid line: Miles theory as extended by Fabrikant and Janssen, dashed: measurements of Snyder et al. (1981) as summarized by eq. (5.9), symbols: estimations compiled by Plant (1982), this figure is taken from Janssen et al. (1994). (b) growth rate for a non-dimensional wavenumber $kz_0 = 10^{-4}$ (filled triangles) compared to numerical model results with connected circles by Mastenbroek (1996) and the Plant (1982) data (other symbols), that figure is taken from Belcher (1999).

surface, only feel a reduced wind stress as they are 'sheltered' by the longer waves (Hara and Belcher, 2002). In the presence of long waves, we thus expect that the growth rate of shorter waves is strongly reduced.

5.1.4 In summary

Wind is a source of energy ($S_{in} > 0$) for all spectral components such that $U/(C\cos\theta_u - \theta) > 1$. In the spectral plane, this corresponds to a region bounded by the straight line defined by $U/(C\cos\theta_u - \theta) = 1$. The other components, with $U/(C\cos\theta_u - \theta) < 1$ are a sink of energy for the waves ($S_{out} < 0$), and thus a source of energy for the wind.

The wind generation source term can be written as

$$S(k,\theta) = S_{\rm in}(k,\theta) + S_{\rm out}(k,\theta) = \sigma\beta E(k,\theta), \tag{5.12}$$

where the non-dimensiona growth parameter β is of the order of $30\rho_a u_\star/C/\rho_w$ for $1 < U/(C\cos\theta_u - \theta) < 3$, and a much smaller negative number, typically -2×10^{-6} for $U/(C\cos\theta_u - \theta) < 1$. This negative part appears to be non-linear with a magnitude of β that increases with the steepness of the swell.

In general it is expected that the growth rate of one component is also a function of the amplitude of other components, but that effect is very poorly known.

5.2 Weakly non-linear evolution

Because waves are not exactly linear, they produce many interesting effects: presence of harmonics, recurrence patterns, instabilities ... that are further discussed in chapter 18. Here we will focus on the evolution of the wave spectrum that comes from the exchange of energy between different spectral components.

This spectral evolution is generally described as a wave-wave interaction process, which is a particular case of wave scattering. In the case of a continuous spectrum, this effect is also known as 'weak turbulence', as it exhibits Kolmogorov-type solutions with a cascade of energy towards the short waves as well as an inverse cascade towards the longer waves. The rate of change of the spectrum due to this non-linear effect was determined by Klaus Hasselmann (1960,1962) and Vladimir Zakharov (1968),

starting from the Euler equations and assuming a quasi-Gaussian sea state. These two publications used different methods that are equivalent, as shown by (e.g. Elfouhaily et al., 2000; Resio et al., 2001). The confirmation of this theory using more complete equations of motions is fairly recent (Tanaka, 2001; Korotkevich et al., 2008). The experimental verification in the case of a pair of monochromatic wave train was first performed by McGoldrick et al. (1966), who showed that two wave trains of different frequencies and directions can create a third wave train with yet another frequency and direction.

Hence, within the wave spectrum, there is a continuous exchange of energy between components that strongly modifies the shape of the spectrum. This exchange is strongest for steep waves. The only remaining doubts about this theory are its applicability to shallow water or in cases with strong variations of depth or currents on the scale of the wavelength.

5.2.1 Wave-wave interation theory

When solving the Euler equations, we can keep the non-linear terms that were discared by Airy, and write the solution as an expansion in powers of the wave slope $\varepsilon = ka$ (see eq. 18.13). One then finds a first order solution that is a superposition of Airy waves

$$\zeta_1 = \sum_{\mathbf{k},s} Z(\mathbf{k},s) \mathrm{e}^{\mathrm{i}[\mathbf{k}\cdot\mathbf{x} - s\sigma t]} \tag{5.13}$$

and that can be introduced into the second order equations.

In order to make things simple, let us replace the full boundary conditions (18.3), by something more simple,

$$\left[\frac{\partial}{\partial t^2} - gk\tanh(kD)\right]\zeta = g\boldsymbol{\nabla}\zeta\cdot\boldsymbol{\nabla}\zeta. \tag{5.14}$$

At second order this gives the following forced harmonic oscillator equation

$$\left[\frac{\partial}{\partial t^2} - gk\tanh(kD)\right]\zeta_2 = g\boldsymbol{\nabla}\zeta_1\cdot\boldsymbol{\nabla}\zeta_1. \tag{5.15}$$

If there are components $(\mathbf{k},\sigma)$ such that $\mathbf{k} = \mathbf{k}_1 + \mathbf{k}_2$ et $\sigma = \sigma_1 + \sigma_2$ then the solution contain resonances. Phillips (1960) showed that such components do not exist because the dispersion relation of gravity waves does not have an inflexion point, hence there is no resonance at second order and the solution is bounded with a simple expression of the second order amplitudes as a function of the first order amplitudes,

$$\zeta_2 = \sum_{\mathbf{k}_1,s_1}\sum_{\mathbf{k}_2,s} A(\mathbf{k}_1,\mathbf{k}_2,s_1,s_2) Z(\mathbf{k}_1,s_1) Z(\mathbf{k}_2,s_2) \mathrm{e}^{\mathrm{i}[(\mathbf{k}_1+\mathbf{k}_2)\cdot\mathbf{x} - (s_1\sigma_1+s_2\sigma_2)t]} \tag{5.16}$$

with $A(\mathbf{k}_1,\mathbf{k}_2,s_1,s_2)$ a constant coefficient given by

$$A = \mathbf{k}_1\cdot\mathbf{k}_2 / \left[s_1\sigma_1 s_2\sigma_2 - gk\tanh(kD)\right]. \tag{5.17}$$

The actual Euler equation (18.3) has a few extra terms but it is the same principle with a similar result, only the actual value of A changes. This second order elevation is the generalization of the first harmonic of a monochromatic waves: if the first order only contains waves of frequency f, the the second order has components with frequency $2f$ and 0.

Things get more exciting when resonances exist. Resonances at second order exist for dispersion relation with an inflexion point, which is the case of gravity-capillarity waves or in the presence of sea ice, but we will not discuss this here. For gravity waves Phillips (1960) showed that resonanced occur at third order. The third order amplitude is a solution of a forced oscillator equation that looks like the wind-forced waves (22.25),

$$\left[\frac{\partial}{\partial t^2} - gk_4\tanh(k_4D)\right] Z_3(\mathbf{k}_4) = \sum_{k_1,k_2,s_1,s_2,s_3} B(\mathbf{k}_1,\mathbf{k}_2,\mathbf{k}_3,s_1,s_2,s_3) Z(\mathbf{k}_1,s_1) Z(\mathbf{k}_2,s_2) Z(\mathbf{k}_3,s_3) \mathrm{e}^{\mathrm{i}[(\mathbf{k}_1+\mathbf{k}_2+\mathbf{k}_3)\cdot\mathbf{x} - (s_1\sigma_1+s_2\sigma_2+s_2\sigma_3)t]} \tag{5.18}$$

in which $\mathbf{k}_3 = \mathbf{k}_4 - \mathbf{k}_1 - \mathbf{k}_2$. The right hand side is resonant for $\mathbf{k}_4 = \mathbf{k}_1 + \mathbf{k}_2 - \mathbf{k}_3$ and $\sigma(k_4) = \sigma_1 + \sigma_2 - \sigma_3$. This resonance condition is satisfied for an inifinite number of quadruplets ($\mathbf{k}_1$, $\mathbf{k}_2$, $\mathbf{k}_3$, $\mathbf{k}_4$), as illustrated in figure 5.3, for the case of deep water. Resonances also exist in shallow water, only the shape of the curves are changed.

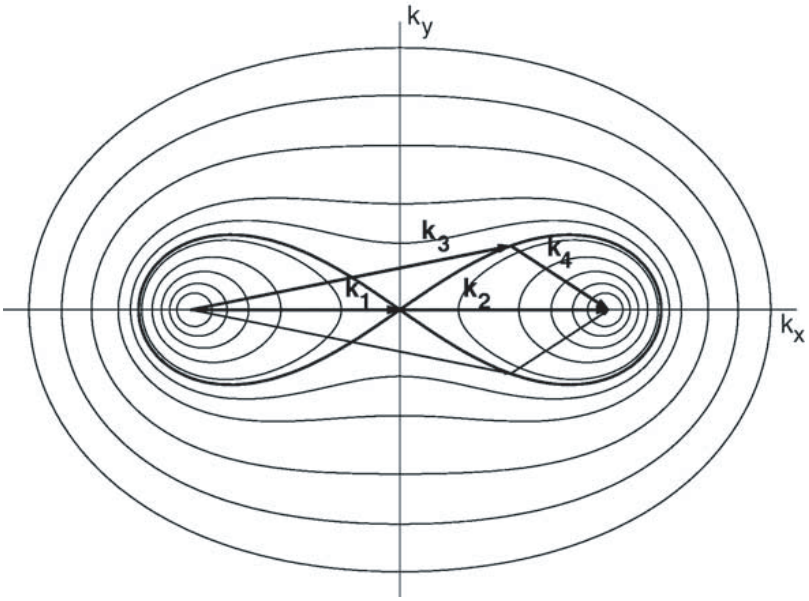

Figure 5.3: Geometric arrangement of wavenumbers that produce resonant interations in deep water, and particular case of the quadruplet used in the Discrete Interaction Approximation (DIA), taken from van Vledder (2006).
The resonance conditions $\mathbf{k}_4 = \mathbf{k}_1 + \mathbf{k}_2 - \mathbf{k}_3$ and $\sigma(k_4) = \sigma_1 + \sigma_2 - \sigma_3$ mean that for a given $\mathbf{k}_1 + \mathbf{k}_2$, $\mathbf{k}_3$ must be on the curve where $\mathbf{k}_1$ lies: each curve corresponds to a fixed value of $\sigma_1 + \sigma_2$. A practical parameterization uses a single configuration $\mathbf{k}_1 = \mathbf{k}_2 = \mathbf{k}$, $k_3 = (1+\lambda)^2 k$ and $\sigma_1 + \sigma_2 = \gamma\sigma$, which imposes $k_4 = (1-\lambda)^2 k$. This DIA, as adjusted by Hasselmann et al. (1985b), uses $\lambda = 0.25$ et $\gamma = \sqrt{2}$. The angle of the ∞-shaped curve near the origin with the x-axis, when $\mathbf{k}_3 \simeq \mathbf{k}_1$ is the same 35° angle as in the next figure. Each curve corresponds to a different value of γ.

A particular case corresponds to $\mathbf{k}_1 = \mathbf{k}_2$, as in the figure. Any component $\mathbf{k}_3$ that lies on the thick black curve shaphed like ∞, will interact resonantly with components $\mathbf{k}_1$ and $\mathbf{k}_4$. This was verified in the laboratory in the case where $\mathbf{k}_3$ and $\mathbf{k}_1$ are at right angles (McGoldrick et al., 1966), with the creation of the new wave component $\mathbf{k}_4$.

The fact that not all combinations of wavenumbers are resonant reduces the number of dimensions of the interaction space from 6 to 3. In other words, the components with wavenumber vector $\mathbf{k}_4$ interact with components $\mathbf{k}_1$, $\mathbf{k}_2$ and $\mathbf{k}_4$ that follow some particular curves in spectral space. Assuming that the surface elevation is Gaussian makes it possible to neglect the correlations of 4 different wave trains (Hasselmann, 1962), giving a rate of change of the energy for time scales much larger that the wave period,

$$\begin{aligned} \frac{\partial E(\mathbf{k}_4)}{\partial t} &= S_{\mathrm{nl}}(\mathbf{k}_4) \\ &= \int |T(\mathbf{k}_1,\mathbf{k}_2,\mathbf{k}_3,\mathbf{k}_4)|^2 \, \delta(\mathbf{k}_1+\mathbf{k}_2-\mathbf{k}_3-\mathbf{k}_4)\, \delta(\sigma_1+\sigma_2-\sigma_3-\sigma_4) \\ &\quad \times \{E(\mathbf{k}_1)\,E(\mathbf{k}_2)\,[E(\mathbf{k}_3)+E(\mathbf{k}_4)] - E(\mathbf{k}_3)\,E(\mathbf{k}_4)\,[E(\mathbf{k}_1)+E(\mathbf{k}_2)]\} \end{aligned} \tag{5.19}$$

where δ is always zero except $\delta(0) = 1$, and the coefficient T is an algebric expression similar to A in eq. (5.17) but much more complex, and given by Herterich et Hasselmann (1980), or, with a simpler form, by Zakharov (1999). The practical calculation of this coefficient and its integration requires a careful handling of singularities (e.g. Gorman, 2003).

The positive term $E(\mathbf{k}_1)\,E(\mathbf{k}_2)\,[E(\mathbf{k}_3)+E(\mathbf{k}_4)]$ in eq. (19.21) comes from the third order amplitude squared in (18.39), and the negative term $-E(\mathbf{k}_3)\,E(\mathbf{k}_4)\,[E(\mathbf{k}_1)+E(\mathbf{k}_2)]$ is due to the correlations between first and fifth order terms in eq. (18.43). This negative part is critical to conserve the total wave energy. In general the coefficient T decreases as the difference between wavenumbers is larger. In other words, the interaction of very different wavelengths or directions is much weaker than the interaction of components that are very similar. A rough estimate of the time scale of spectral evolution is $\varepsilon^4 T_p$.

Faster evolutions due to non-linear effects exist that are not represented by S_{nl}. These faster changes

are oscillations of the energies that do not contribute directly to the long term evolution of the wave spectrum.

5.2.2 Conservation properties

The source term S_{nl} conserves the total wave energy, namely,

$$E_{\mathrm{tot}} = \rho_w g \int E(\mathbf{k})\,\mathrm{d}\mathbf{k} \tag{5.20}$$

as well as the wave momentum vector, which will be discussed further in the next chapter,

$$\mathbf{M}^w = \rho_w g \int \mathbf{k}\frac{E(\mathbf{k})}{\sigma}\mathrm{d}\mathbf{k}, \tag{5.21}$$

and the wave action,

$$A = \int \rho_w g \frac{E(\mathbf{k})}{\sigma}\mathrm{d}\mathbf{k}. \tag{5.22}$$

As we will see in chapter 7, the conservation of wave action in general is related to the invariance of the phase-averaged physical situation by a change of the wave phases. In particular, wave action - and not wave energy - is conserved when waves propagate across current gradients without energy dissipation.

The conservation of the two scalar quantities A and E in a non-linear system imposes the presence of transfers of energy, also known as 'cascades', towards both short and long wave components (Zakharov and Zaslavskii, 1982). Indeed, once integrated over directions, $S_{\mathrm{nl}}(k)$ is the rate of change of the energy for a given wavelength. Assuming that there is only a transfer of energy from components with $k < k_t$ to shorter waves with $k > k_t$, we would have both

$$\int_0^{k_t} S_{\mathrm{nl}}(k)\mathrm{d}k = -\int_{k_t}^{\infty} S_{\mathrm{nl}}(k)\mathrm{d}k \tag{5.23}$$

and

$$\int_0^{k_t} S_{\mathrm{nl}}(k)/\sigma\mathrm{d}k = -\int_{k_t}^{\infty} S_{\mathrm{nl}}(k)/\sigma\mathrm{d}k, \tag{5.24}$$

which is not possible since the division by σ makes the first integral relatively bigger than the second. Hence there is a flux of energy towards both long and short waves, which explains part of the increase in wavelength as the waves develop with time or fetch. Also, the conservation of momentum $\mathbf{M}^w$, further imposes that the energy transferred towards high frequency cannot be in the same direction, but rather in oblique or opposed directions. This property is tighly linked to the resonant conditions that is a consequence of the dispersion relation. Investigating the evolution of a narrow-peaked spectrum, Longuet-Higgins (1976) showed that the energy tends to flow away from the peak towards high frequencies at directions $\arctan(1/\sqrt{2})$ rad $\simeq 35°$ (figure 5.4). Under the effect of nonlinear interactions alone, a narrow spectrum thus tends to have a split tail with two peaks separated by about 70°, which agrees with the observations of wind sea spectra at frequencies $1.5f_p < f < 2f_p$ (Hwang et al., 2000; Long and Resio, 2007), as shown in figure 4.8.

Without forcing from the wind and assuming that the dissipation occurs only at the smallest scales, the wave spectrum tends to evolve towards a self-similar shape known as the Kolmogorov-Zakarov spectrum, with a decay towards high frequencies that is proportional to f^{-4}. In reality, the presence of forcing and dissipation at the dominant scales makes the wave spectra different from this self-similar solutions.

5.2.3 Other properties of wave-wave interactions

Besides the fluxes towards both ends of the spectral domain, the non-linear interactions also have a very strong local smoothing effect. If one takes a spectrum near equilibrium and introduces a local perturbation, the 4-wave interactions will very rapidly remove this disturbance giving a smooth spectrum. This smoothing is faster for steeper waves. For a wind sea, this can happen in less than 100 periods, (figure 5.5), which is much faster than the theoretical dimensional argument saying that S_{nl} acts on a time scale of $\varepsilon^6 T_p$. In the case of swells, with a much weaker steepness, it is possible that the interactions produce a significant broadening of the directional spectrum, without a noticeable shift in frequency (T.H.C. Herbers, personal communication, 2001).

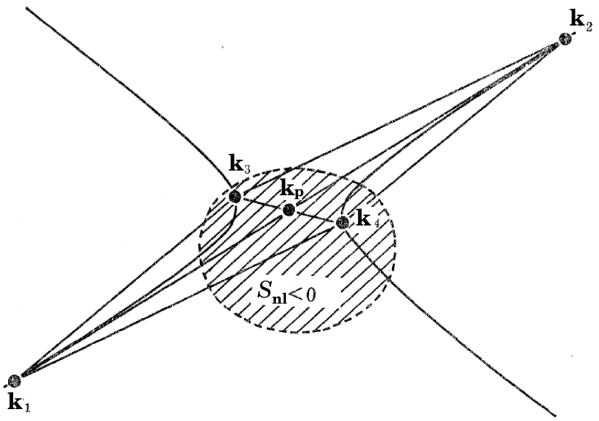

Figure 5.4: Non-linear interactions and bimodal spectral distributions.
The interaction of wave components with wavenumber vectors $\mathbf{k}_1$, $\mathbf{k}_2$, $\mathbf{k}_3$ and $\mathbf{k}_4$, when $\mathbf{k}_3 \simeq \mathbf{k}_4$. Since $\mathbf{k}_1 + \mathbf{k}_2 = \mathbf{k}_3 + \mathbf{k}_4$, the 4 wave vectors make a parallelogram. taking $\mathbf{k}_3$ and $\mathbf{k}_4$ symmetric about the spectral peak $\mathbf{k}_p$ and taking the x-axis in the direction of $\mathbf{k}_p$, one gets $k_{p,y} = 0$ and $k_1 = \sqrt{k_p^2 + 2k_p\Delta k_{1,x} + \Delta k_{1,x}^2 + \Delta k_{1,y}^2}$, the latter equation also applies to the three other wave vectors. Expanding for small values of $X_1 = \Delta k_{1,x}/k_p$ and $Y_1 = \Delta k_{1,y}/k_p$ gives $\sigma_1 = \sqrt{gk_1} \simeq \sqrt{gk_p}\left(1 + 0.5X_1 - 0.125X_1^2 + 0.25Y_1^2\right)$,. The resonant conditions read $X_1 + X_2 = 0$ $Y_1 + Y_2 = 0$ et, for the frequencies $\sigma_1 + \sigma_2 = 2\sigma_p(1+\alpha)$ becomes $2Y_1^2 - X_1^2 = 8\alpha$. That is the equation of an hyperbola with a asympote at an angle $\arctan(1/\sqrt{2})$ relative to the x-axis (figure adapted from Longuet-Higgins, 1976) .

5.2.4 Practical calculation of wave-wave interactions

The calculation of the full integral $S_{\rm nl}$ is unfortunately a little too expensive today for operational wave forecasting, except for large scale coarse models, due to the three-dimensional integral needed for each spectral component and at each grid point where the source terms are evaluated. Such calculations are thus confined to research applications. Operational wave models use some form of approximation, and the Discrete Interaction Approximation by Hasselmann et al. (1985a) is the most common. That approximation preserves the conservation properties of the full integral by using only a subset of the resonant quadruplets $\mathbf{k}_1$, $\mathbf{k}_2$, $\mathbf{k}_3$, et $\mathbf{k}_4$. The original form of the DIA is only valid in deep water.

The shape of $S_{\rm nl}$ produced by the DIA can differ significantly from the exact solution. It has been adjusted to give the right order of magnitude for the transfer of energy to low frequencies in a wind sea, which is very important for the wave development. That choice, has some side-effects on other unconstrained parameters such as the directional wave distribution which is too broad for $1.5 < f_p < f < 4f_p$.

Several intermediate methods have been developed with some already used in operational wave forecasting (e.g. Komatsu and Masuda, 1996).

5.3 Dissipation

Many processes contribute to the dissipation of wave energy, or more exactly, the conversion of mechanical wave energy into other forms of energy, in particular turbulence in the water and air.

Wave breaking is generally the most important sink of energy for wind seas. In the case of periodic waves, breaking results from an instability that develops near the wave crest when the orbital velocity appraoches the phase speed[1]. This criterion gives a maximum possible wave steepness that is

$$H_{\max}/L \simeq 0.14 \tanh(kD) \tag{5.25}$$

as first determined by Miche (1944a). The factor $\tanh(kD)$ happens to be also the ratio between the amplitude of elevations a and the amplitude of the orbital velocities at the surface in the case of linear waves. It is likely that a similar criterion applies to random waves. Indeed, water moving forward faster

[1]In the case of a stationnary wave, instability occurs when the vertical acceleration approaches g.

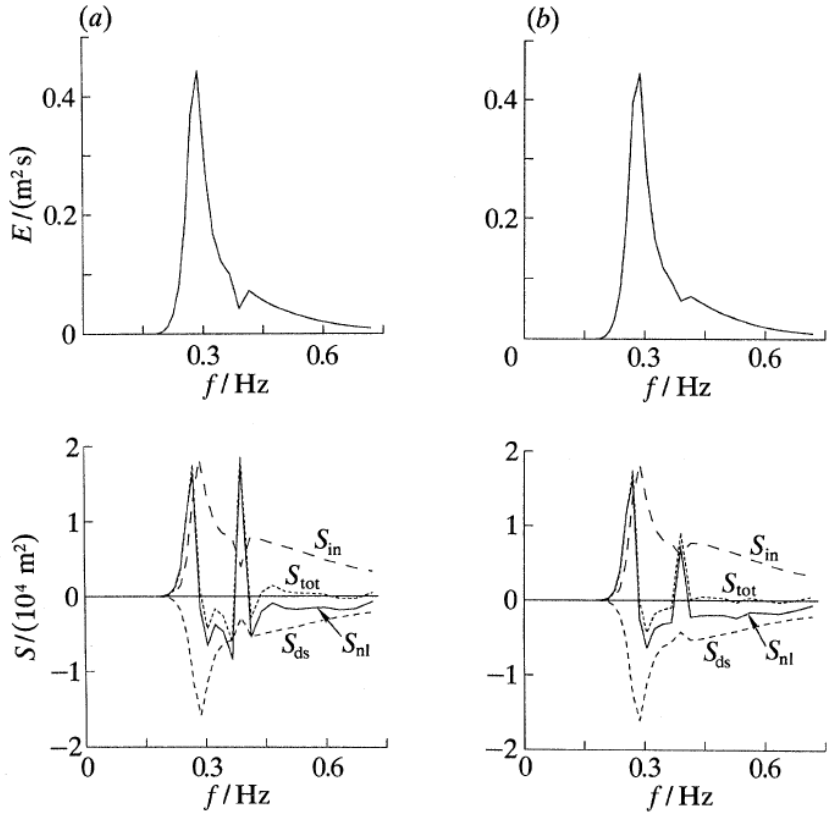

Figure 5.5: Illustration of the smoothing effect of non-linear interactions.
A spectrum with a gap, evolves rapidly towards a smooth spectrum. Top-left: initial spectrum, right: spectrum after 3 minutes, which is less than 100 dominant periods. Bottom: source terms for wind generation $S_{\rm in}$, wave-wave interactions $S_{\rm nl}$, and dissipation $S_{\rm ds}$. Figure taken from Young and van Vledder (1993) .

than the crest will shortly find itself over air and ready to overturn. In deep water, the Miche criterion (5.25), gives the Stokes limit, $ka_{\rm max} = \pi H_{\rm max}/L = 0.44$.

Laboratory observations by Melville and Rapp (1988) and Stansell and MacFarlane (2002) show that non-stationary breaking waves have orbital velocities u that approach the phase speed. One of the important difficulties is to relate this orbital velocity to the wave spectrum, because, for real and thus nonlinear waves, u increase much faster than a when approaching the breaking limit. Also, breaking is defined for individual waves, which are not easily related to the spectrum. Many authors have sought criteria for wave breaking based on the vertical acceleration, but this is not a good indicator of breaking (e.g. Holthuijsen and Herbers 1986).

5.3.1 A classification of breaking waves

Breaking waves of different sizes look different. The shortest gravity waves, with wavelengths $0.1 < L < 1$ m (i.e. $f > 1.25$ Hz) do not make any bubbles. This is because an increase in the area of the air-water interface requires an energy that is the surface tension T times the excess surface, hence the short waves do not have enough energy to make bubbles when the break. Instead, short waves produce micro-breakers (Banner and Phillips, 1974) that are characterized by a strong curvature of the surface and the generation of capillary ripples on the forward face ahead of the breaking point. These capillary waves are strongly damped by viscosity that absorbs a large part of the energy lost during breaking. Observations reveal that short waves break very often, with a probability that increases from 11% for a wind speed of 4.5 m/s to 80% for 7.4m s^{-1} (Siddiqui and Loewen, 2007). These micro-breakers play an important role in setting the surface temperature and the gas fluxes at the air-sea interface because they disrupt the viscous surface layer (figure 5.6.a).

Longer waves are energetic enough to produce bubbles with a particular noise. This ambiant noise is an important factor in the performance of sonar systems (e.g. Lu et al., 1990; Ma et al., 2005). Injecting

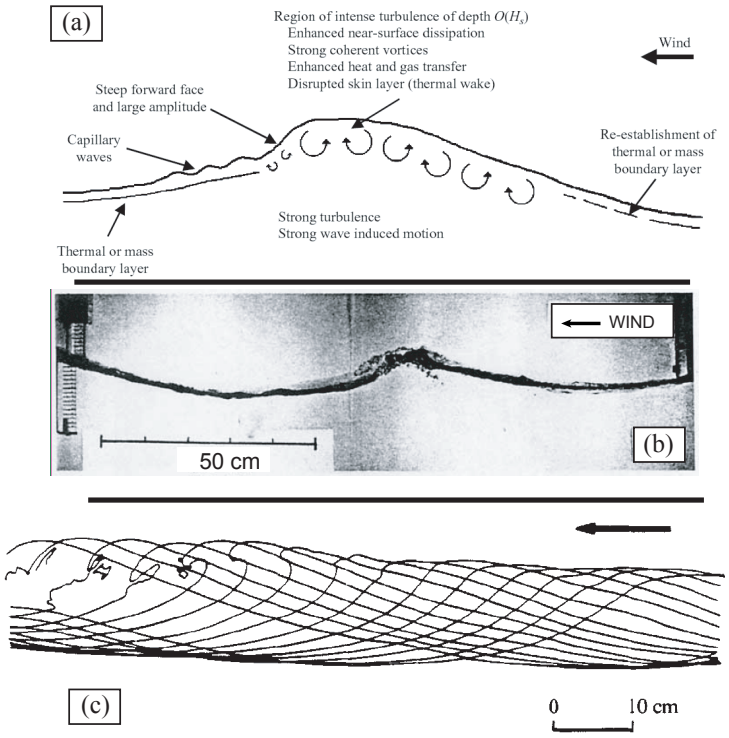

Figure 5.6: Features of breaking waves from short to longer waves.
(a) Schematic of a micro-breaking waves viewed sideways, the vertical scale of the boundary layer is exaggerated (from Siddiqui and Loewen, 2007, ©Cambridge University Press)), (b) breaking of a short wave with entrainment of air at the crest (from Koga, 1982), (c) evolution of a breaking wave in the case of a plunging breaker with one wave profile every 0.04 s (from Bonmarin, 1989, ©Cambridge University Press) .

the bubbles at depths also requires a conversion of kinetic energy into potential energy, that can take up as much as half of the energy lost in the whole breaking process (Lamarre and Melville, 1991). It should be noted that long waves can contribute to the breaking of short waves, either because the long waves are breaking or because they produce a straining of the short waves that locally increases the short wave steepness. Wave breaking of all scales produce vorticity in the water column which is important for upper ocean mixing, in particular for the diurnal cycle of sea surface temperature.

Several types of breakers are usually defined. When the breaking wave is quasi-stationary with a gentle forward slope, it is a spilling breaker. A steeper waves that trap a tube of water near the crest, is a plunging breaker (figure 5.6.c). Finally a waves that rapidly collapses on a steep shoreline is surging breaker.

5.3.2 Parameterizations of dissipation due to breaking

A global energetic appraoch

Near the shore or on offshore shoals, the water is shallow enough that the dominant waves are not dispersive. In that case the question of wave breaking is greatly simplified by considering the total energy E_t instead of the spectrum. Since waves near the shore often have a well-defined direction we may consider that the wave energy is radiated in a single direction, that of the spectral peak. By analogy with a hydraulic jump, as detailed in section 23.4.1, the rate of energy dissipation per unit surface is

$$\epsilon(H,D,T) \simeq \frac{1}{L}\epsilon_1(D-H/2, D+H/2) \approx \frac{1}{4}\rho g \frac{(BH)^3}{DT} \tag{5.26}$$

where B is a tuning factor that is close to 1... empirical adjustments are often useful to produce accurate simulations, and this is one of the better constrained coefficients. Obviously, as B comes to the third power, a small change in B can be a significant change in the modeled dissipation rate.

Effect of wave height distributions

Since the wave height H is very important for the dissipation rate, we should determine what is the period and height of the waves that actually break. Experimental data shows that the breaking waves have a probability distribution $p_B(H,T)$ that is different from the distribution $p(H,T)$ of all – breaking or not – waves. We can define a weighting function W that gives the breaking wave distribution from the full wave distribution,

$$p_B(H,T) = p(H,T)W(H,T). \tag{5.27}$$

The dissipation rate per unit time and per unit horizontal surface is thus an average over all heights and should equal the sum of all spectral components,

$$\epsilon_{\text{tot}} = \int \epsilon(H,D,T)W(H,T)p\,(H,T)\,\mathrm{d}H = \rho g \int_{\mathbf{k}} S_{\text{dis}}\,(\mathbf{k})\,\mathrm{d}\mathbf{k}. \tag{5.28}$$

In deep water, neither the orbital velocity nor the pressure gradient are uniform over the vertical. The energy flux is thus clearly different from the shallow water value. Hence the depth D that appears in the dissipation rate ϵ should be – at the very least – replaced by a relevant length scale $\widetilde{h}$. Chawla and Kirby (2002) proposed to use $\widetilde{h} = \tanh(kD)/k$ which goes to D when kD goes to zero. In order to reproduce the wave evolution in both deep and shallow water, Filipot et al. (2010b) have redefined B as a function of kD with $B = 0.185/\tanh[(kD)^{1.5}]$. This leads to

$$\epsilon(H,D,T) = \frac{1}{8\pi}\rho g k\,(BH)^3\sqrt{\frac{gk}{\tanh(kD)}} \tag{5.29}$$

The choice of $\widetilde{h}$ can be debated and should be determined from an energy balance such as eq. (23.11).

5.3.3 Breaking wave statistics in shallow water

Finally, the dissipation rate requires a definition of $W(H,T)$ and $p\,(H,T)$. In shallow water, the energy is usually integrated across frequencies, and in that case we only need $W(H)$ and $p\,(H)$. The latter is often taken to be the Rayleigh distribution p_R (figure 22.8). For W, two different choices have been made. The first choice by Battjes and Janssen (1978) is based on the idea that all breaking waves have the same height corresponding to the depth limitation $H = \gamma D$ in which γ is a known constant, and the probability of occurence of these waves is simply given by the Rayleigh distribution, namely $Q_B = p_R(h > \gamma D)$. The resulting functions $p(H)$ and $W(H)$ thus have a singularity at $H = \gamma D$. On the problem of this first approach is that it can lead to unphysical parameters such as $Q_B > 1$, which is not very nice for a probability (Janssen and Battjes, 2006).

The second choice is an empirical determination of W from observations. After days of counting waves passing by a fixed location in the surf zone, Thornton and Guza (1983) have proposed the empirical expression

$$W(H) = \left(\frac{H_{\text{rms}}}{\gamma D}\right)^4 \tag{5.30}$$

where γ plays a role similar to the γ in Battjes and Janssen (1978). One reason why they chose this particular form, is that it allows an analytic integration of eq. (5.28) that gives,

$$\epsilon_{\text{tot}} = \frac{3}{16}\pi^{1/2}\rho g\frac{B^3}{\gamma^4 D^5} f_p H_{\text{rms}}^7. \tag{5.31}$$

in which f_p is the peak frequency.

Breaking wave statistics in deep water

Many applications, including underwater acoustics, remote sensing and the investigation of air-sea fluxes, rely on some characterization of breaking waves. The investigation of breaking waves has been limited for a long time ot the estimation of the whitecap coverage in which the active part and the residual foam was separated (e.g. Monahan and Woolf, 1989). This coverage was found to be strongly related to the wind speed, with an increase from very low values for pour $U_{10} < 7$ m s^{-1}, to about 1 % for $U_{10} \simeq 10$ m s^{-1}, 6 % for $U_{10} \simeq 20$ m s^{-1}, and much more for yet higher wind speeds. In fact, these

variations in foam coverage and aspect are the basis of the Beaufort scale (see table A.1) that is still used to determine the wind speed from a visual inspection of the sea.

Wave breaking can also occur without any wind, due to the convergence of wave energy associated to current gradients or the bottom topography. Most authors have distinguished a 'depth-induced' wave breaking that occurs near the shore in the 'surf zone', from the 'whitecapping' that occurs in deep water, usually in the presence of wind. This distinction can be fuzzy in the case of shallow tidal flats, which is why we preferred to have a single breaking definition (Filipot and Ardhuin, 2012).

The fraction of sea surface covered by foam or the breaking probability used in shallow water is not sufficient to fully characterize wave breaking. Hence Phillips (1985) proposed a spectral description of breaking and introduced the breaking spectrum Λ, which is the density of breaking crest length per unit surface and per unit vector speed $\mathbf{c}$ of the breaking fronts. With this definition, the length $\Lambda(\mathbf{c})\mathrm{d}c_x\mathrm{d}c_y$

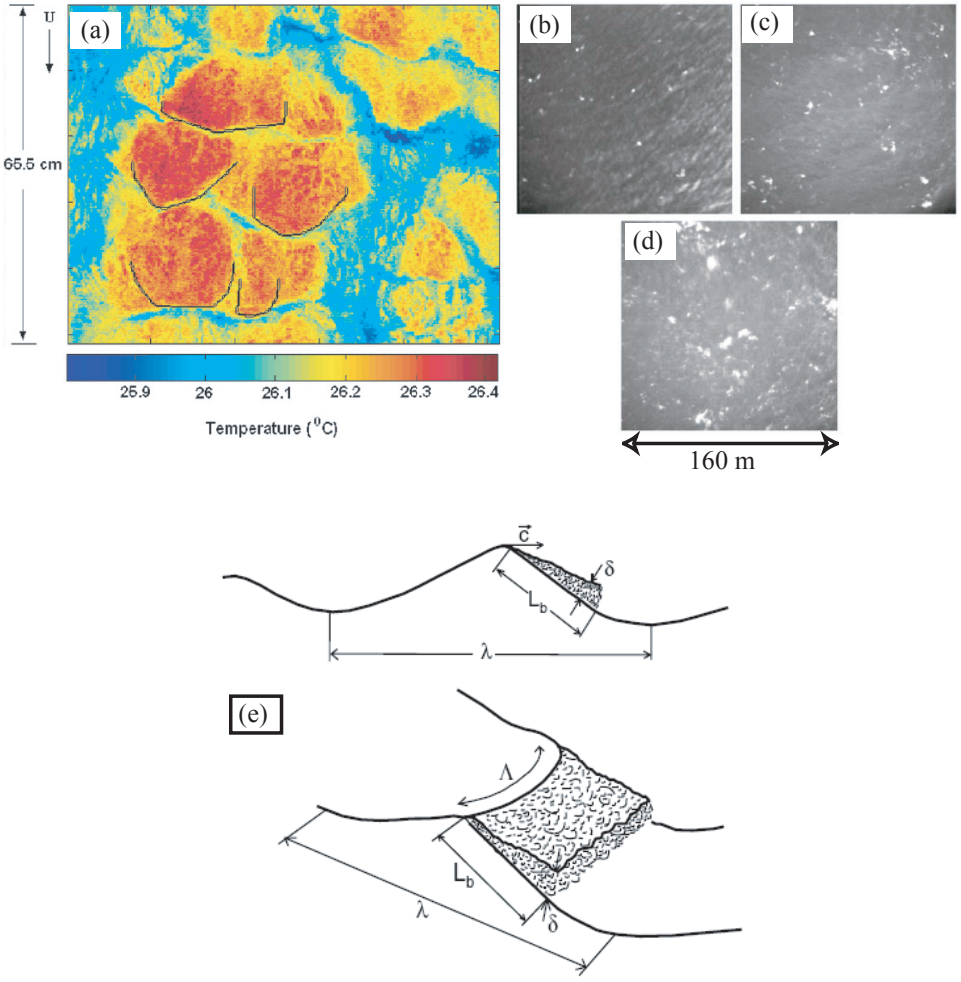

Figure 5.7: Breaking fronts
(a) Detection of breaking front, in black, using infrared imagery of micro-breakers (picture from Jessup and Phadnis 2005) , (b), (c), (d) foam coverage for wind speeds of 7, 10 and 14 m s^{-1} (Melville and Matusov 2002), and (e) schematic defining Λ (from Reul and Chapron 2003).

is the total length of all breaking fronts per unit sea surface that move at a speed $\mathbf{c} = (c_x, c_y)$ within a speed interval $\mathrm{d}c_x$ and $\mathrm{d}c_y$. In general c is about 0.8 times the phase speed C of the dominant waves that are breaking, due to modulation effects (Banner et al., 2014). Such a decomposion of the breaking waves was motivated by the observation by Duncan (1981, 1983) in the laboratory that the dissipation is proportional to c^5.

Other interesting quantities derived from Λ include the fraction of the sea surface wiped by breaking fronts per unit time $\int c\Lambda \mathrm{d}c_x\mathrm{d}c_y$. Assuming that the breaking waves have self-similar shapes, Λ can also be used to provide a an estimate of the mean foam thickness (Reul and Chapron, 2003).

The investigation of breaking wave properties has thus focused onthe estimation of Λ from observations or models. This is not an easy task, requiring high resolution video data in both optical and infrared

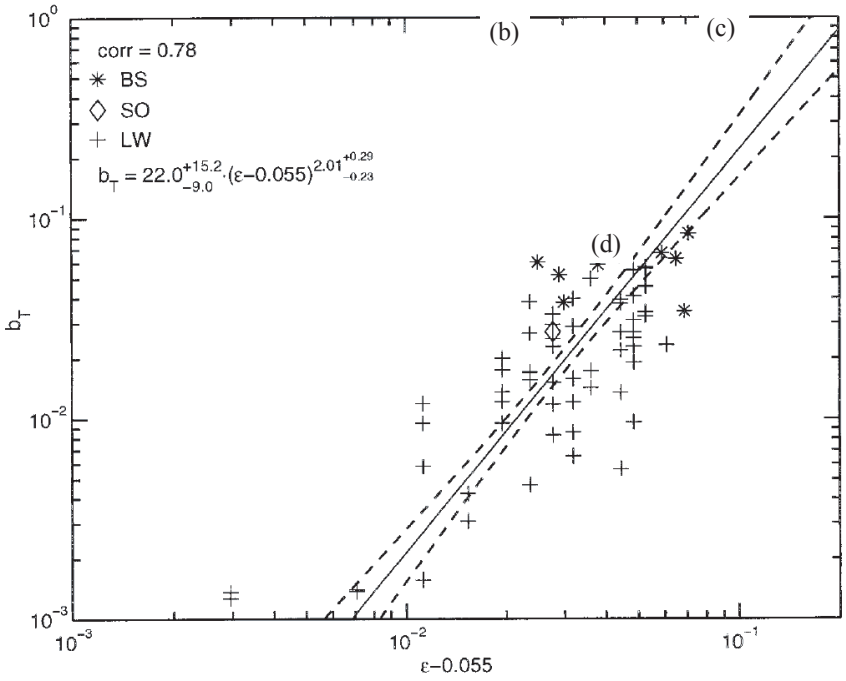

Figure 5.8: Breaking probability and saturation
The probability of breaking of dominant waves b_T is linked to the steepness of the dominant waves ε which is related to the saturation $\varepsilon^2 \simeq 4B(\mathbf{k})$ with $\Delta\theta = \pi$ and $\Delta k \simeq 0.6k$. The threshold over which breaking is observed is $\varepsilon = 0.055$, which corresponds to $B(\mathbf{k}) \simeq 1 \times 10^{-3}$.

as illustrated in figure 5.7 (e.g. Sutherland and Melville, 2013). More classical measurements of surface elevation time series have also been associated to a visual or acoustic indentification of breaking waves (Banner et al., 2000; Babanin et al., 2001; Manasseh et al., 2006). These studies have led to the conclusion that the breaking of dominant waves is not associated to a fixed threshold, but that statistically, the probability of breaking waves can be predicted from the energy level of dominant waves. There is a fixed threshold, when the energy is put in non-dimensional form, over which breaking occurs. There is thus a link between the breaking probability and the 'saturation' spectrum $B(\mathbf{k})$ introduced by Phillips (1985) and defined by

$$B(k,\theta) = \int_{\theta-\Delta\theta}^{\theta+\Delta\theta} \int_{k-\Delta k}^{k+\Delta k} \cos^p(\theta-\theta') k^2 E(k,\theta') \mathrm{d}k \mathrm{d}\theta'. \tag{5.32}$$

As pointed out by Phillips (1984), using a local definition of B with $\Delta\theta$ and Δk very small makes sense only if the spectrum is relatively smooth. Indeed, for a narrow spectrum, B could be very large with very small amplitude waves, even going to infinity for monochromatic waves. In their analysis Banner et al. (2000) used $\Delta\theta = \pi$, $p = 0$ and $\Delta k \simeq 0.6k$. In fact, it is difficult to investigate breaking statistics for small values of $\Delta\theta$, due to the greater statistical uncertainty. In practice the breaking probability is associated to the presence of steep waves, and these can exist only if wave trains with neighboring wavenumbers and directions can interact to form wave groups that live long enough to let the waves evolve towards breaking. The basic interaction is first a linear superposition, and the eventual evolution up to breaking is obviously nonlinear (e.g. Song and Banner, 2002).

Besides, the fact that B has no dimensions suggests that breaking mainly depends on the shape of the waves, while other factors (wind, current ...) are only secondary. After a first demonstration for dominant waves, a threshold for B has also been proposed for the shorter compoents (Banner et al., 2002).

We note that if B is constant then the wavenumber spectrum integrated over directions decays like k^{-3} and, assuming that waves are linear, the frequency spectrum decays like f^{-5}. Besides, a constant non-dimensional spectrum means that all the scales have the same shape: the waves are self-similar. We had found before that non-linear wave-wave interactions tend to impose a f^{-4} shape to the spectrum. Well, this shape is not possible beyond some frequency where it crosses the f^{-5} asymptote as the steepness of the waves must be limited by breaking.

5.3.4 A spectral approach

In order to decompose the overall dissipation rate $\epsilon_{\rm tot}$ across the spectrum one can use an empirical approach by distributing the total dissipation with particular shape factor, e.g. using a distribution of the dissipation proportional to f^2, as is often done for depth-induced breaking in the surf zone. In that case, waves are almost not dispersive and it makes sense to combine all components.

In other conditions, it makes sense to decouple the disspation of wave components that have very different wavelengths and directions. In that case we can define a parametrization that is consistent with the data of Banner et al. (2000).

A first step is thus to determine the breaking probability for different wave 'scales': these scales are spectral regions within which the frequencies and directions are close enough that their superposition produce well defined wave groups with long-lived wave crests that have enough time evolve towards breaking. We can then link the breaking probability to B which, taking $p = 2$ is a non-dimensional variance of the orbital velocity.

The second step is to atribute to each spectral component that contribute to a given scale the braking probability and dissipation rate. This gives a dissipation source term

$$S_{\rm dis,s}\left(\mathbf{k}\right) = \int_{\mathbf{k}} h(\mathbf{k}'-\mathbf{k}) p\left(B(\mathbf{k}')\right) q\left(B'(\mathbf{k}')\right) \mathrm{d}\mathbf{k}' E\left(\mathbf{k}\right). \tag{5.33}$$

in which the integral over $\mathbf{k}'$ is the deconvolution from the scales to the spectral components with a filter h, with p the breaking probability for the a give scale, and q the dissipation rate per unit crest length. This approach was formalized by Filipot et al. (2010a); Filipot and Ardhuin (2012).

An intermediate approach is to define an empirical relationship between one definition of B and the dissipation rate (van der Westhuysen et al., 2007; Ardhuin et al., 2010; Rogers et al., 2010; Romero et al., 2012). The formulation of Ardhuin et al. (2010) introduced a partial integration over directions for B in order to enhance the directional spreading of the resultin wave spectrum,

$$S_{\rm ds}(f,\theta) = \sigma C_{\rm ds}\left[\max\left\{\frac{B\left(f,\theta\right)}{B_r} - 1, 0\right\}\right]^2 F(f,\theta) + S_{{\rm ds},c}(f,\theta). \tag{5.34}$$

where

$$B\left(f,\theta\right) = 2\pi \int_{\theta-\pi\theta}^{\theta+\pi} k^3 cos^2\left(\theta-\theta'\right) F(f,\theta')/C_g \mathrm{d}\theta', \tag{5.35}$$

with $B_r = 0.0009$ is a threshold for breaking that is consistent with the estimate of Banner et al. (2000).

All these parametrizations combine this kind of spontaneous dissipation rate with the dissipation of waves that are steep, and an induced $S_{\rm dis,c}$ dissipation rate, in which the effect of long waves on short waves is parameterized. One parameterization for that effect by Ardhuin et al. (2010) assumes that the short waves are 'wiped out' by the long waves. A first approximation is that a breaking wave with a period at least M times the short wave period considered will lead to a complete disspation of the short waves encoutered by the long wave breaking front. We can first estimate the number of long waves that overtake ther short waves per unit time, it is the integral of $|\mathbf{C}-\mathbf{C}'|\,\Lambda(\mathbf{C})d\mathbf{C}$. This gives an induced dissipation source term

$$S_{{\rm ds},c}(f,\theta) = \int_0^{f/M} |\mathbf{C}-\mathbf{C}'|\,\Lambda(f',\theta')\mathrm{d}f'\mathrm{d}\theta' F(f,\theta), \tag{5.36}$$

where we have considered that $\mathbf{C}'$ is roughly the same as the phase speed of the waves with frequency f' and direction θ'.

Most numerical wave models today use empirical expressions for the dissipation rate that are adjusted to reproduce simple situations like fetch-limited growth and full development. Some of these parametrizations can have funny behaviors in the presence of swells, shallow water of strong current gradients. In general one extra dissipation term for depth-induced breaking is used in order to properly dissipate waves in the surf zone. The parametrization of Filipot and Ardhuin (2012) is unique in being able to dissipate waves in both deep and shallow water, but it still needs to be further tested in intermediate water depth and over current gradients.

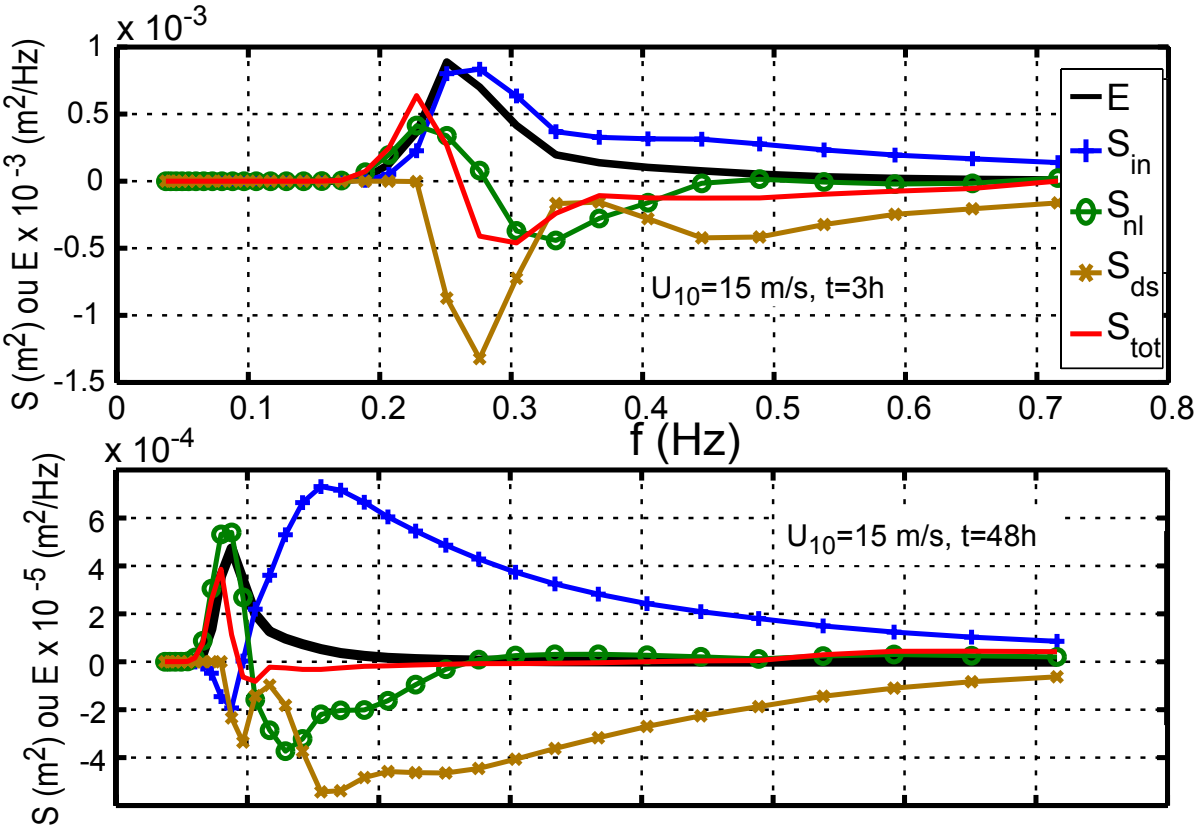

Figure 5.9: Source term balance
Source terms for a wind speed of 15 m/s with a uniform sea starting from rest at $t = 0$. (a) spectrum and source terms after 3 hours, (b) after 2 days.

5.4 Spectral energy balance

Given the uncertainties on generation and dissipation processes the empirical parameters in these two source functions are usually adjusted so that the integration of the full spectral evolution equation

$$\frac{\mathrm{d}E(\mathbf{k})}{\mathrm{d}t} = S_{\mathrm{in}}(\mathbf{k}) + S_{\mathrm{nl}}(\mathbf{k}) + S_{\mathrm{dis}}(\mathbf{k}) \tag{5.37}$$

reproduces as well as possible the observations of fetch-limited growth (e.g. Kahma and Calkoen, 1992) and other observations, such as the the slanting fetch data reported by Ardhuin et al. (2007). Eq. (5.37) where the total derivative is a rate of change following wave packets along rays, is most often written in Eulerian form. In the absence of currents it is,

$$\frac{\partial E(\mathbf{k})}{\partial t} + \boldsymbol{\nabla}_{\mathbf{x}} \cdot (\mathbf{C}_g E(\mathbf{k})) + \boldsymbol{\nabla}_{\mathbf{k}} \cdot (\mathbf{C}_k E(\mathbf{k})) = S_{\mathrm{in}}(\mathbf{k}) + S_{\mathrm{nl}}(\mathbf{k}) + S_{\mathrm{dis}}(\mathbf{k}) \tag{5.38}$$

in which $\boldsymbol{\nabla}_{\mathbf{x}}$ and $\boldsymbol{\nabla}_{\mathbf{k}}$ are divergence operators in physical and wavenumber space, respectively, $\mathbf{C}_g$ and $\mathbf{C}_k$ are the corresponding propagation speeds. $\mathbf{C}_g$ is the vector group speed, which points into the direction of the wavenumber $\mathbf{k}$, and $\mathbf{C}_k$ is the rate of change of the wavenumber $\mathbf{k}$, which is due to the bottom slope and the Earth curvature. Indeed, waves follow geodesics, which are great circles on a spherical Earth. Hence their direction, relative to the north pole, change during propagation.

Among the three source terms, S_{in} defines the range of frequencies where the wind sea is generated, with phase speeds less than the wind speed, this is why it requires very strong winds to produce long waves that will radiate as swells. At low frequencies S_{in} is weakly negative. The energy provided by the wind via S_{in} is redistributed by the wave interaction term S_{nl} with a flux to both high and low frequencies. The low frequency flux makes it possible to have fully developed waves that actually travel faster than the wind, with a peak frequency up to 1.2 times U_{10}. The dissipation term S_{ds} removes the excess of energy due to strong wave steepness.

The sum of the three terms gives the trend of the spectral evolution, which, integrated in time gives the evolving spectrum, with an example on figure 5.9. All operational wave models use a discretization of the energy balance equation (5.38), with finite differences in time.

Most differences between models, at least for the windsea part of the spectrum, are due to differences in the parametrizations. Figure 5.10 shows and example of different parametrizations. Todays most accurate model results have been obtained with the parametrizations by Rascle and Ardhuin (2013). There are still problems at short fetch and for high frequencies, with a poor representation of the directional distribution and an overestimation of the energy level at $f > 3f_p$.

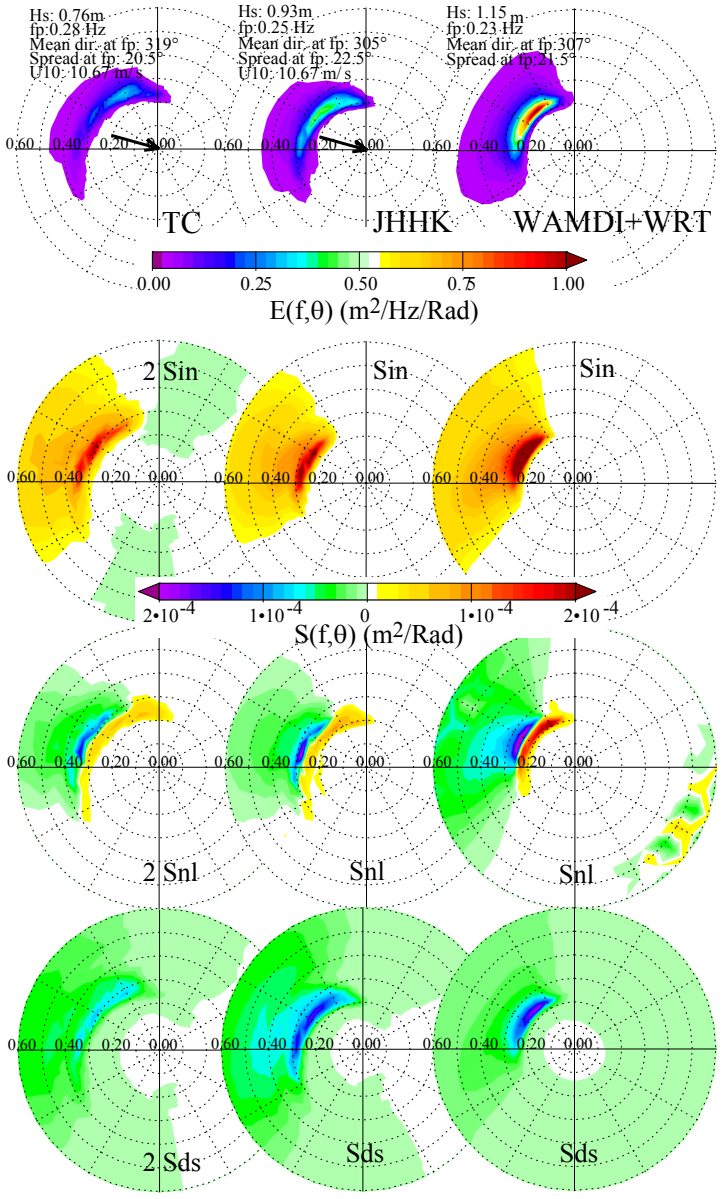

Figure 5.10: Three sets of parameterizations, three different balances
Source terms for a wind speed of 10 m/s at a fetch of 40 km. Left: parametrization by Tolman and Chalikov (1996) with much weaker input and disspation, center: WAM-Cycle 4 (Janssen et al., 1994), right WAM-Cycle 3 in which the DIA parametrization has been replaced by an exact calculation of the interactions. The Tolman and Chalikov (1996) terms have been multiplied by 2 in order to be in the same range. Picture from Ardhuin et al. (2007).

Chapter 6

Waves and momentum

6.1 Stokes drift

The displacements of fluid parcels caused by waves is dominated by the periodic oscillations $\widetilde{\xi}_h$ and $\widetilde{\xi}_3$ derived in chapter 2 for linear waves. For many application this first approximation may not be sufficient. Let us examine what has been neglected. To be exact, the position $(\mathbf{x}(t), z(t))$ of a fluid parcel is the sum of its velocities at the successive positions (e.g. Phillips, 1977, p. 43),

$$(\mathbf{x}(t), z(t)) = (\mathbf{x}(0), z(0)) + \int_0^t \left(\mathbf{u}\left(\mathbf{x}(t'), z(t'), t'\right), w\left(\mathbf{x}(t'), z(t'), t'\right)\right) \mathrm{d}t'. \tag{6.1}$$

To the first order in steepness $\varepsilon = ka$, the velocity equals the velocity at the initial position,

$$\left(\mathbf{u}\left(\mathbf{x}(t'), z(t'), t'\right), w\left(\mathbf{x}(t'), z(t'), t'\right)\right) \simeq \left(\mathbf{u}\left(\mathbf{x}(0), z(0), t'\right), w\left(\mathbf{x}(0), z(0), t'\right)\right). \tag{6.2}$$

Integrating in time this gives a periodic motion, $(\mathbf{x}(t), z(t)) = (\mathbf{x}(0), z(0)) + (\xi_h, \xi_3)$ as given by eqs. (2.30)–(2.31).

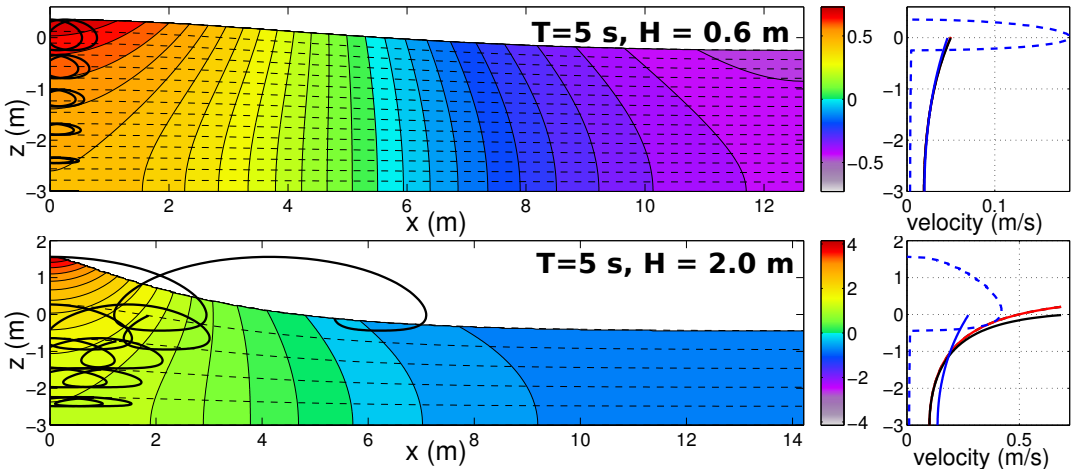

Figure 6.1: Left: Horizontal velocity field at $t = 0$ and particle trajectories integrated over 2 Eulerian periods. Solid lines are isotachs and dashed lines are streamlines in the frame of reference moving with the wave phase speed. Right: vertical profile of Eulerian mean water velocity (dashed, velocity is set to zero in the air for computing the average), Generalized Lagrangian mean (red), Lagrangian mean (black) and Lagrangian mean from the linear approximation (blue). Both top and bottom panels are computed with streamfunction theory to 80th order (Dalrymple, 1974). Non-linear terms are only significant in the bottom case.

However, the exact calculation (figure 6.1) shows that the motion is not periodic. This is because the velocity varies over the displacement distance. That variation introduces a correction of the position

that is of second order in the wave amplitude. This is given by the following Taylor expansion

$$\begin{aligned}\mathbf{u}\left(\mathbf{x}(t'),z(t'),t'\right) &= \mathbf{u}\left(\mathbf{x}(0),z(0),t'\right)\\ &\quad+\mathbf{u}_2\left(\mathbf{x}(0),z(0),t'\right)\\ &\quad+\xi_h(t')\cdot\boldsymbol{\nabla}\mathbf{u}\left(\xi_h(0),\xi_3(0),t'\right)+\xi_3(t')\frac{\partial}{\partial z}\mathbf{u}\left(\xi_h(0),\xi_3(0),t'\right)+O(\varepsilon^3),\end{aligned}\tag{6.3}$$

where $\mathbf{u}_2$ is the gradient of the second order potential ϕ_2, which comes in the solution of non-linear wave equation (18.3). That term can be rather complex to compute, and it is done in chapter 19. However, we do not need to worry about that term because the average over time of $\mathbf{u}_2$ is zero. We will thus only consider the last two terms which are given by products of linear terms.

First of all $\xi_h(t)$ is 90 degrees out of phase with $\mathbf{u}$, and $\boldsymbol{\nabla}\mathbf{u}$ is also 90 degrees out of phase with $\mathbf{u}$. Hence $\xi_h(t)$ and $\boldsymbol{\nabla}\mathbf{u}$ are in phase and their product has a non-zero average, $\mathbf{k}\sigma a^2\cosh^2(kz+kh)/[2\sinh^2(kD)]$. Physically this corresponds to the fact that the orbital velocity at the crest is in the same direction as the crest motion, hence particles ride with the crest longer than they stay in the trough where particles move opposite to the wave propagation. Likewise, ξ_3 is in phase with $\partial\mathbf{u}/\partial z$, which corresponds to the fact that the horizontal velocity increases vertically, and thus a particle goes forward faster when it is up compared to when it is down. That other product gives also a non-zero average, $\mathbf{k}\sigma a^2\sinh^2(kz+kh)/[2\sinh^2(kD)]$. These two effects add up to give the Stokes drift, defined as

$$\mathbf{U}_s\equiv\frac{1}{T_L}\int_0^T\mathbf{u}\left(\mathbf{x}(t'),z(t'),t'\right)\mathrm{d}t'=\sigma\mathbf{k}a^2\frac{\cosh(2kz+2kh)}{2\sinh^2(kD)}(1+O(\varepsilon)),\tag{6.4}$$

where T_L is the Lagrangian period, namely the time it takes for a parcel starting from a crest to loop to the next crest. The bottom panel in figure 6.1 clearly shows that the Lagrangian period is longer than the Eulerian period: after two Eulerian period the particles that started at the crest are not yet back to the crest, because they have moved forward ahead of the next crest.

In deep water ($kD\gg1$), U_s goes to

$$\mathbf{U}_s=\sigma\mathbf{k}a^2\exp(2kz).\tag{6.5}$$

This speed U_s is the average drift speed of a water parcel and it is directed in the direction of wave propagation. It is a mean Lagrangian velocity. Hence the parcel displacement is not exactly periodic and the parcels move forward (figure 2.3). This drift velocity decreases strongly with depth, in deep water this decrease is twice as fast as the orbital velocity, as shown on figure 2.3.

First of all, it should be emphasized that we have computed a second order drift from a linear wave field. The top-right panel in figure 6.1 clearly shows that for a nearly linear wave the Stokes drift is dominated by the contribution of linear wave field (blue profile). There is a widely held misconception that Stokes drift is a property of non-linear waves. This is wrong. In fact, the Stokes drift is a quadratic property, just like the wave energy. Linear waves have a Stokes drift, just like they have an energy.

This correspondence between Stokes drift and energy is a very profound physical property (Andrews and McIntyre, 1978b). The Stokes drift computed here is the pseudo-momentum of the wave field. When integrated over the vertical it is

$$\mathbf{M}^w=\rho_w\int_{-h}^0\mathbf{U}_s\mathrm{d}z=\frac{\cosh(kD)}{2\sinh(kD)}\rho_w\sigma a^2=\rho_w g\frac{a^2}{2C}=\frac{E_t}{C}\tag{6.6}$$

with E_t the wave energy per unit surface. Eq. (6.6) is a very general result in physics for all types of waves. It is the same result as the momentum of a photon $p=E/c$, where c is the speed of light. For non-linear waves of finite amplitude, the exact relationship is $\mathbf{M}^w=2E_c/C$, where E_c is the mean kinetic energy per unit surface (Longuet-Higgins, 1984, see chapter 18.2).

Finally, this transport can also be computed from the Eulerian velocity, integrated from the bottom to the crest level,

$$\mathbf{M}^w=\rho_w\left\langle\int_{-h}^{\zeta}\mathbf{u}\mathrm{d}z\right\rangle=\int_{-a}^{a}\langle\rho\mathbf{u}\rangle\,\mathrm{d}z\tag{6.7}$$

These two estimates of the transport correspond to the two different views of the Stokes drift. In the Eulerian point of view, the mass transport only happens between the crests and the troughs, with a profile that is a parabola for linear waves. In the Lagrangian point of view the drift happens over the entire water column (figure 6.2).

Finally, we also note that there is also a Stokes drift in the air, which is also in the direction of propagation and has a profile that decays vertically up, like the profile of Stokes drift in deep water. It is easily computed by the same method that was used here in the water.

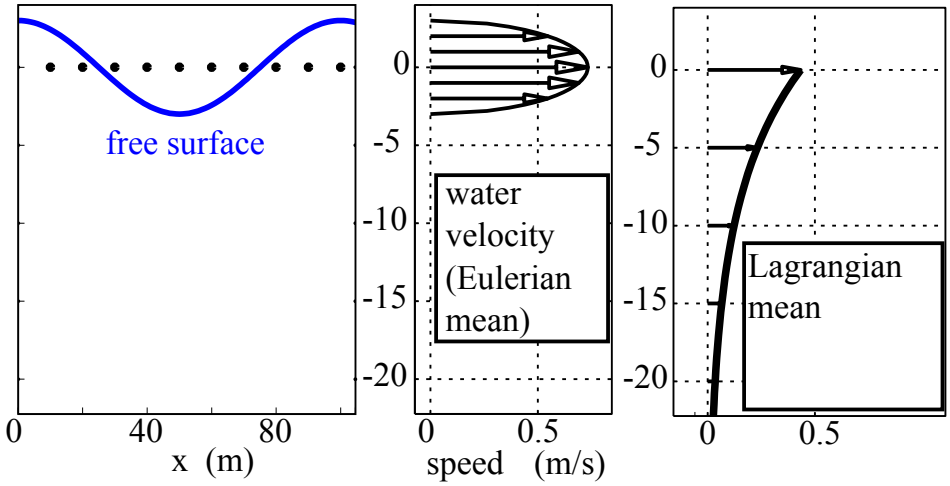

Figure 6.2: Mass transport from an Eulerian and Lagrangian point of views, computed here for an amplitude $a = 30$ m, wavelength $L = 100$ m in 30 m water depth, using linear wave theory.

6.2 The 'shear' of the Stokes drift

Another interesting property of the Stokes drift is that it has a strong vertical shear, in particular in deep water, but also for strongly nonlinear waves in shallow water (Miche, 1944a). This may seem paradoxical that an irrotational flow, with zero vorticity, has an average with a strong shear. This apparent paradox comes from the fact that the curl operator does not commute with the Lagrangian average. Another funny property is that the Lagrangian average of dw/dx is also non-zero, although the motion is periodic in x (Ardhuin and Jenkins, 2006).

The shear of the Stokes drift also has the very nice property to persist in the presence of strong mixing, because the mixing is usually done by eddies that have time scales longer than the wave period. Hence one should be very careful to apply to the wave motion the eddy viscosity ideas that are usual for currents. Indeed, the assumption that the effect of turbulence is analogous the the molecular viscosity scaled up by a factor 100 or more does not work with waves: if it were the case the waves would dissipate over very short distance and swells would never be recorded from remote storms. The 'eddy viscosity' idea is thus a very dangerous idea in the presence of oscillations, and turbulence closures should generally be visco-elastic and not just viscous (e.g. Miles, 1996).

This persistence of the vertical shear of the drift makes the ocean surface boundary layer special and tends to tilt vorticity that is perpendicular to the wind into the wind direction, promoting the generation of rolls aligned in the wind. These are known as Langmuir circulations (Langmuir, 1938), which is a key component of the ocean mixed layer. These properties of the upper ocean will be further discussed in chapter 10.

6.3 Random waves and practical estimation

Although the Stokes drift plays an important role, it is very difficult to measure in the ocean because it requires the measurement of both the Eulerian velocity and the drift at the same place, and drift if usually measured at the surface only with objects that can be also affected by the direct influence of the wind or the radiation stress of the very short waves. Indeed, no object or surfactant drifts exactly like the water surrounding it, and only non-intrusive methods using for example infrared technology (Veron et al., 2008) or surface wave dispersion (Laxague et al., 2018) can provide unambiguous measurements.

As a result, almost all estimates of the Stokes drift are based on the measurement of the wave spectral properties and the use of linear wave theory because the Stokes drift for a random wave field with no phase-correlations between the wave components is simply derived from eq. (6.3), as done by Kenyon (1969). The horizontal Stokes drift vector is thus,

$$(U_S, V_S) = \int_0^\infty 2\sigma k \frac{\cosh(2kz + 2kh)}{2\sinh^2(kD)} \int_0^{2\pi} (\cos\theta, \sin\theta) E(f,\theta) \mathrm{d}\theta \mathrm{d}f. \tag{6.8}$$

The inner integral can be replaced by the moments a_1 and b_1 that are directly measured by wave buoys (see chapter 17 for details),

$$(U_S, V_S) = \int_0^\infty 2\sigma k \frac{\cosh(2kz + 2kh)}{2\sinh^2(kD)} (a_1(f), b_1(f)) E(f) \mathrm{d}f. \tag{6.9}$$

The broad directional spectrum at high frequency contributes little to the total surface drift (Peureux et al., 2018). As a result, the vertical profile of the Stokes drift can have a strong shear but weaker than predicted by simple parameterizations such as the one by Breivik et al. (2016), or when using parametric spectra such as the one by Elfouhaily et al. (1997).

Finally we note that non-linear effects typically enhance the drift, such as shown in figure 6.1. But there is no published theory giving the expression for nonlinear corrections to the Stokes drift for a random wave spectrum. That can be derived using the surface elevation second order spectrum (Janssen, 2009; Leckler et al., 2015).

6.4 Radiation stresses and the flux of wave momtum

Just like the wave energy is radiated by the wave field, the wave momentum is also radiated away. Considering monochromatic waves (i.e. with a single period and direction) propagating along the x-axis, there is a flux of momentum across any surface perpendicular to the propagation direction. By definition, there are two ways to move momentum in the x direction,

- by pushing things around: the pressure forces transmit momentum from one water column to the next,
- by advecting the momentum density per unit volume ρu with the velocity u.

The usual definition of the momentum flux associated to waves, and called the 'radiation stress', is the flux of momentum when the waves are present minus the flux when waves are absent. It is a strange definition because the interaction of waves and currents make it impossible to have the exact same current without the waves, in practice it means that we assume the sea level to remain the same and we just set the orbital velocity to zero and the pressure becomes the hydrostatic pressure. A more rigorous definition is given in Andrews and McIntyre (1978b) and discussed in chapter 24. Anyway, let us make this thought experiment of removing the waves, we define the first component of the radiation stresses by a phase average of the wave effects,

$$S_{xx}^{\mathrm{rad}} = \overline{\int_{-h}^{\zeta} p + \rho_w u^2 \mathrm{d}z} - \int_{-h}^{\overline{\zeta}} p_0 + \rho_w \widehat{u}^2 \mathrm{d}z, \tag{6.10}$$

where the second term correspond to the pressure p_0 in the absence of waves (but with the same mean sea level) and $\widehat{u}$ is the the mean (current) velocity.

When the waves are present, the pressure is obtained by integrating the vertical component of the momentum equation (we take $v = 0$ because waves propagate only along the x-axis)

$$\int_z^\zeta \left[\frac{\partial \rho_w w}{\partial t} + \frac{\partial \rho_w uw}{\partial x} + \frac{\partial \rho_w w^2}{\partial z} + \frac{\partial p}{\partial z} + \rho_w g \right] \mathrm{d}z = 0 \tag{6.11}$$

The first term yields

$$\int_z^\zeta \frac{\partial \rho_w w}{\partial t} \mathrm{d}z = \frac{\partial}{\partial t} \int_z^\zeta \rho_w w \mathrm{d}z - \rho_w w\left(\zeta\right) \frac{\partial \zeta}{\partial t}, \tag{6.12}$$

the second yields,

$$\int_z^\zeta \frac{\partial \rho_w uv}{\partial x} \mathrm{d}z = \frac{\partial}{\partial x} \int_z^\zeta \rho_w uw \mathrm{d}z - \rho_w u\left(\zeta\right) w\left(\zeta\right) \frac{\partial \zeta}{\partial x} \tag{6.13}$$

the third yields

$$\int_z^\zeta \frac{\partial \rho_w w^2}{\partial z} \mathrm{d}z = \rho_w w^2\left(\zeta\right) - \rho_w w^2\left(z\right), \tag{6.14}$$

and, assuming $p\left(\zeta\right) = 0$, the fourth term gives the pressure at elevation z,

$$\int_z^\zeta \frac{\partial p}{\partial z} \mathrm{d}z = -p\left(z\right). \tag{6.15}$$

Gathering all this and using the surface kinematic boundary condition (2.5) gives,

$$p = \rho_w g\left(\zeta - z\right) + \frac{\partial}{\partial t}\int_z^\zeta \rho_w w \mathrm{d}z + \frac{\partial}{\partial x}\int_z^\zeta \rho_w uw \mathrm{d}z - \rho_w w^2. \tag{6.16}$$

We now take the average over a wave period and because linear wave theory has $\overline{uw} = 0$, we find

$$\overline{p} = \rho_w g\left(\overline{\zeta} - z\right) - \rho_w \overline{w^2}. \tag{6.17}$$

We can now compute the different pieces that make up S_{xx}^{rad}. It is straightforward to generalize the calculation to the flux of x_α momentum in the x_β direction, where both x_α and x_β can be either x or y. Namely,

$$S_{\alpha\beta}^{\mathrm{rad}} = \overline{\int_{-h}^{\zeta} \rho_w u_\alpha u_\beta \mathrm{d}z} + \delta_{\alpha\beta}\left(\int_{-h}^{\overline{\zeta}} \overline{p} - p_0 \mathrm{d}z + \overline{\int_{\overline{\zeta}}^{\zeta} p \mathrm{d}z}\right). \tag{6.18}$$

We note that the pressure only come in S_{xx}^{rad} and S_{yy}^{rad} because pressure is a *normal* stress. In our case of $v = 0$ and with waves propagating along the x axis, we clearly have $S_{xy}^{\mathrm{rad}} = S_{yx}^{\mathrm{rad}} = 0$.

Now replacing the velocity and pressure in $S_{\alpha\beta}^{\mathrm{rad}}$ with linear wave theory, the first piece

$$\overline{\int_{-h}^{\zeta} \rho_w u_i u_j \mathrm{d}z} \tag{6.19}$$

only comes into S_{xx}, and we actually have calculated almost the same integral in chapter 2. Indeed, the energy flux is the same integral with pu instead of u^2. For linear waves, $u = p/C\rho_w$, where $C = \omega/k$ is the phase speed. Hence the first piece of S_{xx} is equal to $E_t C_g/C$. This is very nice, this is the flux of wave momentum, just like $C_g E_t$ is the flux of wave energy.

For the last piece and for $z \simeq \zeta$ we may replace p by $\rho_w g\zeta$. That piece yields $\rho_w g\overline{\zeta^2}/2$, which is equal to the potential energy, namely $E_t/2$. Finally, we use the linear wave expression for p to get the second piece of S_{xx}^{rad},

$$\int_{-h}^{\overline{\zeta}} \overline{p} - p_0 \mathrm{d}z = \rho_w g D\overline{\zeta} - \rho_w g \frac{a^2 k}{\sinh\left(2kD\right)}\int_{-h}^{\overline{\zeta}} \sinh^2\left(kz + kD\right)\mathrm{d}z \tag{6.20}$$

using now the fact that

$$\sinh^2 x = \left(\cosh 2x - 1\right)/2 \tag{6.21}$$

we obtain

$$\int_{-h}^{\overline{\zeta}} \sinh^2\left(kz + kh\right)\mathrm{d}z = \frac{1}{4k}\left(\sinh\left(2kD\right) - 2kD\right) \tag{6.22}$$

and our second piece of S_{xx} becomes

$$\int_{-h}^{\overline{\zeta}} \overline{p} - p_0 \mathrm{d}z = \rho_w g D\overline{\zeta} + \frac{\rho_w g}{2} E\left(2\frac{kD}{\sinh\left(2kD\right)} - 1\right). \tag{6.23}$$

Finally, the third piece is

$$\overline{\int_{\overline{\zeta}}^{\zeta} p \mathrm{d}z} = \rho_w g \frac{\overline{\zeta^2}}{2} = \rho_w g \frac{E}{2}. \tag{6.24}$$

It is common practice to remove the $\overline{\zeta}$ term from $S_{\alpha\beta}^{\mathrm{rad}}$ because this is the hydrostatic pressure that varies with the sea level. Finally we have,

$$S_{xx}^{\mathrm{rad}} = \rho_w g E\left(\frac{C_g}{C} + \frac{kD}{\sinh\left(2kD\right)}\right) = \rho_w g E\left(2\frac{C_g}{C} - \frac{1}{2}\right) \tag{6.25}$$

$$S_{yy}^{\mathrm{rad}} = \rho_w g \frac{E}{2}\frac{2kD}{\sinh\left(2kD\right)} \tag{6.26}$$

$$= \rho_w g \frac{E}{2}\left(2\frac{C_g}{C} - 1\right) \tag{6.27}$$

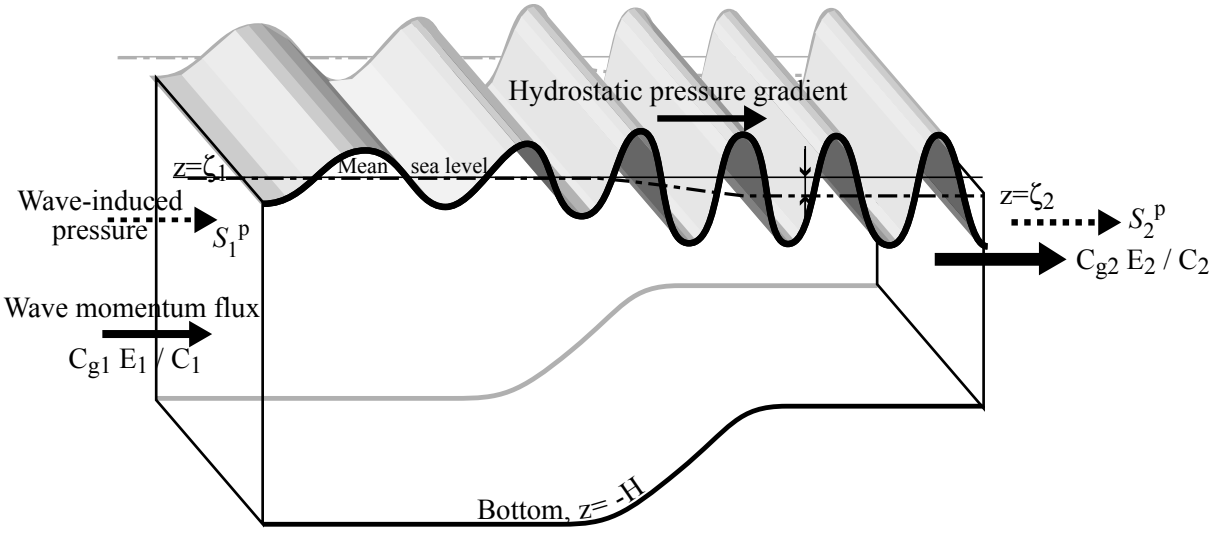

Figure 6.3: Momentum fluxes associated to waves propagating over a variable bathymetry from left to right, towards shallower water. The radiation stress S_{xx} is the sum of the flux of wave momentum $\rho_w g E C_g/C$ and the pressure correction $S^p = 0.5\rho_w g E(2C_g/C - 1)$. This pressure correction goes to zero in deep water. Here a difference between $S^{\rm rad}_{xx} = \rho_w g E C_g/C + S^p$ at points 1 and 2 drives a lowering of the mean water level from $\overline{\zeta} = \zeta_1$ to $\overline{\zeta} = \zeta_2$. This phenomenon is called the set down.

For waves propagating in any azimuth θ relative to the x-axis, the non-isotropic part of $S^{\rm rad}_{\alpha\beta}$ is modified. The orbital velocity u becomes $u\cos\theta$ and the v component becomes $v\sin\theta$. Hence $S^{\rm rad}_{xy}$ and S^{rad}_{yx} are not zero anymore,

$$S^{\rm rad}_{xx} = \rho_w g\left[E\frac{C_g}{C}\cos^2\theta + \frac{E}{2}\left(2\frac{C_g}{C} - 1\right)\right] \tag{6.28}$$

$$S^{\rm rad}_{yy} = \rho_w g\left[E\frac{C_g}{C}\sin^2\theta + \frac{E}{2}\left(2\frac{C_g}{C} - 1\right)\right] \tag{6.29}$$

$$S^{\rm rad}_{xy} = S^{\rm rad}_{yx} = \rho_w g E\frac{C_g}{C}\sin\theta\cos\theta. \tag{6.30}$$

This result was obtained using linear wave theory. For periodic non-linear waves, $S^{\rm rad}$ is actually very close to the linear theory result, with a difference that is less than 5% for $kD < 0.3$.

In general the radiation stress is thus the sum of the wave momentum flux and a correction for the change in mean pressure in the presence of waves. If the wave field varies in space, a divergence of the radiation stress is like a force exerted by the waves on the mean flow. In the absence of wave breaking the usual response to this force is a change in mean sea level, as illustrated in figure 6.3. This type of effect is discussed in more detail in chapter 16 which deals with nearshore hydrodynamics.

Chapter 7

Wave propagation over varying currents

7.1 Current effects on waves: propagation

7.1.1 A uniform current

For waves over a flat bottom, in the absence of any friction, the shape of waves and their motion is unchaged by a Eulerian uniform horizontal current $\mathbf{U}$. This is easily seen by changing the reference frame to a reference frame in which the current is zero. This is obtained with a position $\mathbf{x}'$ defined as

$$\mathbf{x}' = \mathbf{x} + \mathbf{U}t. \tag{7.1}$$

In particular the phase in the moving reference frame is given by eq (7.2), and it is transformed back to the fixed reference frame as

$$\Theta' = \mathbf{k}\cdot\mathbf{x} - \mathbf{k}\cdot\mathbf{U}t - \sigma t + \Theta_0, = \mathbf{k}\cdot\mathbf{x} - \omega t + \Theta_0 \tag{7.2}$$

where we have defined the absolute radian frequency,

$$\omega = \sigma + \mathbf{k}\cdot\mathbf{U}. \tag{7.3}$$

The effect of a uniform current is thus a simple Doppler shift of the phase, which gives a modification of the phase speed and group speed,

$$\mathbf{C}' = \mathbf{C} + \mathbf{U} \tag{7.4}$$
$$\mathbf{C}'_g = \mathbf{C}_g + \mathbf{U}, \tag{7.5}$$

where $\mathbf{C}'$ and $\mathbf{C}'_g$ are the phase and group speed in the fixed reference frame. σ is called the relative radian frequency. We note that the general definition of the group speed still holds, $\mathbf{C}'_g = (\partial\omega/\partial k_x, \partial\omega/\partial k_y)$.

7.1.2 Wave amplification when current changes in the propagation direction

Taking a current $U(x)$ in the direction of progation x, or in the opposite direction, varying only in this same direction, the waves kinematics must adjust to this variation in current speed. For slow variations on the scale of the wavelength, we use the approximation by Wentzel, Kramers, Brillouin et Jeffreys (WKBJ), i.e. the waves are locally sinusoidal, and the conservation of the number of crests (which holds for linear monochromatic waves), and which gives a constant absolute frequency ω because the medium in which the waves propagate is constant (an interesting case where ω is not conserved is when the water depth changes in time). As a result the intrinsic frequency σ must adjust. If the current accelerates in the direction of propagation, then σ must be reduced because $\mathbf{k}\cdot\mathbf{U}$ is positive. Because σ grows with k, the wavelength increases. Conversely, for waves propagating against an accelerating current, $\mathbf{k}\cdot\mathbf{U}$ is negative, hence σ and k must increases to keep ω constant.

A first application can be done in the case of deep water waves with a known radian frequency σ_1, propagating from a region 1 without current, to a region 2 where a current of magnitude U is uniform and opposite to the waves.

For linear waves, the number of crests is conserved, which can be written as a conservation of the absolute frequency,

$$\sigma_2 - k_2 U = \sigma_1. \tag{7.6}$$

Combined with the dispersion relation $\sigma_1^2 = gk_1$ and $\sigma_2^2 = gk_2$, this gives us a second order equation for the unknown relative frequency σ_2,

$$\frac{U}{g}\sigma_2^2 - \sigma_2 + \sigma_1 = 0. \tag{7.7}$$

This second-order polynomial equation has two solutions, but we shall only consider the one that gives $\sigma_1 = \sigma_2$ when U goes to zero,

$$\sigma_2 = \sigma_1 \frac{1 - \sqrt{1 - 4\alpha}}{2\alpha} \tag{7.8}$$

with $\alpha = U\sigma_1/g$, the ratio of the current velocity and the phase speed $C_1 = g/\sigma_1$ in region 1. We note that there is no real solution for $\alpha < 0.25$, in that situation the waves are blocked by the current and cannot propagate in region 2. In the limiting case, $\alpha = 0.25$, we have $\sigma_2 = 2\sigma_1$ and the local group speed C_{g2} is equal to U. In that case there is no wave energy flux, because the mean wave energy velocity is $C_g - U = 0$.

We can further investigate the case when $\alpha \ll 1$. In that case, we may write the following expansion,

$$\sqrt{1 - 4\alpha} = 1 - 2\alpha - 2\alpha^2 + O(\alpha^3) \tag{7.9}$$

which gives

$$\sigma_2 \simeq \sigma_1(1 + \alpha), \tag{7.10}$$

$$k_2 = k_1(1 + 2\alpha). \tag{7.11}$$

This means that the intrinsic wave period σ is shortened in proportion to the ratio $\alpha = U/C_1$ and the wavelength is shortened by twice that amount.

In order to know what happens to the wave height, we may consider the energy balance, as we shall do later. But be careful, this situation is precisely a situation where the wave energy is not conserved, even without any dissipation. What is conserved is the total energy in the system (waves + current), and in practice the waves and currents exchange energy. In the absence of dissipation, this interaction happens with the conservation of another quantity, the wave action, which we may define for monochromatic waves as

$$A = \frac{gE}{\sigma}. \tag{7.12}$$

With a properly defined control volume, the equality of the action fluxes gives,

$$\frac{E_2}{\sigma_2}(C_{g2} - U) = \frac{E_1}{\sigma_1} C_{g1}. \tag{7.13}$$

which gives an amplification of the wave energy

$$E_2 = E_1 \frac{\sigma_2}{\sigma_1} \frac{C_{g1}}{C_{g2} - U} \simeq E_1(1 + 4\alpha + O(\alpha^2)) \tag{7.14}$$

in which three factors are important:

- the increase of σ makes it necessary to increase E to keep A constant, this amplification comes with a transfer of energy from the current to the waves, this gives the factor $\sigma_2/\sigma_1 \simeq (1 + \alpha)$.

- the fact that the advection velocity involves the current, C_g is replaced by $C_g - U$, this accounts for half of the total effect because $U/C_g = 2\alpha$.

- the fact that the intrinsic group speed has been reduced because the wave have become shorter (σ has increased).

7.1.3 Effects of current gradients in the transverse direction: rays and refraction

Just like changes in water depth discussed in chapter 12, currents induce a modification of the phase speed. As a result, any current gradient in the direction transverse to the wave propagation will cause refraction, namely a gradual turning of the wave crests. The particularity of cases with current is that the direction of the phase advection can be different from the direction perpendicular to the crests. The directions in which rays bend follows Fermat's principle, namely waves will always take the path that gives the shortest propagation time. As a result, waves will focus in a jet that flows in the direction opposite to the wave propagation direction (as shown in Figure 7.1) and diverge in a jet of same direction.

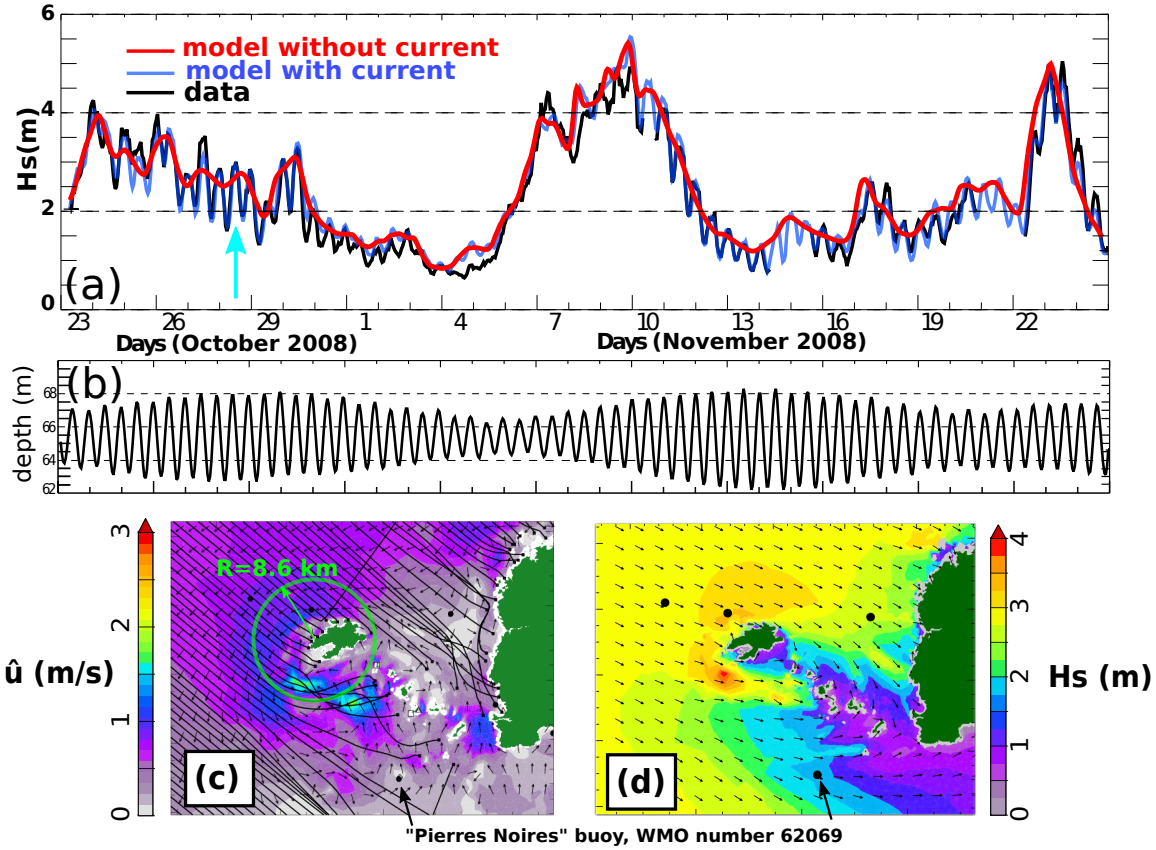

Figure 7.1: Example of strong impact of currents on wave heights due to wave refraction by currents. The top panel shows a time series of H_s recorded at the wave buoy 'Pierres Noires' (WMO number 62069) and modeled with WAVEWATCH III, while the middle panel shows the water depth at the buoy. The bottom maps show the (c) currents provided by the numerical model MARS2D and the corresponding wave rays for $T = 10$ s computed by integration of eqs. (7.16)–(7.18), and (d) shows H_s and mean wave directions, both for October 28, 2008, at 11:00 AM UTC (corresponding to blue arrow in a). Clearly, the wave height has a strong tidal modulation which is due to currents. The typical curvature radius of the rays is around 10 km in the current jet located south-west of the island of Ouessant. This jet peaks 1.5 hours after the high tide, and deviates the waves away from the Pierres Noires buoy, located 20 km down-wave (Adapted from Ardhuin et al., 2012b).

Landau and Lifshitz (1960) gave a simple result on the curvature of the rays followed by wave groups in a medium with varying mean flow velocity. This was re-derived by Dysthe (2001) for surface gravity waves. In the limit of a weak current, $\widehat{u} \ll C$, the radius of curvature of the rays is

$$R = \frac{1}{\partial\theta/\partial s} = \frac{C_g}{\boldsymbol{\nabla} \times \widehat{\mathbf{u}}_h} \tag{7.15}$$

where $\boldsymbol{\nabla} \times \widehat{\mathbf{u}}_h$ is the vertical vorticity of the flow. This result was recently applied by Gallet and Young (2014) to explain the deviation, of the order of 10°, of remote swells recorded off the southern California coast, and Lavrenov (1986) explained the formation of freak waves in the Agulhas current by

this refraction effect. Figure 7.1 shows an example off the West coast of France where the very strong vorticity of tidal currents, of the order of 0.001 s^{-1} is enough to bend wave rays for $T = 10$ s waves with a radius of curvature of 8.6 km.

The equations of wave rays are the trajectories followed by wave packets in time, these are identical to the propagation equations, before discretization, that are solved by spectral models like WAVEWATCH III (equations 2.9 to 2.11 in Tolman et al., 2014)

$$\frac{\mathrm{d}\mathbf{x}}{\mathrm{d}t} = \mathbf{C}_g + \widehat{\mathbf{u}}_h \,, \tag{7.16}$$

$$\frac{\mathrm{d}k}{\mathrm{d}t} = -\frac{\partial\sigma}{\partial D}\frac{\partial D}{\partial s} - \mathbf{k}\cdot\frac{\partial\widehat{\mathbf{u}}}{\partial s} \,, \tag{7.17}$$

$$\frac{\mathrm{d}\theta}{\mathrm{d}t} = -\frac{1}{k}\left[\frac{\partial\sigma}{\partial D}\frac{\partial D}{\partial m} - \mathbf{k}\cdot\frac{\partial\widehat{\mathbf{u}}}{\partial m}\right] \,, \tag{7.18}$$

where $\mathbf{x}$ is the horizontal position along the ray, D is the water depth, θ is the local intrinsic wave direction, $\mathbf{C}_g$ is the vector intrinsic group speed, pointing in direction θ, s is a coordinate in the direction[1] θ and m is a coordinate perpendicular to s. These ray equations are the same as those used by Mathiesen (1987), with the addition of finite depth and bottom refraction effects.

In practice the importance of refraction on wave height depends on the current structure. Gradients that are perpendicular to the dominant wave propagation and are coherent over long distances will be most effective in creating a variability in the significant wave height.

7.1.4 Waves over vertically sheared currents

In the presence of vertical shear, the Doppler shift $\mathbf{k}\cdot\mathbf{U}$ for linear waves can be estimated by solving the Rayleigh equation (22.8). Biesel (1950) gave solutions in the limit $kD \ll 1$ and for a constant shear, with a current varying from $\widehat{u}_{-D}$ at the bottom to $\widehat{u}_0$ at the surface. The phase speed is then

$$C = \left[\left(\frac{U_0 - U_{-D}}{2}\right)^2 + gD\right]^{1/2} \tag{7.19}$$

For more general current profiles and water depths, Kirby and Chen (1989) gave an approximate solution in the limit of small variations of U compared to σ/k,

$$C = \frac{\sigma}{k} + 2\int_{-D}^{0} \mathbf{k}\cdot\widehat{\mathbf{u}}\frac{\cosh(2kz+2kD)}{\sinh(2kD)}\mathrm{d}z \tag{7.20}$$

7.1.5 Practical importance of currents

In practice, current effects on waves combines the 'bunching' or 'concertina' effect described in section 7.1.2 due to a converge in the current, with the refraction, associated with current vorticity. A third effect is the enhancement of wave generation in waves against currents due to the relative wind. When we use the frame of reference moving with the current $\widehat{\mathbf{u}}$, the wind speed in that frame of reference changes from $\mathbf{U}_{10}$ to $\mathbf{U}_{10} - \widehat{\mathbf{u}}$. In practice one should thus correct the wind speed provided by a weather forecasting model to force the wind-wave generation... except for real adjustement of the wind to the presence of the current which are generally not included in weather models. Hence, the true wind is reduced by opposing currents so that the wind-wave forcing should be something between the modeled $\mathbf{U}_{10}$ and $\mathbf{U}_{10} - \widehat{\mathbf{u}}$, say $\mathbf{U}_{10} - r\widehat{\mathbf{u}}$. Numerical experiments for large scale currents suggests that on average $r \simeq 0.5$ is the right order of magnitude when adjusted to the fully coupled atmosphere-current solution (J. Bidlot, personal communication 2010). This is very important for the ocean dynamics, and forcing an ocean circulation model with $r = 1$ generally gives a work of the wind against the eddies that is too strong and produces a strong underestimation of the eddy kinetic energy (Renault et al., 2016b), with influences on the position of western boundary currents such as the Gulf Stream (Renault et al., 2016a).

In figure 7.2, we show an example of modelled current effects on waves in the Drake passage, between Chile and Antarctica. The variability of wave heights is investigated by computed the spatial spectrum of H_s. We find that the variation in wave heights at large scales is dominated by the effect of refraction, whereas at scales around 10 km, the variability is mostly due to the relative wind and advection effects.

[1] Due to the presence of the current, s differs from the along-ray direction.

Although standard processing of satellite altimeter data at scales shorter than 80 km (e.g. figure 7.2.d) is dominated by noise, adaptative denoising method are now producing data that validate this strong effect of currents (Quilfen et al., 2018).

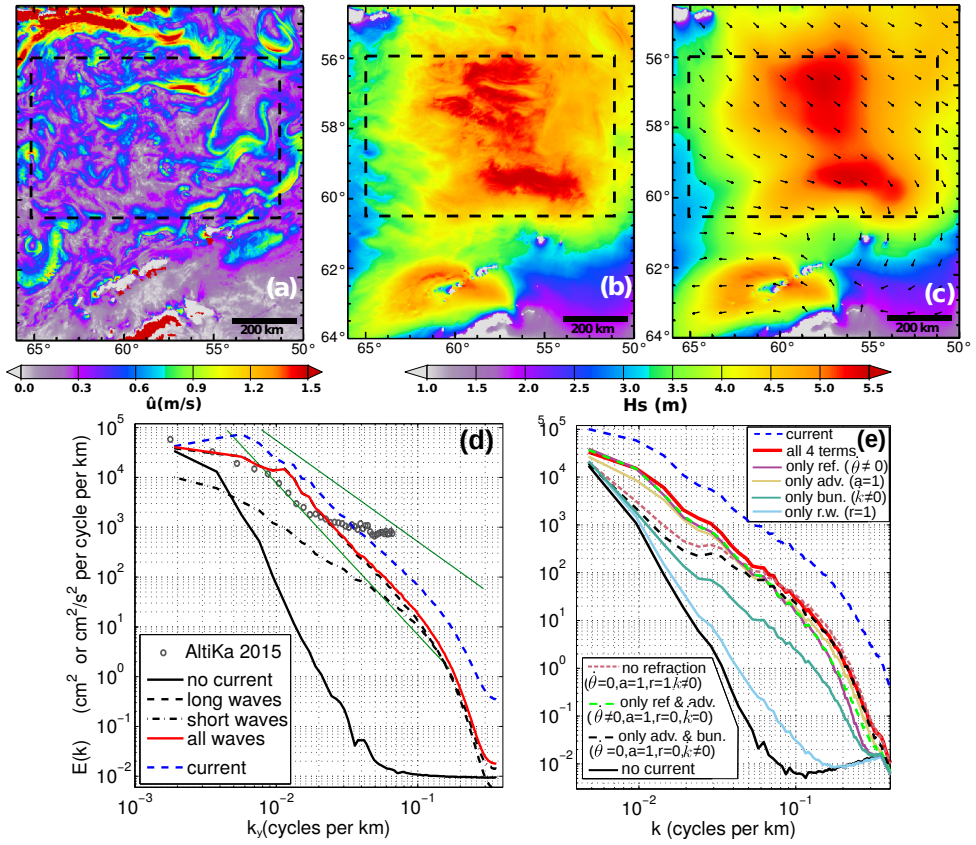

Figure 7.2: Maps for September 16 at 18:00 UTC for (a) surface current magnitude modeled by MITgcm (b) the modeled significant wave height when the current forcing is included in WAVEWATCH III (c) significant wave height without effects of currents and wind directions (arrow). The dashed box is the region used for spectral analysis. (d) Spectra of the modeled zonal current and H_s along the north-south direction, with contributions of waves of periods shorter or longer than 6 s, along-track measured spectra from AltiKa is shown for comparison, and power laws k^{-2} and k^{-3} are shown in green. (e) Omnidirectional spectrum of H_s and contributions of the current through the four different terms of the wave action equation (7.42) can be revealed by progressively switching off the different terms: refraction $\dot{\theta}$, change in wavenumber $\dot{k}$, relative wind r, and advection by u_E and v_E in $\dot{\lambda}$ and $\dot{\phi}$. Adapted from Ardhuin et al. (2017c).

7.2 Wave effects on currents

To make it as simple as possible we first follow the approach of Phillips (1977), in which the velocity field $\mathbf{u}$ is the sum of a current $\widehat{\mathbf{u}}$, that we assume uniform over the vertical, and a perturbation $\mathbf{u}'$ such that its average is zero, at least for the points of space that are always in the water.

7.2.1 Mean flow equations integrated over the vertical

A systematic discussion of wave effects on currents started with Longuet-Higgins and Stewart (1964), and we follow their derivation. The three-component momentum vector $\rho(u, v, w)$ can be advected in any direction, giving a flux tensor $\rho u_i u_j$. When one considers only velocity fluctuations $\mathbf{u}'$, the momentum flux due to the self-advection of momentum is the usual Reynolds stress $-\rho u_i' u_j'$, which is used in the analysis of turbulence. The divergence of this flux is equivalent to a macroscopic force that accelerates the fluid particles, which is easily understood by considering the momentum balance over an elementary cube.

Longuet-Higgins and Stewart (1964) introduced a similar tensor caused by waves, the radiation stress $S^{\rm rad}$, that is confined to the two horizontal dimensions, it represents a flux of momentum that comes from the average of the wave-induced Bernoulli pressure $p+u^2$. Compared to Taylor expansion methods, the present approach is easier because the non-linear wave effects are directly included by using conservation equations.

Starting from the conservation of momentum in any horizontal direction α, with our notation u_α is either the u or the v component, [2]

$$\frac{\partial}{\partial t}\left(\rho_w u_\alpha\right)+\frac{\partial}{\partial x_\beta}\left(\rho_w u_\alpha u_\beta+p\delta_{\alpha\beta}\right)+\frac{\partial}{\partial z}\left(\rho_w u_\alpha w\right)+\varepsilon_{\alpha\beta i}f_i\rho_w u_\beta=\rho_w\nu\frac{\partial^2 u_\alpha}{\partial z^2}, \tag{7.21}$$

in which there is an implicit sum over the repeated indices, here β, and where $\varepsilon_{\alpha ji}f_i u_j$ is the α component of the vector product of the Coriolis parameter vector with the speed vector. In the following we classically consider only the vertical Coriolis parameter f_3.

To be sure that we understand the implicit sum, an explicit form of the equation for the u component is,

$$\frac{\partial}{\partial t}\left(\rho_w u\right)+\frac{\partial}{\partial x}\left(\rho_w u^2+p\right)+\frac{\partial}{\partial y}\left(\rho_w uv\right)+\frac{\partial}{\partial z}\left(\rho_w uw\right)-f_3 v=\rho_w\nu\frac{\partial^2 u}{\partial z^2}, \tag{7.22}$$

Integrating over the vertical, and using the boundary conditon at the surface and bottom, $w(\zeta)=\partial\zeta/\partial t+\mathbf{u}\cdot\boldsymbol{\nabla}\zeta$, yields

$$\begin{aligned}\frac{\partial}{\partial t}\int_{-h}^{\zeta}\rho_w u_\alpha \mathrm{d}z \quad &+ \quad \frac{\partial}{\partial x_\beta}\int_{-h}^{\zeta}\left(\rho_w u_\alpha u_\beta+\delta_{\alpha\beta}p\right)\mathrm{d}z+\varepsilon_{\alpha\beta3}f_3\int_{-h}^{\zeta}\rho_w u_\beta \mathrm{d}z\\ &= \quad p_a\frac{\partial\zeta}{\partial x_\alpha}-p(-d)\frac{\partial h}{\partial x_\alpha}+\rho_w\nu\frac{\partial u_\alpha}{\partial z}|_{z=\zeta}-\rho_w\nu\frac{\partial u_\alpha}{\partial z}|_{z=-h}\end{aligned} \tag{7.23}$$

We now take the average over wave phases [3].

The second integral in 7.23, gives, on average[4], using $u=\widehat{u}+u'$,

$$\overline{\int_{-h}^{\zeta}\rho_w u_\alpha u_\beta \mathrm{d}z} \quad = \quad \rho_w\int_{-h}^{\overline{\zeta}}\widehat{u}_\alpha\widehat{u}_\beta \mathrm{d}z+\rho_w\widehat{u}_\alpha\overline{\int_0^{\zeta}u'_\beta \mathrm{d}z}+\rho_w\widehat{u}_\beta\overline{\int_0^{\zeta}u'_\alpha \mathrm{d}z}+\overline{\int_{-h}^{\zeta}\rho_w u'_\alpha u'_\beta \mathrm{d}z}. \tag{7.24}$$

We now define the α-component of the total mass transport vector as[5],

$$M_\alpha=\overline{\int_{-h}^{\zeta}\rho_w u_\alpha \mathrm{d}z} \tag{7.25}$$

and the wave-induced mass transport, also known as the Stokes transport[6], and the difference of these two is the mass transport due to the mean flow

$$M_\alpha^m=M_\alpha-M_\alpha^w=\overline{\int_{-h}^{\zeta}\rho_w\widehat{u}_\alpha \mathrm{d}z}=\widehat{u}_\alpha\overline{\int_{-h}^{\zeta}\rho_w\widehat{u}_\alpha \mathrm{d}z}=\rho_w D\widehat{u}_\alpha. \tag{7.26}$$

We can thus re-write eq. (7.24) as

$$\overline{\int_{-h}^{\zeta}\rho_w u_\alpha u_\beta \mathrm{d}z} \quad = \quad \frac{1}{\rho_w D}\left(M_\alpha^m M_\beta^m+M_\alpha^m M_\beta^w+M_\beta^m M_\alpha^w\right)+\overline{\int_{-h}^{\zeta}\rho_w u'_\alpha u'_\beta+\delta_{\alpha,\beta}p \mathrm{d}z} \tag{7.27}$$

$$= \quad \frac{1}{\rho_w D}\left(M_\alpha M_\beta-M_\beta^w M_\alpha^w\right)+\overline{\int_{-h}^{\zeta}\rho_w u'_\alpha u'_\beta \mathrm{d}z}. \tag{7.28}$$

[2] Taking into account viscosity and the air pressure p_a allows to include the surface and bottom stress, which are not in the derivation by (Phillips, 1977, page 62).

[3] Phillips (1977) uses a horizontal average but as a result the obtained equatiosn are only valid at scales larger than the wavelength. Using the phase average allows to keep sub-wavelength variations such as in the case of partial standing waves, see Ardhuin et al. (2008c).

[4] This is here that we use the fact that $\widehat{u}$ is independent of z, otherwise we would have an extra term coming from the vertical current profile, that would be equivalent to a horizontal mixing term (Svendsen and Putrevu, 1994).

[5] This notation differs from Phillips (1977) who used $\widetilde{M}_\alpha$.

[6] The decomposition 7.28 and this definition of the Stokes transport require, to be well defined, an analytical extension of the velocity field u' in the air. This is not the real velocity field which, like the density, is very different from this extension. A nice way to avoid this issue is to use an average that follows the up-and-down motion of the sea surface (e.g. Ardhuin et al., 2008b).

The conservation of the vertical momentum is, neglecting viscosity and turbulence,

$$\frac{\partial}{\partial t}\left(\rho_w w\right)+\frac{\partial}{\partial x}\left(\rho_w uw+p\right)+\frac{\partial}{\partial y}\left(\rho_w vw+p\right)+\frac{\partial}{\partial z}\left(\rho_w w^2\right)=-\rho_w g. \tag{7.29}$$

A vertical integration gives, after using the surface kinematic boundary condition,

$$p(z)=p_a+g\int_z^\zeta \rho_w \mathrm{d}z+\frac{\partial}{\partial t}\int_z^\zeta \rho_w w\mathrm{d}z+\frac{\partial}{\partial x_\beta}\int_z^\zeta \rho_w u_\beta w\mathrm{d}z-\rho_w w^2(z). \tag{7.30}$$

in which the second term is the hydrostatic pressure, and the third vanishes only if the spatial average is independant of time – which is not the case in the presence of waves travelling in opposite directions as shown in chapter 21 – the fourth term vanishes for a motion that is periodic in time, and the last term is the mean dynamic pressure which is zero only if the velocity is zero. If we make all these assumptions the bottom pressure is hydrostatic,

$$p(-h)=\rho_w gD+p'. \tag{7.31}$$

As a result the mean value of the right hand side of (7.23) is

$$\tau_{a,\alpha}-\tau_{b,\alpha}+\rho_w gD\frac{\partial h}{\partial x_\alpha}=\tau_{a,\alpha}-\tau_{b,\alpha}+\frac{\partial}{\partial x_\alpha}\left(\frac{1}{2}\rho_w gD^2\right)-\rho_w gD\frac{\partial\overline{\zeta}}{\partial x_\alpha}, \tag{7.32}$$

where $\tau_{a,\alpha}$ and $\tau_{b,\alpha}$ are the α-components of the surface and bottom stress. The correlation $p'\partial h/\partial x_\alpha$ has been included in $\tau_{b,\alpha}$ as it represents the form drag on the bottom, while the other part of $\tau_{b,\alpha}$ is the skin friction given by the average of the viscous stress.

We now have (Smith, 2006),

$$\boxed{\frac{\partial M_\alpha}{\partial t}+\frac{\partial}{\partial x_\beta}\left(\frac{M_\alpha M_\beta-M_\alpha^w M_\beta^w}{\rho_w D}+S_{\alpha\beta}^{\mathrm{rad}}\right)+\varepsilon_{\alpha\beta 3}f_3 M_\beta=-\rho_w gD\frac{\partial\overline{\zeta}}{\partial x_\alpha}+\tau_{a,\alpha}-\tau_{b,\alpha}.} \tag{7.33}$$

where the radiation stresses are defined by Phillips (1977) as the difference between the momentum flux and the flux in the absence of waves,

$$S_{\alpha\beta}^{\mathrm{rad}}=\overline{\int_{-h}^{\zeta}\rho_w u_\alpha u_\beta+\delta_{\alpha\beta}p\mathrm{d}z}-\frac{1}{2}\rho_w gD^2\delta_{\alpha\beta}-\rho_w\widehat{u}_\alpha\widehat{u}_\beta D. \tag{7.34}$$

The expression for S^{rad} using linear wave theory is given in chapter 6.

The same procedure applied to the mass conservation equation yields

$$\boxed{\frac{\partial M_\beta}{\partial x_\beta}+\rho_w\frac{\partial D}{\partial t}=0.} \tag{7.35}$$

Equations (7.33) and (7.35) are the basic equations used in nearshore hydrodynamics, in their most simple form. They can be used to explain a wide variety of phenomena, from changes in the mean sea level, along-shore currents in the surf zone, infra-gravity waves .... All these will be discussed in chapter 16. The assumptions made by Phillips (1977) are fairly restrictive. Removing many of these, we present in chapter 24 an extenstion of the wave-current interaction theory to three dimensions.

We note that the mass transport M_α can be expressed with a mean velocity U_α ad $M_\alpha=\rho_w DU_\alpha$. This mean velocity includes the Stokes drift, which usually has a strong vertical gradient, even possibly in the surf zone (Ardhuin et al., 2008c) and the mean current which can also have a strong vertical shear. This mean speed can thus be very different from a measured mean velocity (Eulerian mean), and also different from a tracer mean speed if tracers are not homogeneously distributed over the vertical, as it is the case for suspended sediment.

7.2.2 Total energy

From the momentum equation the energy equation can be derived. With a viscous dissipation rate ϵ per unit volume and the stress tensor $p\delta_{ij}+\tau_{ij}$, in which i and j can be any of the three directions x, y and z,

$$\frac{\partial}{\partial t}\left(\rho_w\frac{u_i u_i}{2}+gz\right)+\frac{\partial}{\partial x_j}\left[u_i\left(\rho_w\frac{u_i u_j}{2}+gz+\delta_{ij}p+\tau_{ij}\right)\right]=\epsilon. \tag{7.36}$$

Following the derivation of Phillips (1977, page 63), and defining the total depth-integrated mechanical energy per unit surface as

$$E_a = \overline{\int_{-h}^{\zeta} \rho_w \left(\frac{1}{2}u_i u_i + gz\right) \mathrm{d}z} = \frac{1}{2}\frac{M_\alpha M_\alpha}{\rho_w D} + \widehat{u}_\alpha M_\alpha^w + \frac{1}{2}\rho_w g(\overline{\zeta}^2 - h^2) - \frac{1}{2}\rho_w \widehat{u}_\alpha \widehat{u}_\alpha + \rho_w g E + E', \quad (7.37)$$

in which $\rho_w g E$ is the wave energy per unit surface and E' is the turbulent energy.

Integrating (7.36) over depth and using eq. (7.34) for S^{rad}, we get

$$\begin{aligned} \frac{\partial E_a}{\partial t} &+ \frac{\partial}{\partial x_\alpha}\left(U_\alpha E_a + F_\alpha + \rho U_\alpha g h^2 + \widehat{u}_\beta S^{\mathrm{rad}}_{\alpha\beta}\right) \\ &= -\overline{[wp + \tau_{i3}u_i]_{-h}^{\zeta}} + \overline{(u_\alpha p + \tau_{i\alpha}u_i)\frac{\partial \zeta}{\partial x_\alpha}} + \overline{\int \epsilon \mathrm{d}z}, \end{aligned} \quad (7.38)$$

in which the energy flux F_α is

$$F_\alpha = \overline{\int_{-h}^{\zeta} u_\alpha \left[\frac{1}{2}\rho_w u_i'^2 + \rho_w g(z-h) + p + \tau_i \alpha\right] \mathrm{d}z}. \quad (7.39)$$

7.3 Energy exchange and wave action

We can then subtract the mean flow energy $[U_\alpha \times$ (7.33)$+(gh - U_\alpha^2/2)\times$(7.35)$]$ from (7.38) to obtain the wave energy evolution equation[7],

$$\rho_w g \frac{\partial E}{\partial t} + \frac{\partial}{\partial x_\alpha}\left[\rho_w g E\left(\widehat{u}_\alpha + C_{g\alpha}\right)\right] + S^{\mathrm{rad}}_{\alpha\beta}\frac{\partial \widehat{u}_\beta}{\partial x_\alpha} = \phi_{aw} - \phi_{oc} - \phi_{bf}, \quad (7.40)$$

where $\phi_{aw} = -\overline{wp + \tau'_{i3}u'_i|_{z=\zeta}}$ is the mean wind to wave energy flux per unit surface, ϕ_{oc} is the part of $-\epsilon$ associated to wave breaking and dissipation in the water column, and ϕ_{bf} is the wave energy lost through bottom friction, which will be further discussed in chapter 14.

The term of particular interest to us is the gain or loss of wave energy $S^{\mathrm{rad}}_{\alpha\beta}\partial\widehat{u}_\beta/\partial x_\alpha$, when they propagate through current gradients, even without dissipative processes. This is indeed an exchange of energy between waves and currents.

To simplify this term, one can introduce the wave action $A = \rho_w g E/\sigma$ (Bretherton and Garrett, 1968; Andrews and McIntyre, 1978b), and using the evolution equation for the wave number, we obtain (see Phillips, 1977, for details)

$$\frac{\partial A}{\partial t} + \frac{\partial}{\partial x_\alpha}\left[A\left(\widehat{u}_\alpha + C_{g\alpha}\right)\right] = \frac{\phi_{aw} - \phi_{oc} - \phi_{bf}}{\sigma}. \quad (7.41)$$

The action like the energy and the momentum is a quadratic quantity. It can be decomposed into a spectrum $N(k,\theta,\phi,\lambda,t) = E(k,\theta,\phi,\lambda,t)/\sigma$ where ϕ and λ define the horizontal position, here the longitude and latitude. The spectral wave action equation is (Komen et al., 1994)

$$\frac{\partial}{\partial t}N + \frac{\partial}{\partial \phi}\left(\dot{\phi}N\right) + \frac{\partial}{\partial \lambda}\left(\dot{\lambda}N\right) + \frac{\partial}{\partial k}\left(\dot{k}N\right) + \frac{\partial}{\partial \theta}\left(\dot{\theta}N\right) = \frac{S}{\sigma}, \quad (7.42)$$

where S is the sum of the source terms that represent the interactions with winds, bottom, wave-wave interactions and dissipation, and θ is the wave propagation azimuth, the angle between North and the wave propagation direction. The propagation speeds in physical and spectral space are given by Tolman (1990),

$$\dot{\phi} = \left(C_g \cos\theta + \widehat{v}\right) R^{-1} \quad (7.43)$$

$$\dot{\lambda} = \left(C_g \sin\theta + \widehat{u}\right)\left(R\cos\phi\right)^{-1} \quad (7.44)$$

$$\dot{\theta} = C_g \sin\theta \tan\phi R^{-1} + \sin\theta \frac{\partial \omega}{\partial \phi} - \frac{\cos\theta}{\cos\phi}\frac{\partial \omega}{\partial \lambda}(kR)^{-1} \quad (7.45)$$

$$\dot{k} = -\frac{\partial \sigma}{\partial D}\frac{\mathbf{k}}{k} \cdot \boldsymbol{\nabla} D - \mathbf{k} \cdot \boldsymbol{\nabla}\widehat{\mathbf{u}}, \quad (7.46)$$

[7]Here it is assumed that $\widehat{u}$ is a vertically-uniform current. In a more general case $\widehat{u}$ is replaced by u_A as defined by eq. (2.55). There are still discussions about the interpretation of this, but it was derived by Andrews and McIntyre (1978b).

where R is the radius of the Earth, $\widehat{u}$ and $\widehat{v}$ are the zonal (towards the East) and meridional (towards the North) components of the horizontal current $\widehat{\mathbf{u}}$.

In the absence of dissipative processes, $S = 0$ and the wave action is conserved. This is a general physical result and the action is an adiabatic invariant. It is the same for a pendulum of varying length, $A = E/\sigma$ is conserved, not E. More exactly, the total wave action, integral of $A(k, \theta)$ over the spectrum, is conserved for adiabatic processes that are independent of the wave phases. This is Noether's theorem. Wave action is thus conserved by 4-wave interactions discussed but it is not conserved with shallow-water 3-wave interactions. In the context of wave-particle equivalence, A is equivalent to the number of particles.

As we have seen in section 7.1.2, the conservation of wave action can be used to investigate the amplification of waves across a current convergence.

7.4 Wave momentum and mean flow momentum

One of the difficulties when comparing model equations to measurements, is that eq. (7.33) and (7.35) express the change of M_α which combines the Stokes drift and the mean flow. These two parts of the total momentum have very different behaviors, and it is unlikely that turbulence acts on both in the same way and thus requires different mixing parametrizations. Hasselmann (1971) was among the first to point out this problem, followed by Garrett (1976), and more recently Smith (2006). We will follow Garrett's arguments. There are thus two classes of wave-averaged momentum equations, those that work on the total momentum, and those that work only on the current momentum, as summarized in figure 7.3.

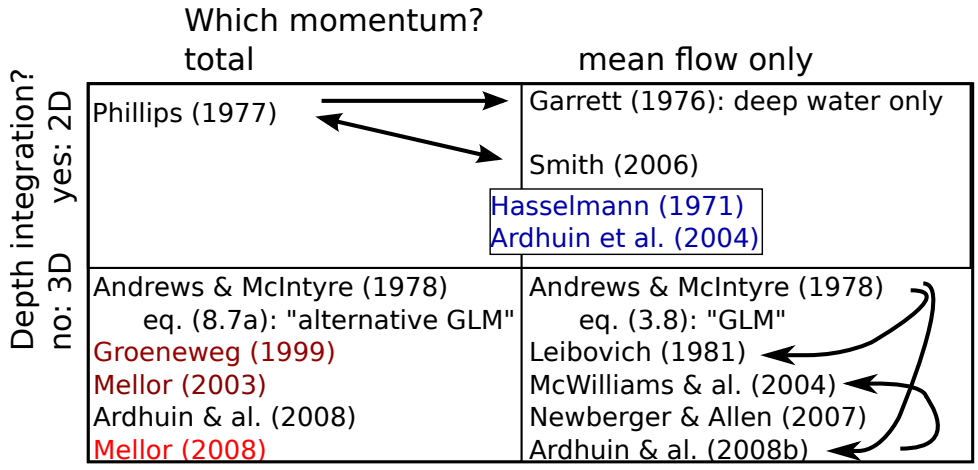

Figure 7.3: General organization of wave-averaged theories according to their choice of momentum variable and depth integration. Names that appear in different shades of red correspond to theories that are not fully consistent with their originating hypotheses. In the case of 3D theories for the total momentum, the problem generally comes from the vertical flux of momentum and are particularly acute on a sloping bottom, not explicitly considered by Groeneweg (1999). In the case of Mellor (2008), the inconsistency arises from different averagings of different terms in the same equation, resulting in a strange mix of Eulerian and Lagrangian mean equations. Other theories not listes here are even less consistent and completely forgot about this vertical flux. The theory of Hasselmann (1971), extended by Ardhuin et al. (2004a) does not quite fit the decomposition in mean flow and wave momentum as the momentum fluxes between the two (the interaction stresses) are not the same as the known fluxes (Ardhuin, 2006a). An arrow from a to b indicates a derivation link: b can be derived from a. Reproduced from Bennis et al. (2011).

7.4.1 Wave momentum

The wave momentum is also sometimes called the pseudo-wave momentum (McIntyre, 1981). For a modulated wave train with a narrow frequency range around $\sigma/(2\pi)$ it is $\mathbf{M}^w = \mathbf{k}E/\sigma = \mathbf{k}A$. This is the momentum of the oscillations associated with waves, it is generally compensated by a motion at the

scale of the modulations. For example, in the case of an isolated wave packet the total momentum may be zero but there is this pseudo-momentum that is compensated by an opposite momentum in the flow that varies on the scale of the packet.

We have the evolution equation for A, we thus need an evolution equation for $\mathbf{k}$ to get the momentum equation for $\mathbf{M}^w$.

With a generalized wave phase $\Theta \simeq \mathbf{k}\cdot\mathbf{x} + \mathbf{k}\cdot\mathbf{u}_A t - s\sigma t$ for the component $(\mathbf{k}, s)$, we have

$$\boldsymbol{\nabla}\Theta = \mathbf{k} \tag{7.47}$$

$$\frac{\partial\Theta}{\partial t} = -\mathbf{k}\cdot\mathbf{u}_A - s\sigma = \omega. \tag{7.48}$$

and thus

$$\frac{\partial\mathbf{k}}{\partial t} + \boldsymbol{\nabla}\left(\sigma + \mathbf{k}\cdot\mathbf{u}_A\right) = 0, \tag{7.49}$$

which is also known as the 'conservation of number of wave crests'. Using the linear wave dispersion relation, it gives,

$$\frac{\partial k_\alpha}{\partial t} + \left(\widehat{u}_{A\beta} + C_{g\beta}\right)\frac{\partial k_\alpha}{\partial x_\beta} = -k_\beta\frac{\partial\widehat{u}_{A\beta}}{\partial x_\alpha} - \frac{k\sigma}{\sinh 2kD}\frac{\partial D}{\partial x_\alpha}, \tag{7.50}$$

where $\widehat{u}_{A\beta}$ is the β-component of the current that advects the wave action. For a vertically-uniform current and neglecting nonlinear effects it is the Eulerian current $\widehat{u}_{A\beta} = \widehat{u}_\beta$. In a more general case see Kirby and Chen (1989) and Weber and Barrick (1977).

Combining the equations for A and k and taking $u_{A\beta} = \overline{u}_\beta$, we get,

$$\frac{\partial M^w_\alpha}{\partial t} + \frac{\partial}{\partial x_\beta}\left[(\overline{u}_\beta + C_{g\beta})M^w_\alpha\right] = \rho_w g\int k_\alpha\frac{S_{tot}}{\sigma}\mathrm{d}\mathbf{k} - M^w_\beta\frac{\partial\overline{u}_\beta}{\partial x_\alpha} - \rho_w S^J\frac{\partial D}{\partial x_\alpha}. \tag{7.51}$$

in wich S^J is a 'Bernoulli pressure head' term

$$S^J = \frac{1}{D}\int_{\mathbf{k}}\left(C_g - \frac{C}{2}\right)\frac{E\left(\mathbf{k}\right)}{C}\mathrm{d}\mathbf{k} = g\int_{\mathbf{k}}\frac{kD}{\sinh 2kD}E\left(\mathbf{k}\right)\mathrm{d}\mathbf{k}. \tag{7.52}$$

Eq. (7.51) expresses the conservation of wave momentum that is advected at the speed $\overline{\mathbf{u}} + \mathbf{C}_g$, and modified via the source term by the processes that contribute to a change in wave action, and a force $-\rho_w S^J\partial D/\partial x_\alpha$, in the presence of depth gradients. That force compensates for the changes in the wave momentum flux (Ardhuin, 2006a).

7.4.2 Mean flow momentum

Removing the wave momentum (7.51) from the total momentum (7.33), and using $M_\alpha = M^m_\alpha + M^w_\alpha$, with $M^m_\alpha = \rho_w\overline{u}_\alpha D$ for a depth-independant current, we obtain (Smith, 2006),

$$\begin{aligned}\frac{\partial M^m_\alpha}{\partial t} &+ \frac{\partial}{\partial x_\beta}\left(\int_{-h}^{\overline{\zeta}}\rho_w\overline{u}_\beta\overline{u}_\alpha\mathrm{d}z\right) + \overline{u}_\alpha\frac{\partial}{\partial t}\left[\rho_w D\right] + \varepsilon_{\alpha\beta3}f_3 M^m_\beta + \left[\rho_w g D - p^w_0\right]\frac{\partial\overline{\zeta}}{\partial x_\alpha}\\ &= -\varepsilon_{\alpha\beta3}\left(f_3 + \Omega_3\right)M^w_\beta - \rho_w\frac{\partial}{\partial x_\alpha}\left(DS^J\right) + \tau^a_\alpha - \tau^w_\alpha - \tau^b_\alpha - \tau^{\mathrm{dis}}_\alpha + \rho_w S^J\frac{\partial D}{\partial x_\alpha},\end{aligned} \tag{7.53}$$

where Ω_3 is the vertical component of the mean flow vorticity, DS^J is the difference between the radiation stresses and the flux of wave momentum on the one hand and on the other hand the Eulerian mean pressure that is, at the surface

$$p^w_0 = -\int_{\mathbf{k}}\sigma^2 E\left(\mathbf{k}\right)\mathrm{d}\mathbf{k}. \tag{7.54}$$

Finally, $\tau^a_\alpha - \tau^{\mathrm{aw}}_\alpha$ is the net flux of momentum from the wind to the mean flow with

$$\tau^{\mathrm{aw}}_\alpha = \rho_w g\int_{\mathbf{k}}\frac{k_\alpha S^{\mathrm{in}}(\mathbf{k})}{\sigma}\mathrm{d}\mathbf{k}, \tag{7.55}$$

and

$$\tau^{\mathrm{wo}}_\alpha = \rho_w g\int_{\mathbf{k}}\frac{k_\alpha S^{\mathrm{dis}}(\mathbf{k})}{\sigma}\mathrm{d}\mathbf{k}, \tag{7.56}$$

is the flux of wave momentum going to the ocean due to wave dissipation due to breaking and interaction with ocean turbulence, excluding the dissipation due to bottom friction[8] or swell dissipation by air-sea friction (Ardhuin et al., 2009a).

Finally we can gather the S^J terms in (7.53) following Smith (1990, 2006),

$$\begin{aligned}\frac{\partial M^m_\alpha}{\partial t} &+ \frac{\partial}{\partial x_\beta}\left(\int_{-h}^{\overline{\zeta}} \rho_w \overline{u}_\beta \overline{u}_\alpha \mathrm{d}z\right) + \overline{u}_\alpha \frac{\partial}{\partial t}\left[\rho_w D\right] + \varepsilon_{\alpha\beta 3} f_3 M^m_\beta + \left[\rho_w g D - p^w_0\right] \frac{\partial \overline{\zeta}}{\partial x_\alpha} \\ &= -\varepsilon_{\alpha\beta 3}\left(f_3 + \Omega_3\right) M^w_\beta - \rho_w D \frac{\partial S^J}{\partial x_\alpha} + \tau^a_\alpha - \tau^{\mathrm{aw}}_\alpha - \tau^b_\alpha - \tau^{\mathrm{wo}}_\alpha. \end{aligned} \tag{7.57}$$

[8] for bottom friction see Longuet-Higgins (2005)

Chapter 8

Numerical modeling in deep water

Numerical wave models are used for a wide variety of applications. These include navigation safety, ocean engineering for marine energy (oil and gas or renewables) or ship design, coastal engineering. Wave models are used both for forecasts and hindcasts, for deterministic simulations or ensemble predictions.

Because waves also have impacts on the atmosphere, ocean, sea ice, or sediments, wave models are increasingly used in Earth System models, coupled with other dynamical models. This coupling is most important in shallow waters (storm surges, wave-driven currents ...) and specific aspects of coastal and shallow water wave modelling will be discussed in chapter 15. Our purpose here is to give indications about the validity and limitations of wave models. As we focus on deep water, it removes the specific issues of bottom friction, refraction, shoaling, making the question of wave evolution more simple. The first question to consider is: what is deep water? From chapter 2, the ratio of the wavelength and water depth represented by kD, is one criteria. Typically when $kD > 2$ the effect of shoaling and refraction can usually be neglected.

This chapter only deals with spectral phase-averaged models, based on the wave action equation (7.42), following the first numerical model of Gelci et al. (1957). The practical problem is to obtain the most accurate result, either for a forecast for the coming days a climate projection over long terms, or a restrospective simulation (hindcast), using limited computational resources and time. This leads to trade-offs between expensive calculations, for example the 4-wave interactions, and cheaper parametrizations. The choice of the numerical method also has a strong impact on the model cost, with benefits that may be visible only for some parameters.

What are the main factors that control the model accuracy?

- Because waves are generated by winds, and propagate in a medium characterized by a bottom topography, currents and obstacles (small islands, sea ice ...), the quality of these forcing fields is determinant, and the accuracy of winds is certainly the most important.

- The second most important factor is the accuracy and behavior of the parametrizations use for all the processes represented in the source terms S in eq. (7.42). These parameterizations should be *robust*, meaning that they should work under all circumstances from calm seas to hurricane-force winds, in the presence or absence of swells ... Many model errors can be traced to poor parametrizations. No parametrizations is perfect but some definitely produce more accurate results than others.

- Finally, there is no method to solve eq. (7.42) to the accuracy of the computer round-off error at an acceptable computational cost. The numerical integration methods are thus based on approximations that lead to numerical diffusion. Also, numerical limiters in the evolution are used by many models, so that the numerical result may be very different from the actual solution of the wave action equation (e.g. Tolman, 2002b). One infamous example is the effect of semi-implicit integration of the source terms in time when large time steps are used (Hargreaves and Annan, 2000). This particular issue motivated the use of an adaptative time step for source term integration in the WAVEWATCH III model (Tolman et al., 2014).

The overall model quality is thus the result of many choices. As a user, you should be very careful about supposedly 'default' model settings: this means that somebody has chosen for you, however reasonable that choice may be in usual conditions, it may be not be the best choice for your particular application. As a user of a wave model you may not have the freedom to choose, and the choice of model

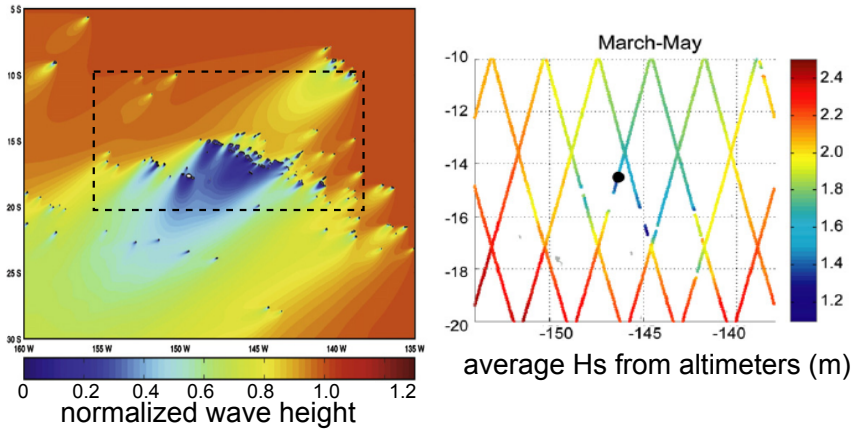

Figure 8.1: Left picture: example of wave attenuation due to propagation across many islands, here the Tuamotus, for a case of swell from the North-East, which almost never happens in this region, as computed on a 3.6 km grid. These islands would not be resolved in a typical ocean global grid (reproduced from Chawla and Tolman, 2008) and require a sub-grid parameterization as introduced by Tolman (2003). The dashed box corresponds to the extent of the right panel which shows the mean values of H_s recorded by TOPEX and Jason (reproduced from Andréfouët et al. (2012), showing the very strong sheltering in real conditions with both windsea and swell, with swell usually coming from the South-West.

or forcing may be imposed because it is more or less easily available and easy to use. Whatever the circumstances, you should be aware of the impact on the model results. Also you may end up frustrated by model result that exhibit unphysical behavior: such as the stronger growth of wind sea in the presence of swell or a broadening of the directional wave spectrum in shallow water. You may thus want to try yourself and improve on the existing models. Hopefully the next sections will be interesting advice. As for the swell effect of wind growth, we have not get a full physical model that would give the proper reduction in wind sea growth (García-Nava et al., 2012), but at least, going from the parameterization by Janssen et al. (1994) to the one by Ardhuin et al. (2010) you will not see anymore the wind sea wave height jump up when swell arrives.

As mentioned, the most important choices that define the model accuracy are the model forcing, model parametrizations, and numerical schemes. Models may also assimilate measurements to correct past estimates of the waves. However, contrary to atmospheric or oceanic circulation models, assimilation is not necessary to obtain accurate forecasts and hindcasts. For all these choices, the most accurate result is not necessarily obtained with the most complex choice, because some errors are often compensated by other errors.

Finally, models are usually good only for the parameters for which they have been validated, and for the ranges of these parameters in which we have data. Remember that there are very few measurements of the full frequency-direction spectrum, so that the modeled spectral shapes can be really bad, especially at high frequencies. When one predicts that the 100-year significant wave height off the west coast of France is 18 m, based on a model that has only been validated up to 14 m, this is a real extrapolation.

8.1 Forcing

8.1.1 Bathymetry and islands

If you have never run a numerical wave model, it probably sounds trivial that the ocean depths and shape of the shoreline should be known. In practice, though, it is not always easy. Global databases such as ETOPO (Sloss, 1993) and GSHHS (Wessel and Smith, 1996) can have important errors, with large error in water depth over continental shelves, and some islands misplaced by a few kilometers. Even at global scales and coarse resolutions, it is important to take into account subgrid islands such as the Tuamotus or Aleoutian islands in the Pacific (Tolman, 2003), as illustrated in figure 8.1.

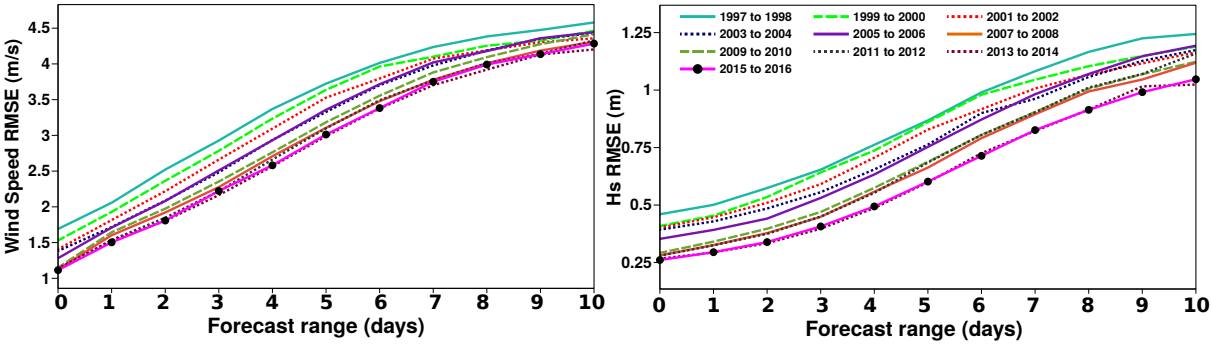

Figure 8.2: Root mean square error (RMSE) as a function of the forecast range, 0 corresponding to the analysis, in the operational systems ran at ECMWF. These modeled wind speed and wave heights are compared to buoy measurements over a year centered in winder (August to July). Only every other year is shown (Picture courtesy of J. Bidlot).

8.1.2 Wind fields: analyses, forecasts, re-analyses

Although there are many measurements of surface winds based on satellite radiometers or scatterometers, the coverage they provide is not enough to use a forcing field defined from these data only. Hence it is most common to use winds from an atmospheric circulation model. In these models, the near-surface wind speed, usually 10 meters, is not a an dynamical parameter because these models usually have a vertical discretization in pressure levels that does not follow a constant height. This surface wind, possibly corrected for stability effects in the form of a *neutral* wind, is in fact diagnosed from the atmospheric boundary layer parameterization. As a result there are significant differences between models. For example, for wind speeds exceeding 30 m/s, the winds provided by the European Center (ECMWF) as part of their operational analyses were typically 10% slower than those of the U.S. weather service (NCEP) for the year 2005. Given that there are very few reliable data at high wind speeds, it is difficult to decide which is more accurate correct. As a result, the wave model parameterizations are adjusted differently to the different forcing fields.

If you are a scientist, you will probably try to get the most accurate wind fields. If you are an engineer, you may be in a rush or may not have access to the most accurate database. When it comes to wind vectors, the most accurate model analyses and forecasts over the recent years and most of the globe, are those provided by the European Center for Medium Range Weather Forecasting (ECMWF). Although their data policy may soon change, these are usually not freely available. The anlysis is the combination of model and observation that is expected to produce the most accurate estimate of the state of the atmosphere, providing the initial conditions from which the forecast in produced.

ECMWF, like most Numerical Weather Prediction (NWP) organizations, produces both deterministic analyses and forecasts, a single simulation, and ensemble predictions, which consist of a set of simulations that is designed to explore the possible variations of the atmospheric state. ECMWF spatial resolution of the deterministic product was reduced to 0.25 degree in 2008, 0.125 degree in 2011, and 9 km in March 2016. Their system, like those at all NWP centers is constantly improving to take the best advantage of computer power, new observations, new model parametrizations and assimilation methods.

You may find details about ECMWF's Integrated Forecasting System (IFS) on their website with a nice quarterly newsletter. It can be a good idea to check on the quality of other sources by looking at the wind and wave model verification http://www.jcomm-services.org/Wave-Forecast-Verification-Project.html, presented by Bidlot (2008).

Wind analyses and deterministic forecasts have made enormous progress over the last 20 years (e.g. Janssen, 2008), thanks to an increase in computational power that allows higher resolution, more complex parameterizations and sophisticated data assimilation. This has gone with a dramatic increase in number and quality of observations. Figure 8.2 shows the reduction in errors in both analyses and forecasts for winds speeds and wave heights in ECMWF operational deterministic forecasting system.

Because of this continuous improvement of model quality, a time series of operational hindcasts is not homogeneous in time. Hence, a statistical analysis of extreme events based on operational analysis will probably have spurious trends. In order to reproduce past events as well as possible, recent versions of the atmospheric models have been re-run to produce re-analyses. In this case the only source of non-homogeneities are the observations assimilated. It is indeed not possible to go back in time and add a

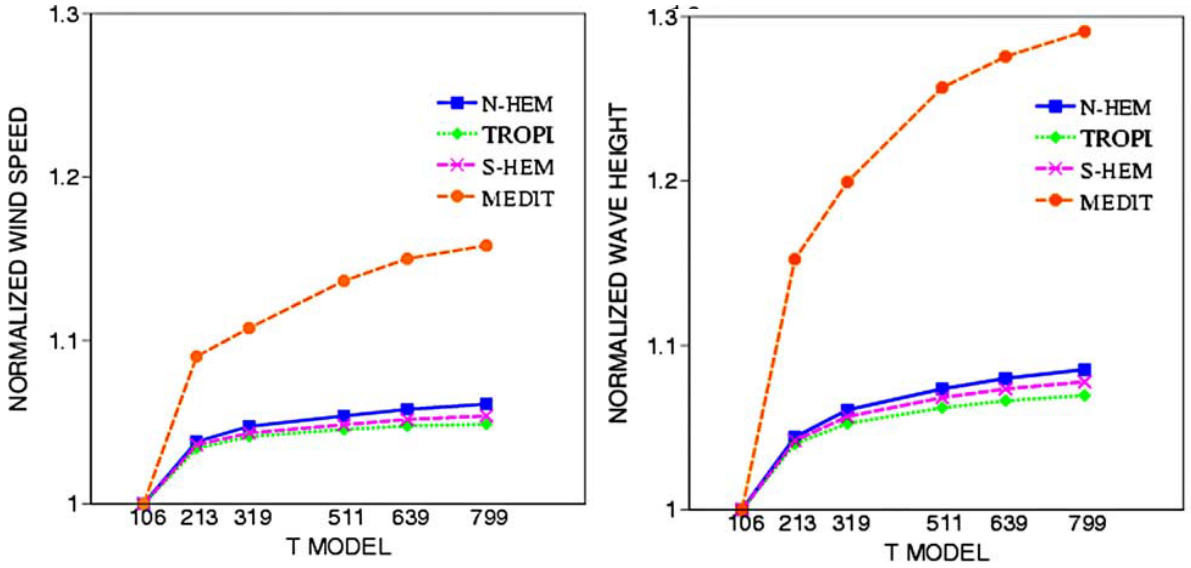

Figure 8.3: Average wind and wave height in the Northern Hemisphere, Southern Hemisphere and Mediterranean sea, obtained in different runs of the ECMWF model in which the spatial resolution is changed. The resolutions of Gaussian grids T106, T213, T319, T511, T639, et T799 correspond to 188, 94, 63, 39, 31, and 25 km. Wind speed and wave height values have been divided by the values obtained for the coarsest of these grids. Taken from (Cavaleri and Bertotti, 2006, ©Elsevier).

few satellites. For this reasons, some atmospheric reanalyzes start in 1978, when enough satellite data is available for a reasonable estimate of the atmospheric circulation. This is the case of the Climate Forecast System Reanalysis (CFSR Saha et al., 2010) and ERA-Interim (Dee et al., 2011). Other re-analyses go back to 1958 (Kobayashi et al., 2015), and Compo et al. (2011) have produced a re-analysis from 1871 to 2008.

As we have seen, the highest waves require very high winds, and the quality of re-analyses for estimating past wave heights critically depends on the capability of the atmospheric models to resolve the gradients in small storms, in particular for tropical storms or polar lows. As a result, some wave re-analyses like ERA40 are notorious for understimating wave heights because of underestimated winds (Caires and Sterl, 2005). Unfortunately for that aspect, the ongoing project for a fitfh generation re-analysis (ERA5) at ECMWF favored an ensemble approach, rather than single and higher resolution model.

8.1.3 Coastal winds

In coastal regions, closed or semi-closed basins surrounded by mountains, such as the northern Mediterranean, the winds from global models are often inaccurate due to a lack of resolution of the land topography that channels winds. A striking view of this is in figure 8.3 (Cavaleri and Bertotti, 2006). In this case, a solution can be to use higher resolution local area models. However, it must be noted that the quality of the nested grid result, owes much to the boundary conditions and the quality of the parent model. Sometimes a statistical correction of coarse grid can be a better option (Signell et al., 2005).

8.1.4 Observed winds

Winds over the oceans are measured by altimeters, scatterometers (or their higher resolution cousins, SARs) and radiometers with increasing coverage and accuracy. It is now possible to have data everywhere over the oceans at a resolution of about 12 km, and every 12 hours. Although 12 hours is long compared to the time scale of evolution of the wind fields and we cannot use this data as such to force a wave model, it is possible to blend this with atmospheric models to improve the realism of modelled winds (e.g. Bentamy et al., 2007).

Although some of that data is assmilated into atmospheric models, these models often reject the highest winds that are often too far from their first guess. As a result, it is always a good thing to check the consistency of modeled winds against data. Although traditional scatterometers that use Ku or C

are not able to discriminate wind speeds beyond 25 m/s, the use the measured Doppler shift (Mouche et al., 2012) or cross-polarizations (Vachon and Wolfe, 2011; Mouche and Chapron, 2015), has been demonstrated with SAR data to be able to better constrain higher wind speeds, and will be used in future scatterometers. The recent use of L-band, which is more sensitive to longer waves than Ku or C, has also been shown to be sensitive to the highest wind speeds (Reul et al., 2006).

8.1.5 Currents

The main issue with ocean currents is to get accurate estimations of current fields, at the relevant resolution (Ardhuin et al., 2017c). This is relatively simple for tide-dominated environment for which numerical models are reasonably goog (e.g. Ardhuin et al., 2012a), it is much more delicate for regions dominated by quasi-geostrophic dynamics, where deterministic ocean circulation forecasts have limited skills, and even more so where internal waves are the main source of surface current gradients (Osborne and Burch, 1980) due to the required high resolution to resolve these features. As a result, most operational wave forecasting systems take into account tidal currents, at best.

8.1.6 Sea ice

Wave-ice interaction is the topic of chapter 25. To summarize it here, the presence of ice has a strong impact on wave growth and disspation, and a knowledge of ice concentration is required in any ocean basin that has some ice, the Arctic of course, but all three oceans (Atlantic, Indian and Pacific) are strongly influenced by ice, at least in their southern hemisphere part, and many regional seas an lakes also freeze up: the Baltic, Caspian, the Great Lakes... Experimental evidence shows that waves are not generated by the wind in ice-covered regions, and the ice can damp the waves very rapidly, in particular the high frequency components.

8.2 Numerics

8.2.1 Wave models are big

The problem of numerical wave modelling at oceanic scales is often a question of compromise between spectral and spatial resolution. Indeed, our wave action spectrum is a 4-dimensional beast that we have to integrate in time. All models today use a fixed discretization into $N_f \simeq 30$ frequencies and $N_\theta \simeq 30$ directions. The wave action equation 7.42 is thus a set of $N_f \times N_\theta \simeq 1000$ hyperbolic advection equations that are coupled via the source term S and the refraction and shoaling terms. Each equation for a component (f_i, θ_j) is a 2-dimensional partial differential equation (PDE) that represents advection equation with source term. This is a fairly standard problem to solve, with the transport velocity $\mathbf{C}_g + \mathbf{U}$ varying in space and possibly in time. If the spatial discretization is a regular mesh with only 100 by 100 points, hence a spatial discretization into 10,000 nodes, the overal problem has 10 million unknowns: all the values of our gigantic wave action matrix. As result, wave models typically use a lot of memory. For example at ECMWF, with the IFS system, the wave model uses about as much as the entire atmosphere.

Now, every time I think of it, it makes me mad that most of these unknowns are zeros: waves over 25 s period do not happen very often, but they do happen once in a while in the biggest storms (Hanafin et al., 2012). One trick could be to adjust the spectral grid to remove the components for which we have zeros on the entire grid or in a subgrid. At the same time, the recent extension of wave models to add shoreline reflections (Ardhuin and Roland, 2012) and sources of low-frenquecy infragravity waves (Ardhuin et al., 2014) have replaced these zeros by small numbers that can be significant for some applications. Still, if you do not activate these options, there should be a way to make models faster by avoiding to compute zero plus zero times zero equals zero.

8.2.2 Spectral discretization

In frequencies, one needs to choose

- the spacing between frequencies: it is usualy exponential, with $f_{i+1} = X_{fr} f_i$ where X_{fr} is a constant close to 1.1. The reason for this geometric progression is that it simplifies the calculation of the 4-wave interaction term S_{nl}: in deep water the geometric arrangement of the interacting waves is the same from one frequency to the next. The choice of $X_{fr} = 1.1$ is relatively coarse, as a JONSWAP spectrum will have only one or two frequencies inside of the peak. However, going to

$X_{fr} = 1.05$ will double the number of frequencies, if you used 30 it now jumps to 60, and double the cost of the model.

- a minimum frequency $f_{\min}$: this should be low enough to allow waves to develop. In the open ocean, it is possible to get a peak period of 25 s (Hanafin et al., 2012), and you probably need a couple of frequency bands below that to allow the spectrum to roll back, this means that $f_{\min} = 0.037$ Hz may already be too high. Ardhuin et al. (2014) have also gone as low as 0.003 Hz to model the infragravity part of the spectrum which will be discussed in chapter 13. However, adding these frequencies means using a lager number N_f of frequencies, and also the computation cost for these low frequencies can be higher due to numerical constraints: these long period waves have larger group velocities, and explicit schemes will require a smaller time step.

- a maximum frequency $f_{\max}$, this is dictated by the lowest winds that you want to represent properly: to catch the peak of the wind sea you need to have $f_{\max} > 1.2X_{fr}g/(2\pi U_{10})$. For a fairly frequent wind speed of 5 m/s, this means that $f_{\max} \simeq 0.4$ Hz is not enough. Still, this was used recently in many global models. Also, if you want to investigate properties of high frequency waves or backscatter for remote sensing, you probably want $f_{\max} > 0.7$ Hz. Finally, most wave model ignore viscous dissipation (Dore, 1978) and capillary effects. These cannot be ignored for $f_{\max} > 2$ Hz.

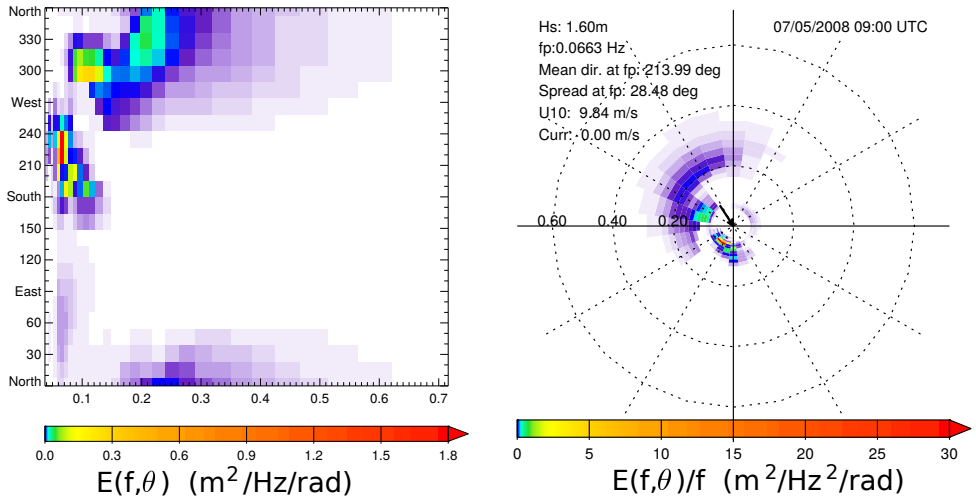

Figure 8.4: Example of spectral discretization: here these modeled spectra use 32 frequencies from 0.037 Hz to 0.72 Hz with $X_{fr} = 1.1$, and 24 directions. The same spectrum is shown in cartesian and polar coordinates. Note that the polar representation is nice to show the waves in the direction from where they are arriving, but it squeezes all the dominant waves near the center, making it difficult to see the details. Here the spectrum in polar coordinates is divided by the frequency f which compensates a little for the squeezing: the total energy is still the area in the plot times the value plotted.

For the directions, with a directional spread that is about 20° for the wind sea peak, a resolution of 15° (i.e. 24 directions), can be satisfactory with 2 points in the peak – the spread is the half-width of the spectrum in the limit of a narrow Gaussian shape. As wind-waves turn into swell, the spread can be as low as 5°, and it can be useful to have a higher directional resolution. Again this comes at a cost: more direction means larger spectra, more memory and computational time.

8.2.3 Spatial discretization

Given the cost induced by spectral discretization, the spatial discretization can be optimized in several ways. First of all, one should consider the necessary resolution. In the absence of currents, the gradients in the wave field are given by the wind field and the shoreline geometry. There are thus several options, from a regular grid in latitude and longitude to a triangle-based mesh (Benoit et al., 1996; Roland and Ardhuin, 2014, e.g.), or mosaics of grids with different resolutions (Tolman, 2008) or quad-trees (Popinet et al., 2010; Li, 2010). In particular, high resolution is desirable in hurricanes, and moving or adaptive grids have thus been designed for this (Tolman and Alves, 2005; Popinet et al., 2010). All these options are available in the WAVEWATCH III modelling framework.

8.2.4 Integration methods

There are two large classes of methods used for this type of multi-dimensional PDE.

- a global resolution with an iterative method: this is the method of Patankar (1980) which has been applied in the SWAN model Booij et al. (1999).
- A splitting method following Yanenko (1971). In that case the several terms of the equation are integrated in succession,

$$\frac{\partial N}{\partial t} + \text{advection} = 0 \tag{8.1}$$
$$\frac{\partial N}{\partial t} + \text{refraction} = 0 \tag{8.2}$$
$$\frac{\partial N}{\partial t} = S/\sigma. \tag{8.3}$$

  In the limit of small time steps, this is equivalent to the full integration. This approach is used in WAM (WAMDI Group, 1988), and for most options of WAVEWATCH III (Tolman, 2002d), and in TOMAWAC the first two steps are combined (Benoit et al., 1996).

The first approach can be interesting at very high resolution, typically in the nearshore, when used with implicit methods that are not constrained to have very small time steps. It is used in SWAN (Booij et al., 1999) and has been implemented in a research version of WAVEWATCH III (Huchet et al., 2015).

The great benefit of the second approach, is that the splitting allows to adapt the time step to the time scale of evolution of each term. This is fully used in WAVEWATCH III, with an adaptative time step for the source term integration, and different time steps for the advection and refraction.

In order to limit the computational time to something acceptable, wave models use limiters: the rate of change of evolution is limited to ensure stability while keeping large time steps. These limiters can completely change the solution (Tolman, 2002b; Roland and Ardhuin, 2014), so that it is a good practice to test that a model gives similar results when reducing all time steps by a factor 2. When a splitting approach is used, different limiters can be applied to different pieces of the equation. For example, WAVEWATCH III has a limiter on refraction (waves cannot turn by more than $\Delta_\theta = 2\pi/N_\theta$ over one refraction time step $\Delta_{t,r}$: if the bottom slope of current gradient require a faster rotation then the rotation speed is limited to $\Delta_\theta/\Delta_{t,r}$. Limiters for source term integration are a bit more complex.

8.2.5 Source term integration

The source terms link all spectral components together, including high frequencies that can evolve very fast. For that reason and also because the source term balance $S_{\rm in} + S_{\rm nl} + S_{\rm ds}$ is generally not well reproduced at high frequencies by parameterizations (e.g. Zieger et al., 2015), the spectrum above a diagnostic frequency f_d is usually prescribed to decrease like f^{-5}. This cannot reproduce the observed broadening of the directional spectrum with increased frequencies (e.g. Banner et al., 1989; Leckler et al., 2015) but it is a shortcut to keep the models within reasonable bounds. In the ECWAM model f_d is set to be the maximum of 2.5 times the mean frequency of the wind sea and 3 times the Pierson-Moskowitz frequency (Bidlot, 2012).

A stable integration of the source terms is possible with an implicit integration,

$$N(t+\Delta_t) = N(t) + \frac{S(t)\Delta_t}{\sigma(1-\alpha\Delta_t \partial S/\partial N/\sigma)}. \tag{8.4}$$

With $\alpha = 0.5$ this is accurate to second order in time, but $\alpha = 1$ generally performs better for the short wave components (Hargreaves and Annan, 2000). Still, one should be careful that source term integration is sensitive to the choice of time step it if is constant. As a result, even at frequencies $f < f_d$, a limiter is used for spectral evolution. The design of this limiter is discussed in Tolman (2002b).

8.2.6 Spatial propagation

The early wave models such as WAM (WAMDI Group, 1988) have chosen the cheap but robust first order 'upwind' scheme. In only one dimension, the wave propagation direction is given by a sign s, going

towards $x > 0$ if $s = 1$ and in the opposite direciton if $s = -1$. The upwind advection scheme is thus

$$N(x, t + \Delta_t) = N(x, t) - \frac{\Delta_t}{\Delta_x} \left[C_g(x) N(x) - C_g(x - \Delta_x) N(x - \Delta_x, t) \right] \quad \text{if} \quad s = 1 \tag{8.5}$$

$$N(x, t + \Delta_t) = N(x, t) + \frac{\Delta_t}{\Delta_x} \left[C_g(x + \delta_x) N(x + \delta_x) - C_g(x) N(x, t) \right] \quad \text{if} \quad s = -1. \tag{8.6}$$

The name upwind expresses the idea that the information is taken from where it is coming. That scheme is stable when the Courant number $C_g \Delta_t / \Delta_x$ is less than 1. This condition is known as the CFL condition after the work of Courant, Friedrichs and Lewy (Courant et al., 1928).

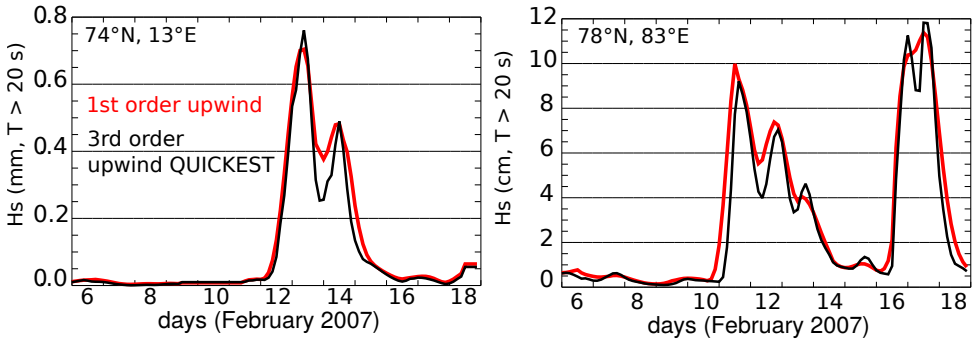

Figure 8.5: Time series of modeled wave height (computed over wave periods longer than 20 s) at two locations of the Arctic, using the first order upwind scheme, or the third order upwind QUICKEST scheme - including the Garden Sprinkler Effect correction of Tolman (2002a).

The main defect of the first order upwind scheme is its large numerical diffusion: a localized packet of energy tends to disperse in space. This dispersion effect is not always bad because real waves are dispersive, but the physical dispersion is only a function of the spectral resolution. A much reduced diffusion can be obtained by using higher order schemes, such as the third order upwind QUICKEST scheme of Leonard (1991). This is obvious in figure 8.5, which shows time series of wave heights in the ice-free part of the Arctic, in February 2007. The two biggest storm of the year in the North Atlantic occured on February 9 and 10, sending swell to the Arctic. This swell is modeled to arrive on 13 and 14 February off the East coast of Greenland at (74°N,13°W), and the two peaks are less separated with the first order than with the third order scheme. Things are worse as waves propagate further, and the two peaks are almost indistinguishable north of Siberia on February 16 and 17, at (78°N,83°E). As a result, the investigation of the potential diffusion effect of sea ice on these swells (Ardhuin et al., 2016) would not be possible with a first order scheme. That first order scheme is still used at ECMWF.

It is also troubling that the mean values are different, because the diffusion in the first order scheme strongly depends on the orientation relative to the grid: the discrete directions that travel along the grid axis are much less diffused. This shows up as north-south beams of energy in the case of slowly moving storms, such as Tropical Cyclone Dora, shown in figure 8.6. To reduce that effect, the usual trick is to shift the directions by $\Delta_\theta/2$: instead of using 0, 15°, 30° ... one uses 7.5°, 22.5°, 37.5° ... Now, instead of a maximum along the meridian, we get a weak minimum (see top-left and bottom-left panels in figure 8.6).

When numerical diffusion is strongly reduced, the dispersion of the wave field can be less than expected from the physical dispersion, giving an anomalous effect of the spectral discretization, known as the 'garden sprinkler effect' (GSE). Without any GSE correction, the upwind QUICKEST scheme gives the beautiful flower pattern in figure 8.6: because each spectral component has its own speed and direction, waves from a very small source separate as they propagate away from the source as discrete blobs of energy, instead of a smooth pattern that would be obtained with a very fine spectral discretization in frequency and direction. The solution to correct this GSE is to introduce some explicit diffusion (Tolman, 2002a).

Such differences are much less visible for fast moving storms, such as the more powerful cyclone Gamede which struck La Reunion island on February 25.

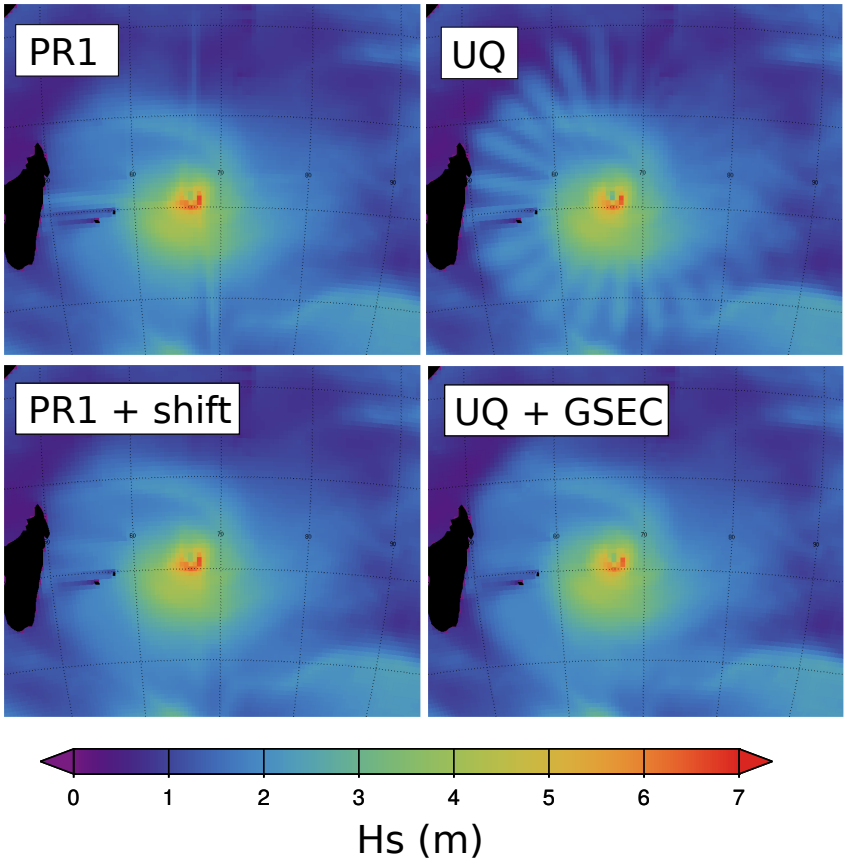

Figure 8.6: Example of wave heights for Tropical Cyclone Dora, in the Southern Indian ocean, using 4 different numerical schemes. 'GSEC' is the GSE correction scheme of Tolman (2002a). All model runs use 24 directions.

8.3 Parameterizations of physical processes

Because of the complexity of wave evolution processes that were briefly described in chapter 5, and further discussed in chapters 22 and 23, there is no generally agreed upon parameterization for wave generation and dissipation. Also, the non-linear wave interaction that is based on the theory of Hasselmann (1962) is too costly to be computed accurately for routine applications. Hence several parameterizations have been proposed to reproduce the non-linear source function. The most common is the Discrete Interaction Approximation by Hasselmann et al. (1985b), which keeps the energy, action and momentum conservation properties of the full non-linear interaction, at the price of an overestimation of the flux of energy to high frequency, among other side effects.

For wave generation and dissipation, the parameterizations proposed by the WAMDI Group (1988), Komen et al. (1994), Tolman and Chalikov (1996), Banner and Morison (2006), Ardhuin et al. (2010), Rogers et al. (2010), and many others, have tried to represent the magnitude of the wind to wave energy and momentum fluxes, as well as the overall balance that gives the wave growth. We cannot describe here in details all the flavours of the proposed parameterizations, nor give all details about their impact in the model solutions, which is the topic of an abundant record of scientific publications. We will try to summarize what we believe to be the most salient aspects and side effects of a few common parametrizaion, looking here only at the resulting wave spectra and derived parameters. In the context of coupled models (wave-atmosphere or wave-ocean or wave-sea ice...) one should probably focus more on the fluxes of energy and momentum than on the shape of the wave spectrum. This will be discussed in chapter 10.

What follows is mostly taken from a few recent papers by Rascle and Ardhuin (2013), Roland and Ardhuin (2014) and Stopa et al. (2016a), and focuses on large scale oceans away from the ice-covered regions. Modelling in and around ice-covered regions will be discussed in chapter 25. Although we mostly discuss the parameterization proposed in these papers and in Zieger et al. (2015), as implemented in the WAVEWATCH III model (version 5.16), other papers, such as van Vledder et al. (2016), have discussed

other models.

Figure 8.7 shows maps of systematic (bias) and total error in H_s from the same model ran with four different parameterizations, compared to altimeter data. Altough it is difficult to associate a particular error pattern to a single feature of the parameterization, the reduction in error from 1988 (top, WAM Cycle 3) to 2013 (Rascle and Ardhuin, 2013), shows that some of the errors have been well identified. In this case, they are mostly associated to swell dissipation and spurious swell - windsea interactions. The next section discusses how such errors can be detected and corrected.

8.3.1 A model development and validation strategy

Historically, the validation of wave models started with the reproduction of academic cases followed by fetch-limited growth and then application to a few real cases (e.g. WAMDI Group, 1988). Although this approach is still valid, it is not sufficient: indeed, the parameterization proposed by Tolman and Chalikov (1996) had input and dissipation terms 3 times smaller than those of Janssen et al. (1994), but still it gave pretty much the same fetch-limited growth curve and performed reasonably well in regional modeling cases. However, Tolman (2002d) had to strongly modify the dissipation for the swells to arrive at reasonable results for oceanic basin scales, as shown in figure 8.7. This demonstrated, as now realized by anybody who tried to improve the global models (e.g. Ardhuin et al., 2010; Zieger et al., 2015), that the swell dissipation coefficient is the single most sensitive parameter in a basin-scale or global wave model.

Today, with all the readily available data, including satellite altimeters, in situ buoys and wave mode synthetic aperture radar spectra, it is possible to adjust the empirical parameters in wave models, adjusting the full model (forcing, numerics and parameterizations). Indeed, the academic cases used with very high spectral resolution are good for debugging a model but they tell very little of the true model performance when using say 24 directions and 30 frequencies.

Many critics of the Tolman and Chalikov (1996) parameterization put forth the idea that it had too many 'tunable coefficients', which was indeed a problem if you wanted to modify it, but was the simple consequence that it was a fit to the detailed numerical calculations of air flow over waves performed by Chalikov (1993). In contrast, Janssen (1991) had managed to summarize his numerical modelling of wind profile coupled to the wave spectrum by replacing the surface roughness by a simple Charnock-like relationship, which only reproduced part of the full model beahviour, namely a stronger wave growth at short fetch. That made the Janssen (1991) parameterization of the wind input more amenable to further modification. However, the Janssen (1991) parameterization is very sensitive on the shape of the high frequency spectrum tail, so that the results it gives in Banner and Morison (2006) or Ardhuin et al. (2010) are very different from the original form.

Given the complexity of the air-sea interface, it is not very surprizing to have many degrees of freedom in the form of adujstable parameters. More important is the strategy to adjust them separately, typically by using a set of well defined wave evolution conditions and measured parameters to which the model can be adjusted. Following Ardhuin et al. (2010) we can propose the algorithm,

1. Start from a reasonable set of physically plausible processes with quantified magnitudes or at least orders of magnitudes

2. Test wave growth and value of H_s under 10 m/s wind, after 24 hours: this should be of the order of 2.3 m: this controls the difference of input and dissipation $S_{in} + S_{ds}$

3. Reproduce the November 3, 1999 case of slanting fetch-limited growth, first analyzed in Ardhuin et al. (2007). In particular the mean direction as a function of frequency depends strongly on the magnitude of S_{in}. The directional spreading also gives an indication on the balance of source terms and their directional distribution.

4. Adjust the sheltering and cumulative terms in order to reproduce the observed variability of mean square slopes (from altimeters) and vertical acceleration variance (from buoys)

5. check on the decay of pure swells using one of the many cases sampled by SARs, for both large and small amplitude swells.

6. Verify the biases of swell peak periods against buoy data, and frequency-dependent biases in the energy content of the spectrum.

7. Once the deep water evolution is correct, later adjust bottom friction (see chapter 14), then sea ice effects (see chapter 25).

8.3.2 Overall performance for common parameters

We will not show time series of model and observations, as can be obtained using buoy data. Such illustrations can be found in all publications. Instead we will use the globally available estimates of H_s provided by satellite altimeters. Figure 8.7 shows typical error statistics over the global ocean when using ECMWF operational analysis for the wind forcing, NCEP operational analyses for the sea ice concentration, and Ifremer/CERSAT iceberg statistics for the southern ocean (Tournadre et al., 2012). All these simulations use the DIA parameterization for the non-linear evolution, but different parameterizations for the generation by the wind and various dissipation processes.

All four simulations have a near zero mean bias, but there are regional biases, particularly with the parameterization by Tolman and Chalikov (1996), as adjusted by Tolman (2002c). The more recent parameterizations generally perform better, but there can be local advantages, like the lower rms errors of TC off West Africa. The differences between the BJA and TEST451 parameterizations are mainly in

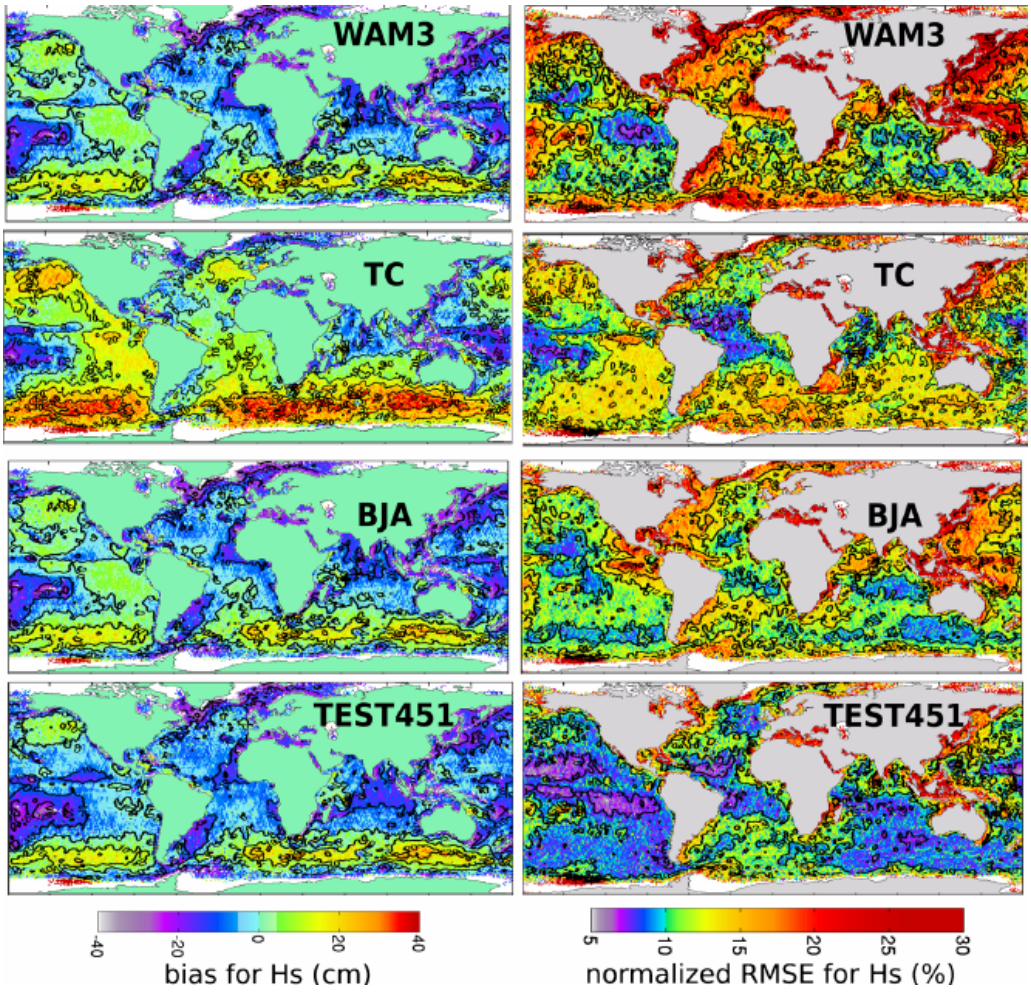

Figure 8.7: Bias and normalized root mean square (RMS) error against altimeter data for the year 2007, using the same forcings but 4 different parameterizations of the wind input and dissipation: WAM Cycle 3 (WAMDI 1988), TC (Tolman and Chalikov 1996, including the Tolman 2002c adjustment), BJA (Bidlot et al. 2005) and TEST451 (Rascle and Ardhuin 2013). Solid lines in the right column correspond to contours at the 7.5, 10, 12.5, 15 and 20% levels.

the dissipation source function.

8.3.3 Parameterization of the dissipation $S_{\rm ds}$

The dissipation used by Bidlot et al. (2005) and later adjustments (Bidlot, 2012), are based on the initial proposition by Hasselmann (1974), later adjusted by Komen et al. (1984), that the dissipation rate is

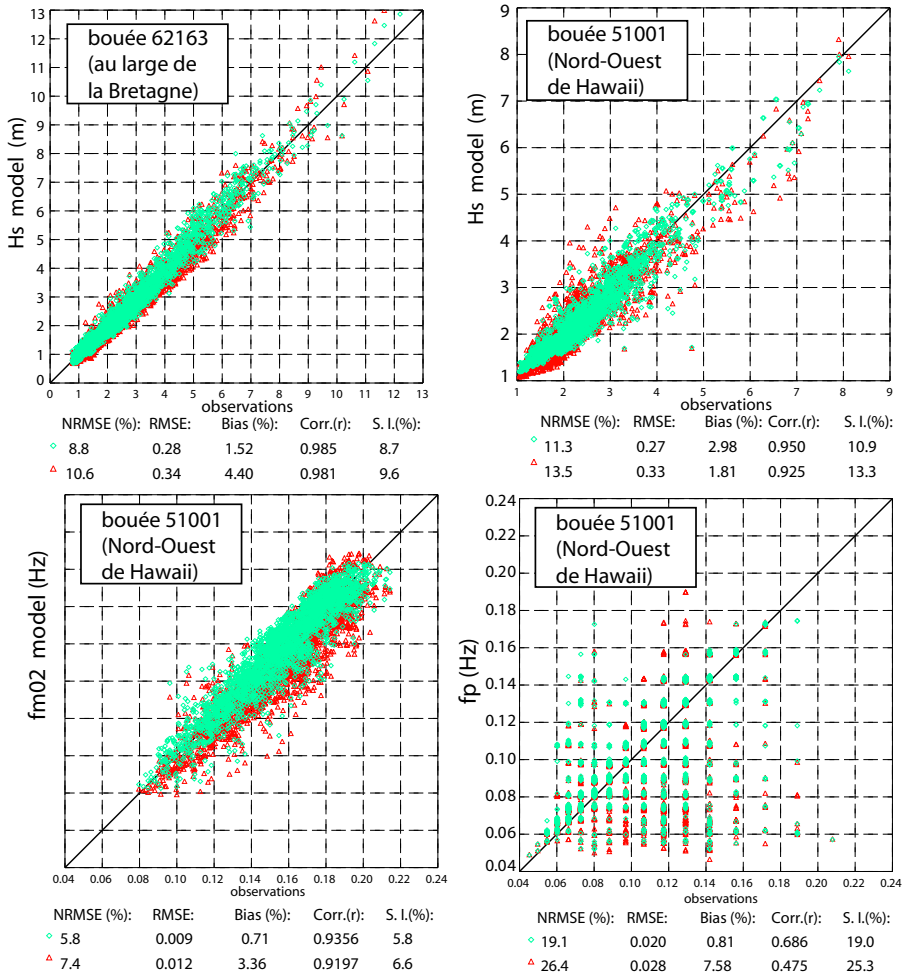

Figure 8.8: Example of scatter plot comparing two model runs, with the Bidlot et al. (2005) parameterization and the Ardhuin et al. (2010) parameterization, described below. Data for the full year 2007 is used at two locations: the Meteo-France - UK Met Office buoy 62163, located off the French Atlantic coast, and the NOAA buoy 51001, located North-West of Hawaii. all observed data has been averaged over 3 hours in order to reduce statistical uncertainties.

defined for the entire spectrum by single mean steepness defined from the full spectrum,

$$S_{ds}\left(k,\theta\right)^{\mathrm{WAM}} = C_{ds}\overline{\alpha}^2\overline{\sigma}\left[\delta_1\frac{k}{\overline{k}} + \delta_2\left(\frac{k}{\overline{k}}\right)^2\right]N\left(k,\theta\right) \tag{8.7}$$

where C_{ds} is a non-dimensional constant, δ_1 and δ_2 are constant weights. This expression uses a mean wavenumber

$$\overline{k} = \left[\frac{\int k^p N\left(k,\theta\right)\mathrm{d}k\mathrm{d}\theta}{\int N\left(k,\theta\right)\mathrm{d}k\mathrm{d}\theta}\right]^{1/p} \tag{8.8}$$

where $p = 0.5$ in the version used by Bidlot et al. (2005). The corresponding mean frequency is

$$\overline{\sigma} = \left[\frac{\int \sigma^p N\left(k,\theta\right)\mathrm{d}k\mathrm{d}\theta}{\int N\left(k,\theta\right)\mathrm{d}k\mathrm{d}\theta}\right]^{1/p}, \tag{8.9}$$

This spectral average gives a mean steepness

$$\overline{\alpha} = E\overline{k}^2 \tag{8.10}$$

This parameterization gives unrealistic variations of the wind sea dissipation in the presence of swell (Ardhuin et al., 2007): the windsea dissipation can be much reduced by the addition of swell. This

spurious effect contributes to the larger scatter in the western part of ocean basins which are dominated by wind seas, with the occasional presence of swells.

As explained in chapter 5, today's understanding of wave breaking and swell dissipation processes, although not complete, have led to parameterizations in which the steepness is more local in spectral space. For example Ardhuin et al. (2010) have proposed to use

$$S_{\rm ds}^{\rm sat}(f,\theta) = \sigma C_{\rm ds}\left\{0.3\left[\max\left\{\frac{B\,(f)}{B_r}-1,0\right\}\right]^2+0.7\left[\max\left\{\frac{B'\,(f,\theta)}{B_r}-1,0\right\}\right]^2\right\}F(f,\theta)+S_{\rm ds,c}(f,\theta). \tag{8.11}$$

with two different steepnesses, one that is integrated in directions,

$$B'\,(f,\theta) = 2\pi\int_{\theta-\Delta_\theta}^{\theta-\Delta_\theta} k^3 cos^2\,(\theta+\theta')\,F(f,\theta')/C_g {\rm d}\theta', \tag{8.12}$$

and the other that is the same for all directions

$$B\,(f,\,) = \max\left\{B'(f,\theta),\theta\in[0,2\pi[\right\}, \tag{8.13}$$

with a threshold $B_r = 0.0009$ so that waves are expected to break if $B > B_r$ (Banner et al., 2000, 2002).

Because the first term of eq. (8.11), in curly brackets, is unable to give an energy balance at high frequency, a 'cumulative term' $S_{\rm ds,c}(f,\theta)$ is added that produces dissipation of the short waves induced by long waves. Hence, starting from a global steepness, we have come to a local steepness, and we are now slowly trying to determine the mutual interactions of the different components through the dissipation term. This will likely keep us busy for many years to come.

Compared to BJA, a 'sheltering term' was also added by Banner and Morison (2006, 2010), reducing the input for high-frequency waves. Ardhuin et al. (2008a) found that this term was necessary to reproduce parameters associated to the high frequency part of the spectrum, with further adjustments discussed by Rascle and Ardhuin (2013).

The other dominant factor at global scales, is the parameterization of swell dissipation as first realized by Tolman (2002c). Indeed, swells account for the majority of wave energy over most of the globe (Chen et al., 2002), and given that dissipation is the only source term for swells away from the storm, a small change of the dissipation rate can lead to very large biases. The swell wave height also depends on the wave heights in the storm. Figure 8.9 shows a typical example, with the storm wave height overestimated by the Tolman and Chalikov (1996) parameterization and a swell dissipation overestimated by Bidlot et al. (2005) and Zieger et al. (2015) for very large propagation distances.

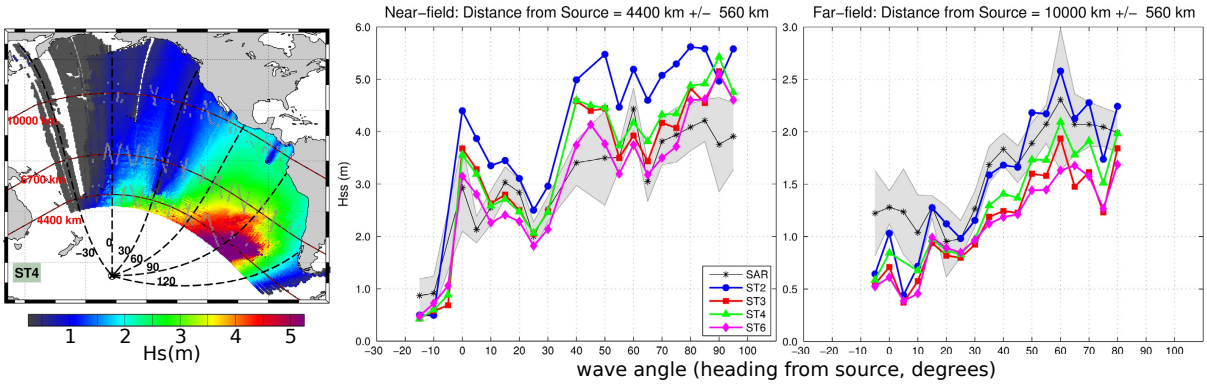

Figure 8.9: Typical model result for swell wave height attenuation away from storms. The left panel shows the modelled swell field using the TEST451 parameterizations described in Rascle and Ardhuin (2013), and the center and right panel compares the measured swell height near and far away from the storm, to modeled results with different parameterizations. ST2 is Tolman and Chalikov (1996), as adjusted by Tolman (2002c), ST3 in Bidlot et al. (2005), ST4 is Rascle and Ardhuin (2013), and ST6 corresponds to Zieger et al. (2015). Adapted from Stopa et al. (2016a).

8.3.4 Beyond H_s, T_p ...

Besides the common sea state parameters, H_s, $T_{m0,2}$ ..., a wave model can be used to compute many other parameters, estimated from the spectrum or from the fluxes associated to source terms. How good

are all these?

Some parameters like the mean square slope and the surface Stokes drift are strongly influenced by the high frequency part of the spectrum. For example, the Stokes drift vector at the sea surface is given by,

$$\mathbf{U}_{ss} = \int_0^{\infty} \int_0^{2\pi} \mathbf{k}\sigma \frac{\cosh(2kD)}{\sinh^2(kD)} E(f,\theta) d\theta df \tag{8.14}$$

in which $\cosh(2kD)/\sinh^2(kD) \to 2$ as $kD \to \infty$. In deep water, if all waves go in the same direction, $\mathbf{U}_{ss}$ is thus proportional to the third moment of the frequency spectrum, m_3 as defined by eq. (3.15).

For $\mathbf{U}_{ss}$ or the mean square slope, the dissipation parameterizations that are based on a mean steepness can introduce spurious effects of long waves on short waves that generally give a poor representation of Stokes drift variability. This is illustrated in figure 8.10 (see also figure 8 in Ardhuin et al., 2010). Hence, an empirical approximation that gives U_{ss} as a function of H_s and wind speed can be a better

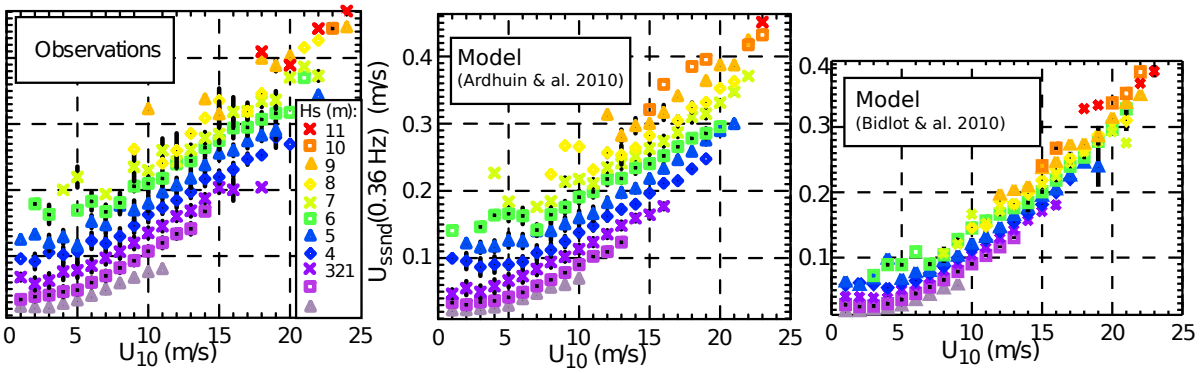

Figure 8.10: Surface Stokes drift for all wave components with a frequency below 0.36 Hz, at the location of NOAA buoy 46005, off the U.S. West Coast. In this calculation we have assumed that all waves travel in the same direction, giving a non-directional Stokes drift U_{ssnd}. The true directional spreading typically gives a true Stokes drift that is 15% less. Observed and modeled values were binned as a function of wind speed U_{10} and wave height. For each bin, the mean value is plotted and the black bars represent half the standard deviation of the bin. We find that over 90% of the variance of U_{ssnd} is explained by U_{10} and H_s. When using the parameterization by Bidlot et al. (2005), the variability is not well reproduced.

choice than some model results (see eq. (C3) in Ardhuin et al., 2009b).

Chapter 9

Extreme waves and historical storms

9.1 Extreme significant wave heights

The maximum measured and modeled wave heights are associated with storms. However, because it takes both a high wind speed and a large fetch and duration to produce large waves, the largest waves are generally caused by storms with high winds that move at a speed close to the group speed of the dominant waves. Figure 9.1 illustrates that H_s generally exceeds 16 m once every 10 years in a good fraction of the North Atlantic: the biggest waves on Earth are found between Ireland and Iceland.

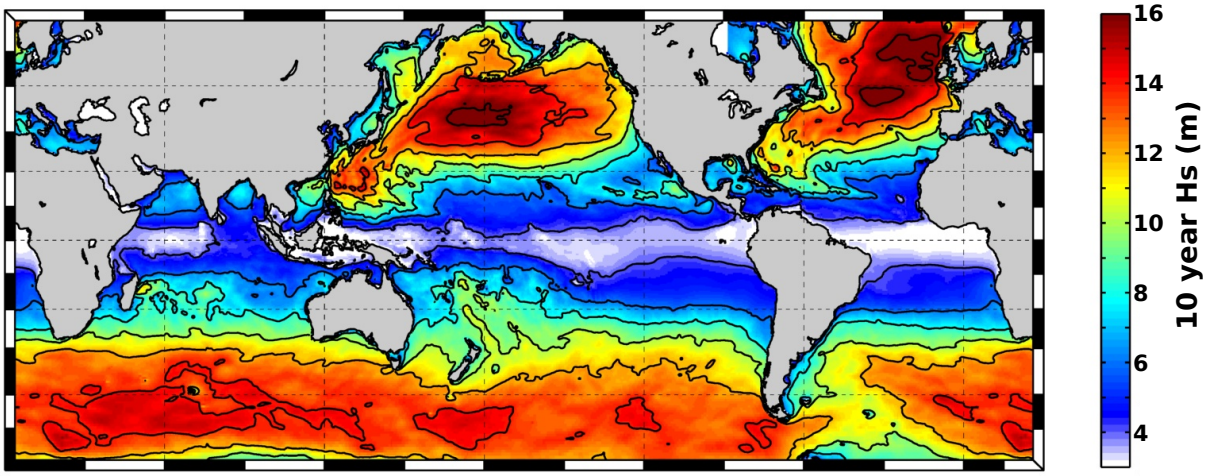

Figure 9.1: Estimate of the 10-year significant wave height (the expected maximum value of H_s that occurs every 10 years) based on a 30-year hindcast, from 1985 to 2015, using WAVEWATCH III forced by CFSR winds Saha et al. (2010), and fitting yearly maxima with a Generalized Extreme Value distribution. Image courtesy of J. Stopa.

Wind speeds in tropical storms can be much faster, probably exceeding 70 m/s in the Typhoon Haiyan that hit the Philippines in 2014, but the motion of these storms does not generally lead to the largest wave heights (see also Quilfen et al., 2010).

The pattern on maxima is thus very different in the tropics where they are related to individual storm tracks, and in the higher latitudes where the broad structures of extra-tropical storm give large values of H_s over a wide region. For example the maximum in the Gulf of Mexico (around 11 m) in figure 9.1 is the result of the passage of a single storm: Hurricane Katrina, which led to widespread damage and coastal flooding (e.g. Resio and Westerink, 2008). Using a different time frame, say around 1900 instead of 2000, would probably have highlighted a different maximum, around Galveston, Texas, associated to the 1900 hurricane that hit that part of the coast. Because it is not possible to know where the next tropical storm tracks will be, an assessment of coastal hazards usually uses empirical storm tracks with randomly shifted positions to investigate the local impact of a track displacement.

The highest-ever measured value of H_s is 20.1 m, using 1-Hz altimeter data from Jason 2. This measurement was made over the North-Atlantic storm Quirin, in February 2011. Although the wind

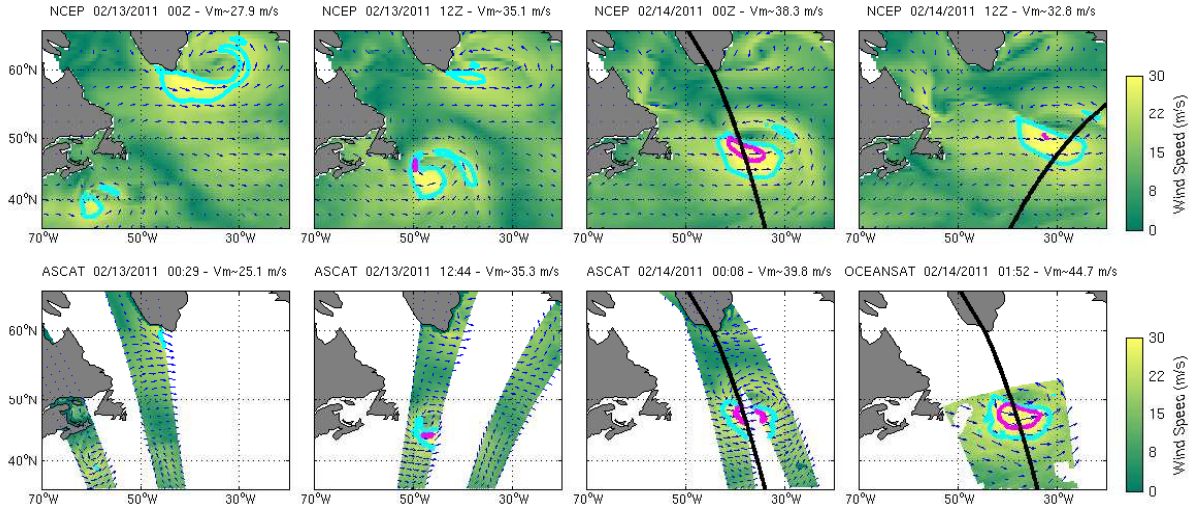

Figure 9.2: Modeled winds (top panel, every 12 hours from 13 February at 00h00 to 14 February at 12h00) and observed (bottom) during the development of the storm Quirin in February 2011. The light blue and magenta contours give the limit of tropical storm ($U_{10} > 24.5$ m/s) and hurricane force ($U_{10} > 32.7$ m/s) wind speeds.

speed probably approached 40 m/s, these waves were associated to a storm travelling at the right speed across the Atlantic, amplifying the dominant waves along its path, which resulted in an effective fetch exceeding 2000 km and a duration larger than 48 hours.

For different regions of the world, different storms have been recorded as particularly severe. In the United States, these are usually associated to hurricanes such as the 1969 Hurrican Camille, or combination of North-Easter storms and hurricanes (e.g. the 1991 Perfect Storm that inspired the movie, see Bromirski, 2001).

9.2 Physical processes at high wind speeds

Parameterizations in wave models have been developed for wind speeds ranging from 5 m/s (Snyder et al., 1981) to 20 m/s or so. At higher wind speeds, the physical properties of the sea surface and the airflow above it is expected to be significantly different. The sea surface is characterized by the presence of foam and spray (e.g. Holthuijsen et al., 2012). In particular, Kelvin-Helmholz or other instabilities can play a leading role Soloviev et al. (2014). It may be surprising that wave models actually work pretty well for H_s up to 18 m (Rascle and Ardhuin, 2013), but this is probably because these large waves mostly occur in regions when the wind is not so extreme, but rather where storms move with the waves.

9.3 Variability and trends of sea state parameters

As waves are related to ocean winds, so does the variability in wind speeds strongly impacts the waves. The El-Nino Southern Oscillation has a very big impact on waves across the Pacific (Bromirski et al., 2005; Stopa and Cheung, 2014), and North Atlantic storms are strongly affected by the North Atlantic Oscillations (e.g. Dodet et al., 2010; Charles et al., 2012). Given this very large interannual variability, it is very difficult to estimate long term trends, such as associated to global change. The studies by Hemer et al. (2013), Wang et al. (2014), and Shimura et al. (2016) show that the shift of high winds speed regimes towards high latitude generally leads to a reduction in wave height at latitudes under 50 degrees, and an increase at higher latitudes. However, the trends for extremes are a complex combination of the number and intensity of tropical storms with the extra tropical storms, so that the extreme wave heights may rise in some regions and decrease in others (Shimura et al., 2016). The case of the Arctic is particular, with a general increase in wave height that is associated to a reduced extent of sea ice (Stopa et al., 2016b).

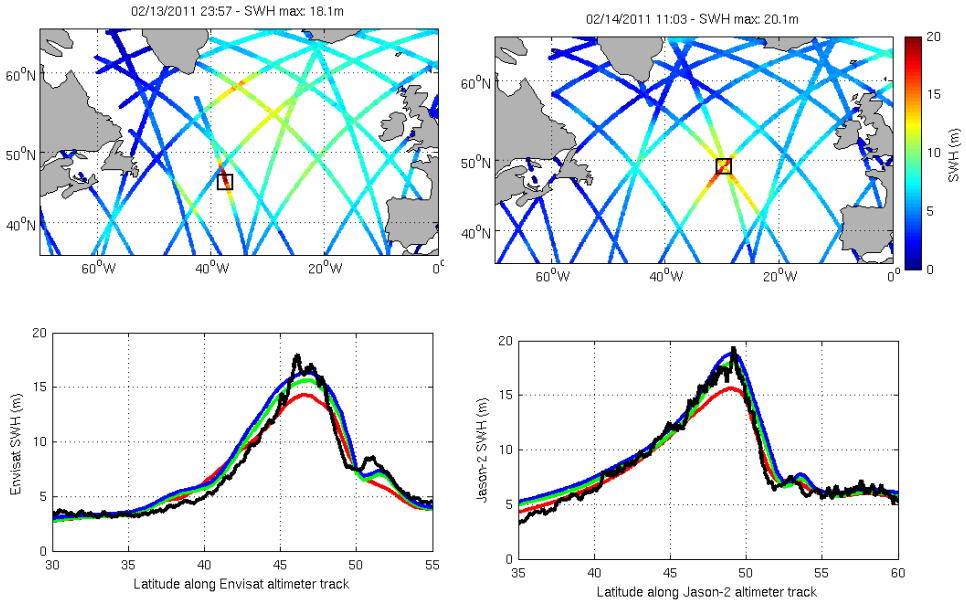

Figure 9.3: Measured H_s from altimeters on 13 and 14 February 2012. Bottom: measured (black) and modeled (color) wave heights using different wind forcings: red is ECMWF operational analyses, green is NOAA/NCEP analyses, and blue is the wind speed from NOAA/NCEP enhanced by 10%.

Chapter 10

Air-sea interactions: wind stress and mixing

Fluxes of any quantity (momentum, heat, mass, carbon dioxide or other gases ...) between the ocean and the atmosphere is very often parameterized as the difference in the volumic density of this quantity between the air and atmosphere, multiplied by an exchange coefficient. This exchange coefficient itself is generally parameterized as a mean velocity difference across the air-sea interface, for practical reason the norm of the vector difference of the wind at 10 m height $\mathbf{U}_{10}$ minus the quasi-Eulerian current at some depth $\widehat{\mathbf{u}}$ multiplied by a non-dimensional exchange coefficient C_e. That coefficient generally represents the full complexity of the ocean surface, the presence of bubble in the water, spray in the air, and the geometry of the interface. Because turbulent transport can be much more efficient, the proper scale for trhe velocity is rather the friction velocity $u_\star$, which means that generally $C_e \ll 1$. The magnitude of this exchange has profound impact on both the ocean and atmosphere, and natural phenomena such as hurricanes are very sensitive to exchanges of heat and momentum. Here we will particularly focus on the fluxes of momentum and energy, looking only at their impact ont the ocean. In general the feedback on the atmosphere cannot be neglected.

A self-similarity theory of turbulence in which big eddies feed smaller eddies following Kolmogorov, gives the Monin-Obukhov theory for the turbulence and associated fluxes in the atmospheric and marine boundary layers (Monin, 1962; Zilitinkevitch and Chalikov, 1968). This was well verified over land (Businger et al., 1971), and in particular it is usual to correct the wind speed $\mathbf{U}_{10}$ to a neutral wind speed $\mathbf{U}_{10N}$ to take into account the source of turbulence coming from buoyancy, in the unstable case of warm water under cold air. A detailed account can be found in Schlichting (1979).

The ocean mixed layer in its top few meters is strikingly different from the atmospheric side, due to the extra source of turbulence coming from ocean waves, mostly due to wave breaking but also associated to the strectching of turbulence by the Stokes drift. This was only revealed in the 1990s and the full details are still being explored, including the interaction of boundary layer turbulence with ocean fronts, internal waves and other features (e.g. Suzuki et al., 2016).

10.1 Sea state influence on air-sea fluxes

10.1.1 Wind stress and drag coefficient

For the horizontal momentum, which is a two-component horizontal vector (U, V), the flux is a also vector (τ_x, τ_y) and the exchange coefficient that relates these two quantities C_e should generally be a tensor. However, it is most often replaced by a scalar C_{DN} parameterized as follows, which makes the big assumption that the flux vector, which is usually called "wind stress", is aligned with the wind vector at 10 m,

$$\boldsymbol{\tau} = \rho_a C_{DN} U_{10N} \mathbf{U}_{10N}, \tag{10.1}$$

where the neutral wind speed is the equivalent wind speeds that gives the same stress in the atmospheric stratification is neutral. It was found in most experiment that C_{10N} tends to be higher for relatively young waves as shown in figure 10.1.

However, in general the wave age is correlated to the wind speed, so that it is very difficult to isolate wave age effects. In their recent review of wind stress parameterization for wind speeds 0 to 25 m/s,

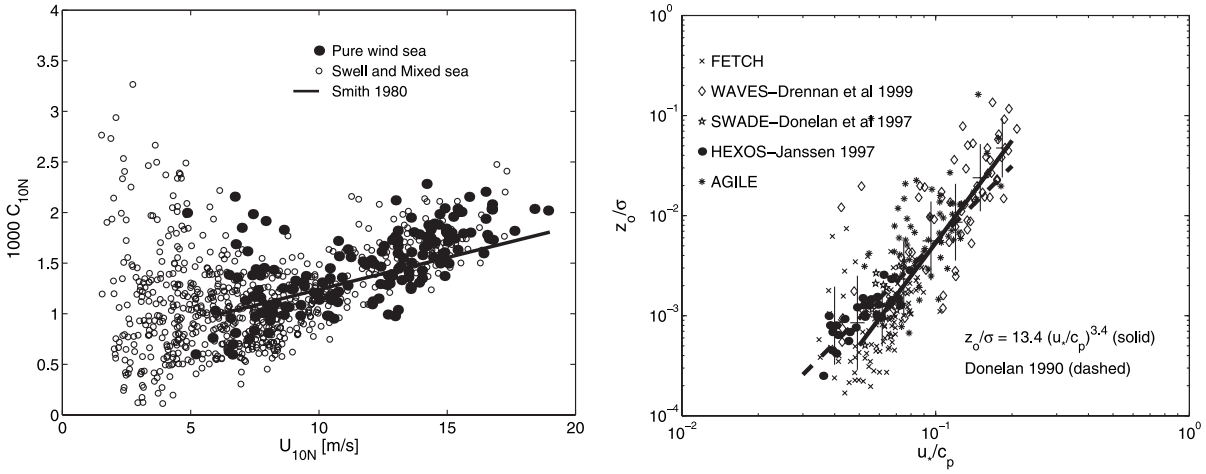

Figure 10.1: Effect of sea state on the wind stress.
Left: measured neutral drag coefficient C_{10N}, during the FETCH experiment in the Mediterranean. Right: variation of the roughness length z_0, normalized by a typical wave amplitude $\sigma = H_s/2$ for various experiments. Figure reproduced from Drennan et al. (2003).

Edson et al. (2013) concluded that the updated COARE 3.5 parameterization gives a good reproduction of the wind stress as a function of the neutral wind speed alone.

For higher wind speeds, several estimates of the stress suggest that the value of C_d may decrease, possibly associated to a full separation of the boundary layer. Figure 10.2 shows several drag coefficient from observations and as used in the ECMWF atmospheric model, for which the drag takes into account the waves (Janssen, 2004).

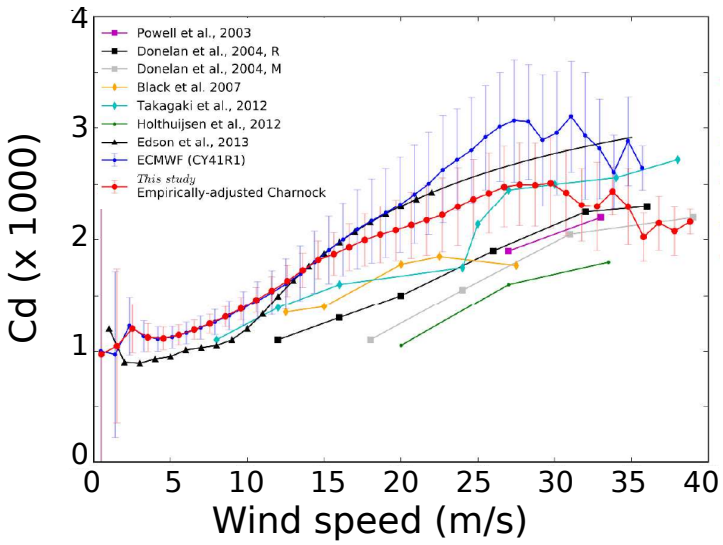

Figure 10.2: Left: Comparison of drag coefficient for ECMWF (CY41R1) parameterization, empirically-adjusted Charnock parameterization and observations (Donelan et al., 2004, 'R' or 'M' corresponds to different measurements techniques Reynolds or Momentum Budget. Adapted from Pineau-Guillou et al. (2018).

10.1.2 Swell and stress direction

Besides the magnitude of the wind stress, waves also modify the stress direction. This is particularly noticeable at low wind speeds in the presence of swell. Indeed, the wind stress may be opposite to the wind direction for wind speeds below 3 m/s, as the wave are loosing momentum to the atmosphere and

generating a low-level jet of wave-driven wind (Semedo et al., 2009; Hogstrom et al., 2009). It is more frequent to observe systematic deviations of the wind stress and wind speed directions when waves and wind are not aligned (Potter et al., 2015).

10.1.3 Other effects

Waves generally have an impact on all air-sea exchanges, not just momentum. This includes mass fluxe (see Veron, 2015, for a recent review of spray generation) and gas transfer (e.g. Brumer et al., 2017). Also in the presence of an ice layer, wave-ice interactions should be taken into account. These are discussed in chapter 25.

10.2 Drift and mixing

10.2.1 Momentum flux for the Eulerian mean current

Knowing the wind stress is a first step in determining how the ocean is forced, but this is not enough to tell how much of that momentum goes into currents as most of it generally goes through the wave field. It is only when the wave momentum is constant that the momentum flux from the wind goes entirely to the ocean circulation. In general, we can use the wave energy balance with source terms S_{in} and S_{dis} presented in Chapter 5, to compute the wave momentum balance. This was done at the end of Chapter 7, when we introduced the momentum flux from wind to waves τ^{aw} and the flux from waves to ocean τ^{wo} .

10.2.2 Quasi-Eulerian currents

The interaction of waves and currents is the topic of onging research, in particular the effects of vertically sheared currents on the waves. A general description of these interaction in three dimensions is given in chapter 24. Here we will consider the much more simple case of a horizontally homogeneous ocean. The wave-averaged momentum equation (24.37) for the mean current $\widehat{\mathbf{u}}$ then takes the following form (Hasselmann, 1970; Xu and Bowen, 1994),

$$\frac{\partial \widehat{\mathbf{u}}}{\partial t} = -f\mathbf{e}_z \times (\widehat{\mathbf{u}} + \mathbf{U}_s) + \frac{\partial}{\partial z}\left[K_z \frac{\partial \widehat{\mathbf{u}}}{\partial z}\right] - \mathbf{T}^{\text{wo}} \tag{10.2}$$

The solution is determined by the surface boundary conditions, and the profiles of the mixing coefficient K_z, and the momentum injected by the waves $\mathbf{T}^{\text{wo}}$ which is a depth-distributed force such that the momentum flux defined by eq. (7.56) is

$$\tau_\alpha^{\text{wo}} = \int_{-h}^{\overline{\zeta}} T_\alpha^{\text{wo}} \mathrm{d}z. \tag{10.3}$$

The solution can be obtained by solving (10.2) with a turbulent closure that gives an estimate of K_z. Following Prandtl (1904), the usual turbulence closure has an addy viscosity that increases with the distance from the boundary (Schlichting, 1979) and involves a velocity scale q associated to the turbulent motion,

$$K_z = qS_M l, \tag{10.4}$$

where the turbulent kinetic energy per unit mass is $q^2 = \overline{u_i' u_i'}$, $S_M \simeq 0.39$ is a constant. With this, the most simple model uses a prescribed mixing length l that is the maximum distance from the surface or the base of the mixed layer.

$$\begin{aligned} l &= \max\{-\kappa D_m \varsigma, \kappa z_{0-}\} \quad \text{for} \quad (-h+\overline{\zeta})/2 < z < \overline{\zeta} \\ l &= \max\{\kappa D_m (1+\varsigma), \kappa z_{0b}\} \quad \text{for} \quad -h < z < (-h+\overline{\zeta})/2, \end{aligned} \tag{10.5}$$

where D_m is the thickness of the mixed layer. The roughness length z_{0-} yields a non-zero value of K_z at the surface, which is consistent with measurements (e.g. Kitaigorodskii, 1994). Thorpe et al. (2003b) and other authors have suggested that z_0 is of the order of H_s, the significant wave height, and should be more precisely related to the height of the breaking waves[1].

[1] Ocean circulation models before the year 2000 used to ignore these effects, and could have very small values of K_z at the surface, e.g. Large et al. (1994), which could give highly unrealistic values of the surface drift when using very high vertical resolutions.

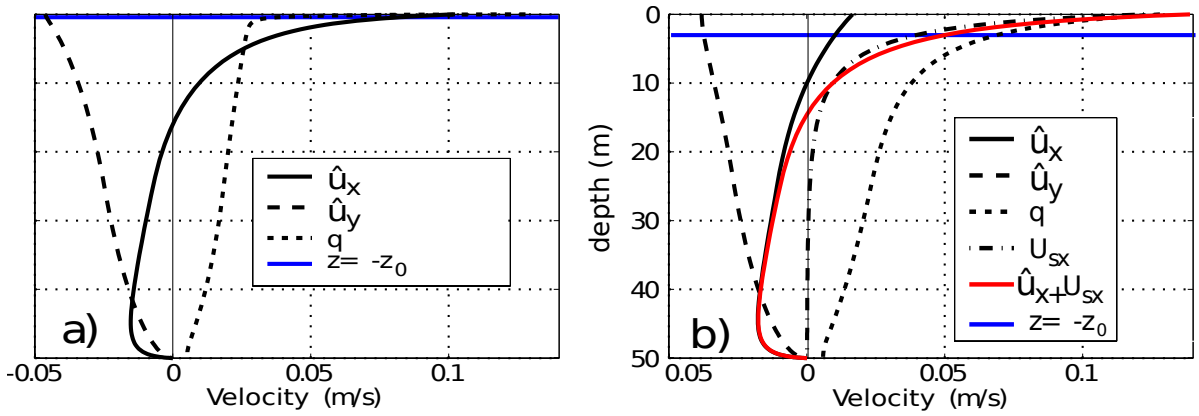

Figure 10.3: Upper ocean current profiles for a wind speed $U_{10} = 10$ m/s
(a) Profiles with a very low value of z_0, representing an unrealistic situation without waves (b) profiles with a realistic value of z_0. In terms of drift velocity, the much lower value of the surface current is compensated by the Stokes drift. The velocity scale q is the square root of the turbulent kinetic enenergy (TKE). A realistic surface flux of q is needed to get the realistic TKE profile in (b). (Figure courtesy of Nicolas Rascle).

More complex models consider also an equation of evolution for q, and one must also define the surface boundary condition for q. For example Mellor and Yamada (1982) use the following equations

$$lqS_q \frac{\partial q^2}{\partial z} = \alpha_{\rm CB} \frac{\rho_a^0}{\rho_w^0} u_\star^3 \quad \text{at} \quad \varsigma = 0, \tag{10.6}$$

$$lqS_q \frac{\partial q^2}{\partial z} = 0 \quad \text{at} \quad \varsigma = -1, \tag{10.7}$$

where $S_q = 0.2$. The mixing coefficient for q^2 is lqS_q, and $\alpha_{\rm CB}$ is the ratio of the energy flux coming from ocean waves (presumably due to wave breaking), and the fruction velocity cubed. This coefficient was particulary discussed by Craig and Banner (1994) and many following authors (Terray et al., 2000; Mellor and Blumberg, 2004; Rascle and Ardhuin, 2009, 2013). Typically $\alpha_{\rm CB}$ is of the order of 100.

For a simple estimation we consider a fully developed sea state, and we assume that $\mathbf{T}^{\rm wo}$ is concentrated near the surface so that we can replace these terms in (10.2) by a local source of momentum in the surface boundary condition. Namely the net momentum flux coming from the wind and waves is balanced by vertical mixing,

$$\tau_a - \tau_\alpha^{\rm aw} + \tau_\alpha^{\rm wo} = \rho_w K_z \frac{\partial \widehat{u}_\alpha}{\partial \varsigma} \quad \text{on} \quad \varsigma = 0. \tag{10.8}$$

In fact, in the presence of a strong surface mixing the numerical solution is not very sensitive to the forcing in the boundary condition or as a body force concentrated near the surface (Rascle et al., 2013).

Assuming a fully delveloped sea state the momentum flux $\tau_\alpha^{\rm aw}$ that goes to the wave growth is canceled by the dissipation terms and we have

$$\tau_a = \rho_w u_\star \mathbf{u}_\star = \rho_w K_z \frac{\partial \widehat{u}_\alpha}{\partial \varsigma} \quad \text{on} \quad \varsigma = 0, \tag{10.9}$$

with $u_\star$ is the wind friction velocity.

Until the 1990s, all ocean circulation models used very small values of mixing at the surface (e.g. Large et al., 1994), corresponding here to low values of z_{0-}, such as in Figure 10.3.a. This can give very high values of the surface current,s depending on the vertical resolution, up to the usally observed 3% of the wind speed (Huang, 1979) or more. But Agrawal et al. (1992) found that the disspation of TKE was much higher in reality, by at least one order of magnitude, so that the mixing must have been strongly underestimated. Recent models have clearly shown that higher surface mixing values are more realistic. For example Mellor and Blumberg (2004) use $z_0 = 0.8H_s$ to get a better fit to measure sea surface temperatures in the Gulf of Alaska. This gives a much weaker surface quasi-Eulerian velocity. This mixing induced by wave breaking is particularly important for relatively shallow mixed layers such

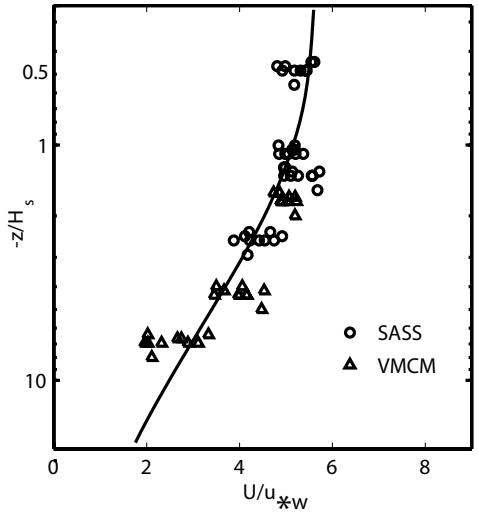

Figure 10.4: Quasi-Eulerian velocities near the sea surface.
Two types of current-meters (SASS and VMCM) provide mean current velocities that have been corrected for wave motion. $u_{\star w} = (\rho_a/\rho_w)^{1/2} u_\star$ is the friction velocity in the water (Figure from Terray et al. 2000). The difference in current velocity between the surface and the thermocline is of the order of 0.5% of the wind speed U_{10}.

as found in the Arabian Sea in summer (Janssen, 2011), or caused by the diurnal cycle of heating (Noh, 1996; Noh and Kim, 1999).

There are very few measurements of velocity profiles of Eulerian or Lagrangian velocity within the upper few meters of the surface. Observations by Santala and Terray (1992) show an Eulerian current that does not exceed 0.5% of the wind speed, see fiugre 10.4. How general is that? Is it still true if we can measure within a few centimeters of the surface, or right at the surface? This is not known yet but several techniques using thermal imagery or polarimetry and wave dispersion should be able to answer these questions.

10.2.3 Stokes drift

The difference between the Lagragian mean velocity, which is the speed or water particles and the speed that advects tracers (temperature, salinity ...), and the quasi-Eulerian velocity is the Stokes drift. To lowest order, this Stokes drift can be computed from the wave spectrum (Chapter 6). For random wave field in deep water, eq. (6.5) gives (Kenyon, 1969),

$$U_s(z) = \int\int 2\sigma k \cos(\theta) E(f,\theta) \exp(2kz) \mathrm{d}f \mathrm{d}\theta, \tag{10.10}$$

$$V_s(z) = \int\int 2\sigma k \sin(\theta) E(f,\theta) \exp(2kz) \mathrm{d}f \mathrm{d}\theta. \tag{10.11}$$

Clearly this expression has a strong contribution from short waves, and thus should be largely influenced by the local wind. Still, for any given wind speed, the surface Stokes drift value U_{Ss} has a root mean square variability of the order of 40%, particularly for relatively low wind speeds, below 7 m/s, as shown in figure 10.5.

Based on direction spectra measured by surface-following buoys, Ardhuin et al. (2009b) found that the surface Stokes drift U_{Ss} could be estimated fairly accurately, with a root-mean-square error of the order of 20%, by an expression as a function of the wind speed and wave height,

$$U_{\mathrm{Ss}}(f_c) \simeq 3.7 \times 10^{-4} \left[1.25 - 0.25 \left(\frac{0.5}{f_c} \right)^{1.3} \right] U_{10} \min\left\{ U_{10}, 14.5 \right\} + 0.025 \left(H_s - 0.4 \right), \tag{10.12}$$

in which f_c is the frequency up to which the Stokes drift is taken into account. This expression was validated for $0.3 < f_c < 0.6$ Hz.

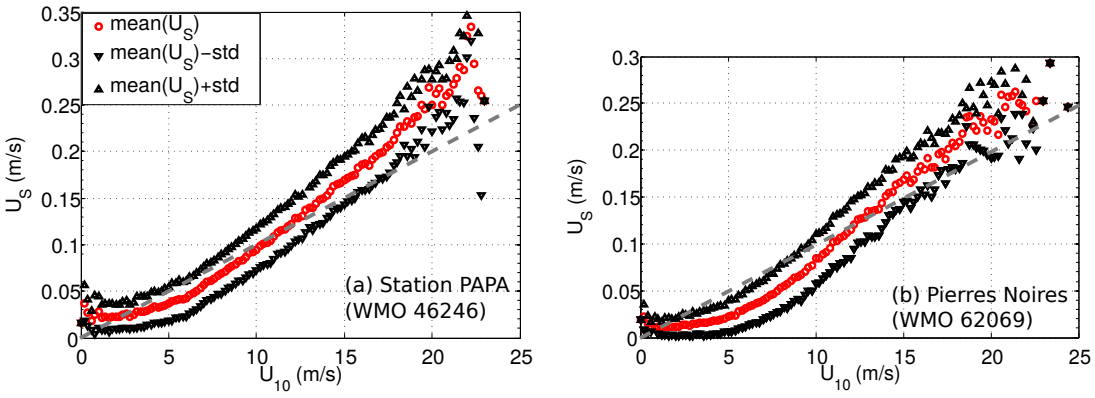

Figure 10.5: Example of mean value (in red) of the surface Stokes drift vector norm $U_{ss} = |(U_{ss}, V_{ss})|$ as a function of wind speed for two locations: station PAPA in the North-East Pacific, and buoy 62069 off the French Atlantic coast. These are obtained by integrating the wave spectrum up to 0.5 Hz. The black symbols show the mean plus or minus one standard deviation for each wind speed. The dashed grey line is $U_S = 0.01U_{10}$.

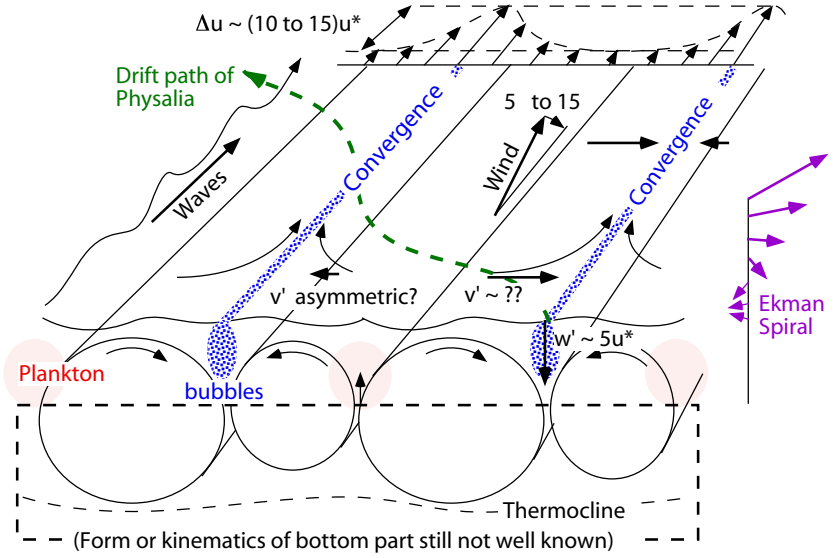

Figure 10.6: Langmuir cells (figure by J. A. Smith)

When subtracting this Stokes drift from HF radar data they found that the quasi-Eulerian current was of the order of 0.4 to 0.8% of the wind speed, with important variations due to inertial oscillations, and, in the Northern hemisphere, a mean direction 60 degrees to the right of the wind. The model proposed here adds the Stokes drift to the quasi-Eulerian velocity and matches relatively well observations of surface drift and mixing (Rascle et al., 2006). The effect of stratification is particularly discussed by Rascle and Ardhuin (2009).

The present model gives both a strong vertical shear of the drift velocity (mostly due to the Stokes drift) and a strong mixing (caused by wave breaking). Still the modeled drift is low by 0.5 to 1.5% of U_{10} compared to the typical 3% surface drift. One possible reason is that surface drift objects are trapped in convergence zones where the mean velocity is faster than that of the surrounding water. These convergence zones are associated to Langmuir cells.

10.3 Langmuir circulation

Indeed the velocities in the upper ocean are not homogeneous horizontally (Weller et al., 1985). Many observations, starting with Langmuir (1938) have revealed lines of convergence where foam, flotsam, sargassum and any buoyant material gathers at the surface (Thorpe et al., 2003a). These lines are

roughly aligned with the wind direction, and correspond to the surface convergence of the rolls that form the Langmuir circulation (Figure 10.6). These rolls emerge due to an instability of the mean vertical shear $\partial \widehat{u}/\partial z$ that is stretched by the Stokes drift shear $\partial U_s/\partial z$ and thus get their energy from the wave field via the turbulent kinetic energy production term $\overline{u'w'}\partial U_s/\partial z$, as detailed in chapter 24. The momentum balance that gives these rolls was further analyzed by Suzuki and Fox-Kemper (2016). These rolls have been observed in most experiments in the ocean and in the laboratory (e.g. Thorpe, 1992; Melville et al., 1998; Smith, 1999), including in shallow water (Marmorino et al., 2005). They are well reproduced in Large Eddy Simulations (e.g. Noh et al., 2004; Harcourt and D'Asaro, 2006; Sullivan and McWilliams, 2010) and can interact with mixed layer fronts (Suzuki et al., 2016).

The parameterization of Langmuir circulation in models that do not resolve them is the topic of active research (e.g. Li and Fox-Kemper, 2017).

Chapter 11

Waves and ocean remote sensing

Waves are usually the first type of motion that you see at the sea surface, and they appear in all remotely sensed data. In some cases, the direct wave influence can be averaged out of the signal. In other cases there is a residual bias due to the presence of waves. This is the case in range measurements with altimeters (e.g. Minster et al., 1991), velocity measurement with Doppler systems (Chapron et al., 2005; Nouguier et al., 2018), surface brighness temperature measurements used to infer sea surface temperature or salinity (Reul and Chapron, 2003). Wave shapes and motion also introduce a variance in the measured quantity which can be useful in the case of sea level measurement with altimetry, or can blur the signal beyond recognition in SAR imagery or interferometry (Peral et al., 2015). All these effects are opportunities for measuring wave parameters, or measuring other processes thanks to their influence on waves.

11.1 Back-scatter from a rough surface

The patterns observed on the sea surface depend on the surface properties (slopes, velocities, whitecaps ...) but also on the viewing geometry and on instrument parameters (electromagnetic wavelength polarization) and on processing details (real aperture, synthetic aperture ...), it is thus difficult to give a comprehensive accounts of the many different looks that the same piece of ocean can have.

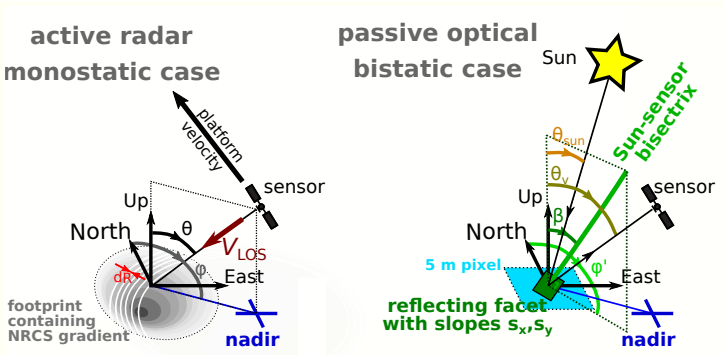

Figure 11.1: Two typical examples of observation geometry of the ocean. Left: observation with a radar looking sideways, the radar is both the source and the receiver of the signal, this is a monostatic measuremnt with ocean apparent properties determined by the incidence angle θ_v and azimuth of the line of sight, as well as radar wavelength and polarization. Right: observation of the sun reflection of the sea surface. Here, for this bistatic geometry, the important direction is not the line of sight but the direction of the sun-sensor bisectrix.

For electromagnetic wavelengths much shorter than the shortest waves (a few millimeters), the ocean surface is locally smooth and the reflection can be completely described by geometrical optics: we can decompose the sea surface in elementary "facets" that are locally flat and reflect the light in the specular direction. When looking in the sun glitter, the apparent brightness of the the ocean depends on the probability that the piece of ocean considered (a "pixel") contains the slope that corresponds to a

bistatic reflector of the sun. For pixels smaller than a few hundreds of meters, the brightness of these pixels fluctuates due to the finite number of "specular points" (Longuet-Higgins, 1960).

A first good approximation for the slope PDF is that it follows a Guassian distribution for the two dimensions that are the slopes $s_x = \partial\zeta/\partial x$ and $s_y = \partial\zeta/\partial y$ along the x and y directions. In this section we will now choose to have the x direction in the wind direction. Under this Gaussian approximation the slope PDF is completely determined by slopes variances $\text{mss}_x = \langle s_x^2 \rangle$ and $\text{mss}_y = \langle s_y^2 \rangle$ as,

$$p(s_{x,y}) \simeq p_G(s_x, s_y) = \frac{1}{2\pi} \exp\left[-\frac{1}{2}\left(\frac{s_x^2}{\text{mss}_x} + \frac{s_y^2}{\text{mss}_y}\right)\right]. \tag{11.1}$$

All measurements, pioneered by Cox and Munk (1954) and confirmed by Bréon and Henriot (2006), have shown that the variances of crosswind and downwind slopes grow linearly with the wind speed, as shown in figure 11.2.a, with a faster growth of the downwind slopes. The total mean square slope (mss) is the sum of these two components, with a value around 0.029 for a wind speed of 5 m/s, corresponding to a root mean square slope of 0.17, or an angle of the sea surface of 10 degrees relative to the horizontal. In practice the mss also varies with the state of development of the wind sea, by up to 20% (± 1 dB in Nouguier et al., 2016), and the presence of current gradients, by about 10% (e.g. Rascle et al., 2017). The largest local changes in mss are associated to the presence of oily films at the sea surface that can strongly damp the shortest wave components.

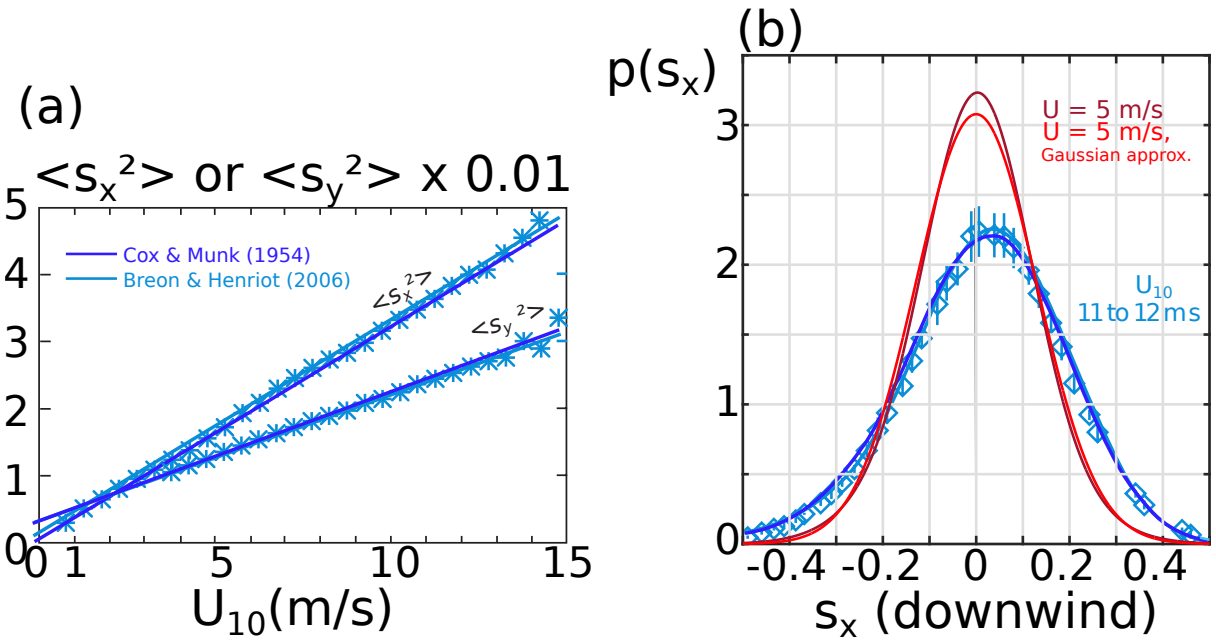

Figure 11.2: (a) variation of the downwind and crosswind slope varianace with wind speed. (b) example of slope PDF for a given mean square slope, corresponding to a widn speed of 5 m/s or in the range 11 to 12 m/s. Adapted from Munk (2009)

For a given slope (or view direction), the PDF (or image brightness) changes if the mss changes. In figure 11.2.b, the PDF increases for small slopes when the mss drops from 0.06 (for 11.5 m/s wind) to 0.03 (for 5 m/s wind, or for higher winds but in the presence of surface slicks), and it decreases for larger slopes. Hence the contrast in the sun reflection in an optical or radar image depends on viewing geometry: near the center of the sun glint (or near the vertical for a monostatic radar) a slick flat surface will appear bright, but it will be dark away from the center (at higher incidences for a monostatic radar) as shown in the photograph in figure 11.3 for a bistatic viewing geometry.

The Gaussian approximation can be corrected with a Gram-Charlier expansion based on the measurements of the mean surface slope, which is not zero, as well as the asymetry and skewness of the waves(Cox and Munk, 1954; Munk, 2009). As shown in Fig. or low wind speeds, non-Gaussian effects mostly introduce a larger probability of near-zero slopes and high slopes, but little change of the probability around $s_x = \text{mss}_x$. These can be associated to nonlinear Stokes-type corrections to the linear wave profile. At higher wind speeds, the asymetry becomes significant, and the most likely surface slope

Figure 11.3: .

is not at zero, but at slightly positive value of $\partial\zeta/\partial x$ that corresponds to the larger area of the rear face of the waves compared to the front face of the waves, the latter being steeper and shorter.

In the case of longer wavelenghts, i.e. all main radar bands used in ocean remote sensing from Ka band (8 mm wavelength) to L band (20 cm or so), the surface is indeed rough and, although specular reflection is still relevant at near-nadir viewing angles, particularly strong reflection occurs when the phases of the surface topography combine constructively with the phases of the incident radar waves: this is Bragg scattering and it typically explains most of the reflections at large incidence angles θ_v.

11.1.1 near-nadir incidences

For near-vertical angles the power recorded on a radar is well described by the theory for a nearly Gaussian distribution of surface slopes, completely determined by the mss. In general, the mss is largely determined by the wind speed, but it is also modified by the stage of development of the wave field, increasing for more mature waves that generally correspond to higher wave heights, as shown in figure 11.4.b.

A flat surface gives a strong return near zero incidence (vertical sounding) and the return power decreases as 1/mss. For incience angles larger than about 10° in Ku-band, the return increases with the roughness.

11.1.2 higher incidence angle

For large incidence angles the reflection is proportional to the amplitude of waves in the radar look direction and with a wavelength equal to $\lambda_e/(2\sin\theta_i)$ where λ_e is the electromagnetic wavelength. These waves are called 'Bragg waves'. A similar scattering of waves by a periodic medium was described by

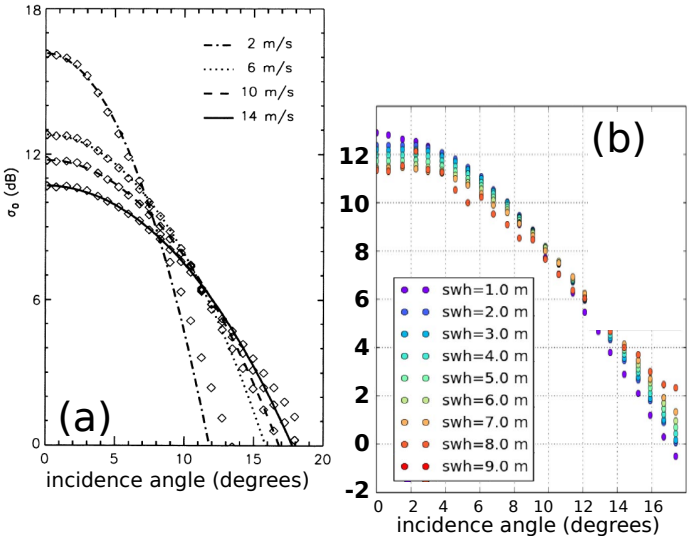

Figure 11.4: (a) Average backscatter power from the TRMM radar (from Freilich and Vanhoff, 2003) (b) Same variation for a given wind speed, as a function of wave height (from Nouguier et al., 2016).

Bragg (1913) in the case of X-ray diffraction, and is thus known as Bragg scattering, although it was first studied by Rayleigh (1896) for the reflection of sound waves at a wavy surface. This generally applies to incidence angles above 30°, and is used in the remote sensing of winds with "scatterometers" as well as the measurement of currents with HF-radars having wavelength of several meters and using grazing incidence angles (close to 90°).

11.2 Various applications

11.2.1 Roughness and surface current gradients

Waves with wavelengths under 3 m are the main contribution to the surface slope variance (e.g. Cox and Munk, 1954; Vandemark et al., 2002), and these short waves are strongly modified by current gradients (e.g. Phillips, 1984). As a result, current gradients have a clear signature in the mean square slopes and the measured back-scatter intensity for incidences 0 to 20°, as shown in figure 11.5. This property has been particularly investigated by Kudryavtsev et al. (2012); Rascle et al. (2014, 2017), with the objective of estimated current gradients from optical imagery in the 'sun glint', i.e. for incidence angles close to the specular reflection direction of the sun. The quantitative analysis of glint data is generally based on the wave action equation as given in chapter 7.

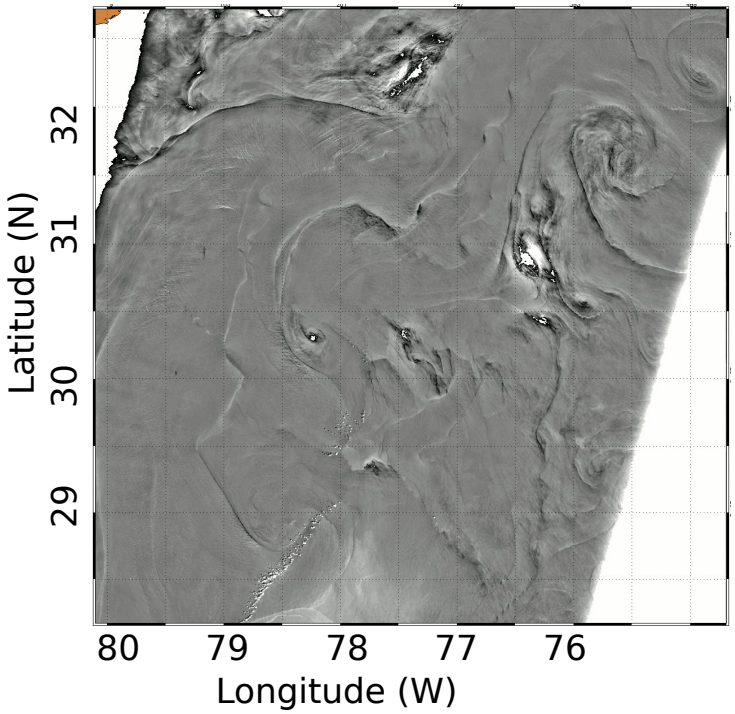

Figure 11.5: Surface roughness observed by the MERIS instrument on board ENVISAT.

Part II

Waves in coastal and nearshore environments

Chapter 12

Linear shoaling, refraction and reflection

In chapter 2, we assumed that the wave field had spatially homogeneous amplitudes, propagating over a flat bottom. We will now allow the water depth to vary, which, like variations in the current velocity in chapter 7, causes important wave modifications.

12.1 Wave shoaling

In the absence of current, wave rays are orthogonal to wave crests are streamlines for the energy. Considering two rays of the same monochromatic wave train, parallel in a region where C is uniform (for instance in deep water, $KD >> 1$, and without current) and spaced from Δl, the energy flux between those two rays $C_g E \Delta l$ is conserved along this 'tube'. All these properties can be demonstrated from Laplace equation and from the boundary conditions at the surface and at the bottom, assuming that amplitudes and phase velocities vary slowly.

Without current and for a beach with an uniform topography along the y-axis (longshore), wave propagation along the x-axis have therefore rectilinear rays et Δl does not change along the tube defined par two of its rays. Hence, the spectral density of energy E matches the group velocity C_g changes (see figure 2.50) so that the energy flux $C_g E$ remains constant. In particular, in the coastal area, $C_g = (gD)^{1/2}$, therefore, the spectral density of energy increases as $H^{-1/2}$. Yet, E is proportional to the mean or significant wave height squared $H_{\text{rms}} = 2^{-1/2} H_s$ and $H_s = 4\,(E/\rho g)^{1/2}$. Therefore, the wave height increases as $D^{-1/4}$. In practice the wave height is limited for wave breaking when D approaches zero.

This modification of the wave height due to variations of the group velocity is called shoaling. But on a real shoal, which has a finite length, the non-uniformity of the depth along the crests also causes refraction.

12.2 Refraction

We showed in chapter 2 that the wave phase velocity was a function of frequency and water depth. In presence of an horizontal current $\mathbf{U}(\mathbf{x})$, vertically uniform, we observe a Doppler shift as well. The wave angular frequency, in a fixed referential becomes then, $\omega = \sigma + \mathbf{k} \cdot \mathbf{U}$, and the phase speed is :

$$C = \frac{\omega}{k} = \left[\frac{g}{k} \tanh(kD)\right]^{1/2} + \frac{1}{k}\mathbf{k} \cdot \mathbf{U} \tag{12.1}$$

The phase speed C changes induce the refraction phenomenon, discovered by Snel and Descartes in optics.

Without current, this effect is perceptible from the moment that the water depth is less than half the wave length ($kD < \pi$). Considering two areas with uniform water depths D_1 and D_2 for $x < 0$ and $x > 0$, then the Snel law (also attributed to Descartes[1]) applies and expresses the wavenumber k_y at the boundary,

[1]The Dutch mathematician Willebrord Snel discovered the refraction law in 1621, but it was only published in 1703

$$\frac{\sin\theta_1}{C_1} = \frac{\sin\theta_2}{C_2} \tag{12.2}$$

Where θ_1 et θ_2 are the angles between the propagation direction and the x-axis. This results applies to a beach with a topography uniform along the y-axis. In this situation, $\sin\theta/C$ is conserved by refraction (figure 12.1).

All the results of geometric optics apply, replacing light velocity by C, in particular Fermat's principle: the integral of C along a trajectory is minimum in the variational sense. Hence, a bump at the bottom acts like a optical converging lens while a trough will be divergent. This explains why waves converge towards capes, increasing their height. Waves propagating against a localized current vein (the current speed is zero outside the current vein) are deviated toward its center. In addition to being shortened due to the Doppler effect, waves are higher and steeper, hence more dangerous, as in the Aguhlas current.

We can obtain a differential equation for the trajectories followed by waves from that same principle. These trajectories are also called rays of characteristics. Let (x, y, θ) be the position and direction of waves in a single point of the ray, and s the curvilinear coordinate along the ray, without current,

$$\frac{\mathrm{d}x}{\mathrm{d}s} = \cos(\theta), \tag{12.3}$$

$$\frac{\mathrm{d}y}{\mathrm{d}s} = \sin(\theta), \tag{12.4}$$

$$\frac{\mathrm{d}\theta}{\mathrm{d}s} = \frac{1}{C}\frac{dC}{dh}\left[\frac{dh}{dx}\cdot\sin(\theta) - \frac{dh}{dy}\cdot\cos(\theta)\right]. \tag{12.5}$$

Without current, the motion of a wave packet is given by his speed $\mathrm{d}s/\mathrm{d}t = C_g$ in the direction θ.

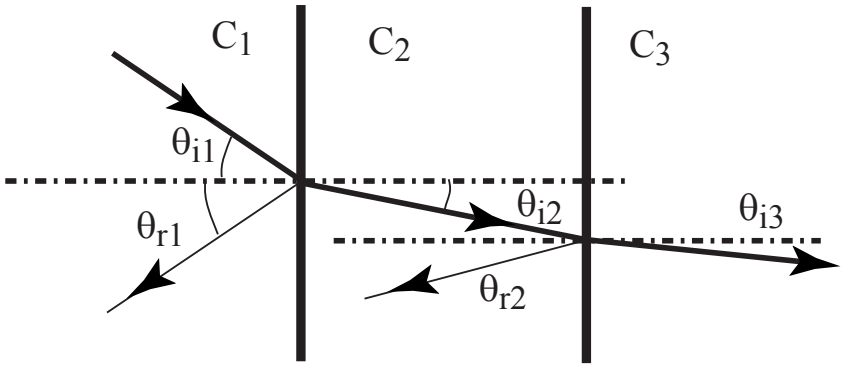

Figure 12.1: Propagation directions for incident or reflected waves, for each part of two phase speed C discontinuities. For a natural topography, refraction is steady and the intensity of reflected waves is generally weak.

With a current $\mathrm{d}s/\mathrm{d}t = |\mathbf{C}_g + \mathbf{U}|$ and the wave propagation direction is different from the direction perpendicular to wave crests. These "rays" have long been calculated by hand (Munk and Traylor, 1947) before numerical methods took over Dobson (1967).

It is very insightful to look at wave plans, the diagrams showing the ray spacing from directions parallel offshore. (see example in figure 12.2). From the energy flux conservation between two rays, a ray spacing l narrower than the offshore spacing l_0 means that the local wave height increases. This is the case in front of Long Beach pier for the 20 s south swell. This augmentation only due to refraction, is of a factor $\sqrt{l_0/l}$, than needs to be multiplied by the shoaling coefficient $\sqrt{C_{g0}/C_g}$. This combination gives a seven-fold increase in wave height that explains the destruction of the Long Beach Pier in April 1930 due to a unusual south swell (Lacombe, 1950). Indeed ,only the very long swells can feel the topography by 200 m depth. The pier has been rebuilt since its destruction but with a slightly different configuration.

in Christian Huygens's book *Dioptrica* where Snel is named in latin (Snellius) which leads to the frequent errors of the English speakers that write his name Snell instead of Snel. The french philosoph René Descartes gives the Snel law in his treaty *La dioptrique*, an appendix of his famous *Discours de la méthode pour bien conduire sa raison et chercher la vérité dans les sciences* publish in Leiden in 1637 and apparently inspired from Snel's work, although Descartes repeated Snel's experiments in 1626 and 1627.(Source: the MacTutor history of mathematics archive, University of St Andrews, Scotland, http://www-groups.dcs.st-andrews.ac.uk/∼history)

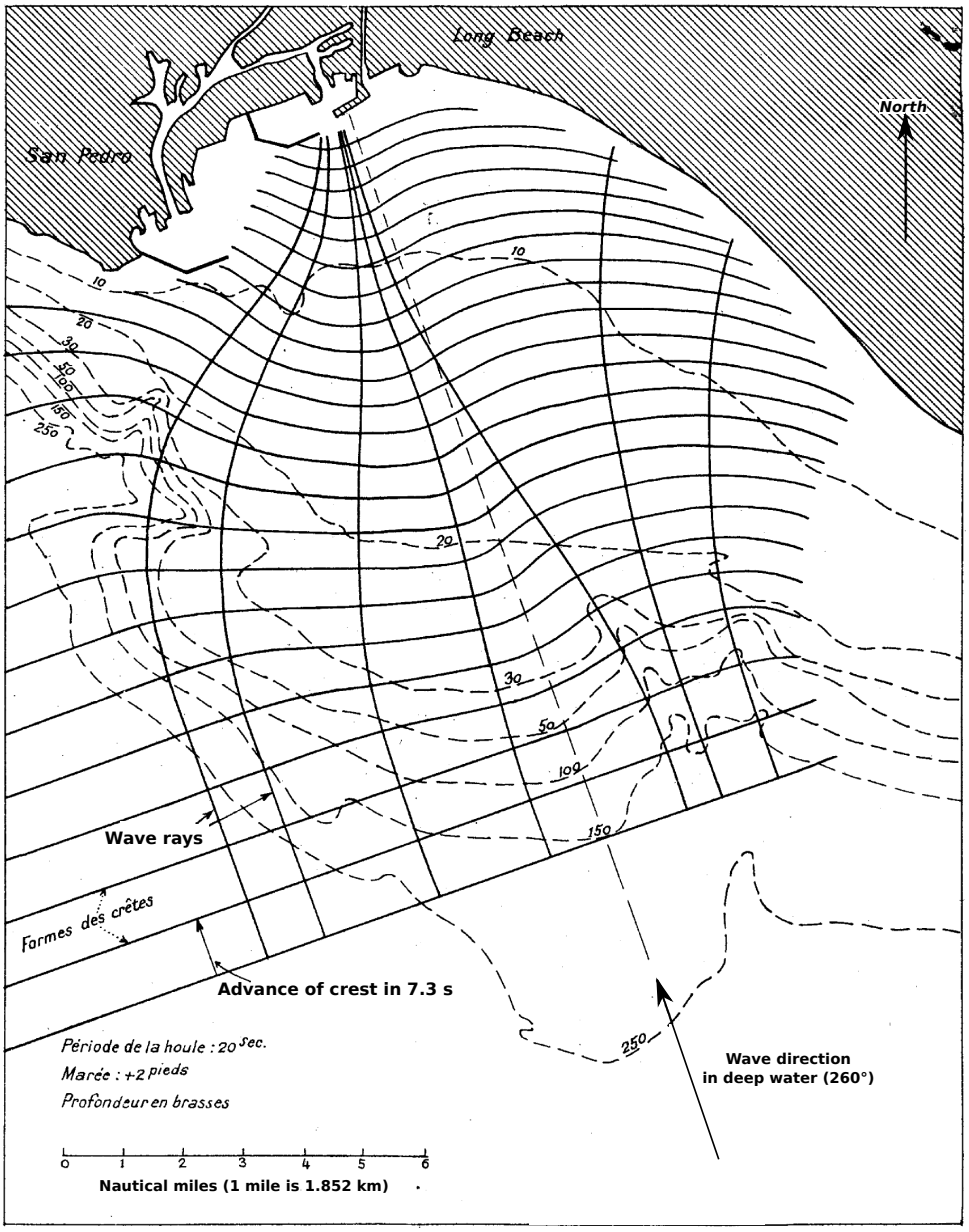

Figure 12.2: Refraction diagram for waves of 20 s period from 160° at Long Beach harbor, California From Lacombe (1950). Note the units on the dashed depth contours: 1 fathom is 1.83 m.

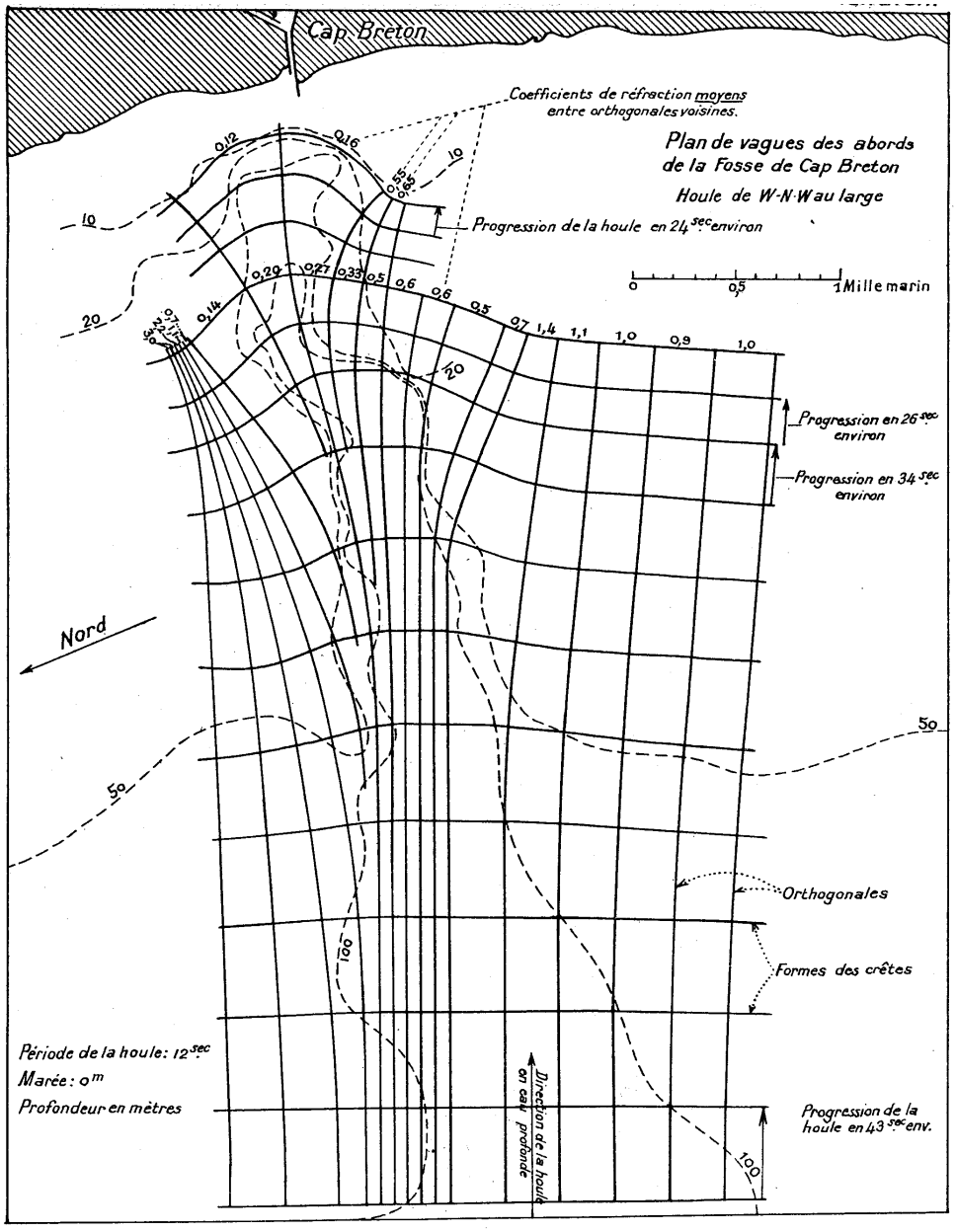

Figure 12.3: Refraction diagram over the Gouf de Cap Breton
From Lacombe (1950).

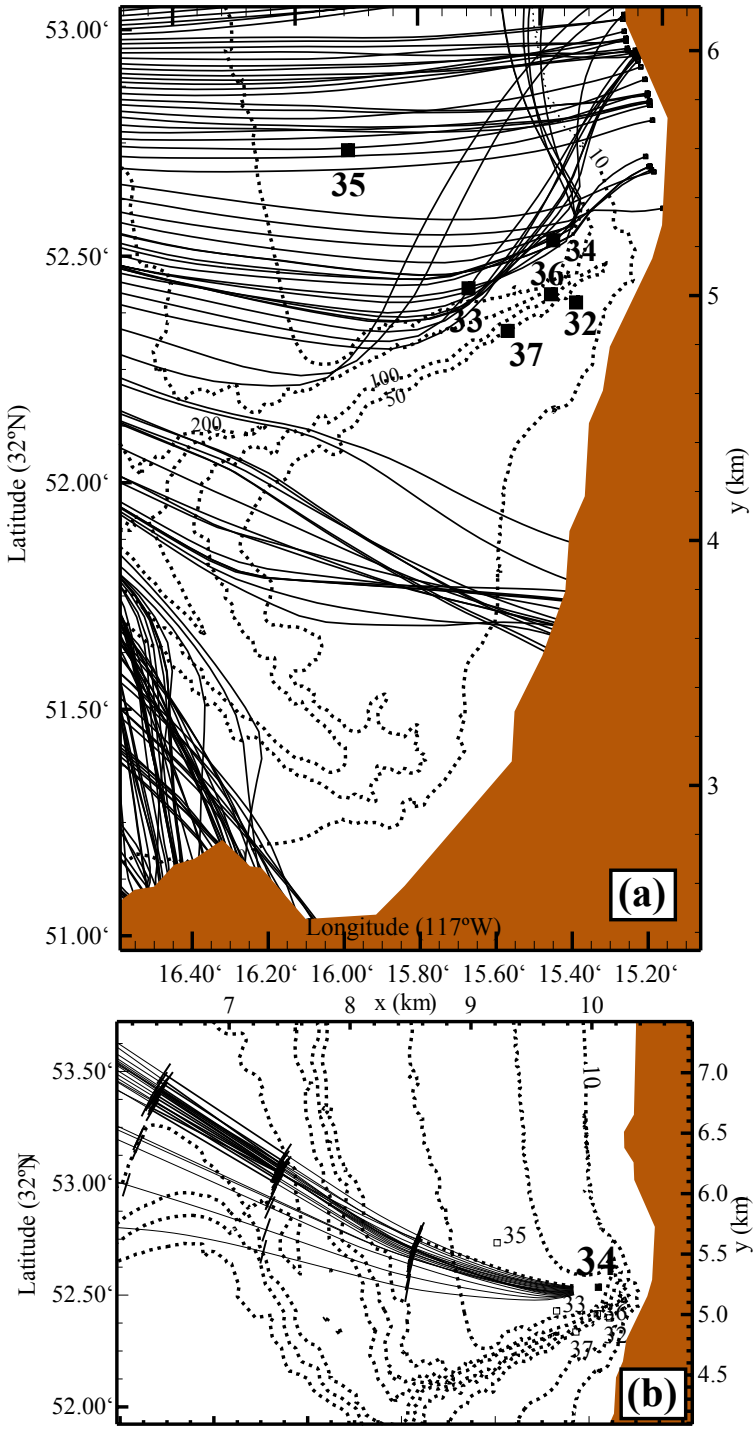

Figure 12.4: Examples of two wave rays methods
a. "Traditional" computation for a west swell with a 15-s period, near La Jolla, California. The location of some the wave buoys deployed during the NCEX experiment is indicated by numbers 32 to 37 and the 10, 50, 100 et 200 m isobaths are shown by the dashed lines. From Magne et al. (2007). b. computation of back-trajectories from point 34, for the same period $T = 15\ s$ and arrival directions evenly spaced with a 1° interval. Only the wave rays reaching offshore, and able to bring energy at point 34 are shown (this is true only within the optical geometry approximation, and by neglecting the wave reflection at the shore. Regular marks are visible along the ray and correspond to the distance covered by the group velocity within time intervals of 60 seconds.)

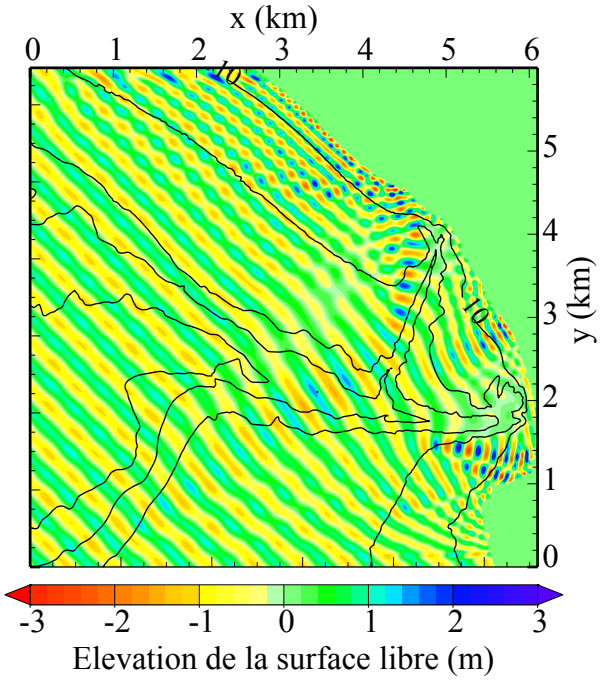

Figure 12.5: Example of propagation of a monochromatic 16 s period, 1 m amplitude offshore swell. Computation made with the finite differences elliptical extended Berkhoff model, from Athanassoulis et Belibassakis (1999)

This computation for Long Beach can be compared to the one for 12-s waves at Cap Breton, France (figure 12.3).

When using a numerical calculation, back-trajectories from a fixed point are more reliable (see for instance in figure 12.4.b). That latter method avoids the occurrence of singularities such as caustics that occur when forward-propagated rays cross. When using backward ray tracing, we use the equality of the of the spectral densities in the coordinates (k_x, k_y), between two points A et B of the same ray. Hence for a zero source term, and in the stationary case without current, using (3.9), equation (5.38) gives

$$E_A(f,\theta_A) = E_B(f,\theta_B)\frac{C_{g,B}k_A}{C_{g,A}k_B}, \tag{12.6}$$

where θ_A et θ_B the ray directions when they cross A and B, respectively. One may hence transform an offshore spectrum to the coast to account for refraction and shoaling. In this situation, we shall often assume that the offshore spectrum is relatively uniform. Reciprocally, we may also estimate an offshore sea state from coastal measurements. This technique can easily be extended to non-stationary situations by adding a time shift between A and B corresponding to the propagation duration, i.e., the integral of $1/C_g$ along the ray. The difficulty of these calculations are limited to the ray tracing that can be done once for all for stationary media (when the tide effect is negligible). This transformation method of a sea state from offshore to the coastline is often very precise, especially for situations dominated by shoaling and refraction (O'Reilly and Guza, 1993; Ardhuin et al., 2003b; Ardhuin, 2006b; Magne et al., 2007).

If wave rays happen to cross, a caustic appears and the wave height becomes infinite. In practice, the wave amplification is finite, since the wave rays of the different spectral components are not at the same location. Yet, for monochromatic wave, the wave height is *in fine* limited by wave breaking or diffraction.

12.3 Diffraction

So far, we have considered that the wave amplitude and the properties of the medium in which they propagate vary slowly in comparison to the wave period on wave length (WKB approximation).

It has been noticed earlier that for caustics due to refraction of a monochromatic wave, this WKB approximation is not valid. This assumption is not verified in the vicinity of obstacles such as breakwaters.

For small amplitude waves, neglecting the wind effect and the bottom friction, one may use the linearized equations. Over a flat bottom and with such obstacles, a solution for ϕ can be found with the following equation

$$\phi = \hat{\phi}(\mathbf{x}) \frac{\cosh(k_0 z + k_0 D)}{\cosh(k_0 D)} \mathrm{e}^{-\mathrm{i}\omega t} \quad + \quad \text{c. c.}, \tag{12.7}$$

where $\omega^2 = g k_0 \tanh(k_0 D)$. ϕ verifies the cinematic boundary conditions at the bottom and surface. The Laplace equation, simplifies into the Helmoltz equation,

$$\nabla^2 \hat{\phi} + k^2 \hat{\phi} = 0. \tag{12.8}$$

The elliptic nature of that equation imposes a solution method with boundary conditions imposed along a closed contour. Taking a wave train $\hat{\phi}$ that varies slowly on the scale $\tilde{\mathbf{x}} = \varepsilon x$, then $\hat{\phi} = \hat{\Phi}(\tilde{\mathbf{x}}) \mathrm{e}^{\mathrm{i}S(\mathbf{x})}$, with a local wavenumber $\mathbf{k} = \boldsymbol{\nabla} S$, that also varies slowly. This gives

$$\begin{aligned}
\nabla^2 \hat{\phi} &= \boldsymbol{\nabla} \cdot \left(\boldsymbol{\nabla} \hat{\Phi} \mathrm{e}^{\mathrm{i}S} \right) && (12.9)\\
&= \boldsymbol{\nabla} \cdot \left[\left(\varepsilon \boldsymbol{\nabla} \hat{\Phi} + i \mathbf{k} \hat{\Phi} \right) \mathrm{e}^{\mathrm{i}S} \right] && (12.10)\\
&= \left[\varepsilon^2 \nabla^2 \hat{\Phi} + 2\mathrm{i}\varepsilon \mathbf{k} \cdot \boldsymbol{\nabla} \hat{\Phi} + \left(\mathrm{i}\varepsilon \boldsymbol{\nabla} \cdot \mathbf{k} - k^2 \right) \hat{\Phi} \right] \mathrm{e}^{\mathrm{i}S} && (12.11)\\
& && (12.12)
\end{aligned}$$

At zero order in ε, the variations of the amplitude $\hat{\Phi}$ are neglected to keep only the phase variations, $S(\mathbf{x})$, and we obtain $|k| = k_0$ meaning that wave trains propagate exactly like plane waves. At first order, we neglect the spatial derivatives of $\hat{\Phi}$. One may show (Mei, 1989, chapter 3, see also Ardhuin et Herbers 2002) that if the bottom slope is of order ε as well, other terms, in addition to $\hat{\phi}$ are required to satisfy the kinematic boundary condition at the surface and we get the action conservation equation,

$$\frac{\partial}{\partial t} \left(\frac{E}{\sigma} \right) + \boldsymbol{\nabla} \cdot \left(\frac{E}{\sigma} \mathbf{C}_g \right) = 0. \tag{12.13}$$

Diffraction appears at second-order terms, and waves tend to turn towards regions with lowest wave amplitudes.

Berkhoff (1972) used the approximation, now known as the mild slope approximation, that ϕ verifies the polarization and dispersion relations of linear waves over a flat bottom. After some calculations, we obtain (see for instance Mei, 1989, chapter 3) the so-called mild-slope equation (or Berkhoff's equation).

$$\boldsymbol{\nabla} \cdot (C C_g \boldsymbol{\nabla} \zeta) + \omega^2 \frac{C_g}{C} \zeta = 0. \tag{12.14}$$

The mild slope equation (12.14) is an extension of the Helmoltz equation to a mild bottom slope. This equation is widely used in coastal engineering for determining harbor agitation, using finite elements numerical models. Results of this type of model are shown in figure 12.5.

Radder (1979) proposed a parabolic approximation of the elliptic equation, by neglecting the ζ gradients in the propagation direction, which conserves the diffraction effects. Such a model (called refraction-diffraction model) has been used for swell forecasting over the Californian Coastline (http://cdip.ucsd.edu), from offshore prediction. The Californian continental shelf is indeed narrow enough to neglected the local generation of waves.

However, contrary to what happens in the vicinity of coastal structures, the diffraction can generally be neglected in this region (O'Reilly et Guza 1991, Peak 2004). hence during the Near Canyon EXperiment (NCEX) offshore La Jolla, California, that lasted over three months, only one swell had been measured with a frequency low enough to justify the use of a model solving Berkhoff's equation. In this situation the Berkhoff's model provided slightly more accurate results than the ray tracing method and only at a limited number of locations. This location corresponds to spots where the wave field varies strongly over a distance that commensurates with the wave length, as for instance over Scripps canyon, with a variation of a factor 5 in the wave amplitude over a distance shorter that the wavelength (figure 12.6).

One may often just use the refraction computation (figure 15.3). This kind of approach take into account the details of the bathymetry and of the spectral shape, which is very important form complex coastline.

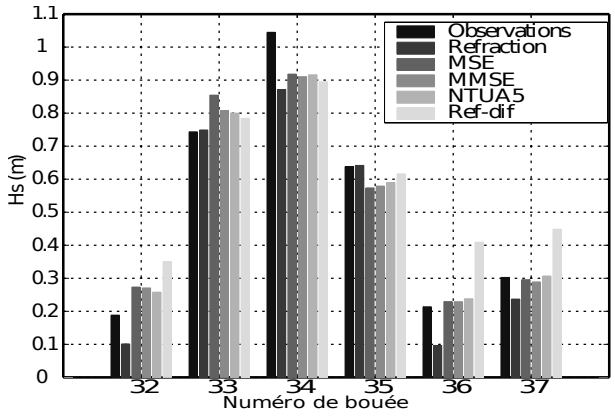

Figure 12.6: Wave observations and modeling during NCEX.
The significant wave heights (H_s) for the frequency band 0.04-0.08 Hz are computed from the spectra generally observed from 1:30 to 4:30 pm UTC, on November 30 2003. The buoy location are shown on figure 12.4. The models used are: a ray back-tracing ("refraction", O'Reilly & Guza 1991) three elliptical models and a parabolic approximation of the Berkhoff equation ("Ref-dif" Kirby 1986). The three models use the same numerical code and solve Berkhoff's equations ("Mild Slope Equation" or MSE, 1972), their version modified by Massel (MMSE, 1993) and their extension by the coupling of three evanescent modes and a local mode (NTUA5, Athanassoulis et Belibassakis 1999). The difference that appears between the refraction model and the elliptical models at buoys 32, 36 and 37 is related to the wave transmission by tunnel effect across the canyon, despite its large depth (see also Thomson et al. 2005). This tunnel effect can not be represented in the geometric optics approximation over which relies the ray tracing of the refraction model. Figure from Magne et al. (2007).

12.4 Reflection

Any variations of the water depth or current velocity - the wave guide parameters - result in partial reflections. These reflections are significant only if the above cited variations are large over the wave length scale. This is the case when the waves approach the coastline.

12.4.1 Reflection at the shoreline

Hence, the magnitude of the reflection, that can be characterized by the ratio $R = a_r/a_i$ of the reflected and incident wave amplitudes, increases strongly with the bottom slope β and with the wave period T. Miche (1951) studied monochromatic waves over a constant bottom slope and reported that R^2 is

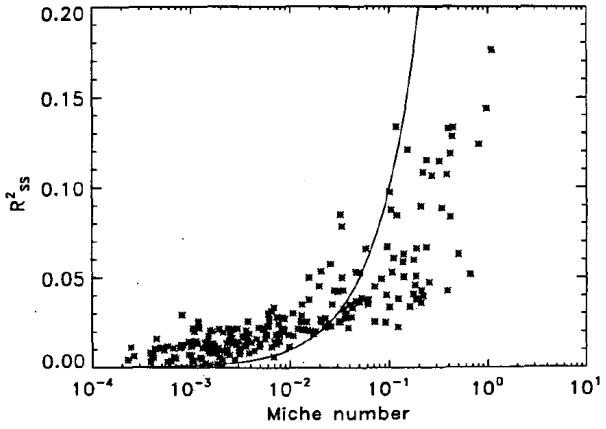

Figure 12.7: Energy Reflection coefficient R^2 as a function of the Miche number M, From Elgar et al. (1994), copyright American Meteorological Society.

roughly equal to the coefficient

$$M = \frac{0.0016 g^2 \tan^5 \beta T^4}{H_\infty^2}, \tag{12.15}$$

where H_∞ is the offshore wave height, in the case $M < 1$ and $R = 1$ for $M > 1$. The only precise study published on the topic of in situ random waves shows that, using H_s instead of H, Miche parameter M effectively gives an order of magnitude of the reflection coefficient for swells and wind seas (figure 12.7).

The study of Elgar et al. (1994) suggests that $R^2 > M$ for $M < 0.05$ and $R^2 < M$ for $M > 0.1$. A better approximation, $R^2 = \min\{0.007(\log_{10}(M) + 5) + 0.2M, 1\}$, has been implemented by Ardhuin and Roland (2012) in the WAVEWATCH III model. Besides, for a given sea state, the reflection decreases toward high frequencies.

Casual observation of wave reflection from a beach suggests that, in addition to the reflection there is also a generation of short wave components, that are radiated toward the open ocean. To our knowledge, this has not yet been discussed in scientific publications.

12.4.2 Reflection by underwater topography

The variations h' of the water depth at the wave length scale also impact waves. One way to represent this effect in the spectral evolution equation consists in decomposing the topography variation h' in sine waves of wavenumber l,

$$h'(\mathbf{x}) = \sum_{\mathbf{l}} B_{\mathbf{l}}(\widetilde{\mathbf{x}})\, e^{i\mathbf{l}\cdot\mathbf{x}}, \tag{12.16}$$

and to calculate the interaction of the wave spectrum with each sine wave. Strictly speaking, we obtain a wave forcing by the topography as obtained in Chapter 2 for the wind turbulence (Hasselmann, 1966). At fist order in bottom slope ($\varepsilon = lh$), we obtain a resonance between two waves with wave numbers $\mathbf{k}$ et $\mathbf{k}'$, such as $k = k'$, that exchange energy thanks to bottom ripples with wave number $\mathbf{l} = \mathbf{k} - \mathbf{k}'$. This leads to an energy transfer in other directions (figure 12.9).

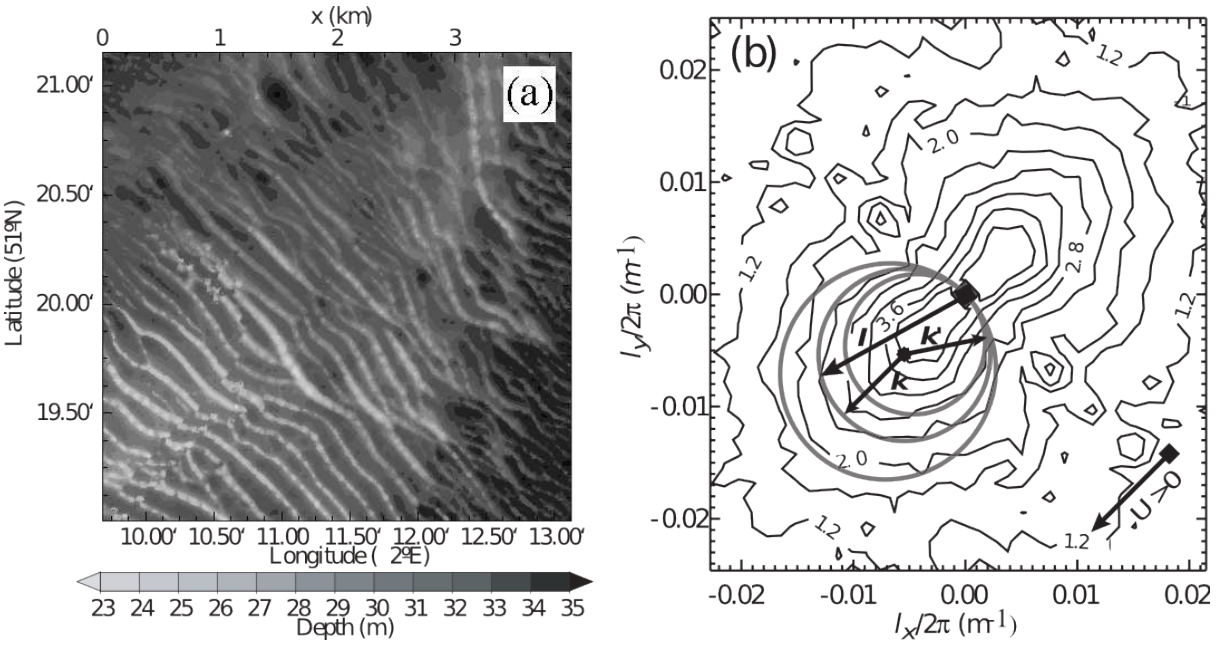

Figure 12.8: Bathymetry of a region with underwater dunes in the south of the North Sea. On the spectrum (b) of this bathymetry, the contours indicate the value $log_{10}[4\pi F_B(\mathbf{l})]$ with F_B the bottom spectrum. The circles indicate the components $\mathbf{l}$ that interact with waves of 12.5 s period coming from the North-West (wave number $\mathbf{k}$) for 3 current speeds, -2, 0 et 2 m/s. .

The local effect of this Bragg diffusion is a modification of the directional wave spectrum. If the bottom topography is dominated by large scales ($l << k$), the result is an increase of the waves directional spreading, that corresponds to a shortening of the wave crest length, rendering the wave field appearance messier.

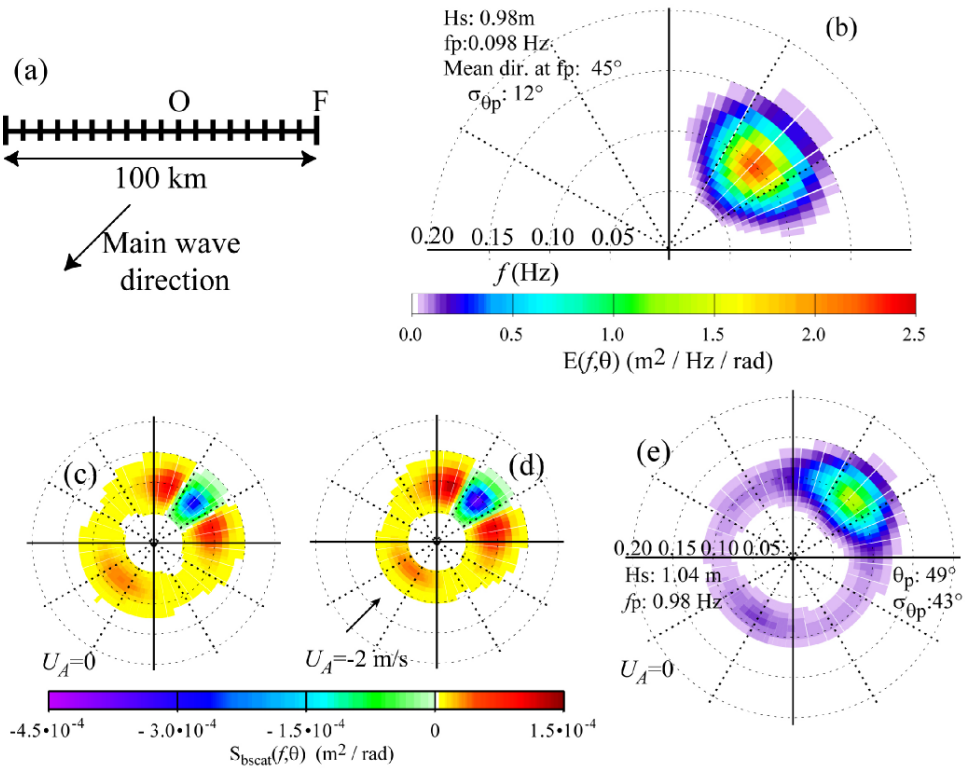

Figure 12.9: Example of spectral evolution caused by bottom reflection for the wave spectrum shown in figure 12.8 and applied in 20 m depth
(a) computation domain, (b) incident spectrum imposed at point F, (c) and (d) evolution term of the spectrum with and without current, (e) spectrum at point O, 40 km inside the domain after 5 hours of propagation. The frequency is here the relative frequency $\sigma/(2\pi)$.

For a topography with a large spectral density at $l = 2k$, the wave are back-scattered (Heathershaw, 1982) and the wave height decreases in the initial direction of wave propagation. For random waves this effect takes the form of a bottom induced scattering term S_{bscat} (Ardhuin and Magne, 2007), which typically produces a broadening of the directional spectrum when important depth variations are present at the scale of the wavelength.

12.4.3 Summary

In Shallow water ($D < 0,5L$), waves are influenced by the bottom in addition to wave-wave interaction and interaction with atmosphere. Leaving apart wave breaking that occurs in the direct vicinity of the beach, the bottom effect depends on the relative amplitude of the waves and of the bottom topography. All these effects are supposed independent of each other, and independent of the wave-wave interaction or of the interaction between waves and atmosphere (e.g. Komen et al., 1994). This leads to a spectral evolution equation that takes into account all the processes as source terms. This is thus an extension of the deep-water action balance given by eq. (7.42) with additional source terms,

$$S = S_{\text{in}} + S_{\text{nl}} + S_{\text{dis}} + S_{\text{fric}} + S_{\text{bscat}} + \cdots \tag{12.17}$$

Chapter 13

Nonlinear wave shoaling

13.1 Introduction

Chapter 3 has shown how random waves can be usually treated as a sum of linear waves with random phases. Chapter 5 presented how it evolves under the influence of weak non-linearities as described by a wave action equation. Non-linearities actually become stronger in shallow water when the waves are less dispersive ($kD << 1$), and we have to reconsider the non-linear effects. In chapter 2 we have introduced the two small parameters $\varepsilon = ka$ and $\delta = a/D$. The nonlinear effects that we will discuss here occur when the parameter $U_r = \delta^3/\varepsilon^2 = a/k^2D^3$ is of order 1. This parameter was introduced by Ursell (1953). The regime $U_r \ll 1$ corresponds to the weak nonlinearity already discussed in chapter 5.

The stronger non-linearity that occurs for $U_r = O(1)$ correspond to a near-resonance at second order, i.e. $k_3 \simeq k_1 + k_2$ and $f_3 = f_1 \pm f_2$, with the plus sign giving super-harmonics of higher frequency, and the minus sign giving sub-harmonics of very low frequency or infragravity waves. These interactions can also be seen as a non-linear wave scattering by the bottom topography with $\mathbf{k}_3 = \mathbf{k}_1 + \mathbf{k}_2 + \mathbf{k}_b$ where $\mathbf{k}_b$ is the wavenumber of the topography (Liu and Yue, 1998; Groeneweg et al., 2015).

Instead of going back to the full Euler equations, several approximations have been proposed to simplify the problem but keep the nonlinearity. In particular, assuming $kD << 1$ allows to derive a simplified set of equations.

13.2 Boussinesq and KdV equations

Both the Boussinesq and (Korteweg and de Vries, 1895, ,KdV for short) equations were first derived by Boussinesq (1872), we will here use the form given by Peregrine (1967).

For wave propagating in one dimension these give the KdV equation,

$$\frac{\partial \zeta}{\partial t} + \sqrt{gD}\left(\frac{\partial \zeta}{\partial x} + \frac{3}{2D}\zeta\frac{\partial \zeta}{\partial x} + \frac{D^2}{6}\frac{\partial^3 \zeta}{\partial x^3}\right) = 0. \tag{13.1}$$

This is asymptotically valid for $kD << 1$ and $ka << 1$. For a constant depth D, solutions of the KdV equation include quasi-periodic recurrent amplitudes (Fermi et al., 1955) caused by the near resonances $k_3 \simeq k_1 + k_2$ which exist when $kD << 1$.

Interestingly, the KdV equation can be solved exactly using the inverse scattering transform, which expresses the solution as a superposition of interacting waves trains and solitary waves also known as cnoidal waves or solitons (Osborne et al., 1996). Among these cnoidal waves, the classical solitary wave solution is,

$$\zeta = \frac{a}{\cosh^2\left[\sqrt{3a/D^3}\,(x - Ct)\right]} \tag{13.2}$$

with a propagation speed

$$C = \sqrt{gD}\left(1 + \frac{a}{2D}\right) \tag{13.3}$$

In this solitary wave the dispersive effect of the finite water depth is exactly canceled by the dispersive effect of the finite amplitude, so that the wave propagate without changing form. The KdV equation is also one of the asymptotic limits of the non-linear Schrodinger equation that describes the evolution of narrow-banded waves in deep water 2003).

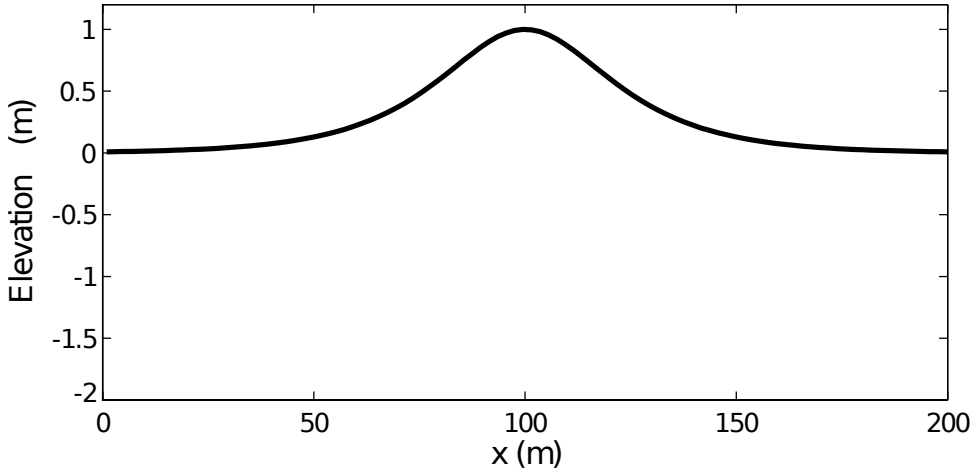

Figure 13.1: Solitary wave given by eq. (13.2) that is a solution of the KdV equation (13.1) in the case $D = 10$ m

The two-dimensional version of the KdV equation is the Boussinesq equation with many forms developed to improve on its dispersive properties, i.e. trying to extend it beyond $kD \ll 1$ (Nwogu, 1993; Nadaoka et al., 1997). Other extensions for finite amplitude have been performed by Serre and others (Lannes and Bonneton, 2009; Dias and Milewski, 2010). Some of these equations have been called fully nonlinear Boussinesq equations but, although they are indeed valid for finite amplitude, they are not correct for waves that are nearly breaking and always have round crests, not sharp like a nearly breaking wave.

13.3 Wave evolution

As waves shoal, the reduction in group speed C_g comes with an increase in the significant wave height H_s, in particular for a shore-normal incidence $\theta = 0$. That effect is less severe for oblique propagation

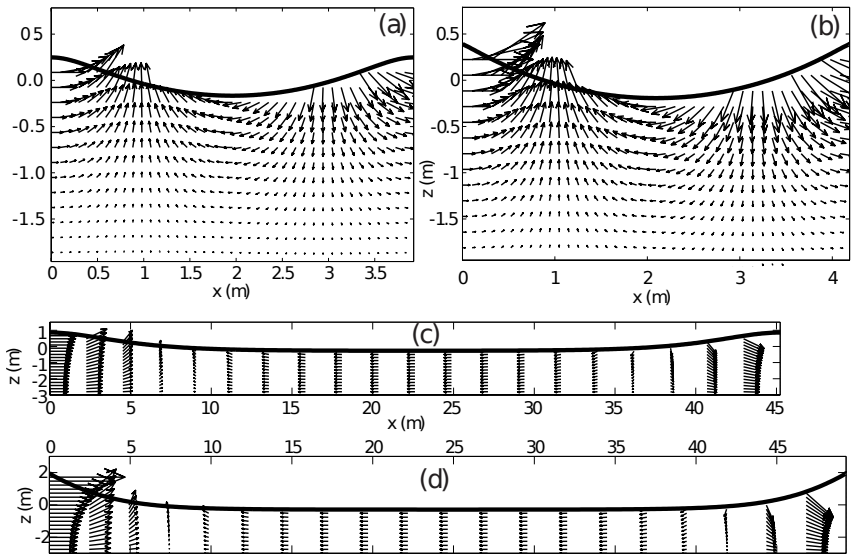

Figure 13.2: Wave profiles computed using the numerical solution method byDean (1965) and Dalrymple (1974) at 60th order for a 3 m water depth, in the case of deep water waves in (a) and (b) with a period $T = 1.5$s ($kD \simeq 5$), and shallow water in (c) and (d) with $T = 8$s, $kD \simeq 0.45$. The arrows represent orbital velocities. Waves in (a) and (c) are moderately nonlinear ($U_c/C \simeq 0.3$), whereas those in (b) and (d) are nearly breaking ($U_c/C = 0.97$).

as the conserved energy flux is $C_g H_s^2 \cos\theta/16$ and $\cos\theta$ increases due to refraction. The wavelength L also reduces as $C = L/T$ slows down and the period remains constant. This increase in height H and decrease in wavelength L make the steepness H/L increase.

13.3.1 Waves over a flat bottom

For a monochromatic wave over a flat bottom, Miche (1944a) studied the shape of the waves of maximum steepness. In the frame of reference moving with the phase speed C, it appears that a singularity develops when the orbital velocity U_c approaches C. Figure 13.2 shows the difference between waves with $U_c/C \simeq 0.3$ and $U_c/C = 0.97$. When $U_c/C \simeq 0.3$, waves in deep water look linear whereas waves in shallow water look like cnoidal waves. As U_c/C approaches 1, the crest become triangular with an angle of 120°, as was already found by Stokes for the deep water case.

Hence, using $U_c/C = 1$ as a sufficient condition for wave breaking, Miche used an analytic stream-function expansion from the wave crest to find that the maximum wave height $H_{\max}$ is

$$H_{\max}/L \simeq 0.14 \tanh(kD) \tag{13.4}$$

In the limit $kD \to 0$, this Miche limit is $H_{\max}/D \simeq 0.28\pi = 0.87$. The deep water limit $kD \to \infty$ gives the previously known $kH/2 = 0.44$. Miche's approximation is very accurate. Figure 13.3.a shows that it can be improved a little by using

$$H_{\max}/L \simeq 0.10 \tanh(kD) + 0.0298 \tanh^2(kD). \tag{13.5}$$

It should be noted that, so far, we have used $H = 2a$ and $E = a^2/2$. In shallow water this does not

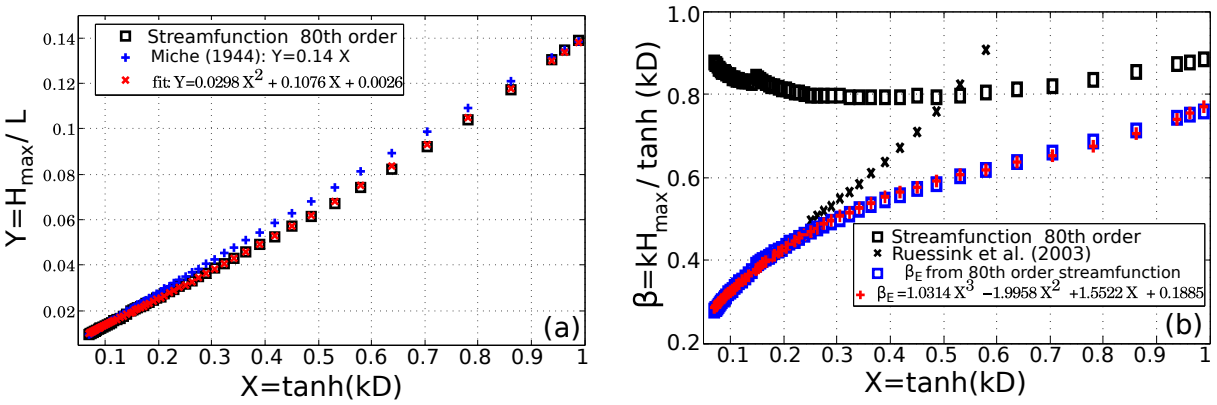

Figure 13.3: Steepness of nearly breaking waves, $Y = H_{max}/L$. The original breaking criterion of Miche (1944) is recalled. A new criterion, using a second order polynomial fit for H/L as a function of $X = \tanh(kD)$ is given. The bottom panel shows the alternative steepness parameters β defined from the wave height, or β_E defined from the wave energy. In the case of Ruessink et al. (2003), his γ parameter is interpreted as H_{max}/D, and transformed to β_E, using the peak wavenumber k_p to estimate $\bar{k}$ (adapted from Filipot et al., 2010a).

hold anymore, and the error on the wave height can be a factor 3 or more. Even if it is probably less important on a sloping bottom, as we will see below, if one wants to apply a limit on the wave height when using wave energy, we can first define a generalized maximum wave steepness from the height

$$\beta = kH_{\max} \tanh(kD) \tag{13.6}$$

or from the wave energy

$$\beta_E = k\sqrt{E_{\max}/8} \tanh(kD). \tag{13.7}$$

This parameter varies with kD in a way that is very close to the estimated variation of the model parameter γ used in the wave breaking parameterization by Ruessink et al. (2003). This γ parameter is often interpreted as $H_{\max}/D$, the fact that it follows β_E and not β suggests that it should rather be interpreted as $\sqrt{E_{\max}/8}/D$.

13.3.2 Sloping bottom and the Iribarren number

Besides the water depth, the local bottom slope also has an influence on the shape of breaking waves, as shown in figure 13.4. These different wave breaking shapes can be predicted using the surf similarity

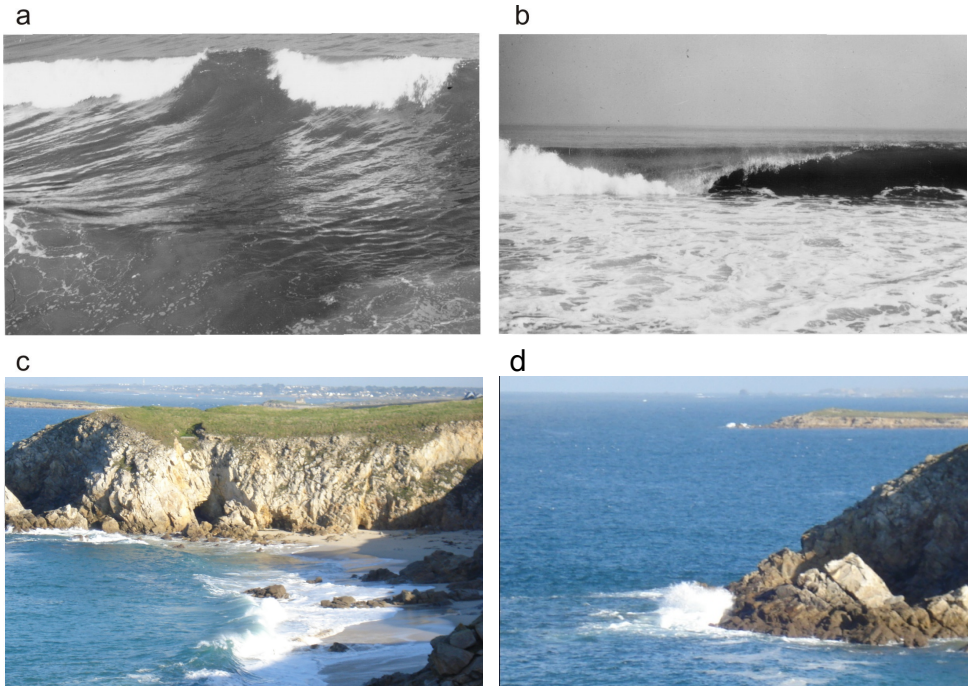

Figure 13.4: Examples of (a) spilling, (b) plunging breakers, taken from Coastal Engineering Manual - Part II (2002). (c et d) are not so nice pictures of a surging breaker on a steep beach and on a rocky point (Ruscumunoc beach, Plouarzel, France).

parameter, proposed by Iribarren and Nogales (1949) and further discussed by Battjes (1974). This is also called the Iribarren number,

$$\xi_0 = \frac{\tan\beta}{\sqrt{H_0/L_0}} = \frac{\tan\beta}{\sqrt{2\pi H_0/(gT^2)}} \tag{13.8}$$

where $\tan\beta$ is the slope of the shoreline, H_0 and L_0 are the height and wavelength of the waves in deep water (before shoaling), which is not always easy to define since shoaling is not the only process involved in transforming the waves from deep water to the shoreline.

Depending on the value of ξ_0 the breaking of waves takes three forms

- spilling for $\xi_0 < 0.5$. Foam is generated at the crest of the wave and spills over the front face. Apart for this foam, the crest keeps its front-back symmetry, and can later evolve in an asymmetric saw-tooth shape.
- plunging for $0.5 < \xi_0 < 3.3$. This is characterized by a ballistic jet of water ahead of the crest, creating a tube of air trapped by the water. The jet produces further splashes as it partially bounces on the sea surface.
- surging for $\xi_0 > 3.3$: in that case the wave breaks right at the shoreface.

For the steepest slopes, waves can be reflected without breaking (Carrier and Greenspan, 1958).

On sandy beaches, which generally have moderate slopes, one can distinguish the surf zone where the waves break, from the swash zone which is the region of the beach which gets wet and dry during a wave cycle.

13.3.3 Wave shapes

The shape of a waves evolves from nearly symmetric front-back shapes outside of the surf zone with a strongly asymmetric shape in the inner surf zone that resembles a hydraulic jump with a rapid rise of

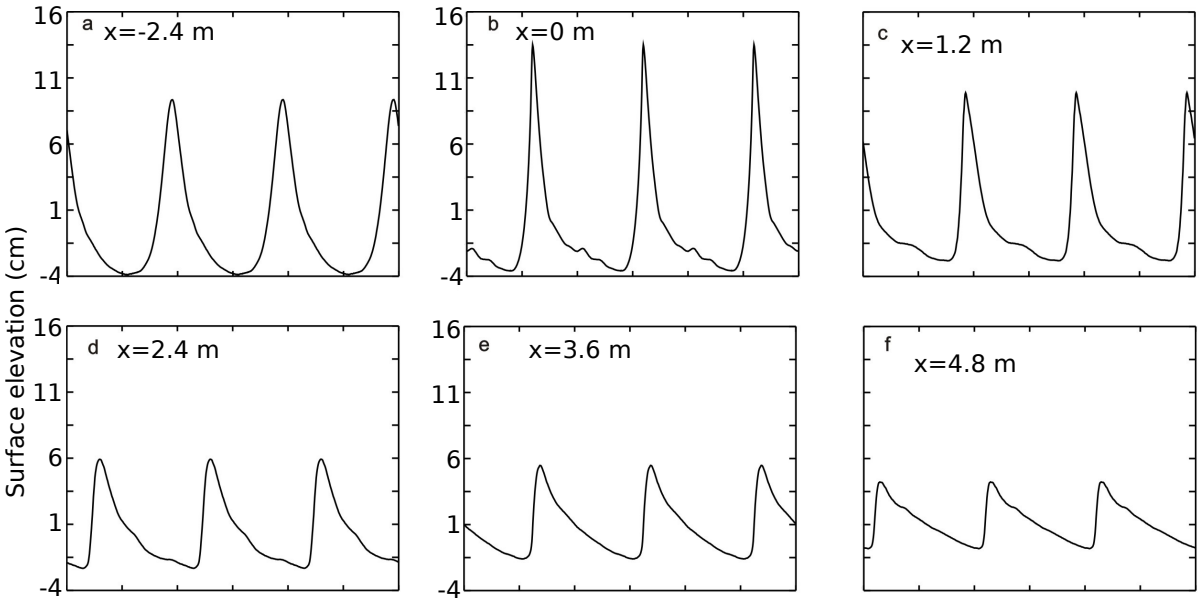

Figure 13.5: Time series of surface elevation before and after wave breaking, for monochromatic waves with $T = 2.2$ s and $H_0 = 0.115$ m over a laboratory beach of constant slope $\beta = 1/35$ (taken from Cox, 1995). These are spilling breakers with an Iribarren number $\xi_0 = 0.23$. The distance is measured from the point $x = 0$ of incipient breaking.

the surface elevation on the forward face of the waves, as shown on figure 13.5 for laboratory spilling breakers. These wave shapes are fairly different from the flat bottom solutions shown in the previous section. This shock-like behavior has been particularly well studied in the shallow water limit(Bonneton et al., 2004). On the contrary top-bottom asymmetry decreases. The front-back asymmetry is associated to a strong acceleration of the flow under the crest, which is very important for sediment transport. In particular, Hoefel and Elgar (2003) have shown how the asymmetry could explain the onshore migration of sand bars.

13.3.4 Wave spectra and bi-spectra

In the case of random waves, the wave evolution is more complex. Looking at the energy only, it is

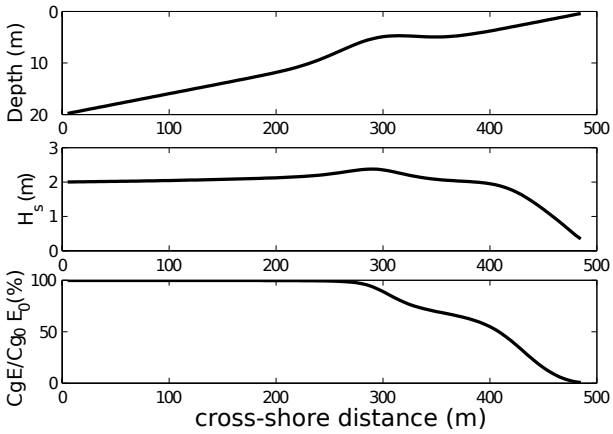

Figure 13.6: Evolution of significant wave height during breaking
Results of the model by Thornton and Guza (1986) for a wave period $T = 12$ s and 20° incidence angle in 20 m depth. Waves propagate over a schematic beach with a mean slope $\beta = 0.04$ and a bar at $x = 300$ m.

possible to have a good approximation of the evolution of the wave energy with a wave dissipation parameterized following the hydraulic jump model presented in chapter 23. This was first developed in

models for the total wave energy by Battjes and Janssen (1978) and Thornton and Guza (1983). An example result from the model by Thornton and Guza, is shown in figure 13.6.

Although the wave height is a key parameter, the important application to sediment transport and beach morphodynamics requires more than information on energy only. First of all, orbital velocities at the bottom, which determine the re-suspension of sediments, require a knowledge of the wave spectrum, or at least wave periods. Hence these energy models have been extended in the form of wave action equations by defining suitable wave breaking parameterizations (e.g. Filipot and Ardhuin, 2012). However, the spectral evolution also exhibits the development of harmonics and their progressive release over varying bathymetry. These processes and the reproduction of the important asymmetry of the waves requires an investigation of the relative phase of the wave components. The relative phases of the different components are given by the bi-spectrum, which is defined as a generalization of the spectrum (our equation 3.3),

$$B(\omega_i,\omega_j) = \langle a_{m,i} a_{m,j} a_{m,i+j} \rangle. \tag{13.9}$$

This bi-spectrum is a complex number. Just like the spectrum is the Fourier transform of the 2-point correlation function, the bi-spectrum is the 2D Fourier transform of the 3-point correlation function of a time series,

$$S(\tau_1,\tau_2) = \langle \zeta(t)\zeta(t+\tau_1)\zeta(t+\tau_2)\rangle \tag{13.10}$$

$$B(\omega_1,\omega_2) = \frac{1}{(2\pi)^2}\int_{-\infty}^{\infty}\int_{-\infty}^{\infty} S(\tau_1,\tau_2)\mathrm{e}^{-\mathrm{i}\omega_1\tau_1-\mathrm{i}\omega_2\tau_2}\mathrm{d}\tau_1\mathrm{d}\tau_2. \tag{13.11}$$

More properties of the bi-spectrum in the context of ocean waves are discussed in Hasselmann et al. (1963). We will particularly note that B is zero for a Gaussian wave field. The skewness and asymmetry of the time series are given by integrals of the bi-spectrum,

$$\langle \zeta^3(t)\rangle = 12\sum_n\sum_l \mathcal{R}\left[B(\omega_n,\omega_l)\right] + 6\sum_n \mathcal{R}\left[B(\omega_n)\right] \tag{13.12}$$

$$\left\langle \left(\frac{\partial\zeta}{\partial t}\right)^3 \right\rangle = 12\sum_n\sum_l \Im\left[B(\omega_n,\omega_l)\right] + 6\sum_n \Im\left[B(\omega_n)\right] / \left(\langle\zeta^2(t)\rangle\right)^{3/2}, \tag{13.13}$$

where $\mathcal{R}$ and $\Im$ stand for the real and imaginary parts respectively.

For practical purposed the bi-spectrum is generally normalized to obtain a bi-coherence $b(\omega_1,\omega_2)$, with values between 0 and 1, and a bi-phase $\beta(\omega_1,\omega_2)$,

$$b(\omega_i,\omega_j) = \frac{|B(\omega_i,\omega_j)|}{\sqrt{\left\langle |a_{m,i}a_{m,j}|^2\right\rangle\left\langle |a_{m,i+j}|^2\right\rangle}}, \tag{13.14}$$

$$\beta(\omega_i,\omega_j) = \arctan\left[\frac{\Im[B(\omega_i,\omega_j)]}{\mathcal{R}[B(\omega_i,\omega_j)]}\right]. \tag{13.15}$$

In the absence of phase-correlations between different components, $b = 0$ all waves are free and propagate at the linear phase speed. The other extreme are the harmonics of a monochromatic waves for which $b = 1$, which are bound to the underlying wave and propagate at its velocity, different from the linear phase speed.

Real waves in shallow water are intermediate between these two extremes and harmonics are partially locked and can be released as free waves by changes in the bottom topography (e.g. Sénéchal et al., 2003).

Elgar and Guza (1985) have made one of the first analyses of the bi-spectral evolution on a gently sloping beach as part of the Nearshore Sediment Transport Study (NSTS) experiment. Figure 13.7 shows the evolution of time series of surface elevation, estimated from bottom-mounted pressure gauges, and the statistical representation of phase-relationships give by the bi-coherence. From a superposition of uncorrelated waves in 9 m depth, the spectrum evolves with the generation of harmonics that, on this particular beach, remain locked in phase and exchange energy. In 3.9 m depth, the bi-coherence already has 3 peaks at 0.06, 0.12 and 0.18 Hz that show the non-linear interaction of the main peak and its harmonics. In other cases with a more complex topography, Sénéchal et al. (2003) showed the the harmonics can become free and the bi-coherence can be reduced after wave propagation over a bar.

A representation of this effect as a 'triad' interactions source term in the wave action equation can be expressed theoretically from the bi-spectrum (Herbers and Burton, 1997; Becq, 1998). However, the integration of an evolution equation for the bi-spectrum comes at a considerable cost, although this is still much less than the cost of a phase-resolving models. As a result, most spectral wave models have adopted relatively crude parameterization of the triad interactions (e.g. Eldeberky and Battjes, 1995).

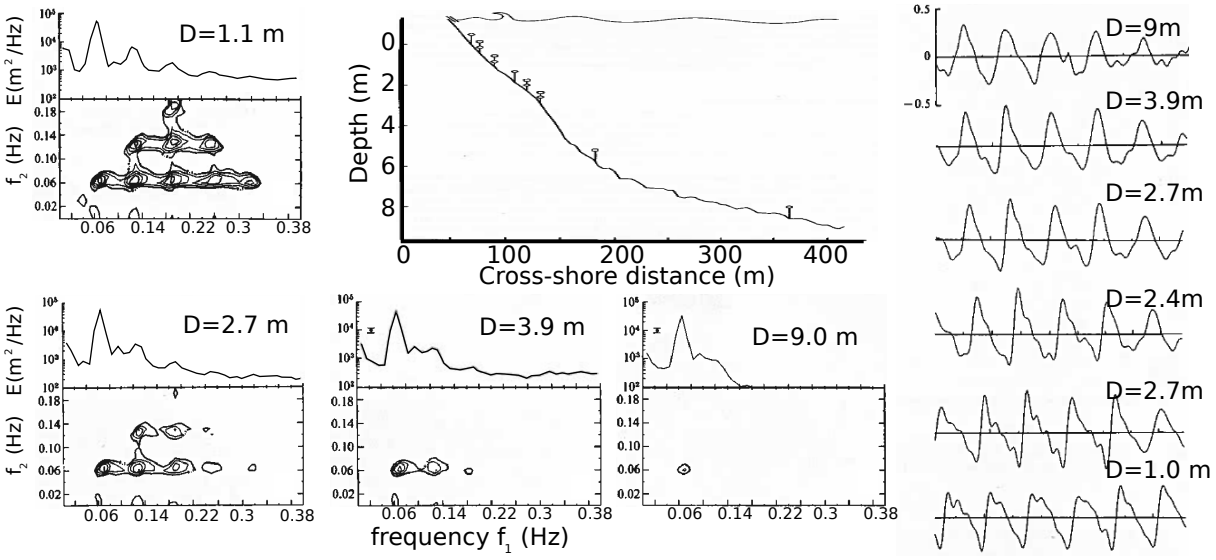

Figure 13.7: Spectral and bi-spectral evolution recorded on February 2, 1980.
The position of bottom-mounted pressure gauges is shown in the upper-middle panel, from 9 m depth to 1.1 m depth. Short pieces of the time series of surface elevation at the different sensors is shown in the right panel. Left and bottom panels show spectra $E(f_1)$ and and associated bi-coherence $b(f_1, f_2)$ at selected locations. Adapted from Elgar and Guza (1985).

13.4 Infragravity waves

13.4.1 Observations

In the same way that sum interactions $f = f_1+f_2$ give rise to harmonics, difference interactions $f = f_1-f_2$ also produce very low frequency components that are called infragravity waves, that we will often shorten as 'IG waves'. This beating pattern was first investigated by Munk (1949). Infragravity water level oscillations are often dominant in the swash, with a typical range of periods between 30 s (0.033 Hz) and 5 minutes (0.003 Hz). Figure 13.8 shows spectra of surface elevation from off-shore of the surf zone to the swash zone, with a typical wind-sea spectrum transforming into a spectrum dominated by motions at frequencies below 0.04 Hz. These long period oscillations of the water level are readily observed by video

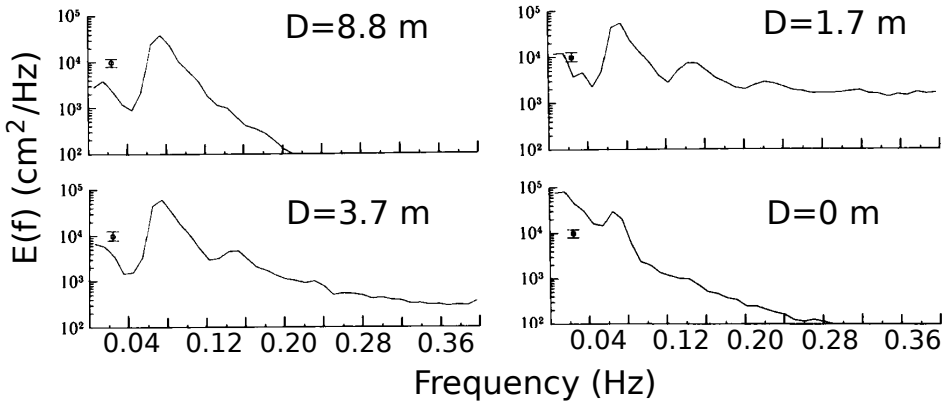

Figure 13.8: Spectra of surface elevation recorded in Santa Barbara on February 4, 1980.
Measurements at $D = 0$ m were performed with a run-up wire: the elevation is not at a fixed position in x but along the beach profile. Adapted from Elgar and Guza (1985).

systems, as shown in figure 13.9 and their analysis is very important for the understanding of coastal hazards.

The contribution of IG waves to the run-up is relatively larger for small beach slopes (Stockdon et al., 2006), with some exceptions. The highest measured IG wave heights, around 2.5 m, was recorded on the

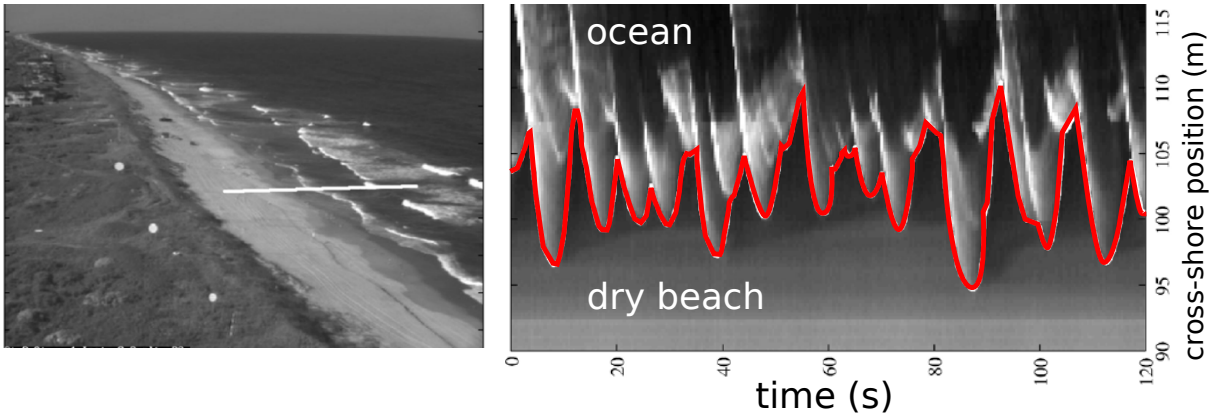

Figure 13.9: Measurement of run-up using a video system
Left: Snapshot of the beach at Duck, North Carolina, with the white line marking the position of a transect. Right: time-stack of pixel grey values along this transect. The red line marks the detected edge of the water: using the beach profile $h(x)$ this gives a time series of run-up. Adapted from Stockdon et al. (2006).

cliff of the small island of Banneg, France, as shown in figure 13.8.

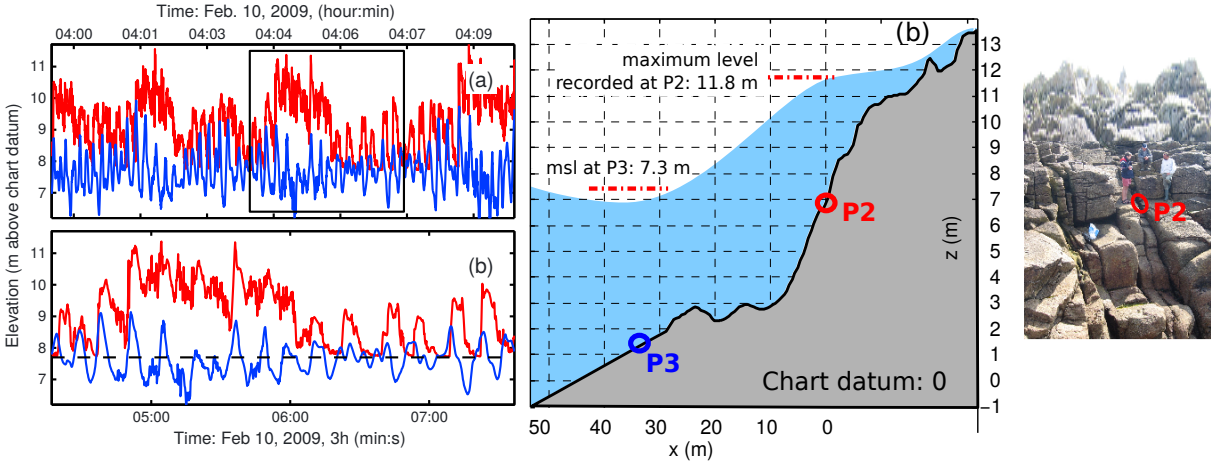

Figure 13.10: Large infragravity wave heights measured on Banneg Island, France.
Left: (a) Time series of pressure converted to surface elevation from the sensors at the top of the cliff (P2, red) and the bottom of the cliff (P3, blue). A typical burst of high water levels, lasting 90 s, is enlarged in (b). Center: cliff profile and schematic of water level at the time of highest recorded pressure. Right, picture of the cliff from P3, at low tide. Adapted from Sheremet et al. (2014).

13.4.2 Theories for IG waves generation

A first theoretical explanation for the formation of infra-gravity waves was given by Whitham (1962a) and Longuet-Higgins and Stewart (1962), looking at the flow response to the passage of wave groups. They actually gave two derivations, the first follows the perturbation method used in chapter 2 and 19. The second method, which we will use here, is only applicable when wave groups are long compared to the water depth, and uses the wave-averaged mass and momentum equation, (7.33) and (7.35). Neglecting the Coriolis force, advection, and surface and bottom friction, these become, for waves propagating in the x direction only

$$\frac{\partial M}{\partial t} = -\rho_w g D \frac{\partial \overline{\zeta}}{\partial x} - \frac{\partial S_{xx}^{\mathrm{rad}}}{\partial x}, \tag{13.16}$$

$$\frac{\partial M}{\partial x} = -\rho_w \frac{\partial \overline{\zeta}}{\partial t}. \tag{13.17}$$

These are exactly the equation of long waves (i.e. in the shallow water limit),forced by $S_{xx}^{\rm rad}$. For a narrow wave spectrum, we note that $S_{xx}^{\rm rad}$ is attached to the wave groups and travels at the speed C_g, the solution of such a forced wave is bound to travel with the forcing, so that the time derivative is equal to $-C_g$ times the horizontal gradient.

We recall eq. (6.25) that gives $S_{xx}^{\rm rad} = \rho_w g E(2C_g/C - 0.5)$, which is always positive. Taking a particular case of modulation of energy $E = E_0 + E_1 \cos[Kx(1-C_g t)]$, we have $S_{xx}^{\rm rad} = S_0 + S_1 \cos[Kx(1-C_g t)]$ we look for solutions of the form, $M = M_1 \cos[Kx(1-C_g t)]$ and $\overline{\zeta} = A_1 \cos[Kx(1-C_g t)$. Replacing in our mass and momentum equation, this gives,

$$C_g M_1 = -\rho_w g D A_1 - S_1 \tag{13.18}$$

$$M_1 = -C_g \rho_w A_1, \tag{13.19}$$

which gives the transport and elevation amplitudes of the bound long wave,

$$M_1 = -\frac{CgS_1}{gD - C_g^2} \tag{13.20}$$

$$A_1 = -\frac{S_1}{\rho_w (gD - C_g^2)}. \tag{13.21}$$

This solution thus gives a total transport M_1 by the long and short waves that is partly compensating the modulation of the wave-induced transport $\rho_w C_g E_1/C$. Because the compensation is not exact, the net divergence of the flow is driving a change in mean sea level, with a lower level where the wave energy E_1 is larger. It should be noted that this bound wave response has a singularity in the limit of shallow water when $C_g \to \sqrt{gD}$, this is the limit into which the interaction of two short waves and the long wave becomes resonant.

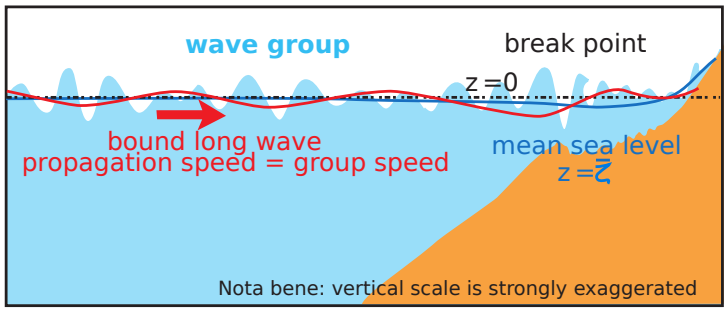

Figure 13.11: Schematic of bound infragravity waves associated to wave groups.

This 180° phase shift between the wave energy and the long waves was indeed verified in some experiments, typically just outside the surf zone on gently sloping beaches, but it is typically less in the surf zone (Elgar and Guza, 1985). This may be due to the difference between the flat bottom solution where the long wave is exactly bound, and the real case of a varying depth in which the long wave is partially free. For a general wave spectrum with waves in all directions, the theoretical bound response is integral over all possible pairs of waves, as detailed in chapter 19, and the theory is well verified over a flat bottom (Herbers et al., 1994). The free and bound IG wave energy can be separated using a bi-spectral analysis (Herbers et al., 1994). Free IG energy usually dominates even in 8 m depth, and even more so in deeper water (Herbers et al., 1995).

It is also possible that other mechanisms generate long period oscillations. In particular, over coral reefs, the modulation of the position of the initial wave breaking with wave groups can produce mean sea level oscillations that are rather in phase with the wave groups (Symonds et al., 1982).

13.4.3 Free wave radiation from the coast

Whatever the details of the generating process, it is clear that bound waves traveling with the incoming wave groups are released and partially dissipated in the surf zone where the groups are dissipated. Because the phase speed of the released waves is much larger than that of the incident waves, most of the energy is strongly trapped by refraction along the coast.

Observations compiled by Ardhuin et al. (2014) suggest that the free IG wave spectrum near the coast can be parameterized as,

$$A_{IG} = H_s T_{m0,-2}^2 \tag{13.22}$$

$$E_{IG}(f) = 1.2\alpha_1^2 \frac{kg^2}{C_g 2\pi f} \frac{(A_{IG}/4)^2}{\Delta_f} [\min(1., 0.015\text{Hz}/f)]^{1.5} \tag{13.23}$$

$$E_{IG}(f,\theta) = E_{IG}(f)/(2\pi), \tag{13.24}$$

where $\alpha_1 = 6 \times 10^{-4}$ s^{-1} might vary with bottom topography, and $\Delta_f = 0.0279$ Hz. The k/C_g factor accounts for the shoaling of a broad directional spectrum, while the frequency shape of the spectrum is given by the other terms. In the shallow water limit, i.e. kD going to zero, this spectrum is constant up to $f = 15$ mHz and decreases like $f^{-1.5}$ for higher frequencies. In that frequency range, this asymptote is identical to the form $\tanh(kD)^{-1.5}$ given by Godin et al. (2013). The differences at lower frequencies may be due to the fact that, in particular for $f < 2$ mHz, the measured wave field in the open ocean is mostly driven by atmospheric pressure and not IG waves radiated from shorelines (Filloux, 1980; de Jong et al., 2003).

Eq. (13.24) gives an estimate $\widehat{H}_{IG}$ of the infragravity wave height,

$$H_{IG} = 4\sqrt{\int_{0.05\ \text{mHz}}^{30\ \text{mHz}} \widehat{E}_{IG}(f)\mathrm{d}f}. \tag{13.25}$$

A global model with such a source of free infragravity waves at the coast gives average IG wave heights shown in figure 13.12.

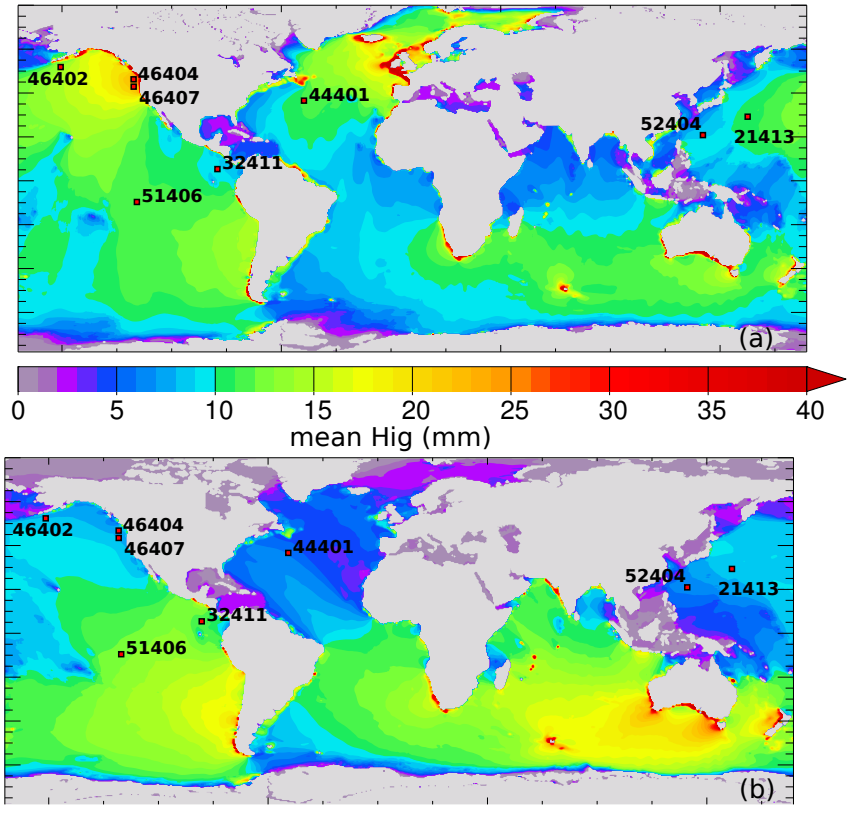

Figure 13.12: Mean values of H_{IG} over (a) January and February 2008, (b) June and July 2008. Small squares with numbers correspond to the location of DART stations used for model validation. Taken from Ardhuin et al. (2014).

Chapter 14

Bottom boundary layer: processes and parameterizations

Bottom friction is a complex process because the bottom is generally a complex medium that can combine sand, mud, rocks, plants and animals. Also the bottom topography can strongly vary in the case of mobile sediments, with wave-generated ripples. Finally, flow in the bottom boundary layer may be turbulent, which requires a turbulence closure of the flow equations.

The wave bottom boundary layer connects the region of potential flow where the oscillatory wave-induced velocity is given by eq. (2.26) to the sea bed where the velocity is zero. This boundary layer is very thin, typically 10 cm or less. This is much less than the boundary layer of the mean current. As a result, when a current is present, the wave boundary layer also affects the friction for the current.

We will consider here the case of a linear monochromatic waves. The velocity above the boundary layer is given by eq. (2.26),

$$u_+(x,t) = \frac{\sigma a}{\sinh(kD)} \cos(kx - \omega t + \Theta_0), \tag{14.1}$$

Because the wave propagates at the phase velocity C, the horizontal advection of any quantity X by the velocity u is $u\partial X/\partial x$, which can be neglected compared to $\partial X/\partial t$ because the first term is u/C smaller than the second, and u/C is typically less than 0.2. Let us define $u_\delta(x,z,t) = \langle u(x,z,t)\rangle - u_+(x,t)$, in which the brackets $\langle . \rangle$ represent a Reynolds average, over the realizations of the turbulent flow.

The conservation of the horizontal momentum component reads

$$\frac{\partial \widetilde{u}}{\partial t} = -\frac{1}{\rho_w}\frac{\partial p}{\partial x} - \frac{\partial u_+}{\partial t} + G \tag{14.2}$$

with G the divergence of the vertical momentum fluxes due to viscosity or turbulence,

$$G = \nu \frac{\partial^2 \widetilde{u}}{\partial z^2} + \frac{\partial \langle u'w' \rangle}{\partial z}. \tag{14.3}$$

Because the thickness of the boundary layer δ is much less than the wavelength, the pressure gradient in the boundary layer equals the pressure gradient outside the boundary layer, which is balanced by the acceleration,

$$-\frac{1}{\rho_w}\frac{\partial p}{\partial x} = \frac{\sigma^2 a}{\sinh(kD)} \sin(kx - \sigma t) = \partial u_+/\partial t. \tag{14.4}$$

This is another way to write the Bernoulli equation (see also Mei, 1989).

Replacing (14.4) in (14.2) one obtains

$$\frac{\partial u_\delta}{\partial t} = G, \tag{14.5}$$

with the matching condition

$$u_\delta \to 0 \quad \text{pour} \quad z \gg \delta. \tag{14.6}$$

14.1 Viscous solution

The laminar situation is very interesting because it has an analytical solution that allows to show general properties of the boundary layer. In the laminar case $G = \nu\partial^2\widetilde{u}/\partial z^2$ and the solution is

$$u_\delta(x,z,t) = \frac{\sigma a}{\sinh(kD)}\mathrm{e}^{-z_+}\cos\left(kx-\sigma t-z_+\right) \tag{14.7}$$

with

$$z_+ = (z+h)/\sqrt{2\nu/\sigma} = (z+h)/\delta, \tag{14.8}$$

in which we have used the definition

$$\delta \equiv \sqrt{2\nu/\sigma} \tag{14.9}$$

that gives an order of magnitude of the boundary layer thickness.

The full velocity profile is thus $u = u^+ + u_\delta$. Because of the $-z_+$ term in the phase, the velocity u in the boundary layer has a phase ahead of the the free stream velocity u^+. This phase advance grows with z_+ but it only impacts a smaller fraction of velocity for larger values of z_+. This advance is due to the importance of the friction term in the momentum balance, which gets added to the pressure gradient and inertia. A linear friction for laminar flow is proportional to $-u$ and thus in phase with the pressure gradient $\partial p/\partial x$, whereas inertia $\rho_w\partial u/\partial t$ has a phase lags of 90°.

From the velocity solution, we obtain the dissipation rate of wave energy per unit surface, as given by the work of the viscous stress. Once divided by the wave energy E_t per unit surface, one gets the attenuation coefficient

$$\beta_\nu = \frac{\langle \rho_w \nu u \partial u/\partial z\rangle}{\rho_w g a^2/2} \tag{14.10}$$

Using the solution in eq. (14.7) we get

$$\frac{\partial u_\delta}{\partial z} = -\frac{\sigma a}{\sinh(kD)}\frac{\mathrm{e}^{-z_+}}{\sqrt{2\nu/\sigma}}\left[\cos\left(kx-\sigma t-z_+\right)-\sin\left(kx-\sigma t-z_+\right)\right] \tag{14.11}$$

in which only the first term correlates with u, and gives

$$\beta_\nu = -\frac{\sigma^3\delta}{2g\sinh^2(kD)}. \tag{14.12}$$

The spectral dissipation rate is thus of the following form

$$S_{\mathrm{bfric}}(\mathbf{k}) = -\frac{\sigma^3\delta}{2g\sinh^2(kD)}E(\mathbf{k}). \tag{14.13}$$

As we have seen in chapter 6, the dissipation of wave energy also comes with a loss of momentum at the rate $\beta_\nu E/C$ for a monochromatic wave train. So what happens to that momentum?

14.2 Streaming

Because momentum is conserved, we have to investigate where it goes, and thus look into the mean current. For this we also need the vertical velocity w_δ associated to u_δ. It is simply given by the conservation of mass $\partial w_\delta/\partial z = -\partial u_\delta/\partial x$, with the result

$$w_\delta = -\frac{2k\delta\sigma a}{\sinh(kD)}\mathrm{e}^{-z_+}\left[\cos\left(kx-\sigma t-z_+\right)+\sin\left(kx-\sigma t-z_+\right)\right]. \tag{14.14}$$

The phase shift between the boundary layer and the free stream has interesting consequences. Indeed, the conservation of mean flow momentum is

$$\frac{\partial\overline{uw}}{\partial z} = \nu\frac{\partial^2 U}{\partial z^2}. \tag{14.15}$$

Following Phillips (1977), one easily gets

$$\overline{(u+u_\delta)(w+w_\delta)} = \frac{\sigma^2a^2k\delta}{4\sinh^2(kD)}\left[\frac{2}{\delta}\mathrm{e}^{-z_+}\sin(z_+)-1+2\mathrm{e}^{-z_+}\cos z_+-\mathrm{e}^{-2z_+}\right]. \tag{14.16}$$

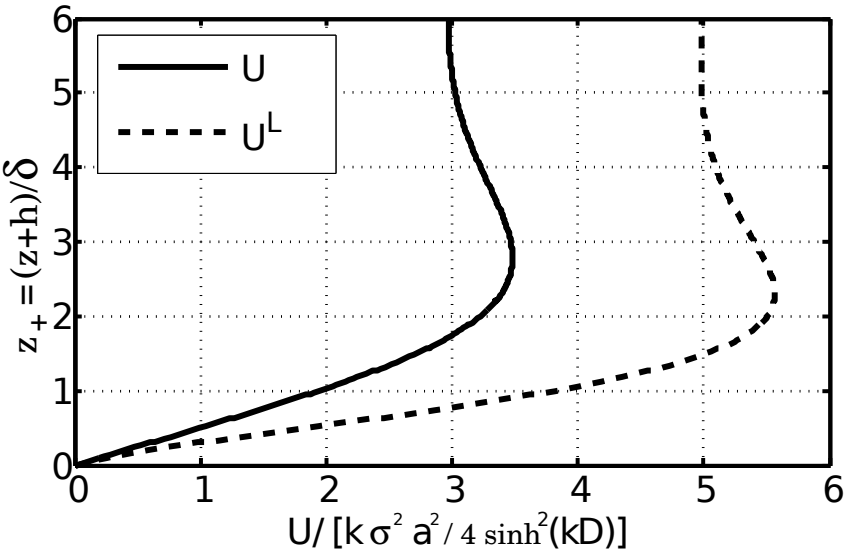

Figure 14.1: Mean current known as 'streaming', induced by a monochromatic wave train. Profiles of the Eulerian mean and Lagrangian mean velocities in the boundary layer for a constant viscosity ν, with $\delta = \sqrt{2\nu/\sigma}$.

As z_+ goes to very large values ($z + D \gg \delta$), the momentum flux goes to

$$\lim_{z_+\to\infty} \rho_w \overline{uw} = -\frac{\rho_w \sigma^2 a^2 k\delta}{4\sinh^2(kD)}. \tag{14.17}$$

This is exactly the momentum lost by the waves per unit time and unit horizontal surface. Hence, the momentum lost by the waves is taken up by the mean flow, and the waves accelerate a near boundary 'streaming current' that was first reported by de Caliginy (1878). The steady state corresponds to a situation in which the bottom friction for the mean current passes on this momentum to the sea floor (Longuet-Higgins, 2005).

The integration of eq. (14.15) gives

$$U(z) = \frac{\sigma a^2 k}{4\sinh^2(kD)} \left[3 - 2\,(z_+ + 2)\,\mathrm{e}^{-z_+}\cos z_+ - 2\,(z_+ + 2)\,\mathrm{e}^{-z_+}\sin z_+ + \mathrm{e}^{-2z_+}\right]. \tag{14.18}$$

We can also update our estimation of the Stokes drift from chapter 6, now using $\widetilde{u}$ and $\widetilde{w}$. This gives a mass transport velocity $\overline{U}^L = U + U_s$ (Longuet-Higgins, 1953),

$$\overline{U}^L = \frac{\sigma a^2 k}{4\sinh^2(kD)} \left[5 - 8\mathrm{e}^{-z_+}\cos z_+ + 3\mathrm{e}^{-2z_+}\right]. \tag{14.19}$$

We note that this mass transport velocity at the top of the boundary layer is *independent* of the value of ν, because the same viscosity appears in the wave dissipation and in the friction for the current. An infinitely small viscosity gives the same current at the top of the boundary layer as strong viscosity, only the thickness of the boundary layer changes, whereas there is no mean current for a zero viscosity. The mass transport velocity reaches 2.5 times the Stokes drift we had estimated in chapter 2. The effect of bottom friction on near-bed currents is thus considerable, which is very important for sediment transport. The velocity profiles are shown in figure 14.1. The boundary layer introduces a significant change in the velocity profile between the bottom and $z = -h + 2.5\delta$, where the velocity amplitude is maximum. The effective thickness of the boundary layer is thus close to 2.5δ. We note that the velocity profile is linear near the bed, and its vertical derivative gives the bottom stress, fond $\rho_w \nu \partial U/\partial z$,

$$\rho_w \nu \frac{\partial U}{\partial z} = \frac{\sigma^2 a^2 k\delta}{4\sinh^2(kD)} = \beta_\nu E/C. \tag{14.20}$$

The loss of wave momentum to the bottom means that it is not the full radiation stress that is relevant for the change in sea level (Longuet-Higgins, 2005; Ardhuin, 2006a).

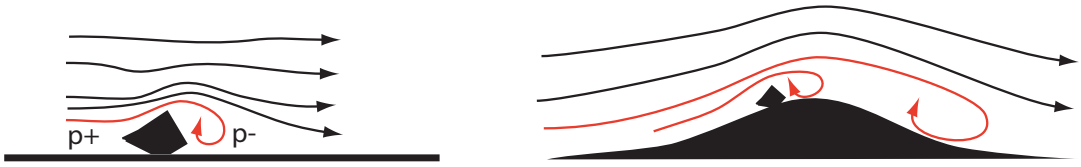

Figure 14.2: Schematic of the flow in the boundary layer, showing the importance of flow detachment from the boundary that induces a drag.
Detachments can occur at all scales, from the grain size to ripples or coral elements (e.g. Monismith et al., 2015).

In the presence of partially standing waves, the situation is a little more complicated, and the streaming is directed towards the surface elevation nodes, which is probably the cause of the formation of multiple sand bars (Heathershaw, 1982).

14.3 Turbulent boundary layer

In practice the boundary layer is often turbulent, as very well observed in the laboratory by Jensen et al. (1989). In the presence of a mean current, the wave boundary layer is thinner than the current boundary layer so that the waves define the roughness felt by the current. As a result a change in wave height can lead to a change in tidal currents and tidal range (Wolf and Prandle, 1999). As the effect of currents on the boundary layer is generally weaker, we will firs assume that the mean current is zero.

Defining a Reynolds number from the free stream wave displacement amplitude $a_{\rm orb}$ and velocity amplitude $u_{\rm orb}$,

$$\mathrm{Re} = \frac{a_{\rm orb} u_{\rm orb}}{\nu} \tag{14.21}$$

a transition to turbulence is observed for a smooth bottom for $\mathrm{Re} > 10^5$. For a wave period of 10 s and monochromatic waves, this corresponds to a $a_{\rm orb} \simeq 0.5$ m. In practice the bottom roughness, even with fin sand, is enough to make the boundary layer turbulent for much lower amplitudes (Jonsson, 1967). The bottom roughness is defined by all the elements of topography of horizontal scales less than the typical orbital amplitude $a_{b,\rm rms}$.

Following Prandtl, turbulence is characterized by eddies with a typical diameter $\kappa\delta$ at a distance δ from the bed. These eddies turn around in time that is of the order of $\kappa\delta/u_\star$. The equivalent viscosity (or eddy viscosity) K_z is defined by a linear relation between the momentum flux and the velocity shear

$$u_\star^2 = \overline{u'w'} = K_z \partial u/\partial z. \tag{14.22}$$

When the flux $u_\star^2$ is constant, Prandtl's mixing length $l = \kappa(z+D)$ gives $K_z = \kappa(z+D)u_\star$, leading to a log profile. Namely the solution of $\partial u/\partial z = u_\star/(\kappa z)$ is

$$u(z) = \frac{u_\star}{\kappa} \log\left(\frac{z}{z_0}\right). \tag{14.23}$$

The eddies mix the flow on a time scale that is the $u_\star/l$. When this is is faster than the wave period we are in the boundary layer. Thus, an order of magnitude for the boundary layer thickness is given by

$$\delta = u_\star/(\kappa f) \approx \sqrt{K_z/f}/\kappa. \tag{14.24}$$

The friction velocity $u_\star$ is often related to the velocity u_∞ outside of the boundary layer, with a friction coefficient f_w, this gives $u_\star^2 = 0.5 f_w u_\infty^2$. Experiments typically give a highly variable f_w, with values under 0.3. Typically f_w is a function of the ratio of the size of roughness elements k_s and the orbital displacement A, and of the Reynolds number Re. In particular f_w decreases when A/k_s increases, and the wave boundary layer thickness is typically less than 10 cm.

Using eq. (14.2) and (14.3) a parameterization of the turbulent term G following Prandtl mixing length ideas gives ($u'w' = K_z \partial u/\partial z$) with $K_z = \kappa(z+D)u_\star$. This leads to the following equation (Kajiura, 1968; Grant and Madsen, 1979),

$$\frac{\partial}{\partial z^\star}\left(z^\star \frac{\partial u_\delta}{\partial z^\star}\right) + \mathrm{i}\widetilde{u} = 0, \tag{14.25}$$

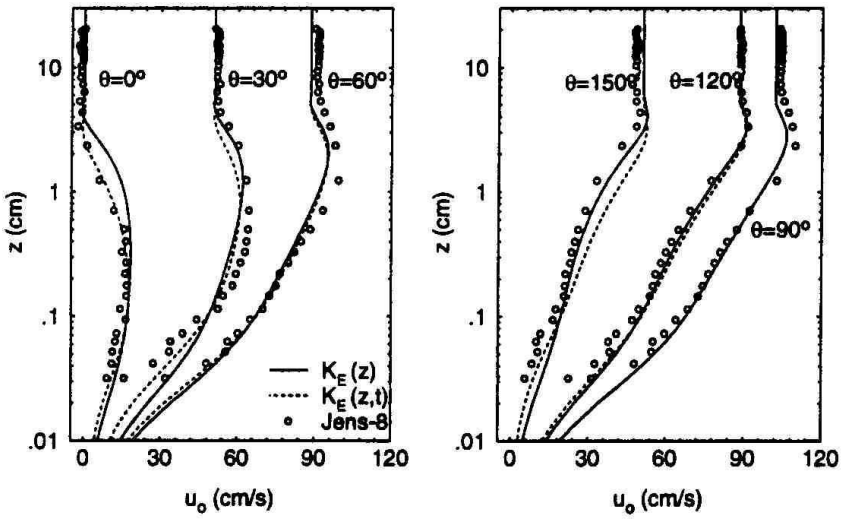

Figure 14.3: Comparison of velocity profiles in the bottom boundary layer observed by Jensen et al. (1989) at high Reynolds numbers and the model of Wiberg (1995). This case has a wave period of 10 s, with an amplitude of velocity oscillations of 1 m s^{-1}. The solid line represents model results using $K_z = \kappa u_\star (z + D)e^{-z^\star}$ that is time-independent, and the dashed line is the model with a time-varying K_z. Left panel: acceleration phase, right panel: deceleration. This figure is taken from Wiberg (1995). We note that the laboratory experiment of Jensen et al. (1989) uses a U-shaped tube and thus does not include wave propagation effects such as the bottom streaming.

with $z^\star = \omega(z + D)/(\kappa u_\star)$. This equation has an analytical solution. The boundary conditions of u_δ going to zero when $z^\star$ is large gives

$$u = \left[1 - \frac{\mathrm{ker}(2\sqrt{z^\star}) + \mathrm{ikei}(2\sqrt{z^\star})}{\mathrm{ker}(2\sqrt{z_0^\star}) + \mathrm{ikei}(2\sqrt{z^\star})}\right] u_+, \tag{14.26}$$

where $z_0^\star$ is the non-dimensional roughness $z_0^\star = \omega z_0/(\kappa u_\star)$. For a smooth sandy bottom with well sorted grain sizes, Nikuradse (1933) gives $z_0 = D_{50}/30$ where D_{50} is the median sand grain size.

The Kelvin functions ker and kei are similar to a logarithm for $z^\star \to 0$, and oscillate for $z^\star \to \infty$. The general result is that the velocity amplitude is largest near the top of the boundary layer, and has a phase that leads the free stream oscillation (figure 14.3).

Using this solution and taking the limit $z^\star \to 0$, one gets the stress at the bottom and the wave energy dissipation rate, in the form of eq. (14.33) below. But we will first have to determine the bottom roughness.

This linear eddy viscosity model was extended to more realistic profiles, including a decrease of K_z outside of the boundary layer and its variation with the wave phase. These modifications have a very limited impact on the results (Trowbridge and Madsen, 1984; Jensen et al., 1989; Wiberg, 1995; Davies and Villaret, 1999; Marin, 2004). In particular the velocity profile is well reproduced by the linear and time-independent eddy viscosity (figure 14.3). Still, there can be an impact on the shear stress at the bed, with consequences for the resuspension of sediments due, among other things, to the asymmetry between the acceleration and deceleration phases of the flow. Such flows are generally better captured by a $k - \omega$ turbulence closure (e.g. Marieu et al., 2008).

14.4 Bottom roughness

For a rocky seafloor, the bottom geometry may be complex, but at least it is fixed. In the case of sand, silt and mixtures the shape of the bottom and the associated roughness is modified by the flow and can also be strongly impacted by animals living in the sediment. Here we will discuss the case of a solid bottom, and leave the possibility of mud liquefaction for later (e.g. Jaramillo et al., 2009).

14.4.1 Sand and ripples

For a sandy seafloor, ripples are generally formed by the oscillatory wave motion, and these ripples determine the roughness and thus the dissipation rate of wave energy (Zhukovets, 1963; Nielsen, 1992). Starting from a flat seafloor, we can assume that the roughness of the flow over sand grains is the same as measured by Nikuradse (1933) in pipes in which sand was glued with lacquer. He found that $z_0 = 30k_N$ where k_N is the grain diameter. This scale k_N is also called the Nikuradse roughness. In practice the sand grains may not have all the same diameter and it is customary to use the median grain size D_{50}. Another issue is that the bottom is not flat and thus it is not just the grains that contribute to the roughness (that part is called "skin friction") but there is also a "form drag" associated to the bottom geometry. This form drag generally varies with the amplitude of the flow characterized by the orbital diameter which is the length of orbits of water particles just outside the wave bottom boundary layer.

When the effects of a mean current are neglected, the bottom boundary layer can have three flow regimes, depending on the ratio of friction and buoyancy forces acting on sediment grains. This ratio is the Shields number, and we generally consider the maximum value over a wave period defined as

$$\psi_{\max} = \frac{f'_w u^2_{\max}}{(s-1)gD}, \tag{14.27}$$

where f'_w is a skin friction factor, s is the sediment grain density normalized by the density of seawater, e.g. $s = 2.65$ for quartz, D is the grain size (Shields, 1936).

When $\psi_{\max}$ is low, the skin friction is not enough to set grains in motion and the bottom shape is fixed, possibly due to previous motions when waves were bigger. This is also called "relict roughness". This does not mean that the roughness z_0 is constant, because z_0 is a function of both the bottom shape and the flow. In that regime the dissipation of wave energy is weak.

In a turbulent regime, the dissipation source term can be put in the following quasi-linear form, as proposed by Madsen et al. (1990),

$$S_{\rm fric}(f,\theta) = \lambda(f) \times E(f,\theta) \tag{14.28}$$

$$\lambda(f) = -f_e u_{\rm b,rms} \frac{(2\pi f)^2}{2g\sinh^2(kD)}, \tag{14.29}$$

where the friction factor f_e is the ratio of the average dissipation rate and the cube of the root mean square velocity.

as the orbital velocity increases, $\psi_{\max}$ may exceed the threshold ψ_c and sand grains start moving. At that point, it only takes a few wave periods to form sand ripples. For quartz sand, the threshold ψ_c ranges from 0.03 to 0.1, depending on the grain size D (e.g. Soulsby, 1997). The formation of these ripples enhances the form drag, and thus the dissipation rate of wave energy, corresponding to larger values of f_e. Random wave experiments by Madsen et al. (1990) show that f_e is maximum for $\psi_{\rm rms} \simeq 1.2\psi_c$, where $\psi_{\rm rms}$ is estimated from the rms orbital velocity amplitude in (14.27) instead of $u_{\max}$. For example, fine sand ($D = 0.15$ mm) in 25 m depth and a wave period T_p=12 s give this maximum dissipation for $H_s = 1.5$ m. Beyond this threshold for sediment motion, any increase of the orbital velocity leads to smoother ripples and a reduction of f_e.

For very large values of $\psi_{\max}$, of the order of $10\psi_c$ (Li and Amos, 1999), a layer of sediment called the 'sheet flow' is fluidized and oscillates with the water column. At that stage, ripples are completely wiped out. Grain collisions become an important factor in the sediment layer. In that regime, the dissipation factor f_e grows with ψ. The three regimes of relict roughness, actively formed ripples and sheet flow are illustrated in figure 14.4.

Using dimensional analysis and numerical modeling, Andersen (1999) showed that ripples self-organize to reach wavelengths of the order of $\lambda = 0.63d$ where d is the orbital diameter of water parcels above the boundary layer, and their slopes are of the order of 15%. This is typically observed for random waves in depths larger than 10 m, replacing d by $2^{1/2}d_{\rm rms}$ (Traykovski et al., 1999; Ardhuin et al., 2002). In very shallow water, it seems that ripple wavelengths are shorter and scale with the grain size (Dingler, 1974; Wiberg and Harris, 1994).

The determination of wave energy dissipation reduces to a parameterization of f_e that must take into account ripples (Graber and Madsen, 1988; Tolman, 1994; Ardhuin et al., 2003b).

It is common to use a representative grain size for the sediment, usually the median diameter D_{50} for which we may estimate a critical Shields number ψ_c, above which grains start to move. It is also

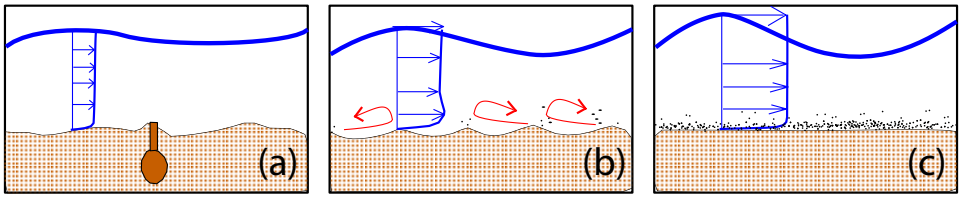

Figure 14.4: Three regimes of the boundary layer over a sandy bottom
(a) Relict roughness with possible contribution from benthic fauna. (b) ripple formation. (c) sheet flow. The ocean wave wavelength L and the depth are not to scale $L \approx 100$ m, compared to $\lambda \simeq 1$ m for the ripple wavelength. Horizontal arrows represent the velocity profile under wave crests. Curvy arrows in (b) represent the eddies in the wake of ripples.

common to use root mean square values for the wave forcing at the top of the bottom boundary layer, in particular the orbital velocity $u_{\rm b,rms}$ and displacement $a_{\rm b,rms}$,

$$u_{\rm b,rms}^2 = \int_{\mathbf{k}} \frac{8\pi^2 f^2}{\sinh^2(kD)} E(\mathbf{k})\, d\mathbf{k}, \tag{14.30}$$

$$a_{\rm b,rms}^2 = \int_{\mathbf{k}} \frac{2}{\sinh^2(kD)} E(\mathbf{k})\, d\mathbf{k}. \tag{14.31}$$

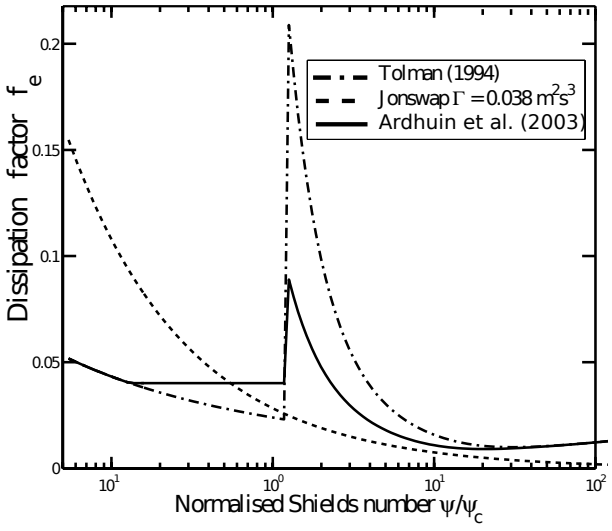

Figure 14.5: Example of dissipation factors f_e as a function of the r.m.s. Shields number $\psi_{\rm rms}$
The solid line is the parameterization by Tolman (1994), for fine sand ($D_{50} = 0.15$ mm), and a wave period $T = 14$ s. This parameterization was adjusted to SHOWEX field data by Ardhuin et al. (2003a). The dashed line correspond to an equivalent value of f_e given by the JONSWAP parameterization, which does not take into account the varying bottom roughness.

The boundary layer model gives a skin friction factor f'_w, a Shields number $\psi_{\rm rms} = f'_w u_{\rm b,rms}^2 / [g(s-1) D_{50}]$, and a total friction factor that includes skin and form drag f_w, that is the ratio of the shear stress τ and $u_{\rm b,rms}^2$,

$$\frac{z_0}{l} = \sqrt{\frac{2}{f'_w \text{ ou } f_w}} \frac{D_{50} \text{ ou } k_N}{30\kappa\, a_{\rm b,rms}}, \tag{14.32}$$

$$f'_w \text{ or } f_w = \frac{\kappa^2}{2\left[\ker^2\left(2\sqrt{z_0/l}\right) + \mathrm{kei}^2\left(2\sqrt{z_0/l}\right)\right]}\ . \tag{14.33}$$

where z_0/l is a non-dimensional roughness length, κ is von Karman's constant ($\kappa = 0,4$), ker and kei are the Kelvin functions of order 0 and 1.

When $\psi_{\rm rms}/\psi_c < 1,2$, k_N is given by the relic roughness and may weakly increase with the orbital diameter $a_{\rm b,rms}$ because larger horizontal scales contribute to the roughness when the flow amplitude increases. When $\psi_{\rm rms}/\psi_c > 1,2$ k_N can be taken as the sum of a ripple roughness k_r and a sheet flow roughness 'sheet flow' k_s. For example, Madsen et al. (1990) and Wilson (1989) give

$$k_r = a_{\rm b,rms} \times 1.5 \left(\frac{\psi_{\rm rms}}{\psi_c} \right)^{-2.5}, \tag{14.34}$$

$$k_s = 0.57 \frac{u_{\rm b,rms}^{2.8}}{\left[g\left(s-1\right) \right]^{1.4}} \frac{a_{\rm b,rms}^{-0.4}}{\left(2\pi\right)^2}. \tag{14.35}$$

Another approach to bottom friction that is completely empirical, goes back to the analysis of the JONSWAP experiment by Hasselmann et al. (1973). In his analysis K. Hasselmann had initially thought that the bottom stress would be quadratic with a relation given by Hasselmann and Collins (1968), so that the dissipation rate may be cubic in the wave amplitude, with a theoretical formulation given for a Gaussian velocity distribution. The JONSWAP data contradicted this view, and K. Hasselmann ended up fitting a dissipation rate that is proportional to the spectrum of the velocity variance at the bottom,

$$S_{\rm fric,JONSWAP}\left(f,\theta\right) = -\Gamma \left[\frac{2\pi f}{g \sinh\left(kD\right)} \right]^2 E\left(f,\theta\right). \tag{14.36}$$

The only justification for this expression was that the near-bottom tidal current $\widehat{u}$ could have played a role and would give $\Gamma = g c_b \widehat{u}$ where c_b is the drag coefficient of Hasselmann and Collins (1968). The JONSWAP data gives a mean value $\Gamma = 0{,}038$ m^{2}s^{-3}, but it ranges from 0.0019 to 0.160 m^{2}s^{-3}). It may be surprising that this parameterization have been widely used, even in the absence of mean current. It is probably because, by chance, it follows the general trend over a sandy bottom shown in figure 14.5. However, it fails in many cases (figure 14.6).

As for the effect of a mean current, what is happening in the wave bottom boundary layer will be discussed in the next section. Other wave-turbulence interaction effects are probably similar to what is happening near the surface, with a production of turbulence kinetic energy due to the Stokes drift stretching of the turbulence, at the rate $\overline{u'w'}\partial U_s/\partial z$, which can be large in the presence of tidal currents (see chapter 24).

14.4.2 Rocks

The strong dissipation over coral reefs can be attributed, to a large extent, to the very large roughness of corals. Lowe et al. (2007) and Monismith et al. (2015) gave detailed analyses of this situation.

14.5 Joint wave and current boundary layers

The joint interaction of waves, current and turbulence can be relatively complex and Madsen (1994) has extensively studied this problem, showin that the roughness for random waves could be given by a single parameter. A recent review and analysis is given by Zou (2004).

The theory distinguishes a wave boundary layer $z + H < \delta_{wc}$, in which the wave stress $\tau_w = \rho_w u_{\star w}^2$ and the current stress $\tau_c = \rho_w u_{\star c}^2$ add up to give a total stress $\tau_{wc} = \rho_w u_{\star wc}^2$, that is the net momentum flux towards the bottom, and a thicker current-only boundary layer $z + H > \delta_{wc}$ in which the stress is given by the current stress only $\tau = \rho_w \overline{u'w'} = \tau_c$.

Following the analysis by Grant and Madsen (1979), the Eulerian mean horizontal momentum equation is

$$\kappa \left| u_{\star c} \right| z \frac{\partial \widehat{u}}{\partial z} = u_{\star c}^2 \quad \text{where} \quad \left(z+H\right) > \delta_w c, \tag{14.37}$$

with the momentum mixed by eddies of sizes controled by the distance to the bottom, following Prantl. Close to the bottom, turbulence comes from shear production by both the current and the wave-induced velocities so that the current velocity is mixed by this combined turbulence

$$\kappa \left| u_{\star c} \right| z \frac{\partial \widehat{u}}{\partial z} = u_{\star wc}^2 \quad \text{where} \quad \left(z+H\right) < \delta_w c. \tag{14.38}$$

These two equations can be solved separately giving

$$\widehat{u} = \frac{u_{\star c}}{\kappa} \ln \frac{z}{z_{0c}} \quad \text{where} \quad \left(z+H\right) > \delta_w c, \tag{14.39}$$

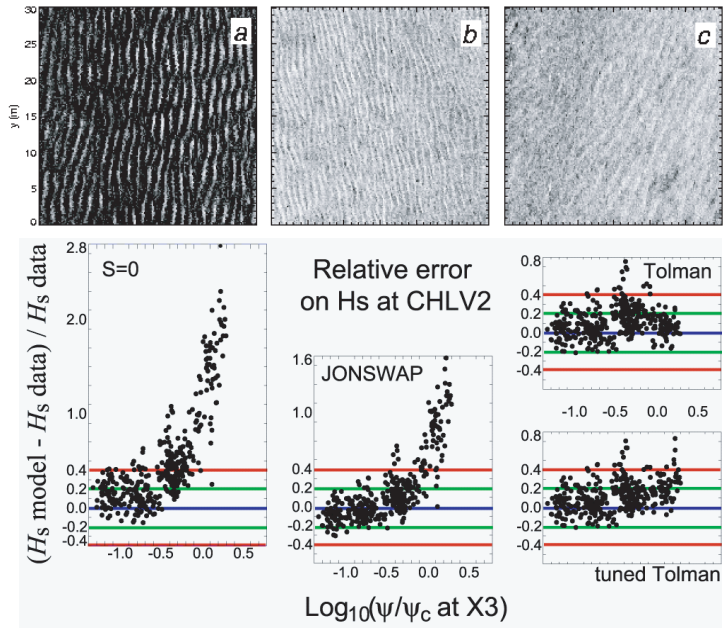

Figure 14.6: Sand ripples and wave dissipation
Top: three ripple fields observed with a sidescan sonar, each square is 30 m across (Ardhuin et al., 2002). Bottom: comparison of modeled and measured wave heights, normalized by the measured wave height at the location of the Chesapeake Lighthouse in 18 m depth, during swell-dominated conditions for the SHOWEX experiment (Ardhuin et al., 2003a). The left panel shows the case in which the model has no dissipation, and the modeled H_s can be 4 times the measured value. The center panel uses the JONSWAP parameterization, with $\Gamma = 0{,}038$ m^{2}s^{-3}, and the right panels are based on Grant and Madsen (1979) as modified by Tolman (1994) and Ardhuin et al. (2003b) to include ripple formation and relic ripple roughness. This last parameterization is now called the SHOWEX parameterization.

and,

$$\widehat{u} = \frac{u_{\star c}}{\kappa}\frac{u_{\star c}}{u_{\star wc}}\ln\frac{z}{z_{1c}} \quad \text{where} \quad (z+H) < \delta_w c. \tag{14.40}$$

Because $\widehat{u}$ is continuous, we get

$$\boxed{z_{0c} = z_{0wc}^{\epsilon}\delta_{wc}^{1-\epsilon}.} \tag{14.41}$$

where z_{0wc} is the roughness for the wave motion, and $\epsilon = u_{\star c}/u_{\star m}$ with $u_{\star m}$ the maximum combined friction velocity, defined by

$$u_{\star m}^2 = u_{\star wm}^2 + u_{\star c}^2 \tag{14.42}$$

in which $u_{\star wm} = \max(u_{\star w})$ for monochromatic waves. In the case of random waves, it is logical to use the r.m.s. value.

This theory thus gives a wave-induced modification of the bottom roughness applicable to the current. Mellor (2002) showed that a wave-averaged numerical model could use an enhancement of the turbulent kinetic energy due to wave dissipation, and the resulting mean current profile is similar to the result of a $k-l$ turbulence closure with a modified bottom roughness. Such an approach can be extended to add other sources of turbulence like wave breaking, which may influence bottom friction in the surf zone (Feddersen et al., 2003) .

The equation (14.38) for z_{0c} misses the source of momentum due to wave dissipation, which is responsible for streaming. Mathisen and Madsen (1996) have thus modified the equivalent roughness to shift the velocity profile by $-\widehat{u}(\delta_{wc})$, namely,

$$z_{0a} = z_{0c}\exp\left[\kappa\widehat{u}(\delta_{wc})/u_{\star c}\right]. \tag{14.43}$$

Near the bottom this gives $\widehat{u}(z) = u_{\star c}/\kappa\ln(z/z_0 a) = u_{\star c}/\kappa\ln(z/z_0 c) - \widehat{u}(\delta_{wc})$.

This adjustment of the roughness gives a mean velocity $\widehat{u}$ at the elevation $-H+\delta_{wc}$. In practice this may change the effective z_0 from 1 to 3 cm (Mathisen and Madsen, 1996).

Chapter 15

Numerical wave modelling at regional to beach scales

The quality of coastal wave models solution depends on many factors, and is more complex than open ocean situations. This is reviewed by Roland and Ardhuin (2014). In general, the important aspects are,

- *the forcing*: waves are generated by the wind, and are strongly influenced by currents, varying water depth, and any obstacles (small islands, sea ice, icebergs ...). All these forcing fields should thus be defined as accurately as possible, starting with the winds, but not forgetting currents that are generally stronger in coastal regions.
- *parameterizations of physical processes*: many errors, in particular in coastal areas are due to deficiencies in source term parameterizations. In particular, coastal regions can be often fetch-limited, and the growth of waves when wind is oblique relative to the shoreline can reveal errors in the magnitude of the wind generation and whitecapping source terms (Ardhuin et al., 2007). Also, bottom friction is a dominant factor when the water depth is less than half the dominant wavelength, and bottom properties can have a very large impact the dissipation rate of wave energy (Roland and Ardhuin, 2014; Monismith, 2007).
- *Numerics*: Although some numerical methods are clearly worse than others, there is no perfect method that would be fast and accurate enough to deal with the very localized depth-induced breaking. For resolutions coarser than 100 m, explicit triangle-based grids using residual distribution (RD) schemes (Csík et al., 2002; Ricchiuto et al., 2005) may well be the most efficient (Roland and Ardhuin, 2014). At higher resolution, the CFL constraint of explicit schemes makes them prohibitvely expesing, and one may have to live with low order schemes and their diffusion.

La qualité d'ensemble du résultat dépend donc des choix, explicites ou implicites, dans ces trois domaines: forçage, paramétrages, méthodes numériques, ces dernières peuvent aussi inclure les méthodes d'assimilation. Dans tous ces domaines, les choix les plus complexes ne sont pas forcément les meilleurs, et le choix optimal dépend beaucoup de la configuration à traiter (simulation à grande échelle, propagation côtière avec ou sans courants ...).

Toutefois, on n'a souvent pas trop de choix: tel code est imposé parce qu'il fait partie d'une chaîne de modélisation ou bien parce qu'il est plus facile à mettre en oeuvre, ou bien parce qu'il donne un résultat plus rapidement. Cela n'est pas forcément très grave. Par contre il convient d'avoir conscience de ce que cela implique en terme de qualité du résultat.

Par ailleurs, les paramétrages sont généralement ajustés aux forçages et aux schémas numériques. Changer le forçage, par exemple utiliser les vents fournis par le Centre Européen (CEPMMT ou ECMWF en anglais)au lieu de ceux du service météorologique des Etats-Unis (le National Center for Environmental Prediction - NCEP - , qui dépend de la National Ocean and Atmosphere Administration - NOAA) peut avoir des effets assez inattendus. En effet les vents du NCEP sont en moyenne 0.5 m/s plus forts que ceux du CEPMMT, et les statistiques des vents extrêmes sont elles aussi très différentes.

Enfin, les modèles ne sont généralement bons que pour les paramètres sur lesquels ils ont été validés et dans les intervales de valeurs où ils ont été validés. Ainsi prévoir que la hauteur significative centenaire au large de la Bretagne est de 18 m sur la base d'un modèle qui n'a été validé que jusqu'à 14 m est une réelle extrapolation. Les phénomènes extrêmes sont très mal compris et les paramétrages et les forçages dans ces cas peuvent très bien se révéler insuffisants. Toutes ces questions sont l'objet de ce chapitre.

15.1 Forcing fields

15.1.1 Winds, currents and water levels

Là où le scientifique ira généralement chercher ce qu'il y a de mieux, l'ingénieur doit souvent faire avec ce qu'il a. Pour le vent, les meilleures analyses et prévisions à l'échelle globale sont actuellement fournies par le CEPMMT, disponible depuis début 2008 à une résolution de 0.25 degré par pas de 3h. Il peut tout de même être prudent de vérifier la qualité d'autres sources, par exemple en consultant les statistiques compilées dans le cadre de la vérification des modèles par le JCOMM, disponible sur le site internet http://www.jcomm-services.org/Wave-Forecast-Verification-Project.html, voir par exemple Bidlot (2008).

En effet, sur certaines régions les analyses et prévisions d'autres centres météorologiques peuvent s'avérer meilleures, comme c'est le cas pour le U.K. Met Office et le NCEP en océan Indien, et pour Météo-France dans certaines régions de la mer du Nord (figure **??**).

Du coup, les séries temporelles issues des modèles atmosphériques opérationnels ne sont pas homogènes, et le rejeu d'évènements passés fait plus souvent appel à des ré-analyses: les modèles actuels sont utilisés pour reproduire le passé... la seule source d'inhomogénéité est alors le champ d'observations, assimilé lors de la ré-analyse. La question de l'homogénéité temporelle de la qualité du forçage est déterminante pour étudier les évolution climatiques. De nombreux efforts on été fait pour améliorer cette homogénéité. Dans le cas de la réanalyse ERA40 du CEPMMT, on peut citer Caires and Sterl (1979) qui ont développé une méthode de correction de ERA40 à partir d'observations.

15.2 Numerics

La première approche pose quelques problèmes de principe quand on veut utiliser des schémas numériques pas trop diffusifs. Un des principaux défauts est que les schémas numériques qui ne sont pas d'ordre 1 (et donc pas trop diffusifs) sont soit non-linéaires (ce qui rend la résolution itérative quasi-impossible) soit produisent des oscillations, et donc, potentiellement des valeurs négatives. C'est le théorème de Godunov. Dans le modèle SWAN ces valeurs négatives sont redistribuées suivant les directions afin de garder un énergie positive partout. Malheureusement cette procédure introduit une diffusion dans l'espace des directions, ce qui limite l'intérêt du schéma d'ordre 2 (figure 15.1). Par ailleurs, la résolution de l'ensemble du système d'un bloc alors que les vitesses d'advection sont très diverses dans les différentes dimensions, peut produire des erreurs numériques importantes, et la convergence vers la solution exacte peut être très lente.

Pour la deuxième approche, le problème est l'erreur liée à la séparation des modes. Elle tend vers zéro quand le pas de temps tend vers zéro, mais en pratique elle est finie, et d'autant plus importante que le terme source est une fonction non-linéaire variant rapidement en fonction du spectre ou des dimensions d'espace.

Afin de ne pas utiliser des pas de temps trop petits, l'ensemble des méthodes utilise en général des limiteurs: le changement du spectre lors de l'intégration est artificiellement limité. Ces limiteurs peuvent avoir un effet très important sur la solution numérique (Tolman, 2002b). Dans le code SWAN, comme l'ensemble de l'équation est résolue en même temps le limiteur peut avoir pour effet de limiter la réfraction lorsque le nombre de Courant devient trop élevé, c'est en particulier le cas pour des vagues sur de forts gradients de courant, il faut donc y prendre garde.

Enfin, en pratique l'intégration du spectre est généralement limitée à une fréquence diagnostique f_d au delà de laquelle on suppose que le spectre décroît de façon régulière, comme f^{-5} par exemple. Cette astuce évite d'avoir à trop réduire le pas de temps pour résoudre les temps d'évolution très rapides des vagues les plus courtes. Malheureusement, la forme du spectre n'est pas aussi simple, et il vaut mieux de pas prendre f_d trop bas. Dans le modèle WAM du centre Européen, f_d est fixé à 2.5 fois la fréquence moyenne $f_{m,0,-1}$ de la partie du spectre ou le terme de génération S_{in} est positif. Ce facteur 2.5 est trop faible si on s'intéresse aux propriétés telles que la pente moyenne de la surface.

15.3 Parameterizations of physical processes

15.3.1 Bottom friction

15.4 Validation

La qualité des résultats en zone côtière est beaucoup plus difficile à obtenir et à interpréter. Outre les incertitudes sur les spectres au large, il faut rajouter des effets liées au courants, souvent plus forts près des côtes, le frottement sur le fond, etc. Pour des côtes assez découpées, les résultats à la côte sont très sensible aux directions au large (directions moyennes et étalement angulaire) du fait des effets d'abri et de forte réfraction. Ainsi sur la figure 15.3, on peut constater que la tempête du 5 mai 2004 (H_s = 5.3 m à Iroise) est bien atténuée aux Blancs Sablons (H_s = 1.2 m), et complètement absente à Bertheaume (H_s = 0.4 m). Cet effet est normal car il s'agit d'une tempête de nord-ouest. Au contraire, le 25 avril, les vagues d'ouest sont très peu atténuées à

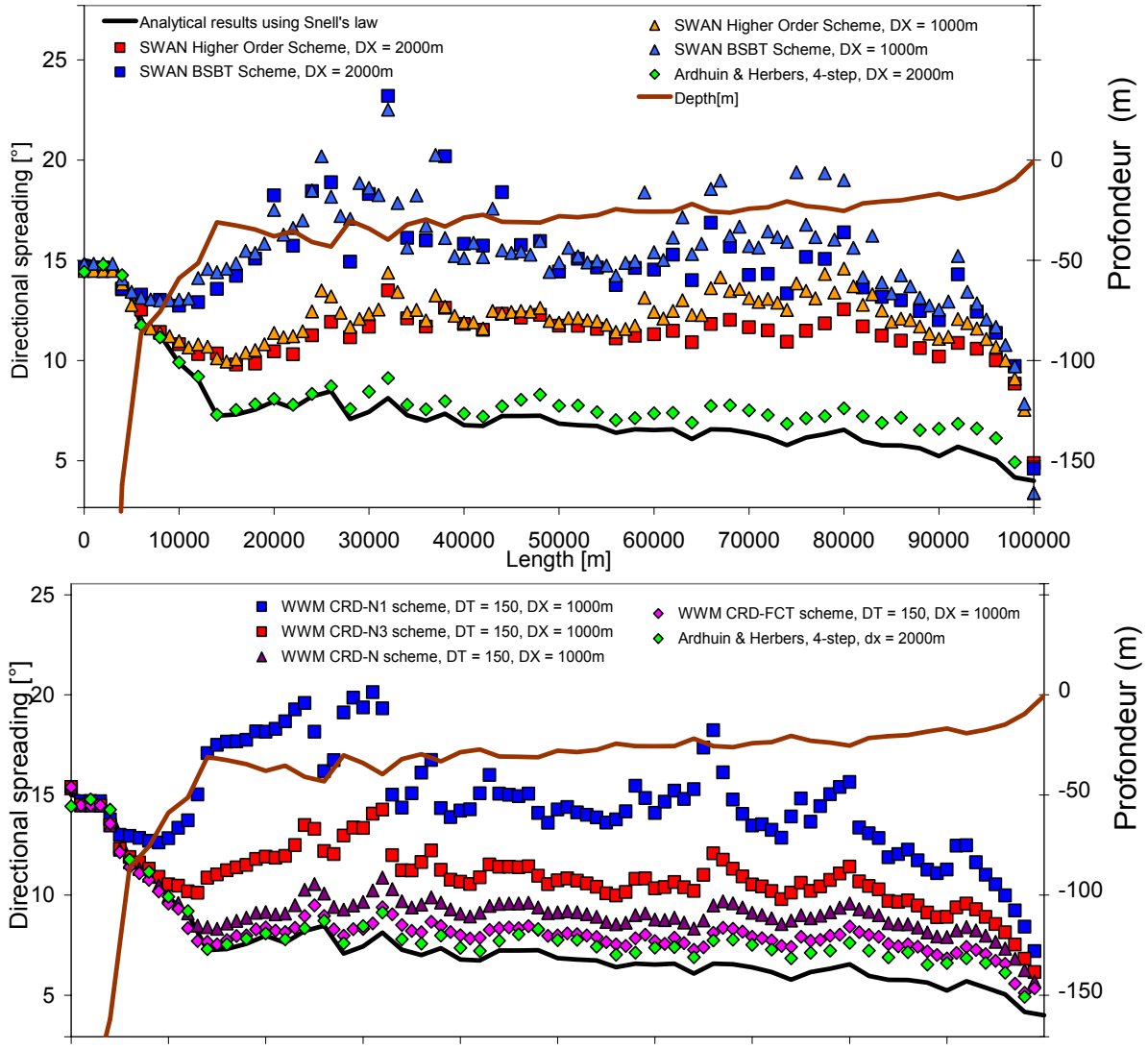

Figure 15.1: Mise en évidence de la diffusion numérique sur l'étalement directionnel d'une houle de période 15 s de largeur angulaire 15° au large se propageant sur un plateau continental bosselé dont la topographie est indiquée par la courbe marron (échelle à droite). Trois modèles sont testés, le tracé de rayon partiel de Ardhuin et coll. (2003) avec des rayons intégrés sur un total de 600 s, le code SWAN avec les schémas d'ordre 1 et d'ordre supérieur, et le code WWM de Roland (2008) avec un maillage non-structuré et différents schémas d'advection. Les schémas N1 et N2 sont implicite tandis que les schémas N et FCT sont explicites avec différents ordres (Abgrall 2006). Ces schémas ont aussi été implémentés dans le code WAVEWATCH III. Figures tirées de Roland (2008).

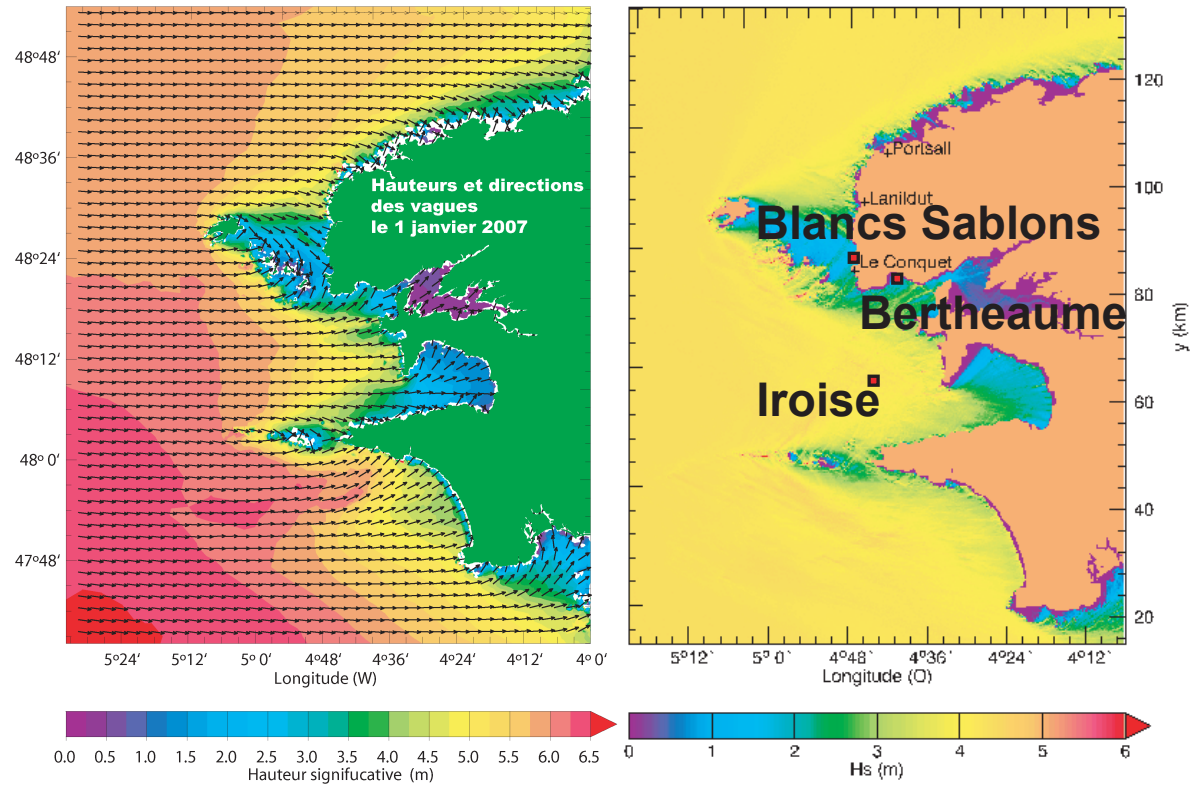

Figure 15.2: Exemples de carte de hauteur des vagues en mer d'Iroise, calculée avec la version non-structurée du code WAVEWATCH III (schéma CRD-N de Csik), et, pour un autre jour, avec un modèle de propagation linéaire (refraction-diffraction). On retrouve les mêmes structures. On remarque que les conditions aux limites au large sont supposées homogènes dans le modèle de réfraction-diffraction.

Bertheaume, et beaucoup plus faibles aux Blancs Sablons. Différents modèles numériques peuvent donner des résultats sensiblement différents. Tout d'abord on peut remarque qu'un calcul de propagation seule (modèle de réfraction-diffraction), sans prise en compte de la génération locale par le vent, est déjà assez précis. Ensuite, il est probable que l'effet de des courants, négligés dans ce calcul soit assez important.

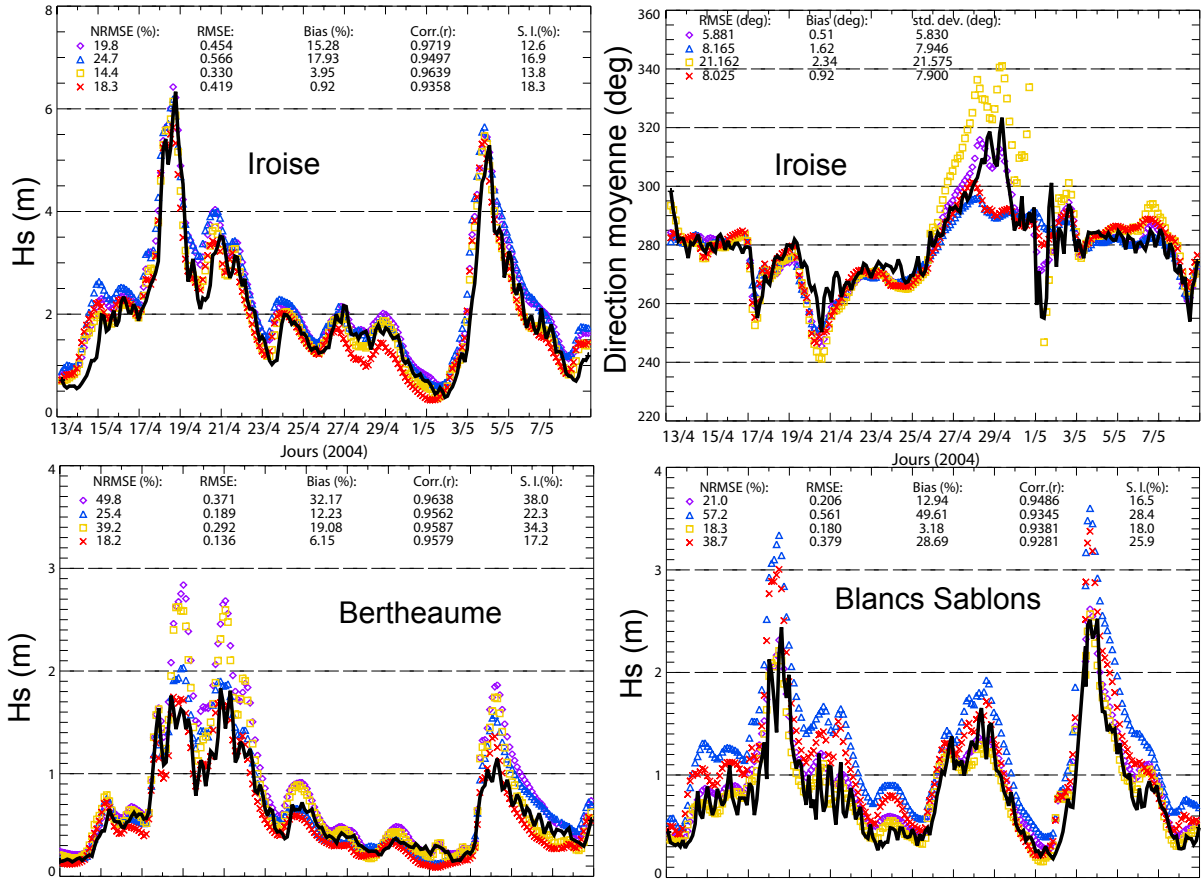

Figure 15.3: Evaluation de modèles de propagation en mer d'Iroise
En haut, résultats pour la bouée Iroise en termes de hauteur (Hs), et direction moyenne. En violet le calcul est fait avec la version non-structurée du code WAVEWATCH III utilisant le paramétrage décrit ici, en bleu par tracé de rayons forcés par le spectre calculé en un point au large d'Ouessant avec le même paramétrage, en orange avec WAVEWATCH III non-structuré et le paramétrage de Bidlot et coll. (2005) et en rouge par tracé de rayons à partir d'un spectre calculé avec le paramétrage de Bidlot et coll. (2005). On constate un assez bon accord général. En bas, comparaisons entre observations aux bouées Bertheaume et Blancs Sablons (voir figure 15.2).

Chapter 16

Waves and nearshore circulation: water levels and currents

La surcote (ou décote quand elle est négative) est définie comme la variation du niveau moyen de la mer qui n'est pas associée à la marée astronomique. Une définition exacte nécessite de définir la durée de cette moyenne. En pratique on considère toutes les variations qui ne sont pas associées aux vagues, avec une moyenne sur au moins 30 secondes. Les vagues contribuent beaucoup aux variations du niveau de la mer, en particulier pour un littoral en pente forte. Même pour les faibles pentes de la topographie du golfe du Mexique, il a été estimé que les vagues ont contribué environ 1 m aux 8 m de surcote qui ont conduit à l'inondation de la Nouvelle Orléans en 2005, lors du passage de l'ouragan Katrina (Resio and Westerink, 2008). Sur les côtes françaises métropolitaines, les plus fortes surcotes mesurées, environ 4 m, ont été enregistrées sur l'île de Bannec, dans l'archipel de Molène, avec une falaise exposée à la houle de l'Atlantique (Ardhuin and Magne, 2010). Cette surcote à Bannec est due à plus de 80% à l'effet des vagues, comme nous allons le voir. Ce n'est donc pas un phénomène anodin, si bien qu'il est possible que l'évolution des risques de submersion marine dans les années à venir soit beaucoup plus sensible à une modification de la forme et probabilité des tempêtes extrêmes, qu'à la lente et inexorable montée du niveau de la mer associée au réchauffement global.

16.1 Mean flow equations

Nous avons vu au chapitre **??** que, par rapport à une situation sans vagues, la présence de l'agitation induit un terme supplémentaire dans les équations intégrées de conservation de la quantité de mouvement (7.33) et (7.35): la divergence de $S^{\rm rad}$, tenseur des contraintes de radiation. En définissant la profondeur moyenne $D=\overline{\zeta}+h$ et le flux de masse total (dû aux vagues et au courant moyen) comme $\mathbf{M}=\rho\widehat{\mathbf{u}}D+\mathbf{M}$, la vitesse moyenne du transport de masse est $\mathbf{U}=\mathbf{M}/\left(\rho D\right)=\widehat{\mathbf{u}}+\mathbf{M}^{w}/\left(\rho D\right)$.

Ici nous allons négliger la force de Coriolis, et nous placer d'abord en situation stationnaire pour ré-écrire (7.33) sous la forme

$$\boxed{\frac{\partial}{\partial x}\left(U_xM_x+S_{xx}^{\rm rad}\right)+\frac{\partial}{\partial y}\left(U_xM_y+S_{yx}^{\rm rad}\right)=-\rho gD\frac{\partial\overline{\zeta}}{\partial x}+\tau_{x,{\rm s}}+\tau_{x,{\rm f}}} \tag{16.1}$$

$$\boxed{\frac{\partial}{\partial x}\left(U_yM_x+S_{xy}^{\rm rad}\right)+\frac{\partial}{\partial y}\left(U_yM_y+S_{yy}^{\rm rad}\right)=-\rho gD\frac{\partial\overline{\zeta}}{\partial y}+\tau_{y,{\rm s}}+\tau_{y,{\rm f}},} \tag{16.2}$$

où $(\tau_{x,{\rm s}},\tau_{y,{\rm s}})$ et $(\tau_{y,{\rm f}},\tau_{y,{\rm f}})$ sont les tensions en surface et au fond respectivement. La divergence du flux de quantité de mouvement est donc équilibrée par la pression hydrostatique, le vent et la friction au fond. ï

16.2 Mean sea level: set-down and set-up

Soit une plage et un champ de vagues uniforme dans la direction (Oy), toutes les dérivées par rapport à y deviennent nulles. En particulier, la conservation de la masse (7.35) devient

$$\frac{\partial M_x}{\partial x}=0, \tag{16.3}$$

donc M_x est constant, et pour une plage imperméable, $M_x=0$. Au passage, on note que le courant moyen doit équilibrer le flux de masse dû aux vagues qui est concentré près de la surface. Le courant doit donc s'inverser en profondeur: c'est le courant de retour ('undertow' en anglais).

La conservation de la quantité de mouvement dans la direction x donne

$$\frac{\partial}{\partial x}S_{xx}^{\text{rad}} = -\rho g D \partial \frac{\overline{\zeta}}{\partial x} + \tau_{a,x} + \tau_{b,x} \tag{16.4}$$

Prenons des vagues d'incidence normale $\theta = 0$ et supposons que $\tau_{a,x} = \tau_{b,x} = 0$, alors on obtient la pente moyenne de la surface

$$\frac{\partial \overline{\zeta}}{\partial x} = -\frac{1}{\rho g D}\frac{\partial}{\partial x}\left[\frac{C_g E}{C}\left(2 - \frac{\sinh 2kD}{\sinh 2kD + 2kD}\right)\right] \tag{16.5}$$

Sans résoudre cette équation différentielle, on remarque que lorsque les vagues ne déferlent pas, $C_g E$ est conservé et C diminue vers la plage donc S_{xx}^{rad} augmente vers la plage si la profondeur D diminue régulièrement et $\partial\overline{\zeta}/\partial x$ est négatif: le niveau moyen s'abaisse vers la plage ('set-down').

En supposant $\overline{\zeta} << h$, on peut remplacer D par h et on trouve (en exercice... un truc: comme la fréquence est conservée, en différenciant $\omega^2 = gk\tanh kD$ on a une relation entre $\partial k/\partial x$ et $\partial D/\partial x$):

$$\overline{\zeta} = -\frac{a^2 k}{2\sinh(2kD)} \tag{16.6}$$

où a est l'amplitude locale des vagues. On peut montrer que cette relation est indépendante de la direction des vagues au large, en appliquant la loi de Snel.

Juste au point de déferlement, de profondeur h_d, on peut supposer que $kD << 1$ et $H_v = 2a = \gamma h_d$ et donc

$$\overline{\zeta} = -\frac{\gamma}{16}H_v. \tag{16.7}$$

En reprenant les valeurs de la figure **??** pour une houle de période $T = 12s$, et d'incidence $\theta = 20°$, la hauteur maximale avant déferlement était $2,3$ m, ce qui donne, avec $\gamma = 0,4$ une décote de 6 cm.

Dans la zone de déferlement, le flux d'énergie n'est plus conservé et la hauteur des vagues est limitée par la profondeur, en gros $2a = H_v = \gamma D$ et donc

$$E = \rho g \gamma^2 D^2/8. \tag{16.8}$$

On peut aussi faire l'approximation de l'eau peu profonde $kD << 1$ et donc $C_g = (gD)^{1/2}$ ce qui donne

$$S_{xx}^{\text{rad}} = \frac{3}{16}\rho g \gamma^2 \left(h + \overline{\zeta}\right)^2 \tag{16.9}$$

qui équilibre le gradient de pression hydrostatique

$$\frac{3}{16}\gamma^2 2\left(h + \overline{\zeta}\right)\frac{\partial}{\partial x}\left(h + \overline{\zeta}\right) = -\left(h + \overline{\zeta}\right)\frac{\partial \overline{\zeta}}{\partial x} \tag{16.10}$$

qui se simplifie en

$$\frac{\partial \overline{\zeta}}{\partial x} = -B\frac{\partial h}{\partial x} \tag{16.11}$$

avec

$$B = \left[1 + \frac{1}{3\gamma^2/8}\right]^{-1} \tag{16.12}$$

et s'intègre en

$$\overline{\zeta} = -Bh + A_0. \tag{16.13}$$

La constante A_0 est donnée par la condition au point de déferlement, de profondeur h_d, et

$$\overline{\zeta} = -B\left(h_d - h\right) + \overline{\zeta}_d. \tag{16.14}$$

$(h_d - h)$ étant positif dans la zone de déferlement, on a une surélévation du niveau moyen, une surcote de vague (wave set-up), qui est maximale à la côte. En réutilisant les valeurs numériques ci-dessus (houle incidente de hauteur 2 m), on a pour $h = 0$, à la côte, $\overline{\zeta} = 26$ cm.

16.2.1 Application pratique

En pratique, on constate que le frottement sur le fond est très important pour la surcote lorsque la profondeur devient faible ($D < 2$ m). Or le frottement sur le fond est assez mal connu et semble augmenter avec du déferlement des vagues (Feddersen et al., 2003), ce qui est cohérent avec la connaissance de la couche limite de fond. Les paramétrages actuels du frottement sur le fond sont capable de produire un bon accord entre surcotes mesurées et observées pour $D > 1$ m, mais pas pour les très petits fonds (figure 16.1). Par ailleurs, comme les erreurs sont probablement associées à un paramétrage imprécis du frottement au fond, il est illusoire de vouloir améliorer les résultats avec des modèles théoriques plus complexes que (16.1), par exemple fondés sur les équations de Boussinesq.

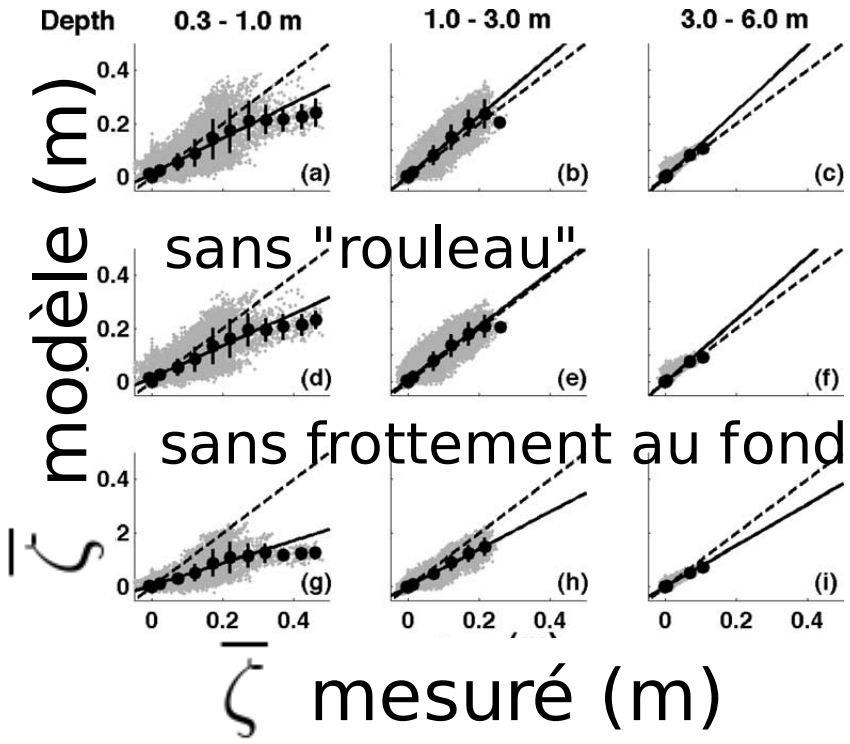

Figure 16.1: Surcotes induites par les vagues sur la plage: mesures et modèles
Les observations de niveau moyen pendant plusieurs moins ont été analysées et comparées à trois approximation de l'équation (16.1). Le "rouleau de déferlement" ajouté dans le modèle consiste à prendre en compte la quantité de mouvement piégée dans le paquet d'écume porté par les vagues, il a tendance a décaler vers la plage le transfert de quantité de mouvement et donc contribue à une augmentation du niveau d'eau. Toutefois, l'effet du rouleau est négligeable par rapport à l'effet attendu du frottement au fond. Ici le frottement a été paramétré via une viscosité turbulente qui dépend de la hauteur des vagues. Ce frottement est proche des valeurs données par (16.21) avec un coefficient $0.018 < C_f < 0.028$ qui est plus fort que ce qui est généralement utilisé pour le courant le long de la côte, et qui pourrait être associé à l'orientation des faciès sédimentaire, avec des crêtes de rides face à la côte. Tiré de Apotsos et al. (2007), droits réservés à l'American Geophysical Union.

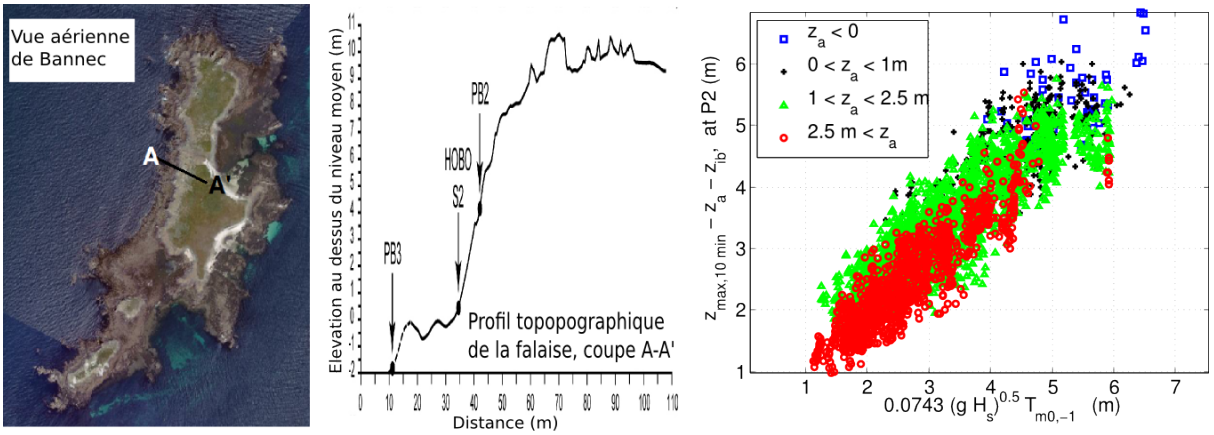

Figure 16.2: Niveau maximal de l'eau observé à Bannec pour chaque intervalle de 10 minutes entre octobre 2008 et mars 2009, en fonction de l'indice de hauteur de Hunt par 20m de fond au large, calculé avec un modèle numérique. Les observations sont des mesures de pression converties en hauteur d'eau, après correction de l'effet -réel - de baromètre inverse et de la marée astronomique. Les mesures sont classées en fonction de la hauteur de la marée astronomique. Le modèle numérique est une version du non-structurée du code WAVEWATCH III, forcé par le vent du CEPMMT et des conditions aux limites au large issues des modèles WAVEWATCH III utilisés dans le cadre des projets Prévimer et IOWAGA (Ardhuin and Magne, 2010).

Ainsi, on est souvent amené à utiliser des paramétrages empiriques de la surcotes, qui peuvent s'avérer plus précis qu'une résolution déterministe de l'équation (16.1). De nombreux auteurs ont proposé de relier la surcote (niveau moyen) et le niveau maximal (qui prend en compte le jet de rive) à un nombre réduit de paramètres. Ainsi Hunt (1959) a considéré un paramètre du type

$$H_H = T_{m0,-1}\sqrt{gH_s} \tag{16.15}$$

pour le dimensionnement des digues avec H_s la hauteur des vagues au large du point de déferlement. Les observations montrent que les niveaux moyen et maximal atteint par l'eau sont fonction de l'indice de hauteur de Hunt H_H. Ils sont aussi fonction de la géométrie du profil des profondeurs, dans la direction perpendiculaire à la côte. Pour un profil donné, on peut trouver une très bonne correspondance entre H_H et les niveaux mesurés, comme le montre la figure 16.2 pour le niveau maximal mesuré sur l'île de Bannec.

Toutefois, on n'a pas toujours le loisir de disposer de mesures pour déterminer une relation empirique entre H_H et d'autres paramètres, et les niveaux d'eau. On peut alors essayer d'appliquer des formules empiriques génériques, du type de celles données par Stockdon et al. (2006), et déterminées à partir d'observations. Pour le niveau moyen, ils donnent,

$$\overline{\zeta} \simeq 0.14\beta_f H_H \tag{16.16}$$

où β_f est la pente de la plage au niveau de la ligne d'eau. Cette formule est indicative, et elle n'explique que la moitié de la variance du signal dans les données collectées par ces auteurs. Cette proportion augmente toutefois à près de 70% si l'on considère des conditions fortement dissipatives. Ainsi pour $\xi_0 < 0.3$, la relation

$$\overline{\zeta} \simeq 0.0064H_H \tag{16.17}$$

apparait plus fiable.

Cette surcote s'ajoute à la marée, aux surcotes de tempêtes et à l'effet de baromètre inverse, et peut être très importante pour l'érosion côtière, ou les inondations, comme à Venise où les grosses vagues correspondent aux vents du Sud et tous ces effets s'additionnent. Son effet au large est par contre très faible car le gradient de pression lié à la pente de la surface exerce une force considérable quand il est intégré sur de grandes profondeurs (Ardhuin et coll. 2004).

Par ailleurs, pour l'étude du risque de submersion, ce n'est pas forcément le niveau moyen qui est le plus pertinent car les ondes longues forcées par les vagues et le jet de rive sur la côte peuvent faire monter de l'eau bien au dessus du niveau moyen. Les ingénieurs s'intéressent alors plutôt à la quantité d'eau susceptible de franchir une dune ou un ouvrage. Il faut alors prendre en compte la végétation et bien d'autres facteurs. On peut à ce sujet consulter Pullen et al. (2007).

16.3 The longshore current

Près de la plage les vagues ne sont jamais tout à fait uniformes le long de la plage, et des différences de hauteurs de vagues suivant (Oy) créent un gradient de surcote le long de la plage, et donc une circulation le long de la plage qui explique le transport de sable derrière les ouvrages de protection (formation de tombolos...). Mais ce n'est pas la seule source de circulation le long de la plage. Nous avons, pour le moment seulement, utilisé l'équation (16.1) pour la composante x de la quantité de mouvement. Lorsque les vagues sont uniformes dans la direction (Oy) mais ont un angle d'incidence θ, l'équation (16.2) pour la composante y donne

$$\frac{\partial S_{xy}^{\text{rad}}}{\partial x} = \tau_{y,\text{s}} + \tau_{y,\text{f}} \tag{16.18}$$

et

$$S_{xy}^{\text{rad}} = E\frac{C_g}{C}\sin\theta\cos\theta. \tag{16.19}$$

Or $\sin\theta/C$ est conservé par la loi de Snel, et le d'énergie flux vers la plage $= EC_g/\cos\theta$ est conservé... en dehors de la zone de déferlement seulement. Il ne se passe donc rien de plus à cause des vagues hors de la zone de déferlement (on a déjà mis en évidence la décote) car S_{xy}^{rad} y est constant. Par contre, dans la zone de déferlement, S_{xy}^{rad} diminue si $\sin\theta > 0$ et augmente si $\sin\theta < 0$ vers la plage et donc la divergence de S^{rad} induit une force qui pousse l'eau le long de la plage. Puisque nous sommes dans un cas stationnaire et en négligeant la tension de vent $\tau_{y,\text{s}}$, seule la tension au fond peut maintenir l'équilibre, et comme elle est en général dans le sens opposé au courant moyen V, le courant moyen est vers les $y > 0$ si $\sin\theta > 0$.

En prenant une loi de friction quadratique instantanée

$$\mathbf{T}(t) = -C_f\left|(\mathbf{U}+\mathbf{u})\right|(\mathbf{U}+\mathbf{u}) \tag{16.20}$$

on montre facilement (Longuet-Higgins, 1970) que pour $|V| << \overline{|u|}$ et de faibles valeurs de θ, la tension devient

$$\tau_{y,\text{f}} = -\overline{\rho C_f\left|u\right|(V+v)} \tag{16.21}$$

où V est le courant moyen suivant (Oy) et (u,v) est la vitesse orbitale des vagues au fond.

$$u = \frac{gD}{2C}\cos(kx-\omega t) \tag{16.22}$$

$$\overline{|u|} = \frac{gD}{\pi C} \tag{16.23}$$

$$\tau_{y,\text{f}} = -\rho C_f\frac{gD}{\pi C}V \tag{16.24}$$

et donc V, le courant moyen le long de la plage est donné par

$$V = -\frac{\pi C}{\rho C_f g D}\frac{\partial\left(EC_g\cos\theta\right)}{\partial x}\frac{\sin\theta_0}{C_0}. \tag{16.25}$$

Ce courant, la dérive littorale, peut être très intense, de l'ordre de 1 m s^{-1}, et son orientation moyenne dépend du climat de vagues, déterminant le transport de sable le long de la plage.

L'équation (16.25) est le modèle de Thornton et Guza (1986), qui utilise la dissipation d'énergie des vagues $\partial EC_g\cos\theta/\partial x$ prévue par le modèle de transformation des vagues de Thornton et Guza (1983), décrit au paragraphe 5.3.3. En revenant à nos vagues $H = 2$ m, $T = 12$ s et $\theta_0 = 20°$, on trouve une valeur maximale du courant de 2 m s^{-1} (voir figure **??**). Ce modèle comporte assez de paramètres 'libres', en particulier C_f (on peut 'bidouiller') pour permettre de reproduire les observations. Les premières vérifications furent faites lors de l'expérience NSTS (Nearshore Sediment Transport Study) en 1980, sur les plages de Torrey Pines (au Nord de San Diego) et Leadbetter (Santa Barbara). L'hypothèse $|V| << \overline{|u|}$ faite par Longuet-Higgins (1970) pour la forme paramétrée de la tension est assez dérisoire car pour une couche limite oscillante (chapitre 3), la tension n'est plus tout à fait quadratique, cela n'a pas empêché Thornton et Guza (1986) d'étudier en détail l'effet de la non-linéarité de τ_y en fonction de V quand $V \sim \overline{|u|}$. On peut améliorer le modèle en ajoutant une diffusion horizontale de quantité de mouvement qui réduira un peu les gradients de V. Beaucoup de travail a aussi été fait récemment sur le mécanisme exact du transfert de quantité de mouvement entre les vagues et le courant. Il a en particulier été mis en évidence que le "rouleau" (le paquet d'écume transporté par une vague qui déferle) pouvait jouer le rôle d'un "tampon à quantité de mouvement" et retarder le transfert entre les vagues et le courant.

16.4 Cross-shore flows

On vient de voir que, dans ce chapitre, la description de la couche limite au fond était assez sommaire, or pour des applications au transport sédimentaire, la représentation des vitesses au voisinage du fond est très importante. Les oscillations des vagues au dessus de la couche limite et la non-linéarité des contraintes peuvent forcer un

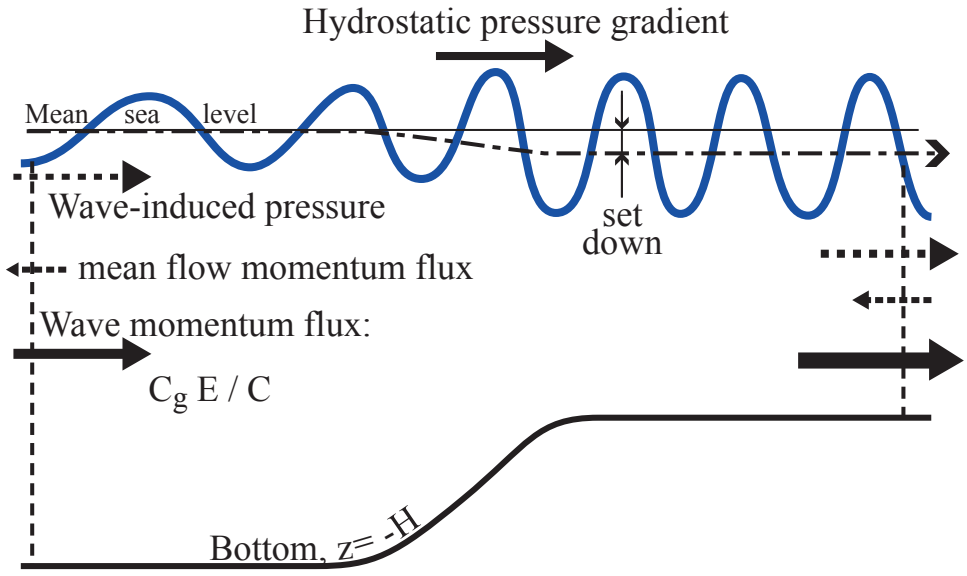

Figure 16.3: Equilibre des forces pour des vagues au-dessus d'une marche lissée.
En absence de réflexion et de dissipation des vagues, la force correspondant à la divergence du flux de quantité de mouvement induit par les vagues se combine avec la pression moyenne. Cette combinaison est généralement équilibrée par un gradient de pression hydrostatique associé au gradient de la surface libre. L'accélération de la circulation moyenne (petites flèches en pointillés) n'apporte, en général, qu'une faible correction à cet équilibre. En absence de réflexion, il n'y a pas de force exercée par le fond, outre la pression hydrostatique.

courant au dessus de la couche limite (Longuet-Higgins, 1953) dans le sens de propagation des vagues (voir aussi Mei, 1989, chapitre 9).

Enfin, car il faut bien s'arrêter quelque part, le courant de dérive littoral forcé par les contraintes de radiation est lui-même instable à cause de son fort cisaillement, et ses méandres génèrent des oscillations (Oltman-Shay et coll., 1989) de très grande période ('far infragravity waves'). Le courant de dérive est aussi fortement couplé à la bathymétrie et est la source des courants de baïne ('rip currents'), dirigés vers le large.

16.5 Séparation des qdm vagues et circulation

Les deux termes en S^J dans (7.53) représentent la pression moyenne induite par les vagues, qui agit logiquement sur la circulation moyenne, et une force supplémentaire $\rho_w S^J \partial D/\partial x_\alpha$ qui compense la force $-\rho_w S^J \partial D/\partial x_\alpha$ qui agit sur la PQDM dans (7.51). Il apparaît donc que ce deuxième terme est une interaction entre la circulation moyenne et l'état de mer, il n'y a donc pas d'interaction avec le fond. Ainsi, en absence de frottement sur le fond et sans réflexion des vagues, la force moyenne exercée par le fond sur la colonne d'eau n'est que la pression hydrostatique. Il n'y a pas de force moyenne sur l'écoulement susceptible de modifier la quantité de mouvement des vagues ou de l'écoulement moyen et la réfraction et le levage ne sont pas la conséquence d'une force exercée par le fond, mais seulement le résultat d'une modification du guide d'onde, sans échange d'énergie ou de quantité de mouvement avec l'extérieur (Longuet-Higgins 1967, 1977, Ardhuin 2006).

On peut alors reconsidérer le problème de vagues unidirectionnelles se propageant au-dessus d'une marche d'escalier lissée avec un changement de profondeur de h_1 à h_2 (Whitham 1962, section 2). Nous sommes d'accord avec Whitham sur la conservation du flux de masse $E_1/C_1 + \rho_w(h_1 + \overline{\zeta}_1)U_1 = E_2/C_2 + \rho_w(h_2 + \overline{\zeta}_2)U_2$, mais par contre, pour la quantité de mouvement notre conclusion est différente de la sienne. La différence de flux de PQDM $C_{g2}/C_2E_2 - C_{g1}/C_1E_1$ ne correspond pas à la force exercée sur la marche, comme suggéré par Whitham, mais à une force exercée sur l'écoulement moyen, à laquelle s'ajoute le gradient de la pression induite par les vagues S^J pour donner les tensions de radiation classiques. Dans le cas d'une dissipation négligeable, l'ensemble des deux termes est compensé par une variation de la surface libre: la décôte (figure 16.3). Cette conclusion est vérifiée expérimentalement par les mesures de la dépression du niveau moyen faites par Saville (1961, voir aussi l'analyse faite par Longuet-Higgins and Stewart 1963, et Phillips 1977) et Bowen et coll. (1968).

En outre il doit aussi y a avoir une divergence de la circulation moyenne pour compenser la divergence de la dérive de Stokes. Toutefois, la divergence correspondante de quantité de mouvement moyen (flèches courtes en pointillés sur la figure 16.3) est généralement beaucoup plus faible que les tensions de radiation à cause du rapport des flux de quantité de mouvement et de masse des vagues, qui est égal à la vitesse de groupe C_g, qui est

en générale plus grande que le rapport correspondant pour la circulation moyenne, égal au courant en moyenne verticale. Dans des cas ou la réflexion des vagues est importante, la force de diffusion $\mathbf{T}^{\mathrm{bscat}}$ doit aussi être prise en compte car elle est exercée par le fond, et annule la partie correspondante de la divergence du flux de quantité de mouvement.

On doit donc clairement séparer trois forces horizontales induites par les vagues,

- la force de pression induite par les vagues, qui est typiquement équilibrée par la décôte dans les cas conservatifs. Après intégration sur la vertical elle est égale à $-\rho_w \partial S^J / \partial x_\alpha$.
- la force de vortex qui est due au cisaillement de courant et à l'advection croisée de quantité de mouvement des vagues par le courant et du courant par les vagues
- la force exercée sur la circulation moyenne correspondant à la divergence de la pseudo-quantité de mouvement (PQDM), corrigée des effets de réflexion des vagues par la topographie, et de la perte de PQDM par frottement sur le fond.

En effet, la fraction de la PQDM perdue par frottement sur le fond n'est que temporairement communiquée à la circulation, en contribuant au courant de ruissellement (Russel and Osorio 1958), avant de finir dans le fond via un cisaillement moyen (Longuet-Higgins 2005).

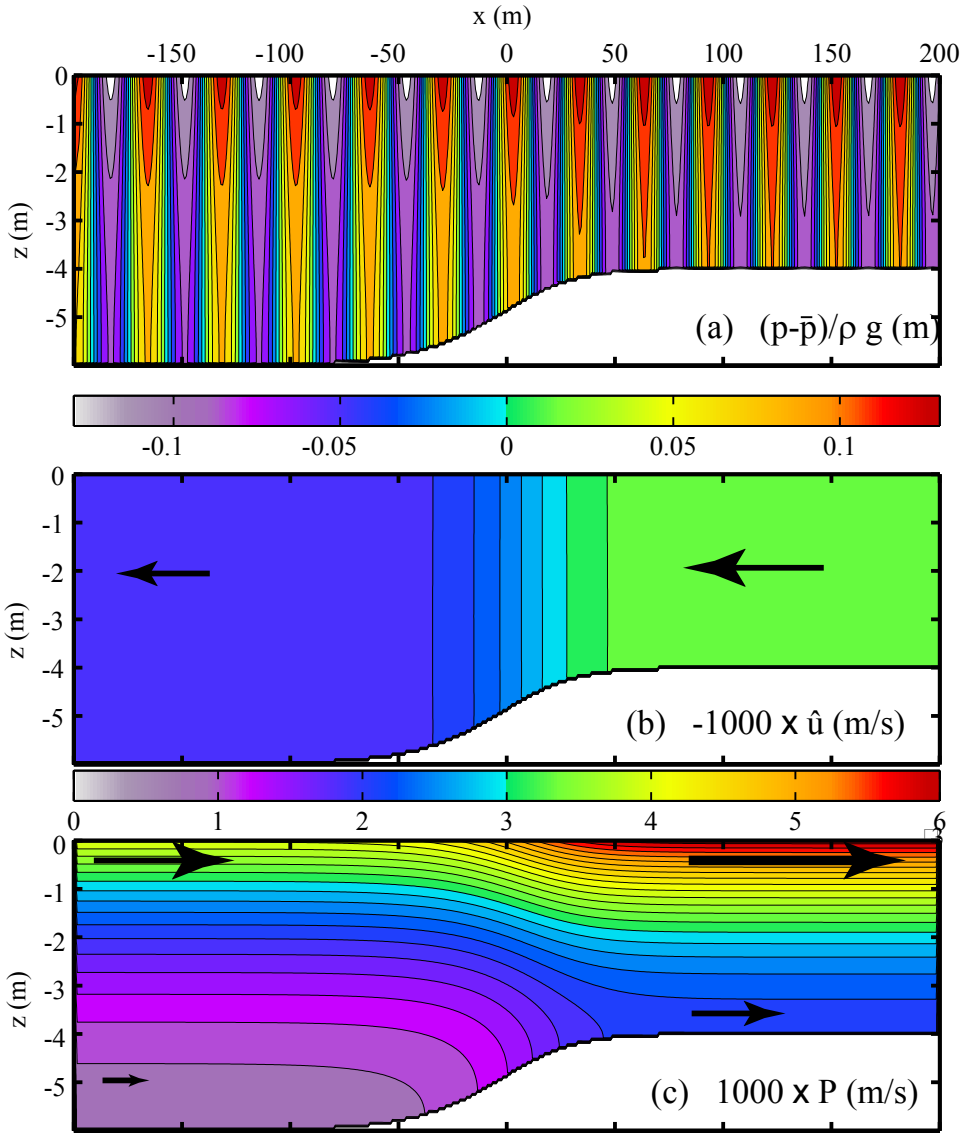

Figure 16.4: Ecoulements Eulériens et Lagrangiens moyens pour des vagues au-dessus d'une marche lissée.
(a) Perturbation de pression $(p-\overline{p})/(\rho_w g)$ à $t=0$ telle que calculée avec le modèle NTUA-nl2 (Belibassakis and Athanassoulis 2002), qui résoud l'équation de Laplace à l'ordre 2 en pente des vagues, pour des vagues d'amplitude $a=0.12$ m. (b) Courant Eulérien moyen $-\widehat{u}$, et (c) composante horizontale de la pseudo-quantité de mouvement P_1, qui est ici égale à la dérive de Stokes. Les flèches indiquent le sens de l'écoulement.

Part III

Advanced wave topics

Chapter 17

Practical estimation of the wave spectrum

17.1 General properties of discrete Fourier transforms

Time series can be obtained from many sensors, for example; a pressure gauge in the water at at fixed depth, a range measurement from a laser or radar mounted on a platform or ship, velocity from underwater acoustic or electromagnetic systems, accelerometer in a floating system. In the laboratory, it is common to measure the surface elevation with resistive or capacitive wave gauges. These times series thus consist of a signal $\zeta(t)$ or $p(t)$ sampled at a fixed frequency f_s, typically $1 < f_s < 4$ Hz in the ocean, and $f_s \sim 10\ Hz$ or more in the laboratory because laboratory waves are generally shorter and also, in the laboratory, the internal memory and power consumption of instruments is less of an issue: either they are directly cabled to the acquisition system or the experiment is short enough. In general, it is very important that f_s is at least 4 times the expected frequency of the signal of interest. Indeed, representing a cosine wave with only 4 points is already relatively coarse. As a result, some of the signal (the very short waves) is not resolved.

Assuming we have such a series of discrete surface elevations $\zeta(n)$ with $1 \leq n \leq M$. The duration of the recording is $(M-1)/f_s$. All data processing softwares have a discrete Fourier transformation routine that will provide

$$Z_m = \frac{1}{M}\sum_{n=1}^{M} \zeta(n) \mathrm{e}^{-2\mathrm{i}\pi(m-1)(n-1)/M}. \tag{17.1}$$

17.1.1 Spectral resolution

For any frequency index m, the complex amplitude Z_m is large when the signal ζ actually contains fluctuations at the frequency $f_m = (m-1)/Mf_s$. The complex amplitudes contain both amplitude and phase information, i.e. $Z_m = |Z_m| \exp[\mathrm{i}\arg(Z_m)]$. The Fourier transform is simply a projection of the signal onto the elementary functions that are the complex exponentials, or if you prefer sines and cosines, with all frequencies $f_m = (m-1)/Mf_s$ where m goes from 1 to M. We note that the difference between frequencies f_m and f_{m+1} is the spectral resolution $df = f_s/M$. Because f_s is the inverse of the sampling interval dt, we have $df = 1/(Mdt)$, which is the inverse of the record duration. Namely, the frequency resolution is the same as the lowest frequency which is at $m = 2$, and it such that the lowest period equals the record duration. We recall that $m = 1$ is the average value of the signal.

17.1.2 Nyquist frequency

The decomposition of a discretized real signal with M pieces of information into M frequencies cannot produce M amplitudes and frequencies that are independent, that would be $2M$ pieces of information. Indeed, the frequencies from $M/2f_s$ to Mf_s do contain the same information as those between 0 $(M/2-1)f_s$, as shown in figure 17.1.

With the definition given by eq. (17.1), $Z_m = \overline{Z_{M+2-m}}$, where the overbar is the complex conjugate, so that the modululs of the spectrum is symmetric around $m = M/2$. This index $M/2$ corresponds to the Nyquist frequency $f_N = f_s/2 = M/2df$. The symmetry means that above f_N there is no new information. In other words, f_N is the highest resolvable frequency. At this Nyquist frequency, a cosine wave is only represented by 2 points over a period.

The continuous spectral density $F(f)$ is obtained in the limit when the spectral resolution df goes to zero of the following expression

$$F(f = (m-1)f_s/M) = 2\frac{Z_m\overline{Z_m}}{df}. \tag{17.2}$$

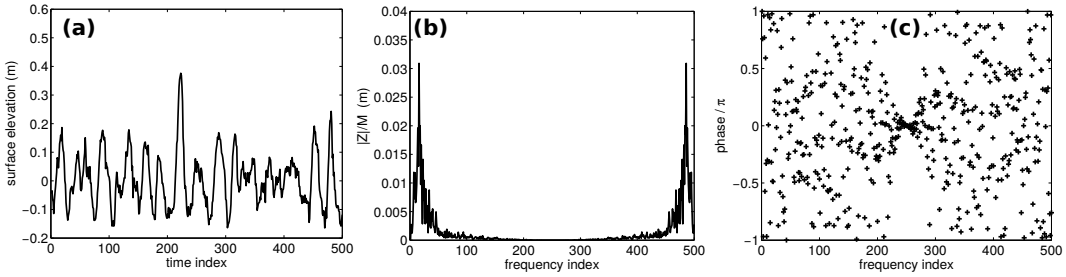

Figure 17.1: (a) Example of surface elevation time series sampled at 12 Hz, (b) Discrete Fourier transform amplitude of the signal, and (c) phase of the same signal.

The factor 2 comes from the combination of positive and negative frequencies in the interval $[0, f_N]$. That definition is called the single-sided spectrum. For some applications it may be convenient to keep the double-sided spectrum defined without this factor 2, for f in the range $[0, 2f_N]$ or $[-f_N, f_N]$. In practice, the zero spectral resolution is never achieved because it corresponds to an infinitely long record. We are therefore stuck to finite spectral resolutions df, and thus a discrete spectrum sampled at df, corresponding to record lengths over which the random variable of interest is stationary.

17.1.3 Co-spectra

In the same manner, we can define the co-spectrum of two variables a and b having Fourier transforms dA and dB,

$$C_{ab}(f = (m-1)f_s/M) = \frac{A_m \overline{B_m}}{df} = P(f) + \mathrm{i}Q(f), \tag{17.3}$$

where P and Q are real numbers, the co-spectra in phase and quadrature.

We note that the product of two Fourier transforms is the Fourier transform of the convolution of the two functions. When these two functions are the same, this result tells us that the spectrum is the Fourier transform of the auto-correlation function. When the two functions are different, the co-spectrum is the Fourier transform of the correlation function.

17.2 Spectra from time series

17.2.1 Filtering of data and aliasing

For any physical parameter, the complex amplitude at a frequency above f_N is the complex conjugate of the amplitude at a frequency below f_N: $dZ(N-m) = \overline{dZ(m)}$. In other words, the energy above the Nyquist frequency is aliased at lower frequencies. This is one reason for applying a low-pass filter before the Fourier transform, in order to remove signals that would otherwise be aliased.

For example, a signal of period 1 s sampled every second ($f_s = 1$ Hz) is constant. In general, any signal with frequency higher than the Nyquist frequency gives an apparent frequency in the range $[0 f_s/2]$, with a value obtained by folding back the spectrum along a vertical line at $f = f_s/2$ or $f = 0$ as many times as necessary, until falling in $[0 f_s/2]$. Figure 17.2 shows an example of a true signal (in red) with frequency at 9/10 which gives 1-9/10=1/10 by aliasing. This is well known problem in oceanography in the case of the measurement of tides from satellite data. In the case of ocean waves, it is really necessary to measure waves with a sampling frequency that is at least 4 times the dominant frequency.

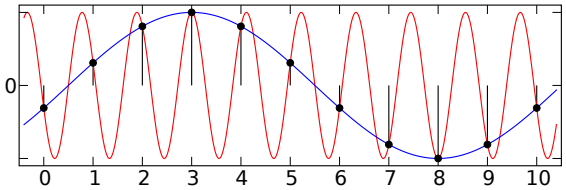

Figure 17.2: Example of spectral aliasing. A signal with period 10/9, in red, and sampled with a step of 1 (black dots) gives an apparent period of 10, in blue. (Moxfyre, wikimedia commons).

In practice the high frequency roll-off of the wave spectrum, for $f > f_p$ in particular for pressure or velocity at the ocean floor, means that this filtering may not be necessary for the surface elevation. Figure 17.3 shows

an example of the filtering of a surface elevation record and its impact on the spectrum. Here the filter helps in reducing the noise associated with the measurement method. The worst filter is clearly the boxcar (or moving

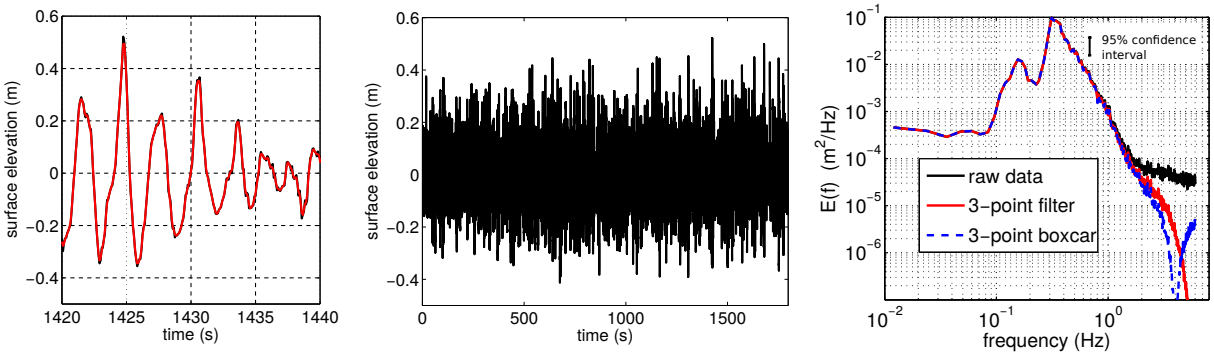

Figure 17.3: Example of surface elevation measured by stereo-video from the Katsiveli platform, in 20 m depth, on Octoebr 4, 2011 (see Leckler et al., 2015; Aubourg et al., 2017, for further detailed analysis of this dataset). (a) small piece of record around $t = 1430$ s with (red) and without (black) a 3-point smoothing filter (b) full record (1780 s) (c) spectra of the time series with different filters applied.

average) filter with equal weight given to the consecutive data values, this does not suppress very well the shortest components.

17.2.2 Windows, Gibbs phenomenon and averaging

The discrete Fourier transform of signal ζ that takes values at locations 1 to N, corresponds to the Fourier transform of a periodic signal that would repeat itself with $\zeta(n+mM) = \zeta(n)$ for any n and m. If $\zeta(1) \neq \zeta(M)$, then this periodic function has a sharp jump from $\zeta(M)$ to $\zeta(M+1)$. Such a jump can give a strong spectral signature, all across the spectrum.

This artifact is known as the Gibbs phenomenon, and it is generally removed by multiplying the signal $\zeta(n)$ by a window function $W(n)$ which goes to zero or very small values for both $n = 1$ and $n = N$. Obviously the spectrum of $\zeta(n) \times W(n)$ is different from the spectrum of $\zeta(n)$. The first obvious effect is that the variance of the signal has been reduced by a factor that is the average of W^2. That is easily corrected for.

Let use the time series shown in figure 17.3.b. We first start with a small piece of only 1000 points. The original time series, in black in figure 17.4.a gives the power spectral density in figure fig:anaspec:spectre1.b. If the time series is brought to zero at both ends (in red) by multiplying with a Hann window, then the spectrum is transformed. However, because of the random fluctuations of the spectral estimates this is not obvious. Indeed waves are random and the surface elevation is nearly-Gaussian. As a result, the complex Fourier amplitudes are also random and Gaussian, so that they modulus, which is the power spectral density follows a χ^2 distribution with two degrees of freedom.

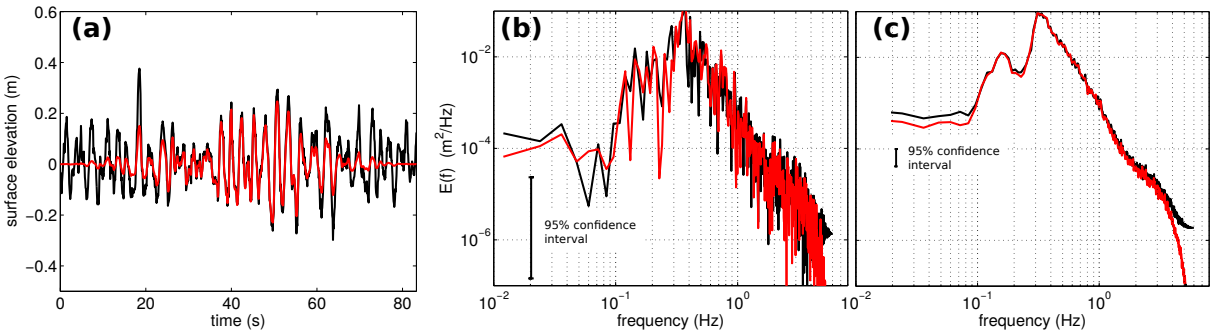

Figure 17.4: (a) First 1000 points of time series shown in (17.3).b, with (red) and without (black) multiplication by a Hann window. (b) Resulting spectra (c) Average spectra using Welch's method with 21 independent windows and thus 42 degrees of freedom.

Using figure 17.5, we find that the expected ratio of the lower and upper bound of a 95% confidence interval is 146. This number is the ratio of $\chi^2_{2,0.975}$ and $\chi^2_{2,0.025}$, that give the probabilities that $\chi^2_n > \chi^2_{n,\alpha}$ is equal to the acceptance threshold α.

Percentage Points of Chi-Square Distribution

Value of $\chi^2_{n;\alpha}$ such that Prob$[\chi_n^2 > \chi^2_{n;\alpha}] = \alpha$

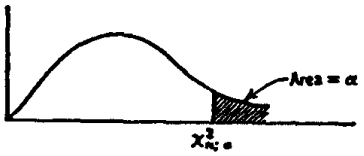

	α									
n	0.995	0.990	0.975	0.950	0.900	0.10	0.05	0.025	0.010	0.005
1	0.000039	0.00016	0.00098	0.0039	0.0158	2.71	3.84	5.02	6.63	7.88
2	0.0100	0.0201	0.0506	0.103	0.211	4.61	5.99	7.38	9.21	10.60
3	0.0717	0.115	0.216	0.352	0.584	6.25	7.81	9.35	11.34	12.84
4	0.207	0.297	0.484	0.711	1.06	7.78	9.49	11.14	13.28	14.86
5	0.412	0.554	0.831	1.15	1.61	9.24	11.07	12.83	15.09	16.75
6	0.676	0.872	1.24	1.64	2.20	10.64	12.59	14.45	16.81	18.55
7	0.989	1.24	1.69	2.17	2.83	12.02	14.07	16.01	18.48	20.28
8	1.34	1.65	2.18	2.73	3.49	13.36	15.51	17.53	20.09	21.96
9	1.73	2.09	2.70	3.33	4.17	14.68	16.92	19.02	21.67	23.59
10	2.16	2.56	3.25	3.94	4.87	15.99	18.31	20.48	23.21	25.19
11	2.60	3.05	3.82	4.57	5.58	17.28	19.68	21.92	24.73	26.76
12	3.07	3.57	4.40	5.23	6.30	18.55	21.03	23.34	26.22	28.30
13	3.57	4.11	5.01	5.89	7.04	19.81	22.36	24.74	27.69	29.82
14	4.07	4.66	5.63	6.57	7.79	21.06	23.68	26.12	29.14	31.32
15	4.60	5.23	6.26	7.26	8.55	22.31	25.00	27.49	30.58	32.80
16	5.14	5.81	6.91	7.96	9.31	23.54	26.30	28.85	32.00	34.27
17	5.70	6.41	7.56	8.67	10.08	24.77	27.59	30.19	33.41	35.72
18	6.26	7.01	8.23	9.39	10.86	25.99	28.87	31.53	34.81	37.16
19	6.84	7.63	8.91	10.12	11.65	27.20	30.14	32.85	36.19	38.58
20	7.43	8.26	9.59	10.85	12.44	28.41	31.41	34.17	37.57	40.00
21	8.03	8.90	10.28	11.59	13.24	29.62	32.67	35.48	38.93	41.40
22	8.64	9.54	10.98	12.34	14.04	30.81	33.92	36.78	40.29	42.80
23	9.26	10.20	11.69	13.09	14.85	32.01	35.17	38.08	41.64	44.18
24	9.89	10.86	12.40	13.85	15.66	33.20	36.42	39.36	42.98	45.56
25	10.52	11.52	13.12	14.61	16.47	34.38	37.65	40.65	44.31	46.93
26	11.16	12.20	13.84	15.38	17.29	35.56	38.88	41.92	45.64	48.29
27	11.81	12.88	14.57	16.15	18.11	36.74	40.11	43.19	46.96	49.64
28	12.46	13.56	15.31	16.93	18.94	37.92	41.34	44.46	48.28	50.99
29	13.12	14.26	16.05	17.71	19.77	39.09	42.56	45.72	49.59	52.34
30	13.79	14.95	16.79	18.49	20.60	40.26	43.77	46.98	50.89	53.67
40	20.71	22.16	24.43	26.51	29.05	51.81	55.76	59.34	63.69	66.77
60	35.53	37.48	40.48	43.19	46.46	74.40	79.08	83.30	88.38	91.95
120	83.85	86.92	91.58	95.70	100.62	140.23	146.57	152.21	158.95	163.65

For $n > 120$, $\chi^2_{n;\alpha} \approx n\left[1 - \frac{2}{9n} + z_\alpha\sqrt{\frac{2}{9n}}\right]^3$ where z_α is the desired percentage point for a standardized normal distribution.

Figure 17.5: Table of χ^2 distributions. This table gives the confidence intervals for the estimation of spectra with $n = 2N$ degrees of freedom, where N is the number of independent spectra used.

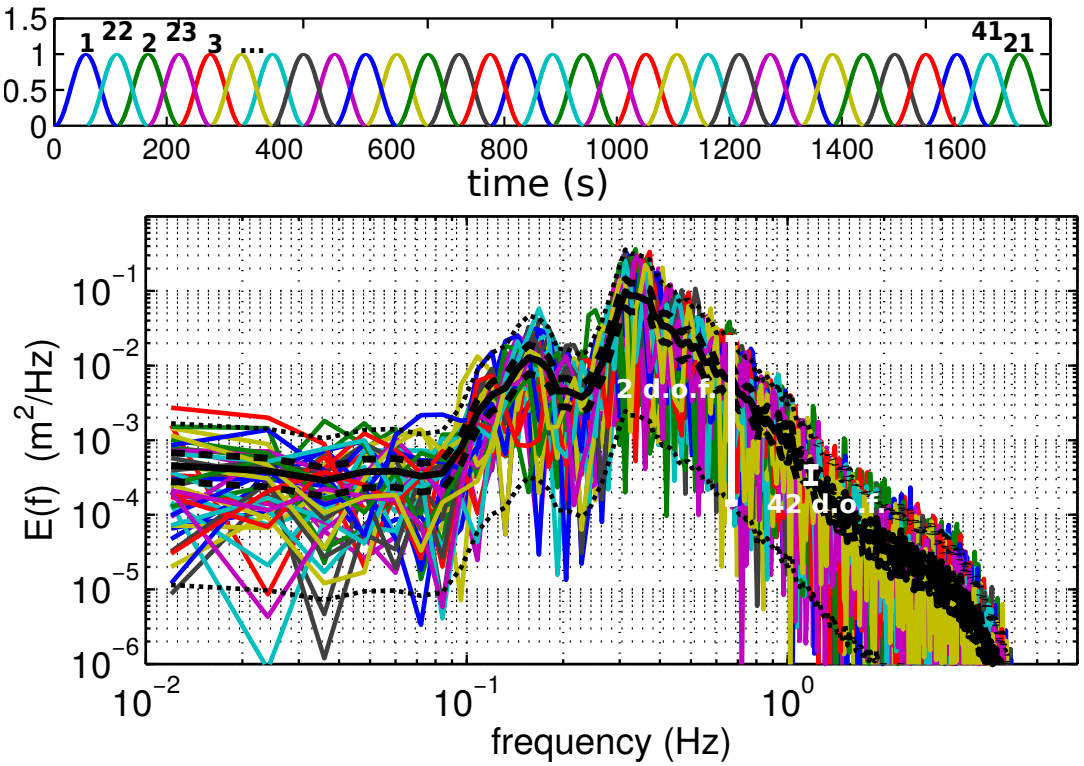

Figure 17.6: (a) Succession of the Hann windows applied to the data, with 21 independent windows and 20 overlapping windows, from number 22 to 41. The solid line is the mean spectrum and the dotted and dashed line show the expected 95% confidence intervals for 2 and 42 degrees of freedom. à 95%.

For an expected value $\widehat{E}$, the Gaussian statistics theory predicts a 95% probability that the estimate of $E(f)$ is in the range $[E_1, E_2]$ with $E_1 = 0.0506\widehat{E}$ and $E_2 = 7.38\widehat{E}$. In other words, the random fluctuations of the spectrum estimated by a single Fourier transform typically spans two orders of magnitude.

That is fairly annoying. There are two ways to reduce this uncertainty: the first, which is most easily done in the laboratory is to run more experiments, repeating the same conditions, with random wave phases, and average the results. For measurements in the field, this is the same as processing a longer time series, but it only makes sense if the conditions are stationary: same wind, same wave age, same current, etc. In practice, this stationarity constraints limits the length of records from half an hour to a few hours. As we average N spectra together, the number of degrees of freedom increases to $2N$. Here we have used 21 independent spectra, and we get an uncertainty that narrows like $1/\sqrt{N}$ for large N. For 20 spectra, the ratio E_2/E_1 is $59.34/34.43 \simeq 1.7$ at 95% confidence.

Because the Hann window practically removes part of the data, Welch (1967) has defined a method in which the windows are shifted by half their length, as shown in figure 17.6.a. The lower panel shows the 21+20 spectra estimated, and the average result.

Another method that is almost equivalent to Welch's is the smoothing of the spectrum, also known as band-averaging. Because the Fourier transform of a shorter window has a coarser resolution, both methods effectively trade off the spectrum accuracy against the spectral resolution. An extension of such methods is the use of wavelet transforms (e.g. Liu and Babanin, 2004) which aims at localizing events in both time and frequency.

Whatever the choice of method, without any prior knowledge on the signal, the product of the spectra uncertainty and the square root of the frequency uncertainty remains constant. Thus the optimal choice of df is up to the user. For wind seas, the typical relative width of the spectrum is 0.1, and for a typical peak period of 0.1 Hz, resolving the peak requires $df < 0.01$ Hz. For swells one may like to have an even narrower frequency resolution. In the example above, $df = 0.012$ Hz is enough for the relatively short wind sea found in the Black Sea.

17.2.3 Interpretations and further developments

The general idea of spectral analysis is to decompose a signal into its basic constituents. If waves were indeed linear, the Fourier components would be truly independent and the spectrum would give the energy of different wave components. In practice, there is a significant level of nonlinearity, which actually dominates the frequency spectrum $E(f)$ at frequencies above 3 to 4 times the wind sea peak (e.g. Leckler et al., 2015). As a result, the

interpretation of these high frequencies ($f > 1$ Hz in the example above) as the energy of linear waves is wrong. Several methods have been developed to try to separate linear and non-linear components, including higher order analysis (Hasselmann et al., 1963) which is illustrated in chapter 13. This question has inspired other nonlinear methods, such as the Empirical Mode Decomposition method by Huang et al. (1998).

17.3 Spectral analysis of directional buoy data

17.3.1 Case of 3-axis displacements or accelerations

We have seen in section 3.2.1 that the spectrum of x-component velocity at the ocean bottom is given from the surface elevation spectrum multiplied by a transfer function,

$$E_{Ux}(f,\theta) = \frac{\sigma^2 \cos^2\theta}{\sinh^2(kD)} E(f,\theta). \tag{17.4}$$

The same method applies to spectra of displacements, velocity and slopes at the sea surface. For a water particle at the surface, the spectra of displacement in the three directions are given by (2.31),

$$E_x(f) = \frac{1}{\tanh^2(kD)} \int_0^{2\pi} E(f,\theta) \cos^2\theta \mathrm{d}\theta \tag{17.5}$$

$$E_y(f) = \frac{1}{\tanh^2(kD)} \int_0^{2\pi} E(f,\theta) \sin^2\theta \mathrm{d}\theta \tag{17.6}$$

$$E_z(f) = \int_0^{2\pi} E(f,\theta)\, \mathrm{d}\theta. \tag{17.7}$$

We note that this last spectrum is the usual elevation spectrum $E(f)$, also called heave spectrum, with a minor modification due to the fact that it is not obtained at a fixed position (x, y) but at a positions that moves with x and y. As a result, the shape of the waves and the shape of the spectrum are modified, with a strong reduction in the contribution of nonlinear harmonics: a surface buoy signal looks much more linear than a wave staff or stereo video record.

The co-spectra of horizontal and vertical displacements are

$$C_{xz}(f) = \frac{\mathrm{i}}{\tanh(kD)} \int_0^{2\pi} E(f,\theta) \cos\theta \mathrm{d}\theta, \tag{17.8}$$

$$C_{yz}(f) = \frac{\mathrm{i}}{\tanh(kD)} \int_0^{2\pi} E(f,\theta) \sin\theta \mathrm{d}\theta. \tag{17.9}$$

$$C_{xy}(f) = \frac{1}{\tanh^2(kD)} \int_0^{2\pi} E(f,\theta) \sin\theta\cos\theta \mathrm{d}\theta. \tag{17.10}$$

These co-spectra are thus related to the mean direction and directional spread, through the directional moments introduced in section 3.2.2

$$a_1(f) = \int_0^{2\pi} E(f,\theta) \cos\theta \mathrm{d}\theta, \tag{17.11}$$

$$b_1(f) = \int_0^{2\pi} E(f,\theta) \sin\theta \mathrm{d}\theta, \tag{17.12}$$

$$a_2(f) = \int_0^{2\pi} E(f,\theta) \cos(2\theta) \mathrm{d}\theta, \tag{17.13}$$

$$b_2(f) = \int_0^{2\pi} E(f,\theta) \sin(2\theta) \mathrm{d}\theta. \tag{17.14}$$

To summarize, starting from the displacement time series $x(t)$, $y(t)$) and $z(t)$ one obtains the spectra and co-spectra $C_{xx}(f)$, $C_{yy}(f)$, $C_{zz}(f)$, $C_{xz}(f)$, $C_{yz}(f)$, $C_{xy}(f)$. Using $\cos(2\theta) = \cos^2(\theta) - \sin^2(\theta)$ and $\sin(2\theta) = 2\sin\theta\cos\theta$, they give the following directional moments, in which $\Im$ stands for the imaginary part,

$$a_1(f) = -\Im(C_{xz}(f))/\left[C_{zz}(f)\left(C_{xx}(f)+C_{yy}(f)\right)\right] \tag{17.15}$$

$$b_1(f) = -\Im(C_{xy}(f))/\left[C_{zz}(f)\left(C_{xx}(f)+C_{yy}(f)\right)\right] \tag{17.16}$$

$$a_2(f) = \left(C_{xx}(f)-C_{yy}(f)\right)/\left(C_{xx}(f)+C_{yy}(f)\right) \tag{17.17}$$

$$b_2(f) = 2C_{xy}(f)/\left(C_{xx}(f)+C_{yy}(f)\right) \tag{17.18}$$

$$\tag{17.19}$$

from which we get directional parameters, with mod the modulo operator,

$$\theta_1(f) = \text{mod}\ (270. - \text{atan2}(b1, a1) \times 180/\pi, 360) \tag{17.20}$$

$$\sigma_1(f) = \left[2\left(1 - \sqrt{a_1^2(f) + b_1^2(f)}\right)\right]^{0.5} \times 180/\pi \tag{17.21}$$

$$\theta_2(f) = \text{mod}\ (270. - 0.5\text{atan2}(b2, a2) \times 180/\pi, 360) \tag{17.22}$$

$$\sigma_2(f) = \left[0.5\left(1 - \sqrt{a_2^2(f) + b_2^2(f)}\right)\right]^{0.5} \times 180/\pi \tag{17.23}$$

These 4 parameters can be used in statistical estimators to obtain the directional spectrum $E(f, \theta)$. A commonly used estimator is the Maximum Entropy Method of Lygre and Krogstad (1986). See also the review by Benoit et al. (1997).

17.3.2 Case of other systems with 3 variables or more

in the above method, we can replace x and y by the slopes $\partial\zeta/\partial x$ and $\partial\zeta/\partial y$ as done in the pitch-and-roll buoys developed by Cartwright and Smith (1964) and still widely used. For example, most of the 3-m discuss buoys operated by the U.S. National Data Buoy Center are based on this measurement (Steele et al., 1992). Also, the horizontal velocities at any given level, (u, v). These give access to the heave spectrum $E(f)$ and the same directional moments a_1, b_1, a_2 and b_2.

In order to go beyond these first 5 parameters, one can built an array of instruments. The cloverleaf buoy of Mitsuyasu et al. (1975) was such an attempt, and arrays of pressure gages or lasers have been routinely used. Today's optical techniques (Benetazzo, 2006; Fedele et al., 2013; Laxague et al., 2015) are other ways to get to more details about the sea surface.

17.4 Some links between spectral and wave-by-wave analysis

The spectrum $E(f)$ gives the distribution of the surface elevation variance as a function of time scales. As discussed in chapter 1, one can also chop the signal in individual waves and study the statistics of their properties. A model for the sea surface elevation could be a signal of constant amplitude with a random frequency modulation. In that case, Woodward (1952)'s theorem tells us that the spectrum of the signal is the distribution of its frequencies $P_f(f - f_c)$ where f_c is the carrier frequency,

$$E(f) = \frac{a^2}{2} P_f(f - f_c). \tag{17.24}$$

Extension of that theorem by Blachman and McAlpine (1969) with an additional amplitude modulation makes it applicable to ocean waves. As shown by Elfouhaily et al. (2003) the spectrum is then given by the joint probability distribution of wave heights and periods $P(a, f)$ with $a = H/2$ and $f = 1/T$. Separating linear (naked) and full (dressed) spectra, Elfouhaily et al. (2003) showed that the peak region is dominated by linear components

$$E_{bare}(f) = \frac{1}{2} \int a^2 P(a, f) da. \tag{17.25}$$

At high frequency the nonlinear contributions dominate the spectrum which can be interpreted as fast modulations of the short components. Taking into account that effect leads to asymetries α et β (see figure 17.7), and the dressed spectrum

$$E_{\text{dressed}}(f) = E_{\text{nu}}(f) + \frac{1}{2}\left[\int \alpha^2 P(\alpha, f/2) da + \int \beta^2 P(\beta, f/2) da\right] \simeq E(f) \tag{17.26}$$

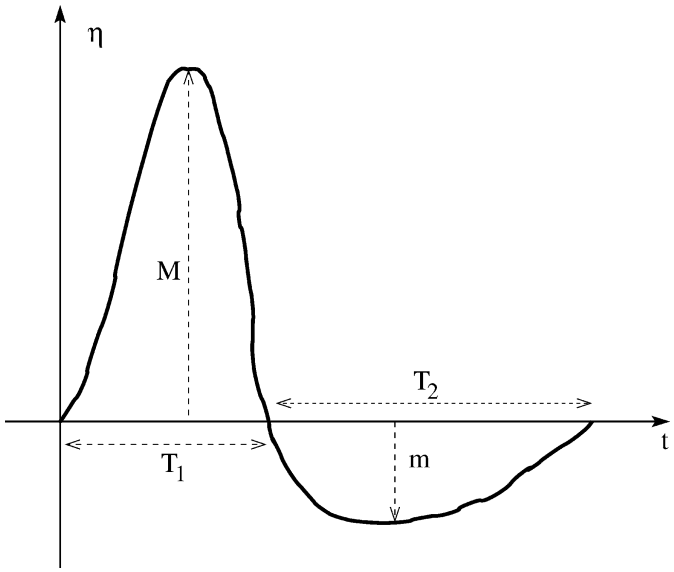

Figure 17.7: Definition of parameters M ,m, T_1 et T_2 used to estimate the amplitude $a = (M - m)/2$, period $T = T_1 + T_2$, vertical asymetry $\alpha = (M + m)/2$ and horizontal asymetry $a\pi(T_1 - T_2)/(T_1 + T_2)/2$ (from Elfouhaily et al. (2003), ©Elsevier). Here $m < 0$, because m is defined as the trough level between two up-crossing zeros that define the start and end of the wave.

Chapter 18

Nonlinear waves over a flat bottom

In this chapter we investigate the consequences of two nonlinear parameters which are the **steepness** $\varepsilon_1 = ka$, and the amplitude normalized by the water depth $\varepsilon_2 = a/D$. The linear theory of 2 was obtained in the limit of $\varepsilon_1 = 0$ and $\varepsilon_2 = 0$. After giving the full equations for nonlinear wave motion, this chapter focuses on the properties of monochromatic waves. The next chapter will consider the solution up to second order in ε_1 but extended to a random wave field.

18.1 Dimensional analysis and importance of ε_1 and ε_2

In order to simplify the equations, we will assume here that the mean water level is $\overline{\zeta} = 0$, so that the mean water depth is $D = h$.

The wave equation for irrotational waves includes non-linear terms in addition to the linear term given in chapter 2. These come from the advection in the momentum equation or u^2 and w^2 terms in the Bernoulli equation,

$$\frac{\partial \phi}{\partial t} = -\frac{1}{2}\left[|\boldsymbol{\nabla}\phi|^2 + \left(\frac{\partial \phi}{\partial z}\right)^2\right] - \frac{p}{\rho_w} - gz + C(t), \tag{18.1}$$

and the surface kinematic boundary condition,

$$w = \frac{\partial \phi}{\partial z} = \mathbf{u}\cdot\boldsymbol{\nabla}\zeta + \frac{\partial \zeta}{\partial t} = \boldsymbol{\nabla}\phi\cdot\boldsymbol{\nabla}\zeta + \frac{\partial \zeta}{\partial t} \quad \text{sur} \quad z = \zeta. \tag{18.2}$$

Taking ∂(18.1 at z=ζ)$/\partial t$ +$g\times$(18.2) in order to eliminate the linear ζ terms, gives [1]

$$\frac{\partial^2 \phi}{\partial t^2} + g\frac{\partial \phi}{\partial z} = g\boldsymbol{\nabla}\phi\cdot\boldsymbol{\nabla}\zeta - \frac{1}{2}\frac{\partial \zeta}{\partial t}\frac{\partial^2 \phi}{\partial z \partial t} - \frac{1}{2}\left(\frac{\partial}{\partial t} + \frac{\partial \zeta}{\partial t}\frac{\partial}{\partial z}\right)\left[\boldsymbol{\nabla}\phi\cdot\boldsymbol{\nabla}\phi + \left(\frac{\partial \phi}{\partial z}\right)^2\right] + C'(t), \quad \text{at} \quad z = \zeta. \tag{18.3}$$

We note that the non-linearity comes from the terms on the right hand side but also from the fact that eq. (18.3) is valid at $z = \zeta$, which is unknown. Indeed, a Taylor expansion around $z = 0$ adds many terms, for example

$$\left.\frac{\partial^2 \phi}{\partial t^2}\right|_{z=\zeta} \simeq \frac{\partial^2 \phi}{\partial t^2} + \zeta\frac{\partial^3 \phi}{\partial t^2 \partial z} + \frac{1}{2}\zeta^2\frac{\partial^4 \phi}{\partial t^2 \partial z^2} + ...\Big|_{z=0} \tag{18.4}$$

Before solving this, a question arises: should we really keep all these terms? Do they have the same importance? This is where a dimensional analysis of eq. (18.3) is necessary. This requires to define scales for time and space.

Because we are studying waves, they are naturally characterized by a wavelength $L = 2\pi/k$, a period T, and their amplitude a. Besides, the water depth $D = h + \overline{\zeta}$ comes in the bottom boundary condition. Finally, gravity g is constant and naturally links space and time scale. We can recall the Reech-Froude law for hydrodynamics: if time is multiplied by α, then space is multiplied by α^2, and velocities by α.

We can thus consider that the time scale is fixed by the spatial scale and our problem is thus only a function of the ratios of the different space scales. Since we have a, k et D, we can make two independent ratios which can be $\varepsilon_1 = ka$, $\varepsilon_2 = a/D$, or $\mu = kD$. The combination of the last two gives the Ursell (1953) number

$$Ur = \varepsilon_2/\mu^2 \tag{18.5}$$

It is common to use ε_1 and Ur. We will see below that a Froude number $\alpha = ga/C^2$, where C is the phase speed, can also have interesting properties (Kirby, 1998).

[1] Be careful that, when computing ∂(18.1)$/\partial t$ at $z = \zeta$, you should not forget that ζ is a function of time.

Let us now look at the different terms in eq. (18.3) following the analysis of Kirby (1998). We take

$$x' = k_0 x, \tag{18.6}$$
$$y' = k_0 y, \tag{18.7}$$
$$t' = k_0 C_0 t, \tag{18.8}$$
$$\zeta' = \zeta/a. \tag{18.9}$$

This gives $\phi' = \phi/\phi_0$ where $\phi_0 = C\alpha/k$ and the Froude number is

$$\alpha = ga/C^2. \tag{18.10}$$

For the vertical coordinate we choose a scale Z, giving $z' = z/Z$. Eq. (**??**) thus becomes

$$\frac{\partial^2\phi'}{\partial t'^2} + \frac{g}{Zk_0^2C_0^2}\frac{\partial\phi'}{\partial z'} = \alpha\boldsymbol{\nabla}\phi'\cdot\boldsymbol{\nabla}\zeta' - \frac{a}{Z}\frac{\partial\zeta'}{\partial t'}\frac{\partial^2\phi'}{\partial z'\partial t'} - \left(1+\frac{akC}{Z}\frac{\partial\zeta'}{\partial t'}\frac{\partial}{\partial z'}\right)\alpha\left[\boldsymbol{\nabla}\phi'\cdot\frac{\partial\boldsymbol{\nabla}\phi'}{\partial t'} + \frac{1}{k_0^2Z^2}\frac{\partial\phi'}{\partial z'}\frac{\partial^2\phi'}{\partial t'\partial z'}\right] + \frac{C'(t)}{\phi_0k_0^2C_0^2}, \quad \text{at} \quad z' = \frac{a}{Z}\zeta'. \tag{18.11}$$

If one chooses $Z = 1/k$, then $\alpha = a/Z = \varepsilon_1$ and the linear wave equation only requires $\varepsilon_1 \ll 1$. Choosing instead $Z = D$, will also require $\varepsilon_2 = a/D \ll 1$. Hence the linear wave theory requires both $\varepsilon_1 \ll 1$ and $\varepsilon_2 \ll 1$. It is easy to verify that the solution given in chapter 2 are indeed consistent with these assumptions.

18.2 Finite amplitude solutions

18.2.1 Stokes expansion for weak non-linearity

The common method, introduced by Stokes (1880) is to expand the solution to the nonlinear equations in powers of ε_1, which is most appropriate for deep water waves,

$$\phi = \phi_1 + \phi_2 + \phi_3 + ..., \tag{18.12}$$
$$\zeta = \zeta_1 + \zeta_2 + \zeta_3 + ..., \tag{18.13}$$

in which each term of index n is of order ε^n. Levi-Civita (1925) proved that this expansion was convergent for monochromatic waves. For general random waves, ϕ_1 is the solution to the linear equations (2.15), and thus ϕ_1 is a linear sum of monochromatic waves as determined in chapter 2,

$$\phi_1 = \sum_{\mathbf{k},s}\frac{\cosh(kz+kh)}{\cosh(kh)}\Phi^s_{1,\mathbf{k}}\left(\widetilde{t}\right)\mathrm{e}^{\mathrm{i}(\mathbf{k}\cdot\mathbf{x}-s\sigma t)}, \tag{18.14}$$

where σ and $\mathbf{k}$ are related by the linear dispersion relation (2.22).

Tke long term evolution of the amplitudes $\Phi^s_{1,\mathbf{k}}$ on time scales $\widetilde{t}$ is not constrained by the linear equations which give constant amplitudes, but this evolution will be part of the solution at higher orders.

When we collect all terms of second order, we have a wave equation for ϕ_2, which is forced by products of ϕ_1 and ζ_1. The full second order solution is given in chapter 19.

We also note that at third order, one obtains a modification of the phase speed. For monochromatic waves in deep water this is (Stokes, 1880)

$$C = gk\left[1+k^2a^2\right]. \tag{18.15}$$

Stokes waves are generally unstable any small perturbation will grow to produce shorter and longer components that will exchange energy with the initial wave. This is known as the instability of Benjamin and Feir (1967). Finite amplitude growth was further analyzed by Chalikov (2007).

18.2.2 Numerical methods for finite amplitude periodic waves

The analytical calculation of the amplitude of different harmonics is becomes very tedious at higher order and has only been completed up to fifth order by De (1955). Beyond fifth order, several method can provide very accurate numerical solutions (Dean, 1965; Dalrymple, 1974; Schwartz, 1974). Such methods have been used by Longuet-Higgins and Fenton (1974) to show that energy and phase speed first grow and then decrease as the wave height increases. Hence, the

Here we use the streamfunction method of Dean, as extended by Dalrymple to allow for a linear current shear such that the velocity potential still satisfies Laplace's equation. This iterative method fits the Fourier amplitudes of the velocity potential to minimise the deviations from a constant pressure along the sea surface. This easily produces the first 100 harmonics for waves that can be really steep, with orbital velocities at the crest $u_{\max}$ up

to 98% of the phase speed C, as shown in figure 18.1. We recall that periodic waves break when 100% is reached and no periodic waves can exist with orbital velocities These near-breaking waves are particularly interesting for exploring the kinematics and energetics of breaking waves, although real breaking waves can be very different due to their non-stationary shapes. Cokelet (1977)) introduced the small parameter

$$\epsilon = \left[1 - \frac{q_{\rm crest}^2 q_{\rm trough}^2}{C^4}\right]^{1/2} \tag{18.16}$$

with $q_{\rm crest}$ and $q_{\rm trough}$ the orbital velocities at the crest and trough in the frame of reference moving with the wave, so that $q_{\rm crest} = u_{\max} - C = 0$ in the case of nearly breaking wave. This parameter is clearly between 0 et 1 and allows an expansion in powers of ϵ for nearly breaking waves.

18.2.3 Kinematics of finite amplitude waves

Finite amplitude waves are characterized by flat trough and steeper crests, in particular in shallow water. The orbital velocities are even more asymetric with much larger velocities at the crest than in the troughs. At the limit when $u_{\max}/C = 1$ the surface slope is discontinuous with a 120° angle at the crest.

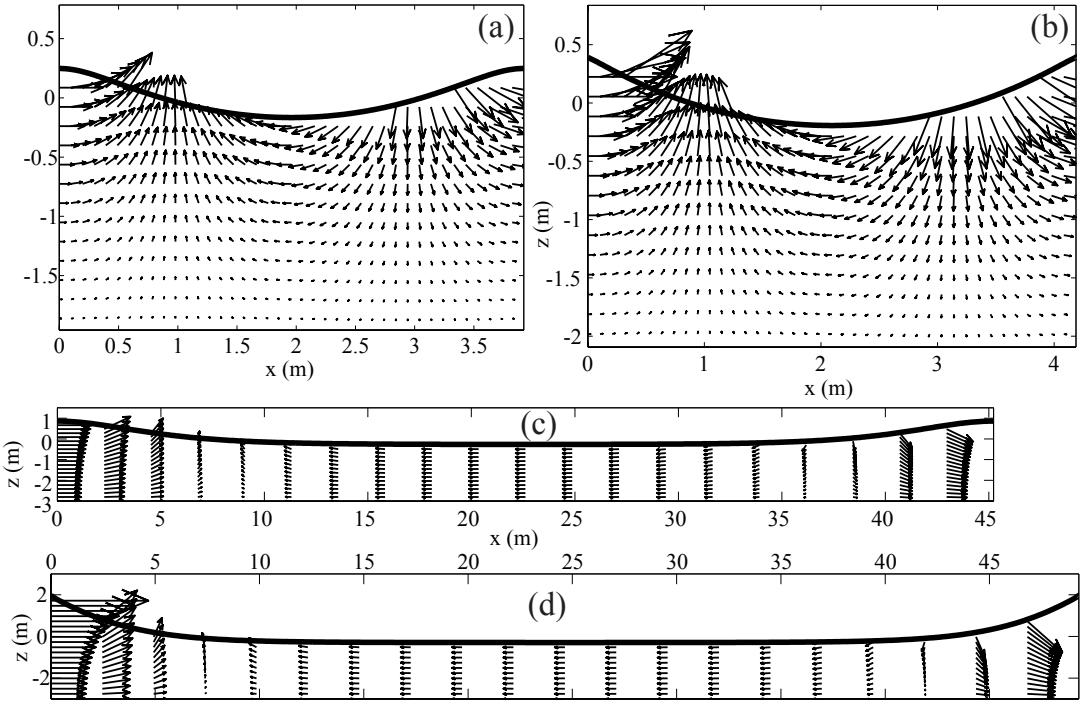

Figure 18.1: Surface elevations and velocity fields at 60th order using Dalrymple (1974)'s numerical method for a water depth of 3 m. (a) and (b) are deep water waves with a period of 1.5 s, so that $kD \simeq 5$. (c) and (d) are shallow water waves of 8 s period. The nonlinearity is intermediate for (a) and (c), with $u_{\max}/C \simeq 0.3$, and extreme in (b) and (d) with $u_{\max}/C \simeq 0.97$.

These nonlinear effects have several consequences. In particular the phase speed, energy and Stokes drift are slightly higher (up to 10% in deep water, much more in shallow water) than predicted by linear theory with the same surface elevation variance (Cokelet, 1977). If accurate estimations of wave kinematics are needed, the linear theory may not be good enough. To know how far the nonlinear solution differ from the linear theory, it is possible to compute numerically the finite amplitude solutions. For example, in the shallow water limit, the surface Stokes drift can exceed several times the linear value (Ardhuin et al., 2008c).

18.2.4 Integral properties

The properties of periodic finite amplitude waves over a flat bottom still follow some exact relations. Here we reproduce the results of (Cokelet, 1977). For any water level z_0 below the wave troughs (i.e. such that

$-h < z_0 < \min(\zeta)$) we may define,

$$\mathcal{M} = \frac{1}{L}\int_0^L \rho_w \zeta \mathrm{d}x = \rho_w \overline{\zeta}, \tag{18.17}$$

$$\mathcal{C} = \frac{1}{L}\int_0^L \rho_w u(x,z_0)\mathrm{d}x = \rho_w \overline{u}, \tag{18.18}$$

$$M^w = \overline{\int_{-h}^{\zeta} \rho_w u \mathrm{d}z}, \tag{18.19}$$

$$E_c = \frac{1}{2}\overline{\int_{-h}^{\zeta} \rho_w \left(u^2+w^2\right)\mathrm{d}z}, \tag{18.20}$$

$$E_p = \overline{\int_{\overline{\zeta}}^{\zeta} \rho_w g z \mathrm{d}z}, \tag{18.21}$$

$$S_{xx} = \overline{\int_{-h}^{\zeta} \left(p+\rho_w u^2\right)\mathrm{d}z} - \overline{\int_{-h}^{\zeta} p^H \mathrm{d}z} = \overline{\int_{-h}^{\zeta} \left(p+\rho_w u^2\right)\mathrm{d}z} - \frac{1}{2}\rho_w g D^2, \tag{18.22}$$

$$F = \overline{\int_{-h}^{\zeta} \left[p + \frac{1}{2}\rho_w\left(u^2+w^2\right) + \rho_w g\left(z -_z eta\right)\right] u \mathrm{d}z}, \tag{18.23}$$

$$\overline{u_b^2} = \frac{1}{L}\int_0^L u^2\left(x,-h,t\right)\mathrm{d}x. \tag{18.24}$$

In the frame of reference moving at the phase speed, the following three quantities are are independent of the horizontal position x. These are the mass flux per unit crest length,

$$-Q = \int_{-h}^{\zeta} \rho_w \left(u-C\right)\mathrm{d}z = -\rho_w C d. \tag{18.25}$$

the dynamic pressure

$$R = \frac{p}{\rho_w g} + \frac{1}{2g}\left[\left(u-C\right)^2 + w^2\right] + \left(z+h\right), \tag{18.26}$$

and the momentum flux per unit crest length

$$S = \int_{-h}^{\zeta} \left[p + \left(u-C\right)^2\right]\mathrm{d}z. \tag{18.27}$$

These quantities are used in other relations

$$M^w = \rho_w C D - Q, \tag{18.28}$$

$$2E_c = C M^w - \rho_w \mathcal{C}, \tag{18.29}$$

$$S_{xx} = 4E_c - 3E_p + \rho_w \overline{u_b^2} + \rho_w C^2 \tag{18.30}$$

$$F = C\left(3E_c - 2E_p\right) + \frac{1}{2}\overline{u_b^2}\left(M^w + \rho_w C D\right) + C\mathcal{C}Q \tag{18.31}$$

$$K = 2\frac{\mathcal{M}}{\rho_w} + \overline{u_b^2} + C^2, \tag{18.32}$$

$$R = \frac{1}{2}K + h, \tag{18.33}$$

$$S = S_{xx} - 2C M^w + D\left(C^2 + \frac{1}{2}D\right), \tag{18.34}$$

where K is Bernoulli's constant, linked to the surface dynamic boundary condition of constant pressure along the sea surface,

$$K = \left(u-C\right) + w^2 + 2\zeta \quad \text{pour} \quad z = \zeta \tag{18.35}$$

18.2.5 Nonlinear corrections to Airy waves

Using periodic numerical solutions, one may propose empirical corrections for various quantities. For example, figure 18.2 shows the expected correction for the wave momentum M_w, as a function of the parameters H/D and kD.

18.3 Nonlinear theory for random waves

La non-linéairité des vagues aléatoires aboutit à plusieurs effets sur le spectre des vagues. Tout d'abord, le transfert d'énergie entre composantes 'libres' est décrit par la théorie de Hasselmann (1960) déjà présentée au chapitre 18.

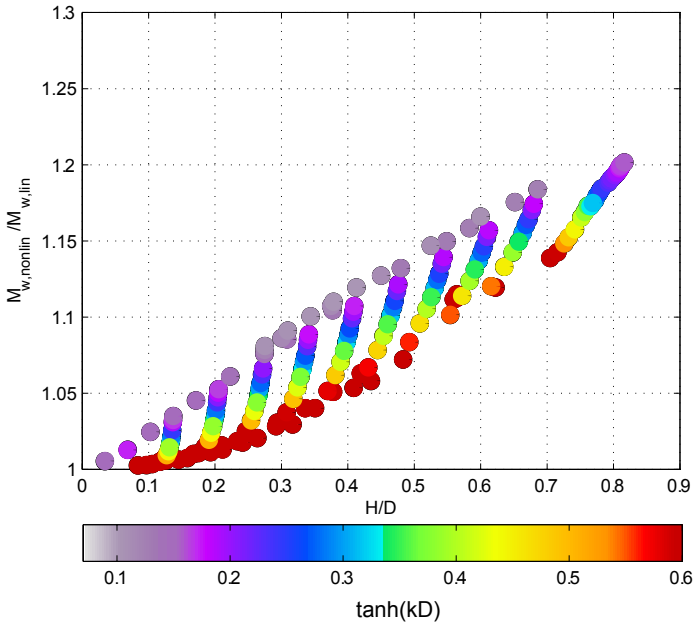

Figure 18.2: Ratio of the wave momentum for periodic waves of finite amplitude and linear waves with the same surface elevation variance. This was computed using the streamfunction theory of Dean and Dalrymple (1974) with orders 80 à 120.

18.3.1 Dispersion relation

Par ailleurs la relation de dispersion est modifiée. Cet aspect est particulièrement important pour la mesure de courants à partir de la relation de dispersion (radar HF ou autres techniques). Barrick and Weber (1977) ont montré que pour des vagues de nombre d'onde k_B et de direction θ_B, la correction de second ordre par rapport à la relation de dispersion linéaire est, en eau profonde (Broche et al., 1983; Ardhuin et al., 2008c),

$$C_2(k_B,\theta_B) = \frac{\sqrt{g}}{2} k_B^{3/2} \int_0^\infty \int_0^{2\pi} F(x,\alpha) E(f,\theta) \mathrm{d}\theta \mathrm{d}f,$$

où, si on définit, $y = x^{1/2} = f/f_B$ and $a = \cos\alpha$,

$$F(x,\alpha) = y\left\{2a - y + 3xa\right\} + y \sum_{\varepsilon=\pm 1} \frac{\varepsilon - a}{a_\varepsilon - (1+\varepsilon y)^2} \left\{ (ya - x)\left(a_\varepsilon + (1+\varepsilon y)^2\right)/2 + (1+\varepsilon y)\left(1 + \varepsilon x a + \varepsilon y\left(x + \varepsilon a\right) - a_\varepsilon\right)\right\}, \tag{18.36}$$

avec

$$a_\varepsilon = \left(1 + x^2 + 2\varepsilon x a\right)^{1/2}. \tag{18.37}$$

Pour $x < 1$, alors $F(x,0) = 4x^{3/2}$, et pour $x > 1$, $F(x,0) = 4x^{1/2}$ (Longuet-Higgins and Phillips, 1962). En général $F(x,\alpha) \simeq F(x,0)\cos\alpha$, avec les erreurs les plus importantes pour $x = 1$, où $F(x,\alpha) > F(x,0)\cos\alpha$ pour $|\alpha| < \pi/3$, ce qui peut donner une erreur de 2 to 5% par rapport à l'approximation $F(x,\alpha) \simeq F(x,0)\cos\alpha$.

18.3.2 Harmoniques

Comme pour des vagues périodiques, le fait qu'il n'y ait pas d'interactions résonnantes (pour les vagues de gravité) à l'ordre 2, permet de calculer de manière explicite le spectre des harmoniques, qui est une correction nonlinéaire du spectre. Plusieurs méthodes ont été développées, mais certaines sont incomplètes car, pour être cohérent, il faut non seulement prendre en compte les termes du type $\Phi^2_{2,2}(\mathbf{k})$ qui résultent du produit d'amplitudes de vagues linéaires $\Phi^2_1(\mathbf{k}')\Phi^2_1(\mathbf{k}-\mathbf{k}')$, mais aussi les termes du type $\Phi_{3,1}(\mathbf{k})\Phi_{1,1}(\mathbf{k})$ avec $\Phi_{3,1}(\mathbf{k})$ les amplitudes d'ordre 3. C'est justement ce qu'avait oublié de faire Weber and Barrick (1977).

Les solutions correctes sont fournies par Creamer et al. (1989) et Janssen (2009). Cette dernière approche est bien adaptée à la modélisation numérique: en faisant travailler le modèle sur les variables canoniques que sont les amplitudes modifiées par la transformation de Krasitskii (1994), on obtient les harmoniques par un post-traitement des spectres résultats pour revenir dans l'espace des variables naturelles, avec les harmoniques. Ce type d'approche est utile pour calculer des efforts sur des structures en mer (e.g. Prevosto et Forristall 2002) mais aussi pour la zone littorale où cela peut permettre de prendre en compte une bonne partie de la génération des harmoniques.

Il semble que la théorie n'est pas encore tout à fait au point pour appliquer cette méthode dans des conditions de profondeur et courant variable, mais elle suggère une alternative interessante au calcul (faux) des interactions de 3 vagues dans les modèles à phase moyennée.

18.4 Evolution non-linéaire du spectre: quadruplets

18.4.1 En eau profonde

Pour un spectre continu de vagues, on se retrouve dans la même situation que pour la résonance forcée par le vent, avec une évolution des amplitudes de la même forme que (22.35). Pour des temps d'évolution longs devant la période des vagues, l'évolution du terme d'ordre 3

$$E_{3,3}(\mathbf{k}) = \frac{|\mathrm{d}Z_3(\mathbf{k})|^2 + |\mathrm{d}\Phi_3(\mathbf{k})|^2}{2\mathrm{d}\mathbf{k}} \tag{18.38}$$

tend vers une expression du type de (22.36)

$$\frac{\partial E_{3,3}(\mathbf{k})\,(\mathbf{k})}{\partial t} = \frac{\pi}{2}\int |B|^2 E(\mathbf{k}_1)E(\mathbf{k}_2)E(\mathbf{k}_3)\mathrm{d}\mathbf{k}_1\mathrm{d}\mathbf{k}_2\mathrm{d}\mathbf{k}_3. \tag{18.39}$$

On peut donc calculer l'évolution du spectre

$$E(\mathbf{k}) = E_2(\mathbf{k}) + E_4(\mathbf{k}) + E_6(\mathbf{k}) + ... \tag{18.40}$$

où l'on a négligé les ordres pairs qui sont rigoureusement nuls dans le cas d'un état de mer Gaussien, car ce sont les produits d'un nombre impair de variables aléatoires Gaussiennes. C'est le travail accompli par Hasselmann (1960,1962). On connait en effet les contributions d'ordre 2,

$$E_2(\mathbf{k}) = 2\frac{|\mathrm{d}Z_1(\mathbf{k},+)|^2}{\mathrm{d}\mathbf{k}} \tag{18.41}$$

d'ordre 4, pour lequel on n'a plus d'équipartition de l'énergie, il faut donc combiner énergie potentielle (termes en Z) et cinétique (termes en Φ),

$$E_4(\mathbf{k}) = \frac{1}{2\mathrm{d}\mathbf{k}}\left\{\overline{|\mathrm{d}Z_2(\mathbf{k})|^2} + 2\mathcal{R}\left[\overline{Z_1(-\mathbf{k})Z_3(\mathbf{k})}\right] + \frac{\sigma^2}{g^2}\overline{|\mathrm{d}\Phi_2(\mathbf{k})|^2} + 2\frac{\sigma^2}{g^2}\mathcal{R}\left[\overline{\Phi_1(-\mathbf{k})\Phi_3(\mathbf{k})}\right]\right\} \tag{18.42}$$

et d'ordre 6,

$$\begin{aligned} E_6(\mathbf{k}) \quad = \quad & \frac{1}{2\mathrm{d}\mathbf{k}}\left\{\overline{|\mathrm{d}Z_3(\mathbf{k})|^2} + 2\mathcal{R}\left[\overline{Z_1(-\mathbf{k})Z_5(\mathbf{k})}\right] + 2\mathcal{R}\left[\overline{Z_2(-\mathbf{k})Z_4(\mathbf{k})}\right]\right. \\ & \left. + \frac{\sigma^2}{g^2}\overline{|\mathrm{d}\Phi_3(\mathbf{k})|^2} + 2\frac{\sigma^2}{g^2}\mathcal{R}\left[\overline{\Phi_1(-\mathbf{k})\Phi_5(\mathbf{k})}\right] + 2\frac{\sigma^2}{g^2}\mathcal{R}\left[\overline{\Phi_2(-\mathbf{k})\Phi_4(\mathbf{k})}\right]\right\} \end{aligned} \tag{18.43}$$

Ainsi il faut calculer jusqu'au cinquième ordre... au moins les termes résonants qui sont importants pour l'évolution du spectre.

18.4.2 Evolution en profondeur finie

Enfin, Janssen et Onorato (2007) ont montré que l'application usuelle du DIA pour des profondeurs intermédiaires, via un coefficient qui augmente quand kD diminue, est probablement erroné. En effet, en résolvant la singularité du coefficient T pour $k_1 = k_2 = k_3 = k_4$ ils montrent que les interactions avec des composantes spectrales proches s'annulent pour $kD = 1.363$ et sont nettement plus faible qu'en eau profonde pour $1.2 < kD < 3$, comme le montre la figure 18.3). A l'heure actuelle, cette variation de l'intensité des interaction n'est prise en compte que dans le modèle du Centre Européen. Il reste encore à vérifier ces prédictions théoriques.

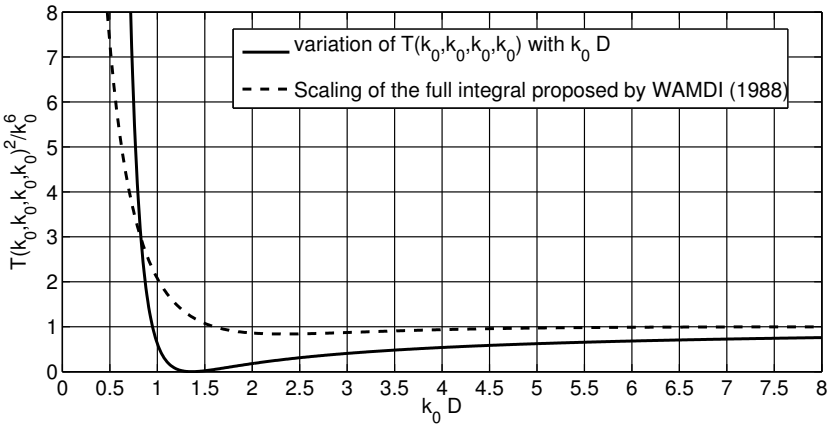

Figure 18.3: Variation de l'intensité des interactions pour des nombres d'onde proches, en fonction de la profondeur adimensionnelle. En pointillés figure la variation préconisée par le groupe WAM (1988), avant les travaux de Janssen et Onorato (2007).

Chapter 19

Waves at second order

19.1 Equations of motion at second order

From the full Bernoulli equation (18.1), the second order approximation is

$$\frac{\partial \phi_2}{\partial t} = -\frac{1}{2}\left[|\boldsymbol{\nabla}\phi_1|^2 + \left(\frac{\partial \phi_1}{\partial z}\right)^2\right] - \frac{p_2}{\rho_w} - gz + C_2(t). \tag{19.1}$$

The usual combination with the surface kinematic boundary condition yields the second order wave equation,

$$\left(\frac{\partial^2}{\partial t^2} + \frac{\partial}{\partial z}\right)\phi_2 + g\frac{\partial \phi_2}{\partial z} = -g\zeta_1\frac{\partial^2 \phi_1}{\partial z^2} + g\boldsymbol{\nabla}\phi_1 \cdot \boldsymbol{\nabla}\zeta_1 - \frac{\partial}{\partial t}\left(\zeta_1\frac{\partial^2 \phi_1}{\partial z \partial t}\right) - \boldsymbol{\nabla}\phi_1 \cdot \frac{\partial \boldsymbol{\nabla}\phi_1}{\partial t} - \frac{\partial \phi_1}{\partial z}\frac{\partial^2 \phi_1}{\partial t \partial z} \quad \text{on} \quad z = 0.$$

The first term on the right hand side comes from the Taylor expansion of the left hand side around $z = 0$, and the four other terms are coming from eq. (18.3).

19.2 Monochromatic waves at second order

Plugging a single monochromatic wave solution with wavenumber $\mathbf{k}_0$, as given in chapter 2, gives second order Stokes solution. For a linear amplitude $a = 2Z^+_{1,\mathbf{k}_0}$, we have $\Phi^+_{1,\mathbf{k}_0} = -iag/(2\sigma)$ and

$$\phi_1 = \frac{\cosh(k_0 z + k_0 h)}{\cosh(k_0 D)}\left(\Phi^+_{1,\mathbf{k}_0} e^{i(\mathbf{k}_0\cdot\mathbf{x} - \sigma_0 t)} + \overline{\Phi}^+_{1,\mathbf{k}_0} e^{-i(\mathbf{k}_0\cdot\mathbf{x} - \sigma_0 t)}\right), \tag{19.2}$$

The solution is,

$$\phi_2 = \frac{\cosh(2k_0 z + 2k_0 h)}{\cosh(2k_0 D)}\left(\Phi^+_{2,2\mathbf{k}_0} e^{i(2\mathbf{k}_0\cdot\mathbf{x} - 2\sigma_0 t)} + \overline{\Phi}^+_{2,2\mathbf{k}_0} e^{-i(2\mathbf{k}_0\cdot\mathbf{x} - 2\sigma_0 t)}\right) + 2\Phi^+_{2,\mathbf{0}} \tag{19.3}$$

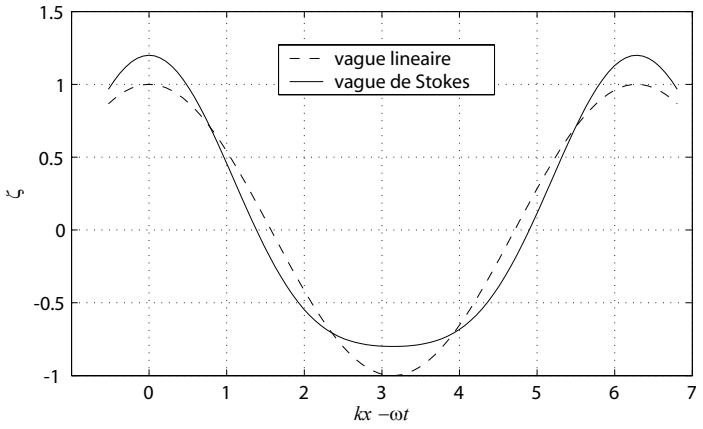

Figure 19.1: Profiles of a linear Airy wave and a second order Stokes wave.

avec

$$\Phi^+_{2,2\mathbf{k}_0} = D(\mathbf{k}_0,\mathbf{k}_0)\frac{\left(\Phi^+_{1,\mathbf{k}_0}\right)^2}{\sigma^2(2k_0)-4\sigma_0^2} \tag{19.4}$$

$$= \frac{3\mathrm{i}\sigma k\cosh(2kh)}{4g\sinh^3(kh)\cosh(kh)}\left(\Phi^+_{1,\mathbf{k}_0}\right)^2, \tag{19.5}$$

and

$$\Phi^+_{2,\mathbf{0}} = 0, \tag{19.6}$$

giving

$$Z^+_{2,2\mathbf{k}_0} = a^2\frac{k\cosh(kh)\left[2+\cosh(2kh)\right]}{32\sinh^3(kh)}, \tag{19.7}$$

and

$$Z^+_{2,\mathbf{0}} = a^2\frac{\sigma^2}{g^2}k^2\left[\tanh^2(2kh)-1\right]. \tag{19.8}$$

The phases of the harmonics are locked with the phase of the linear waves, and the elevation and velocity fields are given by (Dean and Dalrymple, 1991),

$$\zeta = a\cos\left[k(x-Ct)\right] + ka^2\frac{\left[2+\cosh(kD)\right]}{4\sinh^3(kD)}\cos\left[2k(x-Ct)\right] \tag{19.9}$$

$$u = \omega a\frac{\cosh(kz+kD)}{\sinh(kD)}\cos\left[k(x-Ct)\right] + \frac{3}{4}k^2a^2C\frac{\cosh(2kz+2kD)}{\sinh^4(kD)}\cos\left[2k(x-Ct)\right] \tag{19.10}$$

Compared to linear waves, this orbital velocity is higher the crests, and lower under the troughs.

19.3 Second order motion for random waves

Before generalizing to a full wave spectrum, we note tha Miche (1944b) provided the solution for two monochromatic wave trains in opposite directions, which gives a non-zero contribution $C_2(t)$. The general second-order solution, first given by Biesel (1952), comes from using a full superposition of linear waves for ϕ_1 and ζ_1, which are related by eq. (2.25). Here we generally follow the notations used by Hasselmann (1962). We obtain the following wave equation for ϕ_2,

$$\frac{\partial^2\phi_2}{\partial t^2} + g\frac{\partial\phi_2}{\partial z} = \sum_{\mathbf{k}_1,s_1}\sum_{\mathbf{k}_2,s_2} D(\mathbf{k}_1,\mathbf{k}_2)\,\Phi^{s_1}_{1,\mathbf{k}_1}\Phi^{s_2}_{1,\mathbf{k}_2}\mathrm{e}^{\mathrm{i}[(\mathbf{k}_1+\mathbf{k}_2)\cdot\mathbf{x}-(s_1\sigma_1+s_2\sigma_2)t]}. \tag{19.11}$$

The coupling coefficient $D(\mathbf{k}_1,\mathbf{k}_2)$ is given by collecting all the terms from the right hand side ot eq. (19.2). A nice symmetric form (unchanged if $\mathbf{k}_1$ and $\mathbf{k}_2$ are exchanged) is given by Hasselmann (1962)

$$D(\mathbf{k}_1,\mathbf{k}_2) = \mathrm{i}(s_1\sigma_1+s_2\sigma_2)\left[k_1k_2\tanh(k_1h)\tanh(k_2h)-\mathbf{k}_1\cdot\mathbf{k}_2\right] - \frac{\mathrm{i}}{2}\left(s_1\sigma_1\frac{k_2^2}{\cosh^2(k_2h)}+s_2\sigma_2\frac{k_1^2}{\cosh^2(k_1h)}\right). \tag{19.12}$$

This form of $D(\mathbf{k}_1,\mathbf{k}_2)$ can be obtained as follows. One can first expand the products such as $\boldsymbol{\nabla}\phi_1\cdot\boldsymbol{\nabla}\zeta_1$,

$$\boldsymbol{\nabla}\phi_1\cdot\boldsymbol{\nabla}\zeta_1|_{z=0} = \sum_{\mathbf{k}_1,s_1}\mathrm{i}\mathbf{k}_1\Phi^{s_1}_{1,\mathbf{k}_1}\mathrm{e}^{\mathrm{i}(\mathbf{k}_1\cdot\mathbf{x}-s_1\sigma_1t)}\cdot\sum_{\mathbf{k}_2,s_2}\mathrm{i}\mathbf{k}_2Z^{s_2}_{1,\mathbf{k}_2}\mathrm{e}^{\mathrm{i}(\mathbf{k}_2\cdot\mathbf{x}-s_2\sigma_2t)}, \tag{19.13}$$

then replacing $Z^{s_2}_{1,\mathbf{k}_2}$ by $\mathrm{i}s_2\sigma_2\Phi^{s_2}_{1,\mathbf{k}_2}/g$, and collecting the terms

$$\boldsymbol{\nabla}\phi_1\cdot\boldsymbol{\nabla}\zeta_1|_{z=0} = \sum_{\mathbf{k}_1,\mathbf{k}_2,s_1,s_2} -\mathrm{i}\mathbf{k}_1\cdot\mathbf{k}_2\frac{s_2\sigma_2}{g}\Phi^{s_1}_{1,\mathbf{k}_1}\Phi^{s_2}_{1,\mathbf{k}_2}\mathrm{e}^{\mathrm{i}[(\mathbf{k}_1+\mathbf{k}_2)\cdot\mathbf{x}-(s_1\sigma_1+s_2\sigma_2)t]}. \tag{19.14}$$

To get the symmetry, the trick is to write the two sums with $\mathbf{k}_1$ and $\mathbf{k}_2$ switched or not, and take half of their sum,

$$\boldsymbol{\nabla}\phi_1\cdot\boldsymbol{\nabla}\zeta_1|_{z=0} = \sum_{\mathbf{k}_1,\mathbf{k}_2,s_1,s_2} -\mathrm{i}\mathbf{k}_1\cdot\mathbf{k}_2\frac{s_1\sigma_1+s_2\sigma_2}{2g}\Phi^{s_1}_{1,\mathbf{k}_1}\Phi^{s_2}_{2,\mathbf{k}_2}\mathrm{e}^{\mathrm{i}[(\mathbf{k}_1+\mathbf{k}_2)\cdot\mathbf{x}-(s_1\sigma_1+s_2\sigma_2)t]}. \tag{19.15}$$

19.4 Pressure at second order

Using the coupling coefficient D given by Hasselmann (1962, eq. 4.3) for the velocity potentials, our coupling coefficient for the elevation amplitudes is

$$\begin{aligned} D_z\left(\mathbf{k}, s, \mathbf{k}', s'\right) &= -\frac{g^2 D\left(\mathbf{k}, s, \mathbf{k}', s'\right)}{\mathrm{i}s\sigma s'\sigma'\left(s\sigma + s'\sigma'\right)} \\ &= \frac{g^2}{s\sigma s'\sigma'}\left\{\left[\mathbf{k}\cdot\mathbf{k}' - \frac{\sigma^2\sigma'^2}{g^2}\right] + \frac{0.5}{\left(s\sigma + s'\sigma'\right)}\left(\frac{s\sigma k'^2}{\cosh^2(k'h)} + \frac{s'\sigma' k^2}{\cosh^2(kh)}\right)\right\} \end{aligned} \tag{19.16}$$

In the bottom pressure, the additional term arising from the orbital velocity has a coupling coefficient

$$D_{pb}\left(\mathbf{k}, s, \mathbf{k}', s', z\right) = g^2 \frac{kk'\sinh[k(z+h)]\sinh[k'(z+h)] - \mathbf{k}\cdot\mathbf{k}'\cosh[k(z+h)]\cosh[k'(z+h)]}{2s\sigma s'\sigma'\cosh(kh)\cosh(k'h)}. \tag{19.17}$$

The relationship with the coupling coefficient C given by Herbers and Guza (1991, their eq. 4) for the bottom pressure, is given by solving eq. (**??**) for ϕ_2, and then rewriting Bernoulli's equation (19.1), as

$$\frac{p_2}{\rho_w} = \frac{\partial\phi_2}{\partial t} - \frac{1}{2}\left[\left|\boldsymbol{\nabla}\phi_1\right|^2 + \left(\frac{\partial\phi_1}{\partial z}\right)^2\right] \tag{19.18}$$

This gives, for $z = -h$,

$$C = -\frac{D_z(s\sigma + s'\sigma')^2}{g\left[gK\tanh(Kh) - (s\sigma + s'\sigma')^2\right]} + \frac{D_{pb}(z=-h)}{g}. \tag{19.19}$$

ϕ_2 is a solution to Laplace equation and the bottom boundary condition, and its Fourier component $\Phi_{2,\mathbf{k}}$ for the wavenumber $\mathbf{k}$ thus has a vertical structure that is the same as that of ϕ_1, namely it is proportional to $\cosh\left(kz + kh\right)$. The Fourier transform of eq. (**??**) thus gives

$$\frac{\partial^2\Phi_{2,\mathbf{k}}}{\partial t^2} + gk\tanh\left(kh\right)\Phi_{2,\mathbf{k}} = \sum_{\mathbf{k}_1+\mathbf{k}_2=\mathbf{k}, s_1, s_2} D\left(\mathbf{k}_1, \mathbf{k}_2\right)\Phi_{1,\mathbf{k}_1}^{s_1}\Phi_{1,\mathbf{k}_2}^{s_2}\mathrm{e}^{\mathrm{i}-(s_1\sigma_1+s_2\sigma_2)t}, \tag{19.20}$$

et les coefficients de Fourier $Z_{2,\mathbf{k}}$ de ζ_2 en sont déduit via le développement à l'ordre 2 de la condition cinématique en surface,

$$Z_{2,\mathbf{k}} = -\frac{1}{g}\frac{\partial\Phi_{2,\mathbf{k}}}{\partial t} + \sum_{\mathbf{k}_1+\mathbf{k}_2=\mathbf{k}, s_1, s_2} G\left(\mathbf{k}_1, \mathbf{k}_2\right)\Phi_{1,\mathbf{k}_1}^{s_1}\Phi_{1,\mathbf{k}_2}^{s_2}\mathrm{e}^{-\mathrm{i}(s_1\sigma_1+s_1\sigma_1)t}. \tag{19.21}$$

où G est donné par Hasselmann (1962)

$$-\frac{\mathrm{i}}{2}\left(\frac{s_1\sigma_1 k_2^2}{\cosh^2\left(k_2 h\right)} + \frac{s_2\sigma_2 k_1^2}{\cosh^2\left(k_1 h\right)}\right),$$

$$G\left(\mathbf{k}_1, \mathbf{k}_2\right) = \frac{1}{2g}\left[\mathbf{k}_1\cdot\mathbf{k}_2 - g^{-2}s_1 s_2\sigma_1\sigma 2\left(\sigma_1^2 + \sigma_2^2 + s_1 s_2\sigma_1\sigma_2\right)\right]. \tag{19.22}$$

L'équation d'oscillateur forcé (19.27) ne peut conduire à une résonance car la relation de dispersion est telle que $\sigma\left(\mathbf{k}_1 + \mathbf{k}_2\right) \neq \sigma\left(\mathbf{k}_1\right) + \sigma\left(\mathbf{k}_2\right)$ sauf dans la limite de l'eau peu profonde $kh \to 0$, ou pour des vagues de gravité-capillarité. En dehors de ces deux cas, les solutions de second ordre sont donc des vagues d'amplitude limitée et elles sont liées aux solutions du premier ordre. Ces variations d'amplitudes causées par des interactions non-résonnantes peuvent donner lieu a des échanges temporaires d'énergies entre les différentes composantes aussi appelées récurrences (Fermi, Pasta et Ulam 1955).

The dynamic and kinematic boundary conditions a the free surface $z = \zeta$ are

$$p = p_a \tag{19.23}$$

$$w = \frac{\partial\phi}{\partial z} = \boldsymbol{\nabla}\phi\cdot\boldsymbol{\nabla}\zeta + \frac{\partial\zeta}{\partial t}. \tag{19.24}$$

As done in chapter 2, we move the boundary condition on $z = \zeta$ to an equation on $z = 0$ with a Taylor expansion

$$\frac{\partial\zeta}{\partial t} - \frac{\partial\phi}{\partial z} \simeq \boldsymbol{\nabla}\phi\cdot\boldsymbol{\nabla}\zeta + \zeta\frac{\partial^2\phi}{\partial^2 z} \quad \text{on} \quad z = 0. \tag{19.25}$$

Again the combination of eq. (19.1) at $z=\zeta$, where $p=p_a$, and (19.25) allows us to remove the unknown ζ,

$$\left[\left(\frac{\partial^2}{\partial t^2}+g\frac{\partial}{\partial z}\right)\phi_2\right]_{z=0}=-\frac{\partial}{\partial t}\left(\frac{p_a}{\rho_w}\right)-\frac{1}{2}\left\{\frac{\partial}{\partial t}\left[|\boldsymbol{\nabla}\phi|^2+\left(\frac{\partial\phi}{\partial z}\right)^2+2\zeta\frac{\partial^2\phi}{\partial t\partial z}\right]\right\}_{z=0}-g\left\{\boldsymbol{\nabla}\phi\cdot\boldsymbol{\nabla}\zeta+\zeta\frac{\partial^2\phi}{\partial^2 z}\right\}_{z=0}. \tag{19.26}$$

We now replace by the forcing by the first order solution to obtain the forced second order wave equation

$$\left[\left(\frac{\partial^2}{\partial t^2}+g\frac{\partial}{\partial z}\right)\phi_2\right]_{z=0}=\frac{\partial}{\partial t}\left\{-\frac{p_a}{\rho_w}-\sum_{\mathbf{k},s}\sum_{\mathbf{k}',s'}\frac{D\left(\mathbf{k},\mathbf{k}'\right)}{\mathrm{i}\left(s\sigma+s'\sigma'\right)}\Phi^{s}_{1,\mathbf{k}}\Phi^{s'}_{1,\mathbf{k}'}\mathrm{e}^{\mathrm{i}\left[\left(\mathbf{k}+\mathbf{k}'\right)\cdot\mathbf{x}-\left(s\sigma+s'\sigma'\right)t\right]}\right\}, \tag{19.27}$$

where the coupling coefficient $D\left(\mathbf{k},\mathbf{k}'\right)$ is given by Hasselmann (1962),

$$D\left(\mathbf{k},\mathbf{k}'\right)=\mathrm{i}\left(s\sigma+s'\sigma'\right)\left[kk'\tanh\left(kh\right)\tanh\left(k'h\right)-\mathbf{k}\cdot\mathbf{k}'\right]-\frac{\mathrm{i}}{2}\left(s\sigma\frac{k'^2}{\cosh^2(k'h)}+s'\sigma'\frac{k^2}{\cosh^2(kh)}\right). \tag{19.28}$$

As noted by Hasselmann (1963), the forcing terms in the equations are equivalent to a pressure term $\widehat{p}_2$. Replacing $\Phi^{s}_{1,\mathbf{k}}$ by $-\mathrm{i}sgZ^{s}_{1,\mathbf{k}}/\sigma$ it is

$$\begin{aligned}\widehat{p}_2 \quad = \quad & -\rho_w\sum_{\mathbf{k},s,\mathbf{k}',s'}\left\{s\sigma s'\sigma'\left[1-\frac{\mathbf{k}\cdot\mathbf{k}'}{kk'\tanh\left(kh\right)\tanh\left(k'h\right)}\right]\right. \\ & \left.-\frac{1}{2\left(s\sigma+s'\sigma'\right)}\left(\frac{g^2k'^2}{s'\sigma'\cosh^2(k'h)}+\frac{g^2k^2}{s\sigma\cosh^2(kh)}\right)\right\}Z^{s}_{1,\mathbf{k}}Z^{s'}_{1,\mathbf{k}'}\mathrm{e}^{\mathrm{i}\left[\left(\mathbf{k}+\mathbf{k}'\right)\cdot\mathbf{x}-\left(s\sigma+s'\sigma'\right)t\right]}.\end{aligned} \tag{19.29}$$

19.5 The second order spectrum

Because the wave spectrum is a quadratic quantity, the expansion of the surface elevation up to third order

$$\zeta=\zeta_1+\zeta_2+\zeta_3+... \tag{19.30}$$

is needed to evaluate what is ofen called the second order spectrum, but that is in fact a fourth order quantity. The fourth order elevation variance is

$$E=\overline{\zeta_1+\zeta_2+\zeta_3+...}^2=\overline{\zeta_1^2}+2\overline{\zeta_1\zeta_2}+\overline{\zeta_2^2}+2\overline{\zeta_1\zeta_3}+... \tag{19.31}$$

Chapter 20

Wave-wave interactions: general properties of random wave scattering

All wave scattering and wave-wave interaction processes can be expressed as source terms in the wave action evolution equation, it is so general that it also covers wave generation by the wind, microseism generation, wave scattering by bottom, currents, internal waves ... The general theoretical framework is very well described by Hasselmann (1966), and the detailed description of interactions in the case of 4-wave interactions by Hasselmann (1962) can be transposed to many interaction types. This chapter thus insists on key elements of that theory and explains how they apply in other contexts.

20.1 How the interactions of $\mathbf{k}_1$ and $\mathbf{k}_2$ give $\mathbf{k}_3$

20.2 Why resonant interactions emerge

20.3 Large time limit and finite time evolutions

20.4 Amplitude and energy growth

20.5 What if the medium is not homogeneous?

Chapter 21

Ocean waves and microseisms

I thought that this chapter would treat two mechanisms of microseism generation, at the same frequency and at the double frequency. Now it appears that it is getting a bit too long and so this chapter will probably be split into a same-frequency and a double frequency chapters. The two mechanisms only differ by how the ocean waves are able to generate much longer waves with $K << k$, but the following propagation is exactly the same. As a result the sources for the different types of waves, surface Rayleigh waves or body waves, can all be expressed as some coefficient that multiplies the wave-induced pressure spectrum at the sea surface or bottom $F_p(K_x, K_y, f_s)$. For the same-frequency mechanism this is $F_{p1}(K_x, K_y, f_s)$ as given by (Ardhuin et al., 2015, eq. S12), whereas the double-frequency mechanism gives $F_{p2}(K_x, K_y, f_s)$ as given by (Ardhuin and Herbers, 2013, eq. 2.28 with a correction by the bottom pressure 2.31 for waves in finite depth).

21.1 A short history of microseism observations

In the early days of seismology in the late 19th century, a background noise of varying amplitude was detected. Bertelli (1872) performed measurements in Italy and found that the amplitude of these microseisms changed with the passing of storms. By the year 1900, the phenomenon was measured all around the globe, and Algué (1900) related measurements in the Philippines to the passage of Typhoons. All seismometer measurements on Earth contain microseisms. These seismic waves propagate through the solid Earth and oceans, with a displacement amplitude that rarely exceeds 10 microns, and a dominant wave period typically between 3 and 10 s.

From seismograph records, the apparently random signal gives a power spectrum with very robust features. Stutzmann et al. (2000) showed how the noise level generally decreases from island stations to stations deep inside continents, with a classical shape. When the vertical acceleration is considered, the noise generally has 2 broad peaks. The so-called 'secondary' peak lies at periods between 3 and 10 s, typically half of the dominant ocean wave periods, and it is the most energetic. The weaker 'primary' peak has the same period as typical swells, between 10 and 25 s, and a broad interval of noise is found at periods above 30 s. That long period range is called the hum.

In all of these frequency bands, the seismic waves can be separated in different modes,

- Raleigh waves: these are waves that follow the surface of the crust, with a motion in the plane of propagation, and an exponential decrease of the motion amplitude towards the center of the Earth. Within 2000 km from the source, these Rayleigh waves usually dominate the microseisms recorded in the 3 to 10 s period band.
- Love waves: these are waves that follow the surface of the crust, with a motion out of the plane of propagation, and an exponential decrease of the motion amplitude towards the center of the Earth.
- compressive body (P) waves: these waves travel through the Earth mantle, with a motion in the direction of propagation.
- shear body (S) waves: these waves travel through the Earth mantle, with a motion transverse to the direction of propagation, either in the vertical direction, these are then called SV waves, or horizontal direction, and they are called SH waves.

What was a curiosity is now an important source of data for studying the Earth's structure and it can also be used to measure wave properties from land-based seimometers (Zopf et al., 1976). Ongoing efforts are now explaining how and where this noise comes from, which may have some important application for seismology or the study of the ocean wave climate. The acoustic noise field in the ocean is also part of this seismic noise field, with some wave modes that have important signatures in the water column and in the atmosphere. The atmospheric components are called microbaroms and are often studied separately, although they have the same sources. These microbaroms offer unique opportunities to study the upper atmospheric circulation.

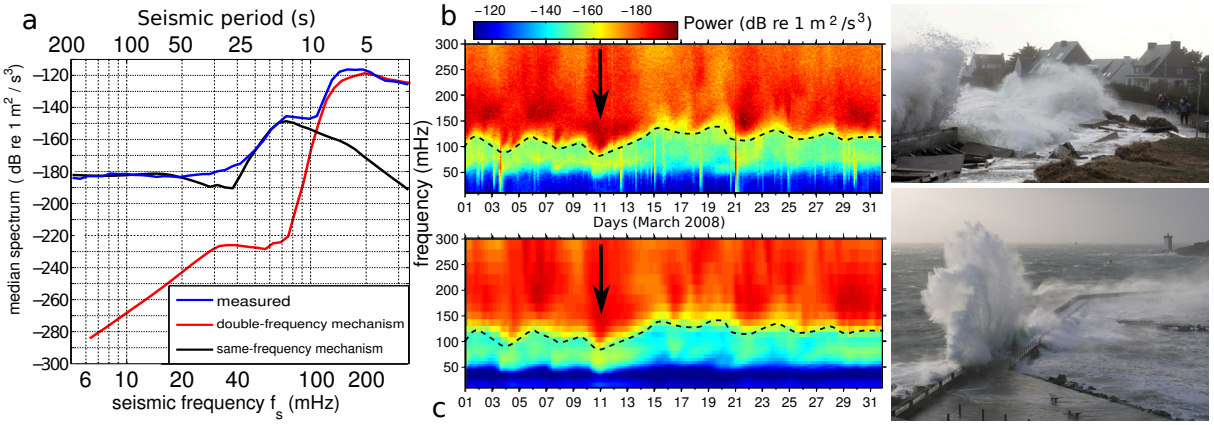

Figure 21.1: Measured and modeled seismic spectra. (a) Median vertical acceleration power spectra in March 2008 at the French SSB seismic station, located near Saint-Etienne, France. (b) observed and (c) modeled spectra in March 2008 following Ardhuin et al. (2015). Light blue to red vertical stripes correspond to earthquakes (not modeled). Contrary to intuition, the direct impact of waves at the shoreline shown on these pictures is not the main source of the microseisms recorded at remote stations. Instead, seismic waves are mostly generated by two mechanisms: a same-frequency mechanism involves wave propagation over varying topography in intermediate water depth, and a double-frequency mechanism that involves the interaction of waves in opposite directions. The dashed line separates the low frequencies where the same-frequency mechanism dominates from the higher frequencies explained by the double-frequency mechanism. The Johanna storm, marked by the vertical arrow on March 10, is conspicuous with powerful and low frequency microseisms. Pictured right: coastal impact of Johanna at Gâvres and Le Conquet, France.

A key feature of the generation of microseisms is that it transfers energy from ocean waves that are slow, with typical phase speeds of 10 m/s, to the much faster seismic waves with speeds of several km/s. How can slow waves excite fast waves?

21.2 The particular case of standing ocean waves

Miche (1944b) was the first to show that, at second order in the wave steepness, the pressure under stationary waves oscillates in time but does not decay with depth. Clearly, we cannot generally assume that $C(t)$ in (2.10) is zero. Taking two propagating waves that give standing waves, with elevations $a\cos(kx-\sigma t)$ and $a\cos(kx+\sigma t)$, going in directions towards $x>0$ and $x<0$. Their sum is the stationary wave,

$$\zeta = 2a\cos(kx)\cos(\sigma t). \tag{21.1}$$

$$w = -2a\sigma\frac{\sinh(kz+kD)}{\sinh(kD)}\cos(kx)\sin(\sigma t). \tag{21.2}$$

$$\tag{21.3}$$

It is particulary interesting to look at the horizontally averaged pressure at depth z using eq. (7.30)

$$\overline{p}(z) = \rho_w g(\zeta - z) + \rho_w \frac{\partial}{\partial t}\overline{\zeta w(\zeta)} - \rho_w \overline{w(z)^2}. \tag{21.4}$$

The last two terms are deviations from the hydrostatic pressure and they give the non-hydrostatic (NH) pressure,

$$\overline{p}_{NH}(z) = -2\rho_w a^2\sigma^2\left[\cos(2\sigma t) + \frac{\sinh^2(kz+kD)}{\sinh^2(kD)}\sin^2(\sigma t)\right]. \tag{21.5}$$

While the second term does not oscillate in time and decays with depth, the first term oscillates at a period equal to half of the propagating wave period, but is uniform over the vertical.

This fluctating pressure, predicted by Miche (1944b), was interpreted by Longuet-Higgins (1950) as the vertical force that is necessary to compensate the fluctuations of the vertical momentum per unit surface

$$M_z = \overline{\int_{-h}^{\zeta}\rho_w w \mathrm{d}z} \simeq \rho_w\overline{\zeta w(\zeta)}. \tag{21.6}$$

This momentum is only non-zero when w and ζ are correlated, and at depth $dM_z/dt = p_{NH}(z\to\infty)$.

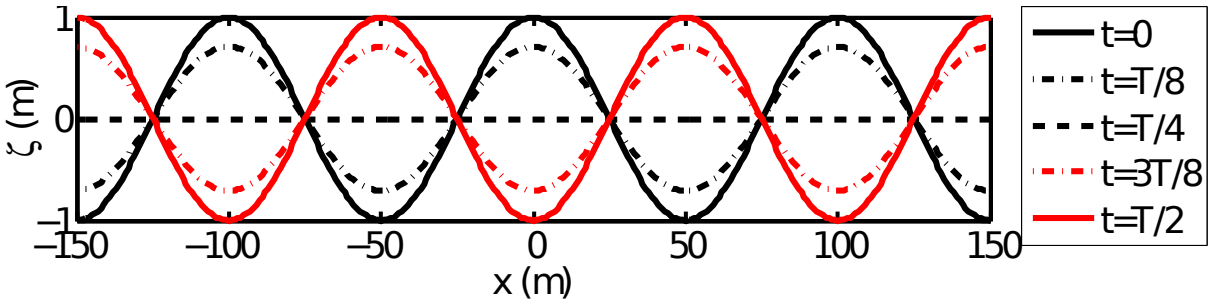

Figure 21.2: Schematic positions of the free surface in a stationary wave at different phases of the period T of the progressive wave.

It should be noted, also, that the first term in pressure $\overline{p}_{NH}$ is lowest when the wave amplitude is maximum, contrary to the second term. In the limit of shallow water $kD \ll 1$ and we have $\overline{p}_{NH}(z) = 0$.

Of course, the surface pressure is not immediately transmitted at large depth, and a more detailed description requires to take into account the compressibility of sea water. In reality, the surface oscillations produce acoustic waves that radiate in the water column (Longuet-Higgins, 1950), and are easily recorded at the ocean bottom (Farrell and Munk, 2008). Eq. (21.5) was verified in the laboratory by Cooper and Longuet-Higgins (1951). Hence, compared to the classical studies of ocean waves, the investigation of seismic and acoustic noise requires to relax two of the hypothesis made in chapter 2. Namely, we will have to take into accound the compressibility of sea water and air, and we will also need to allow the sea bottom to deform under the varying water pressure.

In the case of exactly standing waves, the associated acoustic waves is propagating along the vertical. So this is not yet giving the seismic Rayleigh waves observed on land as surface waves. But the ocean waves are not monochromatic, so that it is much more likely to have interactions of waves with different wavenumbers rather than waves with exactly opposing direction and frequency. In fact, mathematically, the measure of these exactly opposing waves is zero. We thus need to generalize the standing wave to what we will find to be supersonic wave groups in the next section.

21.3 Wave-wave interaction theory for microseism generation

Here we generally follow the method of Hasselmann (1963) with several corrections exposed by Ardhuin and Herbers (2013). In this process we also compute properties of Rayleigh waves in the presence of a water layer, which was first done by Stoneley (1926), and is covered in seismology textbooks such as (Lay and Wallace, 1995, page 133, note the typo with ρ_w and ρ_s excahnged in the dispersion relation).

21.3.1 Wavenumber diagrams and isotropy of microseism sources

We have seen in the previous chapters that wave components of frequency f and wavenumber vector $\mathbf{k}$ can interact with another wave or a change in medium (water depth or current) that has a frequency f' and wavenumber $\mathbf{k}'$, giving rise to a wave of frequency $f_s = f + f'$ and wavenumber $\mathbf{K} = \mathbf{k} + \mathbf{k}'$. The general theory of such interactions was sumarized by Hasselmann (1966), and exposed in chapter 20.

If the phase speed $2\pi(f + f')/|\mathbf{k} + \mathbf{k}'|$ matches the speed of a seismic mode, then there is a resonance and interaction of waves with that seismic mode. In the case of microseisms, the ocean waves transfer energy to the seismic wave. Conversely, the vertical shaking of water, usually in the laboratory, gives rise to standing waves in the water, also known as Faraday waves.

For seismic frequencies f_s around 0.2 Hz, the phase speed of seismic waves is larger 1.5 km/s, such large speed can only be achieved if $K << k$, which imposes $\mathbf{k}' \simeq -\mathbf{k}$, as illustrated on figure 21.3. The two neear-resonant configurations produce seismic waves that travel in very different directions. However, compared to that of the ocean waves, a 1% change in the wave vector $\mathbf{k}$ is generally negligible, because the half-width of the wave spectrum in frequency and direction is generally of the order of 5% or more, and the wave energy spectral density $E(f, \theta)$ is the same if $\mathbf{k}$ changes by only 1%. Hence, at the spectral peak, the source of microseisms is isotropic.

We can distinghish two mechanisms that give rise to these interactions,

- A same-frequency mechanism: $\mathbf{k}'$ corresponds to a change in depth or current, this is usually fixed in time or at least much slower than the waves, hence $f' = 0$ and $f_s = f$, the seismic waves have the same frequency as the ocean waves.
- A double-frequency mechanism: $\mathbf{k}'$ corresponds to another wave component. Since $\mathbf{k}' \simeq -\mathbf{k}$, we also have $|\mathbf{k}'| \simeq |\mathbf{k}|$ and $f \simeq f'$, thus $f_s \simeq 2f$: the microseism have a frequency that is the double of the ocean wave frequency.

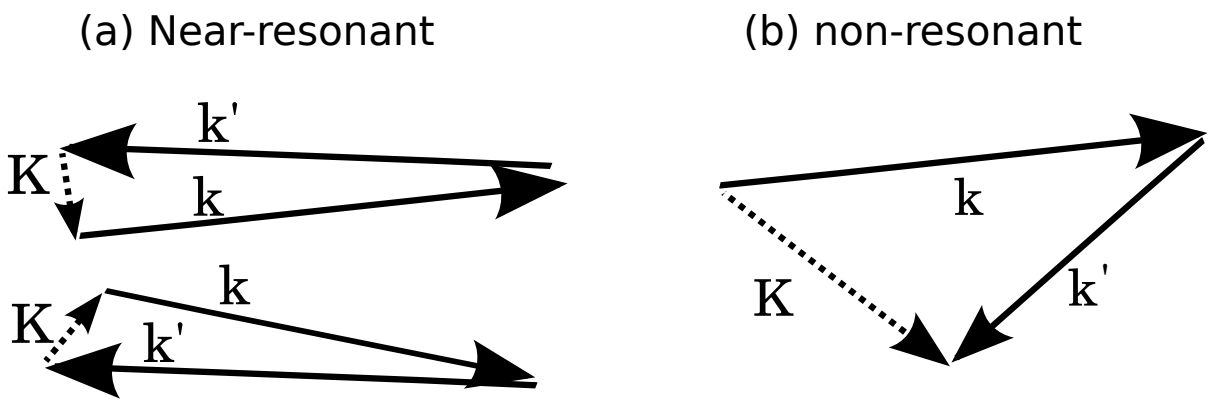

Figure 21.3: Typical configuration of interacting wave components

Figure 21.1 shows that the same-frequency mechanism only explains the hum and primary microseism, while the double-frequency mechanism explains the higher frequency secondary peak. We will now give more theoretical details for each mechanism.

21.3.2 Motion in the water and equivalent wave-induced pressure

We follow here the theory of Hasselmann (1963) made for waves in deep water ($kD >> 1$), including the correction by Ardhuin and Herbers (2013) for finite water depth.

From Longuet-Higgins (1950), we know that at first order the wave motion is given by Airy theory as exposed in chapter 2. At second order, the motion is forced at the surface by the interaction of pairs of linear (first order) solutions. This is thus the exact same problem that is solved in chapter 18, with the only change caused by compressibility, namely the mass conservatin equation that was $\boldsymbol{\nabla}^2\phi + \partial^2\phi/\partial z^2 = 0$ in the incompressible case, is now, assuming that the time-average density ρ_w only varies in the vertical, and ρ' are wave-induced perturbations,

$$\frac{d\rho'}{dt} = \frac{\partial \rho'}{\partial t} + \frac{\partial \phi}{\partial z}\frac{\partial\left(\rho_w + \rho'\right)}{\partial z} + \boldsymbol{\nabla}\phi \cdot \boldsymbol{\nabla}\rho' \quad = \quad -\rho_w \nabla^2 \phi - \rho_w \frac{\partial^2 \phi}{\partial z^2}. \tag{21.7}$$

We now need an equation of state that relates the pressure fluctations p' to density fluctuations ρ', via the sound speed in the water α_w,

$$-\alpha_w^2 \rho' + p' \quad = \quad 0. \tag{21.8}$$

Combining (21.26)–(21.25) and expressing ρ' as a function of p' gives

$$-\alpha_w^2 \rho' + p' \quad = \quad 0 \tag{21.9}$$

$$\frac{dp'}{dt} = \rho_w \alpha_w^2 \left[\nabla^2 + \frac{\partial^2}{\partial z^2}\right]\phi \quad = \quad 0 \tag{21.10}$$

We have thus three unknowns, ρ', p' and ϕ. They are related by eqs. (21.25), (21.10) and a third equation that is unchanged from the incompressible case, namely the Bernoulli equation (18.1).

As detailed in chapter 19 the surface boundary condition contains the interaction of linear ocean waves, and it is equivalent to a surface pressure $\widehat{p}_2$ given by eq. (19.29). The last term of that equation was absent in Hasselmann (1963) because he only considered waves in deep water where $kD \gg 1$, so that it is also missing in Webb (2007). Using (19.29) the surface pressure spectrum can be expressed in terms of quadratic products of the (linear) sea surface elevation spectrum

$$E(k_x, k_y) = 2 \lim_{|d\mathbf{k}|\to 0} \frac{\left|Z^+_{1,\mathbf{k}}\right|^2}{\mathrm{d}k_x \mathrm{d}k_y} \tag{21.11}$$

with a coupling coefficient given by eq. (19.16) that simplifies for $K \simeq 0$ to

$$D_z\left(\mathbf{k}, 1, -\mathbf{k}, 1\right) = -2\sigma^2\left[1 + \frac{1}{4\sinh^2(kh)}\right]. \tag{21.12}$$

For any value of kD, the coupling coefficient given by eq. (21.12) differs from the full second order coefficient for the bottom pressure (e.g. eq. 4 in Herbers and Guza, 1991), which also involves the Bernoulli head (the bracket in eq. 19.1). However, that extra term is also relevant to the generation of seismic noise due to the

bottom boundary condition that couples the solid crust to the water column. Indeed, the second-order pressure perturbation at the bottom writes,

$$p_2(-h) = -\rho_w \frac{\partial \phi_2}{\partial t} + \widehat{p}_{2,\mathrm{bot}}, \tag{21.13}$$

where the Bernoulli head contribution to the pressure can be expressed from the first order wave amplitudes,

$$\widehat{p}_{2,\mathrm{bot}} = \rho_w \sum_{\mathbf{k},s,\mathbf{k}',s'} D_{pb}\left(\mathbf{k},s,\mathbf{k}',s',z=-h\right) Z^s_{1,\mathbf{k}} Z^{s'}_{1,\mathbf{k}'} \mathrm{e}^{\mathrm{i}\Theta(\mathbf{k},\mathbf{k}',s,s')}, \tag{21.14}$$

with a coupling coefficient D_{pb} given by eq. (19.17).

We may interpret the bottom pressure (21.13) as the sum of the surface forcing $\widehat{p}_{2,\mathrm{surf}}$ transmitted to the bottom by ϕ_2, and a direct effect of the Bernoulli head at the bottom which is an additional forcing $\widehat{p}_{2,\mathrm{bot}}$ that partly cancels $\widehat{p}_{2,\mathrm{surf}}$.

We shall see in the next section that the forcing term for seismic noise is $\widehat{p}_{2,\mathrm{surf}} + \cos(lh)\widehat{p}_{2,\mathrm{bot}}$, with $l \leq K \ll k$ the vertical wavenumber in the water. For shallow water gravity waves, $kh \ll 1$ and thus $\cos(lh) \simeq 1$ so that the effective forcing term becomes $\widehat{p}_{2,\mathrm{surf}} + \widehat{p}_{2,\mathrm{bot}}$, which equals the bottom pressure in the incompressible limit. The shallow water asymptote of the spectrum of this total forcing term is very different from the surface pressure only. Compared to eq. (21.22), the $\left[1+0.25/\sinh^2(kh)\right]^2$ factor is now replaced by 1. For $kh \ll 1$, this is a factor $(kh)^4/16$ smaller,

This second order surface pressure is not the only effect of waves, which also appear in the wave equation obtained by eliminating p between (21.10) and (19.1),

$$\alpha_w^2\left[\nabla^2 + \frac{\partial^2}{\partial z^2}\right]\phi = \frac{d}{dt}\left[\frac{\partial \phi}{\partial t} + gz + \frac{1}{2}\left(|\boldsymbol{\nabla}\phi|^2 + \left(\frac{\partial \phi}{\partial z}\right)^2\right)\right] \tag{21.15}$$

$$\alpha_w^2\left[\nabla^2 + \frac{\partial^2}{\partial z^2}\right]\phi - \frac{\partial^2 \phi}{\partial^2 t} - g\frac{\partial \phi}{\partial z} \simeq -\frac{1}{2}\frac{\partial}{\partial t}\left[|\boldsymbol{\nabla}\phi|^2 + \left(\frac{\partial \phi}{\partial z}\right)^2\right]. \tag{21.16}$$

Longuet-Higgins (1950) showed that for $\sigma \simeq 0.5$ s^{-1}, the right hand side in eq. (21.16) was negligible (his F terms). We can thus neglect it for noise generated by wind seas and swell. This term might be important foe longer wave periods.

For the generation of seismic waves, the only relevant interactions are the ones with phase speeds $|\mathbf{k}+\mathbf{k}'|/|s\sigma + s'\sigma'|$ close to the horizontal speed of seismic modes, typically more than 1500 m/s, except for waves over unconsolidated sediments for which the speed could be only a few hunder meter per second. This condition imposes that $\mathbf{k} \simeq -\mathbf{k}'$ and thus $s\sigma \simeq s'\sigma'$, we can thus ignore the other terms and we re-write eq. (19.29) as

$$\begin{aligned}
\widehat{p}_2 &\simeq -\rho_w \sum_{\mathbf{k},\mathbf{k}'\simeq-\mathbf{k},s} \left\{\sigma^2\left[1+\frac{1}{\tanh^2(kh)}\right] - \frac{g^2k^2}{2\sigma^2\cosh^2(kh)}\right\} Z^s_{1,\mathbf{k}} Z^s_{1,\mathbf{k}'} \mathrm{e}^{\mathrm{i}\left[(\mathbf{k}+\mathbf{k}')\cdot\mathbf{x}-2s\sigma t\right]} \\
&\simeq -\rho_w \sum_{\mathbf{k},\mathbf{k}'\simeq-\mathbf{k},s} \left\{\sigma^2\left[\frac{1}{2}+\frac{3}{2\tanh^2(kh)}\right]\right\} Z^s_{1,\mathbf{k}} Z^s_{1,\mathbf{k}'} \mathrm{e}^{\mathrm{i}\left[(\mathbf{k}+\mathbf{k}')\cdot\mathbf{x}-2s\sigma t\right]}
\end{aligned} \tag{21.17}$$

21.3.3 The elementary interaction: a supersonic wave group

Instead of this complete sum, we first detail the simplest case of interaction, with only two monochromatic wave trains in opposite directions with nearly equal periods. Here we take an example with an amplitude a and period $T_a = 12$ s for the first wave train, with a surface elevation $a\cos(k_a x - \sigma_a t)$ and an amplitude b and a period T_b=11.88 s, with a corresponding elevation $b\cos(k_b x + \sigma_b t)$. In the middle of the oceans, with a depth of 5000 m, these two wave trains are in deep water and the difference of the two wavenumbers is $K = k_b - k_a = 5.2\times10^{-4}$ rad/m, corresponding to a wavelength $L = 12$ km, to be compared to the wavelength of the first wave tran that is only 225 m. We thus have wave groups that contain $12000/225 = 53$ waves (figure 21.4). The group speed is $L\times(1/T_a + 1/T_b)$, namely 2 km/s.

because k in eq. (21.17) can be either k_a or $-k_b$, the equivalent wave-induced pressure has 8 different terms. Only 4 of these terms are relevant for seismic wave generation. We have $Z^+_{1,a} = Z^-_{1,a} = a/2$ and $Z^+_{1,b} = Z^-_{1,b} = b/2$, giving

$$\begin{aligned}
\widehat{p}_2 &\simeq -2\rho_w\sigma^2\frac{ab}{4}\left[\mathrm{e}^{\mathrm{i}[(k_a-k_b)x-2\sigma t]} + \mathrm{e}^{\mathrm{i}[(-k_b+k_a)x-2\sigma t]} + \mathrm{e}^{\mathrm{i}[(k_a-k_b)x+2\sigma t]} + \mathrm{e}^{\mathrm{i}[(-k_b+k_a)x+2\sigma t]}\right] \\
&\simeq -2\rho_w\sigma^2 ab\left[\cos\left(Kx+2\sigma t\right)\right]
\end{aligned}$$

This result, given by Ardhuin and Herbers (2013) is the generalization to of the Longuet-Higgins (1950) standing wave. The wave group propagates in the direction of the shortest of the two wave components. This propagation in one dimension is easy to generalize to cases where the wave directions are not exactly opposite but in the directions of two wave vectors $\mathbf{k}_b$ and $\mathbf{k}_a$. The direction of propagation of the second order pressure is in the direction of $\mathbf{K} = \mathbf{k}_b - \mathbf{k}_a$. In the incompressible case, this equivalent pressure is equal to the measured pressure

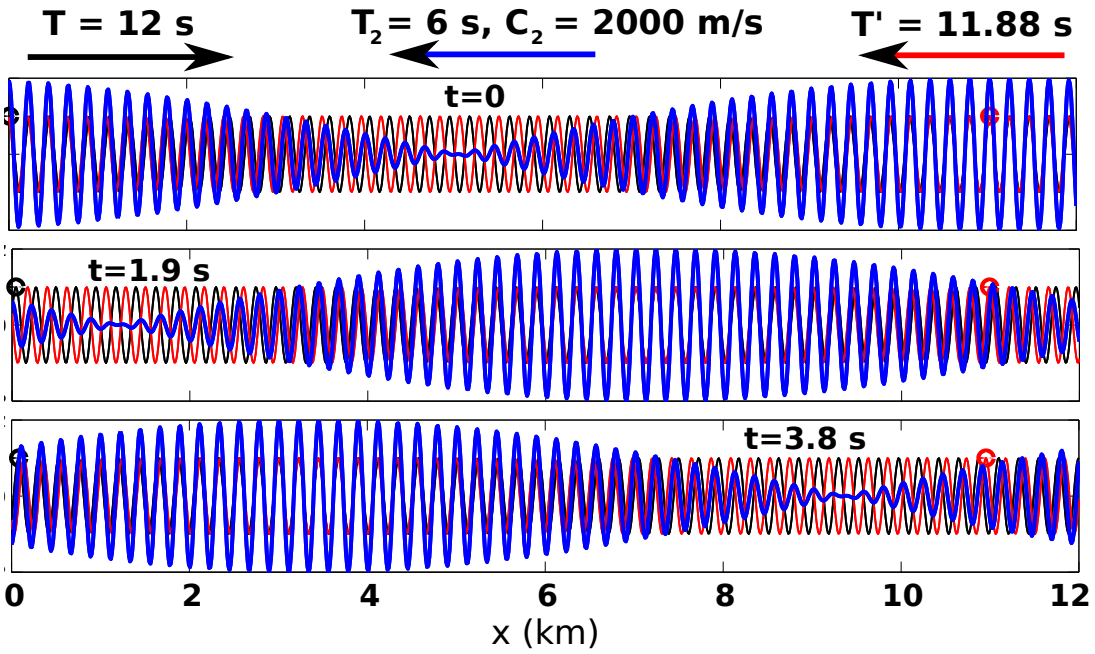

Figure 21.4: Two wave trains with slightly different periods and propagating in opposite directions in deep water interfere to form wave groups. The groups propagate in the same direction as the wave train which has the shorter wave periods. The red and black dots are attached to a crest of their monochromatic component, and these crests travel 100 times slower than the group.

in the water column. In reality, with compressibility we have to solve the equations of motion forced by this surface term, this is done in the following sections.

It is also interesting to consider the pressure at the bottom. Indeed, for finite values of kD the orbital velocity at the bottom induces a pressure oscillation given by the usual Bernoulli term, that is equal to $-(u^2+w^2)/2$, which is out of phase with the surface wave groups, whereas $\widehat{p}_2$ is in phase. As notes by Ardhuin and Herbers (2013), these two terms exactly cancel in the limit $kD \to 0$, which is clear from the incompressible solution for the bottom pressure given by Herbers and Guza (1991).

21.3.4 Sum for a continuous spectrum

In the limit of a continuous spectrum, $2\left|Z^+_{1,\mathbf{k}}\right|^2 \to E(k_x,k_y)\mathrm{d}k_x\mathrm{d}k_y$. The factor 2 is there because we use only positive frequencies (i.e. single-sided spectra), nameliy we gather the variance of the components with amplitudes $Z^+_{1,\mathbf{k}}$ and $Z^-_{1,-\mathbf{k}}$. Liekwise the spectrum of $\widehat{p}_2$ is,

$$F_{p2}(\mathbf{K},f_s) = 2\lim_{|d\mathbf{K}|\to 0, df_s\to 0}\frac{|\widehat{p}_2(\mathbf{K},f_s)|^2}{\mathrm{d}k_{2x}\mathrm{d}k_{2y}\mathrm{d}f_s}, \tag{21.18}$$

where $\widehat{p}_2(\mathbf{K},f_s)$ is the Fourier amplitude of $\widehat{p}_2$ with wavenumber vector $\mathbf{K}$ and frequency f_s. We now replace with eq. (21.17), and transform the ocean wave spectral density $E(k_x,k_y) = C_g E(f)/(2\pi k)$. Now using $f_s = 2f$, we get $\mathrm{d}k_x\mathrm{d}k_y/\mathrm{d}f_2 = \pi k/C_g \mathrm{d}\theta$ et il vient,

$$F_{p2}(\mathbf{K},f_s) \simeq 2\rho_w^2\sigma^4\left[\frac{1}{2}+\frac{3}{2\tanh^2(kD)}\right]^2\int_{k_x,k_y>0} E(k_x,k_y)E(-k_x+k_{2x},-k_y+k_{2y})\frac{\mathrm{d}k_x\mathrm{d}k_y}{\mathrm{d}f_s} \tag{21.19}$$

$$\simeq 2\rho_w^2 g^2 k^2\tanh^2(kh)\left[\frac{1}{2}+\frac{3}{2\tanh^2(kD)}\right]^2\int_{k_x,k_y>0} E(f,\theta)E(f,\theta+\pi)\frac{C_g^2\mathrm{d}k_x\mathrm{d}k_y}{k^2 4\pi^2\mathrm{d}f_s} \tag{21.20}$$

$$\simeq \rho_w^2 g^2\tanh^2(kD)\frac{kC_g}{2\pi}\left[\frac{1}{2}+\frac{3}{2\tanh^2(kD)}\right]^2\int_0^\pi E(f,\theta)E(f,\theta+\pi)\mathrm{d}\theta \tag{21.21}$$

$$\simeq \rho_w^2 g^2\tanh^2(kD) f_s\left(\frac{1}{4}+\frac{kD}{2\sinh(2kD)}\right)\left[\frac{1}{2}+\frac{3}{2\tanh^2(kD)}\right]^2\int_0^\pi E(f,\theta)E(f,\theta+\pi)\mathrm{d}\theta \tag{21.22}$$

In the limit of deep water ($kD \gg 1$), and writing the directional wave spectrum as $E(f,\theta) = E(f)M(f,\theta)$,

this becomes

$$F_{p2}(\mathbf{K} \simeq 0, f_s) = \rho_w^2 g^2 f_s E^2(f) I(f)/2, \tag{21.23}$$

where the 'overlap intergral' I was defined by Farrell and Munk (2008) as

$$I(f) = \int_0^{2\pi} M(f,\theta) M(f,\theta+\pi) \mathrm{d}\theta. \tag{21.24}$$

As a result, there are seismic waves generated at all frequencies, provided that some energy travels in opposite directions. This is also true for capillary waves, although in that case the dispersion relation and surface boundary conditions are different (Farrell and Munk, 2008). From an ocean wave perspective,K is so small compared to k that we can use $K = 0$. However, for the seismic waves, the magnitude and direction of K will determine the type of seismic wave and its direction. Indeed, $K = 0$ correspond to P-waves than travel along the vertical. Because the spectrum F_{p2} is nearly constant for seismic wavenumbers, all the different waves are actually generated at the same time from the same pressure force. In this sense, the wave-induced forcing is equivalent to an oscillating point force at the sea surface.

21.3.5 Free solutions: Rayleigh waves

Motion in the water layer

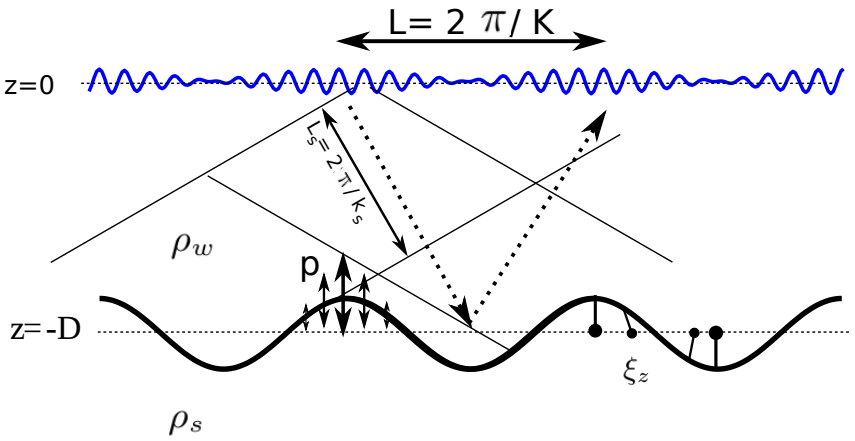

Figure 21.5: Schematic of wave group forcing acoustic waves in a water layer over a solid half-space. The horizontal wavenumber K is set by the forcing, whereas the true acoustic wavelength also involve the vertical component $L_s = 2\pi/k_s = 2\pi/\sqrt{K^2 + l_a^2} = \alpha_w/T$. The dashed arrows give the propagation direction of acoustic waves in the water with the thin solid lines representing the surface of equal phase. The superposition of up-going and down-going waves is a horizontally propagating mode. In practice the angle of propagation of sound waves in Rayleigh modes is less than 65 degrees, as shown in figure 21.7.

Our three equations for perturbations p', ϕ, and ρ_w' in the water (21.9)–(19.1) linearize as

$$-\alpha_w^2 \rho' + p' = 0 \tag{21.25}$$

$$\frac{\partial \rho'}{\partial t} + \frac{\partial \phi}{\partial z}\frac{\partial \rho_w}{\partial z} + \rho_w \nabla^2 \phi + \rho_w \frac{\partial^2 \phi}{\partial z^2} = 0 \tag{21.26}$$

$$\frac{1}{\rho_w} p' + gz + \frac{\partial \phi}{\partial t} = 0. \tag{21.27}$$

Boundary conditions, in the absence of forcing are $p = 0$ at the sea surface, and a coupling with the solid Earth by continuity of vertical velocity $w = \partial\phi/\partial z$, which is not zero, and stresses.

We can re-write (21.25)–(21.27) with ρ' replaced by p',

$$-\frac{\partial}{\partial t} p' + \rho_w \alpha_w^2 \left[\nabla^2 + \frac{\partial^2}{\partial z^2} + \frac{g}{\alpha_w^2}\frac{\partial}{\partial z}\right]\phi = 0 \tag{21.28}$$

$$\frac{1}{\rho_w} p' + gz + \frac{\partial}{\partial t}\phi = 0 \tag{21.29}$$

and finally, the combination of (21.28) and (21.29) removes p', giving a wave equation,

$$\left[\frac{\partial^2}{\partial t^2} + \alpha_w^2 \left(\nabla^2 + \frac{\partial^2}{\partial z^2} - \frac{g}{\alpha_w^2}\frac{\partial}{\partial z}\right)\right]\phi = 0 \tag{21.30}$$

For a monochromatic wave of phase $\Theta = Kx - \omega t$, the velocity potential is given by the real part of

$$\phi = C\mathrm{e}^{l_a(z+h)}\mathrm{e}^{\mathrm{i}\Theta}. \tag{21.31}$$

Replacing in eq. (21.29) gives a second order polynomial for the unknown l_a,

$$-\omega^2 + \alpha_w^2\left(-K^2 + l_a^2 - \frac{g}{\alpha_w^2}l_a\right) = 0 \tag{21.32}$$

with a solution

$$l_a = \frac{g}{2\alpha_w^2} \pm l. \tag{21.33}$$

The water motion is thus a superposition of two terms with the two possible signs,

$$l = \sqrt{\frac{\omega^2}{\alpha_w^2} - K^2 + \frac{g^2}{4\alpha_w^4}} \simeq \sqrt{\frac{\omega^2}{\alpha_w^2} - K^2} \tag{21.34}$$

giving

$$\phi = \mathrm{e}^{gz/2\alpha_w^2}\left(C\mathrm{e}^{il(z+h)} + D\mathrm{e}^{-il(z+h)}\right)\mathrm{e}^{\mathrm{i}\Theta} \tag{21.35}$$

In the ocean $\alpha_w \simeq 1500m/s$ and $z > -11000$ m, so that the term $gz/2\alpha_w$ varies between 0 et 0.02, and can be neglected for simplicity. For a supersonic forcing ($\omega/K > \alpha_w$) l is real and we get acoustic waves, whereas a sub-sonic forcing ($\omega/K < \alpha_w$) gives evanescent waves, decreasing exponential from the sea surface. These are acoustic-gravity modes.

Motion in the solid Earth

Treating the solid Earth as a homogenous medium with a compression velocity α_s and shear velocity β, given by the Lamé coefficients of the solid,

$$\alpha_s^2 = \frac{\lambda + 2\mu}{\rho_s}, \tag{21.36}$$

$$\beta^2 = \frac{\mu}{\rho_s}. \tag{21.37}$$

The elasticity equation gives Laplace's equation for the velocity potential ϕ_s and the stream function ψ. With the same phase as in the water, $\Theta = kx - \omega t$ a finite amplitude at $z \to -\infty$ gives solutions of the form

$$\phi_s = A\mathrm{e}^{m(z+h)}\mathrm{e}^{\mathrm{i}\Theta}, \tag{21.38}$$

$$\psi = B\mathrm{e}^{n(z+h)}\mathrm{e}^{\mathrm{i}\Theta}. \tag{21.39}$$

The vertical wavenumbers m and n are given by the generalized Bernoulli equation,

$$m = \frac{\mathrm{i}g}{2\alpha_s} + \sqrt{K^2 - \frac{\omega^2}{\alpha_s^2} - \frac{g^2}{4\alpha_s^2}} \simeq \sqrt{K^2 - \frac{\omega^2}{\alpha_s^2}} \quad \text{and} \quad n \simeq \sqrt{K^2 - \frac{\omega^2}{\beta^2}}, \tag{21.40}$$

where A and B are the two constant amplitudes of the velocity potential and streamfuction, that have units of m^2/s. These two unknowns are given by the boundary conditons.

Hence, the horizontal and vertical displacements are given by the real parts of

$$\xi_x = \left(KA\mathrm{e}^{m(z+h)} + \mathrm{i}nB\mathrm{e}^{n(z+h)}\right)\mathrm{e}^{\mathrm{i}\Theta}/\omega, \tag{21.41}$$

$$\xi_z = \left(-\mathrm{i}mA\mathrm{e}^{m(z+h)} + KB\mathrm{e}^{n(z+h)}\right)\mathrm{e}^{\mathrm{i}\Theta}/\omega \tag{21.42}$$

The first term is a compression wave with a velocity field $u_A = \partial\xi_x/\partial t = \partial\phi_s/\partial x$, avec $\phi_s = A\mathrm{e}^{m(z+h)}\mathrm{e}^{\mathrm{i}\Theta}$. The second term is a shear wave with a velocity field $u_B = \partial\xi_x/\partial t = -\partial\psi/\partial z$.

Coupling at the water-solid interface requires to express the stresses in the solid using Hooke's law, which states that the stress is linearly related to the strain,

$$\tau_{zz} = \lambda\left(\frac{\partial\xi_x}{\partial x} + \frac{\partial\xi_z}{\partial z}\right) + 2\mu\frac{\partial\xi_z}{\partial z}, \tag{21.43}$$

$$\tau_{xz} = \mu\left(\frac{\partial\xi_x}{\partial z} + \frac{\partial\xi_z}{\partial x}\right). \tag{21.44}$$

In our case we consider that the water freely slips over the solid, so that the shear stress at the bottom is $\tau_{xz} = 0$ at $z = -h$. Using (21.41)–(21.42) we get,

$$B = \frac{2\mathrm{i}Km}{n^2 + K^2}A. \tag{21.45}$$

This relationship is characteristic of Rayleigh waves.

Coupling of water and solid Earth and pseudo-Rayleigh waves

The boundary condtions $w_+ = w_-$ and $\tau_{zz} + p = 0$ give the following relations that couple the amplitudes A, C and D,

$$A(m - \frac{2K^2 m}{n^2 + K^2}) - \mathrm{i}lE + \mathrm{i}lF = 0, \tag{21.46}$$

$$A\frac{\mathrm{i}}{\omega}\left[-\rho_s m^2 \alpha_s^2 + \lambda K^2 + 4\mu \frac{K^2 mn}{n^2 + K^2}\right] - \mathrm{i}\omega\rho_w E - \mathrm{i}\omega\rho_w F = 0. \tag{21.47}$$

Replacing λ and μ by their expression in terms of α_s and β, this gives

$$A\frac{m\omega^2}{\omega^2 - 2K^2\beta^2} - \mathrm{i}lE + \mathrm{i}lF = 0, \tag{21.48}$$

$$A\frac{\mathrm{i}}{\omega\beta^2}\rho_s\left[-\frac{4\beta^4 K^2 mn}{\omega^2 - 2K^2\beta^2} + \left(\omega^2 - 2K^2\beta^2\right)\right] - \mathrm{i}\omega\rho_w E - \mathrm{i}\omega\rho_w F = 0 \tag{21.49}$$

The last unknown, ω is now given by the sea surface boundary condition. Without forcing, this is $p(z = \zeta) = 0 \simeq p(z = 0)$, and it gives,

$$E = B_2 \mathrm{e}^{-ilh}, \tag{21.50}$$

$$F = -B_2 \mathrm{e}^{ilh}, \tag{21.51}$$

and

$$\frac{m\omega^2}{\omega^2 - 2K^2\beta^2} A - 2il\cos(lh)B_2 = 0 \tag{21.52}$$

$$\frac{\mathrm{i}}{\omega\beta^2}\rho_s\left[-\frac{4\beta^4 K^2 mn}{\omega^2 - 2K^2\beta^2} + \left(\omega^2 - 2K^2\beta^2\right)\right] A - 2\omega\rho_w \sin(lh)_2 B = 0. \tag{21.53}$$

The determinant of this linear system is thus zero, which gives the dispersion relation first given by Stoneley (1926),

$$\tan(lh) = \frac{\rho_s}{\rho_w}\frac{l}{m} \times \frac{4\beta^4 K^2 mn - \left(\omega^2 - 2K^2\beta^2\right)^2}{\omega^4}. \tag{21.54}$$

We also have

$$B_2 = m\frac{(n^2 + K^2) - 2K^2}{(n^2 + K^2)\,(2il\cos(lh))} A = mi\frac{\omega^2}{(2K^2\beta^2 - \omega^2)2l\cos(lh)} A. \tag{21.55}$$

The dispersion relation (21.54) and motion are characteristic of Rayleigh waves, modified by a water layer. Because of this modification, these are usually called pseudo-Rayleigh waves.

The practical of the dispersion relation is complicated by the presence of multiple solutions that are associated with different modes,

Figure 21.6 shows how different values of K are possible due to the multiple branches of the tangent function.

The dispersion relation 21.54 is slightly different from that of Rayleigh waves without an ocean layer, which is

$$\beta^4 K^2 mn - \left(\omega^2 - 2K^2\beta^2\right)^2 = 0. \tag{21.56}$$

We also note that for large depths or short wavelengths ($lh > 3\pi/2$) there are several solutions that correspond to different modes, each with a distinct motion pattern in the water column, while the pattern in the crust remains similar. Figure 21.7 shows the phase speed that are between the sound speed and the shear wave speed. For a given mode, the higher the frequency, the slower the horizontal propagation which tends to the sound speed. The acoustic part in the water thus propagate at shallower angles, becoming horizontal in the limit of high frequency.

For high enough frequencies, the acoustic wavelength is much shorter than the water depth, and the variation in sound speed across the water layer can modify the propagation. In particular, nearly horizontal sound waves can be trapped in the SOFAR channel, and there can be a decoupling of the water layer and solid Earth.

The angle of the acoustic propagation in the water are plotted for $D = 5000$ m in figure 21.8, together with the vertical profiles of velocities in the water and crust. We note that the higher modes, with a lower K, penetrate deeper in the solid Earth.

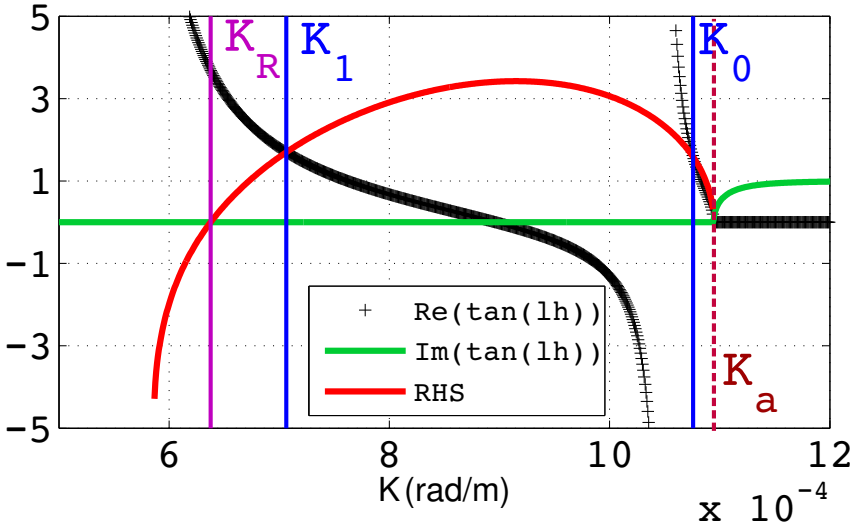

Figure 21.6: Real and imaginary parts of the left hand side and real part of the right hand side of eq. 21.54. This calculation was performed for a water depth $D = 5000$ m, with a sound speed in water of $\alpha_w = 1500$ m/s, a shear wave speed of $\beta = 2800$m/s and water and crust densities of 1000 et 2500 kg/m^3. The chosen seismic frequency is $f_s = 0.263$ Hz, corresponding to a non-dimensional depth $f_s h/\alpha_w = 0.88$. The determinant of the system is zero for three values: one acoustic mode K_a for which $l = 0$ (horizontal propagation) and two seismic Rayleigh modes with wavenumbers K_0 and K_1. For non-dimensional frequencies below 0.34, only the 0 mode exists, and as the frequency increases, K_0 increases and new branches of $\tan(lh)$ appear (in black) giving higher modes, that have a lower value of K. Besides, the zero of the right hand side (in red) gives the wavenumber of Rayleigh waves K_R in the absence of a water layer.

Displacements, pressure, velocity and energy in Rayleigh waves

To finish wth this description of Rayleigh waves, we can express all the wave-related quantities in terms of the ground displacement amplitude at the top of the crust δ,

$$A = \frac{\omega^2 - 2k^2\beta^2}{m\omega^2}\delta \tag{21.57}$$

$$B = \frac{2\mathrm{i}km}{n^2 + K^2}A \tag{21.58}$$

$$B_2 = \frac{\mathrm{i}\omega}{2l\cos(lD)}\delta \tag{21.59}$$

$$\xi_z(z=-D) = \delta\cos\Theta \tag{21.60}$$

$$\phi_s = A\mathrm{e}^{m(z+D)}\mathrm{e}^{\mathrm{i}\Theta} \tag{21.61}$$

$$\psi = B\mathrm{e}^{n(z+D)}\mathrm{e}^{\mathrm{i}\Theta} \tag{21.62}$$

$$\phi = 2\mathrm{i}lB_2\sin(lz)\mathrm{e}^{\mathrm{i}\Theta} \tag{21.63}$$

$$p'(z) = \mathcal{R}\left[\mathrm{i}\rho_w\omega\phi\right] = -\delta\rho_w\omega^2\frac{\sin(lz)}{l\cos(lD)}\cos\Theta. \tag{21.64}$$

From these we can evaluate the seismic wave energy per unit horizontal surface E_s, taking twice the kinetic energy in both water and solid Earth,

$$E_s = \rho_w\int_{-D}^{0}\overline{(u^2+w^2)}\mathrm{d}z + \rho_s\int_{-\infty}^{-D}\overline{(u^2+w^2)}\mathrm{d}z \tag{21.65}$$

$$= T_{E\delta}(D)\frac{\delta^2}{2} \quad \text{with} \tag{21.66}$$

$$T_{E\delta}(D) = \rho_s\left[\frac{(KB/A+m)^2}{2m} + \frac{(nB/A+K)^2}{2n}\right]\left(\frac{A}{\delta}\right)^2 + \rho_w\left\{l^2\left[2D + sin(2lD)/l\right] + K^2\left[2D - sin(2lD)/l\right]\right\}\left(\frac{B_2}{\delta}\right)^2 \tag{21.67}$$

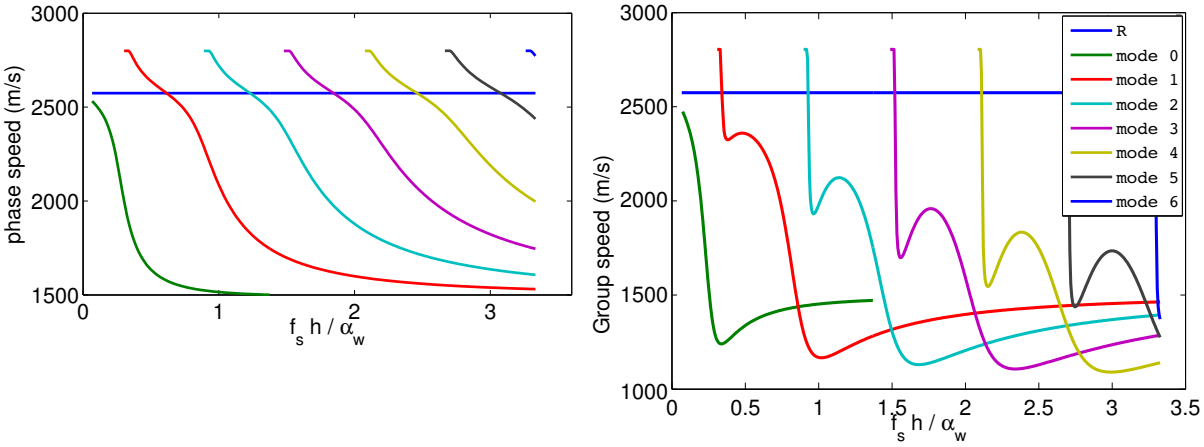

Figure 21.7: Phase speeds and group speeds for Rayleigh waves in the presence of a water layer. Calculations have been made with a water depth $D = 5000$ m, a sound speed in the water $\alpha_w = 1500$ m/s, a shear wave speed of $\beta = 2800$m/s and water and crust densities of 1000 et 2500 kg/m^3. Without the water layer the values are given by the blue line: in that case the Rayleigh waves are not dispersive. We have used seismic frequencies from 0 to 1 Hz, the latter value corresponding to $f_s h/\alpha_w = 3.4$.

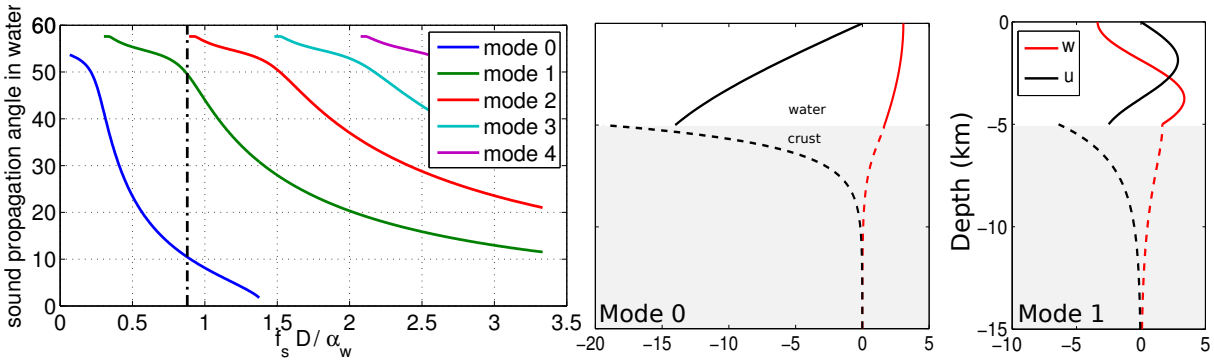

Figure 21.8: (a) Angle of propagation, relative to the hoizontal, of the two acoustic waves that combine to make acoustic modes in the water. The vertical profile of the velocity amplitude for mode 0 and 1 and $f_s D/\alpha_w = 0.88$ are shown in the right panels. For modes 1 and higher, the vertical velocity is zero at the nodes of the vertical standing acoustic wave. The zero-pressure level correspond to the zero-velocity levels, in particular at the surface.

21.4 Forced solutions: Acoustic-Gravity, Rayleigh and body waves

21.4.1 Matrix inversion

Let us now consider what happens with the ocean wave forcing. The surface boundary condition is now $p' = P\mathrm{e}^{\mathrm{i}(Kx-\omega t)}$ at $z = 0$, and $p' = -\rho_w \partial\phi_2/\partial t + P_b \mathrm{e}^{\mathrm{i}(Kx-\omega t)}$ at the bottom. This is now analog to the problem of wave generation by the wind, treated in chapter 22.

Boundary conditions are now, for $kD \gg 1$, and neglect P_b,

$$E\mathrm{e}^{ilh} + F\mathrm{e}^{-ilh} = \frac{\mathrm{i}P}{\rho_w \omega} \tag{21.68}$$

$$\frac{m\omega^2}{\omega^2 - 2k^2\beta^2} A - \mathrm{i}lE + \mathrm{i}lF = 0 \tag{21.69}$$

$$\frac{-\rho_s}{\omega^2 \rho_w}\left[-\frac{4\beta^4 k^2 mn}{\omega^2 - 2k^2\beta^2} + \left(\omega^2 - 2k^2\beta^2\right)\right] A + E + F = 0 \tag{21.70}$$

or, in matrix form,

$$M \begin{pmatrix} A \\ E \\ F \end{pmatrix} = \frac{\mathrm{i}}{\rho_w \omega} \begin{pmatrix} P \\ 0 \\ 0 \end{pmatrix} \tag{21.71}$$

The solution of this system of equation is the sum of a the solutions to the 'homogenous system' (without forcing) and one particular solution with the forcing. That solution can be written using the determinant and co-factors od the matrix [1] M giving

$$A = -2liP/\det M \tag{21.74}$$

with

$$\det M = \frac{2}{\omega\left(\omega^2 - 2K^2\beta^2\right)}\left\{l\rho_s\cos(lD)\left[4\beta^4k^2mn - \left(\omega^2 - 2K^2\beta^2\right)^2\right] - \rho_w m\sin(lD)\omega^4\right\}. \tag{21.75}$$

21.4.2 Four different types of waves and equivalent point force

The amplitude of the seismic displacement as a function of the sea surface pressure amplitude in the form of a gain factor $\delta = G(\omega)P(\omega)$, with the gain

$$G = \frac{2lm(K^2 - n^2)}{(n^2 + K^2)\omega\det M}. \tag{21.76}$$

Contrary to the case without forcing, we can now have waves at all wavenumbers and frequencies, but their amplitude GP varies as shown in figure 21.9. We can distinguish 4 different domains

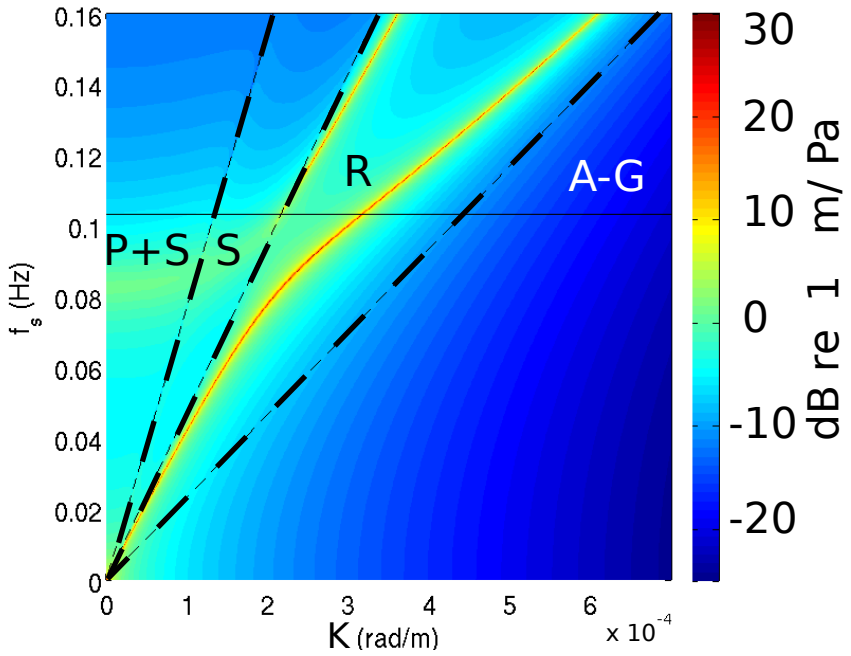

Figure 21.9: Magnitude of the transfer function $G(K, f_s)$ illustrating the singularities along the dispersion relations of the free Rayleigh modes with wavenumbers $K = K_n(f_s)$, that correspond to $\det(M) = 0$. The oblique dashed lines correspond to phase speeds equal to α_c, β, and α_w, and separate the four domains body waves (P+S), mixed body and evanescent waves (S), Rayleigh waves (R) and acoustic-gravity modes (A-G).

- acoustic-gravity waves (AG) for $K/\omega < \alpha_w$: for a monochromatic forcing, these waves vanish exponentially with depth
- free and forced Rayleigh waves for $\alpha_w < K/\omega < \beta$: the free waves are the ones with $\omega = \omega_r$
- evanescent P waves and SV body waves for $\alpha_s < K/\omega < \beta$: the SV propagate down in the solid Earth
- P and SV body waves for $\alpha_s > K/\omega$: both P and SV propagate down in the solid Earth.

[1] For a linear system of three equations

$$\begin{pmatrix} a & b & c \\ d & e & f \\ g & h & i \end{pmatrix}\begin{pmatrix} A \\ E \\ F \end{pmatrix} = \begin{pmatrix} 1 \\ 0 \\ 0 \end{pmatrix}, \tag{21.72}$$

the determinant is

$$\det M = aei + bfg + cdh - ceg - fha - ibd \tag{21.73}$$

and the first co-factor is $ei - fh$ so that $A = (ei - fh)/\det M$, and likewise $E = (fg - di)/\det M$ and $F = (dh - eg)/\det M$.

Ocean waves are random and have a spectrum with a finite width which is typically much wider than the K's of Rayleigh waves, so that waves at a given location excite, simultaneously, a broad range of wave numbers on the wavenumber plane, ans illustrated by figure 21.10. The wave-induced pressure spectrum $F_p(K_x, K_y, f_s)$

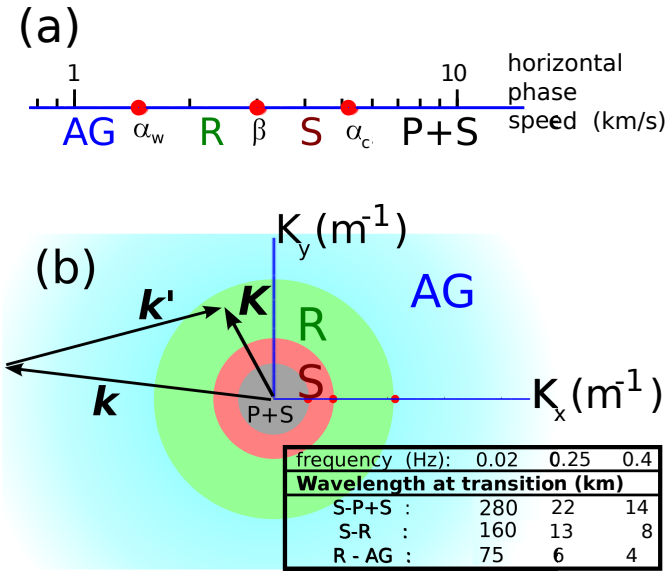

Figure 21.10: (a) The vertical evanescent or propagating nature of the noise field in the solid and liquid layers is defined by the horizontal phase speeds relative to the distinct values of the sound speed in the ocean (α_w), and the shear (β) and compression (α_c) speeds in the crust. From slow to fast, there are the acoustic-gravity (AG) domain, the Rayleigh (R) wave domain, and two body wave domains (S only, and P and S together) (b) For any fixed frequency, the four domains correspond to 4 concentric regions in the wavenumber plane. For three selected noise frequencies generated by OSGW in the infragravity, dominant and high frequency ranges of the forcing wave field, the limiting wavelengths between the four domains are indicated, using $\alpha_w = 1.5$ km/s, $\beta = 3.2$ km/s, $\alpha_c = 5.54$ km/s. One example of interaction is shown with two gravity wave modes that interact to generate a Rayleigh wave (black vectors, not to scale, k and k' should be much larger).

waries smoothly around $K = 0$ and is roughly constant for seismic wavenumbers. Thus, it is simimar to a white spectrum, corresponding to the spectrum of delta function in horizontal (x, y) space. Hence, in terms of the power spectrum of the radiated waves, the ocean wavemotion is equivalent to a vertical oscillating force pushing on a single point of the sea surface with a root mean square value,

$$F_{\rm rms} = 2\pi\sqrt{F_p(K_x = 0, K_y = 0, f_s) dA df_s}, \tag{21.77}$$

where dA is the area over which the forcing is distributed and df_s is the frequency interval of interest. This equivalence is easy to show by computing the spectrum in K_x, Ky of such a force, either directly as a delta function or as a pressure over a small square and taking the size of that square to zero. The spectrum of that force is equal to $F_p(K_x = 0, K_y = 0, f_s)$ for all values of K_x and K_y, unlique the true effect of waves which becomes zero for large K. Also, compared to this point force, the phases of the different seismic modes are independant with real waves whereas they are identical with the point force. As a result, correlations of synthetic traces from a model forced by such point forces may be artificially high, where as power spectral densities should be alright. Such vertical forces were used by Gualtieri et al. (2013) to model the seismic response, which contains all four types of waves, AG, R, P and S. We will now discuss these 4 types of waves.

21.4.3 Rayleigh waves

For a given wavenumber K, there are one or several values of ω that gives a zero determinant, for which G is infinite. Let us call ω_r one of these values, ω_r and K are related by the Rayleigh wave dispersion relation (21.54). In practice the wave forcing is continuous across frequencies and wavenumbers and characterized by a power spectral density $F_p(K_x, K_y, f)$, and in the case of the double-frequency source it is $F_{p2}(K_x, K_y, f)$ given by eq. (21.22). It is thus possible to find the power spectrum of the ground displacement by integrating in frequency across these singularities,

$$F_\delta(K_x, K_y) = \int_0^\infty |G|^2 F_{p3D}(K_x, K_y, \omega) {\rm d}\omega \tag{21.78}$$

or in terms of seismic energy

$$F_E(K_x, K_y) = T_{E\delta}(D) F_\delta(K_x, K_y) \tag{21.79}$$

with $T_{E\delta}(D)$ given by (21.67).

Where the singularities in G can be expanded at $G = G'(\omega)/(\omega^2 - \omega_r^2)$. Following Hasselmann (1962, see also chapter 20), it is easy to prove that the response of a harmonic oscillator forced by a continuous spectrum of density $F_p K_x, K_y, \omega$ with a singularity at $\omega = \omega_r$ integrates to a finite spectral density that grows linearly in time, giving a rate of change,

$$\frac{\partial F_\delta(k_x, k_y)}{\partial t} = S_{DF}(k_x, k_y) = \frac{\pi |G'|^2}{2\omega_r^2} F_p(k_x, k_y, \omega_r). \tag{21.80}$$

In practice we are often in a situation where the wave field changes slowly at the time scale of seismic propagation. In this quasi-stationary situation, assuming seismic energy conservation along rays, we have an energy balance similar to that of ocean waves, with conservation of the spectral densities in $K-$space,

$$\mathbf{U} \cdot \boldsymbol{\nabla} F_E(K_x, K_y) = T_{E\delta}(h) S_{DF}(k_x, k_y), \tag{21.81}$$

where U is the group speed of seismic waves. The seismic spectrum at point $s = 0$ is given by the integral of sources along propagation rays with an along-ray distance s. Introducing the dissipation of seismic waves by anelastic processes, represented by a non-dimensional factor Q, we have

$$F_{\delta,0}(K_x, K_y)(K_x(0), K_y(0)) = \int_O^\infty \frac{T_{E\delta}(s)}{T_{E\delta}(0)} \frac{S_{DF}(K_s(s), K_y(s))}{U(s)} \exp\left[- \int_0^{s'} \frac{\omega}{U(s')Q(s')} \mathrm{d}s' \right] \mathrm{d}s \tag{21.82}$$

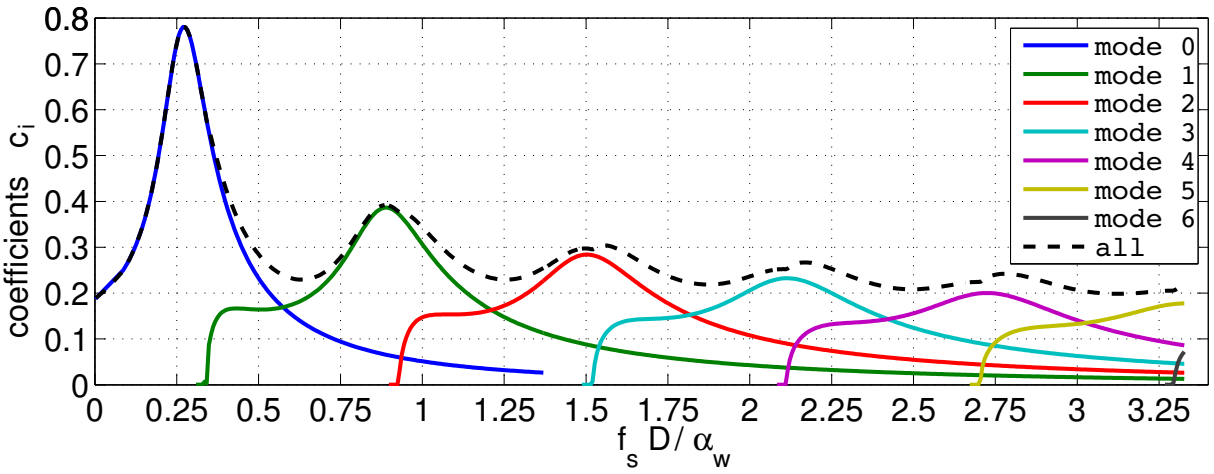

Figure 21.11: Non-dimensional coefficients c_i and $\widetilde{C}$. We note that the peaks of modes $i = 0$ and $i = 1$ occur for depths D that are close to but slightly larger than D $0.25 + i/2$ the acoustic wavelength, just like the resonant modes of an oran pipe. In fact c_i is maximum for a depth that is exactly $0.25 + i/2$ the *vertical* wavelength: because the propagation direction is oblique in the water, what is important for a maximum c_i is the constructive interference of these waves that reflect on the bottom and surface. This figure was drawn for $\alpha_w = 1500$ m s^{-1} and $\beta = 2800$ m s^{-1}. The peak of c_0 is higher for larger values of β/α_w, which is similar to the impedance ratio of the bottom that defines the reflection of waves at the bottom. For example, changing β to 3200 m s^{-1}, the maximum value of c_0 is 1.03.

It is more convenient to work in azimuth and frequency because frequency is conserved during propagation. For the Rayleigh mode number i we have

$$F_{\delta,0}(\omega, \theta_s) = \frac{K(0)}{U(0)} F_{\delta,0}(K_x(0), K_y(0)). \tag{21.83}$$

To simplify our equations we will now assume that Q is independent of the distance along the ray s, and we get

$$F_{\delta,0}(\omega, \theta_s) = \int_O^\infty \frac{S_{DF}(\omega)}{U(s)} \exp\left[-\frac{\omega}{Q} t(s) \right] \mathrm{d}s \tag{21.84}$$

where $t(s)$ is the travel time (propagation time) and

$$S_{DF}(\omega) = \frac{k(0)}{U(0)} \frac{T_{E\delta}(s)}{T_{E\delta}(0)} \frac{S_{DF}(k_x, k_y)}{U(s)}. \tag{21.85}$$

This source is a source of the power spectral density of the vertical elevation variance at point 0, per unit propagation length along a seismic ray. It thus has units of distance times time (m s).

Equations are more simple when this source is written per unit propagation distance

$$S_{DF}(\omega) = \frac{K(0)U(s)}{U(0)K(s)}\frac{T_{E\delta}(s)}{T_{E\delta}(0)}\frac{K(s)S_{DF}(K_x,K_y)}{U^2(s)} \tag{21.86}$$

$$= \frac{K(0)U(s)}{U(0)K(s)}\frac{T_{E\delta}(s)}{T_{E\delta}(0)}\frac{2\pi\omega c_i^2}{\beta^5\rho_s^2}F_{p3D}(K_x,K_y,\omega) \tag{21.87}$$

where c_i is a non-dimensional coefficent that is a function of the non-dimensional depth $\omega D/\alpha_w$ and the seismic mode index i,

$$c_i = \sqrt{\frac{\beta^5\rho_s^2 k_i}{U_i^2 2\pi\omega}\frac{\pi\left|G_i'\right|^2}{2\omega^2}}. \tag{21.88}$$

Going to an extreme simplification, we will assume that U and K are independant of i and D. The seismic source is thus of the order of

$$S_{DF}(f_s) \simeq \frac{2\pi\omega\widetilde{C}^2}{\beta^5\rho_s^2}F_{p3D}(k_x,k_y,f_s). \tag{21.89}$$

where $\widetilde{C}$ combines all the c_i values

$$\widetilde{C}^2 = \sum_{i=0}^{\infty} c_i^2. \tag{21.90}$$

The values of c_i are obtained by finding the roots of the dispersion relation and using eq. (21.88). This gives values such as given in figure (21.11). When combining all modes the coefficient $\widetilde{C}$ varies with the ration of the vertical acoustic wavelength and the water depth D.

21.4.4 body waves

A first theory of body wave generation by ocean waves was proposed by Vinnik (1973), who found that in some regions far from the ocean, the recorded microseism signals were dominated by body waves and not by surface Rayleigh waves. Since that time, many observations of body waves have been performed (e.g. Zhang et al., 2010; Obrebski et al., 2013). The theory of Vinnik did not include the important effect of the water layer. This was corrected by Ardhuin and Herbers (2013) who simply applied the Hasselmann (1963) theory. This theory can explain both P and SV waves, but not the transversally polarized SH waves observed by Nishida and Takagi (2016), which probably require some bottom slopes or mode conversion. The following theoretical expression for the spectrum of P waves was also derived by Gualtieri et al. (2014), and a first quantitative verification was performed by Farra et al. (2016).

In the case of body waves, for $K/(2\pi f_s) > \beta$, there are no singularities and thus the spectrum of the ground displacement is directly given by,

$$F_{\delta,P}(f_s) = f_s E^2(f) I(f)\frac{\rho_w^2 g^2}{\rho_s^2\beta_s^4}c_P^2 \tag{21.91}$$

with a non-dimensional coefficient c_P,

$$c_P^2 = 2\pi\int_0^{\omega_s/\alpha_c}\frac{4l^2m^2\rho_s^2\beta_s^4}{\omega_s^2\det^2(M)}K\mathrm{d}K. \tag{21.92}$$

A similar expression can be written for S waves, and both are illustrated in figure 21.12,

$$F_{\delta,S}(f_s) = f_s E^2(f) I(f)\frac{\rho_w^2 g^2}{\rho_s^2\beta_s^4}c_S^2. \tag{21.93}$$

However, in the range of wavenumbers where S waves exist, $k < \omega_s/\beta$, there can also be evanescent P waves, and the system can approach the singularity for $\omega_s = \omega_{s,j}$ and $k = \omega_s/\beta$. We evaluated numerically the coefficient

$$c_S^2 = 2\pi\int_0^{\omega_s/\beta}\frac{4l^2m^2k^2\rho_s^2\beta_s^4}{\omega_s^2(n^2+k^2)\det^2(M)}K\mathrm{d}K. \tag{21.94}$$

It is striking that the maxima of the coefficients c_P and c_S are much more pronounced that that of c_i for Rayleigh waves,shown in figure 21.11. This is probably due the fact that, in the case of P and S waves, the acoustic waves in the water are propagating closer to the vertical, with a narrow range of angles. As a result, the spatial distribution of sources of body waves is much more constrained by the water depth, and should focus on smaller regions (Obrebski et al., 2013).

For the estimation of the spectrum recorded outside of a source area, it is more convenient to express the local seismic source as a function of the horizontal propagation angle θ, and the vertical take-off angle φ. For P waves, this gives,

$$F_{\delta,P}(f_s,\theta,\varphi) = f_s E^2(f) I(f)\frac{1}{\rho_s^2\beta_s^4}c_{P,\varphi}^2\sin\varphi \tag{21.95}$$

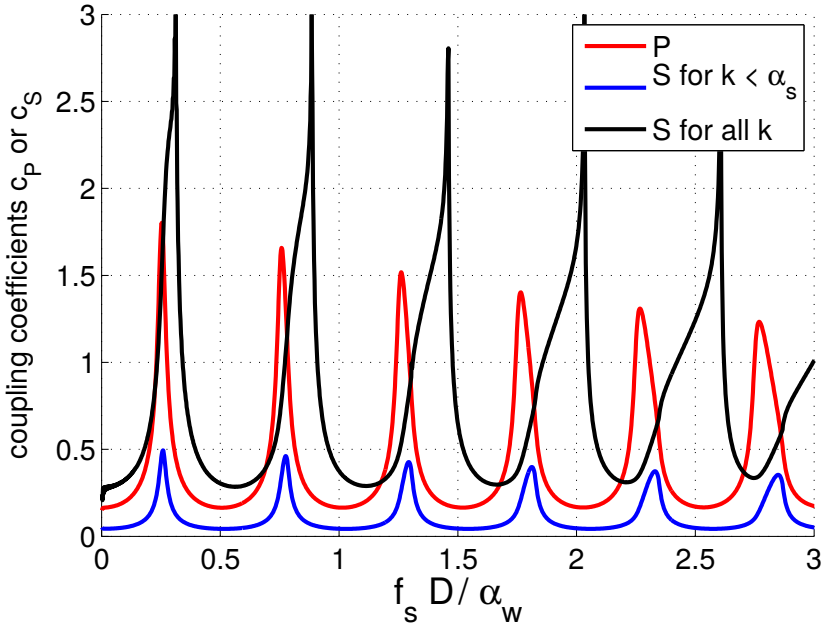

Figure 21.12: Non-dimensionless coefficients c_P and c_S that amplify the wave-induced pressure into ground displacement associated with P and S waves.

with the non-dimensional coefficient $c_{P,\varphi}$ defined by

$$c^2_{P,\varphi} = \frac{4l^2m^2\rho_s^2\beta_s^4}{\omega_s\alpha_c \det^2(M)}\frac{\partial K}{\partial\varphi}, \tag{21.96}$$

which is the normalized source per unit solid angle Ω, so that the average over the half space of downward directions Ω^- is

$$c_P^2 = \int_0^{2\pi}\int_0^{\pi/2} c^2_{P,\varphi}\sin\varphi \mathrm{d}\varphi\mathrm{d}\theta = \int_{\Omega^-} c^2_{P,\varphi}\mathrm{d}\Omega \tag{21.97}$$

as defined by eq. (21.92).

It is noteworthy that the distribution of the P-wave energy with the take-off angle is very close to the one given by a small disk pushing at the top of a uniform half space, as given by Miller and Pursey (1955) and used by Vinnik (1973), although it also varies with the non-dimensional water depth $f_s h/\alpha_w$. The only missing item in the work by Vinnik (1973) is the very strong amplification of the motion for resonant frequencies associated with the water layer. Due to the large impedance contrast at the water-crust interface the relative amplification of P waves is one order of magnitude stronger than for Rayleigh waves. We thus expect a much tighter correspondence of the strong seismic noise sources with the water depths that correspond to a maximum amplification.

Ardhuin and Herbers (2013) estimated that P waves will dominate the signal at large distances from the source. The exact location where P-wave levels overtakes Rayleigh-wave levels depends on the relative attenuation of the two types of waves. With a realistic $Q = 2000$ for the P waves, and $Q = 400$ for the Rayleigh waves, figure 21.14 shows that it occurs at an epicentric angle of $\Delta \simeq 40^\circ$, which is a distance of 4400 km, consistent with the observations reported by Vinnik (1973) using Kazakhstan array data.

21.4.5 acoustic-gravity waves

At the other end of the scale of forcing speeds, for $K/(2\pi f_s) < \alpha_w$, the response in the acoustic-gravity regime is also given by the local forcing.

In order to illustrate the different types of solutions, it is interesting to evaluate the solution for an unbounded ocean, in which sound waves are radiated from the surface only. The velocity field and associated pressure fluctuations are

$$\phi_2 = \frac{1}{\rho_w}\int \frac{\mathrm{i}\omega_s \widehat{p}_2(\mathbf{K},f_s)}{-\omega_s^2+\mathrm{i}gl}\mathrm{e}^{\mathrm{i}[-lz+\Theta(\mathbf{k},\mathbf{k}',s,s')]}\mathrm{d}\mathbf{K}\mathrm{d}f_s \tag{21.98}$$

$$p_2 = \int \frac{\widehat{p}_2(\mathbf{K},f_s)}{1-\mathrm{i}gl/\omega_s^2}\mathrm{e}^{\mathrm{i}[-lz+\Theta(\mathbf{k},\mathbf{k}',s,s')]}\mathrm{d}\mathbf{K}\mathrm{d}f_s \tag{21.99}$$

where p_2 has been obtained using the linearized version of eq. (19.1). The measured pressure signal is the sum of the linear pressure p_1, the second-order wave pressure p_2 given by eq. (21.99), and the Bernoulli correction

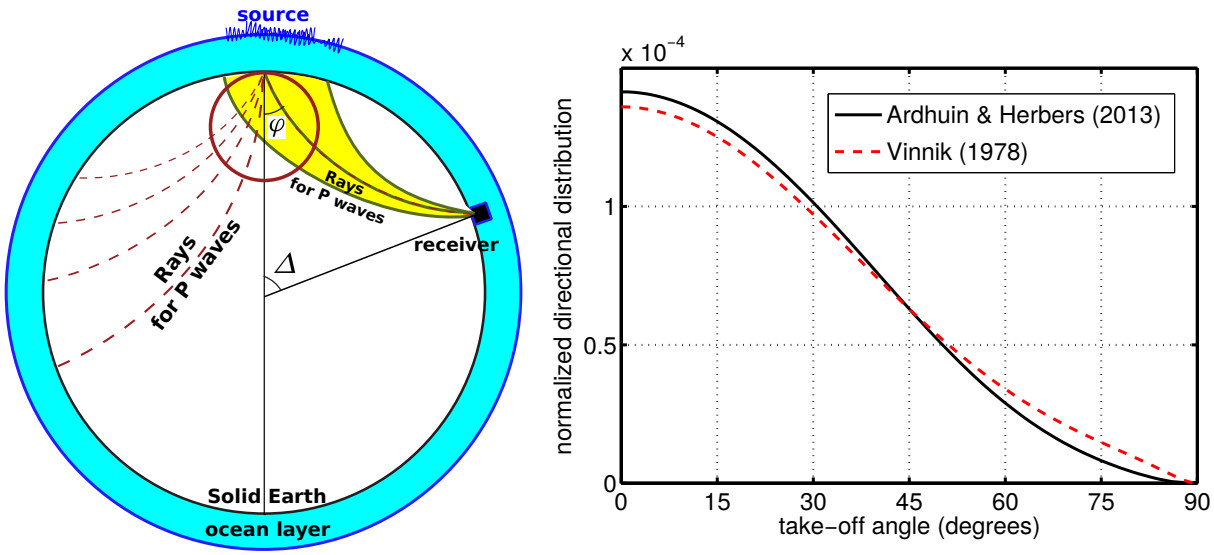

Figure 21.13: Left: schematic of body wave propagation and definitions of take-off angle φ and epicentric angle Δ. Right: Dimensionless coefficients $c_{P,\varphi}$ that amplify the wave-induced pressure into ground displacement. The maximum for a zero take-off angle corresponds to vertically propagating compression waves, and the compression waves that propagate along the crust have a vanishing amplitude.

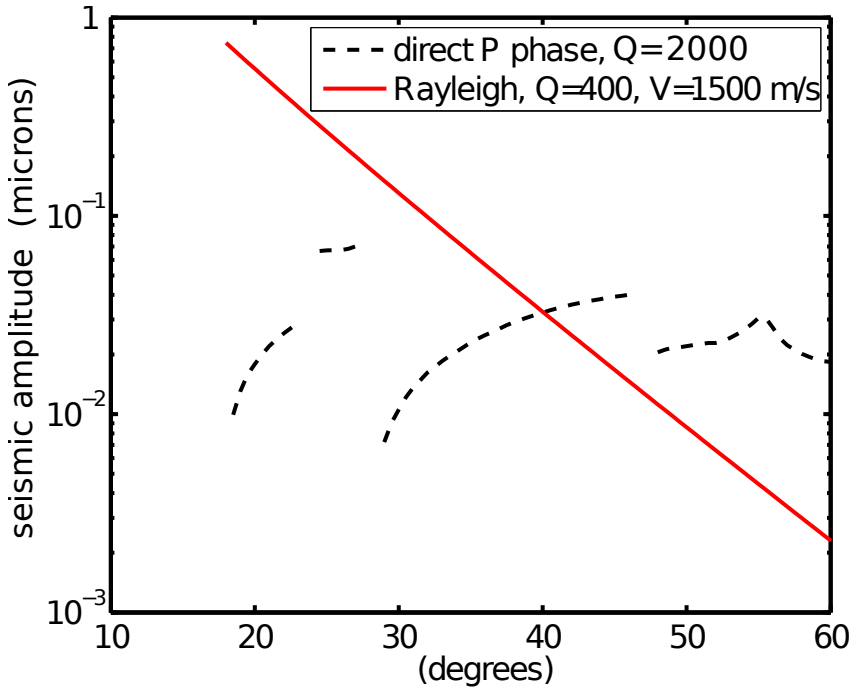

Figure 21.14: Estimates of the rms vertical ground displacement associated with Rayleigh or P waves, as a function of the epicentric angle Δ, for a source of intensity $\int F_{p2,\mathrm{surf}}(\mathbf{K}=0,f)\mathrm{d}f = 4.2\times10^4$ hPa^2 m^2 over a 330 by 330 km square, assuming an attenuation factor $Q = 2000$ for the P waves (Pasyanos et al., 2009), with travel times given by the ak135 reference Earth model (Snoke, 2009).

$p_{2,B}$ given by

$$p_{2,B}(z) = \rho_w \sum_{\mathbf{k},s,\mathbf{k}',s'} D_{pb}\left(\mathbf{k},s,\mathbf{k}',s',z\right) Z^{s}_{1,\mathbf{k}} Z^{s'}_{1,\mathbf{k}'} \mathrm{e}^{\mathrm{i}\Theta(\mathbf{k},\mathbf{k}',s,s')}. \tag{21.100}$$

We note that $p_{2,\mathrm{bot}}$ defined in eq. (21.14) is equal to $p_{2,B}(z=-h)$.

We shall neglect $g|l|/\omega_s^2$, which is bounded by the ratio between the deep water gravity and sound speeds, which is less than 0.1 for wave periods less than 180 s. We express the velocity potential as a sum of propagating (acoustic, l real) and evanescent (acoustic-gravity, l imaginary) modes,

$$\phi_2 = \phi_{2,p} + \phi_{2,e}. \tag{21.101}$$

We get the frequency spectrum of the propagating modes by integrating over the inner regions of the wavenumber space (labelled P+S, S and R in figure 21.10),

$$F_{p2,p}(f_s) = \int_{K<\omega_s/\alpha_w} F_{p2,\mathrm{surf}}(\mathbf{K},f_s)\mathrm{d}\mathbf{K}. \tag{21.102}$$

For this range of wavenumbers $|k-k'| < K < \omega_s/\alpha_w$, and using the relations $\omega_s \simeq 4\pi f$ and, (for small $|f-f'|$), $|k-k'| \simeq 2\pi|f-f'|/C_g \simeq 8\pi^2 f|f-f'|$, we obtain an upper bound for the frequency difference $|f-f'| < g/(2\pi\alpha_w)$ which is close to= 0.001 Hz. Typical ocean wave spectra have a relative frequency half-width σ_f/f that is between 0.03 for swells and and 0.07 for wind-seas (Hasselmann et al., 1973), so that $E(f) \simeq E(f')$ is a good approximation for the interactions that drive long wavelength pressure fluctuations.

The wave spectrum is thus broad enough for us to evaluate $F_{p2,\mathrm{surf}}$ at $K=0$ using eq. (**??**), and take it out of the integral in eq. (21.102). The acoustic spectrum simplifies to

$$F_{p2,p}(f_s) = \frac{\pi\omega_s^2}{\alpha_w^2}\rho_w^2 g^2 f_s E^2(f) I(f). \tag{21.103}$$

This is identical to the expression given by Lloyd (1981).

Gravity noise in an unbounded ocean

The pressure associated with acoustic-gravity modes is the other part of the integral in (21.102), for $K > \omega_s/\alpha_w$. The imaginary wave number l gives a vertical attenuation of the power spectrum by a factor $\mathrm{e}^{-2|l|z}$. With that attenuation we may, for large enough depths, assume that only modes with $K \ll k$ contribute to the result, so that we may take $F_{p2,\mathrm{surf}}(\mathbf{K},f_s) \simeq F_{p2,\mathrm{surf}}(\mathbf{K}=0,f_s)$, and take it out of the integrand. This approximation is valid only up to a maximum wave number $K_{\max}$ that is a small fraction of k, $K_{\max} = \epsilon k$. For numerical applications we used $\epsilon = 0.2$.

With this approximation we have,

$$\begin{aligned} F_{p2,e}(f_s,z) &= F_{p2,\mathrm{surf}}(\mathbf{K}=0,f_s)2\pi \int_{\omega_s/\alpha_w}^{K_{\max}} K\mathrm{e}^{2|l|z}\mathrm{d}K \\ &= F_{p2,\mathrm{surf}}(\mathbf{K}=0,f_s)2\pi \int_{0}^{K_{\max}} |l|\mathrm{e}^{2|l|z}\mathrm{d}|l| \\ &= \frac{\pi}{2z^2}\rho_w^2 g^2 f_s \left[1-\mathrm{e}^{2zK_{\max}}\right] E^2(f) I(f) \end{aligned} \tag{21.104}$$

A previous investigation by Cox and Jacobs (1989) included an extra factor $(1+zK_{\max})$ in front of the exponential term $\mathrm{e}^{2zK_{\max}}$, because they neglected compressibility effects. That term , however, is negligible in the upper part of the water column, and their observations collected within 100 to 290 m of the surface in 4000 m depth, are thus not affected by this small compressibility correction.

As shown in figure 21.15, the oceanic pressure signals can be dominated by linear gravity waves down to depths of a few hundred meters. When looking at the double frequency band, linear waves may only dominate in the top 100 m. At these frequencies, the acoustic-gravity modes have the most important contribution between about 100 to 500 m, provided that $E^2(f)I(f)$ is large enough. Propagating modes should dominate only beyond about 1000 m in the case of an unbounded ocean, or only 300 m, when accounting for the reverberation in a finite depth ocean, assuming a typical tenfold amplification for a sea floor with realistic elastic properties[2]. These depths will be reduced in the case of surface gravity waves with periods shorter than the 15 s swells example shown in figure 21.15.

[2]This amplification depends not only on the impedance ratio of the water and crust, which defines the amplification coefficients c_j derived below, but also on the seismic attenuation coefficient Q, which is discussed in section 4. Realistic calculations following Ardhuin et al. (2011a) typically give a factor 10 to 20 amplification of the sound in the water column due to the bottom elasticity.

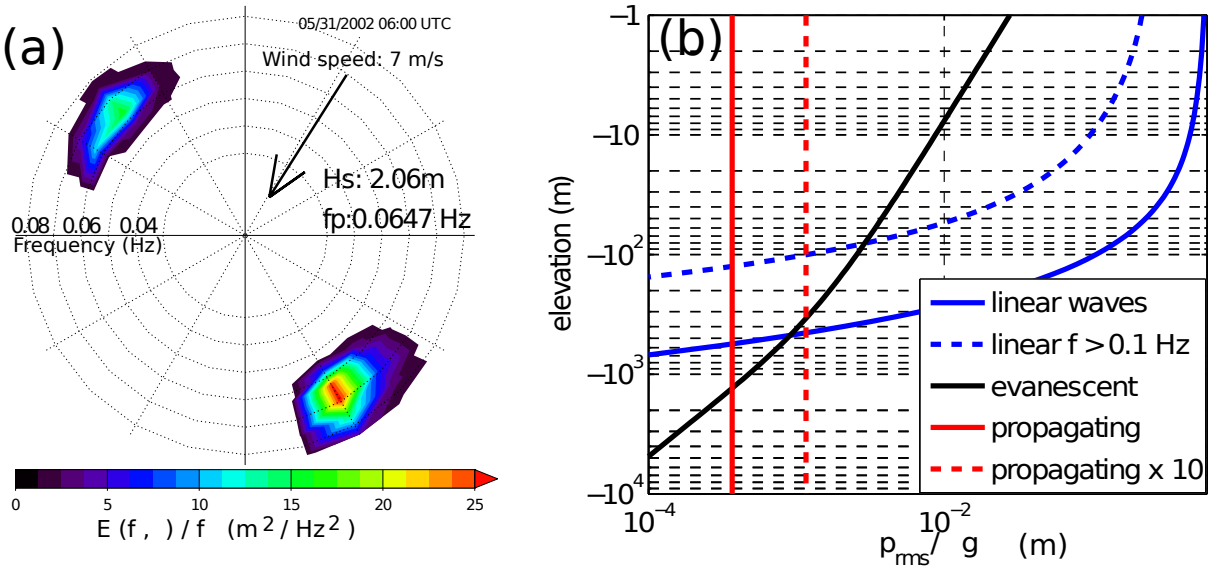

Figure 21.15: Example of (a) directional wave spectrum and (b) resulting profiles of the different contributions to the pressure fluctuations in the ocean, assuming infinite water depth. The ratio of double frequency to linear wave contributions depends on the amplitude of the waves and on the directional spectral shape, because all double frequency contributions are proportional to $E^2(f)I(f)$. This directional spectrum was estimated with a numerical wave model, and corresponds to the loudest noise event recorded at the ocean bottom seismometer H2O, on 31 May 2002 at 25 N, 136 W. This unusual spectrum has large wave energies in opposite directions, radiated from a North Pacific storm and Hurricane Alma (This event is analyzed in detail by Obrebski et al., 2012).

Noise in a finite depth ocean

For large depths compared to the OSGW wavelength, $kh \gg 1$, the finite depth has little effect on the evanescent modes except for a doubling of the motion amplitude near the bottom, as the vertical profiles of the form $\exp(Kz)$ are replaced by $\cosh(Kz + Kh)/\cosh(Kh)$. This is similar to the finite depth effect on linear wave motions. However, the propagating modes radiated by the surface will now undergo multiple reflections at the bottom and sea surface, as shown in figure 21.5. The oceanic acoustic field is tightly coupled to elastic waves in the crust through these reflections.

One of the greatest complications induced by the presence of a bottom is the heterogeneity of the sediment and rock layers below the water column. The natural layering of the crust has a strong influence on the sound reflection and the nature of the seismic modes (e.g. Latham and Sutton, 1966; Abramovici, 1968).

21.5 From the ocean to the atmosphere: microbaroms

The source of noise in the atmosphere can also be derived with the same formalism, as an alternative to the Green functions used by Waxler and Gilbert (2006). Indeed, we may consider the atmospheric motion to be irrotational, so that the equations of motion are identical in the atmosphere and in an unbounded ocean, with the only difference that the atmospheric density is ρ_a and the atmospheric sound speed is α_a. The second-order velocity potential takes the form,

$$\phi_{2,a} \propto \exp[\mathrm{i}(K_x x + K_y y + l_a z - \omega_s t)] \quad \text{for} \quad z > 0, \tag{21.105}$$

with

$$l_a = \sqrt{\frac{\omega_s^2}{\alpha_a^2} - K^2}. \tag{21.106}$$

Because $\rho_w/\rho_a \simeq 1000$, the air motion has only a small $O(\rho_w/\rho_a)$ local influence on the water motion, so that the solutions derived earlier for the water motion remain valid in the presence of air. The air motion, with a velocity potential ϕ_a also obeying eq. (**??**) is fully determined from the water motion via the kinematic boundary conditions on the air and water-sides of the interface (19.25),

$$\frac{\partial \phi_a}{\partial z} - \frac{\partial \phi}{\partial z} \simeq \boldsymbol{\nabla}(\phi_a - \phi) \cdot \boldsymbol{\nabla}\zeta - \zeta \frac{\partial^2 (\phi_a - \phi)}{\partial^2 z} \quad \text{at} \quad z = 0. \tag{21.107}$$

From the first order potential in the air (e.g. Waxler and Gilbert, 2006)

$$\phi_1 = \sum_{\mathbf{k},s} \mathrm{i}s\frac{g}{\sigma} Z^s_{1,\mathbf{k}} \mathrm{e}^{-kz} \mathrm{e}^{\mathrm{i}(\mathbf{k}\cdot\mathbf{x}-s\sigma)} \tag{21.108}$$

we obtain the second order potential,

$$\frac{\partial \phi_{2,a}}{\partial z} = \frac{\partial \phi_2}{\partial z} + \sum_{\mathbf{k},s,\mathbf{k}',s'} D_{za}\left(\mathbf{k},s,\mathbf{k}',s',z\right) Z^s_{1,\mathbf{k}} Z^{s'}_{1,\mathbf{k}'} \mathrm{e}^{\mathrm{i}\Theta(\mathbf{k},\mathbf{k}',s,s')}$$

and a new coupling coefficient

$$D_{za}\left(\mathbf{k},s,\mathbf{k}',s',z\right) = -\frac{2\mathrm{i}sg}{\sigma}\left(kk' + \mathbf{k}\cdot\mathbf{k}'\right). \tag{21.109}$$

We note that for $\mathbf{k}' = -\mathbf{k}$, $D_{za} = 0$, so that the long-wavelength motion with $K \ll k$ simplifies to

$$\frac{\partial \phi_{2a}}{\partial z} \simeq \frac{\partial \phi_2}{\partial z} \quad \text{at} \quad z = 0. \tag{21.110}$$

consistent with the result given by Posmentier (1967) for the interaction of monochromatic wave trains, and in disagreement with a factor 8 correction proposed by Arendt and Fritts (2000).

This gives a pressure spectrum for the propagating atmospheric waves,

$$F_{p2,ap}(f_s) = \int_{K<K_{\max}} \frac{\rho_a^2 \left|l^2\right|}{\rho_w^2 l_a^2} F_{p2,\mathrm{surf}}(\mathbf{K},f_s)\mathrm{d}\mathbf{K} = R(K_{\max})\frac{\pi\omega_s^2}{\alpha_w^2}\rho_a^2 g^2 f_s E^2(f) I(f). \tag{21.111}$$

with the non-dimensional factor

$$R(K_{\max}) = 2\frac{\alpha_w^2}{\omega_s^2}\int_0^{K_{\max}} \frac{\left|l^2\right|}{l_a^2} K\mathrm{d}K == 2\frac{\alpha_w^2}{\omega_s^2}\int_0^{K_{\max}} \frac{\left|l^2\right|}{l_a^2} K\mathrm{d}K. \tag{21.112}$$

In order to avoid the singularity for $l_a = 0$, and atmospheric ducting effects not represented here, we take $K_{\max} = \omega_s/(2\alpha_a)$ which restricts the acoustic propagation directions to be within 30 degrees from the vertical. In that case we have $R(K_{\max}) \simeq 0.54$ instead of $R(K_{\max}) = 0.25$ with the vertical propagation approximation of Waxler and Gilbert (2006), which replaces the l^2/l_a^2 factor in the integral by its value α_a^2/α_w^2 for $K = 0$. Other than that, our expression is consistent with their low Mach number asymptote, i.e. $\sigma/k \ll \alpha_a$ (Waxler and Gilbert, 2006, eq. 61). The present theory also allows the estimation of the evanescent wave components given by wavenumbers $K > \omega_s/\alpha_a$.

21.6 Modeling of seismic spectra using a numerical wave model

While Hasselmann (1963) and Szelwis (1982) already made some order of magnitude estimates of the microseism generated by realistic wave spectra, the first attempt using a numerical wave model was performed by Kedar et al. (2008).

For a seismic frequency $f_s = 0.15$ Hz, the maximum of $\widetilde{C}$ corresponds to a depth $D \simeq 2300$ m. This explains why oceanic ridges are generally stronger sources of microseisms at that frequency (figure 21.16).

21.6.1 Rayleigh wave propagation in a non-homogeneous medium

Les variation de profondeur d'eau ont une importance considerable sur les vitesses de phase et de groupe des ondes sismiques (figure 21.7). On peut donc s'attendre to d'importants phenomenes de refraction des ondes sismique, en particulier au passage du talus continental. En effect, avec une variation du milieu homogene dans la direction y, la propagation d'ondes ne peut se faire entre l'ocean et le continent que pour des angles d'incidences inferieurs to l'angle critique $\arcsin(C_o/C_c)$ avec C_o et C_c les vitesses de phase dans les deux milieux. Pour une frequence sismique de 0.15 Hz par 3000 m de fond ($f_s h/\alpha_s = 0.3$) la vitesse de phase n'est que $C_o = 2000$ m/s, to comparer to la vitesse sur le continent $C_c = 2570$m/s. L'angle critique est donc dejto de 51° et il tombe to 40° pour $h = 5000$ m. Pour prendre en compte ce phenomene on peut utiliser une technique de trace de rayons, comme pour les vagues, mais sa validite, generalement to des echelles plus grande que la longueur d'onde, sera plus limitee du fait de la grande longueur d'onde des ondes sismiques qui peut atteindre 20 km.

Besides, the amplitude of the vertical ground motion δ at the top of the crust is related to the energy flux. Without dissipation and neglecting reflections and lateral variations along direction y, the evolution of δ along the x direction between an ocean with a water depth h and the continent is given by

$$U(h_1)T_{E\delta}(h_1)\delta^2(h_1) = U(0)T_{E\delta}(0)\delta^2(0). \tag{21.113}$$

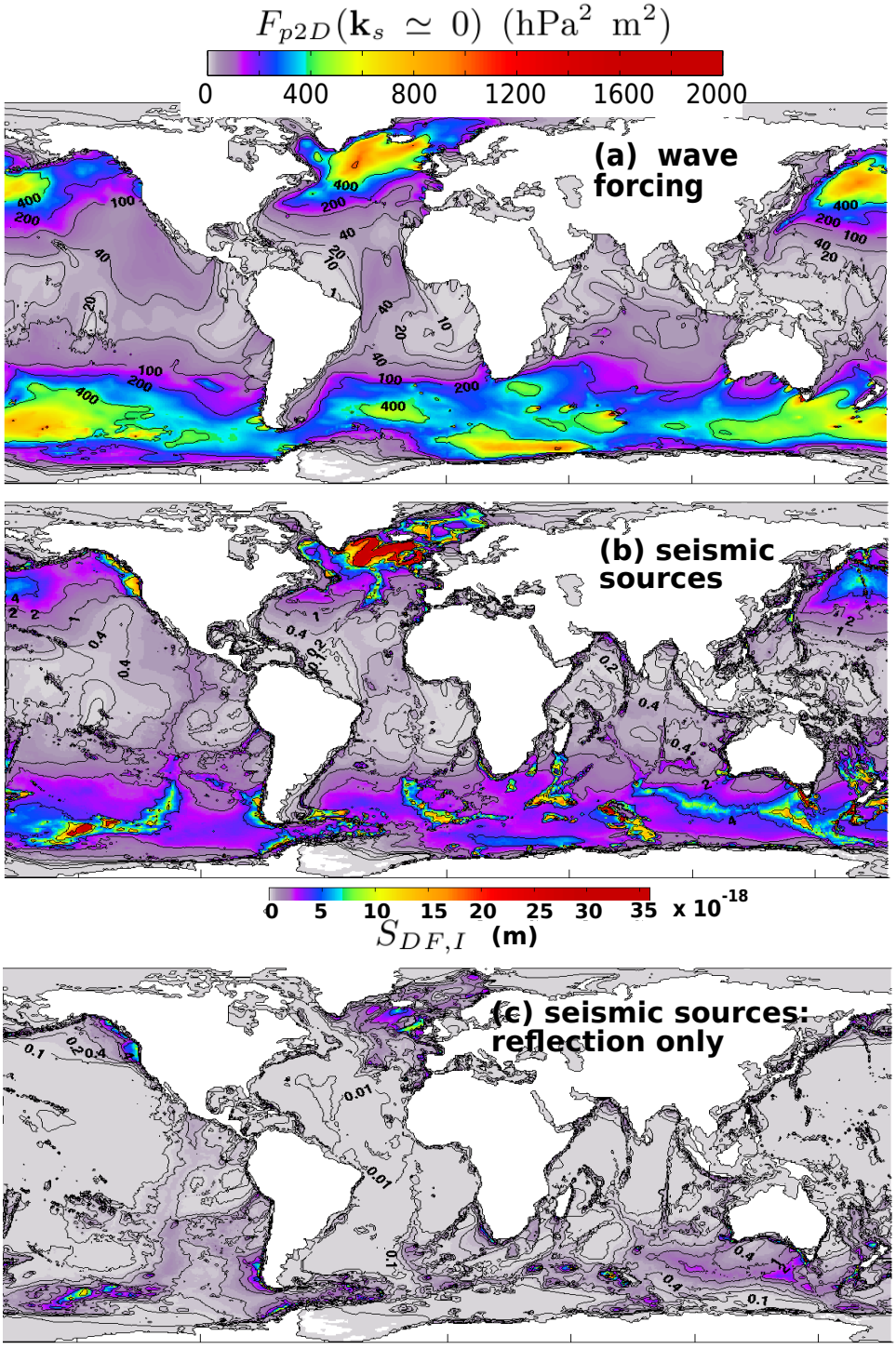

Figure 21.16: Averaged microseism sources averaged over the year 2008 at global scales over the seismic frequency band 0–0.34 Hz, based on a numerical wave model (Ardhuin et al., 2011a). The top panel shows the average wave-induced pressure spectral density $F_{p2D}(k_x = 0, k_y = 0) = \int F_{p3D}(k_x = 0, k_y = 0, f_s)\mathrm{d}f_s$. The middle panel shows the seismic source, which combines the wave-induced pressure and the local amplification factor that varies with water depth $S_{DF}(f_s)$. The bottom panel shows the contribution of coastal reflections only given as the difference of the model run with reflection and the model run without reflection. For reference, without scattering or dissipation a constant source of 10×10^{-18} over a square with side length of 330 km gives an average amplitude $\delta^2_{\mathrm{rms}} = 1\mu\mathrm{m}^2$ at a distance of 1000 km.

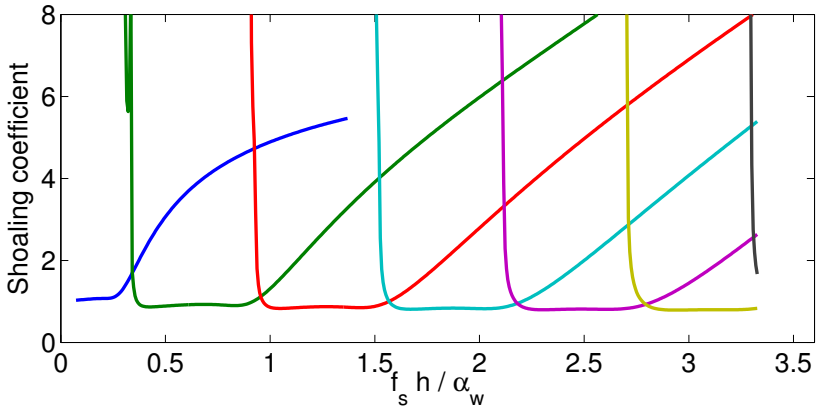

Figure 21.17: Coefficient d'amplification de la variance du deplacement vertical du sommet de la crust terrestre, entre l'ocean et le continent, pour un incidence normale et en fonction de la profondeur oceanique.

avec $V(h_1)$ et $V(0)$ les vitesses de groupe en domaine oceanique et continental, tandis que $T_{E\delta}(h_1)$ et $T_{E\delta}(0)$ sont les coefficient donnant l'energie sismique to partir du deplacement du sommet de la crust.

Hence, just like waves propagating from deep to shallow waters, the variance of the displacement $\delta^2/2$ is amplified by a factor $U(h_1)T_{E\delta}(h_1)/(V(0)T_{E\delta}(0))$ that can be of the order of XX (figure 21.17). Ainsi le mode 0 oceanique se transforme graduellement en une onde de Rayleigh continentale.

Pour les modes superieurs, leur propagation ne peut avoir lieu lorsque la profondeur diminue en dessous de la valeur critique h_c where il disparaissent. Il est possible que ces modes excitent des modes inferieurs jusqu'to finir par transmettre leur energie au mode 0. On remarque que leur structure verticale pour les profondeurs critiques h_c ne presente aucun mouvement dans la crust. Au voinage de h_c ce sont donc des modes purement acoustiques.

Pour un calcul precis du bruit il conviendrait donc de

- prendre en compte la refraction
- utiliser le coefficient d'amplification $V_oM_o/(V_cM_c)$
- estimer la transmission des ondes pour les modes superieurs to 0.

Dans un premier temps nous negligerons ces trois aspects.

21.6.2 Validation of modeled microseism

Les ondes sismiques generees sont attenuees par la dispersion angulaire et par la dissipation et diffusion des ondes sismiques. Ainsi, pour une station sismique to terre, les sources les plus proches donnent un signal qui, toutes choses egales par ailleurs, est plus fort que les sources lointaines. En negligeant les effet de refraction et des ondes sismique, le seul effet de la propagation sur la sphere terrestre est l'attenuation que l'on supposera constante. Ainsi le spectre du deplacement vertical observe to la longitude λ et latitude ϕ est donne par la somme des sources sur l'ensemble de l'ocean,

$$F_\delta(\lambda,\phi,f_s) = \int_{-\pi/2}^{\pi/2}\int_0^{2\pi} \frac{S_{DF}(f_s)}{R_E\sin\alpha}\, \mathrm{e}^{-2\pi f_s \alpha R_E/(VQ)}(R_E^2\sin\phi'\mathrm{d}\lambda'\mathrm{d}\phi')$$

La vitesse de groupe sismique V et le facteur de qualite Q dans (21.114) definissent l'attenuation des ondes sismiques. Pour $V = 1.8$ km s^{-1} et $Q = 150$, l'energie des ondes sismique de frequence $f_s = 0.15$ Hz est diminuee de moitie tous les 200 km. Ces deux parametres dependent de la structure et des non-homogeneites de la croute terrestre. En particulier Q peut varier fortement avec la frequence et le long de la surface terrestre.

En France on a un bon accord entre les spectres sismiques observes et modelises pour $Q \simeq 130$ aux frequences proches de $f_s = 0.14$ Hz (figure 21.18.b) alors que pour certaines stations en Californie il faut reduire Q to pres de 45 (figure 21.18.a). De faibles valeurs de Q impliquent que l'essentiel du bruit sismique vient de regions tres proches de la station de mesure, les sources plus lointaines ayant ete fortement attenuees. En Europe de l'ouest on estime que le bruit sismique est tout autant cause par les vagues qui passent sur la dorsale medio-Atlantique que par l'effet des reflections sur les coast Atlantiques. Les vagues en Mediterranee peuvent aussi be une source significative (figure 21.18.c).

Parce qu'il faut des vagues de same frequence mais de directions opposees pour generer du bruit sismique, les sources sont associees to des houles opposees la mer du vent, ou to la reflexion des vagues, to la coast ou par des icebergs. Avec un modele assez simple de la reflexion to la coast on peut simuler le bruit sismique de facon tres realiste. La principale inconnue etant l'attenuation des ondes sismiques lors de leur propagation.

La figure 21.19 montre la variation au cours de l'annee 2008 de l'amplitude du deplacement sismique vertical δ_{rms} observe et modelise par l'equation (21.114) pour les stations SSB et BKS.

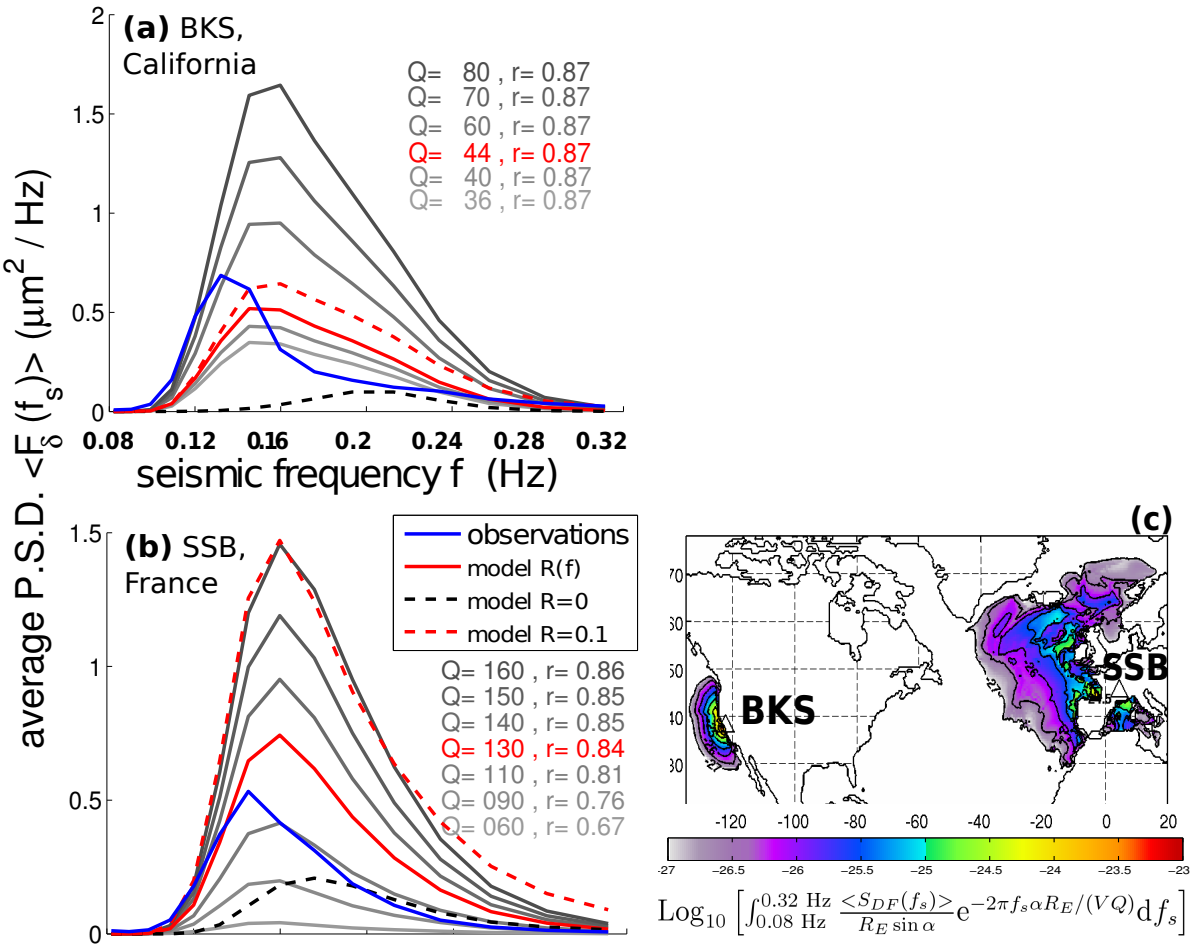

Figure 21.18: (a et b) spectres moyens du deplacement sismique observe et modelise avec differentes valeurs du facteur de qualite Q. Pour la valeur optimale de Q les resultat avec differentes modelisations de la reflection des vagues par la coast sont aussi montres: une reflexion constante de 10%, pas de reflexion du tout ($R = 0$) ou alors une reflection $R(f_s)$ variant lineairement avec la frequence. Dans le cas de SSB cette variation est de $R = 0.06$ pour $f_s = 0.04$ Hz to $R = 0.01$ at $f_s = 0.15$ Hz et pour BKS cette reflexion est augmentee de 50%. (c) Moyenne des contributions au bruit sismique pour l'annee 2008, pour les stations de Berkeley (BKS) et de Saint Sauveur en Rue (SSB), au sud de Saint-Etienne.

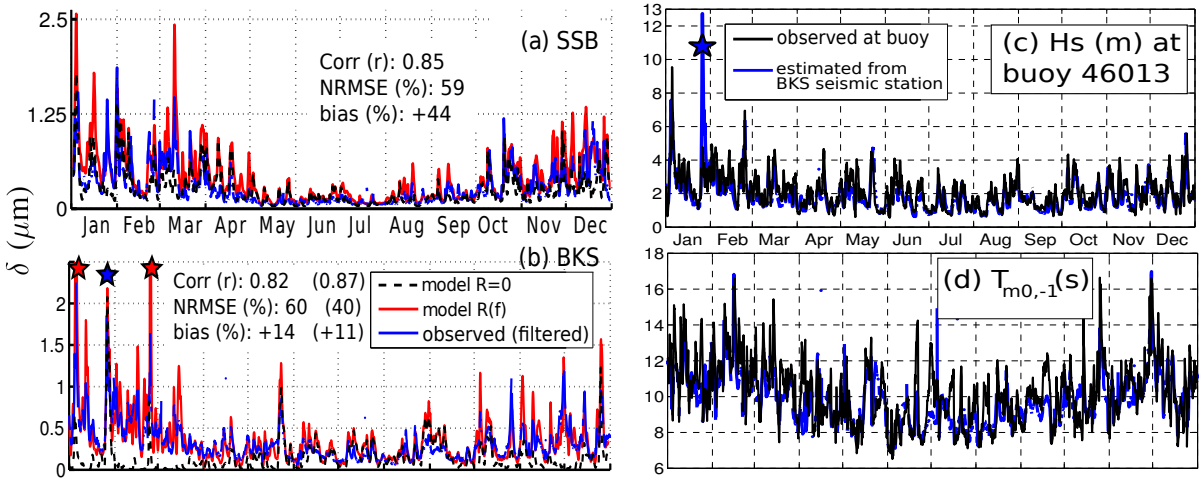

Figure 21.19: Relation entre signal sismique et houle coastal.
Series temporelles du deplacement sismique vertical $\delta_{\rm rms}$ observe et modelise par l'equation (21.114) pour les stations (a) SSB et (b) BKS. (c) et (d) En bas, serie temporelle de hauteurs significatives et periode moyenne des vagues mesurees to 46013 et reconstruite to partir du signal sismique to BKS.

21.7 Measuring waves from microseisms

Microseisms are now widely used to fortomographic analysis of the solid Earth structure (Shapiro et al., 2005), and the monitoring of solid Earth properties. Microseisms can also be used to estimate ocean wave properties. Cette application fut envisagee des les annees 1930 et son utilisation pratique fut mise en oeuvre sur dans les annees 1970 sur la coast ouest des Etats-Unis (Zopf et al., 1976). A cette epoque la technologie de mesure par des bouees en mer n'etait pas encore au point et il n'y avait pas d'autre moyen de mesure fiable.

Cette possibilite d'inverser le signal sismique pour en deduire le spectre des vagues n'est toutefois pas universelle et certains types d'etat de mer peuvent causer d'importantes erreurs. En effet, la relation d'inversion to partir du bruit est typiquement bien calibree pour les situations dans lesquelles la reflexion to la coast est la source principale du bruit. Or une houle opposee to une mer du vent, ou deux houles se faisant face, peuvent aussi generer un tres fort bruit (Obrebski et al., 2012). Dans ce cas la hauteur des vagues pourra be fortement surestimee. Cette source d'erreur dejto discutee par Zopf et al. (1976) est mise en evidence sur la figure 21.19.c pour l'estimation des vagues to partir de la station BKS. Ainsi, le 26 janvier 2008, une situation meteorologique particuliere produit un fort bruit dont on deduit une hauteur significative qui depasse 12 m, soit plus que la hauteur centennale, alors que en realite, la hauteur des vagues n'a pas depasse 5.5 m ce jour lto dans la sone coastal (figure 21.20).

Il convient donc d'ameliorer sensiblement la methode pour arriver to une estimation robuste des parametres d'etat de mer to partir du bruit sismique. Dans le cas de stations sismiques sensibles to une vaste zone de l'ocean l'interpretation quantitative du signal n'est pas simple mais il y a une correlation entre la hauteur des vagues sur l'ensemble de l'Atlantique nord-est et l'intensite du bruit sismique en Europe de l'ouest. Une modelisation numerique des vagues et du bruit peut permettre de filtrer les evenements anormaux (Ardhuin et al., 2012a).

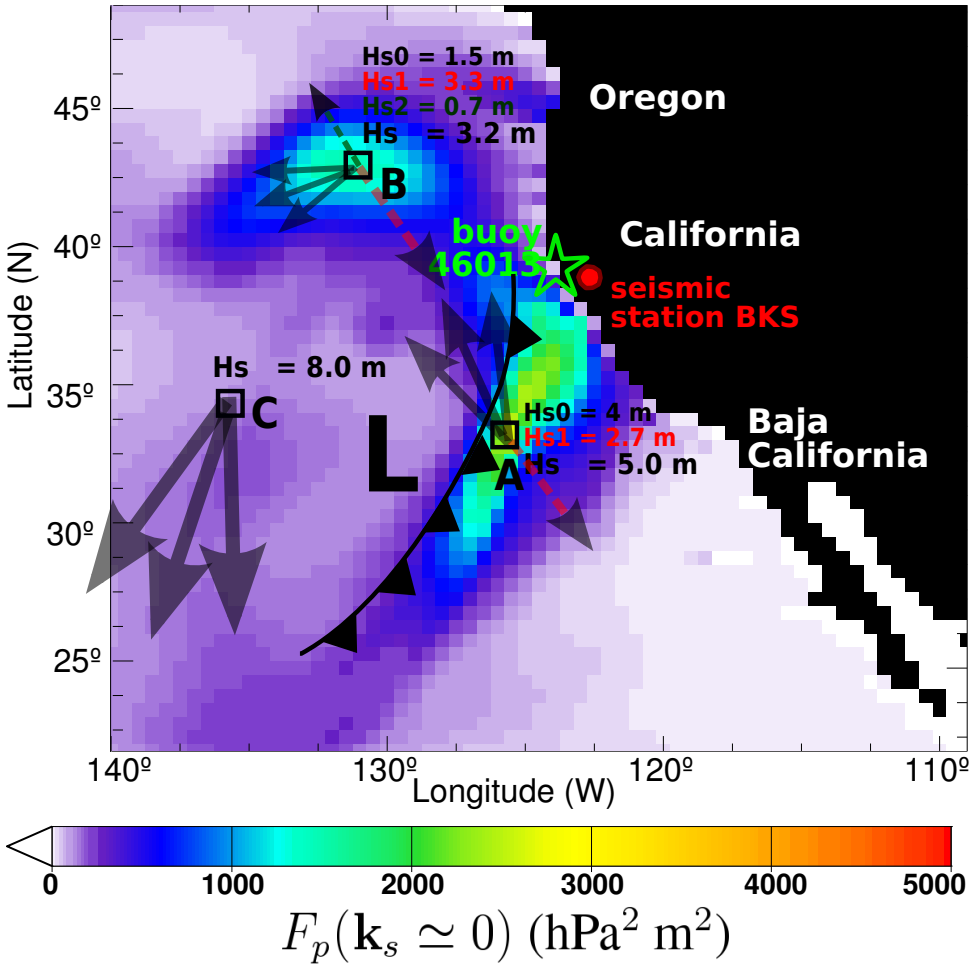

Figure 21.20: Map of the wave-induced second order surface pressure variance, integrated across frequencies (couleurs), on 26 January 2008 at 12:00 UTC, off the California coast. Cette situation correspond to de une forte houle du nord-ouest et une depression (L) centree en 32° N 132° W. Les parametres d'etat de mer sont symbolises pour trois positions (carres), avec la mer du vent (groups of three arrows, and heights H_{s0}), et les houles quand elles existent (dotted arrows and heights H_{s1} and H_{s2}). La depression produit des vents depassant les 25 m/s, ce qui, to l'ouest amplifiela houle incidente en mer forte (H_s jusqu'to 8 m). A l'est de la depression, des mers agitees (4 m) se transforment en houle au nord du front atmospherique (ligne avec triangles). Tous ces champs de vauges produisent deux maxima de pression qui generent des microseismes. Le plus fort (2600 hPa^{2}m^2) s'etend le long du front froid autour du point A, il est cause par la mer du vent qui s'oppose to la houle de nord-ouest. Le second maximum, au point B, vient de l'interaction des deux houles. Enfin on notr que en C, les pressions induites par les vagues sont faibles (200 hPa^{2}m^2) car il n'y a pas de houle opposee to la mer du vent qui pourrait donner une forte valeur de $I(f)$ (eq. 21.24). Si $I(f)$ en C etait aussi fort qu'en A, alors la source microsismique y serait 200 fois plus forte.

Chapter 22

Generation of waves by the wind

22.1 Effects of air viscosity on swell attenuation

Before discussing the generation of wave by the wind, we will look into the opposite and presumably simpler problem of wind generation by waves, or more generally the adjustment of air flow to the water motion taking into account the finite viscosity of the air. This problem was first solved by Dore (1978).

22.2 From air-side turbulence to wave energy: a first theory by Phillips

En supposant que la turbulence du vent est advectée sans modification par un vent moyen U (uniforme sur la verticale et dans la direction de l'axe des x pour simplifier), P_a est de la forme $P_a\,(x - Ut)$ (c'est l'hypothèse de G. I. Taylor, la turbulence est "gelée"). Cela correspond à $\sigma'' = \mathbf{k} \cdot U$.

Pour une pression atmosphérique dont le spectre turbulent est continu,

$$P_a = \sum_{k_a} \Pi_{k_a} \cos\left[k_a\,(x - Ut) + \alpha_{k_a}\right], \tag{22.1}$$

ζ est donné par la superposition de solutions de la forme de (22.33) déphasées de α_{k_a}. Cette superposition est dominée par les composantes qui sont proches de la résonance. L'énergie de chaque composante croît initialement comme t^2, mais la largeur de la bande de fréquence pour laquelle cette croissance a lieu diminue en $1/t$. Le calcul montre que l'énergie des vagues augmente linéairement avec t (eq. 22.36).

On peut alors ajouter des variations suivant y de la fluctuation de pression P_a. Dans ce cas des modes propres de la surface sont excités avec des nombres d'onde k_y non-nuls: ces vagues se propagent dans une direction différente de la direction du vent, donné par la condition de résonance

$$\sigma/k_x = U, \tag{22.2}$$

qui exprime l'égalité de la composante σ/k_x, suivant l'axe des x, de la vitesse de phase des vagues et de la vitesse du vent U. Phillips a aussi ajouté les effets de la tension de surface dans sa théorie, en utilisant la relation de dispersion des vagues de gravité-capillarité. Malheureusement, les valeurs mesurées du spectre des fluctuations de pression turbulente sont insuffisante pour expliquer la croissance des vagues.

22.3 Couplage vent-vagues

Si la croissance linéaire de l'énergie des vagues donnée par la théorie de Phillips (1957) peut expliquer le début de la croissance des vagues, au bout d'un certain temps on ne peut plus supposer que le vent est uniforme car il est modifié par la présence des vagues, au moins au voisinage de la surface. Miles (1957) a mis en evidence un mécanisme de croissance des vagues qui découle de cette modification. Cette théorie a été étendue par la suite par Fabrikant (1976) et appliquée par Janssen (1991). La théorie apparaît bien vérifiée, au moins qualitativement, pour les vagues telles que $C > U_{10}/3$. Pour les vagues plus lentes, il est probable que l'effet d'abri proposé par Jeffreys, en particulier en cas de décollement de l'écoulement d'air, soit important (Giovanangeli et coll. 1999). Belcher et Hunt (1993) ont montré qu'un effet comparable peut aussi se produire en absence de décollement, sous l'effet des variations des propriétés turbulentes.

Dans tous les cas le couplage vent-vagues fait intervenir une modification induite par les vagues de la pression et/ou de la tension de cisaillement dans l'air, de la forme $dPa = \rho_w g \beta dZ$. (voir eq. 5.2).

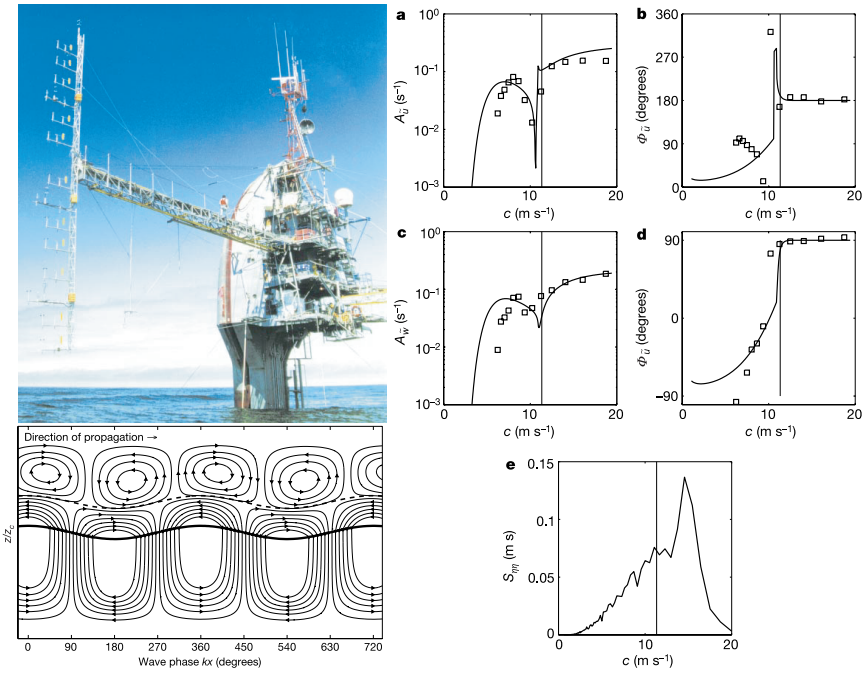

Figure 22.1: Ecoulement dans l'air et niveau critique: mesures de Hristov et coll. (2003). A gauche, une photo de la plateforme de recherche FLIP et un schéma de l'écoulement de l'air au dessus des vagues, dans un référentiel fixe. A droite, solutions numériques de l'équation de Orr-Sommerferld et observations des variations de l'amplitude et de la phase des vitesses pour des vagues de fréquence environ 0.7 f_p: la vitesse des composantes dont les propriétés sont mesurées est indiquée sur le spectre en bas à droite (©Nature Publishing Group).

22.3.1 Equation de Orr-Sommerfeld ou de Rayleigh

La vorticité inhérente au cisaillement vertical du vent oblige à généraliser l'équation de Laplace. Le même problème se pose dans l'étude des ondes internes, avec des applications très importantes en météorologie pour le paramétrage du ralentissement des vents au dessus du relief. En considérant d'abord le cas ou le vent et les vagues sont dans la même direction, on utilise la propriété de divergence nulle pour définir une fonction de courant ψ pour la vitesse induite par les vagues, telle que $u = -\partial\psi/\partial z$ et $w = \partial\psi/\partial x$. En suivant Miles (1957) on se fixe le profil de vitesse $U(z)$ du vent moyen, uniforme en x, et on note ses dérivées premières et secondes U' et U''. En supposant que $|u, w| \ll U$, on peut négliger les termes quadratiques en u et w, y compris les tenseurs de Reynolds, et on a l'équation du mouvement,

$$\rho_a \left(\frac{\partial u}{\partial t} + U\frac{\partial u}{\partial x} + wU' \right) = -\frac{\partial p}{\partial x} \tag{22.3}$$

$$\rho_a \left(\frac{\partial w}{\partial t} + U\frac{\partial w}{\partial x} \right) = -\frac{\partial p}{\partial z}. \tag{22.4}$$

La gravité n'apparait pas: il suffit de redéfinir la pression comme la pression moins la pression hydrostatique.

En utilisant la fonction de courant et en cherchant une solution qui se propage à la vitesse C comme l'élévation de la surface $\zeta = a\mathrm{e}^{\mathrm{i}k(x-Ct)}$. On a donc $\psi = \widehat{\psi}\mathrm{e}^{\mathrm{i}k(x-Ct)}$

$$\rho_a \left[(U-C)\frac{\partial \widehat{\psi}}{\partial y} - U'\widehat{\psi} \right] = p \tag{22.5}$$

$$\rho_a k^2 (U-C)\,\widehat{\psi} = \frac{\partial p}{\partial z}. \tag{22.6}$$

$$\tag{22.7}$$

Classiquement on élimine la pression et on trouve l'équation de Rayleigh, aussi appelée équation de Orr-Sommerfeld,

$$\widehat{\psi}'' - k^2\widehat{\psi} - \frac{U''}{U-C}\widehat{\psi} = 0 \tag{22.8}$$

L'équation de Rayleigh décrit la propagation horizontale d'une onde dans un milieu cisaillé verticalement. Elle sera ainsi utilisée pour étudier l'effet d'un courant variant sur la verticale, et elle est aussi appliquée pour les

ondes internes. On remarque qu'elle diffère de l'équation de Helmholz (2.17) par son dernier terme qui présente une sigularité pour $U = C$. Pour un vent variant logarithmiquement $U = u_\star/\kappa \ln(z/z_0)$ jusqu'à atteindre U_∞ au niveau z_∞ , il existe, pour $C < U_\infty$ un niveau "critique" z_c tel que $U(z_c) = C$ où l'équation de Rayleigh est singulière.

Afin de déterminer le taux de croissance adimensionnel β, il suffit de se rendre compte que (22.5) nous donne une perturbation de pression qui peut être mise sous la forme de l'équation (5.1) et de reconnaître que β est donné par la partie imaginaire de (22.5).

Miles (1957) a montré que β s'obtenait par intégration verticale de $\widehat{\psi}$ donné par l'équation de Rayleigh. Cette intégrale est alors dominée par la singularité au niveau critique z_c et il obtient une expression approchée, en supposant que $\widehat{\psi}$ décroit comme e^{-kz},

$$\beta = -\pi \frac{U''(z_c)}{U'^3(z_c)} k^2 \left(\int_{z_c}^{\infty} \frac{\mathrm{e}^{-kz}}{(U-C)^2} \mathrm{d}z \right)^2 . \tag{22.9}$$

La croissance des vagues est donc largement déterminée par la forme du profil du vent $U(z)$ au voisinage du niveau critique z_c défini par $U(z_c) = C$. L'équation (22.9) permet de calculer le taux de croissance β si on connaît le profil du vent.

22.3.2 Interprétation de Lighthill: Force de vortex

Si le mécanisme de départ est assez clair (les fluctuations de pression en surface), les calculs aboutissant à une valeur de β obscurcissent un peu comment cette corrélation pression-pente des vagues apparaît. Lighthill (1962) a proposé une inteprétation relativement simple du résultat de Miles (1957). Le vent a un profil vertical de vitesse $U(z)$ tel qu'à la surface, il est égal à la vitesse oscillante des vagues. En négligeant la diffusion (turbulente ou visqueuse), la vorticité de l'écoulement bidimensionnel,

$$\Sigma = \frac{\partial U}{\partial z} - \frac{\partial w}{\partial x}, \tag{22.10}$$

est conservée par toute particule. On peut écrire l'accélération dans les équations d'Euler come la somme d'un gradient de pression totale

$$p_{\mathrm{tot}} = p + \frac{1}{2}\rho \left(U^2 + w^2\right) \tag{22.11}$$

et d'une force de vortex $(-\rho\Sigma w, \rho\Sigma U)$:

$$\rho \frac{\partial U}{\partial t} = -\rho\Sigma w - \frac{\partial p_{\mathrm{tot}}}{\partial x} \tag{22.12}$$

$$\rho \frac{\partial w}{\partial t} = \rho\Sigma u - \frac{\partial p_{\mathrm{tot}}}{\partial z} \tag{22.13}$$

En moyenne sur une longueur d'onde (notée $\langle\cdot\rangle$), (22.12) donne

$$\rho \frac{\partial \langle U \rangle}{\partial t} = -\rho \langle \Sigma w \rangle . \tag{22.14}$$

La vorticité Σ est simplement égale à $U'(z)$ pour un écoulement non-perturbé par les vagues, et sa valeur diminue avec z si l'on suppose, avec Miles (1957), $U''(z) < 0$. En présence de vagues qui perturbent l'écoulement par un déplacement des lignes de courant, les variations de Σ sont donc essentiellement dues à une variation de l'altitude des particules. Si on fait un développement en série de Σ autour de z_0, avec $h = z - z_0$ on a

$$\Sigma = U'(z_0) + hU''(z_0) + O\left(h^2\right) \tag{22.15}$$

et donc

$$\rho \frac{\partial \langle U \rangle}{\partial t} = -\rho U''(z_0) \langle hw \rangle . \tag{22.16}$$

Puisque la circulation de l'air résultant de la présence des vagues est advectée avec la vitesse de phase C, l'air à tous les niveaux, excepté le niveau "critique" $z = z_c$ où $U = C$, est déplacé de manière à peu près sinusoïdale avec une fréquence

$$\frac{U(z) - C}{L}, \tag{22.17}$$

où L est la longueur d'onde des vagues. Pour de telles oscillations sinusoïdales, le déplacement vertical h et la vitesse verticale w sont en quadrature et la moyenne de leur produit est nul. Pour des vents plus rapides (en altitude, où l'on peut négliger l'effet des vagues) que la vitesse de phase C des vagues il existe donc un niveau "critique" z_c où $U(z_c) = C$. Juste au dessus de $z = z_c$, une particule d'air qui se trouve à la verticale d'une crête de vague la dépasse, mais avant de se retrouver au dessus du creux de vague suivant son altitude diminue pour se trouver légèrement en dessous de $z = z_c$ car les lignes de courant sont perturbées par la présence des vagues. Du coup, la particule d'air est lentement rattrapée par la crête de vague qu'elle vient de doubler et se retrouve à sa

position initiale par rapport au train de vagues. Mais à $z = z_c$ une particule d'air se déplace à la même vitesse que les vagues, si bien qu'une particule qui monte continue de monter et inversement et $\langle hw \rangle$ est non-nul. w est de la forme

$$w = w_0(z) \cos\left(2\pi \frac{U(z) - C}{L} t\right), \tag{22.18}$$

h est donc

$$h = \frac{w_0(z) L}{2\pi [U(z) - C]} \sin\left(2\pi \frac{U(z) - C}{L} t\right), \tag{22.19}$$

et (22.16) devient

$$\rho \frac{\partial \langle U \rangle}{\partial t} = \frac{\pi}{4} \rho L U''(z_c) w_0^2(z_c) \delta(z - z_c), \tag{22.20}$$

où on a utilisé

$$\lim_{t \to 0} \frac{\sin \sigma t}{\sigma} = \pi \delta(\sigma). \tag{22.21}$$

Pour $U''(z_c) < 0$, la quantité de mouvement est perdue par l'air, au profit des vagues, et correspond à un gain d'énergie S_{in} ("in" pour "wind INput") égal à C fois cette perte:

$$S_{\text{in}} = \frac{\pi}{4} \rho C L U''(z_c) w_0^2(z_c), \tag{22.22}$$

ce qui est une autre manière d'écrire (22.9). Il ne reste plus qu'á déterminer w_0 qui est la perturbation de la vitesse verticale dans l'air, induite par les vagues. Lighthill obtient la valeur de w_0 en calculant d'abord la pression, qui est en équilibre avec la force centrifuge $\rho_a |u, w|^2 / R$. Le rayon de courbure des lignes de courant, R, estimé en supposant que ces lignes de courant suivent la surface à la surface et deviennent progressivement horizontale au fur et à mesure qu'on s'élève ($R \propto \mathrm{e}^{-kz}$). Ensuite il exprime l'équilibre entre le gradient de pression et la force de vortex qui fait intervenir w et obtient une expression pour w_0. On trouve que $w_0(z_c)$ est proportionnel à l'amplitude a des vagues. Le terme de source est donc proportionnel à l'énergie des vagues, et la croissance des vagues est exponentielle.

22.4 Effet d'abri sans décollement

Hristov et coll. (2003) montrent clairement que la perturbation induite par les vagues a une structure très proche de la théorie du niveau critique (figure 22.1). De plus, l'extension de la théorie de Miles (1957) par Janssen (1991) semble donner un bon accord avec les variation de pression au dessus des vagues mesurés par Snyder et al. (1981, figure 5.2). Cependant ces observations ne couvrent que les vagues proche du pic spectral. A haute fréquence le niveau critique est très près de la surface, dans une région ou la turbulence est importante et la vitesse moyenne du vent U est du même ordre que les fluctuations induites par les vagues ou la turbulence.

Afin de représenter l'écoulement sur des vagues lentes, Belcher et Hunt (1993) ont étudié la turbulence près de la surface et sa déformation par les vagues. Leur théorie fait en particulier intervenir un raccordement entre une couche interne, et une couche externe. Dans la couche interne proche de la surface, la turbulence peut être modélisée avec un modèle de type k-l et une longueur de mélange augmentant linéairement avec l'altitude au dessus de la surface ($l = \kappa u_\star \xi_3$), comme en écoulement permanent: on a un comportement de type visqueux. Dans la couche externe la turbulence est composée de grands tourbillons, rapidement déformé par les vagues, sans que les tourbillons ait le temps de transporter de la quantité de mouvement à l'échelle de la période des vagues: on a un comportement élastique (Miles 1996). La séparation entre ces deux couches se fait au niveau ou le temps caractéristique des tourbillons ("eddy turn-over time" en anglais) est égal au temps d'advection par le vent sur une longueur d'onde (voir Janssen 2004 pour une correction de la théorie de Belcher et Hunt 1993). Belcher et Hunt on montré que l'intensification de la turbulence du côté des crêtes de vagues abrité par le vent induit un gradient du tenseur de Reynolds qui est équilibré par une variation de la pression. En même temps les lignes de courant s'écartent un peu plus de la surface du côté abrité. Cette variation de pression est partiellement en phase avec la pente des vagues et donc contribue à la croissance des vagues et à la tension de vent. Le même mécanisme explique très bien la traînée observée pour un vent au dessus de collines. Il s'agit en quelque sorte du même mécanisme que Jeffreys (1925) avait proposé, sans avoir besoin d'un décollement de l'écoulement d'air derrière la crête.

La théorie de Belcher et Hunt (1993) est bien vérifiée par le modèle numérique de Mastenbroek (1996, voir aussi Mastenbroek et al. 1996). Le modèle de Mastenbroek utilise une cloture turbulente au second ordre et donc ne fait pas l'hypothèse d'une viscosité turbulente. Il met clairement en évidence le fait qu'une viscosité turbulente n'est pas adapté à la couche externe.

Des décollements sont toutefois observés, en particulier lorsque les vagues déferlement, ce qui augmente d'autant leur croissance, et la traînée. Ces effet, ainsi que les modulations de la tension de vent sont probablement à l'origine de la sous estimation du taux de croissance pour les vagues jeunes ($C/u_\star$ élevé, figure 5.2, voir Giovanageli et al. 1999). Par ailleurs, pour des vagues très jeunes, le décolement peut littéralement déconnecter l'écoulement d'air du profil des vagues: le point de rattachement de l'air sur la vague étant près de la crête suivante. Ce phénomène est probablement à l'origine de la réduction de la rugosité de l'océan, et du coefficient de traînée, pour les vents très forts (Powell et coll. 2003, Donelan et coll. 2006).

22.5 Pression dans l'air et croissance des vagues

Les mesures de pression faites près de la surface montrent que pour les vagues moins rapides que le vent les fluctuations de pression sont plus importantes que celles des tensions de cisaillement.

En ajoutant la pression atmosphérique p_a, variable, dans l'équation de Bernoulli linéarisée pour $z = \zeta$ on a

$$\frac{\partial \phi}{\partial t} = -\frac{p}{\rho} - g\zeta - \frac{1}{\rho} p_a, \quad \text{sur} \quad z = 0, \tag{22.23}$$

En prenant la transformée de Fourier spatiale, une forme générique des fluctuations de pression est

$$p_a(t) = \mathcal{R}\left[\mathrm{i}\widehat{P}_a \mathrm{e}^{\mathrm{i}(\mathbf{k}\cdot\mathbf{x})}\right], \tag{22.24}$$

avec $\mathcal{R}$ qui représente la partie réelle, $\widehat{P}_a(t)$ une fonction réelle, et $\mathrm{i}\widehat{P}_a(t)$ l'amplitude complexe. En posant $\Theta = (\mathbf{k}\cdot\mathbf{x})$ on a $p_a(t) = -\widehat{P}_a(t)\sin\Theta$.

Puisque l'équation de Laplace et la condition à la limite au fond sont inchangées, ϕ est encore de la forme, $\phi = \mathcal{R}\left(\Phi \mathrm{e}^{\mathrm{i}\Theta}\right)\cosh(kz + kh)/\cosh(KD)$. On peut ainsi dériver (22.23) par rapport au temps puis remplacer ϕ via la condition cinématique en surface linéarisée, $\Phi = -\mathrm{i}gZ/\sigma$, pour obtenir une équation d'évolution pour l'amplitude Z définie par $\zeta = \mathcal{R}\left(Z\mathrm{e}^{\mathrm{i}\Theta}\right)$. Il s'agit de l'équation d'un oscillateur forcé (Phillips 1957, eq. 2.11),

$$\frac{\partial^2 Z}{\partial t^2} + \sigma^2 dZ = -\frac{\mathrm{i}\sigma}{\rho_w g}\frac{\partial \widehat{P}_a}{\partial t}, \tag{22.25}$$

avec $\sigma^2 = gk\tanh(kD)$.

Il s'agit donc de déterminer la forme des fluctuations de pression $dP_a(t)$ et de calculer la réponse de l'océan à ce forçage. On peut tout d'abord prendre une forme générique des fluctuations de pression,

$$p_a(t) = \mathcal{R}\left[\mathrm{i}P_a \mathrm{e}^{\mathrm{i}\Theta'}\right], \tag{22.26}$$

avec $\Theta' = (\mathbf{k}\cdot\mathbf{x} - \sigma' t)$ et P_a une constante.

22.5.1 Pression sinusoïdale résonante

Dans le cas $\sigma' = s\sigma$, avec $s = \pm 1$, la solution générale de (22.25) est la somme d'une solution particulière et de la solution générale sans second membre, soit

$$Z(t) = -\frac{P_a}{2\rho_w g} s\sigma t\cos\Theta' + A\sin\Theta_1 + B\sin\Theta_2 + C\cos\Theta_1 + D\cos\Theta_2. \tag{22.27}$$

avec $\sigma^2 = gk\tanh(KD)$, $\Theta_1 = (\mathbf{k}\cdot\mathbf{x} - \sigma t)$, $\Theta_1 = (\mathbf{k}\cdot\mathbf{x} + \sigma t)$. A, B, C et D sont des constantes que l'on peut déterminer en se donnant les conditions initiales.

En prenant $\zeta = 0$ et $\partial\zeta/\partial t = 0$ pour $t = 0$, on trouve $C = D = 0$, et, pour s= 1, $A = -P_a/(2\rho_w g)$, $B = 0$.

On remarque que l'amplitude des vagues croît linéairement, et que le terme croissant de l'élévation de la pression est en quadrature de phase avec la pression. La densité spectrale d'énergie[1] est $E(\mathbf{k}) = |dZ|^2/\mathrm{d}\mathbf{k}$, et on peut relier sa variation à celle de la densité spectrale de pression $\Pi(\mathbf{k}) = |dP_a|^2/\mathrm{d}\mathbf{k}$. Ainsi, le flux d'énergie entre l'air et l'eau est, en négligeant le terme venant de A ou B,

$$\rho_w g\frac{\partial E(\mathbf{k})}{\partial t} = \frac{\sigma^2 t\Pi(\mathbf{k})}{2\rho_w g}, \tag{22.28}$$

qui s'exprime en Watts pour les unités du système international, de telle sorte que l'intégrale sur l'ensemble des nombres d'ondes est bien un flux en Watts par mètre carré. Ce flux est logiquement égal au travail des forces de pression sur la surface, produit de la vitesse normale à la surface (normale rentrante) par la pression. Pour des pentes faibles la normale est quasiment verticale, et seule la vitesse verticale $w(\zeta) = \partial\zeta/\partial t$ travaille,

$$\rho_w g\frac{\partial E(\mathbf{k})}{\partial t} = -\left\langle \frac{\partial dZ}{\partial t}\overline{dP_a}/\mathrm{d}\mathbf{k}\right\rangle. \tag{22.29}$$

Ainsi le décalage de phase entre la pression et l'élévation permet justement à l'atmosphère d'appuyer vers le bas là où la surface descend, et à aspirer la ou la surface monte, ce qui donne un flux net d'énergie. De la même manière la quantité de mouvement des vagues $\mathbf{k}\rho_w g E(\mathbf{k})/\sigma$ augmente elle aussi, avec un flux égal à la force moyenne exercée sur la surface. Cette force est la force de pression projetée sur l'horizontale, donc le produite entre la pression et la pente de la surface $\mathcal{R}(\mathrm{i}\mathbf{k}dZ)$,

$$\frac{\rho_w g\mathbf{k}}{\sigma}\frac{\partial E(\mathbf{k})}{\partial t} = \mathbf{k}\left\langle \mathrm{i}\frac{dZ\overline{dP_a}}{\mathrm{d}\mathbf{k}}\right\rangle. \tag{22.30}$$

[1] La notation dZ renvoie à la transformée de Fourier-Stieltjes. $|dZ|^2/\mathrm{d}\mathbf{k}$ est équivalent à la variance comprise dans un intervalle $\Delta\mathbf{k}$ autour de $\mathbf{k}$, divisée par la surface $\Delta\mathbf{k}$ de cet intervalle, dans la limite où cette surface tend vers 0.

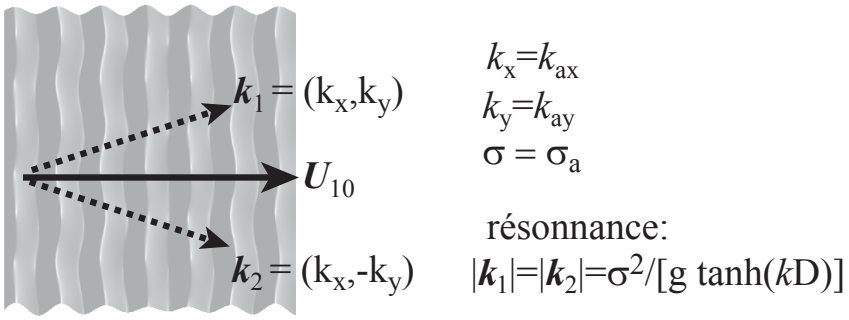

Figure 22.2: Génération de vagues obliques

Dans tous les cas, les vagues répondent aux nombres d'ondes $\mathbf{k}$ et fréquences σ imposés par le forçage atmosphérique. Il n'y a résonance que si le couple $(\mathbf{k}, \sigma)$ est relié par la relation de dispersion (le forçage correspond à un mode propre). Le vent génère donc des vagues dans toutes les directions car le spectre de pression contient de l'énergie pour tous les nombres d'ondes, mais les fréquences sont en général telles que $\sigma_a/k_{ax} < U_{10}$: dans la direction du vent, les perturbations de pression ne se propagent pas plus vite que le vent.

22.5.2 Pression sinusoïdale non-résonante

De la même manière, dans le cas $\sigma'^2 \neq \sigma^2$, la solution générale de (22.25) est de la forme

$$\zeta(t) = -\frac{P_a}{\rho_w g}\frac{\sigma^2}{\sigma^2 - \sigma'^2}\sin\Theta' + A\sin\Theta_1 + B\sin\Theta_2 + C\cos\Theta_1 + D\cos\Theta_2. \tag{22.31}$$

En prenant $\zeta = 0$ et $\partial\zeta/\partial t = 0$ pour $t = 0$, on trouve $C = D = 0$, $A = (dP_a\sigma)/[\rho_w g(\sigma - \sigma')]$, $B = (dP_a\sigma)/[\rho_w g(\sigma + \sigma')]$, ce qui donne,

$$\zeta(t) = \frac{dP_a}{\rho_w g}\frac{\sigma}{\sigma + \sigma'}\left[\sigma\frac{\sin\Theta - \sin\Theta'}{\sigma - \sigma'} + \frac{1}{2}\left(\sin\Theta_1 - \sin\Theta_2\right)\right]. \tag{22.32}$$

On remarque que l'amplitude peut être forte pour σ proche de σ' (figure 22.3). En posant $\Delta = \sigma - \sigma'$, $\Theta = \Theta' - t\Delta$, et on peut faire le développement limité suivant, $\sin\Theta = \sin\Theta'(1 + O(t\Delta)^2) - \sin(t\Delta)\cos\Theta'$, valable pour $t\Delta \ll 1$. Ainsi pour $t\Delta \ll 1$, on a

$$\zeta(t) = \frac{dP_a}{\rho_w g}\frac{\sigma}{\sigma + \sigma'}\left[\sigma t\frac{\sin t\Delta}{t\Delta}\cos\Theta' + O(t^2\sigma\Delta) + \frac{1}{2}\left(\sin\Theta_1 - \sin\Theta_2\right)\right]. \tag{22.33}$$

Cette solution correspond à une croissance linéaire de l'amplitude qui se prolonge tant que $t\Delta \ll 1$ (le premier terme est dominant). La bande de fréquence $\sigma - \Delta_0 < \sigma' < \sigma + \Delta_0$ pour laquelle la croissance reste importante se réduit, avec $\Delta_0 \propto 1/t$.

22.5.3 Pression aléatoire de spectre continu

Dans le cas général, la pression dP_a peut prendre n'importe quelle forme,

$$dP_a = \int d\widehat{P}_a(\sigma'')\mathrm{e}^{\mathrm{i}\sigma'' t}\mathrm{d}\sigma'' \tag{22.34}$$

les cas précédemment étudiés correspondant à $d\widehat{P}_a = \delta(\sigma'' - \sigma')$ avec δ la distribution de Dirac. Il nous faut donc intégrer sur σ'' en remplaçant σ' par σ'' dans les résultats précédents. Les modes résonants $\sigma'' = \pm\sigma$ représentent un ensemble de mesure nulle dans l'espace des σ'', leur contribution peut donc être négligée dans le cas où le spectre est continu. On se retrouve donc avec une intégrale du type suivant, où l'égalité est valable pour toute fonction A qui est analytique,

$$\int_0^\infty A(\sigma')\frac{\sin^2\left[(\sigma - \sigma')\,t\right] + O\left(\sigma - \sigma'\right)}{\left(\sigma - \sigma'\right)^2}\mathrm{d}\sigma' = 2\pi t A(\sigma), \tag{22.35}$$

avec dans notre cas $A(\sigma') = \sigma^4\left|d\widehat{P}_a\right|^2/[\mathrm{d}\sigma'(\rho_w g(\sigma + \sigma'))^2]$, ce qui donne in fine,

$$E(\mathbf{k}) = \sigma^2 t\frac{\pi}{2}\frac{\Pi(\mathbf{k}, \sigma_k)}{(\rho_w g)^2}, \tag{22.36}$$

avec $\Pi(\mathbf{k}, \sigma_k)$ le spectre tridimensionnel de la pression atmosphérique à la surface, où $\sigma_k = \sqrt{gk\tanh(kD)}$.

Ainsi, parmi l'infinité des modes d'oscillations forcés par la pression atmosphérique, les seuls capable d'extraire une quantité significative d'énergie du vent sont les modes propres que sont les ondes libres déterminées au chapitre 1.

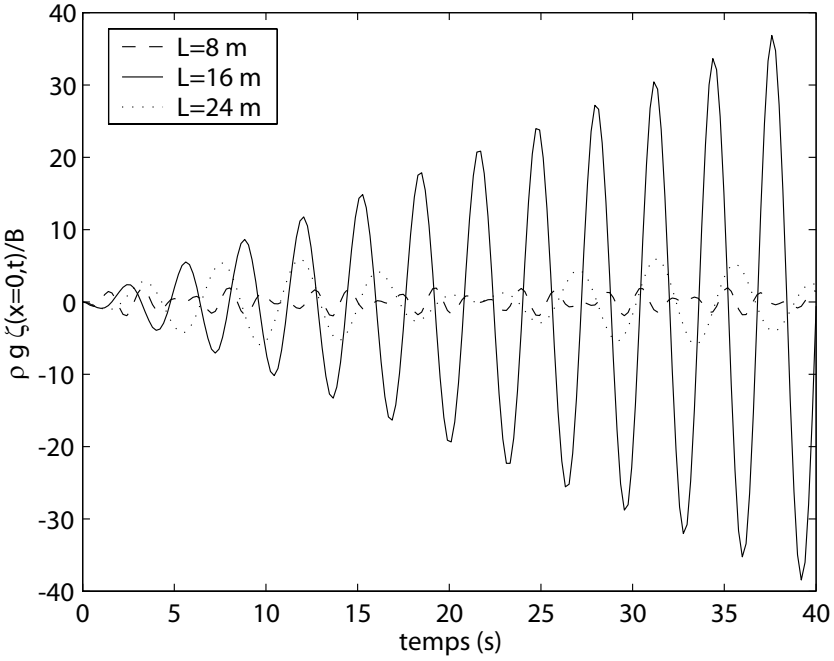

Figure 22.3: Croissance des vagues sous l'effet d'un vent turbulent
Elévation normalisée de la surface, pour un vent $U = 5$ m s^{-1}, et trois longueurs d'onde différentes pour les perturbations turbulentes ($L = 2\pi/k$) en profondeur infinie. En suivant l'hypothèse de Phillips, la pulsation de la pression est $\sigma' = kU$. Dans ce cas la longueur d'onde résonante est $L = 16,03$ m, telle que $\sigma = \sigma'$ soit $k = g/U^2$.

Chapter 23

Wave breaking and dissipation

De nombreux mécanismes contribuent à la dissipation de l'énergie des vagues, ou plutôt au transfert d'énergie mécanique vers d'autres formes de mouvement, en particulier la turbulence. En effet la seule dissipation en chaleur est due à la viscosité.

23.1 Effet de la viscosité dans l'eau

Nous l'avions négligée jusque là, il est temps de savoir pourquoi. La conversion d'énergie mécanique en chaleur par unité de surface océanique est donnée par le travail des contraintes visqueuses sur les vitesses orbitales soit, d'après tout bon cours de mécanique des milieux continus (par exemple article 287 dans Lamb 1932),

$$\begin{aligned}\frac{\partial E}{\partial t} &= -\int_{-\infty}^{+\infty} 2\mu \left[\left(\frac{\partial u}{\partial x}\right)^2 + \left(\frac{\partial v}{\partial y}\right)^2 + \left(\frac{\partial w}{\partial z}\right)^2 \right] \\ &\quad +\mu \left[\left(\frac{\partial u}{\partial z} + \frac{\partial w}{\partial x}\right)^2 + \left(\frac{\partial v}{\partial z} + \frac{\partial w}{\partial y}\right)^2 + \left(\frac{\partial u}{\partial y} + \frac{\partial v}{\partial x}\right)^2 \right] \mathrm{d}z \end{aligned} \tag{23.1}$$

On remarque que cette expression ne fait intervenir que des carrés de différents termes. Grâce au théorème de Parseval on peut donc disséquer cette dissipation en un terme pour chaque composante du spectre. Avec un peu de calcul on arrive à la formule donnée par Lamb (1932), valable pour des vagues de gravité au second ordre en pente des vagues, et quelle que soit la profondeur,

$$\frac{\partial}{\partial t} E\left(f,\theta\right) = -4\nu_w k^2 E\left(f,\theta\right) \tag{23.2}$$

avec ν_w la viscosité cinématique de l'eau (environ $3 \times 10^{-6}\mathrm{m}^2\ \mathrm{s}^{-1}$ à 20°C, et beaucoup plus pour des eaux très froides). En pratique cette dissipation est très faible pour les ondes de gravité, et pour des vagues de période supérieure à 1.3 s, l'effet de la viscosité de l'air est plus important (cf. eq. **??**). Par contre l'effet de la viscosité de l'eau est un terme dominant pour les ondes capillaires (longueurs d'ondes inférieures à 2 cm), et peut donc avoir un effet significatif, via les interactions non-linéaires, sur les ondes mixtes de gravité-capillarité. Dans ces cas il faut aussi, en général, prendre en compte la tension de surface.

23.2 Effets de la turbulence dans l'eau

La turbulence, des plus petites aux plus grandes échelles peut avoir divers effets sur les vagues (Phillips 1961). En particulier les tourbillons et les variations de courant à petite échelle peuvent partiellement réfléchir les vagues (Rayevskiy 1983), tandis que les variations à des échelles plus grandes que la longueur d'onde entraînent une réfraction des vagues (chapitre **??**). Dans tous les cas le transfert d'énergie entre les vagues et la turbulence peut se calculer en considérant l'équation d'évolution de l'énergie cinétique turbulente (ECT, ou TKE en anglais, voir par exemple Phillips 1977). Le taux local de production d'ECT par le mouvement des vagues est,

$$P_{ws} = \rho \sum_{i,j} \overline{u_i' u_j'} \frac{\partial u_i}{\partial x_j}, \tag{23.3}$$

qui s'exprime en Watts par mètre cube dans le système international. u_i est la composante i de la vitesse induite par les vagues, et $\overline{u_i' u_j'}$ est le tenseur des flux turbulents ou tenseur de Reynolds. En supposant que ces flux turbulents sont constants par rapport à la phase des vagues, ce qui peut être une première approximation,

Ardhuin et Jenkins (2006) ont montré que P_{ws} se simplifie. En supposant de plus que le flux $\rho(\overline{u'w'}, \overline{v'w'})$ est uniforme et égal (dans l'eau) à la tension de vent $\tau_a = \rho_a u_\star^2$, on a

$$P_{ws} = \tau_a \cdot \frac{\partial \mathbf{U}_s}{\partial z}, \tag{23.4}$$

avec $\mathbf{U}_s$ la dérive de Stokes. On peut aussi exprimer cette production comme un terme de source pour l'énergie des vagues,

$$\frac{\partial}{\partial t} E(f,\theta) = S_{turb} = -\frac{\rho_a}{\rho_w} u_\star^2 \sigma k \cos(\theta_\star - \theta) \frac{\cosh(2kD)}{\sinh^2(kD)} E(f,\theta) \tag{23.5}$$

qui devient

$$S_{turb} = -2\frac{\rho_a}{\rho_w} u_\star^2 \sigma k \cos(\theta_\star - \theta) E(f,\theta) \tag{23.6}$$

en eau profonde. Teixeira et Belcher (2002) étaient déjà arrivés à la même expression en faisant l'hypothèse d'une distorsion rapide de la turbulence par le mouvement des vagues. Cette hypothèse est très proche de notre hypothèse de non-corrélation de la turbulence avec la phase des vagues. En pratique cette expression donne probablement un ordre de grandeur raisonnable pour l'interaction des vagues avec la turbulence dans la couche de mélange océanique. Elle donne une expression pour la source d'énergie des principaux mouvements turbulents que sont, dans ce cas, les circulations de Langmuir (chapitre **??**) dont le mouvement est effectivement assez lent pour considérer qu'il s'agit d'une distorsion rapide par les vagues. Par ailleurs cette expression indique que les vagues gagnent de l'énergie lorsqu'elles se propagent contre le vent. Il reste à voir si dans ce cas l'hypothèse de non-corrélation est toujours valable. Ce terme est généralement négligeable pour les houles longues, par rapport au frottement à la surface (même s'il est visqueux). Par contre ce terme peut représenter environ 10% de la dissipation de la mer du vent et c'est aussi la source d'énergie probable des circulations de Langmuir, dont le rôle est dominant dans le mélange près de la surface.

23.3 Déferlement

23.4 Paramétrage de la dissipation par déferlement

23.4.1 Approche énergétique globale: compléments du 5.3.2

Parce que les mesures de vitesse orbitale à la crête sont très rares, (Battjes and Janssen, 1978) on redéfini le seuil en vitesse orbitale sous forme de seuil en hauteur de vague, afin de s'appuyer sur la distribution de Rayleigh correspondant assez bien aux observations

$$p(H) = \frac{2H}{H_{\rm rms}^2} \mathrm{e}^{-(H/H_{\rm rms})^2} \tag{23.7}$$

Ils ont alors utilisé une relation empirique assez bien vérifiée: la hauteur maximale des vagues par petits fonds est proportionnelle à profondeur avec un seuil γD, où γ est de l'ordre de 0.3 à 0.8. En prenant γ constant, ce seuil correspond à la limite quand kD tend vers zéro du seuil $H_{\rm max}/L = 0.14\tanh(kD)$ de Miche, soit $H_{\rm max} = 0.14 * 2\pi D$. Les travaux récents de Ruessink et coll. (2003) montrent d'ailleurs que γ est une fonction de kD. Battjes et Janssen (1978) ont obtenu le taux de dissipation des vagues en modifiant la distribution p en imposant que toutes les vagues qui auraient eu une hauteur supérieure à γD sont limitées à γD et donc la probabilité de déferlement p_B est donnée par la fraction des vagues qui ont cette hauteur.

Ensuite le taux de dissipation par unité de longueur de crête ϵ est donné par analogie avec un ressaut hydraulique (figure 23.1).

Conditions de saut et dissipation locale: première approche

Dans un ressaut hydraulique classique, l'écoulement et permanent et le fond est plat, avec des hauteurs d'eau D_1 et D_2 de part et d'autre du ressaut. Dans le référentiel en translation avec le ressaut l'écoulement moyen est permanent et les vitesses U_1 et U_2 sont uniformes sur la verticale avec un débit liquide à travers le ressaut donné par $Q = U_1 D_1 = U_2 D_2$. En faisant un bilan des flux dans un volume de contrôle autour du ressaut et en supposant que, assez loin du ressaut, l'écoulement est hydrostatique, la conservation de la quantité de mouvement donne

$$D_1 U_1^2 + 0.5 g D_1^2 = D_2 U_2^2 + 0.5 g D_2^2. \tag{23.8}$$

On peut déjà éliminer U_1 et U_2 pour obtenir

$$U_1 = \sqrt{\frac{g D_2 (D_1 + D_2)}{2 D_1}} + \Delta_U \tag{23.9}$$

$$U_2 = \sqrt{\frac{g D_1 (D_1 + D_2)}{2 D_2}} + \Delta_U \tag{23.10}$$

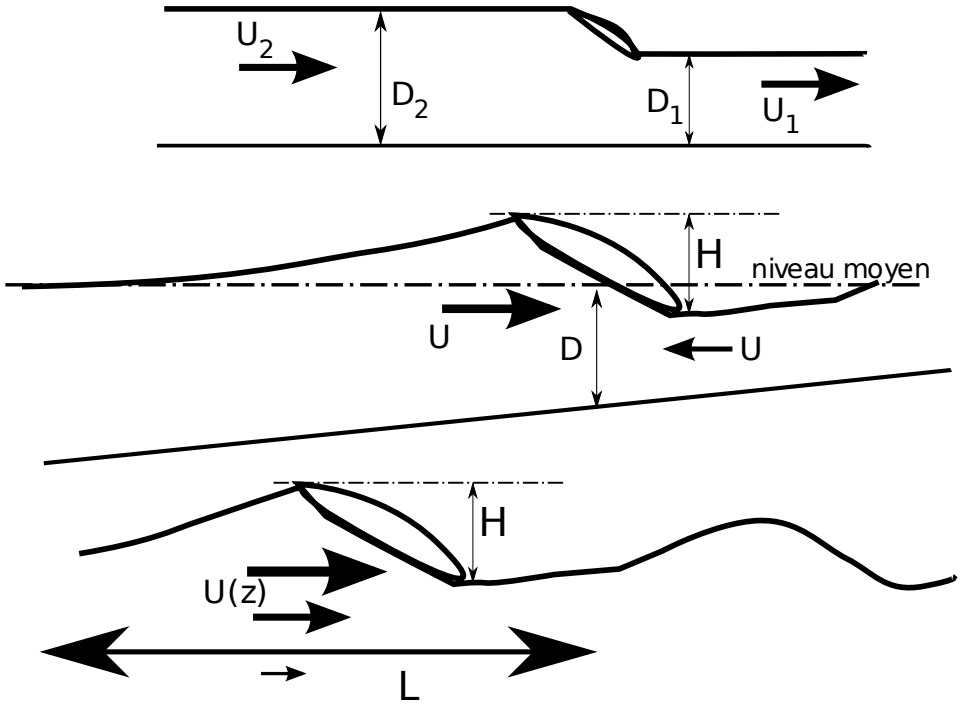

Figure 23.1: Analogie entre un ressaut hydraulique (en haut) une vague déferlante par petits fonds (au milieu) et une vague déferlante par grand fond (en bas).

La constante Δ_U ne peut pas être déterminée

On calcule alors ϵ_1, la perte d'énergie mécanique par unité de temps et par unité de longueur du ressaut, qui, conditions stationnaires oblige, est égale au flux entrant dans le volume de contrôle compris entre les sections verticales en 1 et 2. Ce flux se décompose en flux advectif d'énergie cinétique $\rho_w U^3 D/2$, flux advectif d'énergie potentielle $\rho_w g \int z dz = \rho_w g D^2/2$ et le travail des contraintes sur les bords du volume de contrôle, qui se réduisent ici aux forces de pression, soit $\int pU dz = \int \rho g(D-z) dz U = \rho_w g D^2/2$. Il suffit donc de remplacer les vitesses par (23.9) et (23.10) pour obtenir,

$$\epsilon_1(D_1, D_2) = \frac{\rho_w U_1 D_1}{2}\left(U_1^2 - U_2^2\right) + \rho_w g U_1 D_1 \left(D_2 - D_1\right) = \frac{1}{4}\rho_w g \frac{\left(D_2 - D_1\right)^3}{D_1 D_2} U_1 D_1. \tag{23.11}$$

L'analogie entre les vagues et le ressaut consiste à remplacer $D_2 - D_1$ par la hauteur de la vague H, égaler la profondeur D_1 et D_2 de part et d'autre du ressaut avec profondeur moyenne D, H. Il reste à paramétrer le débit $Q = U_1 D_1$. En suivant Hwang and Divoky (1970), on considère que le flux net à vers la côte est nul, et donc, dans le référentiel qui suit la crête de la vague, la vitesse moyenne est la vitesse de phase C, le débit est donc égal à la hauteur d'eau moyenne que multiplie cette vitesse, soit $U_1 D_1 = CD$. En eau pu profonde $C \simeq \sqrt{gD}$ et la dissipation par unité de surface est donc,

$$\epsilon(H, D, T) \simeq \frac{1}{L}\epsilon_1(D - H/2, D + H/2) \approx \frac{1}{4}\rho g \frac{(BH)^3}{DT} \tag{23.12}$$

où B un facteur d'ajustement voisin de 1: nous avons quitté la géophysique pour aller dans le génie côtier, il faut bien des facteurs de calibration empirique pour arriver à un résultat précis!

23.4.2 Approche spectrale

Si l'on veut maintenant décomposer la dissipation totale ϵ_{tot} sur le spectre on peut utiliser une approche empirique en redistribuant la dissipation sur toutes les composantes de façon proportionnelle à l'énergie ou à l'énergie que multiplie un facteur de forme spectrale (par exemple f^2 pour dissiper plus les hautes fréquences). Ce type d'approche est généralement utilisé par petits fonds car du fait de la non-dispersivité des vagues, la distinction des différentes composantes a peu de sens.

Mais de façon plus générale, on veut pouvoir découpler le déferlement des différentes composantes qui ont des longueurs d'ondes ou directions très différentes. Ce type d'approche permet d'exploiter les observations de probabilités de déferlement par Banner et al. (2000), de manière rationnelle.

Une première étape est de déterminer la probabilité de déferlement par "échelle": ces échelles sont des voisinages spectraux au sein desquels la séparation des nombres d'onde n'a pas de sens physique car on peut

considérer une vagues comme la somme de composantes dont les nombres d'ondes sont proches. Ainsi on relie les probabilités de déferlement à B qui, en choisissant $p = 2$ est une variance de vitesse orbitale adimensionnelle.

Il faut ensuite déconvoluer cette probabilité de déferlement en la distribuant sur les composantes spectrales. Le taux de dissipation spectral associé au déferlement spontané des vagues est ainsi

$$S_{\mathrm{dis,s}}\left(\mathbf{k}\right) = \int_{\mathbf{k}} h(\mathbf{k}' - \mathbf{k}) p\left(B(\mathbf{k}')\right) q\left(B'(\mathbf{k}')\right) \mathrm{d}\mathbf{k}' E\left(\mathbf{k}\right). \tag{23.13}$$

où l'intégrale sur $\mathbf{k}'$ exprime la déconvolution des échelles vers les composantes spectrales avec filtre h, et où p est la probabilité de déferlement par échelle et q est le taux de dissipation par longueur de crête. La formalisation complète de cette démarche est en cours (Filipot et coll. 2008).

Actuellement des approches semi-empiriques (van der Westhuysen et coll. 2007, Ardhuin et al. 2008c) ont abouti a des termes de dissipation par déferlement, qui combine un déferlement spontané $S_{\mathrm{dis,s}}$ avec un déferlement induit par les vagues plus longues, $S_{\mathrm{dis,c}}$, sous la forme,

$$S_{\mathrm{ds}}(f,\theta) = \sigma C_{\mathrm{ds}} \left[\max\left\{\frac{B\left(f,\theta\right)}{B_r} - 1, 0\right\}\right]^2 F(f,\theta) + S_{\mathrm{ds,c}}(f,\theta). \tag{23.14}$$

avec

$$B\left(f,\theta\right) = 2\pi \int_{\theta-\pi\theta}^{\theta+\pi} k^3 cos^2\left(\theta - \theta'\right) F(f,\theta')/C_g \mathrm{d}\theta', \tag{23.15}$$

et un seuil $B_r = 0.0009$ cohérent avec le seuil mesuré par Banner et coll. (2000). Le second terme, $S_{\mathrm{ds,c}}$ représente la dissipation induite par le déferlement de vagues de plus grande longueur d'onde qui "lissent" la surface et entraîne une dissipation des vagues les plus courtes. En première approximation on peut exprimer ce terme à partir de la fonction Λ, en estimant qu'une vague de période au moins M fois plus grande que la vague courte considérée induit une dissipation totale de l'énergie de la vague courte. Il suffit donc de calculer le nombre de vagues longues qui dépassent la vague courte par unité de temps, c'est l'intégrale de $|\mathbf{C} - \mathbf{C}'|\,\Lambda(\mathbf{C})d\mathbf{C}$,

$$S_{\mathrm{ds,c}}(f,\theta) = \int_0^{f/M} \left|\mathbf{C} - \mathbf{C}'\right| \Lambda(f',\theta')\mathrm{d}f'\mathrm{d}\theta' F(f,\theta), \tag{23.16}$$

où on a considéré que la vitesse de phase $\mathbf{C}'$ correspondant aux vagues de fréquence f' et de direction θ'.

La plupart des codes de calcul de l'état de mer utilise encore actuellement des formulations empiriques ajustées pour que les modèles reproduisent les observations de croissance des vagues sous l'effet du vent, et le développement complet de l'état de la mer. De ce fait, ces paramétrages ne sont pas faits pour fonctionner en eau peu profonde ou en présence de forts gradients de courant, et il est d'usage de leur ajouter un terme de déferlement 'bathymétrique' afin de dissiper correctement l'énergie des vagues s'approchant des plages.

Les travaux en cours au SHOM visent justement à aboutir à un paramétrage physique de $P_B(H,T)$ pour éviter la distinction assez difficile et arbitraire entre le 'déferlement bathymétrique' et le 'moutonnement'. Ainsi, Filipot et al. (2010a) ont ajusté un paramétrage commun de la fonction $W(H,T)$ aux observations de Thornton and Guza (1983) et à celles de Banner et al. (2000). On définit d'abord des hauteurs de vagues dans un voisinage spectral autour de la fréquence $f_c = 1/T$,

$$H(f_c) = \int_0^{f_{\max}} U(f_c, f) E(f') df', \tag{23.17}$$

avec U une fenêtre spectrale centrée sur f_c et de largeur proportionnelle à f_c. Une largeur de 0.7 à 1.3 f_c est cohérente avec l'analyse de Banner et al. (2000) et permet de trouver, pour les vagues dominantes, des hauteurs proche de celles données par une analyse vague par vague classique. Filipot et al. (2010a) ont montré que l'on pouvait exprimer une fonction W à partir de vitesses orbitales adimensionnelles,

$$\beta = \frac{\overline{k}(f_c)H(f_c)}{\tanh(\overline{k}(f_c)D} \tag{23.18}$$

sous la forme

$$W_{FAB}(H) = a\left[\frac{\beta}{\widetilde{\beta}}\right]^2 \left\{1 - \exp\left[-\left(\frac{\beta}{\widetilde{\beta}}\right)^p\right]\right\}, \tag{23.19}$$

donnait de bon résultats avec $a = 1.5$ et $p = 4$, comme indiqué en figures 23.2 et 23.3. La constante $\widetilde{\beta}$ joue le rôle de γ dans le modèle de Thornton and Guza (1983), et elle est ici définie comme une fraction de $\beta_{\max}$, valeur de β correspondant aux vagues d'amplitude maximale pour une période T fixée. On obtient alors une répartition en fréquence de la dissipation $S_{ds}(f)$ en utilisant le taux de dissipation (5.29), et en redistribuant la dissipation des vagues de fréquence centrée en f_c sur l'intervalle de fréquence qui contribue à $H(f_c)$.

La répartition en direction pourrait être faite de la même façon en définissant un $H(f_c, \theta_c)$ au lieu de $H(f_c)$. Malheureusement il n'y a pas encore assez de mesures directionnelles du déferlement pour valider et calibrer cette approche.

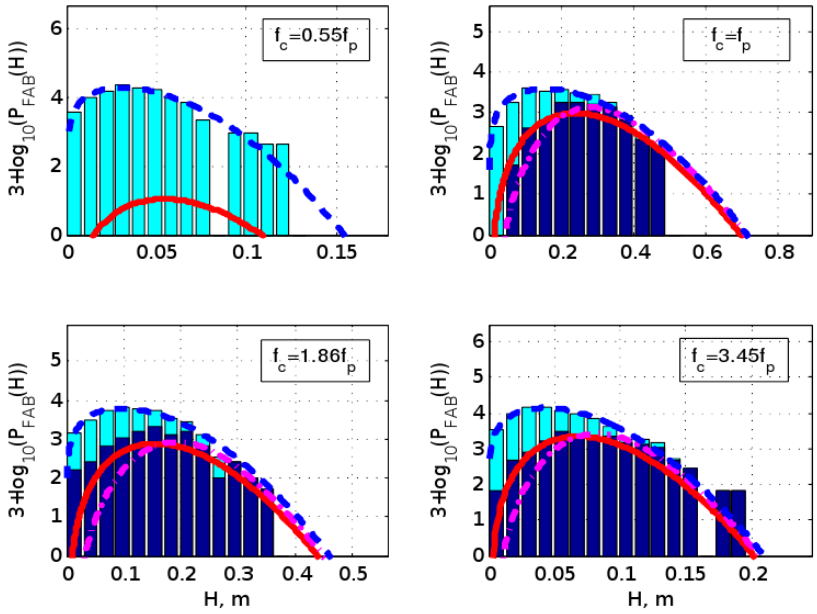

Figure 23.2: Paramétrage des probabilités de déferlement
Illustration de la capacité du paramétrage de W donné par (23.19) à reproduire les observations de déferlement réalisées dans le lac George en Australie, pour des profondeurs intermédiaires, avec k_pD de l'ordre de 1 (tiré de Filipot et al. (2010a)). Chaque figure correspond à une bande de fréquence. Les barres indiquent les observations de $p(H)$ en clair et $p_B(H)$ en foncé, et les courbes sont les paramétrages données par p_R (Rayleigh, pointillés bleus) et $W(H)P_R(H)$ pour $(a = 1.5, p = 4)$ (trait mixte rose) et $(a = 1, p = 2)$ (trait plein rouge) .

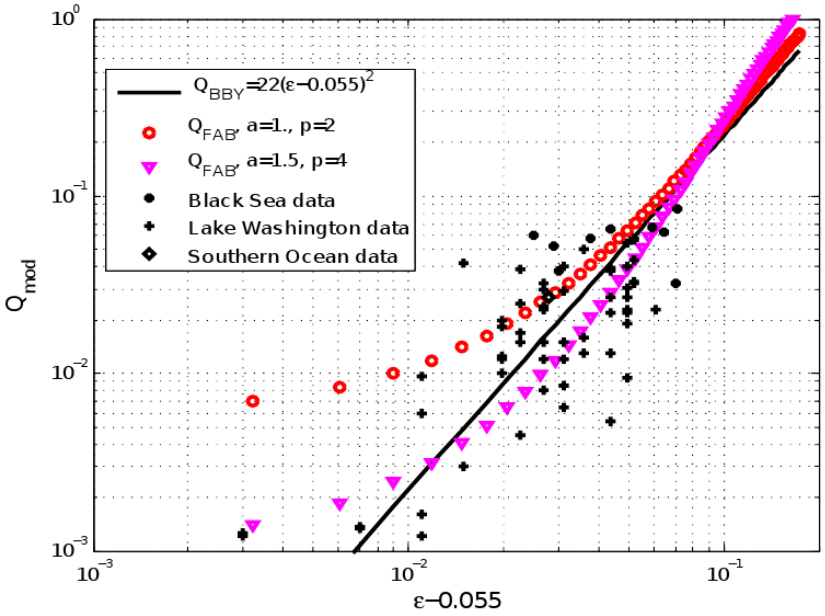

Figure 23.3: Paramétrage des probabilités de déferlement
Illustration de la capacité du paramétrage de W donné par (23.19) à reproduire les observations de déferlement pour les vagues dominantes par grands fonds.

Chapter 24

Wave-current interactions in three dimensions

24.1 Introduction

Parce que la surface monte et descend, faire une moyenne de l'écoulement près de la surface n'a pas beaucoup de sens, sauf pour des mesures car on n'a pas toujours le choix. Du point de vue de la modélisation il est intéressant de résoudre les gradients en surface et donc de séparer clairement l'air et l'eau. Pour cela il faut tranformer au moins la coordonnée verticale. L'approche proposée ici suit celle de Ardhuin et al. (2008c) qui est détaillée dans Delpey (2012) et dans une version simplifiée dans Bennis et al. (2011).

Un jeu d'équation a été obtenu par Mellor (2003) à partir d'un simple changement de coordonnée verticale. La nouvelle coordonnée verticale ς est définie implicitement par,

$$z = s\left(\mathbf{x}, \varsigma, t\right) = \widehat{\zeta} + \varsigma D + \widetilde{s}, \tag{24.1}$$

de telle sorte que $z = \widehat{\zeta} + \widetilde{\zeta}$, la position instantanée de la surface libre, pour $\varsigma = 0$, et $z = -h$, la position du fond, pour $\varsigma = -1$. on rapelle que $D = h + \widehat{\zeta}$.

Les équations du mouvement ont été ainsi transformées et moyennées sur la phase des vagues par Mellor (2003), pour des vagues monochromatiques. On peut appliquer le même principe à des vagues aléatoires (Ardhuin et coll. 2004) en prenant, à l'ordre 1 en pente des vagues,

$$\widetilde{s} = \sum_{\mathbf{k},s_1} \frac{\sinh(kz + kD)}{\sinh(kD)} Z^{s_1}_{1,\boldsymbol{k}} \mathrm{e}^{\mathrm{i}\psi^{s_1}_{1,\mathbf{k}}}. \tag{24.2}$$

Avec cette nouvelle coordonnée, les surfaces où ς est constant sont aussi des lignes de courant pour le mouvement des vagues. Il n'y a donc plus de vitesse verticale induite par les vagues dans ces coordonnées.

Malheureusement Mellor (2003) a négligé la modification des vitesses orbitales par la pente du fond et variations horizontales du champ de vagues. En effet, dans ces cas (2.25)–(2.28) ne sont pas solution exacte de l'équation de Laplace. Or ces effets contribuent des termes du même ordre que les termes retenus par Mellor (Ardhuin et al., 2008b). Or, ces termes relativement complexes n'agissent que sur la pseudo-quantité de mouvement car ils représentent le déplacement vertical de PQDM U_s. Il est donc inutile d'introduire cette complexité si l'on s'intéresse à l'autre partie de la QDM, $\widehat{u} = U - U_s$, la QDM du courant moyen.

Il apparaît donc avantageux de déterminer des équations pour $\widehat{u}$ directement. Or ce travail a déjà été fait par Andrews et McIntyre (1978), il suffit donc de le transcrire en utilisant le mouvement connu des vagues (Ardhuin et coll. 2007b).

En définissant alors $\mathbf{X}$ comme la divergence du tenseur de Reynolds, on peut appliquer la moyenne GLM aux équations de Navier-Stokes en moyenne de Reynolds (RANS). Les équations ci-dessus sont donc une approximation au second ordre en cambrure de la moyenne GLM des équations RANS, elles sont donc baptisées équations "glm2-RANS".

24.2 Mouvements Lagrangiens et Eulériens

Nous avons vu au chapitre 1 que le mouvement orbital des vagues induit une dérive dans le sens de propagation, la dérive de Stokes $\mathbf{U}_s$. Cette dérive est intimement liée aux oscillations verticales et horizontales induites par le mouvement orbital. On peut ainsi séparer le mouvement de dérive d'une particuler en une dérive de Stokes et un courant Eulérien $\widehat{\mathbf{u}}$ qu'on appellera simplement "courant". La dérive de Stokes peut être assez importante. Au large, elle peut dépasser 1.6% de la vitesse du vent en surface, en particulier pour les vents forts (Ardhuin et

al. 2008b). Près de la côte la dérive est amplifiée quand la profondeur diminue et peut atteindre 0.5 m/s dans la zone de déferlement. Pour des vagues de cambrure maximale, Longuet-Higgins (1979) a calculé, en négligeant la viscosité, que la dérive pouvait atteindre 27% de la vitesse de phase. Enfin, le déferlement des vagues peut induire des vitesses importantes, en surface, dans le front déferlant (Melville and Rapp, 1988). Ces deux effets seront négligés dans ce qui suit.

24.2.1 Flux de masse et de quantité de mouvement

On peut définir le flux de masse (aussi appelé transport) moyen $\mathbf{M}^w = \left(M_x^w, M_y^w\right)$ associé aux vagues par la différence entre le transport total $\mathbf{M}$ et le transport du courant Eulérien moyen, $\widehat{\mathbf{M}}$,

$$M_\alpha^w = M_\alpha - \widehat{M}_\alpha = \int_{-h}^{\zeta} \rho_w \left(\widehat{u}_\alpha + \widetilde{u}_\alpha\right) \mathrm{d}z - \int_{-h}^{\widehat{\zeta}} \rho \widehat{u}_\alpha \mathrm{d}z. \tag{24.3}$$

Avec cette définition, le transport induit par les vagues est égal, en absence de courant, au transport total. En utilisant les vitesses issues de la théorie linéaire, on trouve, au second ordre en pente des vagues,

$$\begin{aligned} M_\alpha^w &= \int_0^{\zeta} \rho u_\alpha \mathrm{d}z, & (24.4)\\ &= \rho_w g \frac{E}{C} \frac{k_\alpha}{k}, & (24.5) \end{aligned}$$

On remarque que le flux de masse associé à la propagation des vagues est $1/C$ fois le flux d'énergie.

Si l'on considère que ce flux est la somme des flux entre des niveaux fixes z et $z + \mathrm{d}z$, des vagues monochromatiques ont un flux de profil parabolique, concentré dans la région $-a < z < a$ avec a l'amplitude de ces vagues. Pour des vagues aléatoires le flux sera compris entre le creux le plus bas et la crête la plus haute. C'est le point de vue Eulérien sur la dérive de Stokes.

24.2.2 Moyenne Lagrangienne généralisée

Toutefois cette description ne correspond pas à la dérive de particules en suspension qui suivent la dérive de Stokes telle que définie au chapitre 1 avec le point de vue Lagrangien. La vitesse de dérive d'une particule dans le cas général est la vitesse Lagrangienne $\mathbf{U} = \widehat{\mathbf{u}} + \mathbf{U}_s$. Intégrées sur la verticale les deux expressions du transport $\mathbf{M}^w$ sont indentiques.

En trois dimensions les points de vue Eulériens et Lagrangiens sont tout à fait différents et pour certaines applications (comme le transport de matière en suspension ou l'étude de propriétés près de la surface) il peut être avantageux d'adopter un point de vue Lagrangien. De part les changements de coordonnées qu'elle impose, cette idée peut faire frémir les habitués de la mécanique des fluides. Les vagues permettent toutefois une simplification de taille: les déplacements sont quasi-périodiques. On peut alors définir des changements de coordonnées relativement simples qui aboutissent à des équations tout à fait maniables. En particulier, Andrews and McIntyre (1978a) ont défini une moyenne Lagrangienne généralisée.

Pour tout champ scalaire ϕ, on définit le champ ϕ^ξ à la position moyenne $\mathbf{x}$, par

$$\phi^\xi(\mathbf{x}, t) = \phi\left(\mathbf{x} + \xi(\mathbf{x}, t), t\right) \tag{24.6}$$

On peut définir la moyenne Lagrangienne généralisée si la fonction Ξ telle que $\Xi(\mathbf{x}) = \mathbf{x} + \xi(\mathbf{x}, t)$ est bijective. Dans ce cas il existe un champ de vitesse unique $\mathbf{v}(\mathbf{x}, t)$ tel que quand le point $\mathbf{x}$ se déplace à la vitesse $\mathbf{v}$, alors le point matériel $\mathbf{x} + \xi$ se déplace à la vitesse du fluide $\mathbf{u}^\xi$ (figure 24.1), ce qui s'écrit mathématiquement,

$$\left(\frac{\partial}{\partial t} + \mathbf{v} \cdot \boldsymbol{\nabla}\right) \Xi = \mathbf{u}^\xi \tag{24.7}$$

Pour tout opérateur de moyenne Eulérienne, on note $\overline{\phi(\mathbf{x}, t)}$ la moyenne de $\phi(\mathbf{x}, t)$ (ce peut être une moyenne sur des phases, des réalisations, une moyenne temporelle ou spatiale). Alors on obtient la définition de la moyenne Lagragienne généralisée (GLM) en imposant

$$\begin{aligned} \overline{\xi(\mathbf{x}, t)} &= 0 & (24.8)\\ \overline{\mathbf{v}(\mathbf{x}, t)} &= \mathbf{v}(\mathbf{x}, t). & (24.9) \end{aligned}$$

La vitesse en moyenne GLM est $\overline{\mathbf{u}}^L = \mathbf{v}$, et on peut ainsi définir les moyennes de n'importe quelle variable. Ainsi la moyenne GLM est différente de la moyenne Eulérienne. La différence entre ces deux moyennes est la correction de Stokes (Andrews et McIntyre 1978). La correction de Stokes de la vitesse est, par définition, la vitesse de Stokes

$$\mathbf{U}_s = \overline{\mathbf{u}}^L - \overline{u}. \tag{24.10}$$

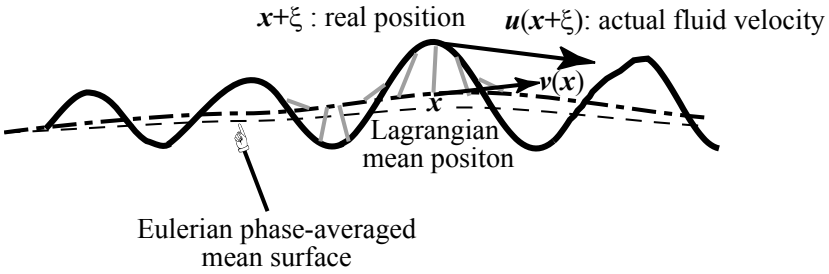

Figure 24.1: Schéma de principe de la moyenne Lagrangienne généralisée

$\overline{\mathbf{u}}^L$ s'interprète simplement comme la vitesse de dérive moyenne des particules d'eau. De manière plus générale, pour un champ continuement différentiable ϕ, la correction de Stokes est donnée par (Andrews et McIntyre 1978a, équation 2.27)

$$\overline{\phi}^L = \overline{\phi} + \overline{\xi_j \frac{\partial \phi}{\partial x_j}} + \frac{1}{2}\overline{\xi_j \xi_k}\frac{\partial^2 \overline{\phi}}{\partial \xi_j \partial \xi_k} + O(\varepsilon_1^3) \tag{24.11}$$

On peut, par exemple, appliquer cette relation pour calculer les gradients moyens de vitesse en présence de vagues (Ardhuin et Jenkins 2006). Pour des vagues monochromatiques, au-dessus d'un fond en pente faible, on rappelle les champs de pression et de vitesse donnés par la théorie d'Airy (1841)

$$\widetilde{p} = \rho_w g a \left[F_{CC}\cos(kx_1 - \omega t)O(\varepsilon_1) + O(\varepsilon_2)\right] \tag{24.12}$$

$$\widetilde{u}_1 = a\sigma\left[\frac{k_1}{k}F_{CS}\cos(kx_1 - \omega t) + O(\varepsilon_1) + O(\varepsilon_2)\right] \tag{24.13}$$

$$\widetilde{u}_2 = a\sigma\left[\frac{k_2}{k}F_{CS}\cos(kx_1 - \omega t) + O(\varepsilon_1) + O(\varepsilon_2)\right] \tag{24.14}$$

$$\widetilde{u}_3 = a\sigma\left[F_{SS}\sin(kx_1 - \omega t) + O(\varepsilon_1) + O(\varepsilon_2)\right] \tag{24.15}$$

avec $k = (k_1^2 + k_2^2)^{1/2}$ et ω le nombre d'onde et la pulsation, $\mathbf{k} = (k_1, k_2)$ le vecteur d'onde, et σ défini par $\sigma^2 = gk\tanh(kD)$, où g est l'accélération de la gravité et D la profondeur d'eau moyenne. Les notation $F_{CS} = \cosh(kz + kD)/\sinh(kD)$ et $F_{SS} = \sinh(kz + kD)/\sinh(kD)$ ont été utilisées.

En intégrant dans le temps on trouve le déplacement des particules fluides,

$$\xi_1 = -a\left[\frac{k_1}{k}F_{CS}\sin(kx_1 - \omega t) + O(\varepsilon_1) + O(\varepsilon_2)\right], \tag{24.16}$$

$$\xi_2 = a\left[\frac{k_2}{k}F_{CS}\sin(kx_1 - \omega t) + O(\varepsilon_1) + O(\varepsilon_2)\right], \tag{24.17}$$

$$\xi_3 = a\left[F_{SS}\cos(kx_1 - \omega t) + O(\varepsilon_1) + O(\varepsilon_2)\right]. \tag{24.18}$$

Pour simplifier les notations, on choisit la direction 1 dans le sens de propagation des vagues. Les corrections de Stokes (24.11) des cisaillements sont alors,

$$\overline{\frac{\partial \widetilde{u}}{\partial z}}^L = \overline{\xi_1 \frac{\partial^2 \widetilde{u}}{\partial x \partial z}} + \overline{\xi_3 \frac{\partial^2 \widetilde{u}}{\partial z^2}} = \frac{a^2}{2}k^2\sigma F_{CS}F_{SS} \tag{24.19}$$

$$\overline{\frac{\partial \widetilde{w}}{\partial x}}^L = \overline{\xi_3 \frac{\partial^2 \widetilde{w}}{\partial x \partial z}} + \overline{\xi_1 \frac{\partial^2 \widetilde{w}}{\partial x^2}} = \frac{a^2}{2}k^2\sigma F_{CS}F_{SS}. \tag{24.20}$$

Ces expressions se généralisent aux vagues aléatoires car les termes de second ordre sont le résultat de corrélations entre termes de premier ordre (voir par exemple Kenyon 1969 pour une discussion similaire). Ainsi, les deux cisaillements moyens sont chacun égaux à la moitié du gradient vertical de la dérive de Stokes U_s,

$$\overline{\frac{\partial \widetilde{u}}{\partial z}}^L = \overline{\frac{\partial \widetilde{w}}{\partial x}}^L = \frac{1}{2}\frac{\partial U_s}{\partial z}, \tag{24.21}$$

avec $u = u_1$, $w = u_3$, $x = x_1$ and $z = x_3$.

Le changement de coordonnée implicitement associé à la moyenne GLM par la fonction Ξ conserve le volume au premier ordre en ε_1, les moyennes obtenues sont donc, en première approximation, des moyennes sur un volume (Jenkins et Ardhuin 2004). On retrouve que la vorticité du mouvement est nulle ($\overline{\partial\widetilde{w}/\partial x}^L - \overline{\partial\widetilde{u}/\partial z}^L = 0$), ce qui

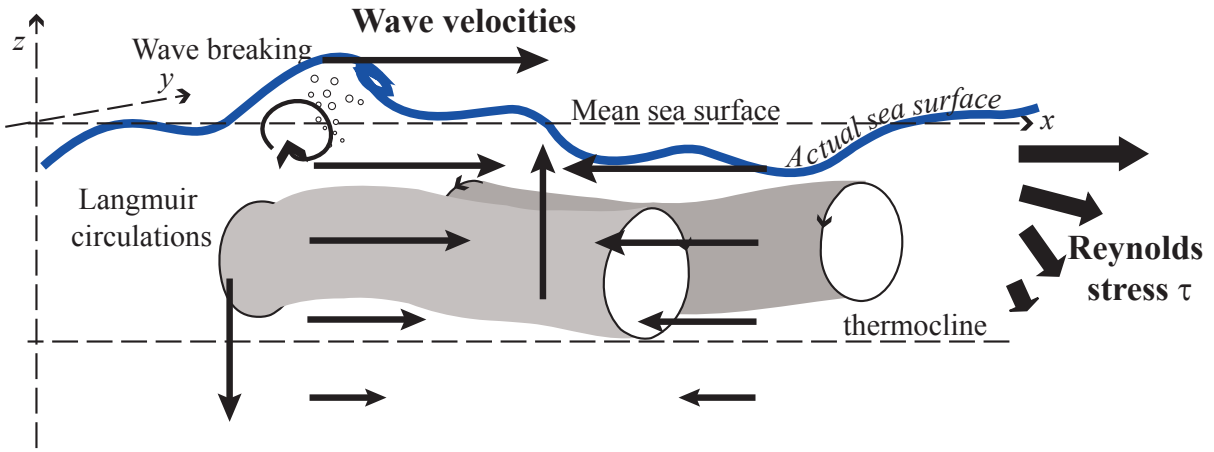

Figure 24.2: Vitesse induite par les vagues (flèches fines) et processus de mélange dans l'océan superficiel. Les flux d'énergie cinétique turbulente entre l'atmosphère et l'océan sont largement supportés par le déferlement d'ondes courtes (e.g. Donelan 1998) et sont en partie transmis par les circulations de Langmuir qui sont un ensemble de tourbillons d'échelles multiples alignés dans la direction du vent et brassant l'ensemble de la couche de mélange. Dans la limite des petites pentes pour les grandes vagues, ces processus ne sont pas modifiés en moyenne et le cisaillement moyen induit par les grandes vagues est donné par (24.21). La production d'énergie cinétique turbulente par interaction des vagues et de la turbulence est donc le flux turbulent vertical de quantité de mouvement horizontale (flèches épaisses) multiplié par la moyenne en volume du cisaillement induit par les vagues. Cette moyenne en volume donne plus de poids aux crêtes par rapport aux creux.

est normal puisque (24.13)–(24.18) ont été déterminées pour un mouvement irrotationnel. Par contre, la vitesse résiduelle U_s est bel et bien rotationnelle[1]. La moyenne non-nulle de $\partial w/\partial x$ pourrait, par erreur, être interprétée comme conduisant à une valeur infinie de w quand x tend vers l'infini, ce qui n'est pas le cas. Cette moyenne correspond plutôt au fait qu'il y a plus d'eau sous les crêtes que sous les creux des vagues, les crêtes contribuent donc plus à la moyenne (figure 24.2). Ces propriétés permettent de calculer la production ou destruction d'énergie cinétique turbulente (ECT) par le cisaillement des vagues. En supposant que la turbulence n'est pas corrélée avec la phase des vagues et en utilisant les hypothèse usuelles d'uniformité horizontale de la couche limite océanique, cette production d'ECT se fait au taux,

$$P_{ws} = \overline{\rho_w u_1' u_3'}^L \left(\overline{\frac{\partial \widetilde{u}}{\partial z}}^L + \overline{\frac{\partial \widetilde{w}}{\partial x}}^L \right) = \overline{\rho_w u_1' u_3'}^L \frac{\partial U_s}{\partial z}, \tag{24.22}$$

comme si la dérive de Stokes était un courant verticalement cisaillé.

24.2.3 Equations *glm*2-RANS pour $\partial \widehat{u}/\partial z = 0$

Afin de simplifier la discussion, nous utiliserons ici la forme des équations GLM donnée par Groeneweg (Groeneweg 1999, eq. 3.12) pour ρ_w constant, ce qui supprime, entre autres, les termes liés à la thermodynamique du fluide,

$$\overline{D}^L \left(\overline{u}_i^L - P_i \right) + \epsilon_{i3j} f_3 \overline{u}_j^L + \frac{1}{\rho_w} \frac{\partial \overline{p}^L}{\partial x_i} - \overline{X}_i^L + gz = \frac{\partial}{\partial x_i} \left[\frac{1}{2} \overline{u_j^l u_j^l} \right] + P_j \frac{\partial \overline{u}_j^L}{\partial x_i}, \tag{24.23}$$

où la dérivée Langragienne D^L est une dérivée en suivant le fluide à la vitesse Langragienne moyenne $\overline{u}^L$.

$$P_i = A^{-x_i} \overline{\xi_{j,i} \left(u_j^l + \epsilon_{jik} \Omega_j \xi_k \right)} \simeq A^{-x_i} \overline{\xi_{j,i} u_j^l} \tag{24.24}$$

est la composante suivant i de la pseudo quantité de mouvement des vagues, soit, dans un langage plus familier, et de manière exacte aux ordres ε_1^2 et ε_2^0, $P_i = U_{si}$. On négligera ici le cisaillement vertical du courant, qui est pris en compte par Ardhuin et al. (2007b). On peut alors utiliser les vitesses et déplacements données par la théorie d'Airy (chapitre 1).

On remarque que les termes quadratiques dans (24.23) et (24.24) ne sont pas affectés par les corrections de premier ordre en ε_2, car ces corrections sont en quadrature avec les termes d'ordre ε_2^0. Il s'agit là d'un grande

[1] Ceci montre la non-commutation de l'opérateur GLM avec l'opérateur rotationnel. L'opérateur GLM commute cependant avec la dérivée Lagrangienne, c'est d'ailleurs l'intérêt principal du GLM (voir Andrews et McIntyre 1978a).

simplification par rapport au calcul à partir de la GLM alternative. Par contre, le cisaillement vertical du courant introduit des termes correctifs qui sont en phase avec les termes d'ordre ε_2^0 (MRL04). Le cisaillement vertical induit donc une modification de $\overline{u_j^l u_j^l}$ et $\mathbf{P}$ que nous négligerons dans un premier temps.

Nous allons calculer les différents termes induits par les vagues, d'abord pour une onde monochromatique dont la variance de l'élévation est $\mathrm{var}_\zeta = a^2/2$. On fera ensuite la superposition des composantes. Considérons d'abord le terme de pression. En utilisant le fait que $\widetilde{u}_\alpha\widetilde{u}_\alpha - \widetilde{w}^2 = \sigma^2\left(F_{CS}F_{CS} - F_{SS}F_{SS}\right)$ est indépendant de z à l'ordre ε_1^2, on peut ajouter $0.5\partial(\widetilde{u}_\alpha\widetilde{u}_\alpha - \widetilde{w}\widetilde{w})/\partial z$ à l'équation sur la verticale (24.23) pour obtenir, toujours à l'ordre ε_1^2,

$$\begin{aligned}\frac{\partial \widehat{w}}{\partial t} &+ \widehat{w}\frac{\partial \widehat{w}}{\partial z} + P_3\frac{\partial \widehat{w}}{\partial z} + (\widehat{u}_\beta + P_\beta)\frac{\partial \widehat{w}}{\partial x_\beta} + \frac{1}{\rho_w}\frac{\partial \overline{p}^L}{\partial z} + g \\ &= \frac{\partial}{\partial z}\left[\left(\overline{\widetilde{u}_\alpha\widetilde{u}_\alpha} + \overline{\widetilde{w}^2}\right)/2 + K_2\right] + P_\beta\frac{\partial}{\partial z}\left(\widehat{u}_\beta + P_\beta\right) + P_3\frac{\partial}{\partial z}\left(\widehat{u}_3 + P_3\right), \end{aligned} \tag{24.25}$$

qui se transforme en

$$\begin{aligned}\frac{1}{\rho_w}\frac{\partial}{\partial z}\left[\overline{p}^L + \rho_w g z - \rho_w\frac{\sigma^2 E}{2}\left(F_{CS}^2 + F_{SS}^2\right) - \rho_w K_2\right] &= -\frac{\partial \widehat{w}}{\partial t} - \widehat{w}\frac{\partial \widehat{w}}{\partial z} \\ - (\widehat{u}_\beta + P_\beta)\frac{\partial \widehat{w}}{\partial x_\beta} + P_\beta\frac{\partial}{\partial z}\left(\widehat{u}_\beta + P_\beta\right) &+ P_3\frac{\partial}{\partial z}\left(\widehat{w} + P_3\right). \end{aligned} \tag{24.26}$$

On ajoute alors le terme uniforme sur la verticale $-\sigma^2 E\left(F_{CC}^2 - F_{SS}^2\right)/2$, et en négligeant les trois premiers termes (hypothèse hydrostatique), l'intégration sur z donne

$$\frac{\overline{p(z)}^L}{\rho_w} = -g\left[(z - z_s) - kEF_{CC}F_{CS}\right] + K_2 + K_1 - \frac{gkE}{4\sinh(2kD)} \tag{24.27}$$

La force K_1 est définie par

$$K_1 = -\int_z^{\overline{\zeta}^L} P_\beta\frac{\partial}{\partial z'}\left(\widehat{u}_\beta + P_\beta\right)\mathrm{d}z' + \int_z^{\overline{\zeta}^L} P_3\frac{\partial}{\partial x_\beta}\left(P_\beta\right)\mathrm{d}z', \tag{24.28}$$

où l'on a utilisé la relation, qui peut se prouver dans la limite des faibles cambrures,

$$P_3 = -P_\alpha(-h)\frac{\partial h}{\partial x_\alpha} - \int_{-h}^{z}\frac{\partial P_\alpha(z')}{\partial x_\alpha}\mathrm{d}z'. \tag{24.29}$$

La constante d'intégration de la pression est donnée par la condition à la surface,

$$\overline{p(\zeta)}^L = -\rho_w g\left(\overline{\zeta}^L - z_s - kEF_{CC}F_{CS} - K_2(\overline{\zeta}^L)/g\right) = \overline{p}_a. \tag{24.30}$$

L'équation (24.41) donne

$$z_s = \overline{\zeta} + \overline{p}_a/(\rho_w g) - K_2(\overline{(\zeta)}^L)/g \tag{24.31}$$

et (24.27) devient

$$\frac{\overline{p}^L}{\rho_w} = \frac{\overline{p}^H}{\rho_w} + gkEF_{CC}F_{CS} + K_1 + K_2 - K_2(\overline{\zeta}^L), \tag{24.32}$$

où p^H est la pression hydrostatique, $p^H = \rho_w g(\overline{\zeta} - z) + \overline{p}_a$.

Au moins sous les creux des vagues, la correction de Stokes pour la pression (24.11) donne la pression Eulérienne moyenne

$$\overline{p} = \overline{p}^L - \rho_w gk\mathrm{var}_\zeta\left(F_{CS}F_{CC} + F_{SS}F_{SC}\right). \tag{24.33}$$

Ainsi l'equation (24.27) donne une relation, valable sous les creux des vagues et à l'ordre ε_1^2, entre la pression Eulérienne moyenne $\overline{p}$ et la pression GLM $\overline{p}^L$,

$$\overline{p} = \overline{p}^H - \rho_w g\mathrm{var}_\zeta kF_{SS}F_{SC}. \tag{24.34}$$

Par ailleurs, (24.12)–(24.18) donne, aux ordres ε_1^2 et ε_2,

$$\frac{1}{2}\left(u_j^l u_j^l\right) = \frac{1}{2}\left[F_{CS}^2 + F_{SS}^2\right]\sigma^2\mathrm{var}_\zeta = \frac{gk\mathrm{var}_\zeta}{2}\left[F_{CC}F_{CS} + F_{SC}F_{SS}\right]. \tag{24.35}$$

En notant la vitesse quasi-Eulérienne $\widehat{\mathbf{u}} = \overline{\mathbf{U}}^L - \mathbf{P}$, l'équation (24.23) devient, pour la vitesse horizontale,

$$\frac{\partial \widehat{u}_\alpha}{\partial t} + (\widehat{u}_\beta + U_{s\beta})\frac{\partial \widehat{u}_\alpha}{\partial x_\beta} + \widehat{w}\frac{\partial \widehat{u}_\alpha}{\partial z} + \epsilon_{\alpha 3\beta}f_3\overline{u}_\alpha^L + \frac{1}{\rho_w}\frac{\partial \overline{p}^H}{\partial x_\alpha} \simeq -\frac{\partial S^J}{\partial x_\alpha} + U_{s\beta}\frac{\partial \widehat{u}_\beta}{\partial x_\alpha} - P_3\frac{\partial \widehat{u}_\alpha}{\partial z}\overline{X}_\alpha^L, \tag{24.36}$$

où S^J est défini par (7.52).

L'équation (24.36) peut se transformer en

$$\frac{\partial \widehat{u}_\alpha}{\partial t} + \widehat{u}_\beta \frac{\partial \widehat{u}_\alpha}{\partial x_\beta} + \widehat{w}\frac{\partial \widehat{u}_\alpha}{\partial z} + \epsilon_{\alpha 3\beta}\left[f_3 \widehat{u}_\alpha + (f_3+\omega_3)\, U_{s\beta}\right] + \frac{1}{\rho_w}\frac{\partial \overline{p}^H}{\partial x_\alpha} = -\frac{\partial}{\partial x_\alpha}\frac{S^J}{\rho_w D} - P_3 \frac{\partial \widehat{u}_\alpha}{\partial z} + \overline{X}^L_\alpha. \tag{24.37}$$

Un paramétrage possible de la source de quantité de mouvement provenant des mouvements diabatiques est

$$\overline{X}^L_\alpha = \frac{\partial R_{\alpha\beta}}{\partial x_\beta} + \frac{\partial}{\partial z}\left(K_z \frac{\partial \widehat{u}_\alpha}{\partial z}\right) - T^{\mathrm{wc}}_\alpha - T^{\mathrm{turb}}, \tag{24.38}$$

avec $R_{\alpha\beta}$ le tenseur de Reynolds turbulent horizontal, tandis que les deux derniers termes correspondent au flux de quantité de mouvement des vagues vers la circulation moyenne.

24.2.4 Transformation de coordonnée implicite associée au GLM

La moyenne des positions des particule aboutit à donner plus de poids là où les particules passent plus de temps (par exemple sur les crêtes des vagues), malgré un déplacement moyen nul pour chaque particule. Ainsi le domaine de validité de l'équation (24.37) est $-h < z < \overline{\zeta}^L$, au lieu de $-h < z < \overline{\zeta}$. Il faut donc faire attention en transformant les coordonnées, par exemple pour utiliser une coordonnée ς. On fait ici la démonstration pour une onde monochromatique dont la variance d'élévation de la surface est var_ζ. Cette démonstration ne faisant intervenir que des quantités d'ordre 2 en ε_1, proportionnelles au spectre de variance de l'élévation de surface $E(\mathbf{k})$, elle se transpose à des vagues alaétoires par simple sommation sur les composantes. Le Jacobien J de la transformation entre coordonnées Eulériennes et GLM est égal à 1 plus une quantité J_2 qui est de second ordre en ε_1,

$$J = 1 + J_2 + O(\varepsilon_1^3) \tag{24.39}$$

$$J_2 = -\frac{kA^{3D}}{\sigma} = -k^2 \mathrm{var}_\zeta \frac{\cosh\left[2k(z+h)\right]}{\sinh^2(kD)}, \tag{24.40}$$

Parce que le GLM n'induit pas d'étirement des coordonnées horizontales, une distance verticale $\mathrm{d}z' = J\mathrm{d}z$ en GLM correspond à une distance Cartésienne $\mathrm{d}z$. Puisque $J < 1$, alors $\mathrm{d}z' > \mathrm{d}z$. Ainsi, la position verticale en GLM est partout plus grande que la moyenne Eulérienne de la position des mêmes particules (voir aussi la discussion de cet effet par McIntyre 1988). Cela peut s'interpréter par le fait que les particules sont plus nombreuses dans les crêtes que dans les creux (figure 24.1). Au second ordre en ε_1, la position GLM moyenne de la surface est donnée par (24.11)

$$\overline{\zeta}^L = \overline{\zeta} + \overline{\zeta}^S = \overline{\zeta} + \xi_\alpha(z=0)\frac{\partial \zeta}{\partial x_\alpha} = \overline{\zeta} + \mathrm{var}_\zeta \frac{k}{\tanh kD}, \tag{24.41}$$

En intégrant sur la profondeur, on définit

$$s_2^G(x,z,t) = -\int_{-h}^{z} J_2(z')\mathrm{d}z' = k\mathrm{var}_\zeta \frac{\sinh\left[2k(z+h)\right]}{2\sinh^2(kD)}. \tag{24.42}$$

et on a bien

$$\int_{-h}^{\overline{\zeta}^L} J\mathrm{d}z = \overline{\zeta}^L + D - s_2^G(0) = D. \tag{24.43}$$

Par analogie avec (24.1) on définit implicitement une nouvelle transformation de coordonnée verticale

$$s_2 = \varsigma D + s_2^G + \overline{\zeta}. \tag{24.44}$$

Tout champ scalaire $\phi(x_1, x_2, z, t)$ se transforme en $\phi^\star(x_1^\star, x_2^\star, \varsigma, t^\star)$, avec les relations

$$\frac{\partial \phi}{\partial t} = \frac{\partial \phi^\star}{\partial t^\star} - \frac{s_{2,t}}{s_{2,\varsigma}}\frac{\partial \phi^\star}{\partial \varsigma} \tag{24.45}$$

$$\frac{\partial \phi}{\partial x_\alpha} = \frac{\partial \phi^\star}{\partial x_\alpha^\star} - \frac{s_{2,\alpha}}{s_{2,\varsigma}}\frac{\partial \phi^\star}{\partial \varsigma} \tag{24.46}$$

$$\frac{\partial \phi}{\partial z} = \frac{1}{s_{2,\varsigma}}\frac{\partial \phi^\star}{\partial \varsigma} \tag{24.47}$$

avec $s_{2,t}$, $s_{2,\varsigma}$ et $s_{2,\alpha}$ les dérivés partielles de s_2 par rapport à t, ς et x_α, respectivement. Nous avons par ailleurs l'identité remarquable

$$s_{2,\varsigma} J = D\left[1 + O(\varepsilon_1^3)\right]. \tag{24.48}$$

On peut enfin transformer l' équation (24.37) en coordonnée ς en utilisant (24.45)–(24.47). Tout d'abord la conservation de la masse en GLM s'écrit (Andrews et McIntyre 1978a),

$$\frac{\partial\left(\rho_w J\right)}{\partial t} + \frac{\partial\left(\rho_w J \overline{u}^L_\alpha\right)}{\partial x_\alpha} + \frac{\partial\left(\rho_w J \overline{w}^L\right)}{\partial z} = 0 \tag{24.49}$$

ce qui donne, dans les nouvelles coordonnées,

$$\frac{\partial\left(\rho_w\widehat{\zeta}\right)}{\partial t}+\frac{\partial\left(D\rho_w U_\alpha\right)}{\partial x_\alpha}+\frac{\partial\left(\rho_w W\right)}{\partial\varsigma}=0, \tag{24.50}$$

avec la vitesse "verticale",

$$W=J\left[\overline{w}^L-\overline{u}_\alpha^L s_{2,\alpha}-s_{2,t}\right], \tag{24.51}$$

qui est définie exactement par le transport Lagrangien à travers les surfaces iso-ς.

La multiplication de (24.37) par $\rho_w s_{2,\varsigma} J$ donne, sous une de ses formes,

$$\begin{aligned}\rho_w D\frac{\partial\widehat{u}_\alpha}{\partial t} &+ \rho_w D\widehat{u}_\beta\frac{\partial\widehat{u}_\alpha}{\partial x_\beta}+\rho_w\widehat{w}\frac{\partial\widehat{u}_\alpha}{\partial\varsigma}+\rho_w D\epsilon_{\alpha 3\beta}\left[f_3\widehat{u}_\alpha+\left(f_3+\omega_3\right)U_{s\beta}\right]\\ &+ D\frac{\partial\overline{p}^H}{\partial x_\alpha}-\rho_w gDJs_{2,\alpha}=-\frac{\partial S^J}{\partial x_\alpha}+\frac{JS^J}{D}\frac{\partial}{\partial\varsigma}\left(s_{2,\alpha}\right)+\overline{X}_\alpha^L,\end{aligned}$$

avec

$$\widehat{w}=J\left[\overline{w}^L-\widehat{u}_\alpha s_{2,\alpha}+s_{2,t}\right]=W+J\widehat{U}_{s\alpha}s_{2,\alpha}, \tag{24.52}$$

la vitesse quasi-Eulérienne à travers les surfaces iso-ς.

L'équation (24.37) est valable de $z=-h$ à $z=\overline{\zeta}^L$ ce qui couvre toute la colonne d'eau en GLM.

24.2.5 Comparaison avec les équations 2D

L'équation correspondant à la quantité de mouvement intégrée sur la verticale est obtenue en multipliant (24.37) par le Jacobien J avant d'intégrer de $z=-h$ à $z=\overline{\zeta}^L$. Pour les termes qui sont déjà d'ordre ε_1^2, comme la force de vortex, cela revient, à l'ordre ε_1^2, à intégrer simplement (24.37) de $-h$ à $z=\overline{\zeta}$. Enfin, pour les termes uniformes sur la verticale (e.g. $\partial p^H/\partial x_\alpha=\partial\overline{\zeta}/\partial x_\alpha$), l'introduction du Jacobien compense exactement la continuation de l'intégrale entre $\overline{\zeta}$ et $\overline{\zeta}^L$. Ainsi

$$\begin{aligned}-\int_{-h}^{\overline{\zeta}^L}J\frac{\partial}{\partial x_\alpha}\left(\frac{S^J}{D}\right)\mathrm{d}z &= -\frac{\partial}{\partial x_\alpha}\left[\rho_w gE\left(C_g/C-\frac{1}{2}\right)\right]+\frac{S^J}{D}\left(\frac{\partial\overline{\zeta}}{\partial x_\alpha}+\frac{\partial h}{\partial x_\alpha}\right)\\ &= -\frac{\partial}{\partial x_\alpha}\left[\rho_w gE\left(C_g/C-\frac{1}{2}\right)\right]+\frac{S^J}{D}\frac{\partial D}{\partial x_\alpha},\end{aligned} \tag{24.53}$$

ce qui correspond au deuxième terme du membre de droite de (7.57). L'intégration verticale des équations 3D donne donc les équations 2D connues.

Le terme adiabatique S^J dans l'équation du mouvement moyen (24.37) est uniforme sur la verticale.

A première vue, tout cela peut paraître très compliqué. Toutefois, on a maintenant explicité la contribution des vagues qui se cachait dans les mystérieux tenseurs de Reynolds: la boîte noire des tenseurs de Reynolds est devenue un peu plus grise, et c'est, pour certains, moins joli. Mais on s'est donné des outils qui sont parmi les plus simples pour manipuler la vitesse juste en surface, et nous en verrons une application assez simple. Dans leur pleine généralité ces équations devraient permettre des simulations 3D réalistes de la zone de déferlement où la circulation est sensible aux profils des tensions de dissipation $T_\alpha^{\mathrm{wc}}+T^{\mathrm{turb}}$.

Chapter 25

Interactions of waves and sea ice

Ice in the ocean is part of the ocean. In the case of sea ice it comes from sea water that freezes as it is cooled by a cold atmosphere, with some addition of snow accumulating on the top. In the case of icebergs, it generally comes from glaciers that feeds the ocean with pieces of ice that is compacted snow that has fallen on continents, and contains no salt.

The interaction of waves and ice is a subject that is very complex. It is made more difficult by the paucity of available measurements. Fortunately, research efforts have been amplified since 2010, in an area where much is still to be discovered. These efforts are motivated by the rapid evolution and poor climate projections of the sea ice cover, in particular in the Arctic. Sea ice has an important role in isolating the ocean from the atmosphere and solar radiation, effectively shutting off heat and gas fluxes and increasing the ocean albedo. As a result, the effects of waves, pushing the ice or enhancing ice formation and melting, are important for understanding the ice edge dynamics and air-sea interaction from weather forecasting to climate projections. Another reason for studying waves in ice, is that the emerging Arctic ocean is a place of increased human activities, with new shipping routes and increasing exploitation of natural resources. As a result, any activity there requires the development of wave forecasting capabilities, in particular around the ice edge.

This chapter discusses several key processes of wave-ice interactions, starting with sea ice and finishing with icebergs which is made special by its very large thickness. In all of these processes , one obvious aspect is that ice is a solid that floats, but a solid that can take many shapes and forms. Ice also deforms, and can break into pieces under the strain caused by ocean waves. Although we start with an account of frazil and pancake ice, it should be remembered that these are probably not the most common ice form. Still, it is estimated that 50% of the Antarctic ice (Gow et al., 1982), and less so in the Arctic, is initially grown as frazil and pancakes. Hence, this early stage of development is a very important one.

Without going in too many details about the physical properties of ice and its consequences for sea ice (see Weeks, 2010), it is important to note that sea water freezing results in the formation of cristals of pure ice that then confine salt to brine pockets and a few other cristals involving, among other carbonates. Also, the freezing of water with salinity above 25 PSU produces sea ice with low salinity (typically 10–20 PSU, made up of ice cristals and brine) and increases the salinity of the surrounding water. That more saline water is denser and will thus lead to some convection in the upper ocean mixed layer. If the original water is brackish (defined here with a salinity under 25 PSU) then the more salty water is less dense, and will be stably floating on less salty water, so that ice formation can develop in a very thin surface layer (Weeks, 2010, p. 48). Here we will not discuss these brackish conditions that are specific to large Arctic estuaries.

When the water is very calm it freezes from the surface as columnar ice crystals, forming large slabs of congelation ice. The wave-induced perturbation facilitates the nucleation of ice cristals that grow into a suspension of small platelets of ice, known as frazil ice. Due to their buoyancy, these frazil cristals concentrate at the sea surface, like a snowstorm flipped upside down.

25.1 From water to pancakes

25.1.1 Suspensions of frazil cristals and effective viscosity

Knowledge on frazil properties mostly come from laboratory experiments, such as those performed by Martin and Kauffman (1981), in which sea water in a wave tank is cooled. As sea water approaches the freezing temperature, around -2° C for a salinity of 35 PSS, disk-shaped ice cristals form with diameters 1–3 mm and thickness of 1 to 10 micrometers, as shown in figure 25.1.a. The volume concentration ϕ of this suspension may vary in the range $0.15 < \phi < 0.45$ depending on the confinement of the water. In particular, the dissipation of waves by the ice induces a compression force due to the convergence of the wave momentum flux. This wave-induced force tends to increase the concentration at the ice edge exposed to the waves.

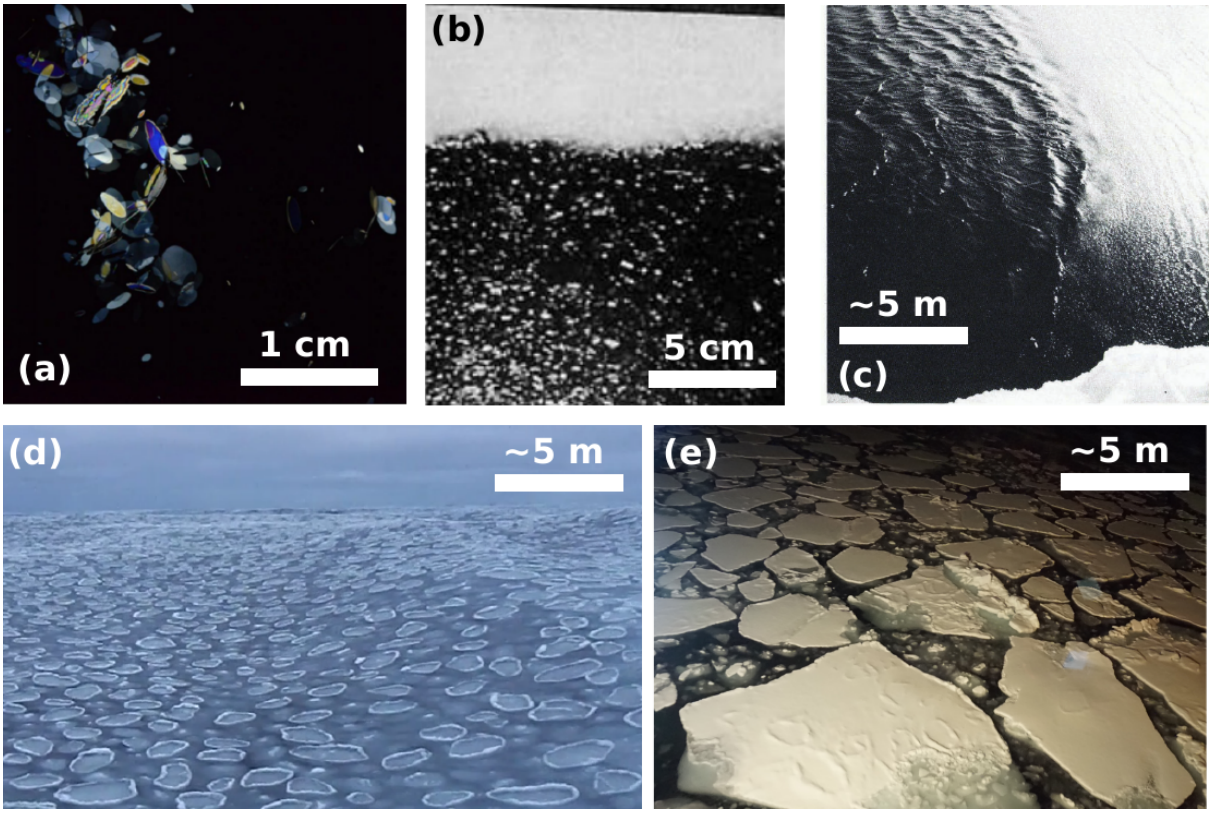

Figure 25.1: From frazil to pancakes.
(a) vertical plane view of frazil cristals viewed with polarized light, and their aggregation (copyright Elsevier, taken from McFarlane et al. (1982). (b) accumulation of frazil in a surface layer under waves. (c) Formation of an ice edge in frazil ice (From Martin and Kauffman, 1981, , copyright Cambridge University Press). (d) Field of pancakes in a storm as recorded by E. Rogers on October 12, 2015 in the Beaufort sea (Rogers et al., 2016). (e) Ice floes resulting from the agregation of pancakes, Beaufort sea, November 1, 2015, picture by H. Shen.

Such a concentration of solid particles enhances the effective kinematic viscosity ν_1 of the suspension compared to that of the fluid component only which, at the freezing point is $\nu_w \simeq 1.83 \times 10^{-6}$ m^2 s^{-1}. The ratio ν_1/ν_w for a concentrated solution of solid glass spheres is expected to vary like (Mooney, 1951)

$$\frac{\nu_1}{\nu_w} = \exp\left[2.5\phi/(1-1.43\phi)\right]. \tag{25.1}$$

This equation gives a factor 2 at $\phi = 0.2$ and a factor 23 at $\phi = 0.45$.

Representing the ocean as a two layer system with different viscosities, ν_1 for the top layer of thickness h_1, and ν_w for the underlying and deep layer, wave attenuation is exponential. A first approximate solution was given by Weber (1987) with a very large viscosity in the surface layer gave a dissipation dominated by the viscosity of the underlying water, independently of the top layer viscosity and thickness, identical to the solution by Dore (1978) for the viscous friction at the air-sea interface. The general solution, including finite depth of the underlying layer is given by Keller (1998). The resulting dissipation can be very strong for waves relatively short compared to the frazil layer, which explains the strong attenuation of waves in figure 25.1.c. However, longer waves are not much attenuated once their wavelength is much larger than h_1.

Now, the empirical coefficient 1.43 in Mooney's eq. (25.1) is strongly dependent on the solid material that is in suspension. Besides, the frazil cristals are not spherical and, for smaller wave amplitudes, these disks tend to stick together (Martin and Kauffman, 1981).

The problem of flat ellipsoids in suspension, instead of spheres, was addressed by de Carolis et al. (2005), who give an effective viscosity in the form of a power law

$$\frac{\nu_1}{\nu_w} = (1-\phi)^K. \tag{25.2}$$

Interpreting the wave attenuations measured by Martin and Kauffman (1981), de Carolis et al. (2005) find that the exponent K is of the order of 15 to 20 to explain the effective viscosities in the range 0.002–0.01 m^2 s^{-1}. They conclude that such high values can only be explained by a dominance of solid-solid interactions, including

collisions, friction and some sticking, and these all very sensitive to strain rate. It is thus expected that the effective viscosity is generally a non-linear function of the strain rate and volume concentration.

As pointed out by Martin and Kauffman (1981), the thickness and concentration of grease ice is modulated by wave-generated roll structures known as Langmuir circulations (see chapter 10). The ice collects in the surface convergence zone of these rolls. Garrett (1976) had envisaged that a localized wave dissipation in the convergence zone, in his case due to wave breaking over the stronger current, could reinforce the rolls. The stronger dissipation due to thicker grease ice could play the same role. These effects may be relevant for the enhancement of air-sea fluxes in leads (Esau, 2007).

25.1.2 Pancake ice

Natural grease does not remain a suspension of ice fragments of similar sizes and shapes. Instead, grease ice evolves to the formation of pancakes. These are agglomerations of frazil that weld together. Once a pancake has started forming, it can grow by the washing of frazil ice over the top of the pancake and its subsequent freezing (Doble et al., 2003). The raised rim of the pancakes, clearly visible as a white skirt in figure 25.1.c, come from their mutual collisions. Pancakes typically grow to diameters of the order of 1 m, and the ocean can be covered by a few layers of a pancakes. Shen et al. (2001) discussed that the maximum diameter of the pancakes observed in the laboratory is generally of the order of 1% of the the dominant wavelength, possibly due to break-up by bending or stretching if the pancakes get larger. This scaling of the pancake diameter with the wavelength was also confirmed by Roach et al. (2018) with video acquired in the Beaufort Sea, but they could not conclude if bending or stretching was the main mechanism that limits the size of pancakes.

Pancakes have thicknesses that rarely exceed a few centimeters, so that they easily raft and form a an ice layer with several pancakes irregularly stacked. The dissipation of energy in this ice layer is certainly dominated by ice-ice friction and collisions. Even though the local surface motions is consistent with orbital wave motion without ice (the ratio of horizontal to vertical motions recorded by buoys is very close to 1), there is a very strong dissipation of short wave components. Several models have been proposed to represent this dissipation, ranging from the viscous layer model of Keller (1998), to more complex visco-elastic models (Wang and Shen, 2010; Rogers et al., 2016). These latter models include different modes of motion and Mosig et al. (2015) show that some of these are often similar to what is predicted by a viscous thin beam model. Unfortunately, all these models are highly empirical, and there is no method for determining a priori the viscosity and elasticity parameters from large scale environmental conditions.

25.2 Dissipation for solid floes: basal friction

When freezing persists, pancakes weld together, leading to a single and continuous layer of ice. The agitation due to waves that has led to the formation of pancakes results in a thicker layer of ice compared to freezing conditions without agitation that produces columnar ice in which the heat is lost to the atmosphere by diffusion through the ice layer.

With such a single ice layer heaving up and down with the wave motion but constrained in its horizontal displacement, the dissipation energy can occur in the boundary layer below the ice. This oscillatory boundary layer is similar to the air-side boundary layer discussed in section 22.1, and the bottom boundary layer discussed in chapter 14. For the case of ice, the problem was treated by Liu and Mollo-Christensen (1988), with the additional effect of ice inertia that we neglect here. Here we consider the finite viscosity of seawater at the freezing point, $\nu_w \simeq 1.83 \times 10^{-6}$ m^2 s^{-1}. For monochromatic waves of radian frequency σ, a boundary layer of thickness $\sqrt{\nu_w \sigma}$ develops in the laminar case, and the attenuation rate of the wave energy in time is

$$\beta_{\mathrm{ice,bfr,v}} = -k\sqrt{\nu_w \sigma/2}. \tag{25.3}$$

This is the same dissipation rate that was found by Phillips (1977) for waves under an inextensible layer of oil (see also Weber, 1987). For a smooth under-ice surface, if we accept the similarity with the bottom boundary layer, this laminar regime is expected to occur for Reynolds numbers $\mathrm{Re} = \sigma a^2/\nu < \mathrm{Re}_c$, with $\mathrm{Re}_c = 1.5 \times 10^5$ (Jensen et al., 1989). Above this value the boundary layer transitions into a turbulent regime. In that case the dissipation rate becomes quadratic,

$$\beta_{\mathrm{ice,bfr,t}} = -f_e u_{\mathrm{orb}}/g, \tag{25.4}$$

where u_{orb} is is the significant orbital velocity amplitude at the water-ice interface. The dissipation factor f_e is obtained from the under-ice roughness in the same way that it was obtained in the turbulent bottom boundary layer in chapter 14.

For random waves, neglecting the effects of the ice layer on the water motion, we use the solution given in chapter 2,

$$u_{\mathrm{orb}} = 2\sqrt{\int_0^\infty \frac{\sigma^2}{\tanh^2(kD)} E(f)\mathrm{d}f}, \tag{25.5}$$

with a significant horizontal displacement

$$a_{\rm orb} = 2\sqrt{\int_0^\infty \frac{1}{\tanh^2(kD)} E(f)\mathrm{d}f}, \tag{25.6}$$

and we use this definition of the Reynolds number, $\mathrm{Re} = u_{\rm orb} a_{\rm orb}/\nu$.

Because the superposition of linear waves gives a Rayleigh distribution of the amplitudes, the transition between laminar and turbulent can happen only for the highest waves, giving a smooth transition of the average dissipation rate β_c. In practive, considering a Rayleigh distribution gives a value of β_c that is very close to the following approximation

$$\beta_c = (1-w)\beta_{\rm ice,bfr,v} + w\beta_{\rm ice,bfr,t}, \tag{25.7}$$

as shown in figure 25.2, where we have used a weight $w = 0.5\,[1 + \tanh((\mathrm{Re} - \mathrm{Re}_c)/\Delta_{\rm Re}]$, and $\Delta_{\rm Re} = 2 \times 10^5$.

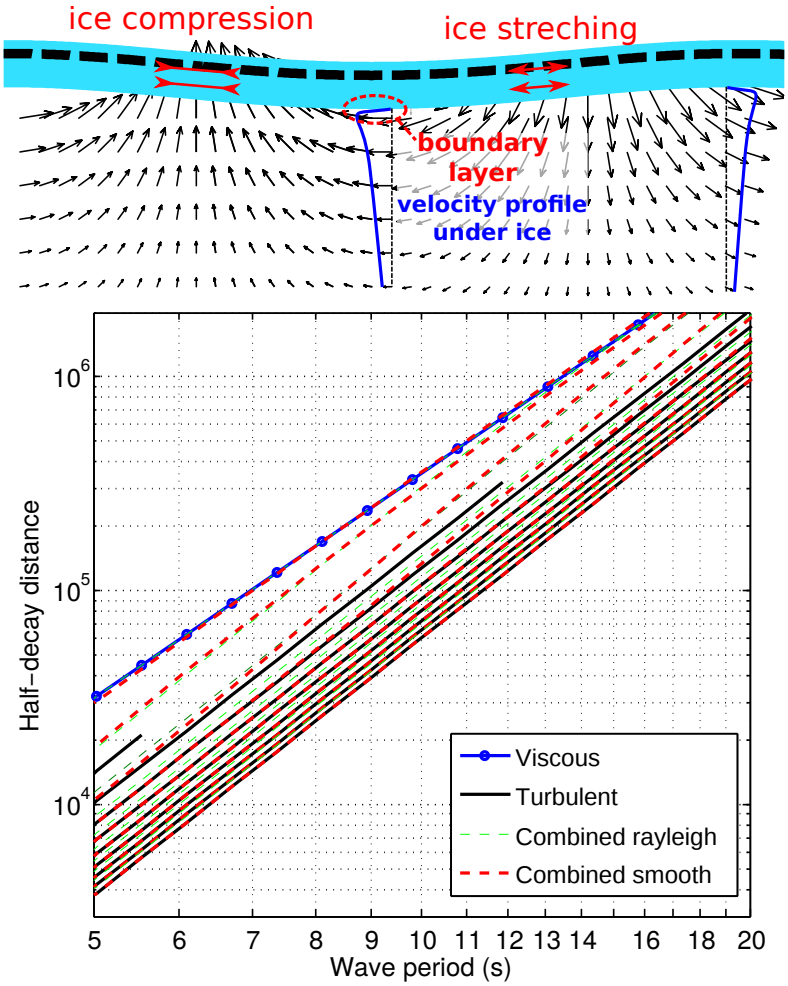

Figure 25.2: Top: schematic of velocities and boundary layer below an ice layer (light blue). Bottom: expected decay distance $X_{1/2} = C_g \ln(2)/\beta_c$ as a function of wave period T, for an under-ice roughness of 0.1 mm, and wave heights ranging from 0.5 to 5 m. The 'combined Rayleigh' solution uses a combination of $\beta_{\rm ice,bfr,v}$ and $\beta_{\rm ice,bfr,t}$ with a weighting depending on a Rayleigh distribution of wave amplitudes, and the 'combined smooth' solution is given by eq. (25.7). Adapted from Stopa et al. (2016c).

It should be noted that even the laminar dissipation is relatively strong, with half-decay distances under 400 km for periods shorter than 10 s, and 30 km under 5 s. This viscous dissipation is larger than what was estimated from buoys in pancake ice in recent experiments (Ardhuin et al., 2018). Rogers et al. (2016) reported imaginary wavenumbers $k_i = 2\ln(2)/X_{1/2}$ of the order of 2×10^{-5} for a period $T = 5$ s, which corresponds to $X_{1/2} = 140$ km, 4 times larger than due to molecular viscosity under an inextensible surface ice sheet. This is possible because the pancakes actually move horizontally and raft to form multiple layers, so that the present theory for β_c gives an overestimate of the wave dissipation in pancake ice. In the case of densely packed thick floes, rafting does not occur and the horizontal ice motion is much weaker than the vertical motion (Fox and Haskell, 2001), in which case the above expression for β_c should be applicable.

25.3 Dissipation for solid floes: flexure and the importance of ice break-up

In other cases, under-ice friction appears insufficient to explain the observed attenuation. This is particularly the case for the large-scale attenuation of swells with periods 18 to 33 s reported by Ardhuin et al. (2016), and illustrated in figure 25.3. In that study of waves measured in the pack, 1500 km from the ice edge, the constant dissipation rate needed to obtain a reasonable agreement with the data corresponds to a spatial decay of the energy, $\alpha = \beta/C_g$, ranging from $\alpha \simeq 4 \times 10^{-6}$ m^{-1} at $T = 20$ s, to $\alpha \simeq 2 \times 10^{-6}$ m^{-1} at $T = 25$ s. These are 12 times the effect of viscous friction below a smooth ice plate as given by eq. (25.3). That seems impossible to explain by the ice morphology alone, with complicated keel structures, often exceeding 10 m below the mean ice level (Doble et al., 2011).

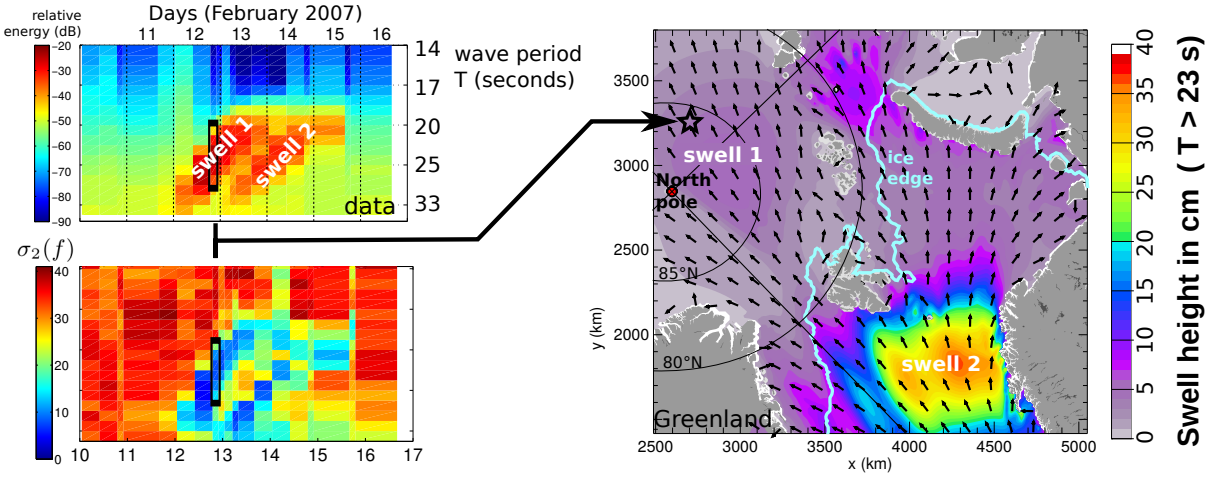

Figure 25.3: Left: Spectrogram of surface elevation and width σ_2 of the directional wave spectrum estimated from second moments a_2 and b_2. The black rectangle highlights the time and frequency range of the spectral peak on February 12 at 18:00 UTC, showing that the directional spreading is around 10° or less when the energy is maximum. Right: model snapshot giving some context to the measured data. The two swell events are due to two distinct storms. Adapted from Ardhuin et al. (2016).

Also, dissipation by basal friction leads to unrealistic high values of swell heights, of a few centimeters, crossing the Arctic from Fram Strait to Alaska (Ardhuin et al., 2016).

25.4 Dispersion relations

Whereas the condition of zero pressure at the free surface and the horizontal momentum balance gives the usual ice-free dispersion relation $\sigma^2 = gk \tanh(kD)$, the presence of ice clearly modifies these two conditions and thus the dispersion relation. A first effect, when ice is not broken in floes shorter than the wavelength, is the resistance to stretching of the sea surface. This same effect is similar to the effect of surface tension, and thus also leads to an increase of the phase speed for the shorter waves. (Fox and Haskell, 2001)

25.5 Scattering of waves by sea ice

25.6 Feedbacks of sea ice formation and melt

Sutherland and Dumont (2018), Stopa et al. (2018)

25.7 Waves and icebergs

Either at large ice shelves around Antarctica or from smaller glaciers around Greenland, icebergs are formed by the calving of ice streams reaching the oceans.

25.7.1 Floating breakwaters

Ardhuin et al. (2011b)

25.7.2 Iceberg break-up and erosion caused by waves

Wagner et al. (2018)

Appendix A

Some useful tables

$Y = X\tanh(X)$	X	$Y = X\tanh(X)$	X	$Y = X\tanh(X)$	X
0.05	0.2255	1.30	1.4511	2.55	2.5795
0.10	0.3216	1.35	1.4934	2.60	2.6273
0.15	0.3973	1.40	1.5360	2.65	2.6753
0.20	0.4627	1.45	1.5788	2.70	2.7234
0.25	0.5218	1.50	1.6218	2.75	2.7716
0.30	0.5767	1.55	1.6651	2.80	2.8200
0.35	0.6284	1.60	1.7085	2.85	2.8684
0.40	0.6778	1.65	1.7523	2.90	2.9170
0.45	0.7255	1.70	1.7962	2.95	2.9657
0.50	0.7717	1.75	1.8405	3.00	3.0145
0.55	0.8168	1.80	1.8850	3.05	3.0634
0.60	0.8611	1.85	1.9297	3.10	3.1123
0.65	0.9046	1.90	1.9747	3.15	3.1613
0.70	0.9476	1.95	2.0199	3.20	3.2104
0.75	0.9902	2.00	2.0653	3.25	3.2596
0.80	1.0324	2.05	2.1110	3.30	3.3088
0.85	1.0744	2.10	2.1570	3.35	3.3581
0.90	1.1163	2.15	2.2031	3.40	3.4075
0.95	1.1580	2.20	2.2495	3.45	3.4569
1.00	1.1997	2.25	2.2961	3.50	3.5063
1.05	1.2414	2.30	2.3428		
1.10	1.2831	2.35	2.3898		
1.15	1.3249	2.40	2.4370		
1.20	1.3668	2.45	2.4843		
1.25	1.4088	2.50	2.5318		

Table A.1: Table of the inverse function of $X\tanh X$. Defining $Y = \sigma^2 D/g$ it gives $k = X/D$, which allows to invert the dispersion relation in the absence of current. For $Y < 0.05$ one should use $X = \sqrt{Y}$, and for $Y > 3.5$ one should use $X = Y$.

État de la mer			Houle
Chiffre du code S	Terme descriptif	Hauteurs en mètres (1)	
0	Calme, sans rides *(calm, glassy)*	0	— Longueur des vagues de la houle *(lengh)*:
1	Calme, ridée *(calm, rippled)*	0 à 0,1	Courte *(short)* 0-100 mètres
2	Belle (vaguelettes) *[smooth, wavelets]*	0,1 à 0,5	Moyenne *(average)* 100 à 200 mètres
3	Peu agitée *(slight)*	0,5 à 1,25	Longue *(long)* plus de 200 mètres
4	Agitée *(moderate)*	1,25 à 2,5	— Hauteur des vagues de la houle *(height)* :
5	Forte *(rough)*	2,5 à 4	Petite *(low)* 0-2 mètres
6	Très forte *(very rough)*	4 à 6	Modérée *(moderate)* 2-4 mètres
7	Grosse *(high)*	6 à 9	Grande *(heavy)* plus de 4 mètres
8	Très grosse *(very high)*	9 à 14	— Lorsqu'il n'y a pas de houle : nulle
9	Énorme *(phenomenal)*	> 14	— Lorsqu'on ne peut déterminer la longueur, la hauteur et la direction : confuse

(1) Hauteur moyenne de la vague obtenue à partir des vagues bien formées, les plus grosses dans le système observé.

1.4.2.1. — Termes descriptifs de l'état de la mer et de la houle.

Figure A.1: The Beaufort scale for sea states

Bibliography

Abdalla, S. and L. Cavaleri, 2002: Effect of wind variability and variable air density on wave modelling. *J. Geophys. Res.*, **107**, 17.

Abgrall, R., 2006: Essentially non oscillatory residual distribution schemes for hyperbolic problems. *J. Comp. Phys.*, **214**, 773–808.

Abramovici, F., 1968: Diagnostic diagrams and transfer functions for oceanic wave-guides. *Bull. Seism. Soc. Am.*, **58**, 426–456.

Adler, R., 1981: *The Geometry of Random Fields*. John Wiley, New York.

Agnon, Y., A. V. Babanin, I. R. Young, and D. Chalikov, 2005: Fine scale inhomogeneity of wind-wave energy input, skewness and asymetry. *Geophys. Res. Lett.*, **32**, L12603.

Agrawal, Y. C., E. A. Terray, M. A. Donelan, P. A. Hwang, A. J. Williams, W. Drennan, K. Kahma, and S. Kitaigorodskii, 1992: Enhanced dissipation of kinetic energy beneath breaking waves. *Nature*, **359**, 219–220.

Airy, G. B., 1841: Tides and waves. *Encyclopedia metropolitana (1817–1845)*, H. J. R. et al., ed., London.

Algué, J., 1900: Relation entre quelques mouvements microséismiques et l'existence, la position et la distance des cyclones à Manille (Philippines). *Congrès international de Météorlogie, Paris*, 131–136.

Alpers, W. R. and C. L. Rufenach, 1979: The effect of orbital motions on synthetic aperture radar imagery of ocean waves. *IEEE Trans. Antennas Propagat.*, **27**, 685–690.

Alves, J. H. G. M. and M. L. Banner, 2003: Performance of a saturation-based dissipation-rate source term in modeling the fetch-limited evolution of wind waves. *J. Phys. Oceanogr.*, **33**, 1274–1298.URL link.

Andersen, K. H., 1999: *The dynamics of ripples beneath surface waves and topics in shell models of turbulence*. Ph.D. thesis, Det Naturvidenskabelige Fakultet Københavns Universitet.URL link.

Andreas, E. L., 2004: Spray stress revisited. *J. Phys. Oceanogr.*, **34**, 1429–1439.

Andréfouët, S., F. Ardhuin, P. Queffeulou, and R. L. Gendre, 2012: Island shadow effects and the wave climate of the Western Tuamotu archipelago (french polynesia) inferred from altimetry and numerical model data. *Marine Pollution Bulletin*, **66**, 415–424.

Andrews, D. G. and M. E. McIntyre, 1978a: An exact theory of nonlinear waves on a Lagrangian-mean flow. *J. Fluid Mech.*, **89**, 609–646.

— 1978b: On wave action and its relatives. *J. Fluid Mech.*, **89**, 647–664, corrigendum: vol. 95, p. 796.

Apotsos, A., B. Raubenheimer, S. Elgar, R. T. Guza, and J. A. Smith, 2007: Effects of wave rollers and bottom stress on wave setup. *J. Geophys. Res.*, **112**, C02003. doi:10.1029/2006JC003549.

Ardhuin, F., 2006a: On the momentum balance in shoaling gravity waves: a commentary of -shoaling surface gravity waves cause a force and a torque on the bottom- by K. E. Kenyon. *Journal of Oceanography*, **62**, 917–922.URL link.

— 2006b: Quelles mesures pour la prévision des états de mer en zone côtière? *Communications de l'Atelier Experimentation et Instrumentation*.URL link.

Ardhuin, F., A. Balanche, E. Stutzmann, and M. Obrebski, 2012a: From seismic noise to ocean wave parameters: general methods and validation. *J. Geophys. Res.*, **117**, C05002. doi:10.1029/2011JC007449.

Ardhuin, F., G. Boutin, J. Stopa, F. Girard-Ardhuin, C. Melsheimer, J. Thomson, A. Kohout, M. Doble, and P. Wadhams, 2018: Wave attenuation through an Arctic marginal ice zone on 12 october, 2015: 2: numerical modeling of waves and associated ice break-up. *J. Geophys. Res.*, **123**, 5652–5668. doi:10.1002/2018JC013784.

Ardhuin, F., B. Chapron, and F. Collard, 2009a: Observation of swell dissipation across oceans. *Geophys. Res. Lett.*, **36**, L06607. doi:10.1029/2008GL037030.

Ardhuin, F., B. Chapron, F. Collard, M. Smith, J. Stopa, J. Thomson, M. Doble, P. Wadhams, B. Blomquist, O. Persson, and C. O. Collins, III, 2017a: Measuring ocean waves in sea ice using SAR imagery: A quasi-deterministic approach evaluated with Sentinel-1 and in situ data. *Remote sensing of Environment*, **189**, 211–222. doi:10.1016/j.rse.2016.11.024.

Ardhuin, F., B. Chapron, and T. Elfouhaily, 2004a: Waves and the air-sea momentum budget, implications for ocean circulation modelling. *J. Phys. Oceanogr.*, **34**, 1741–1755.URL link.

Ardhuin, F., F. Collard, B. Chapron, P. Queffeulou, J.-F. Filipot, and M. Hamon, 2008a: Spectral wave dissipation based on observations: a global validation. *Proceedings of Chinese-German Joint Symposium on Hydraulics and Ocean Engineering, Darmstadt, Germany*, 391–400, iSBN: 3-936146-23-3.URL link.

Ardhuin, F., T. G. Drake, and T. H. C. Herbers, 2002: Observations of wave-generated vortex ripples on the North Carolina continental shelf. *J. Geophys. Res.*, **107**. doi:10.1029/2001JC000986.

Ardhuin, F., F. Dumas, A.-C. Bennis, A. Roland, A. Sentchev, P. Forget, J. Wolf, F. Girard, P. Osuna, and M. Benoit, 2012b: Numerical wave modeling in conditions with strong currents: dissipation, refraction and relative wind. *J. Phys. Oceanogr.*, **42**, 2101–2120.

Ardhuin, F., L. Gualtieri, and E. Stutzmann, 2015: How ocean waves rock the earth: two mechanisms explain seismic noise with periods 3 to 300 s. *Geophys. Res. Lett.*, **42**, 765–772. doi:10.1002/2014GL062782.

Ardhuin, F. and T. H. C. Herbers, 2002: Bragg scattering of random surface gravity waves by irregular sea bed topography. *J. Fluid Mech.*, **451**, 1–33.

— 2013: Noise generation in the solid earth, oceans and atmosphere, from nonlinear interacting surface gravity waves in finite depth. *J. Fluid Mech.*, **716**, 316–348. doi:10.1017/jfm.2012.548.

Ardhuin, F., T. H. C. Herbers, P. F. Jessen, and W. C. O'Reilly, 2003a: Swell transformation across the continental shelf. part II: validation of a spectral energy balance equation. *J. Phys. Oceanogr.*, **33**, 1940–1953.URL link.

Ardhuin, F., T. H. C. Herbers, K. P. Watts, G. P. van Vledder, R. Jensen, and H. Graber, 2007: Swell and slanting fetch effects on wind wave growth. *J. Phys. Oceanogr.*, **37**, 908–931. doi:10.1175/JPO3039.1.

Ardhuin, F. and A. D. Jenkins, 2006: On the interaction of surface waves and upper ocean turbulence. *J. Phys. Oceanogr.*, **36**, 551–557. doi:10.1175/JPO2862.1.

Ardhuin, F., A. D. Jenkins, and K. Belibassakis, 2008b: Comments on 'the three-dimensional current and surface wave equations' by George Mellor. *J. Phys. Oceanogr.*, **38**, 1340–1349. doi:10.1175/2007JPO3670.1.

Ardhuin, F., T. Lavanant, M. Obrebski, L. Marié, J.-Y. Royer, J.-F. d'Eu, B. M. Howe, R. Lukas, and J. Aucan, 2013: A numerical model for ocean ultra low frequency noise: wave-generated acoustic-gravity and Rayleigh modes. *J. Acoust. Soc. Amer.*, **134**, 3242–3259.

Ardhuin, F. and R. Magne, 2007: Scattering of surface gravity waves by bottom topography with a current. *J. Fluid Mech.*, **576**, 235–264.

— 2010: Modélisation des états de mer du globe à la plage : validation de nouveaux paramètres produits par prévimer. *Actes des Xèmes journées Génie côtier-Génie civil, Les Sables d'Olonne*, Centre Français du Littoral, 87–94.URL link. doi:10.5150/jngcgc.2010.002-A.

Ardhuin, F., L. Marié, N. Rascle, P. Forget, and A. Roland, 2009b: Observation and estimation of Lagrangian, Stokes and Eulerian currents induced by wind and waves at the sea surface. *J. Phys. Oceanogr.*, **39**, 2820–2838.URL link. doi:10.1175/2009JPO4169.1.

Ardhuin, F., F.-R. Martin-Lauzer, B. Chapron, P. Craneguy, F. Girard-Ardhuin, and T. Elfouhaily, 2004b: Dérive à la surface de l'océan sous l'effet des vagues. *Comptes Rendus Géosciences*, **336**, 1121–1130. doi:10.1016/j.crte.2004.04.007.

Ardhuin, F., W. C. O'Reilly, T. H. C. Herbers, and P. F. Jessen, 2003b: Swell transformation across the continental shelf. part I: Attenuation and directional broadening. *J. Phys. Oceanogr.*, **33**, 1921–1939.URL link.

Ardhuin, F., N. Rascle, and K. A. Belibassakis, 2008c: Explicit wave-averaged primitive equations using a generalized Lagrangian mean. *Ocean Modelling*, **20**, 35–60. doi:10.1016/j.ocemod.2007.07.001.

— 2017b: Corrigenda of 'explicit wave-averaged primitive equations using a generalized Lagrangian mean'. *Ocean Modelling*, **113**, 185–186. doi:10.1016/j.ocemod.2017.03.017.

Ardhuin, F., N. Rascle, B. Chapron, J. Gula, J. Molemaker, S. T. Gille, D. Menemenlis, and C. Rocha, 2017c: Small scale currents have large effects on wind wave heights. *J. Geophys. Res.*, **122**, 4500–4517. doi:10.1002/2016JC012413.

Ardhuin, F., A. Rawat, and J. Aucan, 2014: A numerical model for free infragravity waves: Definition and validation at regional and global scales. *Ocean Modelling*, **77**, 20–32. doi:10.1016/j.ocemod.2014.02.006.

Ardhuin, F., E. Rogers, A. Babanin, J.-F. Filipot, R. Magne, A. Roland, A. van der Westhuysen, P. Queffeulou, J.-M. Lefevre, L. Aouf, and F. Collard, 2010: Semi-empirical dissipation source functions for wind-wave models: part I, definition, calibration and validation. *J. Phys. Oceanogr.*, **40**, 1917–1941. doi:10.1175/2010JPO4324.1.

Ardhuin, F. and A. Roland, 2012: Coastal wave reflection, directional spreading, and seismo-acoustic noise sources. *J. Geophys. Res.*, **117**, C00J20. doi:10.1029/2011JC007832.

Ardhuin, F., E. Stutzmann, M. Schimmel, and A. Mangeney, 2011a: Ocean wave sources of seismic noise. *J. Geophys. Res.*, **116**, C09004.URL link. doi:10.1029/2011JC006952.

Ardhuin, F., P. Sutherland, M. Doble, and P. Wadhams, 2016: Ocean waves across the Arctic: attenuation due to dissipation dominates over scattering for periods longer than 19 s. *Geophys. Res. Lett.*, **43**, 5775–5783. doi:10.1002/2016GL068204.

Ardhuin, F., J. Tournadre, P. Queffelou, and F. Girard-Ardhuin, 2011b: Observation and parameterization of small icebergs: drifting breakwaters in the southern ocean. *Ocean Modelling*, **39**, 405–410. doi:10.1016/j.ocemod.2011.03.004.

Arendt, S. and D. C. Fritts, 2000: Acoustic radiation by ocean surface waves. *J. Fluid Mech.*, **415**, 1–21.

Athanassoulis, G. A. and K. A. Belibassakis, 1999: A consistent coupled-mode theory for the propagation of small amplitude water waves over variable bathymetry regions. *J. Fluid Mech.*, **389**, 275–301.

Aubourg, Q., A. Campagne, C. Peureux, F. Ardhuin, J. Sommeria, S. Viboud, and N. Mordant, 2017: 3-wave and 4-wave interactions in gravity wave turbulence. *Phys. Rev. Fluids*, **2**, 114802. doi:10.1103/PhysRevFluids.2.114802.

Babanin, A., D. Chalikov, I. Young, and I. Savelyev, 2007: Predicting the breaking onset of surface water waves. *Geophys. Res. Lett.*, **34**, L07605. doi:10.1029/2006GL029135.

Babanin, A., I. Young, and M. Banner, 2001: Breaking probabilities for dominant surface waves on water of finite depth. *J. Geophys. Res.*, **106**, 11659–11676.

Backus, G. E., 1962: The effect of the earth rotation on the propagation of ocean waves over long distances. *Deep Sea Res.*, **9**, 185–197.

Banner, M. L., A. V. Babanin, and I. R. Young, 2000: Breaking probability for dominant waves on the sea surface. *J. Phys. Oceanogr.*, **30**, 3145–3160.URL link. doi:10.1175/1520-0485(2000)030¡3145:BPFDWO¿2.0.CO;2.

Banner, M. L., X. Barthelemy, F. Fedele, M. Allis, A. Benetazzo, F. Dias, and W. L. Peirson, 2014: Linking reduced breaking crest speeds to unsteady nonlinear water wave group behavior. *Phys. Rev. Lett.*, **112**, 114502.

Banner, M. L., J. R. Gemmrich, and D. M. Farmer, 2002: Multiscale measurement of ocean wave breaking probability. *J. Phys. Oceanogr.*, **32**, 3364–3374.URL link.

Banner, M. L., I. S. F. Jones, and J. C. Trinder, 1989: Wavenumber spectra of short gravity waves. *J. Fluid Mech.*, **198**, 321–344.

Banner, M. L. and R. P. Morison, 2006: On modeling spectral dissipation due to wave breaking for ocean wind waves. *Proceedings of the 9th International workshop on wave hindcasting and forecasting, Victoria, Canada*.

— 2010: Refined source terms in wind wave models with explicit wave breaking prediction. part I: Model framework and validation against field data. *Ocean Modelling*, **33**, 177–189. doi:10.1016/j.ocemod.2010.01.002.

Banner, M. L. and W. L. Peirson, 1998: Tangential stress beneath wind-driven air-water interfaces. *J. Fluid Mech.*, **364**, 115–145.

Banner, M. L. and O. M. Phillips, 1974: On the incipient breaking of small scale waves. *J. Fluid Mech.*, **65**, 647–656.

Barber, N. F., F. Ursell, J. Darbyshire, and M. J. Tucker, 1946: A frequency analyser used in the study of ocean waves. *Nature*, 329–335.

Barnett, T. P. and A. J. Sutherland, 1968: A note on an overshoot effect in wind-generated waves. *J. Geophys. Res.*, **73**, 6879–6885.

Barrick, D. E., J. M. Headrick, R. W. Bogle, and D. D. Crombie, 1974: Sea backscatter at HF: interpretation and utilization of the echo. *Proc. IEEE*, **62**, 673.

Barrick, D. E. and B. L. Weber, 1977: On the nonlinear theory for gravity waves on the ocean's surface. Part II: Interpretation and applications. *J. Phys. Oceanogr.*, **7**, 3–10.URL link.

Battjes, J., 1974: *Computations of set-up, longshore currents, run-up and overtopping due to wind-generated waves*. Ph.D. thesis, Delft University of Technology, The Netherlands.

Battjes, J. A. and J. P. F. M. Janssen, 1978: Energy loss and set-up due to breaking of random waves. *Proceedings of the 16th international conference on coastal engineering*, ASCE, 569–587.

Becq, F., 1998: *Extension de la modélisation spectrale des états de mer vers le domaine côtier*. Ph.D. thesis, Université de Toulon et du Var, France.

Belcher, S. E., 1999: Wave growth by non-separated sheltering. *Eur. J. Mech. B/Fluids*, **18**, 447–462.

Belcher, S. E. and J. C. R. Hunt, 1993: Turbulent shear flow over slowly moving waves. *J. Fluid Mech.*, **251**, 109–148.

Belibassakis, K. A., G. A. Athanassoulis, and T. P. Gerostathis, 2001: A coupled-mode model for the refraction-diffraction of linear waves over steep three-dimensional bathymetry. *Appl. Ocean Res.*, **23**, 319–336.

Benetazzo, A., 2006: Measurements of short water waves using stereo matched image sequences. *Coastal Eng.*, **53**, 1013–1032.

Benetazzo, A., F. Ardhuin, F. Bergamasco, L. Cavaleri, P. V. Guimarães, M. Schwendeman, M. Sclavo, J. Thomson, and A. Torsello, 2017: On the shape and likelihood of oceanic rogue waves. *Scientific Reports*, **7**, 8276. doi:10.1038/s41598-017-07704-9.

Benjamin, T. B. and J. E. Feir, 1967: The disintegration of wav trains on deep water. part 1. theory. *J. Fluid Mech.*, **27**, 417–430.

Bennis, A.-C., F. Ardhuin, and F. Dumas, 2011: On the coupling of wave and three-dimensional circulation models : Choice of theoretical framework, practical implementation and adiabatic tests. *Ocean Modelling*, **40**, 260–272.

Benoit, M., P. Frigaard, and H. A. Schäffer, 1997: Analysing multidirectional wave spectra: a tentative classification of available methods. *Proceedings of the 1997 IAHR conference, San Francisco*, The Johns Hopkins University Press, Baltimore, 131–158.

Benoit, M., F. Marcos, and F. Becq, 1996: Development of a third generation shallow-water wave model with unstructured spatial meshing. *Proceedings of the 25th International Conference on Coastal Engineering, Orlando*, ASCE, 465–478.

Bentamy, A., H.-L. Ayina, P. Queffeulou, D. Croize-Fillon, and V. Kerbaol, 2007: Improved near real time surface wind resolution over the mediterranean sea. *Ocean Sci.*, **112**, 259–271.

Berkhoff, J. C. W., 1972: Computation of combined refraction-diffraction. *Proceedings of the 13th International Conference on Coastal Engineering, Vancouver*, ASCE, New York, N. Y., 796–814.

Bertelli, T., 1872: Osservazioni sui piccoli movimenti dei pendoli in relazione ad alcuni fenomeni meteorologiche. *Boll. Meteorol. Osserv. Coll. Roma*, **9**, 10.

Bidlot, J., P. Janssen, and S. Abdalla, 2005: A revised formulation for ocean wave dissipation in CY25R1. Technical Report Memorandum R60.9/JB/0516, Research Department, ECMWF, Reading, U. K.

Bidlot, J.-R., 2008: Intercomparison of operational wave forecasting systems against buoys: data from ECMWF, MetOffice, FNMOC, NCEP, DWD, BoM, SHOM and JMA, September 2008 to November 2008. Technical report, Joint WMO-IOC Technical Commission for Oceanography and Marine Meteorology, available from http://preview.tinyurl.com/7bz6jj.URL link.

— 2012: Present status of wave forecasting at E.C.M.W.F. *Proceedings of ECMWF workshop on ocean wave forecasting, 25–27 June*, 1–16.

Biesel, F., 1950: Etude théorique de la houle en eau courante. *La houille blanche*, **Numéro spécial A**, 279–285.

— 1952: Equations générales au second ordre de la houle irrégulière. *Houille Blanche*, **5**, 372–376.

Blachman, N. M. and G. A. McAlpine, 1969: The spectrum of a high-index fm waveform: Woodward's theorem revisited. *IEEE Trans. Comm. Tech.*, **COM-17**, 201–207.

Bonmarin, P., 1989: Geometric properties of deep-water breaking waves. *J. Fluid Mech.*, **209**, 405–433.

Bonneton, P., V. Marieu, H. Dupuis, N. Sénéchal, and B. Castelle, 2004: Wave transformation and energy dissipation in the surf zone: comparison between a non-linear model and field data. *Journal of Coastal Research*, **39**, 329–333.

Booij, N., R. C. Ris, and L. H. Holthuijsen, 1999: A third-generation wave model for coastal regions. 1. model description and validation. *J. Geophys. Res.*, **104**, 7,649–7,666.

Boussinesq, J., 1872: Théorie des ondes et des remous qui se propagent le long d'un canal rectangulaire horizontal, en communiquant au liquide contenu dans ce canal des vitesses sensiblement pareilles de la surface au fond. *J. Math. Pures Appl.*, **17**, 55–108.

Bowen, A. J., D. L. Inman, and V. P. Simmons, 1968: Wave "set-down" and wave "set-up". *J. Geophys. Res.*, **73**, 2569–2577.

Bragg, W. L., 1913: The structure of some crystals as indicated by their diffraction of x-rays. *Proc. Roy. Soc. Lond. A*, **89**, 248–277.

Breivik, Ø., J.-R. Bidlot, and P. A. Janssen, 2016: A Stokes drift approximation based on the phillips spectrum. *Ocean Modelling*. doi:10.1016/j.ocemod.2016.01.005.

Bréon, F. M. and N. Henriot, 2006: Spaceborne observations of ocean glint reflectance and modeling of wave slope distributions. *J. Geophys. Res.*, **111**, C0605. doi:10.1029/2005JC003343.

Bretherton, F. P. and C. J. R. Garrett, 1968: Wavetrains in inhomogeneous moving media. *Proc. Roy. Soc. of London*, **A302**, 529–554.

Broche, P., J. C. de Maistre, and P. Forget, 1983: Mesure par radar décamétrique cohérent des courants superficiels engendrés par le vent. *Oceanol. Acta*, **6**, 43–53.

Bromirski, P. D., 2001: Vibration from the Perfect Storm. *Geochemistry Geophysics Geosystems*, **2**, 2000GC000119. doi:10.1029/2004GC000768.

Bromirski, P. D., D. R. Cayan, and R. E. Flick, 2005: Wave spectral energy variability in the northeast Pacific. *J. Geophys. Res.*, **110**, C03005. doi:10.1029/2004JC002398.

Brown, G. S., 1977: The average impulse response of a rough surface and its applications. *IEEE J. Oceanic Eng.*, **2**, 67–63. doi:10.1109/JOE.1977.1145328.

Brumer, S. E., C. J. Zappa, B. W. Blomquist, C. W. Fairall, A. Cifuentes-Lorenzen, J. B. Edson, I. M. Brooks, and B. J. Huebert, 2017: Wave-related reynolds number parameterizations of CO2 and DMS transfer velocities. *Geophys. Res. Lett.*, **44**, 9865–9875.

Businger, J. A., J. C. Wyngaard, I. Izumi, and E. F. Bradley, 1971: Flux-profile relationships in the atmospheric surface layer. *J. Atmos. Sci.*, **28**, 181–189.URL link.

Caires, S. and A. Sterl, 1979: On the estimation of return values of significant wave height data from the reanalysis of the european centre for medium-range weather forecasts. *Safety and Reliability*, Bedford and van Gelder, eds., Swets and Zeitlinger, Lisse, The Netherlands, pages 353–361.

— 2005: A new nonparametric method to correct model data: Application to significant wave height from the ERA-40 re-analysis. *J. Atmos. Ocean Technol.*, **22**, 443–459.

Carrier, G. F. and H. P. Greenspan, 1958: Water waves of finite amplitude on a sloping beach. *J. Fluid Mech.*, **4**, 97–109.

Cartwright, D. E. and M. S. Longuet-Higgins, 1956: The statistical distribution of the maxima of a random function. *Proc. Roy. Soc. Lond. A*, **237**, 212–232.

Cartwright, D. E. and N. D. Smith, 1964: Buoy techniques for obtaining directional wave spectra. *Buoy technology, transactions of the International Buoy technology symposium, Washington, D. C.*, National Academy of Sciences, Marine Technology society, 111–136.

Caudal, G., D. Hauser, R. Valentin, and C. L. Gac, 2014: KuROS: A new airborne ku-band doppler radar for observation of surfaces. *J. Atmos. Ocean Technol.*, **31**, 2023–2245. doi:10.1175/JTECH-D-14-00013.1.

Cavaleri, L. and L. Bertotti, 2006: The improvement of modelled wind and wave fields with increasing resolution. *Tellus*, **33**, 553–565.

Cavaleri, L., S. Curiotto, G. D. Porta, and A. Mazzoldi, 1981: Directional wave recording in the northern Adriatic sea. *Nuovo Cimento*, **4C**, 519–534.

CERC, 1977: *Shore protection manual*, volume 3 volumes. U. S. Army Coastal Engineering Research Center.

Chalikov, D., 1993: Comments on "wave-induced stress and the drag of air flow over sea waves" and "quasi-linear theory of wind wave generation applied to wave forecasting". *J. Phys. Oceanogr.*, **23**, 1597–1600.

— 2007: Numerical simulation of the Benjamin-Feir instability and its consequences. *Phys. of Fluids*, **19**, 016602.

Chapron, B., F. Collard, and F. Ardhuin, 2005: Direct measurements of ocean surface velocity from space: interpretation and validation. *J. Geophys. Res.*, **110**. doi:10.1029/2004JC002809.

Charles, E., D. Idier, J. Thiebot, G. L. Cozannet, R. Pedreros, F. Ardhuin, and S. Planton, 2012: Present wave climate in the bay of biscay: Spatiotemporal variability and trends from 1958 to 2001. *Journal of Climate*, **25**, 2020–2039. doi:10.1175/JCLI-D-11-00086.1.

Charnock, H., 1955: Wind stress on a water surface. *Quart. Journ. Roy. Meteorol. Soc.*, **81**, 639–640.

Chawla, A. and J. T. Kirby, 2002: Monochromatic and random wave breaking at blocking points. *J. Geophys. Res.*, **107**, 3067.

Chawla, A. and H. L. Tolman, 2008: Obstruction grids for spectral wave models. *Ocean Modelling*, **22**, 12–25.

Chen, G., B. Chapron, R. Ezraty, and D. Vandemark, 2002: A global view of swell and wind sea climate in the ocean by satellite altimeter and scatterometer. *J. Atmos. Ocean Technol.*, **19**, 1849–1859.

Cokelet, E. D., 1977: Steep gravity waves in water of arbitrary uniform depth. *Proc. Roy. Soc. Lond. A*, **286**, 183–230.

Collard, F., F. Ardhuin, and B. Chapron, 2005: Extraction of coastal ocean wave fields from SAR images. *IEEE J. Oceanic Eng.*, **30**, 526–533.

— 2009: Monitoring and analysis of ocean swell fields using a spaceborne SAR: a new method for routine observations. *J. Geophys. Res.*, **114**, C07023.

Compo, G. P., J. S. Whitaker, P. D. Sardeshmukh, N. Matsui, R. J. Allan, X. Yin, J. B. E. Gleason, B. E., R. S. Vose, G. Rutledge, P. Bessemoulin, S. Brönnimann, M. Brunet, R. I. Crouthamel, A. N. Grant, P. Y. Groisman, P. D. Jones, M. C. Kruk, A. C. Kruger, G. J. Marshall, M. Maugeri, H. Y. Mok, O. Nordli, T. F. Ross, R. M. Trigo, X. L. Wang, S. D. Woodruff, and S. J. Worley, 2011: The twentieth century reanalysis. *Quart. Journ. Roy. Meteorol. Soc.*, **137**, 1–28. doi:10.1002/qj.776.

Cooper, R. I. B. and M. S. Longuet-Higgins, 1951: An experimental study of the pressure variations in standing water waves. *Proc. Roy. Soc. Lond. A*, **206**, 426–435. doi:10.1098/rspa.1951.0079.

Cote, L. J., J. O. Davis, W. Marks, R. J. McGough, E. Mehr, W. J. Pierson, Jr., J. F. Ropek, G. Stephenson, and R. C. Vetter, 1960: The directional spectrum of a wind generated sea as determined from data obtained by the Stereo Wave Observation Project. Technical Report 6, N. Y. U. Coll. of Eng.

Courant, R., K. Friedrichs, and H. Lewy, 1928: Über die partiellen differenzengleichungen der mathematischen physik. *Mathematische Annalen*, **100**, 32–74. doi:10.1007/BF01448839.

Cox, C. and W. Munk, 1954: Measurement of the roughness of the sea surface from photographs of the sun's glitter. *J. Opt. Soc. Am.*, **44**, 838–850. doi:10.1364/josa.44.000838.

Cox, C. S. and D. C. Jacobs, 1989: Cartesian diver observations of double frequency pressure fluctuations in the upper levels of the ocean. *Geophys. Res. Lett.*, **16**, 807–810.

Cox, D., 1995: *Experimental and numerical modelling of surf zone hydrodynamics*. Ph.D. thesis, Univ. of Delaware, Newark.

Craig, P. D. and M. L. Banner, 1994: Modeling wave-enhanced turbulence in the ocean surface layer. *J. Phys. Oceanogr.*, **24**, 2546–2559.URL link.

Craik, A. D. D., 2004: The origins of water wave theory. *Annu. Rev. Fluid Mech.*, **36**, 1–28.

Creamer, D. B., F. Henyey, R. Schult, and J. Wright, 1989: Improved linear representation of ocean surface waves. *J. Fluid Mech.*, **205**, 135–161.

Csík, Á., M. Ricchiuto, and H. Deconinck, 2002: A conservative formulation of the multidimensional upwind residual distribution schemes for general nonlinear conservation laws. *J. Comp. Phys.*, **172**, 286–312.

Dalrymple, R. A., 1974: A finite amplitude wave on a linear shear current. *J. Geophys. Res.*, **79**, 4498–4504. doi:10.1029/jc079i030p04498.

Darbyshire, J., 1957: Attenuation of swell in the north atlantic ocean. *Quart. Journ. Roy. Meteorol. Soc.*, **83**, 351–359.

Darrigol, O., 2003: The spirited horse, the engineer, and the mathematician: Water waves in nineteenth-century hydrodynamics. *Arch. Hist. Exact Sci.*, **58**, 21–95. doi:10.1007/s00407-003-0070-5.

Davies, A. G. and C. Villaret, 1999: Eulerian drift induced by progressive waves above rippled and very rough beds. *J. Geophys. Res.*, **C1**, 1465–1488.

Davis, R. E. and L. A. Regier, 1977: Methods for estimating directional wave spectra from multi-element arrays. *J. Mar. Res.*, **35**, 453–478.

De, S. C., 1955: Contributions to the theory of Stokes waves. *Proceedings of the Cambridge philosophical society*, **51**, 713–736.

de Caliginy, A., 1878: Expériences sur les mouvements des molécules liquides des ondes courantes, considérées dans leur mode d'action sur la marche des navires. *C. R. Acad. Sci. Paris*, **87**, 1019–1023.

de Carolis, G., P. Olla, and L. Pignagnoli, 2005: Effective viscosity of grease ice in linearized gravity waves. *J. Fluid Mech.*, **535**, 369–381. doi:10.1017/S002211200500474X.

de Jong, M. P. C., L. H. Holthuijsen, and J. A. Battjes, 2003: Generation of seiches by cold fronts over the southern north sea. *J. Geophys. Res.*, **108**, 3117. doi:10.1029/2002JC001422.

de Laplace, P. S., 1776: Suite des recherches sur plusieurs points du système du monde (XXV–XXVII). *Mém. Présentés Acad. R. Sci. Inst. France*, 542–552.

Dean, R. G., 1965: Stream function representation of nonlinear ocean waves. *J. Geophys. Res.*, **70**, 4561–4572.

Dean, R. G. and R. A. Dalrymple, 1991: *Water wave mechanics for engineers and scientists*. World Scientific, Singapore, second edition, 353 pp.

Dee, D. P., S. M. Uppala, A. J. Simmons, P. Berrisford, P. Poli, S. Kobayashi, U. Andrae, M. A. Balmaseda, G. Balsamo, P. Bauer, P. Bechtold, A. C. M. Beljaars, L. van de Berg, J. Bidlot, N. Bormann, C. Delsol, R. Dragani, M. Fuentes, A. J. Geer, L. Haimbergere, S. B. Healy, H. Hersbach, E. V. Holm, L. Isaksena, P. Køallberg, M. Köhler, M. Matricardi, A. P. McNally, B. M. Monge-Sanz, J.-J. Morcrette, B.-K. Park, C. Peubey, P. de Rosnay, C. Tavolato, J.-N. Thépaut, and F. Vitart, 2011: The era-interim reanalysis: configuration and performance of the data assimilation system. *Quart. Journ. Roy. Meteorol. Soc.*, **137**, 553–597. doi:10.1002/qj.828.

Delpey, M., 2012: *Etude de la dispersion horizontale en zone littorale sous l'effet de la circulation tridimensionnelle forcée par les vagues*. Ph.D. thesis, Université Européenne de Bretagne, Ecole doctorale des Sciences de la Mer, Brest, France.

Delpey, M., F. Ardhuin, F. Collard, and B. Chapron, 2010: Space-time structure of long swell systems. *J. Geophys. Res.*, **115**, C12037. doi:10.1029/2009JC005885.

Dias, F. and P. Milewski, 2010: On the fully-nonlinear shallow-water generalized Serre equations. *Phys. Lett. A*, **374**, 1049–1053.

Dibarboure, G., F. Boy, J. D. Desjonqueres, S. Labroue, Y. Lasne, N. Picot, J. C. Poisson, and P. Thibaut, 2014: Investigating short-wavelength correlated errors on low-resolution mode altimetry. *J. Atmos. Ocean Technol.*, **31**, 1337–1362. doi:10.1175/JTECH-D-13-00081.1.

Dingemans, M. W., 1997: *Water wave propagation over uneven bottoms. Part 1 linear wave propagation*. World Scientific, Singapore, 471 p.

Dingler, J. R., 1974: *Wave-formed ripples in nearshore sands*. Ph.D. thesis, University of California, San Diego.

Doble, M. J., M. D. Coon, and P. Wadhams, 2003: Pancake ice formation in the weddell sea. *J. Geophys. Res.*, **108**, 3209. doi::10.1029/2002JC001373.

Doble, M. J., H. Skourup, P. Wadhams, and C. A. Geiger, 2011: The relation between arctic sea ice surface elevation and draft: A case study using coincident auv sonar and airborne scanning laser. *J. Geophys. Res.*, **116**, COOE03. doi:10.1029/2011JC007076.

Dobson, F. W., 1971: Measurements of atmospheric pressure on wind-generated sea waves. *J. Fluid Mech.*, **48**, 91–127.

Dobson, R. S., 1967: Some applications of a digital computer to hydraulic engineering problems. Technical Report 80, Department of Civil Engineering, Stanford University.

Dodet, G., X. Bertin, and R. Taborda, 2010: Wave climate variability in the north-east Atlantic ocean over the last six decades. *Ocean Modelling*, **31**, 120–131.

Donelan, M., M. Skafel, H. Graber, P. Liu, D. Schwab, and S. Venkatesh, 1992: On the growth rate of wind-generated waves. *Atmosphere Ocean*, **30**, 457–478.

Donelan, M. A., 1998: Air-water exchange processes. *Physical Processes in Lakes and Oceans*, J. Imberger, ed., American Geophysical Union, Washington, D.C., pages 18–36, iSBN 0-87590-268-5.

Donelan, M. A., A. V. Babanin, I. R. Young, and M. L. Banner, 2006: Wave-follower field measurements of the wind-input spectral function. Part II: parameterization of the wind input. *J. Phys. Oceanogr.*, **36**, 1672–1689.

Donelan, M. A., F. W. Dobson, H. C. Graber, N. Madsen, and C. Mccormick, 2005: Measurement of wind waves and wave-coherent air pressures on the open sea from a moving SWATH vessel. *J. Atmos. Ocean Technol.*, **22**, 896–906.

Donelan, M. A., W. M. Drennan, and A. K. Magnusson, 1996: Nonstationary analysis of the directional properties of propagating waves. *J. Phys. Oceanogr.*, **26**, 1901–1914.URL link.

Donelan, M. A., J. Hamilton, and W. H. Hui, 1985: Directional spectra of wind-generated waves. *Phil. Trans. Roy. Soc. London A*, **315**, 509–562.

Dore, B. D., 1978: Some effects of the air-water interface on gravity waves. *Geophys. Astrophys. Fluid. Dyn.*, **10**, 215–230.

Drennan, W. M., H. C. Graber, D. Hauser, and C. Quentin, 2003: On the wave age dependence of wind stress over pure wind seas. *J. Geophys. Res.*, **108**, 8062. doi:10.1029/2000JC00715.

Duennebier, F. K., R. Lukas, E.-M. Nosal, J. Aucan, and R. A. Weller, 2012: Wind, waves, and acoustic background levels at station ALOHA. *J. Geophys. Res.*, **117**, C03017. doi:10.1029/2011JC007267.

Dulov, V., V. Kudryavtsev, and A. Bolshakov, 2002: A field study of white caps coverage and its modulations by energy containing wave. *Gas Transfer at the Water Surface, Geophysical Monographs 127*, M. A. D. et al., ed., American Geophysical Union, pages 187–192.

Dulov, V. A. and M. V. Kosnik, 2009: Effects of three-wave interactions in the gravity-capillary range of wind waves. *Izv. Atmos. Ocean. Phys.*, **45**, 380–391.

Duncan, J. H., 1981: An experimental investigation of breaking waves produced by a towed hydrofoil. *Proc. Roy. Soc. Lond. A*, **377**, 331–348.

— 1983: The breaking and non-breaking wave resistance of a two-dimensional hydrofoil. *J. Fluid Mech.*, **126**,

507–520.
Dysthe, K. B., 2001: Refraction of gravity waves by weak current gradients. *J. Fluid Mech.*, **442**, 157–159.
Edson, J. B., V. Jampana, R. A. Weller, S. P. Bigorre, A. J. Plueddemann, C. W. Fairall, S. D. Miller, L. Mahrt, D. Vickers, and H. Hersbach, 2013: On the exchange of momentum over the open ocean. *J. Phys. Oceanogr.*, **43**, 1589–1610. doi:10.1175/JPO-D-12-0173.1.
Ehrenmark, U. T., 2005: An alternative dispersion equation for water waves over an inclined bed. *J. Fluid Mech.*, **543**, 249–266.
Eldeberky, Y. and J. Battjes, 1995: Parameterization of triad interactions in wave energy models. *Coastal Dynamics '95*, W. Dally and R. Zeidler, eds., ASCE, 140–148.
Elfouhaily, T., B. Chapron, K. Katsaros, and D. Vandemark, 1997: A unified directional spectrum for long and short wind-driven waves. *J. Geophys. Res.*, **102**, 15781–15796. doi:10.1029/97jc00467.
Elfouhaily, T., M. Joelson, S. Guignard, H. Branger, D. R. Thompson, B. Chapron, and D. Vandemark, 2003: Analysis of random nonlinear water waves: the Stokes-Woodward technique. *C. R. Acad. Sci. Paris*, **331**, 189–196.
Elfouhaily, T., D. R. Thompson, D. Vandemark, and B. Chapron, 2000: Truncated hamiltonian versus surface perturbation in nonlinear wave theories. *Waves in Random Media*, **10**, 103–116.
Elgar, S. and R. T. Guza, 1985: Observation of bispectra of shoaling surface gravity waves. *J. Fluid Mech.*, **161**, 425–448.
Elgar, S., T. H. C. Herbers, and R. T. Guza, 1994: Reflection of ocean surface gravity waves from a natural beach. *J. Phys. Oceanogr.*, **24**, 1,503–1,511.URL link.
Elliot, J. A., 1972: Microscale pressure fluctuations measured within the lower atmospheric boundary layer. *J. Fluid Mech.*, **53**, 351–384.
Esau, I. N., 2007: Amplification of turbulent exchange over wide arctic leads: Large-eddy simulation study. *J. Geophys. Res.*, **112**, D08109. doi:10.1029/2006JD007225.
Ewans, K. C., 1998: Observations of the directional spectrum of fetch-limited waves. *J. Phys. Oceanogr.*, **28**, 495–512.URL link.
Fabrikant, A. L., 1976: Quasilinear theory of wind-wave generation. *Izv. Atmos. Ocean. Phys.*, **12**, 524–526.
Farquharson, G., S. J. Frasier, B. Raubenheimer, and S. Elgar, 2005: Microwave radar cross sections and doppler velocities measured in the surf zone. *IEEE Trans. on Geosci. and Remote Sensing*, **110**, C12024. doi:10.1029/2005JC003022.
Farra, V., E. Stutzmann, L. Gualtieri, M. Schimmel, and F. Ardhuin, 2016: Ray-theoretical modeling of secondary microseism P-waves. *Geophys. J. Int.*, **206**, 1730–1739. doi:10.1093/gji/ggw242.
Farrell, W. E. and W. Munk, 2008: What do deep sea pressure fluctuations tell about short surface waves? *Geophys. Res. Lett.*, **35**, L19605. doi:10.1029/2008GL035008.
Feddersen, F., E. L. Gallagher, R. T. Guza, and S. E. Feddersen, 2003: The drag coefficient, bottom roughness, and wave-breaking in the nearshore. *Coastal Eng.*, **48**, 189–195.
Fedele, F., A. Benetazzo, G. Gallego, P.-C. Shih, A. Yezzi, F. Barbariol, and F. Ardhuin, 2013: Space-time measurements of oceanic sea states. *Ocean Modelling*, **70**, 103–115. doi:10.1016/j.ocemod.2013.01.001.
Fedele, F., G. Gallego, A. Benetazzo, A. Yezzi, and M. A. Tayfun, 2009: Euler characteristics and maxima of oceanic sea states. *Proceedings of the Rogue waves workshop, October 2008, Brest, France*, Ifremer, 145–154.
Fermi, E., J. Pasta, and S. Ulam, 1955: Studies of nonlinear problems. i. *Nonlinear wave motion. Lectures in applied mathematics, vol. 15*, A. C. Newell, ed., Amer. Math. Soc., Providence, R.I., pages 143–156.
Filipot, J.-F. and F. Ardhuin, 2012: A unified spectral parameterization for wave breaking: from the deep ocean to the surf zone. *J. Geophys. Res.*, **117**, C00J08. doi:10.1029/2011JC007784.
Filipot, J.-F., F. Ardhuin, and A. Babanin, 2008: Paramétrage du déferlement des vagues dans les modèles spectraux : approches semi-empirique et physique. *Actes des Xèmes journées Génie côtier-Génie civil, Sophia Antipolis*, Centre Français du Littoral.
— 2010a: A unified deep-to-shallow-water wave-breaking probability parameterization. *J. Geophys. Res.*, **115**, C04022. doi:10.1029/2009JC005448.
Filipot, J.-F., F. Ardhuin, and R. Magne, 2010b: Validation d'un terme source de dissipation par déferlement applicable du large à la côte. *Actes des Xèmes journées Génie côtier-Génie civil, Les Sables d'Olonne*, Centre Français du Littoral, 87–94.URL link.
Filloux, J. H., 1980: Pressure fluctuations on the open ocean floor over a broad frequency range: new program and early results. *J. Phys. Oceanogr.*, **10**, 1959–1971.
Fox, C. and T. G. Haskell, 2001: Ocean wave speed in the antarctic marginal ice zone. *Annales Geophysicae*, **33**, 350–354. doi:10.3189/172756401781818239.
Freilich, M. H. and B. A. Vanhoff, 2003: The relationship between winds, surface roughness, and radar backscatter at low incidence angles from TRMM precipitation radar measurements. *J. Atmos. Ocean Technol.*, **20**, 549–562.
Gain, L., 1918: La prédiction des houles au Maroc. *Annales Hydrographiques*, 65–75.
Gallego, G., A. Yezzi, F. Fedele, and A. Benetazzo, 2011: A variational stereo method for the three-dimensional reconstruction of ocean waves. *IEEE Trans. on Geosci. and Remote Sensing*, **49**, 4445–4457. doi:10.1109/TGRS.2011.2150230.
Gallet, B. and W. R. Young, 2014: Refraction of swell by surface currents. *J. Mar. Res.*, **72**, 105–126.

doi:10.1357/002224014813758959.
García-Nava, H., F. J. Ocampo-Torres, P. A. Hwang, and P. Osuna, 2012: Reduction of wind stress due to swell at high wind conditions. *J. Geophys. Res.*, **117**, C00J11. doi:10.1029/2011JC007833.
Garrett, C., 1976: Generation of Langmuir circulations by surface waves - a feedback mechanism. *J. Mar. Res.*, **34**, 117–130.
Gelci, R., H. Cazalé, and J. Vassal, 1957: Prévision de la houle. La méthode des densités spectroangulaires. *Bulletin d'information du Comité d'Océanographie et d'Etude des Côtes*, **9**, 416–435.
Giovanangeli, J. P., N. Reul, M. H. Garat, and H. Branger, 1999: Some aspects of wind-wave coupling at high winds: an experimental study. *Wind-over-wave couplings*, S. G. Sajjadi, N. H.Thomas, and J. C. R. Hunt, eds., Clarendon Press, Oxford, U. K., 81–90.
Goda, Y., 1985: *Random seas and design of marine structures*. University of Tokyo Press, 323 p.
Godin, O. A., N. A. Zabotin, A. F. Sheehan, Z. Yang, and J. A. Collins, 2013: Power spectra of infragravity waves in a deep ocean. *Geophys. Res. Lett.*, **40**, 2159–2165. doi:10.1002/grl.50321.
Gorman, R. M., 2003: The treatment of discontinuities in computing the nonlinear energy transfer for finite-depth gravity wave spectra. *J. Atmos. Ocean Technol.*, **20**, 206–216.
Gow, A. J., S. F. Ackley, W. F. Weeks, and J. W. Govoni, 1982: physical and structural characteristics of Antarctic sea ice. *Annales Geophysicae*, **3**, 113–117.
Graber, H., E. Terray, M. Donelan, W. Drennan, J. V. Leer, and D. Peters, 2000: ASIS – a new air-sea interaction spar buoy: design and performance at sea. *J. Atmos. Ocean Technol.*, **17**, 708–720.
Graber, H. C. and O. S. Madsen, 1988: A finite-depth wind-wave model. part 1: model description. *J. Phys. Oceanogr.*, **18**, 1465–1483.URL link.
Grant, W. D. and O. S. Madsen, 1979: Combined wave and current interaction with a rough bottom. *J. Geophys. Res.*, **84**, 1797–1808.
Greenslade, D. J. M., 2001: A wave modelling study of the 1998 Sydney to Hobart yacht race. *Aust. Met. Mag.*, **50**, 53–63.
Groeneweg, J., 1999: *Wave-current interactions in a generalized Lagrangian mean formulation*. Ph.D. thesis, Delft University of Technology, The Netherlands.
Groeneweg, J., M. van Gent ad Joana van Nieuwkoop, and Y. Toledo4, 2015: Wave propagation into complex coastal systems and the role of nonlinear interactions. *J. of Waterway, Port Coast. Ocean Eng.*, **141**, 04015003. doi:10.1061/(ASCE)WW.1943-5460.0000300.
Gualtieri, L., E. Stutzmann, Y. Capdeville, F. Ardhuin, M. Schimmel, A. Mangeney, and A. Morelli, 2013: Modelling secondary microseismic noise by normal mode summation. *Geophys. J. Int.*, **193**, 1732–1745. doi:10.1093/gji/ggt090.
Gualtieri, L., E. Stutzmann, V. Farra, Y. Capdeville, M. Schimmel, F. Ardhuin, and A. Morelli, 2014: Modelling the ocean site effect on seismic noise body waves. *Geophys. J. Int.*, **193**, 1096–1106. doi:10.1093/gji/ggu042.
Guimaraes, P. V., 2018: *Surfaces de mer et dissipation d'énergie*. Ph.D. thesis, Ecole Centrale de Nantes.
Hanafin, J., Y. Quilfen, F. Ardhuin, J. Sienkiewicz, P. Queffeulou, M. Obrebski, B. Chapron, N. Reul, F. Collard, D. Corman, E. B. de Azevedo, D. Vandemark, and E. Stutzmann, 2012: Phenomenal sea states and swell radiation: a comprehensive analysis of the 12-16 February 2011 North Atlantic storms. *Bull. Amer. Meterol. Soc.*, **93**, 1825–1832. doi:10.1175/BAMS-D-11-00128.1.
Hara, T. and S. E. Belcher, 2002: Wind forcing in the equilibrium range of wind-wave spectra. *J. Fluid Mech.*, **470**, 223–245.
Harcourt, R. R. and E. A. D'Asaro, 2006: Large Eddy Simulation of Langmuir Turbulence in Pure Wind Seas. *AGU Fall Meeting Abstracts*, A562+.
Hargreaves, J. C. and J. D. Annan, 2000: Comments on –improvement of the short-fetch behavior in the wave ocean model (WAM)–. *J. Atmos. Ocean Technol.*, **18**, 711–715.URL link.
Hasselmann, D. and J. Bösenberg, 1991: Field measurements of wave-induced pressure over wind-sea and swell. *J. Fluid Mech.*, **230**, 391–428.
Hasselmann, K., 1960: Grundgleichugen der seegangsvorhersage. *Schifftechnik*, **7**, 191–195.
— 1962: On the non-linear energy transfer in a gravity wave spectrum, part 1: general theory. *J. Fluid Mech.*, **12**, 481–501.
— 1963: A statistical analysis of the generation of microseisms. *Rev. of Geophys.*, **1**, 177–210.
— 1966: Feynman diagrams and interaction rules of wave-wave scattering processes. *Rev. of Geophys.*, **4**, 1–32.
— 1970: Wave-driven inertial oscillations. *Geophys. Fluid Dyn.*, **1**, 463–502. doi:10.1080/03091927009365783.
— 1971: On the mass and momentum transfer between short gravity waves and larger-scale motions. *J. Fluid Mech.*, **4**, 189–205.
— 1974: On the spectral dissipation of ocean waves due to white capping. *Boundary-Layer Meteorol.*, **6**, 107–127.
Hasselmann, K., T. P. Barnett, E. Bouws, H. Carlson, D. E. Cartwright, K. Enke, J. A. Ewing, H. Gienapp, D. E. Hasselmann, P. Kruseman, A. Meerburg, P. Müller, D. J. Olbers, K. Richter, W. Sell, and H. Walden, 1973: Measurements of wind-wave growth and swell decay during the Joint North Sea Wave Project. *Deut. Hydrogr. Z.*, **8**, 1–95, suppl. A.
Hasselmann, K. and J. I. Collins, 1968: Spectral dissipation of finite depth gravity waves due to turbulent bottom friction. *J. Mar. Res.*, **26**, 1–12.

Hasselmann, K. and S. Hasselmann, 1991: On the nonlinear mapping of an ocean wave spectrum into a synthetic aperture radar image spectrum and its inversion. *J. Geophys. Res.*, **96**, 10713–10729.

Hasselmann, K., W. Munk, and G. MacDonald, 1963: Bispectra of ocean waves. *Time series analysis*, M. Rosenblatt, ed., Wiley, 125–139.

Hasselmann, K., R. K. Raney, W. J. Plant, W. Alpers, R. A. Shuchman, D. R. Lyzenga, C. L. Rufenach, and M. J. Tucker, 1985a: Theory of Synthetic Aperture Radar ocean imaging: a MARSEN view. *J. Geophys. Res.*, **90**, 4659–4686.

Hasselmann, S., K. Hasselmann, J. Allender, and T. Barnett, 1985b: Computation and parameterizations of the nonlinear energy transfer in a gravity-wave spectrum. Part II: Parameterizations of the nonlinear energy transfer for application in wave models. *J. Phys. Oceanogr.*, **15**, 1378–1391.URL link.

Hauser, D., G. Caudal, G. J. Rijckenberg, D. Vidal-Majar, G. Laurent, and P. Lancelin, 1992: RESSAC: a new airborne FM/CW radar ocean wave spectrometer. *IEEE Trans. on Geosci. and Remote Sensing*, **30**, 981–995.

Heathershaw, A. D., 1982: Seabed-wave resonance and sand bar growth. *Nature*, **296**, 343–345.

Hemer, M. A., J. Katzfey, and C. E. Trenham, 2013: Global dynamical projections of surface ocean wave climate for a future high greenhouse gas emission scenario. *Ocean Modelling*, **70**, 221–245.

Herbers, T. H. C. and M. C. Burton, 1997: Nonlinear shoaling of directionally spread waves on a beach. *J. Geophys. Res.*, **102**, 21,101–21,114.

Herbers, T. H. C., S. Elgar, and R. T. Guza, 1994: Infragravity-frequency (0.005-0.05 Hz) motions on the shelf, part I, forced waves. *J. Phys. Oceanogr.*, **24**, 917–927.URL link.

— 1995: Infragravity-frequency (0.005-0.05 Hz) motions on the shelf. part II: free waves. *J. Phys. Oceanogr.*, **25**, 1063–1079.URL link.

Herbers, T. H. C. and R. T. Guza, 1990: Estimation of directional wave spectra from multicomponent observations. *J. Phys. Oceanogr.*, **20**, 1703–1724.URL link.

— 1991: Wind-wave nonlinearity observed at the sea floor. part I: forced-wave energy. *J. Phys. Oceanogr.*, **21**, 1740–1761.URL link.

Herbers, T. H. C. and S. J. Lentz, 2010: Observing directional properties of ocean swell with an acoustic doppler current profiler (ADCP). *J. Atmos. Ocean Technol.*, **27**, 210–225.URL link.

Herbers, T. H. C., R. L. Lowe, and R. T. Guza, 1992: Field observations of orbital velocities and pressure in weakly nonlinear surface gravity waves. *J. Fluid Mech.*, **245**, 413–435.

Herterich, K. and K. Hasselmann, 1980: A similarity relation for the non-linear energy transfer in a finite-depth gravity-wave spectrum. *J. Fluid Mech.*, **97**, 215–224.

Hoefel, F. and S. Elgar, 2003: Wave-induced sediment transport and sandbar migration. *Science*, **299**, 1885–1887.

Hogstrom, U., A. Smedman, E. Sahlee, W. M. Drennan, K. K. Kahma, H. Pettersson, and F. Zhang, 2009: The atmospheric boundary layer during swell: A field study and interpretation of the turbulent kinetic energy budget for high wave ages. *J. Atmos. Sci.*, **66**, 2764–2779.URL link.

Holthuijsen, L., 1983: Stereophotography of ocean waves. *Appl. Ocean Res.*, **5**, 204–209.

— 2007: *Waves in Oceanic and Coastal Waters*. Cambridge University Press, Cambridge.

Holthuijsen, L. H. and T. H. C. Herbers, 1986: Statistics of breaking waves observed as whitecaps in the open sea. *J. Phys. Oceanogr.*, **16**, 290–297.URL link.

Holthuijsen, L. H., M. D. Powell, and J. D. Pietrzak, 2012: Wind and waves in extreme hurricanes. *J. Geophys. Res.*, **117**, C09003. doi:10.1029/2012JC007983.

Huang, N. E., 1979: On surface drift currents in the ocean. *J. Fluid Mech.*, **91**, 191–208.

Huang, N. E., Z. Shen, S. R. Long, M. C. Wu, H. H. Shih, Q. Zheng, N.-C. Yen, C. C. Tung, and H. H. Liu, 1998: The empirical mode decomposition and the Hilbert spectrum for nonlinear and non-stationary time series analysis. *Proc. Roy. Soc. Lond. A*, **454**, 903–995.

Huchet, M., F. Leckler, J.-F. Filipot, A. Roland, F. Ardhuin, M. D. Sikiric, H. Michaud, M. Delpey, and G. Dodet, 2015: On the high resolution coastal applications with WAVEWATCH III. *Proceedings, 14th Int. Workshop of Wave Hindcasting and Forecasting, Key West, Florida*.URL link.

Hunt, I. A., 1959: Design of seawalls and breakwaters. *Journal of Waterways and Harbours Division*, **85**, 123–152.

Hwang, L. S. and D. Divoky, 1970: Braking wave set up and decay on gentle slopes. *Proceedings of the 12th international conference on coastal engineering*, ASCE, 377–389.

Hwang, P. A. and D. W. Wang, 2004: Field measurements of duration-limited growth of wind-generated ocean surface waves at young stages of development. *J. Phys. Oceanogr.*, **34**, 2316–2326.URL link.

Hwang, P. H., D. W. Wang, E. J. Walsh, W. B. Krabill, and R. N. Swift, 2000: Airborne measurement of the wavenumber spectra of ocean surface waves. part ii: directional distribution. *J. Phys. Oceanogr.*, **30**, 2768–2787.URL link.

Iribarren, R. and C. Nogales, 1949: Protection des ports. *Proceedings XVIIth International Navigation Congress, Section II, Communication, 4, Lisbon*, 31–80.

Ivonin, D. V., P. Broche, J.-L. Devenon, and V. I. Shrira, 2004: Validation of HF radar probing of the vertical shear of surface currents by acoustic Doppler current profiler measurements. *J. Geophys. Res.*, **101**, C04003. doi:10.1029/2003JC002025.

Jackson, F. C., W. T. Walton, and P. L. Baker, 1985: Aircraft and satellite measurement of ocean wave directional spectra using scanning-beam microwave radars. *J. Geophys. Res.*, **90**, 987–1004.

Janssen, P., 2004: *The interaction of ocean waves and wind*. Cambridge University Press, Cambridge, 300 pp.

Janssen, P. A. E. M., 1991: Quasi-linear theory of wind wave generation applied to wave forecasting. *J. Phys. Oceanogr.*, **21**, 1631–1642, see comments by D. Chalikov, J. Phys. Oceanogr. 1993, vol. 23 pp. 1597–1600.URL link.

— 2008: Progress in ocean wave forecasting. *J. Comp. Phys.*, **227**, 3572–3594. doi:10.1016/j.jcp.2007.04.029.

— 2009: On some consequences of the canonical transformation in the Hamiltonian theory of water waves. *J. Fluid Mech.*, **637**, 1–44.

— 2011: Ocean wave effects on the daily cycle in SST. *J. Geophys. Res.*, **117**, C00J32. doi:10.1029/2012JC007943.

Janssen, P. A. E. M., K. Hasselmann, S. Hasselmann, and G. J. Komen, 1994: Parameterization of source terms and the energy balance in a growing wind sea. *Dynamics and modelling of ocean waves*, G. J. Komen et al., ed., Cambridge University Press, pages 215–238.

Janssen, P. A. E. M. and M. Onorato, 2007: The intermediate water depth limit of the Zakharov equation and consequences for wave prediction. *J. Phys. Oceanogr.*, **37**, 2389–2400. doi:10.1175/JPO3128.1.

Janssen, T. and J. Battjes, 2006: A note on wave energy dissipation over steep beaches. *Coastal Eng.*, **54**, 711–716.

Jaramillo, S., A. Sheremet, M. A. Allison, A. H. Reed, and K. T. Holland, 2009: Wave-mud interactions over the muddy atchafalaya subaqueous clinoform, louisiana, united states: Wave-supported sediment transport. *J. Geophys. Res.*, **114**, C04002. doi:10.1029/2008JC004821.

Jenkins, A. D. and F. Ardhuin, 2004: Interaction of ocean waves and currents: How different approaches may be reconciled. *Proc. 14th Int. Offshore & Polar Engng Conf., Toulon, France, May 23–28, 2004*, Int. Soc. of Offshore & Polar Engrs, volume 3, 105–111.URL link.

Jensen, B. L., B. M. Sumer, and J. Fredsøe, 1989: Turbulent oscillatory boundary layers at high Reynolds numbers. *J. Fluid Mech.*, **206**, 265–297.

Jessup, A. T. and K. R. Phadnis, 2005: Measurement of the geometric and kinematic properties of microscale breaking waves from infrared imagery using a PIV algorithm. *Meas. Sci. Technol.*, **16**, 1961–1969. doi:10.1088/0957-0233/16/10/011.

Jonsson, I. G., 1967: *Proceedings of the 10th International Conference on Coastal Engineering, Tokyo, Japan*, ASCE, 127–148.

Kahma, K. K., 1981: A study of the growth of the wave spectrum with fetch. *J. Phys. Oceanogr.*, **11**, 1503–1515.

Kahma, K. K. and C. J. Calkoen, 1992: Reconciling discrepancies in the observed growth of wind-generated waves. *J. Phys. Oceanogr.*, **22**, 1389–1405.URL link.

Kahma, K. K. and M. A. Donelan, 1988: A laboratory study of the minimum wind speed for wind wave generation. *J. Fluid Mech.*, **192**, 339–364.

Kajiura, K., 1968: A model of the bottom boundary layer in water waves. *Bull. Earthquake Res. Inst. Univ. Tokyo*, **46**, 75–123.

Kedar, S., M. Longuet-Higgins, F. W. N. Graham, R. Clayton, and C. Jones, 2008: The origin of deep ocean microseisms in the north Atlantic ocean. *Proc. Roy. Soc. Lond. A*, 1–35. doi:10.1098/rspa.2007.0277.

Keller, J. B., 1998: Gravity waves on ice-covered water. *J. Geophys. Res.*, **103**, 7663–7669.

Kenyon, K. E., 1969: Stokes drift for random gravity waves. *J. Geophys. Res.*, **74**, 6991–6994.

Kerbaol, V., 1997: *Analyse spectrale et statistique vent-vagues des images radar Ã ouverture synthÃ©tique : application aux donnÃ©es satellites ERS-1/2*. Ph.D. thesis, Université de Rennes 1.

Kinsman, B., 1965: *Wind waves*. Prentice-Hall, Englewood Cliffs, N. J., 676 p. Reprinted by Dover Phoenix editions, Mineola, N. Y.

Kirby, J. T., 1986: Higher-order approximations in the parabolic equation method for water waves. *J. Geophys. Res.*, **91**, 933–952.

— 1998: Discussion of 'note on a nonlinearity parameter of surface waves' by S. Beji. *Coastal Eng.*, **34**, 163–168.

Kirby, J. T. and T.-M. Chen, 1989: Surface waves on vertically sheared flows: approximate dispersion relations. *J. Geophys. Res.*, **94**, 1013–1027.

Kirincich, A., 2016: Remote sensing of the surface wind field over the coastal ocean via direct calibration of HF radar backscatter power. *J. Atmos. Ocean Technol.*, **33**, 1377–1392. doi:10.1175//JTECH-D-15-0242.1.

Kitaigorodskii, S. A., 1962: Applications of the theory of similarity to the analysis of wind-generated wave motion as a stochastic process. *Izv. Geophys. Ser. Acad. Sci., USSR*, **1**, 105–117.

— 1994: A note on the influence of breaking wind waves on the aerodynamic roughness of the sea surface as seen from below. *Tellus*, **46A**, 681–685.

Kobayashi, S., Y. Ota, Y. Harada, A. Ebita, M. Moriya, H. Onoda, K. Onogi, H. Kamahori, C. Kobayashi, H. Endo, K. Miyaoka, and K. Takahashi, 2015: The JRA-55 reanalysis: General specifications and basic characteristics. *J. Met. Soc. Japan*, **93**, 5–48. doi:10.2151/jmsj.2015-001.

Koga, M., 1982: Bubble entrainment in breaking wind waves. *Tellus*, **34**, 481–489.

Komar, P. D., 1998: *Beach processes and sedimentation*. Prentice-Hall, second edition, 544 p.

Komatsu, K. and A. Masuda, 1996: A new scheme of nonlinear energy transfer among wind waves: Riam method. algorithm and performance. *Journal of Oceanography*, **52**, 509–537.URL link.

Komen, G. J., L. Cavaleri, M. Donelan, K. Hasselmann, S. Hasselmann, and P. A. E. M. Janssen, 1994: *Dynamics and modelling of ocean waves*. Cambridge University Press, Cambridge, 554 pp.

Komen, G. J., K. Hasselmann, and S. Hasselmann, 1984: On the existence of a fully developed windsea spectrum.

J. Phys. Oceanogr., **14**, 1271–1285.URL link.

Korotkevich, A. O., A. Pushkarev, D. Resiod, and V. E. Zakharov, 2008: Numerical verification of the weak turbulent model for swell evolution. *Eur. J. Mech. B/Fluids*, **27**, 631–387.

Korteweg, D. J. and G. de Vries, 1895: On the change of form of long waves advancing in a rectangular canal and on a new type of long stationary waves. *Phil. Mag.*, **39**, 422–443.

Krasitskii, V. P., 1994: On reduced equations in the Hamiltonian theory of weakly nonlinear surface waves. *J. Fluid Mech.*, **272**, 1–20.

Krogstad, H. E., 1992: A simple derivation of Hasselmann's nonlinear ocean-synthetic aperture radar transform. *J. Geophys. Res.*, **97**, 2421–2425.

Kudryavtsev, V., D. Hauser, G. Caudal, and B. Chapron, 2003: A semiempirical model of the normalized radar cross-section of the sea surface 1. background model. *J. Geophys. Res.*, **108**, 8054. doi:10.1029/2001JCOO1003.

Kudryavtsev, V., A. Myasoedov, B. Chapron, J. A. Johannessen, and F. Collard, 2012: Imaging mesoscale upper ocean dynamics using synthetic aperture radar and optical data. *J. Geophys. Res.*, **117**, C04029. doi:10.1029/2011JC007492.

Kudryavtsev, V., M. Yurovskaya, B. Chapron, F. Collard, and C. Donlon, 2017: Sun glitter imagery of surface waves. part 1: Directional spectrum retrieval and validation. *J. Geophys. Res.*, **122**. doi:10.1002/2016JC012425.

Kudryavtsev, V. N., 1994: The coupling of wind and internal waves. *J. Fluid Mech.*, **278**, 33–62.

Kudryavtsev, V. N., V. K. Makin, and B. Chapron, 1999: Coupled sea surface–atmosphere model. 2. spectrum of short wind waves. *J. Geophys. Res.*, **104**, 7625–7639.

Kuik, A. J., G. P. van Vledder, and L. H. Holthuijsen, 1988: A method for the routine analysis of pitch-and-roll buoy wave data. *J. Phys. Oceanogr.*, **18**, 1020–1034.URL link.

Lacombe, H., 1950: Les fluctuations des caractéristiques de la houle par petites profondeurs. les "plans de vagues". *Bulletin d'information du Comité d'Océanographie et d'Etude des Côtes*, 180–187.

Lamarre, E. and W. K. Melville, 1991: Air entrainment and dissipation in breaking waves. *Nature*, **351**, 469–472.

Lamb, H., 1932: *Hydrodynamics*. Cambridge University Press, Cambridge, England, 6th edition, 738 pp.

Landau, L. D. and E. M. Lifshitz, 1960: *Mechanics*. Pergamon Press Addison-Wesley, Reading, MA, 524–526 pp.

Langmuir, I., 1938: Surface motion of water induced by wind. *Science*, **87**, 119–123.

Lannes, D., 2013: *The water waves problem*. American Mathematical Society.

Lannes, D. and P. Bonneton, 2009: Derivation of asymptotic two-dimensional time-dependent equations for surface water wave propagation. *Phys. of Fluids*, **21**, 16601.

Large, W. G., J. C. McWilliams, and S. C. Doney, 1994: Oceanic vertical mixing: a review and a model with nonlocal boundary layer parameterization. *Rev. of Geophys.*, **32**, 363–403.

Latham, G. V. and G. H. Sutton, 1966: Seismic measurements on the ocean floor. *J. Geophys. Res.*, **71**, 2545–2573.

Lavrenov, I. V., 1986: Behavior of the surface gravity wave spectrum on a horizontally nonuniform current. *Izv. Atmos. Ocean. Phys.*, **22**, 398–401.

— 2003: *Wind-waves in oceans: dynamics and numerical simulations*. Springer, Berlin, 376 pp.

Laxague, N. J. M., B. K. Haus, D. Bogucki, and T. Özgökmen, 2015: Spectral characterization of fine-scale wind waves using shipboard optical polarimetry. *J. Geophys. Res.*, **120**, 3140–3156.

Laxague, N. J. M., T. M. Özgökmen, B. K. Haus, G. Novelli, A. Shcherbina, P. Sutherland, C. M. G. B. Lund, S. Mehta, M. Alday, and J. Molemaker, 2018: Observations of near-surface current shear help describe oceanic oil and plastic transport. *Geophys. Res. Lett.*, **44**, 245–249. doi:10.1002/2017GL075891.

Lay, T. and T. C. Wallace, 1995: *Modern Global Seismology*. Academic Press, San Diego, CA, 517 pp., iSBN 0-12-732870-X.

Leckler, F., F. Ardhuin, C. Peureux, A. Benetazzo, F. Bergamasco, and V. Dulov, 2015: Analysis and interpretation of frequency-wavenumber spectra of young wind waves. *J. Phys. Oceanogr.*, **45**, 2484–2496. doi:10.1175/JPO-D-14-0237.1.

Leonard, B. P., 1991: The ULTIMATE conservative difference scheme applied to unsteady one-dimensional advection. *Computational Methods in Applied Mechanical Engineering*, **88**, 17–74.

Levi-Civita, T., 1925: Détermination rigoureuse des ondes permanentes d'ampleur finie. *Matematische Annalen*, **XCII**, 264–314.

Li, J.-G., 2010: Global transport on a spherical multiple-cell grid. *Mon. Weather Rev.*, **139**, 1536–1555. doi:http://dx.doi.org/10.1175/2010MWR3196.1.

Li, M. Z. and C. L. Amos, 1999: Sheet flow and large wave ripples under combined waves and currents: field observations, model predictions and effect on boundary layer dynamics. *Continental Shelf Research*, **19**, 637–663.

Li, Q. and B. Fox-Kemper, 2017: Assessing the effects of Langmuir turbulence on the entrainment buoyancy flux in the ocean surface boundary layer. *J. Phys. Oceanogr.*, **47**, 2863–2886. doi:10.1175/JPO-D-17-0085.1.

Li, X.-M., S. Lehner, and T. Bruns, 2011: Ocean wave integral parameter measurements using envisat asar wave mode data. *IEEE Trans. on Geosci. and Remote Sensing*, **49**, 155–174. doi:10.1109/TGRS.2010.2052364.

Lighthill, M. J., 1962: Physical interpretation of the mathematical theory of wave generation by the wind. *J. Fluid Mech.*, **14**, 385–398.

Liu, A. K. and E. Mollo-Christensen, 1988: Wave propagation in a solid ice pack. *J. Phys. Oceanogr.*, **18**,

1702–1712.
Liu, P. C. and A. V. Babanin, 2004: Using wavelet spectrum analysis to resolve breaking events in the wind wave time series. *Annales Geophysicae*, **22**, 3335–3345.
Liu, P. C., H. S. Chen, D.-J. Doong, C. C. Kao, and Y.-J. G. Hsu, 2008: Monstrous ocean waves during typhoon Krosa. *Annales Geophysicae*, **26**, 1327–1329.
Liu, Y. and D. K. P. Yue, 1998: On generalized Bragg scattering of surface waves by bottom ripples. *J. Fluid Mech.*, **356**, 297–326.
Lloyd, S. P., 1981: Underwater sound from surface waves according to the Lighthill-Ribner theory. *J. Acoust. Soc. Amer.*, **69**, 425–435.
Long, C. E. and D. T. Resio, 2007: Wind wave spectral observations in Currituck Sound, North Carolina. *J. Geophys. Res.*, **112**, C05001. doi:10.1029/2006JC003835.
Long, R. B. and K. Hasselmann, 1979: A variational technique for extracting directional spectra from multi-component wave data. *J. Phys. Oceanogr.*, **9**, 373–381.
Longuet-Higgins, M., 1976: On the nonlinear transfer of energy in the peak of a gravity-wave spectrum: A simplified model. *Proc. Roy. Soc. Lond. A*, **347**, 311–328.
Longuet-Higgins, M. S., 1950: A theory of the origin of microseisms. *Phil. Trans. Roy. Soc. London A*, **243**, 1–35.
— 1952: On the statistical distributions of sea waves. *J. Mar. Res.*, **11**, 245–265.
— 1953: Mass transport under water waves. *Phil. Trans. Roy. Soc. London A*, **245**, 535–581.
— 1960: Reflection and refraction at a random moving surface. II. number of specular points in a gaussian surface. *J. Opt. Soc. Am.*, **50**, 845–850. doi:10.1364/JOSA.50.000845.
— 1967: On the wave-induced difference in mean sea level between the two sides of a submerged breakwater. *J. Mar. Res.*, **25**, 148–153.
— 1970: Longshore currents generated by obliquely incident sea waves, 1. *J. Geophys. Res.*, **75**, 6778–6789.
— 1977: The mean forces exerted by waves on floating or submerged bodies with applications to sand bars and wave power machines. *Proc. Roy. Soc. Lond. A*, **352**, 463–480.
— 1979: The trajectories of particles in steep, symmetric gravity waves. *J. Fluid Mech.*, **94**, 497–517.
— 1984: New integral relations for gravity waves of finite amplitude. *J. Fluid Mech.*, **149**, 205–215, see also Yu and Wu, J. Fluid Mech., 1987.
— 2005: On wave set-up in shoaling water with a rough sea bed. *J. Fluid Mech.*, **527**, 217–234.
Longuet-Higgins, M. S., D. E. Cartwright, and N. D. Smith, 1963: Observations of the directional spectrum of sea waves using the motions of a floating buoy. *Ocean Wave Spectra, proceedings of a conference, Easton, Maryland*, National Academy of Sciences, Prentice-Hall, 111–136.
Longuet-Higgins, M. S. and J. D. Fenton, 1974: On the mass, momentum, energy and circulation of a solitary wave. II. *Proc. Roy. Soc. Lond. A*, **340**, 471–493.
Longuet-Higgins, M. S. and O. M. Phillips, 1962: Phase velocity effects in tertiary wave interactions. *J. Fluid Mech.*, **12**, 333–336.
Longuet-Higgins, M. S. and R. W. Stewart, 1962: Radiation stresses and mass transport in surface gravity waves with application to 'surf beats'. *J. Fluid Mech.*, **13**, 481–504.
— 1963: A note on wave set-up. *J. Mar. Res.*, **21**, 4–10.
— 1964: Radiation stress in water waves, a physical discussion with applications. *Deep Sea Research*, **11**, 529–563.
Lowe, R. J., J. L. Falter, J. R. Koseff, S. G. Monismith, and M. J. Atkinson, 2007: Spectral wave flow attenuation within submerged canopies: Implications for wave energy dissipation. *J. Geophys. Res.*, **112**, C05018. doi:10.1029/2006JC003605.
Lu, N. Q., A. Prosperetti, and S. W. Yoon, 1990: Underwater noise emissions from bubble clouds. *IEEE J. Oceanic Eng.*, **15**, 275–281.
Lund, B., H. C. Graber, H. Tamura, C. O. Collins, and S. M. Varlamov, 2015: A new technique for the retrieval of near-surface vertical current shear from marine x-band radar images. *J. Geophys. Res.*, **120**, 8466–8486. doi:10.1002/2015JC010961.
Lygre, A. and H. E. Krogstad, 1986: Maximum entropy estimation of the directional distribution in ocean wave spectra. *J. Phys. Oceanogr.*, **16**, 2,052–2,060.
Ma, B. B., J. A. Nystuen, and R.-C. Lien, 2005: Prediction of underwater sound levels from rain and wind. *J. Acoust. Soc. Amer.*, **117**, 3555–3565.
Madsen, O. S., 1994: Spectral wave-current bottom boundary layer flows. *Proceedings of the 24th international conference on coastal engineering*, ASCE, 384–397.
Madsen, O. S., P. P. Mathisen, and M. M. Rosengaus, 1990: Movable bed friction factors for spectral waves. *Proceedings of the 22nd international conference on coastal engineering*, ASCE, 420–429.
Magne, R., K. Belibassakis, T. H. C. Herbers, F. Ardhuin, W. C. O'Reilly, and V. Rey, 2007: Evolution of surface gravity waves over a submarine canyon. *J. Geophys. Res.*, **112**, C01002. doi:10.1029/2005JC003035.
Manasseh, R., A. V. Babanin, C. Forbes, K. Rickards, I. Bobevski, and A. Ooi, 2006: Passive acoustic determination of wave-breaking events and their severity across the spectrum. *J. Atmos. Ocean Technol.*, **23**, 599–618.
Marieu, V., P. Bonneton, D. L. Foster, and F. Ardhuin, 2008: Modeling of vortex ripple morphodynamics. *J. Geophys. Res.*, **113**, C09007. doi:10.1029/2007JC004659.

Marin, F., 2004: Eddy viscosity and Eulerian drift over rippled beds in waves. *Coastal Eng.*, **50**, 139–159.
Marmorino, G. O., G. B. Smith, and G. J. Lindemann, 2005: Infrared imagery of large-aspect-ratio Langmuir circulation. *Continental Shelf Research*, **25**, 1–6.
Martin, S. and P. Kauffman, 1981: A field and laboratory study of wave dampin by grease ice. *Journal of Geology*, **27**, 283–313.
Massel, S. R., 1993: Extended refraction-diffraction equation for surface waves. *Coastal Eng.*, **19**, 97–126.
Mastenbroek, C., 1996: *Wind-wave interaction*. Ph.D. thesis, Delft University of Technology, The Netherlands.
Mastenbroek, C., V. K. Makin, M. H. Garat, and J. P. Giovanangeli, 1996: Experimental evidence of the rapid distortion of turbulence in the air flow over water waves. *J. Fluid Mech.*, **318**, 273–302.
Mathiesen, M., 1987: Wave refraction by a current whirl. *J. Geophys. Res.*, **92**, 3905–3912.
Mathisen, P. P. and O. S. Madsen, 1996: Wave and currents over a fixed rippled bed. 2. bottom and apparent roughness experienced by currents in the presence of waves. *J. Geophys. Res.*, **101**, 16,543–16,550, see erratum in Mathisen and Madsen JGR 1999.
McFarlane, V., M. Loewen, and F. Hicks, 1982: Measurements of the evolution of frazil ice particle size distributions. **120**, 45–55.
McGoldrick, L. F., O. M. Phillips, N. E. Huang, and T. H. Hodgson, 1966: Measurements of third-order wave interactions. *J. Fluid Mech.*, **25**, 437–456.
McIntyre, M. E., 1981: On the 'wave momentum' myth. *J. Fluid Mech.*, **106**, 331–347.
— 1988: A note on the divergence effect and the Lagrangian-mean surface elevation in periodic water waves. *J. Fluid Mech.*, **189**, 235–242.
Mei, C. C., 1989: *Applied dynamics of ocean surface waves*. World Scientific, Singapore, second edition, 740 p.
Mellor, G., 2002: Oscillatory bottom boundary layers. *J. Phys. Oceanogr.*, **32**, 3075–3088.
Mellor, G. and A. Blumberg, 2004: Wave breaking and ocean surface layer thermal response. *J. Phys. Oceanogr.*, **34**, 693–698.
Mellor, G. L., 2008: The depth-dependent current and wave interaction equations: A revision. *J. Phys. Oceanogr.*, **38**, 2587–2596.URL link.
Mellor, G. L. and T. Yamada, 1982: Development of a turbulence closure model for geophysical fluid problems. *Rev. Geophys. Space Phys.*, **20**, 851–875.
Melville, W. K. and P. Matusov, 2002: Distribution of breaking waves at the ocean surface. *Nature*, **417**, 58–63.
Melville, W. K. and R. J. Rapp, 1988: The surface velocity in steep and breaking waves. *J. Fluid Mech.*, **169**, 1–22.
Melville, W. K., R. Shear, and F. Verron, 1998: Laboratory measurements of the generation and evolution of Langmuir circulations. *J. Fluid Mech.*, **364**, 31–58.
Miche, A., 1944a: Mouvements ondulatoires de la mer en profondeur croissante ou décroissante. forme limite de la houle lors de son déferlement. application aux digues maritimes. Troisième partie. Forme et propriétés des houles limites lors du déferlement. Croissance des vitesses vers la rive. *Annales des Ponts et Chaussées*, **Tome 114**, 369–406.
— 1944b: Mouvements ondulatoires de la mer en profondeur croissante ou décroissante. Première partie. Mouvements ondulatoires périodiques et cylindriques en profondeur constante. *Annales des Ponts et Chaussées*, **Tome 114**, 42–78.
— 1951: Le pouvoir réfléchissant des ouvrages maritimes exposés à l'action de la houle. *Annales des Ponts et Chaussées*, **121**, 285–319.
Miles, J., 1996: Surface wave generation: a viscoelastic model. *J. Fluid Mech.*, **322**, 131–145.
Miles, J. W., 1957: On the generation of surface waves by shear flows. *J. Fluid Mech.*, **3**, 185–204.
— 1959: On the generation of surface waves by shear flows. part 2. *J. Fluid Mech.*, **6**, 568–598.
Miller, G. F. and H. Pursey, 1955: On the partition of energy between elastic waves in a semi-infinite solid. *Proc. Roy. Soc. Lond. A*, **233**, 55–69.
Minster, J. F., D. Jourdan, C. Boissier, and P. Midol-Monnet, 1991: Estimation of the sea-state bias in radar altimeter Geosat data from examination of frontal systems. *J. Atmos. Ocean Technol.*, **9**, 174–187.
Mitsuyasu, H., F. Tasai, T. Suhara, S. Mizuno, M. Onkusu, T. Honda, and T. Rukiiski, 1975: Observations of the directional spectrum of ocean waves using a cloverleaf buoy. *J. Phys. Oceanogr.*, **5**, 751–761.
Monahan, E. C. and D. K. Woolf, 1989: Comments on "variations of whitecap coverage with wind stress and water temperature". *J. Phys. Oceanogr.*, **19**, 706–709.URL link.
Monin, A. S., 1962: Empirical data on turbulence in the surface layer of the atmosphere. *J. Geophys. Res.*, **67**, 3103–3109.
Monismith, S. G., 2007: Hydrodynamics of coral reefs. *Annu. Rev. Fluid Mech.*, **39**, 37–55. doi:10.1146/annurev.fluid.38.050304.092125.
Monismith, S. G., J. S. Rogers, D. Koweek, and R. B. Dunbar, 2015: Frictional wave dissipation on a remarkably rough reef. *Geophys. Res. Lett.*, **112**, 4063–4071. doi:10.1002/2015GL063804.
Montagne, R., 1922: Le service de prédiction de la houle au Maroc. *Annales Hydrographiques*, 157–186.
Mooney, M., 1951: The viscosity of a concentrated suspension of spherical particles. *Journal of Colloid Science*, **6**, 162–170.
Mosig, J. E. M., F. Montiel, and V. A. Squire, 2015: Comparison of viscoelastic-type models for ocean wave

attenuation in ice-covered seas. *J. Geophys. Res.*, **120**, 6072–6090. doi:10.1002/2015JC010881.
Mouche, A. and B. Chapron, 2015: Global C-band Envisat, RADARSAT-2 and Sentinel-1 SAR measurements in copolarization and cross-polarization. *J. Geophys. Res.*, **120**, 7195–7207. doi:10.1002/2015JC011149.
Mouche, A., F. Collard, B. Chapron, K.-F. Dagestad, G. Guitton, J. A. Johannessen, V. Kerbaol, and M. W. Hansen, 2012: On the use of doppler shift for sea surface wind retrieval from SAR. *IEEE Trans. on Geosci. and Remote Sensing*, **50**, 2901–2909. doi:10.1109/TGRS.2011.2174998.
Munk, W., 2009: An inconvenient sea truth: Spread, steepness, and skewness of surface slopes. *Annu. Rev. Mar. Sci.*, **1**, 377–415. doi:10.1146/annurev.marine.010908.163940.
Munk, W. H., 1949: Surf beat. *Eos Trans. AGU*, **30**, 849–854.
— 1950: Origin and generation of waves. *Proceedings 1st International Conference on Coastal Engineering, Long Beach, California*, ASCE, 1–4.
Munk, W. H., G. R. Miller, F. E. Snodgrass, and N. F. Barber, 1963: Directional recording of swell from distant storms. *Phil. Trans. Roy. Soc. London A*, **255**, 505–584.
Munk, W. H. and M. A. Traylor, 1947: Refraction of ocean waves: a process linking underwater topography to beach erosion. *Journal of Geology*, **LV**, 1–26.
Nadaoka, K., S. Beji, and Y. Nakagawa, 1997: A fully dispersive weakly nonlinear model for water waves. *Proc. Roy. Soc. Lond. A*, **453**, 303–318.
Nielsen, P., 1992: *Coastal bottom boudary layers and sediment transport*. World Scientific Publishing.
Nikuradse, J., 1933: Strömungsgestze in rauhen rohren. Technical Report 361, VDI, (English translation: NACA Tech. Memo. 1292, National Advisory Commission for Aeronautics, Washington D.C., 1950).
Nishida, K. and R. Takagi, 2016: Teleseismic S wave microseisms. *Science*, **353**, 919–921. doi:10.1126/science.aaf7573.
Noh, Y., 1996: Dynamics of diurnal thermocline formation in the oceanic mixed layer. *J. Geophys. Res.*, **26**, 2189–2195.
Noh, Y. and H. J. Kim, 1999: Simulations of temperature and turbulence structure of the oceanic boundary layer with the improved near-surface process. *J. Geophys. Res.*, **104**, 15621–15634.
Noh, Y., H. S. Min, and S. Raasch, 2004: Large eddy simulation of the ocean mixed layer: the effects of wave breaking and Langmuir circulation. *J. Phys. Oceanogr.*, **34**, 720–733.
Nouguier, F., B. Chapron, F. Collard, A. Mouche, N. Rascle, F. Ardhuin, and X. Wu, 2018: Sea surface kinematics from near-nadir radar measurements. *IEEE Trans. on Geosci. and Remote Sensing*, **56**, 6169–6179.URL link. doi:10.1109/TGRS.2018.2833200.
Nouguier, F., A. Mouche, N. Rascle, B. Chapron, and D. Vandemark, 2016: Analysis of dual-frequency ocean backscatter measurements at Ku- and Ka-bands using near-nadir incidence GPM radar data. *IEEE Geoscience And Remote Sensing Letters*, **31**, 2023–2245. doi:10.1109/LGRS.2016.2583198.
Nwogu, O., 1993: Alternative form of Boussinesq equations for nearshore wave propagation. *J. of Waterway, Port Coast. Ocean Eng.*, **119**, 618–637.
Obrebski, M., F. Ardhuin, E. Stutzmann, and M. Schimmel, 2012: How moderate sea states can generate loud seismic noise in the deep ocean. *Geophys. Res. Lett.*, **39**, L11601. doi:10.1029/2012GL051896.
— 2013: Detection of microseismic compressional (p) body waves aided by numerical modeling of oceanic noise sources. *J. Geophys. Res.*, **118**, 4312–4324. doi:10.1002/jgrb.50233.
Oltman-Shay, J., P. A. Howd, and W. A. Birkemeier, 1989: Shear instabilities of the mean longshore current, 2, field observations. *J. Geophys. Res.*, **94**, 18031–18042.
Onorato, M., A. R. Osborne, and M. Serio, 2002: Extreme wave events in directional, random oceanic sea states. *Phys. of Fluids*, **14**, L25–L28.
O'Reilly, W. C. and R. T. Guza, 1991: Comparison of spectral refraction and refraction-diffraction wave models. *J. of Waterway, Port Coast. Ocean Eng.*, **117**, 199–215.
— 1993: A comparison of two spectral wave models in the Southern California Bight. *Coastal Eng.*, **19**, 263–282.
O'Reilly, W. C., T. H. C. Herbers, R. J. Seymour, and R. T. Guza, 1996: A comparison of directional buoy and fixed platform measurements of Pacific swell. *J. Atmos. Ocean Technol.*, **13**, 231–238.
Osborne, A., M. Onorato, and M. Serio, 2003: The nonlinear dynamics of rogue waves and holes in deep water gravity wave trains. *Phys. Lett.*, **A275**, 386–393.
Osborne, A. R., L. Bergamasco, M. Serio, L. Bianco, L. Cavaleri, M. Drago, L. Iovenitti, and D. Viezzoli, 1996: Nonlinear shoaling of shallow water waves: perspective in term of the inverse scattering transform. *Nuovo Cimento*, **19C**, 151–176.
Osborne, A. R. and T. L. Burch, 1980: Coupling between a surface-wave spectrum and an internal wave: modulation interaction. *Science*, **208**, 513–460.
Palubinskas, G., F. Meyer, H. Runge, P. Reinartz, R. Scheiber, and R. Bamler, 2005: Estimation of along-track velocity of road vehicles in SAR data. *Proceedings of SPIE, volume 5982*, SPIE, 1–9.
Pasyanos, M. E., W. R. Walter, and E. M. Matzel, 2009: A simultaneous multiphase approach to determine p-wave and s-wave attenuation of the crust and upper mantle. *Bull. Seismol. Soc. Am.*, **99**, 3314–3325.
Patankar, S., 1980: *Numerical heat transfer and fluid flow: Computational methods in mechanics and thermal science*. Hemisphere Publishing Corp., Washington, DC, 210 pp.
Pawka, S. S., 1983: Island shadows in wave directional spectra. *J. Geophys. Res.*, **88**, 2579–2591.

Peak, S. D., 2004: *Wave refraction over complex nearshore bathymetry*. Master's thesis, Naval Postgraduate School.URL link.

Peral, E., E. Rodriguez, and D. Esteban-Fernandez, 2015: Impact of surface waves on SWOT's projected ocean accuracy. *Remote Sensing*, **7**, 14509–14529. doi:10.3390/rs71114509.

Peregrine, D. H., 1967: Long waves on a beach. *J. Fluid Mech.*, **27**, 815–827.

Perignon, Y., F. Ardhuin, M. Cathelain, and M. Robert, 2014: Swell dissipation by induced atmospheric shear stress. *J. Geophys. Res.*, **119**, 6622–6630. doi:10.1002/2014JC009896.

Pettersson, H., H. C. Graber, D. Hauser, C. Quentin, K. Kahma, W. M. Drennan, and M. A. Donelan, 2003: Directional wave measurements from three wave sensors during the FETCH experiment. *J. Geophys. Res.*, **108**, 8061. doi:10.1029/2001JC001164.

Peureux, C. and F. Ardhuin, 2016: Ocean bottom pressure records from the cascadia array and short surface gravity waves. *J. Geophys. Res.*, **121**, 2862–2873. doi:10.1002/2015JC011580.

Peureux, C., A. Benetazzo, and F. Ardhuin, 2018: Note on the directional properties of meter-scale gravity waves. *Ocean Science*, **14**, 41–52. doi:10.5194/os-14-41-2018.

Phillips, O. M., 1957: On the generation of waves by turbulent wind. *J. Fluid Mech.*, **2**, 415–417.

— 1958: The equilibrium range in the spectrum of wind-generated waves. *J. Fluid Mech.*, **4**, 426–433.

— 1960: On the dynamics of unsteady gravity waves of finite amplitude. *J. Fluid Mech.*, **9**, 193–217.

— 1961: A note on the turbulence generated by gravity waves. *J. Geophys. Res.*, **66**, 2889–2893.

— 1977: *The dynamics of the upper ocean*. Cambridge University Press, London, 336 p.

— 1984: On the response of short ocean wave components at a fixed wavenumber to ocean current variations. *J. Phys. Oceanogr.*, **14**, 1425–1433.URL link. doi:10.1175/1520-0485(1984)014¡1425:OTROSO¿2.0.CO;2.

— 1985: Spectral and statistical properties of the equilibrium range in wind-generated gravity waves. *J. Fluid Mech.*, **156**, 505–531.

Pierson, W. J., 1972: The loss of two British trawlers – a study in wave refraction. *Journal of Navigation*, **25**, 291–304.

Pierson, W. J., G. Neumann, and R. W. James, 1955: *Practical methods for observing and forecasting ocean waves by means of wave spectra and statistics*. U. S. Hydrographic Office, 284 pp.

Pierson, W. J., Jr and L. Moskowitz, 1964: A proposed spectral form for fully developed wind seas based on the similarity theory of S. A. Kitaigorodskii. *J. Geophys. Res.*, **69**, 5,181–5,190.

Pineau-Guillou, L., F. Ardhuin, M.-N. Bouin, J.-L. Redelsperger, B. Chapron, J. Bidlot, and Y. Quilfen, 2018: Strong winds in a coupled wave-atmosphere model during a north Atlantic storm event: evaluation against observations. *Quart. Journ. Roy. Meteorol. Soc.*, **144**, 317–332. doi:10.1002/qj.3205.

Plant, W. J., 1982: A relationship between wind stress and wave slope. *J. Geophys. Res.*, **87**, 1961–1967.

Popinet, S., R. M. Gorman, G. J. Rickard, and H. L. Tolman, 2010: A quadtree-adaptive spectral wave model. *Ocean Modelling*, **34**, 36–49.

Posmentier, E., 1967: A theory of microbaroms. *Geophys. J. R. Astron. Soc.*, **13**, 487–501.

Potter, H., C. O. Collins, III, W. M. Drennan, and H. C. Graber, 2015: Observations of wind stress direction during typhoon Chaba (2010). *Geophys. Res. Lett.*, **42**, 9898–9905. doi:10.1029/2011JC007833.

Powell, M. D., P. J. Vickery, and T. A. Reinhold, 2003: Reduced drag coefficient for high wind speeds in tropical cyclones. *Nature*, **422**, 279–283.

Prevosto, M. and G. Z. Forristall, 2002: Statistics of wave crest from models vs. measurements. *Proceedings of OMAE 2002 21st International Conference on Offshore Mechanics and Arctic Engineering, 23-28 June 2002, Oslo, Norway*, ASME, OMAE2002–28446.

Pullen, T., N. W. H. Allsop, T. Bruce, A. Kortenhaus, H. Schüttrumpf, and J. W. van der Meer, 2007: *Wave overtopping of sea defences and related structures: assessment manual*. Boyens Medien GmbH, 336 p.URL link.

Quilfen, Y., B. Chapron, and J. Tournadre, 2010: Satellite microwave surface observations in tropical cyclones. *Mon. Weather Rev.*, **131**, 421–437.

Quilfen, Y., M. Yurovskaya, B. Chapron, and F. Ardhuin, 2018: Storm waves sharpening in the Agulhas current: satellite observations and modeling. *Remote sensing of Environment*, **216**, 561–571. doi:10.1016/j.rse.2018.07.020.

Radder, A. C., 1979: On the parabolic equation method for water wave propagation. *J. Fluid Mech.*, **95**, 159–176.

Rascle, N. and F. Ardhuin, 2009: Drift and mixing under the ocean surface revisited. stratified conditions and model-data comparisons. *J. Geophys. Res.*, **114**, C02016. doi:10.1029/2007JC004466.

— 2013: A global wave parameter database for geophysical applications. part 2: model validation with improved source term parameterization. *Ocean Modelling*, **70**, 174–188. doi:10.1016/j.ocemod.2012.12.001.

Rascle, N., F. Ardhuin, and E. A. Terray, 2006: Drift and mixing under the ocean surface. a coherent one-dimensional description with application to unstratified conditions. *J. Geophys. Res.*, **111**, C03016. doi:10.1029/2005JC003004.

Rascle, N., B. Chapron, F. Ardhuin, and A. Soloviev, 2013: A note on the direct injection of turbulence by breaking waves. *Ocean Modelling*, **70**, 145–151. doi:10.1016/j.ocemod.2012.09.001.

Rascle, N., B. Chapron, A. Ponte, F. Ardhuin, and P. Klein, 2014: Surface roughness imaging of currents shows divergence and strain in the wind direction. *J. Phys. Oceanogr.*, **44**, 2153–2163. doi:10.1175/JPO-D-13-0278.1.

Rascle, N., J. Molemaker, L. Marié, F. Nouguier, B. Chapron, B. Lund, and A. Mouche, 2017: Intense deformation field at oceanic front inferred from directional sea surface roughness observations. *Geophys. Res. Lett.*, **48**, 5599–5608. doi:10.1002/2017GL073473.

Rayevskiy, M. A., 1983: On the propagation of gravity waves in randomly inhomogeneous nonsteady-state currents. *Izv. Atmos. Ocean. Phys.*, **19**, 475–479.

Rayleigh, L., 1896: *The Theory of Sound*. Macmillan, London, 3rd edition.

Renault, L., M. J. Molemaker, J. Gula, S. Masson, and J. C. McWilliams, 2016a: Control and stabilization of the Gulf Stream by oceanic current interaction with the atmosphere. *J. Phys. Oceanogr.*, **46**, 3439–3453. doi:10.1175/JPO-D-16-0115.1.

Renault, L., M. J. Molemaker, J. C. McWilliams, A. F. Shchepetkin, F. Lemarié, D. Chelton, S. Illig, and A. Hall, 2016b: Modulation of wind work by oceanic current interaction with the atmosphere. *J. Phys. Oceanogr.*, **46**, 1685–1704. doi:10.1175/JPO-D-15-0232.1.

Resio, D. T., J. H. Pihl, B. A. Tracy, and C. L. Vincent, 2001: Nonlinear energy fluxes and the finite depth equilibrium range in wave spectra. *J. Geophys. Res.*, **106**, 6985–7000.

Resio, D. T. and J. J. Westerink, 2008: Modeling the physics of storm surges. *Physics Today*, 33–38.

Reul, N. and B. Chapron, 2003: A model of sea-foam thickness distribution for passive microwave remote sensing applications. *J. Geophys. Res.*, **108**, 3321. doi:10.1029/2003JC001887.

Reul, N., J. Tenerelli, B. Chapron, D. Vandemark, Y. Quilfen, and Y. Kerr, 2006: Smos satellite l-band radiometer: A new capability for ocean surface remote sensing in hurricanes. *J. Geophys. Res.*, **117**, C02006. doi:10.1029/2011JC007474.

Ricchiuto, M., Á. Csík, and H. Deconinck, 2005: Residual distribution for general time-dependent conservation laws. *J. Comp. Phys.*, **209**, 249–289. doi:10.1016/j.jcp.2005.03.003.

Rice, S., 1944: Mathematical analysis of random noise. *Noise and stochastic processes*, N. Wax, ed., Dover Publications Inc. (published 1954), New York, 133–294.

Roach, L. A., M. M. Smith, and S. M. Dean, 2018: Quantifying growth of pancake sea ice floes using images from drifting buoys. *J. Geophys. Res.*, **123**, 2851–2866. doi:10.1002/2017JC013693.

Rogers, W. E., A. V. Babanin, and D. W. Wang, 2010: Observation-consistent input and whitecapping dissipation in a model for wind-generated surface waves: Description and simple calculations. *J. Atmos. Ocean Technol.*, **29**, 1329–1346.

Rogers, W. E., J. Thomson, H. H. Shen, M. J. Doble, P. Wadhams, and S. Cheng, 2016: Dissipation of wind waves by pancake and frazil ice in the autumn beaufort sea. *J. Geophys. Res.*, **121**. doi:10.1002/2016JC012251.

Roland, A. and F. Ardhuin, 2014: On the developments of spectral wave models: numerics and parameterizations for the coastal ocean. *Ocean Dynamics*, **64**, 833–846. doi:10.1007/s10236-014-0711-z.

Romero, L. and K. W. Melville, 2010: Airborne observations of fetch-limited waves in the gulf of tehuantepec. *J. Phys. Oceanogr.*, **40**, 441–465.

Romero, L., W. K. Melville, and J. M. Kleiss, 2012: Spectral energy dissipation due to surface wave breaking. *J. Phys. Oceanogr.*, **42**, 1421–1444.

Ruessink, B. G., D. J. R. Walstra, and H. N. Southgate, 2003: Calibration and verification of a parametric wave model on barred beaches. *Coastal Eng.*, **48**, 139–149.

Russell, R. C. H. and J. D. C. Osorio, 1958: An experimental investigation of drift profiles in a closed channel. *Proceedings of the 6th International Conference on Coastal Engineering*, ASCE, 171–193.

Saha, S., S. Moorthi, H.-L. Pan, X. Wu, J. Wang, S. Nadiga, P. Tripp, R. Kistler, J. Woollen, D. Behringer, H. Liu, D. Stokes, R. Grumbine, G. Gayno, J. Wang, Y.-T. Hou, H. ya Chuang, H.-M. H. a. J. S. Juang, M. Iredell, R. Treadon, D. Kleist, P. V. Delst, D. Keyser, J. Derber, M. Ek, J. Meng, H. Wei, R. Yang, S. Lord, H. van den Dool, A. Kumar, W. Wang, C. Long, M. Chelliah, Y. Xue, B. Huang, J.-K. Schemm, W. Ebisuzaki, R. Lin, P. Xie, M. Chen, S. Zhou, W. Higgins, C.-Z. Zou, Q. Liu, Y. Chen, Y. Han, L. Cucurull, R. W. Reynolds, G. Rutledge, and M. Goldberg, 2010: The NCEP Climate Forecast System Reanalysis. *Bull. Amer. Meterol. Soc.*, **91**, 1015–1057.

Santala, M. J. and E. A. Terray, 1992: A technique for making unbiased estimates of current shear from a wave-follower. *Deep Sea Res.*, **39**, 607–622.

Saville, T., 1961: Experimental determination of wave set-up. *Proc. 2nd Tech. Conf. on Hurricanes, Miami Beach, FL., Nat. Hurricane Res. Proj. Rep. 50*, US Dept. of Commerce, 242–252.

Schlichting, H., 1979: *Boundary layer theory*. McGraw-Hill, seventh edition.

Schumacher, A., 1939: Stereophotogrammetrische Wellenaufnahmen. Wiss. Ergeb. Dtsch. Atlant. Exped. Forschungs Vermessung. Meteor 1925-1927. Technical report.

Schwartz, L. W., 1974: Computer extension and analytic continuation of Stokes' expansion for gravity waves. *J. Fluid Mech.*, **62**, 553–578.

Semedo, A., Ø. Sætra, A. Rutgersson, K. K. Kahma, and H. Pettersson, 2009: Wave-induced wind in the marine boundary layer. *J. Atmos. Sci.*, **66**, 2256–2270.URL link.

Sénéchal, N., H. Dupuis, and P. Bonneton, 2003: Field experiment on secondary wave generation on a barred beach and the consequent evolution of energy dissipation on the beach face. *Coastal Eng.*, **46**, 233–247.

Shapiro, N. M., M. Campillo, L. Stehly, and M. H. Ritzwoller, 2005: High-resolution surface-wave tomography from ambient seismic noise. *Science*, **307**, 1615–1617. doi:10.1111/j.1365-246X.2006.03240.x.

Shen, H. H., S. F. Ackley, and M. A. Hopkins, 2001: A conceptual model for pancake ice formation in a wave field. *Annales Geophysicae*, **33**, 361–367. doi:10.3189/172756401781818239.

Sheremet, A., T. Staples, F. Ardhuin, S. Suanez, and B. Fichaut, 2014: Observations of large infragravity-wave run-up at Banneg island, France. *Geophys. Res. Lett.*, **41**, 976–982. doi:10.1002/2013gl058880.

Shields, A., 1936: Anwendung der ähnlichkeits-Mechanik und der Turbulenz-forschung auf die Geschiebebewegung. *Preussische Versuchsanstalt für Wasserbau und Schiffbau*, **26**, 524–526, translated as California Inst. Technol. W. M. Keck Lab. for Hydraulic Water Res. Report 167.

Shimura, T., N. Mori, and M. A.Hemer, 2016: Projection of tropical cyclone-generated extreme wave climate based on cmip5 multi-model ensemble in the western north pacific. *Coastal Dyn.*, **49**, 1449–1462. doi:10.1007/s00382-016-3390-2.

Siddiqui, M. H. K. and M. R. Loewen, 2007: Characteristics of the wind drift layer and microscale breaking waves. *J. Fluid Mech.*, **573**, 417–456. doi:10.1017/S0022112006003892.

Signell, R. P., S. Carniel, L. Cavaleri, J. Chiggiato, J. D. Doyle, J. Pullen, and M. Sclavo, 2005: Assessment of wind quality for oceanographic modelling in semi-enclosed basins. *J. Mar. Sys.*, **53**, 217–233.

Sloss, P. W., 1993: Global relief cd-rom. Technical report, Marine Geology and Geophysics Division, U. S. National Geophysical Data Center (NOAA/NESDIS/NGDC/MGGD).URL link.

Smith, J. A., 1990: Modulation of short wind waves by long waves. *Surface waves and fluxes*, G. Geernaert and W. Plant, eds., Kluwer Academic, Dordrecht.

— 1999: Observations of wind, waves, and the mixed layer: the scaling of surface motion. *The wind-driven air-sea interface*, M. L. Banner, ed., University of New South Wales, Sydney, Australia, pages 231–238, iSBN O 7334 0586 X.

— 2006: Wave-current interactions in finite-depth. *J. Phys. Oceanogr.*, **36**, 1403–1419.

Snoke, J. A., 2009: Traveltime tables for iasp91 and ak135. *Seismological Research Letters*, **88**, 260–262.

Snyder, R. L. and C. S. Cox, 1966: A field study of the wind generation of ocean waves. *J. Mar. Res.*, **24**, 141–178.

Snyder, R. L., F. W. Dobson, J. A. Elliot, and R. B. Long, 1981: Array measurement of atmospheric pressure fluctuations above surface gravity waves. *J. Fluid Mech.*, **102**, 1–59.

Soloviev, A. V., R. Lukas, M. A. Donelan, B. K. Haus, and I. Ginis, 2014: The air-sea interface and surface stress under tropical cyclones. *Scientific Reports*, **4**, 5306. doi:10.1038/srep05306.

Song, J.-B. and M. L. Banner, 2002: On determining the onset and strength of breaking for deep water waves. Part I: Unforced irrotational wave groups. *J. Phys. Oceanogr.*, **32**, 2541–2558.URL link.

Soulsby, R., 1997: *Dynamics of marine sands, a manual for practical applications*. Thomas Telford Publications, London, 256 pp.

Squire, V., J. Dugan, P. Wadhams, P. Rottier, and A. Liu, 1995: Of ocean waves and sea ice. *Annu. Rev. Fluid Mech.*, **27**, 115–168.

Stansell, P. and C. MacFarlane, 2002: Experimental investigation of wave breaking criteria based on wave phase speeds. *J. Phys. Oceanogr.*, **32**, 1269–1283.URL link.

Steele, K., C.-C. Teng, and D. W.-C. Wang, 1992: Wave direction measurements using pitch and roll buoys. *Ocean Eng.*, **19**, 349–375.

Stewart, R. H. and J. W. Joy, 1974: HF radio measurements of surface currents. *Deep Sea Res.*, **21**, 1039–1049.

Stockdon, H. F., R. A. Holman, P. A. Howd, and A. H. Sallenger, Jr., 2006: Empirical parameterization of setup, swash, and runup. *Coastal Eng.*, **53**, 573–588.

Stokes, G. G., 1849: On the theory of oscillatory waves. *Trans. Camb. Phil. Soc.*, **8**, 441–455.

— 1880: On the theory of oscillatory waves, appendix B. *Math. and Phys. papers*, Cambridge University Press, volume 1, 225–2228.

Stoneley, R., 1926: The effect of the ocean on Rayleigh waves. *Mon. Not. Roy. Astron. Soc.*, **Geophys. Suppl. 1**, 349–356.

Stopa, J. E., F. Ardhuin, A. Bababin, and S. Zieger, 2016a: Comparison and validation of physical wave parameterizations in spectral wave models. *Ocean Modelling*, **103**, 2–17. doi:10.1016/j.ocemod.2015.09.003.

Stopa, J. E., F. Ardhuin, and F. Girard-Ardhuin, 2016b: Wave climate in the Arctic 1992-2014: seasonality and trends. *The Cryosphere*, **10**, 1605–1629. doi:10.5194/tc-10-1605-2016.

Stopa, J. E., F. Ardhuin, R. Husson, H. Jiang, B. Chapron, and F. Collard, 2016c: Swell dissipation from 10 years of envisat asar in wave mode. *Geophys. Res. Lett.*, **43**, 3423–3430. doi:10.1002/2015GL067566.

Stopa, J. E., F. Ardhuin, J. Thomson, M. M. Smith, A. Kohout, M. Doble, and P. Wadhams, 2018: Wave attenuation through an arctic marginal ice zone on 12 october, 2015: 1. measurement of wave spectra and ice features from Sentinel 1A. *J. Geophys. Res.*, **123**, 3619–3634. doi:10.1029/2018JC013791.

Stopa, J. E. and K. F. Cheung, 2014: Intercomparison of wind and wave data from the ECMWF reanalysis interim and the NCEP Climate Forecast System Reanalysis. *Ocean Modelling*, **75**, 65–83.

Stutzmann, E., G. Roult, and L. Astiz, 2000: Geoscope station noise level. *Bull. Seismol. Soc. Am.*, **90**, 690–701.

Styles, R. and S. M. Glenn, 2000: Modeling stratified wave and current bottom boundary layers on the continental shelf. *J. Geophys. Res.*, **105**, 24,119–24,139. doi:10.1029/2001JC000864.

Sullivan, P. P. and J. C. McWilliams, 2010: Dynamics of winds and currents coupled to surface waves. *Annu. Rev. Fluid Mech.*, **42**, 19–42.

Sutherland, P. and D. Dumont, 2018: Marginal ice zone thickness and extent due to wave radiation stress. *J. Phys. Oceanogr.*, **48**, 1885–1901. doi:10.1175/JPO-D-17-0167.1.

Sutherland, P. and W. K. Melville, 2013: Field measurements and scaling of ocean surface wave-breaking statistics. *Geophys. Res. Lett.*, **40**, 3074–3079. doi:10.1002/grl.50584.

Suzuki, N. and B. Fox-Kemper, 2016: Understanding stokes forces in the wave-averaged equations. *J. Geophys. Res.*, **121**, 3579–3596. doi:10.1002/2015JC011563.

Suzuki, N., B. Fox-Kemper, P. E. Hamlington, and L. P. van Roekel, 2016: Surface waves affect frontogenesis. *Geophys. Res. Lett.*, **121**, 3597–3624. doi:10.1002/2015JC011563.

Svendsen, I. A. and U. Putrevu, 1994: Nearshore mixing and dispersion. *Proc. Roy. Soc. Lond. A*, **445**, 561–576.

Sverdrup, H. U. and W. H. Munk, 1947: Wind, sea, and swell: theory of relations for forecasting. Technical Report 601, U. S. Hydrographic Office.

Symonds, G., D. A. Huntley, and A. J. Bowen, 1982: Two-dimensional surf beat: Long wavegeneration by a time-varying breakpoint. *J. Geophys. Res.*, **87**, 492–498.

Szelwis, R., 1982: Modeling of microseismic surface wave source. *J. Geophys. Res.*, **87**, 6906–6918.

Tanaka, M., 2001: Verification of Hasselmann's energy transfer among surface gravity waves by direct numerical simulations of primitive equations. *J. Fluid Mech.*, **444**, 199–221.

Tayfun, A., 1980: Narrow-band nonlinear sea waves. *J. Geophys. Res.*, **85**, 1543–1552.

Teixeira, M. A. C. and S. E. Belcher, 2002: On the distortion of turbulence by a progressive surface wave. *J. Fluid Mech.*, **458**, 229–267.

Terray, E. A., W. M. Drennan, and M. A. Donelan, 2000: The vertical structure of shear and dissipation in the ocean surface layer. *Proc. Symp. on Air-Sea Interaction, Sydney*, University of New South Wales, 239–245.

Thomson, J., S. Elgar, and T. Herbers, 2005: Reflection and tunneling of ocean waves observed at a submarine canyon. *Geophys. Res. Lett.*, **32**, L10602. doi:10.1029/2005GL022834.

Thornton, E. B. and R. T. Guza, 1983: Transformation of wave height distribution. *J. Geophys. Res.*, **88**, 5,925–5,938.

— 1986: Surf zone longshore currents and random waves: field data and models. *J. Phys. Oceanogr.*, **16**, 1,165–1,178.

Thornton, E. B. and R. F. Kraphol, 1974: Wave particle velocity measured under ocean waves. *J. Geophys. Res.*, **79**, 847–852.

Thorpe, S. A., 1966: On wave interactions in a stratified fluid. *J. Fluid Mech.*, **24**, 737–751.

— 1992: The breakup of Langmuir circulation and the instability of an array of vortices. *J. Phys. Oceanogr.*, **22**, 350–360.

Thorpe, S. A., T. R. Osborn, D. M. Farmer, and S. Vagle, 2003a: Bubble clouds and Langmuir circulation: observations and models. *J. Phys. Oceanogr.*, **33**, 122–145.

Thorpe, S. A., T. R. Osborn, J. F. E. Jackson, A. J. Hall, and R. G. Lueck, 2003b: Measurements of turbulence in the upper-ocean mixing layer using autosub. *J. Phys. Oceanogr.*, **33**, 2013–2031.

Toba, Y., 1973: Local balance in the air-sea boundary processes. II partition of wind stress to waves and current. *J. Oceanogr. Soc. Japan*, **29**, 70–75.URL link.

Tolman, H. L., 1990: The influence of unsteady depths and currents of tides on wind-wave propagation in shelf seas. *J. Phys. Oceanogr.*, **20**, 1166–1174.URL link.

— 1994: Wind waves and moveable-bed bottom friction. *J. Phys. Oceanogr.*, **24**, 994–1,009.URL link.

— 1995: On the selection of propagation schemes for a spectral wind wave model. Office Note 411, NWS/NCEP, 30 pp + figures.

— 2002a: Alleviating the garden sprinkler effect in wind wave models. *Ocean Modelling*, **4**, 269–289.

— 2002b: Limiters in third-generation wind wave models. *Global Atmos. Ocean Syst.*, **8**, 67–83.

— 2002c: Testing of WAVEWATCH-III version 2.22 in NCEP's NWW3 ocean wave model suite. Technical report, NOAA/NWS/NCEP/MMAB, oMB contribution number 214.

— 2002d: Validation of WAVEWATCH-III version 1.15. Technical Report 213, NOAA/NWS/NCEP/MMAB.

— 2003: Treatment of unresolved islands and ice in wind wave models. *Ocean Modelling*, **5**, 219–231.

— 2008: A mosaic approach to wind wave modeling. *Ocean Modelling*, **25**, 35–47. doi:10.1016/j.ocemod.2008.06.005.

Tolman, H. L., M. Accensi, H. Alves, F. Ardhuin, J. Bidlot, N. Booij, A.-C. Bennis, T. Campbell, D. V. Chalikov, A. Chawla, J.-F. Filipot, M. Foreman, P. Janssen, F. Leckler, Jian-Guo, K. L. M. Orzech, R. Padilla-Hernández, W. E. Rogers, A. Rawat, A. Roland, M. D. Sikiric, M. Szyszka, H. L. Tolman, B. Tracy, G. P. van Vledder, A. van der Westhuysen, and S. Zieger, 2014: User manual and system documentation of WAVEWATCH-III^{TM} version 2020. Technical Report 316, NOAA/NWS/NCEP/MMAB.

Tolman, H. L. and J.-H. G. M. Alves, 2005: Numerical modeling of wind waves generated by tropical cyclones using moving grids. *Ocean Modelling*, **9**, 305–323.

Tolman, H. L. and N. Booij, 1998: Modeling wind waves using wavenumber-direction spectra and a variable wavenumber grid. *Global Atmos. Ocean Syst.*, **6**, 295–309.

Tolman, H. L. and D. Chalikov, 1996: Source terms in a third-generation wind wave model. *J. Phys. Oceanogr.*, **26**, 2497–2518.URL link.

Tournadre, J., F. Girard-Ardhuin, and B. Legrésy, 2012: Antarctic iceberg distributions 2002–2010. *J. Geophys.*

Res., **117**, C05004. doi:10.1029/2011JC007441.
Traykovski, P., A. E. Hay, J. D. Irish, and J. F. Lynch, 1999: Geometry, migration, and evolution of wave orbital ripples at LEO-15. *J. Geophys. Res.*, **104**, 1,505–1,524.
Trowbridge, J. and O. S. Madsen, 1984: Turbulent wave boundary layers. 1. model formulation and first-order solution. *J. Geophys. Res.*, **89**, 7989–7997.
Tyler, G. L., C. C. Teague, R. H. Stewart, A. M. Peterson, W. H. Munk, and J. W. Joy, 1974: Wave directional spectra from synthetic aperture observations of radio scatter. *Deep Sea Res.*, **21**, 989–1016.
U. S. Army Corps of Engineers, 2002: *Coastal Engineering Manual, Engineering Manual 1110-2-1100*. U. S. Army Corps of Engineers, Washington, D. C.URL link.
Ursell, F., 1953: The long-wave paradox in the theory of gravity waves. *Proceedings of the Cambridge philosophical society*, **49**, 685–694.
— 1999: Reminiscences of the early days of the spectrum of ocean waves. *Wind-over-wave couplings*, S. G. Sajjadi, N. H. Thomas, and J. C. R. Hunt, eds., Clarendon Press, Oxford, U. K., 127–137.
Vachon, P. W. and J. Wolfe, 2011: C-band cross-polarization wind speed retrieval. *IEEE Geoscience And Remote Sensing Letters*, **8**, 456–459. doi:10.1109/LGRS.2010.2085417.
van der Westhuysen, A. J., M. Zijlema, and J. A. Battjes, 2007: Saturation-based whitecapping dissipation in SWAN for deep and shallow water. *Coastal Eng.*, **54**, 151–170.
van Vledder, G. P., 2006: The WRT method for the computation of non-linear four-wave interactions in discrete spectral wave models. *Coastal Eng.*, **53**, 223–242.
van Vledder, G. P., S. T. C. Hulst, and J. D. McConochie, 2016: Source term balance in a severe storm in the southern north sea. *Ocean Dynamics*, **66**. doi:10.1007/s10236-016-0998-z.
Vandemark, D., N. Tran, B. D. Beckley, B. Chapron, and P. Gaspar, 2002: Direct estimation of sea state impacts on radar altimeter sea level measurements. *Geophys. Res. Lett.*, **29**, 2148. doi:10.1029/2002GL015776.
Veron, F., 2015: Sea spray. *Annu. Rev. Fluid Mech.*, **47**, 507–538. doi:10.1146/annurev-fluid-010814-014651.
Veron, F., W. K. Melville, and L. Lenain, 2008: Infrared techniques for measuring ocean surface processes. *J. Atmos. Ocean Technol.*, **25**, 307–326. doi:10.1175/2007JTECHO524.1.
Vinnik, L. P., 1973: Sources of microseismic P waves. *Pure Appl. Geophys.*, **103**, 282–289.
von Gerstner, F. J., 1809: Theorie der wellen. *Ann. Phys.*, **32**, 412–440.
Wagner, T. J., R. W. Dell, I. Eisenman, R. F. Keeling, L. Padman, and J. P. Severinghaus, 2018: Wave inhibition by sea ice enables trans-atlantic ice rafting of debris during heinrich events. *Earth Planetary Sci. Lett.*, **495**, 157–163. doi:10.1016/j.epsl.2018.05.006.
WAMDI Group, 1988: The WAM model - a third generation ocean wave prediction model. *J. Phys. Oceanogr.*, **18**, 1775–1810.URL link.
Wang, R. and H. H. Shen, 2010: Gravity waves propagating into an ice-covered ocean: A viscoelastic model. *J. Geophys. Res.*, **115**, C06024. doi:10.1029/2009JC005591.
Wang, X. L., Y. Feng, and V. R. Swail, 2014: Changes in global ocean wave heights as projected using multimodel cmip5 simulations. *Geophys. Res. Lett.*, **41**, 1026–1034. doi:10.1002/2013GL058650.
Wang, X. L. and V. R. Swail, 2004: Trends of atlantic wave extremes as simulated in a 40-yr wave hindcast using kinematically reanalyzed wind fields. *Journal of Climate*, **15**, 1020–1035.URL link.
Waxler, R. and K. E. Gilbert, 2006: The radiation of atmospheric microbaroms by ocean waves. *J. Acoust. Soc. Amer.*, **119**, 2651–2664.
Webb, S. C., 2007: The earth's 'hum' is driven by ocean waves over the continental shelves. *Nature*, **445**, 754–756. doi:10.1038/nature05536.
Weber, B. L. and D. E. Barrick, 1977: On the nonlinear theory for gravity waves on the ocean's surface. Part I: Derivations. *J. Phys. Oceanogr.*, **7**, 3–10.URL link.
Weber, J. E., 1987: Wave attenuation and wave drift in the marginal ice zone. *J. Phys. Oceanogr.*, **17**, 2351–2361.
Weber, J. E. and E. Førland, 1990: Effect of the air on the drift velocity of water waves. *J. Fluid Mech.*, **218**, 619–640.
Weeks, W. F., 2010: *On sea ice*. University of Alaska Press, Fairbanks.
Welch, P. D., 1967: The use of fast Fourier transform for the estimation of power spectra: a method based on time averaging over short, modified periodograms. *IEEE Trans. Audio and Electroacoustics*, **15**, 70–73.
Weller, R. A., J. P. Dean, J. Marra, J. F. Price, E. A. Francis, and D. C. Boardman, 1985: Three-dimensional flow in the upper ocean. *Science*, **277**, 1552–1556. doi:10.1126/science.227.4694.1552.
Wessel, P. and W. H. F. Smith, 1996: A Global Self-consistent Hierarchical, High-resolution Shoreline database. *J. Geophys. Res.*, **101**, 8741–8743.
Whitham, G. B., 1962a: Mass, momentum and energy flux in water waves. *J. Fluid Mech.*, **12**, 135–147.
— 1962b: Mass, momentum and energy flux in water waves. *J. Fluid Mech.*, **12**, 135–147.
Wiberg, P. L., 1995: A theoretical investigation of boundary layer flow and bottom shear stress for smooth, transitional and rough flow under waves. *J. Geophys. Res.*, **100**, 22,667–22,679.
Wiberg, P. L. and C. K. Harris, 1994: Ripple geometry in wave-dominated environments. *J. Geophys. Res.*, **99**, 775–789.
Wilson, K. C., 1989: Friction of wave-induced sheet flow. *Coastal Eng.*, **12**, 371–379.
Winterwerp, J., R. de Graaff, J. Groeneweg, and A. P. Luijendijk, 2003: Modelling of wave damping at Guyana

mud coast. *Coastal Eng.*, **54**, 249–261, 10.1016/j.coastaleng.2006.08.012.
Wolf, J. and D. Prandle, 1999: Some observations of wave–current interaction. *Coastal Eng.*, **37**, 471–485.
Woodward, P., 1952: The spectrum of random frequency modulation. Technical Report 168, Telecommunications Research Establishement, Great Malvern, Worcs., England.
Wyatt, L. R., 2000: Limits to the inversion of HF radar backscatter for ocean wave measurement. *J. Atmos. Ocean Technol.*, **17**, 1651–1665.
Xu, Z. and A. J. Bowen, 1994: Wave- and wind-driven flow in water of finite depth. *J. Phys. Oceanogr.*, **24**, 1850–1866.URL link.
Yanenko, N. N., 1971: *The method of fractional steps*. Springer-Verlag.
Young, I. R., 1998: An experimental investigation of the role of atmospheric stability in wind wave growth. *Coastal Eng.*, **34**, 23–33.
— 1999: *Wind generated ocean waves*. Elsevier Science, Oxford, 288 pp.
Young, I. R., W. Rosenthal, and F. Ziemer, 1985: A three-dimensional analysis of marine radar images for the determination of ocean wave directionality and surface currents. *J. Geophys. Res.*, **90**, 1049–1059.
Young, I. R. and G. P. van Vledder, 1993: A review of the central role of nonlinear interactions in wind-wave evolution. *Phil. Trans. Roy. Soc. London A*, **342**, 505–524.
Young, I. R., L. A. Verhagen, and M. L. Banner, 1995: A note on the bimodal directional spreading of fetch-limited wind waves. *J. Geophys. Res.*, **100**, 773–778.
Yueh, S. H., W. Tang, A. G. Fore, G. Neumann, A. Hayashi, A. Freedman, J. Chaubell, and G. S. E. Lagerloef, 2013: L-band passive and active microwave geophysical model functions of ocean surface winds and applications to aquarius retrieval. *IEEE Trans. on Geosci. and Remote Sensing*, **51**, 4619–4632.
Yurovskaya, M. V., V. A. Dulov, B. Chapron, and V. N. Kudryavtsev, 2013: Directional short wind wave spectra derived from the sea surface photography. *J. Geophys. Res.*, **113**, C12024. doi:10.1002/jgrc.20296.
Zakharov, V. E., 1968: Stability of periodic waves of finite amplitude on the surface of a deep fluid. *J. Appl. Mech. Tech. Phys.*, **2**, 190–194.
— 1999: Statistical theory of gravity and capillary waves on the surface of a finite-depth fluid. *Eur. J. Mech. B/Fluids*, **18**, 327–334.
Zakharov, V. E. and M. M. Zaslavskii, 1982: The kinetic equation and Kolmogorov spectra in the weak turbulence theory of wind waves. *Izv. Atmos. Ocean. Phys.*, **18**, 747–753.
Zappa, C. J., M. L. Banner, H. Schultz, A. Corrada-Emmanuel, L. B. Wolff, and J. Yalcin, 2008: Retrieval of short ocean wave slope using polarimetric imaging. *Meas. Sci. Technol.*, **19**, 055503.
Zhang, J., P. Gerstoft, and P. D. Bromirski, 2010: Pelagic and coastal sources of P-wave microseisms: Generation under tropical cyclones. *Geophys. Res. Lett.*, **37**, L15301. doi:10.1029/2010GL044288.
Zhukovets, A. M., 1963: The influence of bottom roughness on wave motion in a shallow body of water. *Izv. Geophys. Ser. Acad. Sci., USSR*, **10**, 1561–1570.
Zieger, S., A. V. Babanin, W. E. Rogers, and I. R. Young, 2015: Observation-based source terms in the third-generation wave model WAVEWATCH. *Ocean Modelling*, **96**, 2–25. doi:10.1016/j.ocemod.2015.07.014.
Zilitinkevitch, S. S. and D. V. Chalikov, 1968: Determinint the universal wind-velocity and temperature profiles in the atmospheric boundary layer. *Izv. Atmos. Ocean. Phys.*, **4**, 394–302.
Zopf, D. O., H. C. Creech, and W. H. Quinn, 1976: The wavemeter: a land-based system for measuring nearshore ocean waves. *Mar. Tech. Soc. Journal*, **10**, 19–25.
Zou, Q., 2004: A simple model for random wave bottom friction and dissipation. *J. Phys. Oceanogr.*, **34**, 1460–1467.